

GEOHERMAL PLAY-FAIRWAY ANALYSIS OF WASHINGTON STATE PROSPECTS: PHASE 2 TECHNICAL REPORT

by Corina Forson, Alexander Steely, Trenton Cladouhos,
Mike Swyer, Nicholas Davatzes, Megan Anderson,
Brent Ritzinger, Jonathan Glen, Jared Peacock,
William Schermerhorn, Erick Burns,
and Pete Stelling

December 2017



WASHINGTON STATE DEPARTMENT OF
NATURAL RESOURCES
WASHINGTON GEOLOGICAL SURVEY

This page is left intentionally blank.

Contents

Executive Summary	1
Introduction	1
Washington Geothermal Play Fairway	1
Summary of Phase 2 Activities	2
Updated Conceptual Models.....	2
Revised and New Modeling Methods.....	4
Method Description	4
Heat	6
Permeability	9
Fluid-filled Fractures.....	12
Infrastructure.....	13
Results of New Data Collection.....	15
Mount Baker Study Area	15
Mount St. Helens Study Area (North And South AOIs).....	16
Wind River Valley Study Area.....	19
Opportunistic Data Collection	20
Updated Phase 2 Favorability and Confidence Models	20
Definitions of Terms Used	20
Heat Potential.....	22
Permeability Potential.....	22
Fluid-filled Fractures.....	24
Combined Geothermal Model and Exploration ‘Risk’	24
Infrastructure.....	31
Proposed Validation Activities	31
Overview.....	31
Proposed Validation Activities.....	31
Method Re-evaluation and Improvement	36
Permitting Pathway and Known Constraints	36
Phase 3 Timeline.....	38
References.....	38
Appendix A. Intermediate Favorability and Confidence Results.....	41
Appendix B. Updated Phase 2 Fault Models	62
Appendix C. Results of MT Surveys	63
Mount Baker Study Area	63
Mount St. Helens Northern Study Area	97
Mount St. Helens Southern Study Area	135
Appendix D. Results of Passive-Seismic Surveys.....	163
Appendix E. Results of Potential-Field Surveys.....	176
Appendix F. Results of Electrical Resistivity Surveys.....	206
Appendix G. Results From New Geologic Mapping.....	210
Appendix H. Results From New Geochronology	215
Appendix I. Favorability Model Results at 2-km Depth.....	219
Appendix J. Confidence Model Results	221
Appendix K. Letters of Support.....	224

FIGURES

Figure 1. Locations of study areas in Washington State.	1
Figure 2. Updated conceptual models	3
Figure 3. Phase 2 heat potential and change in confidence from Phase 1	21
Figure 4. Phase 2 permeability potential at 200 m depth and change in confidence.....	23
Figure 5. Phase 2 fluid-filled fracture potential at 200 m depth and overview of confidence	25
Figure 6. Phase 2 Combined favorability models at 200 m depth with overview of confidence ...	26
Figure 7. Phase 2 Combined favorability models at 2 km depth with overview of confidence.....	27
Figure 8. Exploration ‘risk’ models for all three study areas at 200 m depth.....	28
Figure 9. Exploration ‘risk’ models for all three study areas at 2 km depth.....	29
Figure 10. Correlation between combined model favorability and measured temperature gradients in all three study areas.....	29
Figure 11. Infrastructure favorability for all three study areas.....	30
Figure 12. Proposed temperature-gradient holes (TGH) and exploration risk.	32
Figure 13. Proposed temperature-gradient holes (TGH) and infrastructure favorability.....	33
Figure 14. Timeline for conclusion of Phase 2 and proposed validation activities.....	38

TABLES

Table 1. Summary of proposed, funded, and completed activities.	2
Table 2. Relevant GIS parameters for data processing.....	4
Table 3. Major data types, processing steps, and software used.....	4
Table 4. <i>ArcGIS 10.4</i> IDW (Geostatistical Analyst) parameters.	5
Table 5. <i>QGIS</i> Grid (Nearest neighbor) and Interpolate (Cubic spline) parameters.	5
Table 6. <i>QGIS</i> kernel density estimation parameters.	5
Table 7. Typical <i>MATLAB</i> commands for scaling and transforming rasters	6
Table 8. Summary of model favorability layers and extents.	7
Table 9. Heat model favorability parameters.....	8
Table 10. Goodness-of-fit and layer weighting example	8
Table 11. Heat model confidence parameters.	9
Table 12. Poisson’s ratio and Young’s modulus for <i>Poly3D</i> models.....	10
Table 13. Permeability model favorability parameters.....	10
Table 14. Permeability model confidence parameters.	11
Table 15. Fluid-filled fracture model favorability parameters.	12
Table 16. Fluid-filled fracture model confidence parameters.....	13
Table 17. Infrastructure favorability parameters.....	14
Table 18. Summary of final model weights for each study area.....	24
Table 19. Favorability ranking for proposed drill sites and comparison to nearby hot springs and temperature-gradient results.	34
Table 20. Validation metrics for four aspects of temperature-gradient holes.	34
Table 21. Core-analysis activities and goals.	35
Table 22. Structural assessment activities and goals.....	35
Table 23. Proposed drill sites, land status, permitting information, and other logistics.	37

Geothermal Play-Fairway Analysis of Washington State Prospects: Phase 2 Technical Report

by Corina Forson¹, Alexander Steely¹, Trenton Cladouhos², Mike Swyer², Nicholas Davatzes³, Megan Anderson⁴, Brent Ritzinger⁵, Jonathan Glen⁵, Jared Peacock⁵, William Schermerhorn⁶, Erick Burns⁷, and Pete Stelling⁶

¹ Washington Geological Survey
Department of Natural Resources
MS 47007
Olympia, WA 98504-7007

² AltaRock Energy, Inc.
4010 Stone Way North
Suite 400
Seattle, WA 98103

³ Temple University
1901 N. 13th St
Philadelphia, PA 19122

⁴ Colorado College
14 E. Cache La Poudre St
Colorado Springs, CO 80903

⁵ US Geological Survey
MS 989
345 Middlefield Road
Menlo Park, CA 94025

⁶ Western Washington University
MS 9080
516 High St
Bellingham, WA 98225

⁷ US Geological Survey
Oregon Water Science Ctr
2130 SW 5th Ave
Portland, OR 97201

EXECUTIVE SUMMARY

An investment of \$0.7M from the Geothermal Technology Office for Phase 2 of Play Fairway Analysis in Washington State improved existing favorability models and increased model confidence. New 1:24,000-scale geological mapping, 15 detailed geophysical surveys, 2 passive seismic surveys, and geochronology collected during this phase were coupled with updated and detailed structural modeling and have significantly improved the conceptual models of three potential blind geothermal systems/plays in Washington State, the St. Helens Shear Zone, Mount Baker, and Wind River Valley. Results of this analysis reveal the presence of commercially viable undiscovered geothermal resources in all three study areas. The analysis additionally provides a clear definition of the geothermal prospects in terms of the essential elements of a functioning geothermal system, the confidence in these assessments, and associated potential and risk of development.

This report also includes a proposal to validate the modeling results in highly favorable areas for two main reasons: (1) to develop confidence in the modeling approach that will encourage future development of geothermal resources in Washington State inside and outside of the Phase 2 study areas, and (2) to provide actionable results to the DOE, existing industry partners, newly identified developers, and other renewable-energy stakeholders. The proposed validation activities aim to collect new data that will further the understanding of geothermal resource potential in Washington, as well as substantiate the favorability, confidence, and risk models developed in Phases 1 and 2.

INTRODUCTION

Washington Geothermal Play Fairway

The Washington State Geothermal Play is conceptually simple; heat is provided by the injection of magma at shallow crustal levels along the active Cascade volcanic arc and permeability is provided by an extensive network of steep active faults that can effectively transfer heat from deeper sources to reservoirs near the surface. Abundant seismicity, Quaternary crustal shortening between Oregon and Canada (Stanley and others, 1996; McCaffrey and others, 2007), and Holocene fault ruptures (for example, Bucknam and others, 1992; Personius and others, 2014) provide evidence of active tectonics. Hot springs and fumaroles exist around some of the volcanic centers in the state, but the extreme precipitation—over 3 m/yr along much of the Cascade Range—and dense vegetation has likely suppressed the surface expression of geothermal systems in many areas.

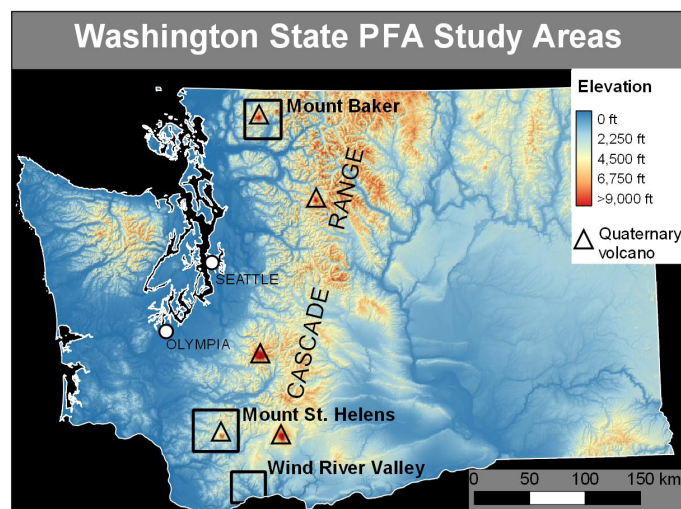


Figure 1. Locations of Play Fairway Analysis (PFA) study areas in Washington State.

Three areas were selected for further study in Phase 1 (Fig. 1) based on the results of a statewide geothermal assessment (Boschmann and others, 2014): the Mount Baker region (MB), the areas north and south of Mount St. Helens (MSH-N and MSH-S) within the St. Helens shear zone (SHSZ), and the Wind River Valley (WRV). The updated conceptual models for each of these areas (Fig. 2) provide context for the datasets and favorability models that follow. Common to each conceptual model are the defining characteristics of a geothermal system: a source of heat, a pathway for heat movement—typically aided by channeled fluid flow along portions of active faults, and a shallow, accessible heat reservoir kinematically maintained within an active fracture network. This whole-system approach promotes the effective transfer of knowledge between similar plays while still allowing for individual differences based on local conditions.

The goal of the Play Fairway Analysis (PFA) in Washington has been to develop a method that effectively identifies favorable regions of enhanced permeability near viable heat sources with the intention of supporting commercial exploration and development of the region. Washington State has a mandate to source 15 percent of its energy portfolio from renewable sources by 2020; the state's largest source of energy is currently hydro-electric which does not qualify as 'renewable' by the Energy Independence Act (I-937).

Summary of Phase 2 Activities

DATA COLLECTION

To support the aims of the Geothermal Technology Center during Phase 2 of Play Fairway Analysis, nearly \$1M in geophysical and geological data collection was proposed. All funded activities (Table 1) were completed on time, within scope, and on or under budget. Additionally, this project benefited from activities performed beyond the scope of work (geophysical modeling of 2D cross sections and lidar acquisition) at no cost. Major relevant findings are presented in the following sections.

REVISED FAVORABILITY AND CONFIDENCE MODELING METHODS

A revision of the Phase 1 methods was required to effectively incorporate the data collected during Phase 2. These improvements focused on the development of a more robust method to evaluate model confidence, characterize potential heat sources, and evaluate the likelihood of encountering fluid-filled fractures at depth. Two new models were developed: a fluid-filled fracture potential model—which is incorporated into the final geothermal model, and an infrastructure model that systematically addresses issues related to the viability of siting, permitting, and drilling. A description of these improvements is provided in the sections below.

UPDATED MODEL WEIGHTS USING THE ANALYTICAL HIERARCHY PROCESS

The weights of individual layers within a model—and the contribution of each model to the final geothermal potential—are calculated using a consensus-based expert opinion

Table 1. Summary of proposed, funded, and completed activities. Solid circles indicate requested, funded, and completed; hollow circles indicate requested but not funded; plus signs indicate activities completed at no cost to the project; dashes indicate not requested.

Method	Mount Baker (MB)	North of Mount St. Helens (MSH-N)	South of Mount St. Helens (MSH-S)	Wind River Valley (WRV)
1:24,000-scale geologic mapping	●	●	○	Compl. 2014
Lidar collection (opportunistic) and interpretation	+	+	+	+
Magneto-telluric survey (MT)	●	●	●	---
Passive seismic surveys	---	●	○	---
Ground-based gravity survey	●	●	●	●
Ground-based magnetic survey	●	●	●	●
2D modeled cross sections using geology and potential fields	+	+	+	+
Aeromagnetic survey	---	---	---	○
Geochronology	---	●	---	●
Electrical resistivity survey	●	●	○	Compl. 2014
Temperature-gradient well	○	---	---	---

approach known as the Analytical Hierarchy Process (AHP) (Saaty, 2008; Goepel, 2013). The AHP is implemented as an Excel spreadsheet and helps groups make complex decisions by having each participant rank input layers as a series of pairwise comparisons with weights that determine the strength of the comparison. The spreadsheet informs the participants how consistent their choices and weights are. Ultimately, layer weights are tabulated and calculated based on the input from all participants. For Phase 2 there were 8 to 10 participants consisting of two geologists from the Washington Geological Survey (WGS), two geologists from AltaRock Energy, four geologists and geophysicists from the U.S. Geological Survey (USGS), two geologists from academic institutions, and one hydrologist from the USGS.

Updated Conceptual Models

MOUNT BAKER STUDY AREA

The updated conceptual model (Fig. 2) of the Mount Baker geothermal play remains speculative with regards to the pathway from the likely heat source (young intrusives or deeper magma below Mount Baker). Volcanic activity at Mount Baker, most recently in 1975, can be responsible for extremely high heat flux below the volcano. Crider and others (2011) calculated that the heat-flux density in the crater increased from an already high 10 W/m² to 180 W/m² in 1975. This thermal increase could theoretically have been supplied by a sphere

of magma 124 m in radius. Much better constrained by the new data is the structure(s) along which hot fluids upwell to the Baker Hot Springs and the nearby TGH with a measured gradient of up to 200 °C/km. Modeling based on ground-based gravity and magnetic data indicates that the structure trends south from the known upwelling locations, suggesting that a new temperature-gradient hole (TGH) drilled 1–2 km south would test this hypothesis, confirm the high heat flow previously measured, and provide an indication of the size of the geothermal resource.

MOUNT ST. HELENS STUDY AREAS

The updated conceptual model (Fig. 2) is customized to the northern area of interest (AOI) and is consistent with the new datasets collected there. The seismically active SHSZ occupies a structural position between two plutons within a north-northwest-trending gravity low. The gravity low is consistent with low-grade metamorphosed sedimentary and volcaniclastic rocks and are likely to be far weaker and more easily fractured than the adjacent intrusives. The abundant seismicity indicates that fractures within the SHSZ are critically stressed. High compressional to shear wave velocity (V_p/V_s) ratios and low magnetotelluric (MT) resistivity suggest the presence of fluids (the geothermal reservoir) within the SHSZ. Within

the AOI this reservoir (between the plutons) could potentially measure 3–4 km east to west and 8 km north to south. Lastly, geologic mapping indicates that a thick sequence of altered volcaniclastics and volcanic flows are found between the plutons and comprise the reservoir cap. The primary uncertainty within the conceptual model is the heat source. The volcanic edifice of MSH is 15 km south and linked by the SHSZ; however, this distance is near the outer limit for vent proximity and geothermal prospects based on a study in Indonesia (Carranza and others, 2008).

WIND RIVER VALLEY STUDY AREA

The conceptual model of Wind River (Fig. 2) features two sets of major faults (northwest striking and northeast striking) which intersect at near right angles above a young, as-yet undiscovered heat source. The new data confirms that the northeast-trending Shipherds fault zone does have a prominent geophysical signature, although not as significant as the northwest-striking Wind River fault which largely controls the drainage organization and topography within the AOI. The existence of a shallow intrusion is still speculative, yet seems required to explain the high heat flow indicated by multiple hot springs and temperature profiles observed from temperature-gradient holes.

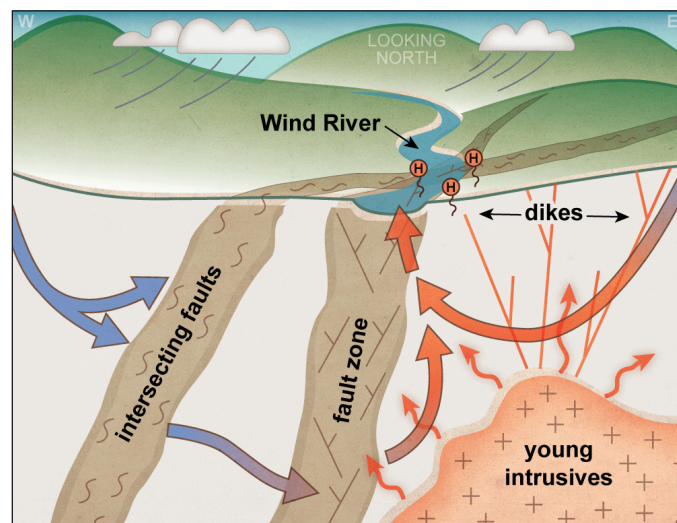
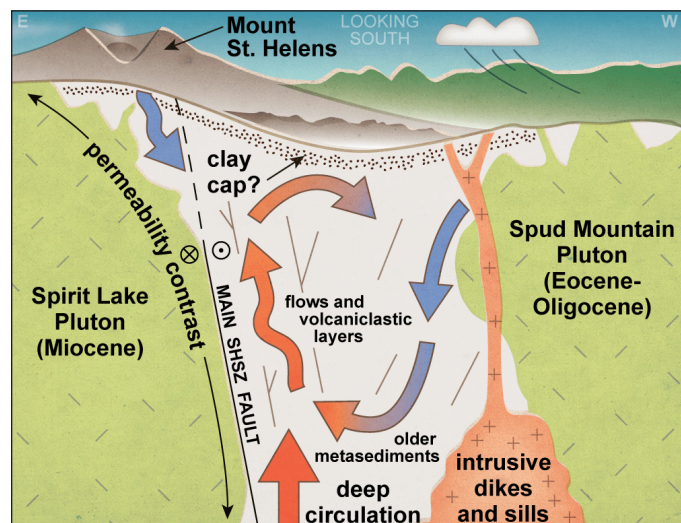
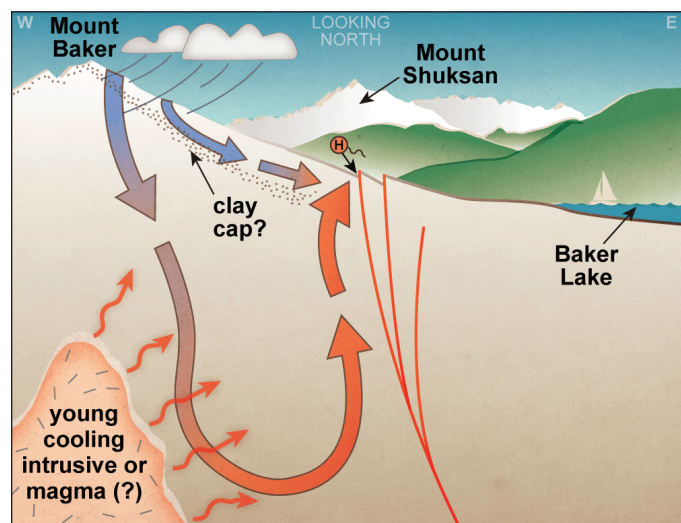


Figure 2. Updated conceptual models for Mount Baker (left), Mount St. Helens (below left), and Wind River Valley (below). Abundant Quaternary volcanism provides heat; active deformation along faults and fractures provides permeable pathways for the convection of geothermal fluids. Models are not to scale; viewing directions are provided in white at the top of each figure.

REVISED AND NEW MODELING METHODS

Method Description

OVERVIEW

Three main geothermal models were developed—heat, permeability, and fluid-filled-fractures—and each model is composed of several data layers. Through the modeling process, input data layers are transformed into scaled rasters that represent favorability and data confidence near the surface (200 m depth) and at a potential geothermal reservoir depth (2 km). This process involves four main steps: (1) initial raster creation from vector data or other observations; (2) scaling of intermediate rasters from initial values into a common 0–1 scale; (3) combination of intermediate rasters for each model using the AHP process to determine relative weighting between each layer; and (4) combination of each model into final favorability, confidence, and exploration risk models for each of the two depths. A fourth model—infrastructure potential—was also developed to assess restrictions on siting and permitting a geothermal well. A description of the major processing steps and relevant parameters is provided directly below. A description of the data layers for each model is also provided and includes scaling parameters and weighting schemes.

GIS PARAMETERS AND SOFTWARE

Unlike the Phase 1 modeling approach, rasters in Phase 2 were generated with a statewide extent. This was done to alleviate the need to impose artificial boundary conditions adjacent to the more-detailed study areas and to aid in expanding the analysis to the remainder of the state. All rasters were created with the same parameters, even if the data only covered a small portion of the area. This approach enabled raster scaling and combination to occur in *MATLAB* which was much more efficient than performing those processes within a GIS program. However, all processing steps can be accomplished within a GIS program.

All GIS processing was performed with the open-source software *QGIS* (version 2.18) with one exception (discussed below) where *ArcGIS 10.4* was used. Raster scaling and combination was accomplished in *MATLAB* (version 2016.b) with the *Image Processing* toolbox. Particular attention was paid

Table 2. Relevant GIS parameters for data processing.

Parameter	Value
Raster cell size	104.355 ft
Raster extent (xmin, xmax, ymin, ymax)	605034, 2551150, 81837, 1355594
Raster dimensions (x pixels, y pixels)	18649, 12206
Initial raster data type	32-bit floating-point (interpolation, regular grids, density) 16-bit unsigned integer (distance/proximity)
Intermediate and final raster data type	8-bit unsigned integer (0-255)
Projection	NAD83(HARN) Washington South (US ft) EPSG: 2907

to data representation. The >227 million cells of the statewide raster extent can consume a large amount of disk space if stored as 32-bit floating-point numbers (~880 mb/raster). Thus, all attempts were made to choose data types that could accurately represent the data with the minimum storage requirements. To this end, intermediate and final rasters use an 8-bit unsigned integer format (0–255) that are only 3–10 mb/raster. For these scaled rasters, a stored value of 255 is equivalent to the maximum favorability or confidence possible (value of 1) and a stored value of 0 is equivalent to the minimum favorability or confidence possible (value of 0). In this way the 0–1 scaling of each scaled raster can be contained within the most efficient data representation. Raster properties and GIS parameters are provided in Table 2.

INITIAL DATA PROCESSING AND RASTER CREATION

All data used in this project can be divided into one of six main categories (Table 3) based on how it relates to geothermal favorability or data confidence: (1) data where proximity to an observation is the most-relevant feature, such as distance to a volcanic vent; (2) data that represent irregular observation of a physical quantity that exists everywhere such as temperature-gradient wells; (3) data from a regular grid that

Table 3. Major data types, processing steps, and software used.

Initial data type	Example	Processing steps	Software and name of tool
Proximity to observation	Distance from volcanic vent	1. Rasterize observation 2. Calculate distance from observation	1. <i>QGIS</i> —Rasterize (Vector to raster) 2. <i>QGIS</i> —Proximity (Raster distance)
Irregular point observations of continuous physical quantity	Temperature gradient from wells	1. Interpolate continuous surface using weighted IDW (inverse-distance weighting)	1. <i>ArcGIS</i> —IDW (Geostatistical Analyst)
Regular point values of a model space	Passive-seismic inversion	1. Interpolate continuous surface over model space using node spacing 2. Interpolate to final grid resolution	1. <i>QGIS</i> —Grid (Nearest Neighbor) 2. <i>QGIS</i> —Interpolate (cubic spline)
Density and quality of observations	Density of fault observations	1. Use KDE (kernel-density estimation) to calculate spatial density of observations	1. <i>QGIS</i> —Kernel density estimation
Simple overlay	Land-use status	1. Rasterize observation	1. <i>QGIS</i> —Rasterize (Vector to raster)
Z-value raster	Elevation	No initial processing required	---

represent a constructed model of a physical quantity, such as a passive-seismic inversion; (4) data where the density and quality of observations are the most-salient features, such as the number of fault observations in an area; (5) data where a point of interest is either inside or outside of a boundary, such as land-use status; and (6) data that already exist as a raster with values, such as a digital elevation model. Within each of these categories data undergo a similar transformation from their original form into an unscaled initial raster and the general procedure is outlined below and summarized in Table 3.

Proximity to observations

Where proximity to an observation is the most-relevant feature a simple procedure is used to transform the original data into an unscaled initial raster. The original observations are rasterized in *QGIS* using the raster parameters in Table 2 and the Rasterize (Vector to raster) tool. The Proximity (Raster distance) tool uses the rasterized observations to produce a distance raster. This distance raster is the unscaled initial raster and generally uses a 16-bit unsigned integer data type (maximum value of 65,535). This maximum value corresponds to a ~20 km radius and was sufficient for most datasets. A 32-bit floating-point data type was used where greater distance was required.

Irregular point observations

Where the original data are irregularly spaced observations of a physical feature that varies continuously (or nearly continuously) across a large region—such as observations of subsurface temperature gradients—a weighted IDW (inverse-distance weighted) interpolation method is used (Table 3). This method interpolates a value at all points between the irregular observations based on two separate weights: the inverse of the distance to the observation (raised to a power of two), and the relative weighting of the observation itself. The inclusion of the observation weight is somewhat uncommon for IDW interpolation and ensures that data which are known to be less meaningful or reliable do not affect the interpolated results as much as data that are very meaningful and reliable. The IDW tool from the Geostatistical Analyst toolbox in *ArcGIS 10.4* was used for this processing because it has the ability to include observation weight. A similar Python-based tool could be written for *QGIS*, but was not undertaken for this project. The IDW tool provides the unscaled initial raster and uses a 32-bit floating-point data type. Processing parameters are provided in Table 4; weighting parameters are discussed further below.

Regular point observations

Several 3D models were developed during Phase 2 that provide values at points with regular spacing and these data were processed in two-steps (Table 3). The first step rasterizes the regular grid with each pixel centered on each observation point and sized according to the grid spacing (typically 300 to 1000 ft). The second step interpolates the coarse raster into the final model scale using a cubic spline interpolation technique. Processing parameters are provided in Table 5.

Table 4. *ArcGIS 10.4* IDW (Geostatistical Analyst) parameters.

Parameter	Value
Z value field	Varies by dataset
Output cell size	104.355 ft
Power	2
Search neighborhood	Standard with 10 minimum and 15 maximum neighbors
Weight field	Varies by dataset

Table 5. *QGIS* Grid (Nearest neighbor) and Interpolate (Cubic spline) parameters.

Processing Type	Parameter	Value
Grid (Nearest neighbor)	Z field	Varies by dataset
	Radius 1 and Radius 2	0 (searches all data)
	Angle	0
Interpolate (Cubic spline)	Attribute	Varies by dataset
	Minimal points	3
	Maximal points	20
	Points per square	5
	Tolerance	140
	Cell size	104.355 ft

Table 6. *QGIS* kernel density estimation parameters.

Parameter	Value
Weight	Varies by dataset
Radius	Varies by dataset
Kernel	Gaussian
Cell size	104.355 ft

Density of observations

For data types where the density and quality of observations are the most-salient feature a kernel density estimation is used to transform the original data into an unscaled initial raster. This process counts the number and weight of observations within a Gaussian-shaped window around each output raster point. The radius of the search window must be specified for each dataset and these values are provided and discussed individually below. General processing parameters are provided in Table 6.

Simple overlay

For data types where the most-salient feature is whether a point of interest falls inside of or outside of a boundary a simple rasterization process is used to transform the original data into a initial raster. This process typically creates a simple raster with discrete categories such as 0 or 1, where pixels within the boundary are a 1 and pixels outside of the boundary are 0.

Z-value rasters

Some data types are used that already exist as a 2D array of pixels with values, such as a raster of elevation or precipitation. No initial processing is required for these datasets.

INTERMEDIATE RASTER TRANSFORMATION AND SCALING

In order to combine the various types of geologic and geophysical data within the play fairway analysis, each initial raster is transformed into a scaled intermediate raster with values that range from 0 (no favorability or no confidence) to 1 (most favorable or most confident). The process is broadly similar for all rasters and follows 5 major steps: (1) set maximum (most favorable) value; (2) set minimum (least favorable) value; (3) divide by range of values; (4) combine individual components into a single layer (only for rasters that have individual outputs for each study area); and (5) each scaled (0–1) intermediate raster is then multiplied by 255 and converted to an 8-bit unsigned integer for efficient data storage. All transformation and scaling steps were performed in *MATLAB (2016.b)* with the help of the Image Processing toolbox to open and save GeoTiff files. Example commands are provided in Table 7; scaling values for each dataset are provided in tables further below.

RASTER COMBINATION

Scaled intermediate rasters are combined in *MATLAB* using relative weights determined using AHP. Each intermediate raster layer is multiplied by its AHP weight and added together. Separate results are made for favorability and confidence at both 200 m and 2 km depths for each model (heat, permeability, and fluid-filled-fractures). These model rasters are then combined into a single final favorability and confidence raster at both depths, also using relative weights from AHP. An exploration risk raster at both depths is created by multiplying the confidence and favorability rasters.

Heat

JUSTIFICATION OF IMPROVEMENTS

A critical element of predicting geothermal potential is derived from the Play-Fairway heat model. It is this component of

prediction that is most easily tested with temperature-gradient exploratory drilling. Because of this strong predictor/validation relationship the Phase 1 modeling approach was evaluated and updated. Based on other Play Fairway Analysis Phase 1 reports, and a more-extensive literature review, several key shortcomings of the Phase 1 model approach were identified and remedied, as summarized below. These changes required correlative updates to the confidence models. A detailed description of methods and intermediate data layers is provided below.

FAVORABILITY MODELING

Intermediate rasters are provided in Appendix A. A summary of each layer and its extent is provided in Table 8.

Model scope

The improved method models the entire state of Washington and clips the final results to each study area instead of modeling each study area individually. Such a step was made possible by the comprehensive geological databases developed by the Washington Geological Survey and removes the need to assign arbitrary boundary conditions at the edge of each study area. This approach also expedites modeling of the remainder of the state once Phase 3 validation results become available.

Continuous instead of discrete

A major refinement was initiated after reviewing how temperature observations (springs, wells, geothermometry) were integrated into the model. In Phase 1, each observation—such as a temperature-gradient well—was given a small ‘radius of influence’ on the order of a few hundred meters. Within this region, favorability could range from low to high depending on the value of the observation; outside of the small region the favorability was zero. This had two effects: (1) it gave the temperature-observation layers a ‘spotted’ appearance, and (2) it biased the favorability estimate by only having values very close to existing data. In effect, this approach made it impossible to predict values at distance from point observations.

An alternative approach adopted for Phase 2 was to model the three temperature observation layers as continuous fields of predicted values which are algorithmically determined from

Table 7. Typical *MATLAB* commands for scaling and transforming rasters where ‘data’ is a 2D array read from a GeoTiff file; ‘data_a’, ‘data_b’, ‘data_c’ are individual rasters that only contain data for a particular study area and need to be combined into a single data layer; ‘mask_a’, ‘mask_b’, ‘mask_c’ are binary or logical data layers that contain 1s where the corresponding data layer has meaningful values and 0s elsewhere.

Processing step	Sub task	Example script
1. Set maximum	Clip values above maximum	<code>data(data>max_value)=max_value;</code>
2. Set minimum	Clip values below minimum	<code>data(data<min_value)=min_value;</code>
3a. Scale to range (all rasters except proximity)	Set base value Divide by range	<code>data=data-min_value; scaled=data/(max_value-min_value);</code>
3b. Scale to range (proximity rasters)	Set base value and flip range Divide by range	<code>flipped=-(data-max_value); scaled=flipped/(max_value-min_value);</code>
4. Clip and combine parts into a single data layer	Combine data Combine mask Mask data Combine masked layers	<code>comb_data=cat(3, data_a, data_b, data_c); comb_mask=cat(3, mask_a, mask_b, mask_c); masked_data=comb_data.*comb_mask; final=max(masked_data,[],3);</code>
5. Scale and convert to 8-bit unsigned integer		<code>scaled=uint8(255*scaled);</code>

Table 8. Summary of model favorability layers and extents.

Input data layer	Brief description	Spatial extent
Heat		
Subsurface temperature observations	Temperature-gradient wells and wells with a bottom-hole temperature; weighted by quality	Statewide
Springs	All springs with a measured water temperature	Statewide
Quaternary volcanic vents	Proximity to vents; distance and weight vary by vent type and age	Statewide
Quaternary intrusive rocks	Proximity to young intrusive rock; weight varies by age	Statewide
Geothermometry	Estimates of reservoir temperature; weighted by quality	Statewide
Permeability		
Fault density	Defines areas where faults are closely spaced or intersecting	All study areas
Max. Coulomb shear stress	Defines regions where elevated shear stress (and fracturing) are likely	Model space in each study area
Dilation tendency	Defines faults and regions where dilational strain is likely	Model space in each study area
Seismic-event density	Defines map-view regions of seismicity; provides inference of active deformation	Statewide
Slip tendency	Defines fault segments likely to slip under current stress conditions	Model space in each study area
Slip gradient	Defines regions along faults where fracture density is high due to complex fault geometry (e.g. fault tips, intersections and accommodation zones)	Model space in each study area
Fluid-filled fractures		
Resistivity (MT)	High conductivity is interpreted as a region of fluid-filled fractures or conductive material	Model space at MB and MSH
V_p/V_s (passive seismic)	High ratios indicate fluid-filled fractures are likely	Model space at MSH-N
V_s (passive seismic ambient noise)	Areas of low shear velocity can indicate high temperature, high fluid porosity, and (or) rock composition.	Model space at MSH-N
Infrastructure		
Land-use restrictions and favorable areas	DNR-owned land and existing or proposed geothermal leases; off-limits areas mask the final model	Statewide
Availability of process water	Mean annual precipitation and proximity to perennial streams and lakes	Statewide
Proximity to viable transmission lines	Buffer of existing 115 kV or greater transmission lines	Statewide
Proximity to existing roads	Permitting and building new roads is difficult	Statewide
Distance from urban centers	Accounts for possible societal effects of induced seismicity	Statewide
Elevation restrictions	Increasing restriction above 4,500 ft due to snow	Statewide

available observations. In this way, for example, the temperature of a well at any location can be predicted instead of biasing the favorability toward existing data. This change required a robust approach to interpolation and attention to data quality for each observation guiding the interpretation. To this end the nonparametric inverse-distance weighting (IDW) method was employed with the added ability to weight each observation based on a set of quality criteria. For each layer the weighting and scaling strategy is outlined below.

Layer weights and scaling

Each input layer has different data-quality parameters or uncertainty metrics that are used to weight their influence on the prediction and are discussed in the section below. Table 9 indicates the scaling used to convert the data from measured values to a common 0–1 rank that can then be combined according to weights determined by AHP for each data type.

Subsurface temperature observations (wells)—The weighting scheme from Phase 1 was modified to retain the well type and well depth ranking so that deep temperature-gradient wells are weighted more heavily than shallow wells with only a bottom-hole temperature (Table 9). The ranking by number

of temperature measurements was moved into the confidence model.

Springs—No weighting was performed on these data in either Phase 1 or Phase 2.

Geothermometry—No weighting of these data was performed in Phase 1, yet there are clear quality indicators which affect observation validity and should be considered. A weighting scheme was developed that uses charge balance, vintage of analysis (average for repeat surveys), and internal consistency between thermometer systems. Each of these rankings was then weighted and combined to determine the overall rank for the observation.

Quaternary volcanic vents—In Phase 1, this layer employed a variable-distance buffer around different volcanic vent types. For Phase 2 the buffer size was improved to better capture the correlation between vent proximity and cumulative geothermal prospects in a similar volcanic-arc play (Indonesia) where ~85 percent of prospects are within 8 km of a stratovolcano and 95 percent are within ~16 km (Carranza and others, 2008). This data was used to set a favorability window around stratovolcanoes of 100 percent up to 8 km that decreases

Table 9. Heat model favorability data layers with processing types, weighting and scaling parameters, and AHP weights.

Data layer	Initial raster processing type	Initial raster weighting criteria	Initial raster weighting value	Intermediate raster scaling criteria	Intermediate raster scaling value	AHP favorability weights
Subsurface temperature observations	Irregular points	<u>Well type</u>				
		TGH (>250 m deep)	1			
		TGH (50–250 m deep)	0.85	<10°C/km	0	0.304
		TGH (<50 m deep)	0.7	>60°C/km	1	
Bottom-hole temp. only (any depth)	0.1					
Springs	Irregular points	No weighting	---	<10°C >50°C	0 1	0.229
Quaternary volcanic vents	Proximity	<u>Vent type</u>	<u>Buffer/limit</u>	<u>Feature age</u>		
		Stratovolcanos	8/16 km	<160 ka	1	0.201
		Calderas, domes, plugs	5/10 km	160–780 ka	0.75	
		Minor vents and cones	2.5/5 km	780–2,500 ka	0.5	
Quaternary intrusive rocks	Proximity	No weighting	---	>10 km <5 km	0 1	0.139
Geothermometry	Irregular points	<u>Charge balance</u>				
		<3%	0.5			
		>12%	0			
		<u>Inter-method discrepancy</u>				
		<15°C	0.25	<20°C	0	0.128
		>100°C	0.05	>100°C	1	
<u>Year of analysis</u>						
>2000	0.25					
<1975	0.05					

linearly to 0 percent at 16 km. Smaller buffers (with identical ratios) are used for the remaining types of volcanic vents.

Phase 1 also employed a tiered age/composition ranking for volcanic vents that created a 14x range in favorability between the most and least favorable combination with little statistical basis for such an extreme range. Although there is a common perception in the geothermal community that high magma viscosity is a strong predictor of stored shallow crustal volcanogenic heat, a robust global statistical analysis from the Alaska Phase 1 Play Fairway Analysis does not support such a relationship. On this basis, the 14x range in favorability from the Phase 1 method seems unsupported by available data and the composition ranking was completely removed. The remaining ranking is based entirely on age and distance from a heat source (Table 9). In this ranking scheme a value of 1 indicates close proximity (2.5 to 8 km, depending on vent type) to a late Quaternary volcanic vent.

Individual shapefile vector buffers are created around each mapped volcanic vent in the state for each vent type and age category (9 separate buffers) at the 100% value distance. These buffers are rasterized and a distance raster is

then calculated. The distance raster is scaled according to the maximum distance for each vent type. The result is 9 scaled (0–1) rasters—where a value of 1 represents the 100%-value buffer and a value of 0 represents all areas beyond the maximum buffer. Each raster is multiplied by its age weighting and summed. Two types of overlapping buffers are possible within this schema: overlaps between different categories (for example, a minor vent next to a caldera) and overlaps within a category (for example, several minor vents in close proximity). A merged buffer was created for within-category overlaps and overlaps between categories were treated as additive with a value ceiling of 1.

Quaternary intrusive rocks—No substantive changes were implemented to this layer for Phase 2 processing. Mapped outcrops of Quaternary intrusive rocks from the seamless 1:100,000-scale digital geologic map of Washington (Wdger, 2016) were rasterized and a distance raster was created from those results. A 100-percent-value buffer was created at 5 km with a linear ramp to 0-percent-value at 10 km, similar to the calderas, domes, and plugs category within the volcanic vent data.

Table 10. Confidence weights for subsurface temperature observation layer use the goodness-of-fit multiplied by the observation weight.

		GOF (complement of relative misfit)		
		perfect match between model and observation	1	0.75
Observation weight	1	1	0.75	0.5
	0.75	0.75	0.5625	0.375
	0.5	0.5	0.375	0.25
	0.25	0.25	0.1875	0.125

CONFIDENCE MODELING

Intermediate rasters are provided in Appendix A.

Observations of temperature (TGH, springs, and geothermometry)

In Phase 1, the confidence modeling focused entirely on observation uncertainty (accuracy of results and location accuracy). This approach was satisfactory because observations were modeled as discrete points with buffers instead of a continuous predictive surface. Two additional components of confidence modeling were introduced in Phase 2: (1) the misfit between input observations and the predictive surface, and (2) the

proximity to the nearest observation (which replaces the Phase 1 observation buffer). The final result is a continuous estimate of confidence that accounts for the map-view distribution of observations, their individual uncertainty or weighting, and the ability of the predictive model to fit the observations.

The model misfit is characterized at each original data point using a goodness-of-fit function that is the complement of the relative misfit: $GOF = |1 - ((O - P) / P)|$ where O is the observed value and P is the predicted value from the interpolated surface. The GOF value is multiplied by the weighting scheme used for initial data transformation (discussed above) to arrive at an intermediate confidence value. This intermediate value characterizes both the model misfit and the original observation weight. Table 10 shows the subsurface temperature observation layer as an example.

To account for the uneven map-view distribution of observations a Gaussian kernel density estimation (KDE) technique with a 5-km radius was employed. Conceptually, this approach treats areas with abundant observations as better-known (more confident) than areas with fewer or no observations. The effect of variable observation confidence (model misfit and observation weight) is accommodated by weighting the KDE by the intermediate confidence value. The resulting KDE raster is scaled so that a value of 1 represents at least one best-quality data point per kernel area (~20 km² for a 5 km radius); a scaled value of 0 represents no data observations.

Observations from geologic maps (vents and intrusive rocks)

The Phase 1 method considered the number and quality of mapped-vent citations and whether the vent had associated geochronology. An example highlights the need for improvement—using the Phase 1 method, new 1:24,000-scale geologic mapping that identified a volcanic vent and used nearby well-dated stratigraphy to constrain its relative age to 10–40 ka would have been ranked a 1 (out of 5), whereas a vent mapped in the 1950s and then compiled at a 1:100,000 scale in the 1970s would be ranked a 5. This approach does not adequately reflect the information most valuable to assessing confidence, namely:

(1) how certain is a mapped feature and its age assignment, and (2) how certain is the absence of a mapped feature (does it reflect an actual absence of the feature or a cursory mapping campaign).

In Phase 2 the modeling was revised to include the scale and vintage of mapping and the proximity to available geochronology (Table 11). The scale of mapping is likely to be a better predictor of mapping quality than the number of sources for a particular feature because it also addresses the issue of certainty in what was not observed. The vintage of mapping is a justified addition because the advent of DEMs in the early 2000s and abundant lidar in the 2010s has greatly aided in identification and characterization of young volcanic features. Density of geochronology is a better predictor of vent-age confidence because it acknowledges that meaningful constraints on the age of a feature can be found in understanding the regional or sub-regional stratigraphy. To these ends, the extent of the best-available mapping in the study areas is weighted for scale of mapping and vintage and combined with a 2.5-km-radius KDE of post-latest Miocene geochronology that could be useful in determining the age of Plio-Pleistocene volcanic and intrusive rocks. These three separate datasets provide confidence estimates for both volcanic vents and intrusive rocks. Because of this, the AHP values for vents (0.201) and intrusive rocks (0.139) were combined and distributed to the three confidence datasets of mapping scale (30%), mapping vintage (30%), and geochronology (40%).

Permeability

JUSTIFICATION OF IMPROVEMENTS

A substantial portion of Phase 2 activities were aimed at improving fault geometry and subsurface characterization; five main changes were implemented in the favorability modeling to highlight these improvements: (1) updated material properties; (2) addition of seismicity and fault density layers; (3) removal of four low-weight Phase 1 layers; (4) refined high-resolution boundary-element stress/strain modeling using the program *Poly3D*; and (5) updated study-area-wide

Table 11. Heat model confidence data layers with processing types, weighting and scaling parameters, and AHP weights.

Data layer	Raster processing type	Weighting criteria	Weighting value	AHP confidence weights	
Subsurface temperature observations	KDE (5 km radius)	Same as favorability (Table 9)	Weighting x GOF	0.304	
Springs	KDE (5 km radius)	Same as favorability (Table 9)	Weighting x GOF	0.229	
Quaternary volcanic vents and intrusive rocks	Overlays of age and scale of mapping	<u>Age of mapping (30%)</u>		0.102	
		Since 2010	1.0		
		2000–2010	0.9		
			Before 2000	0.8	
			<u>Scale of mapping (30%)</u>		0.102
			1:24,000 or better	1.0	
			1:24,000–1:100,000	0.9	
		1:100,000	0.8		
	KDE of geochronology (2.5 km radius)		<u>Age (40%)</u>	0.136	
			<160 ka	1.0	
			160–780 ka	0.75	
			780–2,500 ka	0.5	
			2.5–23 Ma	Ramp from 0.25–0	
Geothermometry	KDE (5 km radius)	Same as favorability (Table 9)	Weighting x GOF	0.128	

slip and dilation tendency modeling. Additional changes to the confidence modeling were required to adequately assess improvements gained through the collection of new data.

FAVORABILITY MODELING

Intermediate rasters for each layer are provided in Appendix A. Material properties in the *Poly3D* model (Poisson's ratio and Young's modulus) were updated using a combination of geophysical observations in the study areas and lithology-specific values from literature (Table 12); these values were assumed to be invariant during Phase 1 modeling. Values of Poisson's ratio (ν) were constrained at MSH-N from the V_p/V_s ratio determined from earthquake passive-seismic tomography using the equation:

$$\nu = \frac{1(V_p/V_s)^2 - 2}{2(V_p/V_s)^2 - 1}$$

Values of V_p/V_s were averaged in the northwest-trending region between the Spirit Lake and Spud Mountain plutons from 0 to 2 km depths for use in this calculation; a Young's modulus was chosen that was appropriate for Neogene marine sediments and volcanics (Waite and Moran, 2009; Zhu, 2012). Values from representative lithologies for the other study areas (Schultz, 1993; Tabor and others, 2003; Zhu, 2012) were chosen and used in the modeling.

Seismic-event density and fault density were added as model inputs using a KDE (Table 13). Seismicity was implicitly considered in some study areas during Phase 1 by informing the modeled fault geometries; its addition in Phase 2 provides a mechanism to explicitly include it. The 5-km-radius

Table 12. Poisson's ratio and Young's modulus for *Poly3D* models.

Study area	Poisson's ratio	Young's modulus (GPa)	Dominant modeled lithology
Mount Baker	0.21	20	Cretaceous argillite
Mount St. Helens	0.3	20	Neogene volcanics
Wind River Valley	0.25	57	Neogene basalt

density kernel is scaled so that a value of 0 represents regions with <1 event/km² and a value of 1 shows regions with >4 events/km². These values were selected because they highlight regions with abundant seismicity and show prominent linear trends associated with major known active fault zones (Appendix A).

The addition of a fault-density layer is conceptually justified by the idea that permeability will generally be higher where there are closely spaced or intersecting faults (Curewitz and Karson, 1997). The new surface mapping and lidar interpretation—coupled with subsurface characterization of fault geometries—provided updated fault maps at each study area (at the 200 m and 2 km depths) which were used for the calculation (Appendix B). Each fault segment was converted to points with ~30-m spacing; a Gaussian kernel density estimator with 500-m radius was used and the results were scaled so that a value of 0 means no nearby fault, 0.5 is a single fault strand, and a value of 1 indicates at least two faults in very close proximity or intersecting. The radius of influence (500 m) is a favorable interpretation of the upper limit of increased fracture density from a moderate-size fault (Johri, 2012).

Table 13. Permeability model favorability data layers with processing types, weighting and scaling parameters, and AHP weights.

Data layer	Initial raster processing type	Initial raster weighting criteria	Initial raster weighting value	Intermediate raster scaling criteria	Intermediate raster scaling value	AHP favorability weights
Fault density	KDE (0.5 km radius)	No weighting	---	0 faults 1 fault 2 closely spaced or intersecting faults	0 0.5 1.0	0.33
Maximum Coulomb shear stress (<i>Poly3D</i> model)	Regular points (100 m model spacing)	No weighting	---	Model min. value Model max. value	0 1	0.187
Dilation tendency (<i>Poly3D</i> model)	Regular points (100 m model spacing)	No weighting	---	Model min. value Model max. value	0 1	0.142 (maximum value of 2D and 3D layers)
Dilation tendency (2D model)	Proximity (0.25 km radius)	No weighting	---	Model min. value Model max. value	0 1	
Seismic-event density	KDE (5 km radius)	No weighting	---	<1 event/km ² >4 events/km ²	0 1	0.138
Slip tendency (<i>Poly3D</i> model)	Regular points (100 m model spacing)	No weighting	---	Model min. value Model max. value	0 1	0.113 (maximum value of 2D and 3D layers)
Slip tendency (2D model)	Proximity (0.25 km radius)	No weighting	---	Model min. value Model max. value	0 1	
Slip gradient (<i>Poly3D</i> model)	Regular points (100 m model spacing)	No weighting	---	Model min. value Model max. value	0 1	0.091

Several Phase 1 model inputs were not considered in the Phase 2 model: fault displacement distribution, tensile fracture density, regional-scale maximum shear strain rate, and surface dilational strain rate. All four inputs were weighted low in Phase 1; the first two largely duplicate other model outputs and the last two did not provide much discrimination power either between study areas or within them. The goal of this change was to reduce model complexity while retaining enough information to assess and predict the variations in normal traction on fault surfaces as a result of regional strain and local stress perturbations along major faults.

A focused *Poly3D* model area was selected at each of the AOIs and run with a significantly higher resolution using a simplified version of the updated fault models. Refined model areas were chosen to overlap the regions of new data collection; node spacing was improved from 305 m to 100 m in order to capture the finer-scale fault structures elucidated during Phase 2 field activities. *Poly3D* is a boundary-element model that characterizes both on- and off-fault deformation resulting from sub-regional strain and from slip along large-scale active structures (Thomas, 1993). Major structures are used to ‘drive’ the stress/strain field and the smaller-scale structures ‘respond’ to the imposed conditions. Major structures were selected from the updated fault model using at least two of the following criteria: collocation of seismic events on fault planes, collocation of faults with appropriately oriented focal mechanisms, collocation of faults with major potential-field boundaries (gravity, MT, seismic velocities), and collocation of faults with abundant field evidence of activity (lidar lineaments along well-mapped and observed faults). A detailed discussion of the *Poly3D* modeling assumptions and methods is available in the Phase 1 report. Separate models were run for five detailed areas (one at MB, two at MSH, and two at WRV); the resulting model

values were normalized to the maximum and minimum values for each individual modeled area.

In addition to the detailed 3D modeling, a 2D slip and dilation tendency model was run for all mapped faults in the study areas. Typical *Poly3D* software applications preclude its use on high-resolution faults/fractures mapped at the surface at scales appropriate for an entire study area, but provide vital insight in how large faults and volcanic deformation centers that cause crustal deformation at the surface and at depth play a role in reservoir permeability. The addition of the computationally simpler slip and dilation tendency allow refinement of the permeability potential outside of the detailed 3D modeling areas. The 2D slip and dilation tendency model results produced scaled favorability for each fault segment; each segment was then buffered with its corresponding favorability value to a distance of 250 m based on the extent of simulated damage zone caused by faults and fault intersections in the *Poly3D* models. Combined layers for slip and dilation tendency were created by finding the maximum value at each pixel between the 3D and 2D models.

CONFIDENCE MODELING

Intermediate rasters for each layer are provided in Appendix A. The collection of six new datasets during Phase 2 (and the addition of existing aeromagnetic data) was a challenge to the Phase 1 uncertainty model which was built to only consider the two datasets that were used at that time. The new data have greatly clarified the location and geometry of faults and the likely permeable pathways; thus a revised confidence model was developed to document the reduction in uncertainty. Because the permeability modeling requires two main inputs—stress/strain boundary conditions and fault geometry—and only fault geometry was substantially modified during Phase 2, the

Table 14. Permeability model confidence data layers with processing types, weighting and scaling parameters, and AHP weights.

Data layer	Raster processing type	Weighting criteria	Weighting value	AHP Phase 2 confidence weights		
				MB	MSH	WRV
Mapped faults	Proximity (0.25 km limit)	Certain	1	0.05	0.175	0.15
		Approximate	0.75			
		Inferred	0.5			
		Concealed	0.25			
		Queried	0.10			
Fault observations	KDE (0.25 km radius)	0 obs/km ²	0	0.05	0.175	0.15
		>1 obs/km ²	1			
Seismicity	KDE (5 km radius)	<1 event/km ²	0	0.05	0.2	0.07
		>4 events/km ²	1			
Gravity surveys	<u>Near surface interpretation</u> KDE (0.5 km radius)	<u>Near surface</u> <0.7 station/km ²	0	0.13	0.15	0.26
	<u>1–3 km depth interpretation</u> KDE (2.5 km radius)	<u>>5 station/km²</u> <u>1–3 km depth</u> 0 stations/km ²	0.5			
		1 station/km ²	0.5			
Magnetic surveys (aeromag and ground-based)	Proximity (0.5 km limit)	No weighting	---	0.33	0.08	0.1
2D modeled cross sections	Proximity (1.5 km limit)	No weighting	---	0.16	0.1	0.1
Lidar lineaments	Proximity (0.25 km limit)	No weighting	---	0.22	0.15	0.17

confidence model focuses on these changes. Additionally, the tensor algebra used in the modeling ensures that confidence is transitive; that is, an increase in confidence of an input parameter also increases the confidence of the model results.

One of the advantages of this method is that it provides a mechanism to vary the weighting of a particular dataset within a more general framework. For example, seismicity was much less influential in constraining fault geometry in the Wind River Valley than at Mount St. Helens, and ground-based magnetic surveys were only available at Mount Baker (Table 14). Because of these differences, separate AHP values were calculated for each study area.

Layer weights and scaling

Mapped faults and fault observations—Conceptually, confidence is high where mapped faults are certain and there are abundant observations of fault kinematics or orientation. A layer was created that combines proximity to mapped faults (weighted by type) and density of fault observations. All mapped faults in the state at 1:24,000 and 1:100,000 scales were combined and duplicate structures removed. Faults were classified according to Table 14 and rasterized separately for each type. A proximity raster was created for each fault type from the rasterized data and these were scaled using a distance of 250 m. The separate rasters were combined by finding the maximum value at each pixel. Fault observations from 1:24,000- and 1:100,000-scale mapping were combined and duplicate observations removed. A KDE of the resulting unweighted observations was created and scaled according to Table 14.

Seismicity—A high density of seismic events can be used to delineate the geometry of active faults in the subsurface, such as along the SHSZ. Fault geometries at depth in regions that lack a large number of events are more uncertain. A layer of seismic event density was developed using the entire catalogue of relocated seismicity in Washington from Czajkowski and Bowman (2014). The layer was scaled so that <1 event/km² was a confidence value of 0, and >4 events/km² was a confidence value of 1.

Gravity and Magnetics—Regions with high station density or flight lines have tighter constraints on the shape and character of the potential field than areas with sparse

coverage. For gravity-field surveys, two station density maps were combined into a single confidence layer: one with a short radius to highlight areas with good near-surface constraints (0–1 km depth) and another with a larger radius to show areas with good resolving power at 1–3 km depths (Table 14); these were combined equally. For magnetic-field surveys a single confidence layer was constructed using the proximity to either aeromagnetic flight lines or ground-based magnetic survey lines, whichever was closest. This approach does not explicitly account for the direction of the flight lines relative to the potential-field gradient—structures perpendicular to flight lines are better constrained than those that are parallel.

Modeled cross sections—A major component of Phase 2 activities was the development of 10 potential-field-constrained 2D cross-sections. Hand samples were collected from all major lithologies in the study areas and magnetic susceptibility and density were measured. Each cross section uses available geologic mapping and models the expected gravity and magnetic field at the surface and compares with the observed values. In this way the cross sections can be iteratively refined to develop a subsurface interpretation that is geologically based and produces a close fit between the predicted and observed potential fields. A confidence layer was developed using the proximity (<1.5 km) to these cross section lines (Table 14).

Lidar—The opportunistic collection of lidar at all study areas is a huge benefit for Phase 2 activities: it was used to identify potentially active faults at all three study areas and served as a base map for new 1:24,000-scale mapping at MSH. Many of the newly identified lineaments are collocated with mapped faults, fault observations, steep potential-field gradients, boundaries in the MT data, and bands of seismicity. A simple confidence layer was developed using proximity (<250 m) to mapped lidar lineaments (Table 14).

Fluid-filled Fractures

JUSTIFICATION OF ADDITION

The Phase 1 modeling did not assess the likelihood of encountering fluid-filled fractures in the subsurface. Based on feedback from the Technical Monitoring Team—and with the addition of new data—this important aspect was more fully considered during Phase 2. Conceptually, large contiguous volumes of fluid-filled fractures are more likely to have permeable

Table 15. Fluid-filled fracture model favorability data layers with processing types, weighting and scaling parameters, and AHP weights.

Data layer	Data availability	Initial raster processing type	Initial raster weighting criteria	Initial raster weighting value	Intermediate raster scaling criteria	Intermediate raster scaling value	AHP weights (MB+MSH-S/MSH-N/WRV)
Resistivity (MT)	MB, MSH-N, MSH-S	Regular points (~250 m spacing)	No weighting	---	$>300 \Omega\text{-m}$ $<10 \Omega\text{-m}$	0 1	0.587/0.318/0
V_p/V_s (passive seismic)	MSH-N	Regular points (~600 m spacing)	No weighting	---	<1.6 (unitless) >1.9 (unitless)	0 1	0/0.310/0
V_s (ambient-noise)	MSH-N	Regular points (~70 m spacing E-W; ~100 m spacing N-S)	No weighting	---	>4 km/s <2 km/s	0 1	0/0.148/0
Seismicity	All	KDE (5 km radius)	No weighting	---	<1 event/km ² >4 events/km ²	0 1	0.413/0.22/1

pathways that allow convective circulation; these regions also provide a reservoir for geothermal heat. Four datasets were used to develop this model—although not all are available in each study area: (1) resistivity models from magnetotelluric (MT) data, (2) V_p/V_s ratios from earthquake tomography, (3) Shear wave velocities (V_s) from ambient-noise tomography, and (4) density of seismic events. These data can also be compared for internal consistency with independent outputs of the permeability potential model such as the maximum coulomb stress (which can be interpreted to predict fracture density). An overview of how these data were used in the model is provided below and in Table 15.

FAVORABILITY MODELING

Highly conductive anomalies in MT data are often associated with warm fluid-filled fractures and reservoirs in geothermal systems (for example, Coso geothermal field; Wannamaker and others, 2004). Such features are interpreted in the resistivity data in all three areas (MB, MSH-N, and MSH-S) and are discussed in the *Results of New Data Collection* section and in Appendix C. However, geophysical properties generally have a non-unique relationship to the presence of fluids since other factors such as salinity, temperature, rock type, and fracture density also play a role. Where possible, this is addressed by combining multiple independent geophysical properties with differing dependencies. The result is improved confidence in the model of fluid favorability. Intermediate rasters for each layer are provided in Appendix A.

High V_p/V_s ratios can indicate regions of fluid-filled fractures because shear waves are slowed more by pore fluid than compressive waves (O'Connell and Budiansky, 1974; Lees and Wu, 2000). The V_p and V_s layers were inverted separately, which could possibly lead to V_p/V_s artifacts although no obvious artifacts were noted in the current dataset. Slow shear-wave velocity (V_s) from ambient-noise tomography can result from many physical properties. However, in a uniform medium at a particular depth, slower shear wave velocities may reflect greater amounts of pore fluid. A detailed description of passive seismic methods and results is provided in Appendix D.

The density of seismic events was included in this model because earthquakes are indicative of subsurface deformation and their presence is a predictor of processes that facilitate fracturing and promote high fracture density. Because seismic-station density is insufficient to accurately assess the

depth of events at the ~2 km model depth the map-view density of events is used.

CONFIDENCE MODELING

MT—The approach to assessing confidence in the MT layer follows the general premise used elsewhere: use the density of observation points and weight them by a quality or uncertainty value. For the MT data, a Gaussian kernel-density estimator of stations with a 2.5-km radius was used and each station was weighted by the model error value (RMS; root-mean square residual) at that station for the corresponding depth slice (Table 15). The errors were scaled for each model so that the maximum error was a confidence value of 0 and the minimum error was a confidence value of 1. In this way, confidence is highest where stations are closely spaced and the resistivity-model errors are low; confidence is low where model errors are high or where stations are sparse.

Seismic tomography—The passive-seismic datasets both provide an uncertainty value for each pixel in the model that implicitly accounts for station density and so a KDE was not used. Uncertainty in the earthquake tomography V_p and V_s data is a function of the combined length of raypaths that traversed each model point and the uncertainty in arrival time. Values from both V_p and V_s were summed in quadrature and the result was scaled so that a confidence value of 0 indicates no raypaths through the pixel in either model and a value of 1 indicates 4 raypaths per pixel (although the raypath length can be distributed unevenly between the V_p and V_s models) (Table 16). The ambient-noise V_s layer used the uncertainty in phase-velocity at each pixel and was scaled so that a confidence value of 0 indicates the highest calculated uncertainty in phase velocity, and a value of 1 indicates the lowest calculated uncertainty in phase velocity. Intermediate rasters are provided in Appendix A.

Infrastructure

JUSTIFICATION OF ADDITION

Geothermal development faces significant restrictions across all of the PFA projects that bear directly on the feasibility of exploration, development, and operations of a geothermal project (Table 17). Restrictions such as unfavorable zoning or land ownership, distance to transmission lines, proximity to seismically sensitive population centers, lack of process water,

Table 16. Fluid-filled fracture model confidence data layers with processing types, weighting and scaling parameters, and AHP weights.

Data layer	Raster processing type	Weighting criteria	Weighting value	AHP confidence weights (MB+MSH-S/MSH-N/WRV)
Resistivity (MT)	KDE (2.5 km radius)	Model max. RMS value Model min. RMS value	0 1	0.587/0.318/0
V_p/V_s (passive seismic)	Regular points (~600 m spacing)	0 raypaths/model point 4 raypaths/model point	0 1	0/0.310/0
V_s (ambient-noise)	Regular points (~70 m spacing E-W; ~100 m spacing N-S)	Model max. error Model min. error	0 1	0/0.148/0
Seismicity	KDE (5 km radius)	<1 event/km ² >4 events/km ²	0 1	0.413/0.22/1

Table 17. Infrastructure favorability data layers with processing types, weighting and scaling parameters, and AHP weights.

Data layer	Raster processing type	Raster weighting criteria	Raster weighting value	AHP favorability weights
Drilling not allowed	Overlay (mask for whole model)	Drilling not allowed	0	Mask
		Drilling allowed (with or without restrictions)	1	
Unfavorable land use	Overlay (mask for whole model)	Major land-use restrictions on drilling	0.5	Mask
		No known major land-use restrictions on drilling	1	
Favorable land use	Overlay	Existing geothermal leases and DNR-owned land	1	0.243
		Proposed geothermal leases	0.5	
		Other land-use category	0	
Process water availability	<u>Precipitation</u> Z-value raster	<u>Precipitation</u> 0 m/yr	0	0.218
		>2 m/yr	0.5	
	<u>Water sources</u> Proximity	>10 km	0	
		0 km	0.5	
Transmission line proximity	Proximity	>45 km	0	0.189
		≤20 km	1	
Road proximity	Proximity	>0.25 km	0	0.171
		0 km	1	
Urban center distance	Proximity	>25 km	0	0.101
		<15 km	1	
Elevation restrictions	Z-value raster	>8,500 ft	0	0.077
		<4500 ft	1	

or adverse environmental factors can all cause a viable geothermal resource to be undevelopable.

FAVORABILITY MODELING

In order to focus validation activities in areas that are most likely to be developable, a statewide infrastructure favorability model was constructed. The model contains six datasets that reflect a comprehensive array of development factors and were combined into a final model using AHP. Intermediate rasters for each layer are provided in Appendix A. Table 17 provides the weighting parameters for the different land types discussed below.

Land ownership, leasing, and zoning restrictions

Un-drillable land: Washington contains many national parks and monuments, wilderness areas, state parks, and other lands upon which geothermal drilling and development is not allowed. These lands were identified and are used as an exclusion filter for the entire infrastructure model. Included in this category are large bodies of water and some lands managed by the Columbia River Gorge Commission near the Wind River study area that are protected because of their value to the scenic Columbia River corridor.

Unfavorable land: The Columbia River Gorge Commission has also set major restrictions on the types of development and allowed drilling operations on many areas along the river. These restricted development areas are used to mask the entire model to reflect the greater difficulty in designing a successful drilling campaign or geothermal development.

Favorable land: Three types of land were identified that have above-average favorability for geothermal development: (1) existing geothermal leases; (2) proposed

geothermal leases on Forest Service land; and (3) state-owned (DNR) land for which geothermal leasing is available. Although development on private land outside of these identified areas is possible, existing leases and leasing options represent a more streamlined path to development and permitting and ensure that industry and land managers have goal alignment.

Availability of process water

Geothermal power production can potentially consume significant quantities of water depending on reservoir characteristics and facility design, and water cooled power plants operate with much greater efficiency than those cooled by air in the summer months. Although most of the play is located in temperate rain-forest with annual rainfall of 2–3 m (study areas average 3.1, 2.9, and 2.3 m/yr from north to south), more-arid portions of the state (and many of the other play-fairway projects) might face location restrictions based on water availability. To approximate regions with potentially abundant versus potentially scarce water resources the 2010 PRISM mean annual precipitation data was combined with proximity to perennial streams, rivers, and major bodies of water. This simple model does not account for water rights, environmental protection, or water loss from evapotranspiration, runoff, aquifer storage, or many other factors that will need to be assessed on a site-specific basis. Equal weight was given to each layer and the maximum and minimum scaling values are provided in Table 17.

Proximity to viable transmission lines

Distances less than ~20 km are considered feasible by industry but adding transmission lines beyond this distance is likely to be a significant impediment to development of power-producing facilities.

Proximity to existing roads

During Phase 3 validation it will not be possible to build new roads due to permits and cost; thus all roads are buffered to a distance of 250 m to ensure that potential drill sites are sufficiently close to existing roads.

Distance from urban centers

Induced seismicity is a byproduct at many geothermal facilities (for example, the Geysers geothermal field; Eberhard-Phillips and Oppenheimer, 1984) and such side-effects are increasingly not tolerated by large population centers (for example, Basel Switzerland, Mignan and others, 2015). The 2010 Census-defined urban areas were buffered to a distance of 15 km with a linear ramp to zero at 25 km.

Elevation restrictions

Washington faces significant snow loads at high elevations that might hinder infrastructure development. Areas above 8,500 ft were considered to be unfavorable and areas below 4,500 ft to be insensitive to this constraint.

CONFIDENCE MODELING

No confidence modeling was performed on these data.

RESULTS OF NEW DATA COLLECTION

Mount Baker Study Area

GEOLOGIC AND GEOMORPHIC MAPPING

Aims

- Interpret recently flown lidar, specifically looking for evidence of active faults.
- Field-check and improve previous geologic mapping.

Data Collected

Lidar with 1-m resolution covering most of the study area was flown in late 2015 and delivered to DNR in July, 2016 as part of the USGS 3DEP program at no cost to this project. Lidar was interpreted and accessible lineaments were field checked. Geological mapping at 1:24,000-scale or better was conducted along and adjacent to lidar lineaments in the Area of Interest (AOI).

Major Findings

- 57 linear features were identified from lidar and several are sub-parallel to or along strike from mapped faults; many lineaments also correspond to strong geophysical gradients and suggest that the geophysical boundaries are perhaps controlled by active faults.
- Abundant fractures are found in exposures along these lineaments.
- Existing 1:100,000-scale mapping is accurate given the density of vegetation.

MAGNETOTELLURIC SURVEY

Aims

- Determine 3D resistivity structure of study area to identify regions of enhanced fluid content, hydrothermal alteration, major structures, and geologic features.

Data Collected

MT data were collected using induction coils and electric dipoles at 28 stations throughout and adjacent to the AOI for a minimum of 20 hours per station. Data were processed and inverted to develop a 3D resistivity model from the surface to ~10 km depth. Details of data collection, inversion, and results are provided in Appendix C.

Major Findings

- A tabular 2–3 km³ conductive zone was discovered from near the Baker Hot Springs to >3 km depth; this is also near a >200 °C/km temperature-gradient well (DNR 83-3). The conductive anomaly is similar in value to the measured resistivity of the hot spring water (~10 Ω-m) and is interpreted as a volume of upwelling hot fluid that perhaps ascends along a steeply north-dipping fault. The conductive zone nears the surface about 200 m east of the hot springs and moves west towards the springs along a surficial geologic boundary (perhaps glacial deposits).
- The hot water discharging at the hot springs does not necessarily flow from beneath Mount Baker, but may be meteoric recharge that flows down along a south-dipping fault to 2–3 km before convecting upwards towards the hot spring.
- Bulk porosity in the conductive anomaly near the hot springs may be 15 percent or higher.
- There are many near-surface conductive anomalies; most are likely related to Quaternary glacial and (or) landslide deposits.
- Deeper conductive anomalies are found in areas where mapped faults intersect or where intersecting faults are interpreted from lidar and other geophysical datasets. This finding appears to support the conceptual model (Fig. 2) of enhanced permeability near geometric fault complexities that promote dilatant failure mechanisms.

GROUND-BASED GRAVITY AND MAGNETIC SURVEYS AND GEOPHYSICAL MODELING

Aims

- Constrain subsurface geology and potential fault locations.

Data Collected

More than 93 km of magnetic data were collected using a backpack-mounted magnetometer and integrated GPS unit with a base-station magnetometer to correct for diurnal field variation. Data were processed and inverted to develop a 3D subsurface model of magnetic regions in addition to map-view

anomalies. This effort was undertaken as part of an outstanding undergraduate senior thesis at Western Washington University.

A total of 495 gravity observations were made in and near the AOI using a nearby base station to compute absolute gravity values and correct for instrument drift. These data were tied into regional gravity measurements through repeat surveys of older stations. Data were processed and used to develop an isostatic gravity map and identify the location of maximum horizontal gradients. Two cross sections were constructed and modeled with the potential field data to constrain the subsurface extension of mapped and inferred structures and provide cross-validation with other geophysical data such as seismicity, seismic tomography and MT. Detailed results are provided in Appendix E.

Major Findings

- 93 km of walked magnetic lines reveal a 1.7-km-long highly magnetic body along the lidar lineament that trends into the hot springs. The size and shape of the body was inversely modeled in 3D and was determined to be a roughly tabular, ~2 km³ volume body that roots down to the northwest near the conductive MT anomaly. The feature is consistent with being either a low-conductivity mafic intrusion—based on its geometry perhaps intruded along a fault zone—or an anomalously magnetic portion of the Permian metavolcanic bedrock—perhaps related to hydrothermal alteration. A steeply southeast- or northwest-dipping fault likely forms the northwest boundary of this feature and corresponds to the strong magnetic gradient, lidar lineament, and location of the hot springs.
- Magnetic data also reveal an intersecting steep northeast-trending magnetic gradient ~0.5 km north of the hot springs. Interaction of the two structures may enhance permeability near the springs.
- Both structures noted above have surface expressions in lidar and bound highly conductive regions in the MT model.
- Many other steep magnetic gradients were identified, several of which lie along lidar lineaments and suggest recent deformation along these relatively large crustal structures.
- 495 new gravity stations significantly update and refine the existing isostatic gravity map of the area. Major density contrasts were identified using algorithmically determined maximum-horizontal gradient lineaments or ‘spots’ and large changes in the orientation of gravity contours. Many of these features correspond well with mapped faults and lidar lineaments.
- Gravity and magnetic data were used to validate three geologic cross sections in the area via a forward-modeling process: a steeply southeast-dipping fault is the simplest hypothesis that agrees with available observations.

ELECTRICAL RESISTIVITY SURVEY

Aims

- Check mapped faults and lidar lineaments for conductive anomalies indicative of fluid pathways or clay caps.
- Improve characterization of shallow fault geometry.

Data Collected

Two 355-m-long Electrical Resistivity (ER) transects were collected: one across a mapped fault and another across lidar lineaments. The IRIS Syscal R1 PLUS 72 electrode system was used to collect data with a dipole-dipole array and 5 m probe spacing. The data were processed using Prosys RES2DINV software and corrected for topography. Detailed logs are provided in Appendix F.

The ER method was not well-suited for this project for two main reasons: (1) the probes cannot get wet, a difficult feat in the temperate rainforest of Washington; (2) the probes must be in a 355-m-long straight line, also difficult in a temperate rain forest in steep terrain. Processed errors were extremely high (12–40 percent). Only one of six transects showed a change in resistivity across a known or suspected (lidar-based) fault. This was particularly frustrating because one of the transects (MSHSZ-ER1) crossed several well-exposed faults with abundant slickenlines and fault gouge, yet showed no correlation with changes in resistivity.

Major Findings

- The MB-ER2 transect at Mount Baker is one of the only transects that showed a change in resistivity near a mapped lidar lineament; this transect also has the lowest error (12.7 percent). A 30-m-tall near-vertical resistivity contrast is found below a 10–20-m-thick conductive cap; the high conductivity zone may represent a clay cap or fluid filled fractures.

Mount St. Helens Study Area (North And South AOIs)

GEOLOGIC AND GEOMORPHIC MAPPING

Aims

- Map geology in northern AOI above the St. Helens Seismic Zone (SHSZ); specifically look for evidence of faulting, permeability pathways, potential heat sources, and hydrothermal alteration to provide information on the distribution of potential reservoir cap rock.
- Interpret newly acquired lidar.

Data Collected

More than 130 km² was mapped at 1:24,000-scale or better in the northern AOI, including more than 100 fault observations and 1,200 outcrop descriptions. The mapping partially overlaps and confirms the results of unpublished field notes and maps from Russ Evarts and Roger Ashley from the mid 1990s; their data was used to extend mapping coverage an additional 25 km² south beyond the Phase 2 mapping effort. A preliminary version of the new geologic mapping can be found in

Appendix G; a final version will be published as a geologic map of the 7.5-minute Elk Rock quadrangle by the Washington Geological Survey by the end of 2019.

Major Findings

- The surface expression of the north-northwest-trending SHSZ is an en echelon array of discontinuous lidar lineaments and newly mapped fault segments with argillic alteration. The soda spring in the northern AOI lies along one such newly mapped structure.
- A diorite intrusion, mapped west of the SHSZ, appears to have altered and magnetized the surrounding country rock, is spatially associated with faults that are commonly silicified, bleached, sulfide-bearing, and often exhibit liesegang banding. This intrusion is late Eocene–early Oligocene (see *Geochronology* below) and is most likely the Spud Mountain pluton of Evarts and others (1987).
- Faults with argillic alteration mostly strike east-northeast to east-southeast but also northwest and likely record slip at relatively shallow crustal levels (<1–2 km). Faults with silicification, sulfides, and liesegang banding predominantly strike north-northeast to northeast likely record slip at deeper crustal levels (2–3 km); these faults are associated with the Spud Mountain pluton, and may have been exhumed by regional eastward tilting (Evarts and others, 1987).
- Faults of both argillic and silicic alteration have slickenlines that record paleo-stress similar to the modern stress field (~north σ_1 , horizontal compression), indicating that most faults in the area have the potential to still be active.

GEOCHRONOLOGY

Aims

- Determine age of newly mapped intrusive igneous rocks and previously mapped but undated rocks to assess their contribution to Quaternary geothermal heat potential.

Data Collected

Three intrusive igneous samples were dated by the OSU Argon Geochronology Lab using the $^{40}\text{Ar}/^{39}\text{Ar}$ method: one from the Spud Mountain pluton, one from a dike and sill complex that cuts the Spud Mountain pluton, and one from a series of basaltic dikes near Coldwater Lake. Detailed results are provided in Appendix H.

Major Findings

- All three samples were latest Eocene to early Oligocene in age and document a previously unrecognized late Eocene period of plutonism.

MAGNETOTELLURIC SURVEY

Aims

- Determine 3D conductivity structure of study area to identify regions of enhanced fluid content, major structures, and geologic features.

Data Collected

MT data were collected using induction coils and electric dipoles at 41 stations (northern AOI) and 15 stations (southern AOI) for a minimum of 20 hours per station. Data were processed and inverted to develop two 3D resistivity models from the surface to ~10 km depth. Both models incorporate constraints and boundary conditions imposed by nearby as-yet unpublished MT data collected for the iMUSH experiment. Details of data collection, inversion, and results are provided in Appendix C.

Major Findings

Northern AOI

- A conductive column rises to just beneath the soda springs in the north part of the AOI and is the preferred drill target based on the resistivity model. The conductive column is ~10 $\Omega\text{-m}$, which may indicate less fluid or perhaps greater mixing with meteoric water than the north-northwest-striking conductive anomaly just to the north (see below). Porosity is estimated at 2–10 percent; the estimate could be improved with conductivity measurements at the spring.
- A 1-km-wide conductive zone (1–30 $\Omega\text{-m}$) strikes north-northwest between 4 and 10 km depth. This conductive anomaly is coincident with and west of seismic events on the SHSZ. It is likely caused by either fluid-filled fractures or conducting phases such as graphite which could be present in Eocene-age organic-rich sediments that may underlie the exposed volcanoclastic rocks. Passive seismic tomography indicates this zone highly attenuates shear waves (see below) and suggests that fluid-filled fractures are more likely than graphite. Porosity is estimated at 5–15 percent in this zone using a modified Archie's equation and assuming a water conductivity close to sea water (1 $\Omega\text{-m}$).
- A second drilling target may be a west-dipping column of high conductivity, but there is no surface manifestation of upwelling fluids.
- Other near-surface features are the resistive blocks on either side of the SHSZ; the Spud Mountain pluton on the west and the Spirit Lake pluton on the east which help to define the overall crustal structure.

Southern AOI

- The main feature is a 1-km-wide conductive (10–30 $\Omega\text{-m}$) anomaly in the northeast that rises to near the surface; this is the preferred drilling target from the resistivity model. Similar to the northern AOI, the anomaly is adjacent to and above seismicity on the SHSZ. Assuming a lithology similar to the north, the lower zone of conductivity may have a lower fracture density—and thus lower fluid content—or mixes with fresh meteoric water. Porosity is estimated at 2–10 percent for the near-surface conductive anomaly.

- Seismicity is more scattered in this AOI and suggests a broader zone of weakness (and perhaps lower fracture density) than in the northern AOI.
- A conductive block on the west of the AOI is most likely plutonic rock.

GROUND-BASED GRAVITY SURVEY AND GEOPHYSICAL MODELING

Aims

- Constrain subsurface geology and potential fault locations.

Data Collected

New gravity measurements were made in the northern (297) and southern (184) AOIs. Raw data were tied to an absolute datum and corrected for instrument drift through the use of a base station and were tied into regional gravity measurements through repeat surveys of older stations. Five new ground magnetic transects were walked with data collection and processing following procedures described at Mount Baker. Hand samples were collected for every major lithology and magnetic susceptibility, magnetic Q, and density values were measured. These data—along with a recently flown aeromagnetic survey—were used to model and match the potential field response along four cross sections. Detailed results are provided in Appendix E.

Major Findings

Northern AOI

- The north-northwest-trending SHSZ is collocated with the western edge of the Spirit Lake pluton, which at this latitude is dense ($\sim 2,700 \text{ kg/m}^3$) and has a magnetic roof ($60 \times 10^{-3} \text{ SI}$, 0.17 A/M). Modeling confirms that this pluton extends from the upper crust perhaps into the mid-crust. Spatial variability in the potential fields along the modeled western edge of the pluton is mimicked by the pattern of microseismicity.
- The western edge of the AOI contains the dense and magnetic Spud Mountain pluton ($2,740 \text{ kg/m}^3$, $25 \times 10^{-3} \text{ SI}$, 0.37 A/M). A suspected north-northwest-trending fault parallels the SHSZ—and coincides with the eastern edge of the Spud Mountain pluton—in the southern part of the AOI, but continues as a linear gravity gradient to the north as the edge of the pluton steps west. Thicker zones of Quaternary or late Tertiary cover are located between this fault and the SHSZ with the thickest sections close to each fault.
- A zone of lower density nonmagnetic rocks (2670 kg/m^3) forms a north-northwest-trending gravity low between the plutons and is consistent with lightly metamorphosed sedimentary rocks or more-felsic intrusive rocks. This lower-density nonmagnetic region encapsulates a highly conductive zone imaged with MT which is moderately to highly magnetic. A hypothesis of warm fluids circulating to shallow depths and precipitating magnetite is consistent with available potential-field observations. This hypothesis is also supported by observations that hornfels

developed above the highly magnetic Spud Mountain pluton contains more magnetite than un-metasomatized rock.

- Shallow warm fluids are most likely in the northern part of the AOI where the shallowest magnetic anomalies are found near the intersection of an E-trending structure and the SHSZ. A shallow conductive column in the MT model just east of the SHSZ is not magnetic and therefore this region is interpreted as a zone of colder return flow instead of upwelling.
- A gravity high bound by east-northeast-trending gradients along the Green River in the north of the AOI indicates a deeply seated cross-structure.

Southern AOI

- A low-density ($2,600 \text{ kg/m}^3$) and nonmagnetic region is collocated with a zone of high conductivity in the MT model and corresponds with the $\sim 160 \text{ ka}$ volcanic vents of Marble Mountain. This region is a gravity low between two more-dense ($2,740 \text{ kg/m}^3$) and nonmagnetic regions interpreted as intrusive volcanic rocks. Cross sections are less-well constrained compared to the northern AOI because of fewer hand-sample measurements.
- A narrow but dense and highly magnetic ($2,700 \text{ kg/m}^3$, $30 \times 10^{-3} \text{ SI}$, 1.12 A/M) zone is adjacent to the column of highest conductivity in the MT model and is interpreted as the basaltic feeder for the $\sim 160 \text{ ka}$ Marble Mountain basalts. Most of this feature is west of the vents. The surface vents are located above small-wavelength gravity lows that may represent buried scoria cones.
- The strongest gravity gradients trend northeast and east and appear to cross the north-northwest trend of sparse seismicity associated with the SHSZ.
- As in the north, the most linear band of seismicity broadly marks the eastern edge of a lower-density region. This boundary appears to be the edge of a large upper to mid-crustal plutonic complex, similar to the Spirit Lake pluton. A strong north-northwest- to west-northwest-trending gravity gradient extends beyond the speculative pluton margin and marks the eastern and northern edge of a very strong gravity low containing the active Mount St. Helens volcanic edifice. Many mapped springs are coincident with this gravity gradient and may indicate that it blocks the northward flow of groundwater.

PASSIVE SEISMIC SURVEY—EARTHQUAKE AND AMBIENT-NOISE TOMOGRAPHY

Aims

Define high-resolution subsurface velocity structure to aid in the interpretation of large-scale geologic boundaries, faults, and regions of fluid-filled fractures.

Data Collected and method overview

A network of 20 broadband seismic stations were deployed from June through November of 2016 and combined with 70 stations from the iMUSH experiment (imush.org) and several

permanent stations from the Pacific Northwest Seismic Network (PNSN). Phase 2 seismic stations used Geotech KS2000M broadband seismometers with Reftek 130 and Smart24 data loggers, iMUSH stations used Guralp CMG-3T broadband seismometers and Reftek 130 data loggers, and PNSN stations are a mixture of short-period and broadband seismometers. The Phase 2 instruments had an array diameter of ~12 km and an average station spacing of 2 km; the iMUSH network has an average array diameter of ~100 km and station spacing of ~10 km. Detailed results are provided in Appendix D.

Earthquake tomography data consisted of P- and S-wave arrival times from ~300 local earthquakes (~60 within the Phase 2 footprint, 40 of which occurred during the deployment). In total there were ~5,300 P-wave and ~2,500 S-wave arrivals which provided raypaths through the model volume, with 559 P-wave and 414 S-wave arrivals observed at Phase 2 stations. Earthquake P- and S- arrival times were picked using the seismic software package Antelope, and inverted to obtain 3-D seismic velocity models with the program *struct3dp*, written by Bob Crosson. This program uses a conjugate-gradient least-squares method with joint hypocenter and velocity inversion using 3D eikonal-based travel time computation (Vidale, 1990; Hole and Zelt, 1995).

Ambient-noise tomography uses the cross-correlated continuous noise between seismic station pairs to provide a fundamental mode Rayleigh wave signal between the stations (Shapiro and Campillo, 2004). These cross correlations are then used to calculate velocities, which can be interpreted for structure. A new technique using radial-vertical cross correlations of ambient noise (Haney and others, 2012) was employed to image small features from a high-frequency dataset. This technique uses a frequency-domain method that calculates phase velocities and is well-suited for short (3 km-long) paths (Ekström and others, 2009; Jin and others, 2015) and thus high-resolution, shallow imaging. Finite-frequency tomography (Lin and others, 2009; Zhou and others, 2005) was also used which calculates the phase velocity tomography for small arrays more accurately than ray theory. Shear velocities are then calculated from phase velocities and are shown as depth slices in the model space where the resolution matrix for phase velocities is nonzero. This technique has been demonstrated in various hydrothermal and geothermal settings, such as Dixie Valley to develop EGS exploration methodology (Lovenitti and others, 2012) and Soda Lake as a cost effective alternative to active source seismic surveys (Tibuleac and others, 2012).

Major Findings

- Earthquakes—There were approximately 20 events in the PNSN catalog within the Phase 2 array footprint during its deployment. These were relocated as a part of the seismic tomographic inversion, and 20 more were detected using the Antelope seismic software. Focal mechanisms were calculated for several of these. Earthquake focal mechanisms along the SHSZ are similar to previous results (Weaver and others, 1987), exhibiting right lateral shear, with T axes oriented in a northwest–southeast direction. Earthquakes ~15 km west-southwest of the SHSZ have T axes oriented closer to east–west.

- Earthquake tomography—Major features of the 3D seismic velocity models include low P- and S-wave velocities along the SHSZ, possibly related to fluids or fractures. High velocities at shallow depths to the east and west of the SHSZ correspond to the Spirit Lake and Spud Mountain plutons. There are high V_p/V_s ratios just to the west of the SHSZ, which could indicate the presence of fluids, since S-waves are more sensitive to fluids and open fractures.
- Ambient-noise tomography—A central region of low velocity is identified and lies adjacent to the SHSZ (Fig. 10). The inferred fault of the SHSZ lies in an area of high velocity gradient; fast velocity is found to the E and slow velocity to the west and northwest. The velocities farther west and northwest (3–4 km/s) could be within the Spud Mountain pluton (Evarts and others, 1987); common shear velocities for diorite at 2–4 km depth are around 3.7–3.8 km/s. The fast velocities (2.2–3.6 km/s) to the east of the fault could be the edge of the Spirit Lake pluton, which should have a velocity near 3.6 km/s at 2–4 km depths. Near-surface porosity can lower the velocities of diorite or granite; however, the low velocities in the center of the map are much lower than the plutons (1.8–3 km/s) and indicates lower density or fractured rock.

ELECTRICAL RESISTIVITY SURVEY

Aims

- Check mapped faults and lidar lineaments for resistive anomalies indicative of fluid pathways or clay caps.
- Improve characterization of shallow fault geometry.

Data Collected

Four resistivity transects were conducted at MSH following the same procedures as at MB. As at MB, these transects failed to respond to known faults with well-developed gouge and geomorphic expression. Because the method did not identify the well-exposed faults in the MSHSZ-ER1 transect, there is little confidence in the remaining sections. The results are compiled in Appendix F but will not be discussed further here.

Wind River Valley Study Area

GEOMORPHIC MAPPING

Aims

- Interpret recently flown lidar, specifically looking for evidence of active faults.

Data Collected

Lidar with 1-m resolution was flown in late 2014, delivered to DNR in 2015 at no cost to this project, and interpreted using 1:24,000-scale mapping from 2014 to ‘field-check’ linear features.

Major Findings

- 86 linear features were identified; approximately 40 percent corresponded to existing mapped faults, observed

small shear zones, or areas of distributed deformation; approximately 30 percent correspond to linear alignments of maximum-horizontal gradients in the new gravity survey.

GEOCHRONOLOGY

Aims

- Determine age of plutonic rock near the St. Martin and Shipherds hot springs and assess whether it could be the source for the elevated heat flow in the area.

Data Collected

A diorite sample from the Buck Mountain pluton was dated by the OSU Argon Geochronology Lab using the $^{40}\text{Ar}/^{39}\text{Ar}$ method. Detailed results are provided in Appendix H.

Major Findings

- A plateau age of ~20 Ma indicates there is a different source of heat for the hot springs. Currently, the most-likely candidate is the source of the abundant nearby late Pleistocene extrusive volcanism (Fleck and others, 2014).

GROUND-BASED GRAVITY SURVEY

Aims

- Constrain subsurface geology and potential fault locations.

Data Collected

604 new gravity measurements were made and four new ground magnetic transects were collected. Data collection and processing followed the same procedure as MSH. These data—along with a previously flown aeromagnetic survey—were used to model and match the potential field response along three cross sections. Detailed results are provided in Appendix E.

Major Findings

- The location of the St. Martin Hot Springs (and source for the Carson Hot Spring Resort) coincides with the intersection between the Wind River fault and the Shipherds fault zone, which are well-defined in the potential fields by linear trends in maximum-horizontal gradient.
- Gravity and magnetic data reveal a major crustal discontinuity running subparallel to the Wind River fault characterized by low density/high magnetization rocks on the southwest and high density/low magnetization rocks on the northeast. A portion of the discontinuity is attributed to near-surface changes in lithology; the remainder require larger as-yet-unexplained changes at depth.
- The Wind River Valley appears to be bound on both its northeast and southwest sides by subparallel structures. Complicated patterns of gradients in the northwest part of the valley preclude the clear continuation of a through-going fault. The gravity and magnetic gradients on the southwest side of the valley appear to trend farther west-northwest at the northern end of the valley.

- The northeast-striking Shipherds fault zone has a prominent geophysical signature and appears to mark the southeast boundary of a major crustal discontinuity. A steep gravity gradient continues northeast from St. Martin Hot Springs, is subparallel to a mapped fault zone, and marks the transition between low density rocks on the southeast and high density rocks on the northwest. A parallel gradient is found in the aeromagnetic data.
- The Brush Creek and Bear Creek faults are both observed in the isostatic gravity data, though Bear Creek is less well defined. The Brush Creek fault is well defined by a sharp gradient subparallel to the mapped fault trace north-northwest of Buck Mountain. Though data is somewhat sparse to the east, this gradient then turns east and converges with the Shipherds fault zone.

Opportunistic Data Collection

GEOCHRONOLOGY AND GEOLOGIC MAPPING

One regional study (Fleck and others, 2014) was completed since the last Washington statewide geochronology and volcanic vent compilation (Boschman and others, 2014) used in the Phase 1 heat model. This study collected over 100 $^{40}\text{Ar}/^{39}\text{Ar}$ ages which were added to the Washington Geochronology Database and incorporated into the heat potential model. Additionally, two 7.5-minute quadrangles in the Wind River study area are nearing publication through the USGS and were provided to DNR by R. Evarts (USGS, written communication, 2016). Faults from these maps were added to the fault model, but fell outside of the smaller Phase 2 AOIs.

UPDATED PHASE 2 FAVORABILITY AND CONFIDENCE MODELS

Definitions of Terms Used

Assessment of geothermal systems is based on combining numerous datasets that each constrain a key element of the geothermal system. For each dataset—and resulting model—distinct metrics were developed.

Favorability and potential—Both terms are used to refer to semi-quantitative assessments of data to develop a holistic geothermal model. In detail, favorability generally refers to the 0–1 value of a dataset and potential generally refers to the weighted sum of several datasets.

Confidence and uncertainty—Both terms refer to a semi-quantitative statement about the certainty of a value. Confidence is the direct complement of uncertainty and is used in Phase 2 instead of uncertainty. The phrase ‘confidence modeling’ refers to the assessment of certainty for both data-layer values and model results. Confidence as defined here then becomes a direct input into the assessment of development risk.

Model risk—The term ‘risk’ is conceptually used here to refer to the favorability of a model weighted by the confidence of the constituent data. This is accomplished by scaling the favorability model by the confidence model; areas of high favorability with high model confidence are less risky than areas with high favorability but low model confidence.

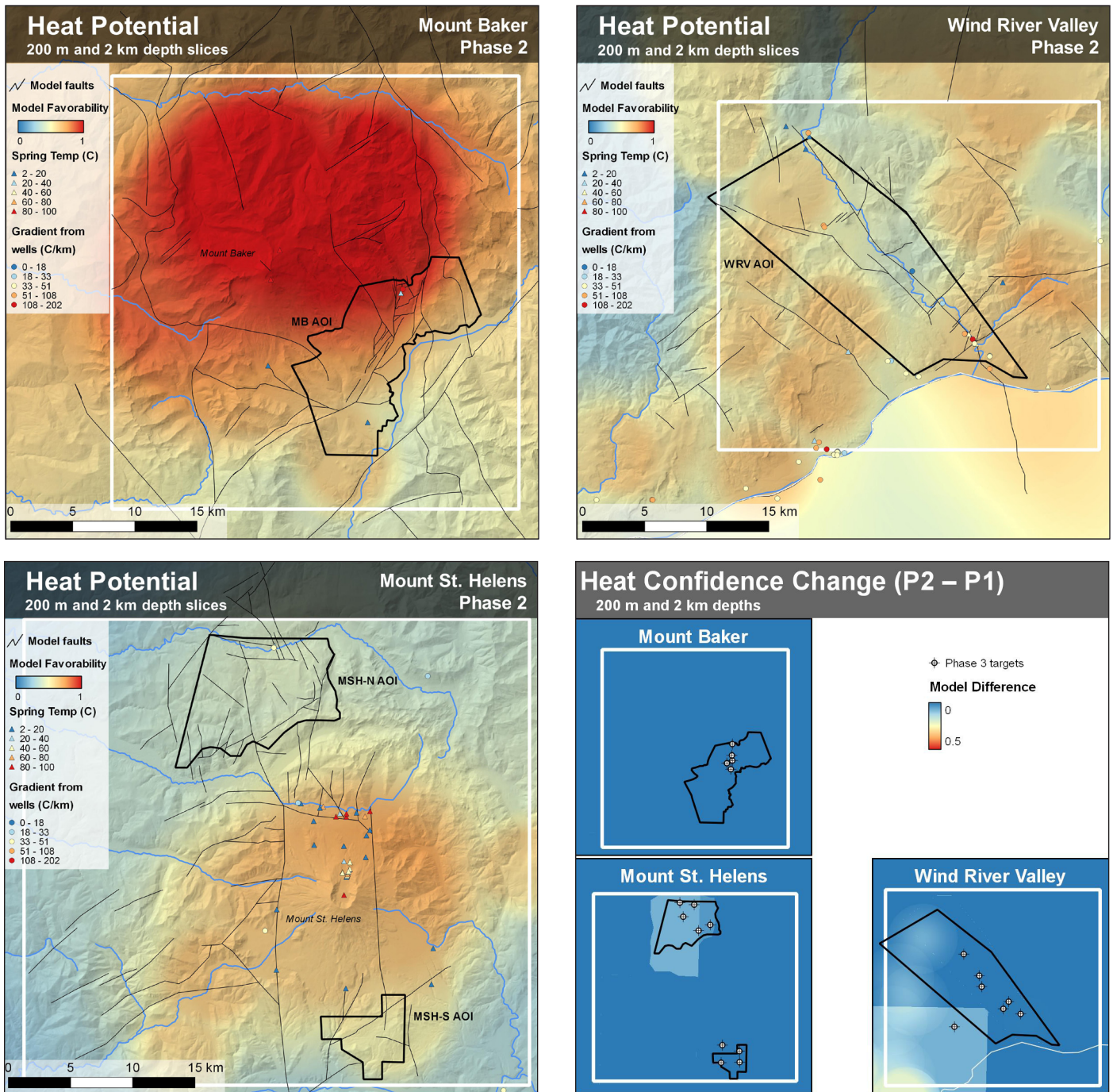


Figure 3. Phase 2 heat potential and change in confidence from Phase 1. Confidence increases are largely the result of new mapping at MSH, and opportunistic data collection near WRV. Individual confidence models are provided in Appendix J.

Heat Potential

PHASE 2 ACTIVITIES AND MODEL ADDITIONS

- Geochronology (MSH and WRV)
- Geologic mapping (MSH; opportunistic at WRV)
- Revised model method

PHASE 2 RESULTS AND CHANGES FROM PHASE 1

The improved modeling method better defines regions of higher heat potential than the Phase 1 method. The Mount Baker area has the highest favorability of all three areas at 200 m depth (Fig. 3) and at 2 km depth (Appendix I), driven largely by the proximity of the Mount Baker volcano, Mount Kulshan Caldera, the young Lake Anne intrusive rock, several other young volcanic cones, and a 200° C/km temperature-gradient hole. Favorability at Mount St. Helens, both north and south of the volcanic edifice, is along the St. Helens Shear Zone, with slightly elevated values in the southern AOI associated with the ~160 ka Marble Mountain volcanic vents and flows. At Wind River Valley, favorability is more-broadly distributed and is strongly influenced by the many temperature-gradient wells and abundant—but small—young volcanic vents. Weights for the input layers are provided in Table 9.

Although Phase 2 geochronology and geologic mapping did not identify young intrusive rocks capable of providing a geothermal heat source, the data from Fleck and others (2014) significantly improved the ages of young volcanic rocks in the Wind River area. The addition of new mapping and age control improved model confidence at MSH and WRV (Fig. 3). Full-size confidence models can be found in Appendix J.

Permeability Potential

PHASE 2 ACTIVITIES AND MODEL ADDITIONS

- Geologic mapping (MSH, opportunistic at WRV and MB)
- Lidar interpretation (all areas)
- Detailed gravity surveys (all areas)
- Ground-based magnetic surveys (MB)
- Electrical resistivity surveys (new data at MSH-N and MB; ER data were already collected at WRV)
- Aeromagnetic surveys (all areas; existing data, newly incorporated)
- 2D geophysical cross section modeling (all areas)
- 3D magnetic susceptibility modeling (MB)
- Refined boundary-element modeling of stress/strain
- Expanded fault slip and dilation tendency modeling
- Addition of seismic event density layer
- Addition of fault density layer
- Revised model method

PHASE 2 RESULTS AND CHANGES FROM PHASE 1

Updating the permeability potential model at 200 m depth (Fig. 4) and 2 km depth (Appendix I) was a focus of Phase 2 activities (Table 13) and shows the largest gains in model confidence. Full-size confidence models are available in Appendix J. As in Phase 1, the most-favorable regions are located in areas of fault complexity (intersections, bends, and stepovers) where modeling suggests dilatant fracturing should occur under current stress conditions and where seismicity indicates deformation is occurring. In all study areas warm and hot springs are commonly associated with higher-favorability regions in the 200 m model, providing some independent verification of the basic modeling strategy.

The permeability layers added in Phase 2 were based on new faults from geologic mapping, geophysics, and lidar interpretation. Further, the permeability model resolution was increased. The new permeability layers provide additional insight into the permeability for each study area, and the revised method has the potential to be applied across all of Washington State and the greater Pacific Northwest region. In the cases of the Mount St. Helens shear zone and Mount Baker, the newly mapped structures did not significantly alter the large-scale results of the *Poly3D* stress model. This is because crustal deformation in these two areas is influenced to a large degree by volcanogenic stress that is additive with regional and local tectonic stress and there were no changes to the volcanogenic stress model in Phase 2.

In the Mount St. Helens area, a modeled stress anomaly in the north matches the thickest part of the high V_p/V_s anomaly (Appendix A). It is hypothesized that the upward bifurcation of the SHSZ at ~7 km depth (Weaver and others, 1987) projects a highly favorable stress state (high dilatancy) upward and to the west under Coldwater Lake, and in the southern part of the geothermal lease area. Regions of favorable modeled stress appear to have a higher density of Oligo–Miocene-age dikes than areas with unfavorable modeled stress (low dilatancy). The cause of this correlation is not entirely clear because of the 20–30 m.y. between when the dikes were emplaced and the current stress state of the area but may suggest that the long-term tectonic stress regime has been relatively constant since the Oligo–Miocene. The abundant but apparently discontinuous east–west-trending faults mapped and modeled in Phase 2 might interact with more throughgoing structures and bring fluids to the surface. However, the Phase 2 *Poly3D* models did not indicate strong support for this contention, perhaps because the two fault sets did not overlap or intersect in the 3D model.

In the Mount Baker area, the measured geodetic strain rates on the flanks of the volcano are two orders of magnitude higher than the surrounding tectonic strain rates (Crider and others, 2011). Thus, the volcanic deformation center model located at 5.8 km depth (Hodge and Crider, 2010) is the most salient source of stress in the *Poly3D* model. This became apparent after modeling two scenarios that had nearly the same result, where (1) the faults were allowed to slip to zero residual shear stress and (2) where the faults had zero displacement. In the *Poly3D* model, the deformation caused by the source under the volcano is combined with the regional tectonic northward

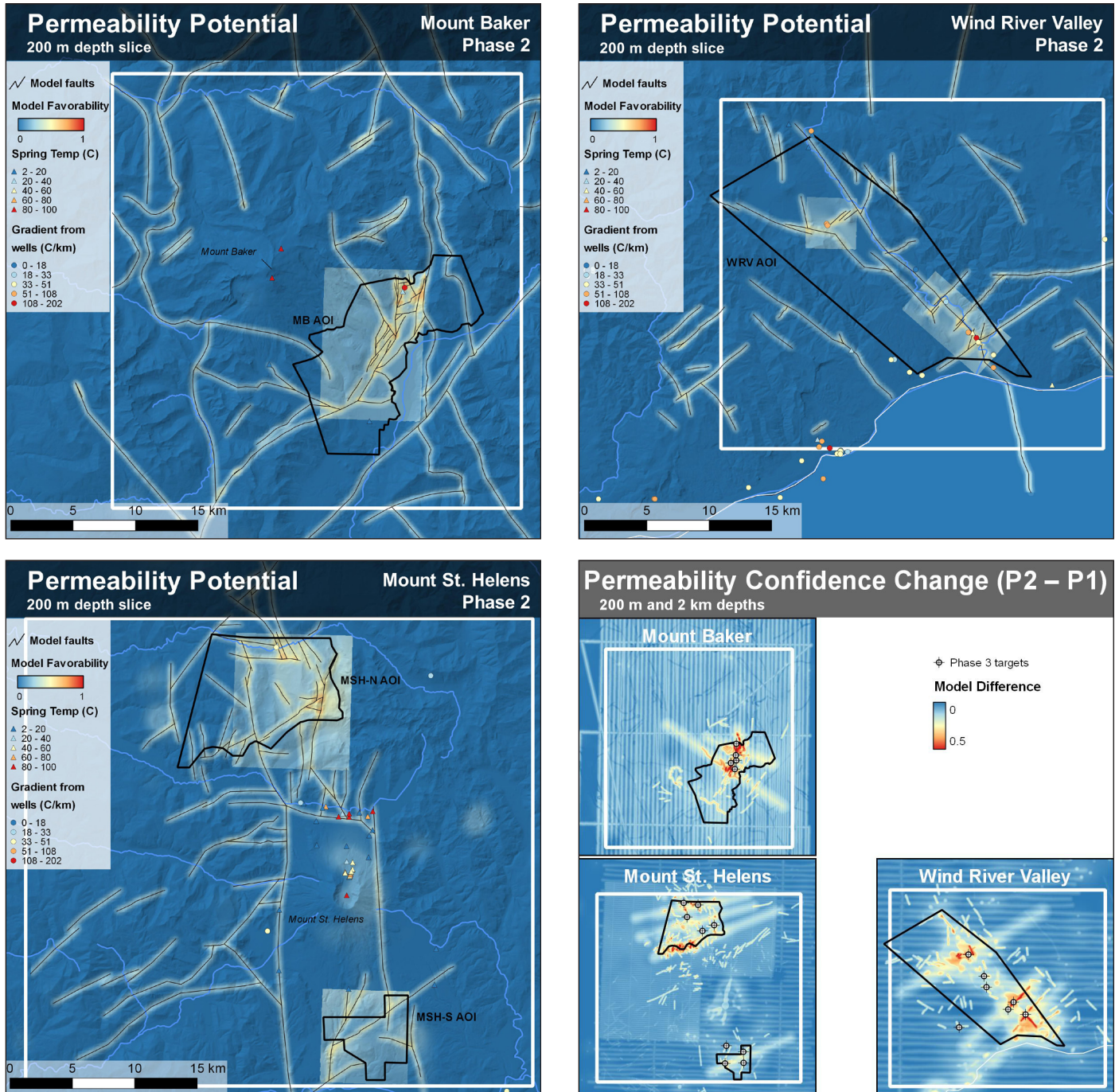


Figure 4. Phase 2 permeability potential at 200 m depth and change in confidence from Phase 1. Confidence increases are the result of new mapping, lidar interpretation, the inclusion of new gravity and magnetic data, modeled cross sections, and updated and refined geomechanical models and opportunistic data collection near WRV. Potential models at 2 km depth are provided in Appendix I and confidence models are provided in Appendix J.

compressional stress and produces two north–south-trending zones of favorable stress (high dilatancy) as much as 10 km east and west of the volcanic edifice. This area of favorable stress includes the Baker Hot Springs and adjacent 200 °C/km TGH in addition to a major conductive anomaly in the MT data.

The Phase 2 *Poly3D* results for Wind River were greatly improved because the main sources of crustal deformation are the fault intersections mapped at the surface (Czajkowski and others, 2013). The southeastern model captured the extent of the damage zones along the faults and around the fault intersections at the surface. Fault geometries were improved with high-resolution gravity data, including the location and extent of the Shipherds fault zone. The *Poly3D* stress model predicts a damage zone around this structure that is consistent with previous geologic mapping (Czajkowski and others, 2014). The lidar collected in the Wind River Valley provided additional constraints on the location and extent of the Brush Creek fault, as well as other structures to the north. Regions of favorable stress in the *Poly3D* model closely matched the location of existing hot springs and high temperature gradients. Some important insights gained from this model are: (1) favorable stress was only modeled on the southeast side of Wind River, rather than in opposite dilational corners of fault intersections as originally hypothesized; (2) the predicted area of influence (fault damage zone) appears to be ~250 m along each side of a fault and ~500 m away from fault intersections, similar to the assumptions made in a statewide geothermal assessment (Boschmann and others, 2014); (3) the Shipherds fault zone appears to be an excellent place to validate the *Poly3D* model predictions for fault damage.

Fluid-filled Fractures

PHASE 2 ACTIVITIES AND MODEL ADDITIONS

- Magnetotelluric surveys (MSH and MB)
- Passive-seismic V_p , V_s , and V_p/V_s tomography (MSH-N only)
- Ambient-noise shear-wave tomography (MSH-N only)

PHASE 2 RESULTS

This model is a new addition over Phase 1 and highlights regions that are most likely to have fluid-filled fractures at 200 m depth (Fig. 5) and at 2 km depth (Appendix I); confidence models can be found in Appendix J. Because data availability is vastly different between sites (Tables 8 and 13), the AHP was conducted on a site-by-site basis and thus comparison of the resulting models should be done with care. In addition, because most of these datasets have non-unique relationships to fluid saturation and temperature; the best results are achieved where multiple lines of evidence are integrated.

At MSH-N, where the most data are available, there is a favorable north-northwest-trending region that lies slightly west of and above the inferred fault defined by the SHSZ. This zone is high in conductivity, has a high V_p/V_s ratio, has slow ambient-noise shear wave velocity, and coincides with a gravitational low. Together, the collocation of these anomalies provide strong support for the presence of fluid-filled fractures;

Table 18. Summary of final model weights for each study area.

Model	MB	MSH-N	MSH-S	WRV
Heat	0.322	0.243	0.322	0.492
Permeability	0.344	0.351	0.344	0.388
Fluid-filled fractures	0.334	0.405	0.334	0.120

the soda springs in the north of the AOI lies along this trend at an intersection of favorable structures. Lower-favorability regions to the west and east correspond to the Spud Mountain and Spirit Lake plutons mapped at the surface and indicated in the sub-subsurface by higher seismic velocities, gravity anomalies, and high resistivity. In the southern AOI, a collocation of seismicity and a highly conductive anomaly in a high-amplitude gravity low provides compelling evidence for fluid-filled fractures.

At Mount Baker, high favorability is largely a product of high-conductivity MT anomalies; there is a small amount of seismicity in the NW part of the AOI near the hot springs. As discussed in *Results of New Data Collection* and in Appendix C, a high-conductivity zone just north of the hot springs is interpreted as a region of fluid-filled fractures that provides a convective pathway from beyond ~3 km depth towards the surface; fluid from this anomaly likely mixes with cold meteoric waters in the last several hundred m before reaching the hot springs.

At Wind River Valley, evidence for fluid-filled fractures at depth is not well captured by the model because only seismic-event density was available. Flowing hot, warm, and cold springs throughout the region and abundant fault and fracture observations along the Wind River—many with small seeps or springs—provides some surface manifestations of fluid-filled fractures at depth. The presence of some seismicity along a northwest trend parallel to the Wind River fault suggests active fracturing of rock at depth.

Combined Geothermal Model and Exploration ‘Risk’

The three main models (heat, permeability, and fluid-filled fractures) were combined into final models at 200 m depth (Fig. 6) and 2 km depth (Fig. 7) that highlight regions with collocated high favorability. Because of differences in data availability, weights were determined individually—using AHP—for each study area (Table 18). This strategy allows favorability values to be compared somewhat equally across all of the study areas; that is, MSH-N is not more favorable than WRV simply because it has more data. Confidence values were combined in a similar way; MSH-N generally has higher confidence than WRV, reflecting the value of integrating multiple independent lines of evidence. Full-size confidence models are available in Appendix J. An exploration ‘risk’ model was developed for each study area and depth that scales the favorability by the confidence values (Figs. 8 and 9). Areas with low confidence have higher risk compared against high-confidence areas.

It is noteworthy that low measured temperature gradients are found largely in areas of low favorability and the highest temperature gradients (in WRV and MB) are found in areas

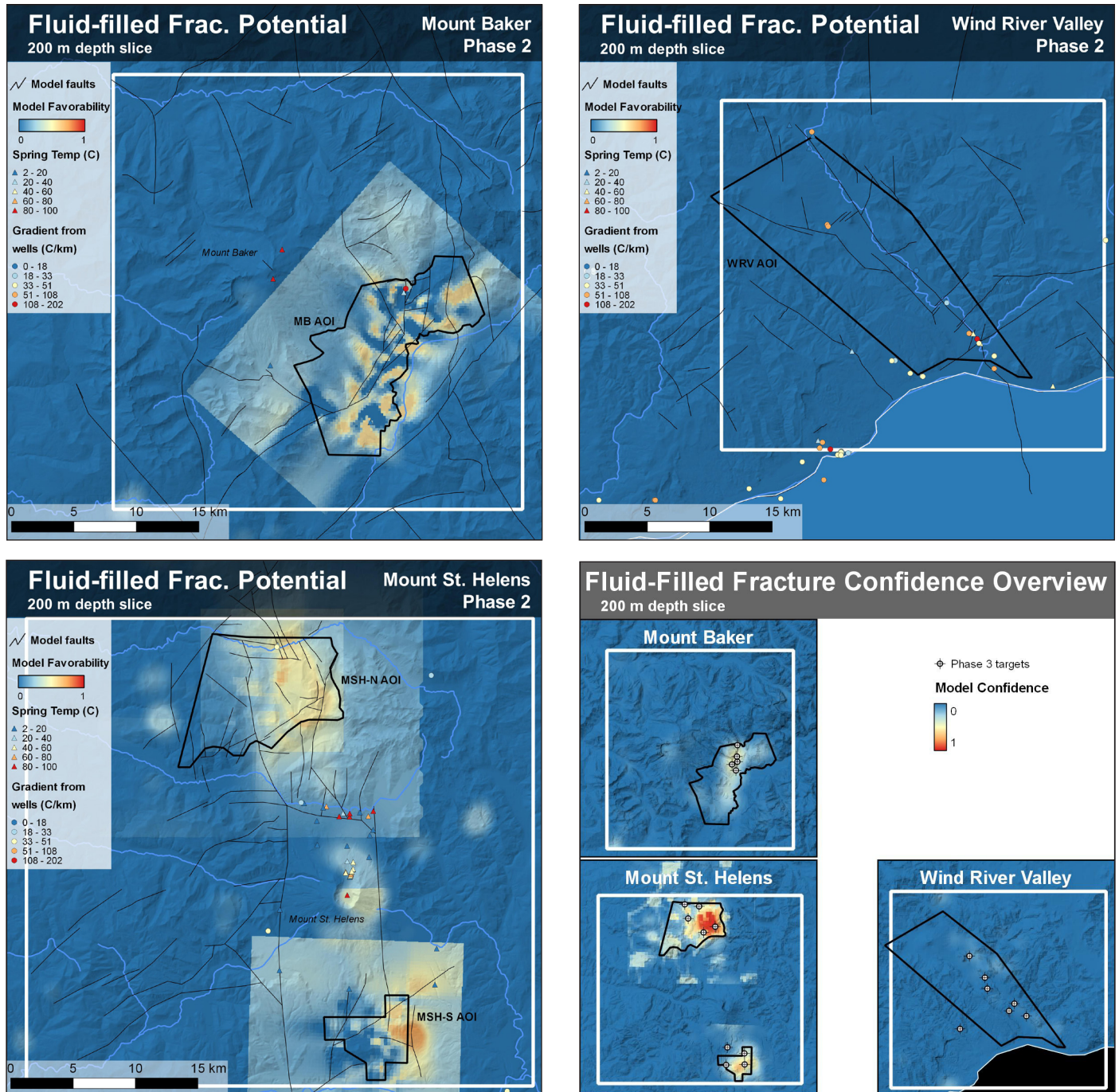


Figure 5. Phase 2 fluid-filled fracture potential at 200 m depth and overview of confidence. Data sets vary substantially between study areas and make comparisons between areas difficult. Potential models at 2 km depth are provided in Appendix I and confidence models are provided in Appendix J.

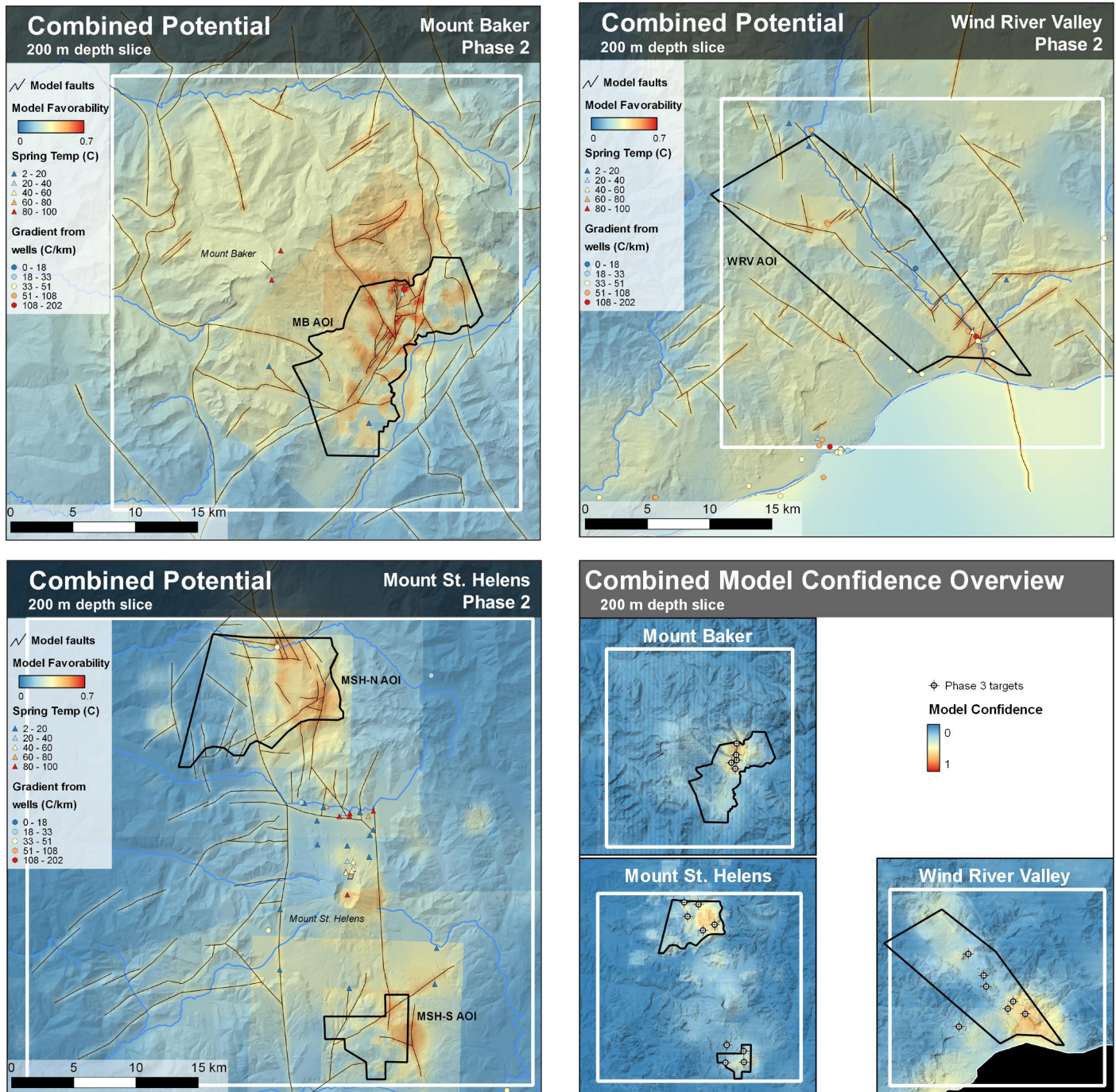


Figure 6. Phase 2 Combined favorability models at 200 m depth with overview of confidence. Full-size confidence models are provided in Appendix J.

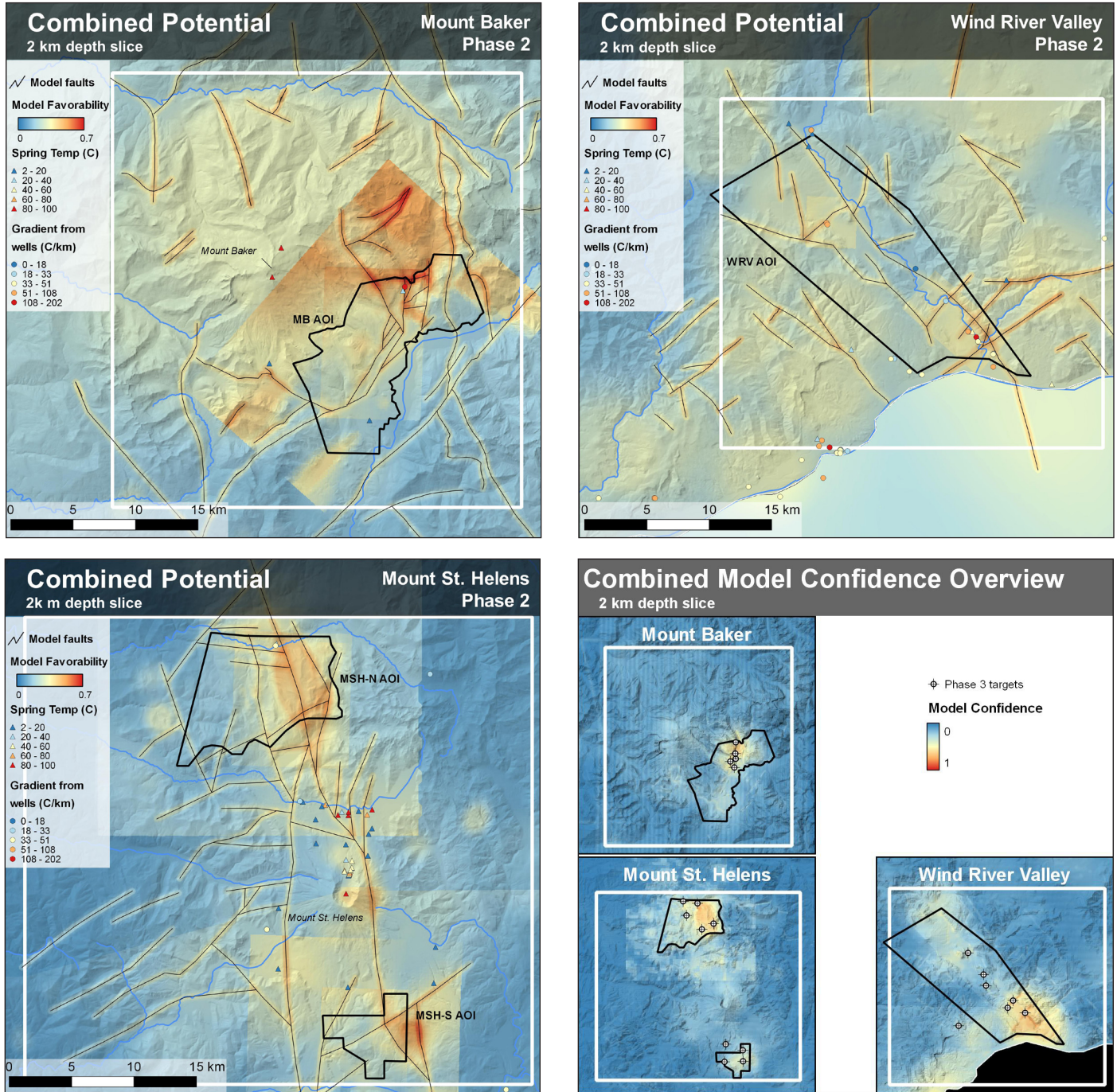


Figure 7. Phase 2 Combined favorability models at 2 km depth with overview of confidence. Full-size confidence models are provided in Appendix J.

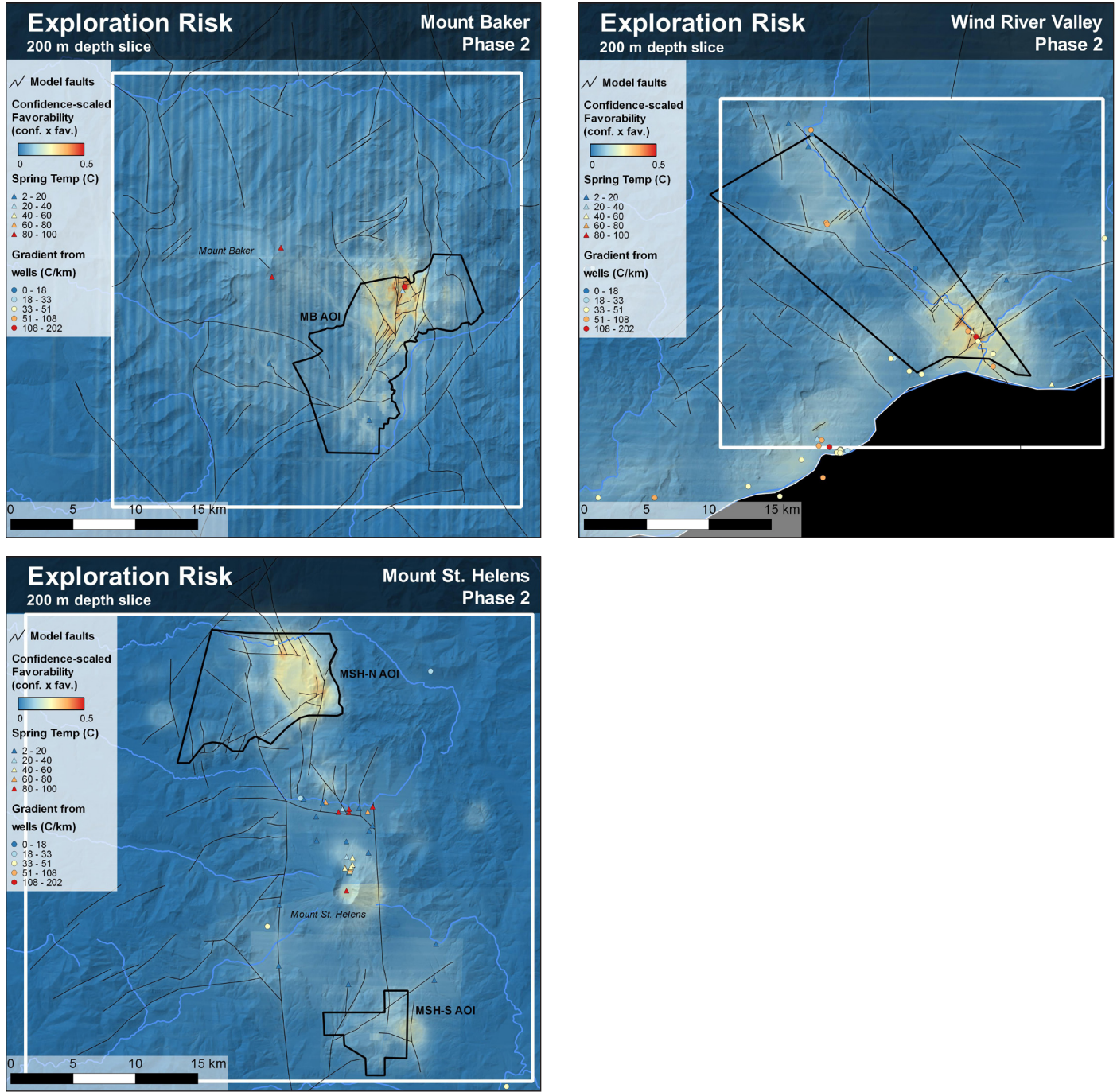


Figure 8. Exploration 'risk' models for all three study areas at 200 m depth.

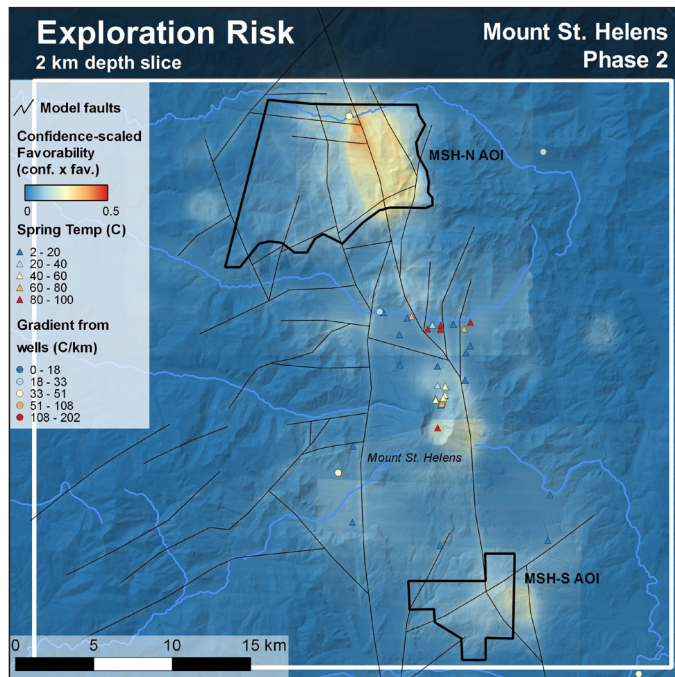
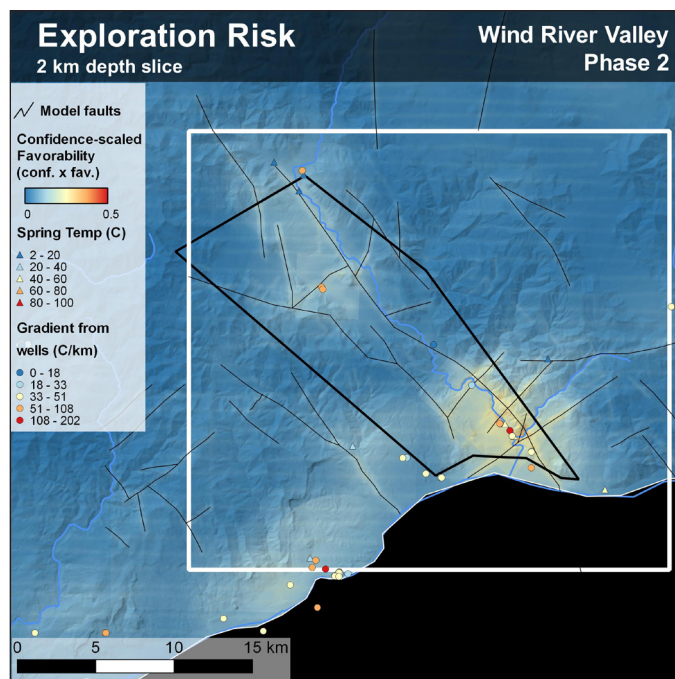
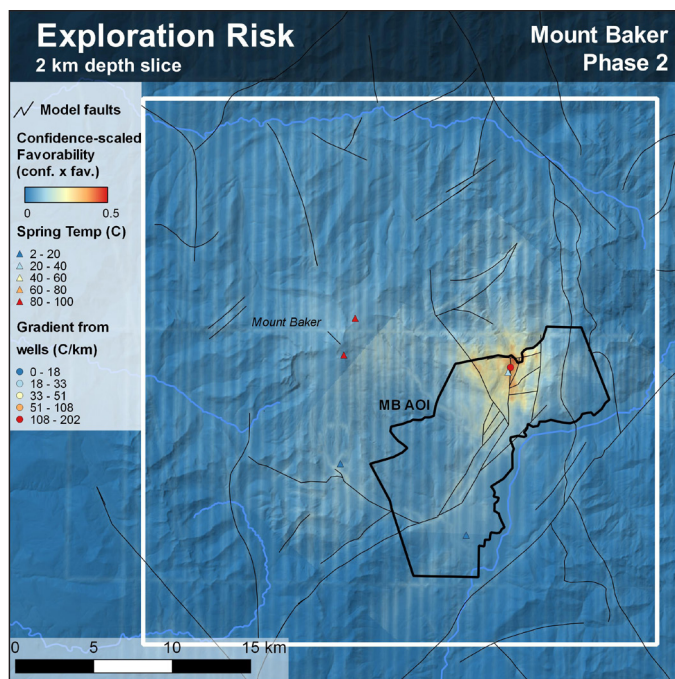


Figure 9. Exploration 'risk' models for all three study areas at 2 km depth (above and to left).

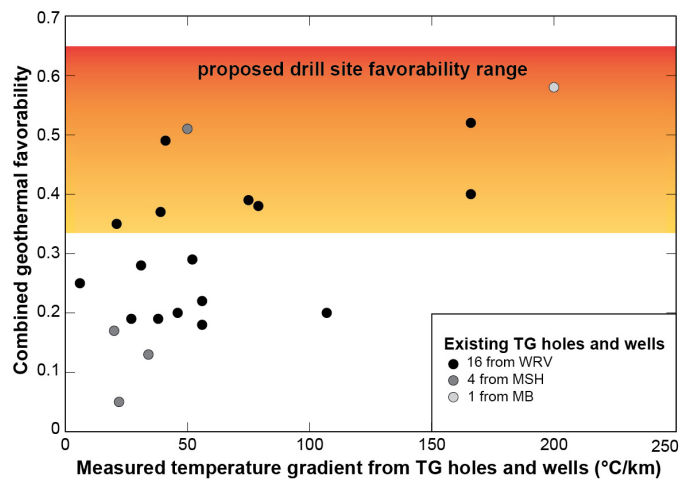


Figure 10. Correlation between combined model favorability and measured temperature gradients in all three study areas

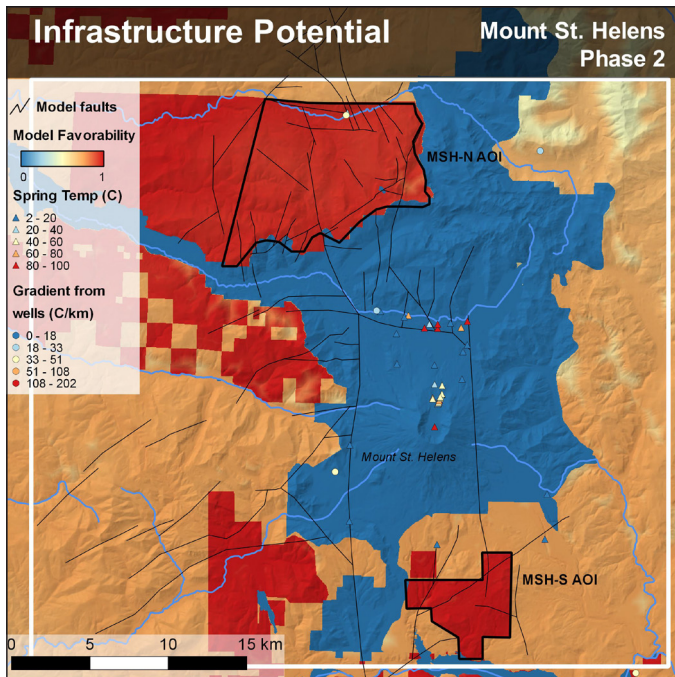
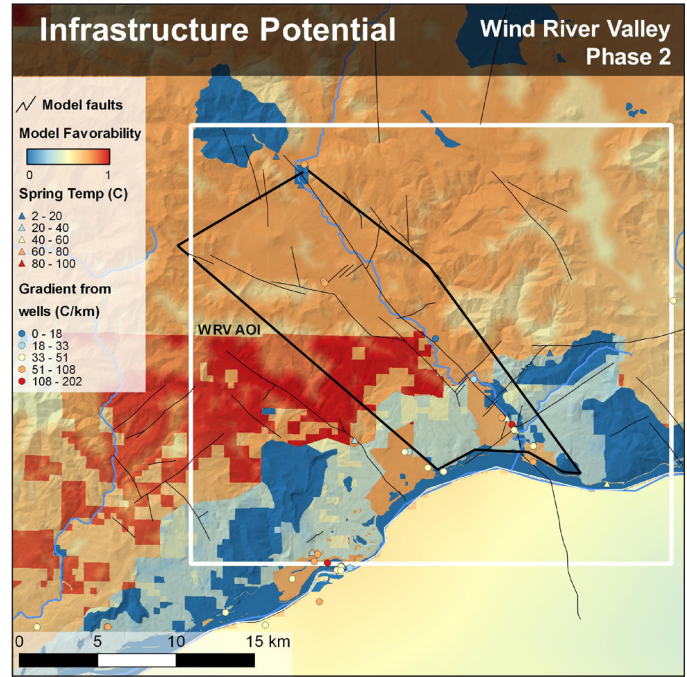
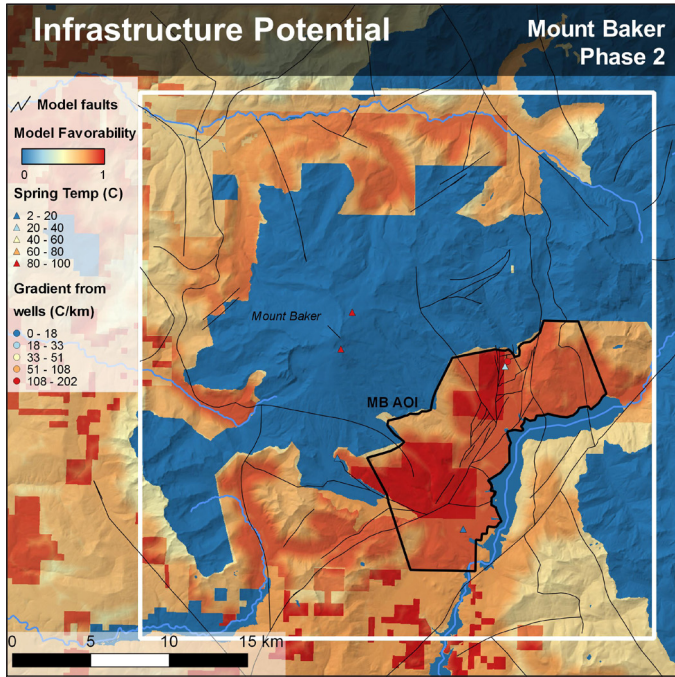


Figure 11. Infrastructure favorability for all three study areas (above and to left).

with the highest favorability (Fig. 10). Favorability values were compiled for all existing temperature-gradient measurements in the study areas as a simple way to assess the predictive power of the model. Although this approach lacks the independence (and high number of data points) of a true training/calibration study, autocorrelation between temperature-gradient measurements and the final model results is low because these data only contribute 4–7 percent towards the final model. A moderate positive correlation ($p=0.001$; $R^2=0.46$) is found but the lack of data near the center of the regression makes such an inference tentative.

Infrastructure

The infrastructure model formalizes many of the known constraints on the ability to successfully site, permit, and drill wells for a geothermal power plant. Model parameters and strategy are discussed in greater detail in the *Revised and New Modeling Methods* section. Model inputs are briefly described in Tables 8 and 17.

The results of this model clearly show areas that are off-limits to drilling and highlight the favorability of the Phase 2 AOIs (Fig. 11). National parks, monuments, and wilderness areas were the biggest off-limit areas; DNR-owned land and existing geothermal leases were the most-extensive favorable areas. Land-use restrictions along the Columbia River Gorge were substantial and are accounted for in this model. All of the areas are generally close to transmission lines; roads in the Mount Baker study area restrict the amount of developable area. All of the areas were located at significant distance from major urban centers, and high elevation was not a significant limiting factor. Process water was non-restrictive, with 2–3 m/yr precipitation and abundant streams and lakes.

PROPOSED VALIDATION ACTIVITIES

Overview

- Use Phase 2 results to guide Phase 3 validation activities
- Strategically drill several temperature-gradient holes (TGH) at high-favorability sites identified by the synthesis of multiple geophysical methods and geologic mapping
- Collect core from 1–3 sections within each TGH and analyze structures, lithology, and alteration; core will be stored for future use
- Perform detailed structural analysis near drill sites to validate permeability potential models
- Perform a method comparison using Washington data and the method developed by the USGS for the Snake River Plain PFA.
- Update geologic and conceptual models at each Area of Interest (AOI) with new drilling results
- Provide updated data layers, favorability/confidence models, and drilling results to promote geothermal development

Proposed Validation Activities

The goal of Phase 3 is to validate the favorability model developed during Phases 1 and 2 in order to reduce future exploration risk and encourage development. Strongly favorable results that confirm the Phase 2 model predictions will enable future developers to quickly implement the model in new areas and fast-track their development schedules. Strongly negative results will be cause for a re-assessment of the method. In both cases, the information gained from the proposed Phase 3 activities—especially temperature-gradient holes—is required to move this Play-Fairway Analysis method from an expert-guided synthesis of indirect, non-unique geophysical measurements to a validated, statistically significant, and executable geothermal exploration tool.

The approach outlined below seeks to provide the greatest amount of positive validation information with available budget constraints. A key component of the Phase 3 activities is to contextualize how either positive or negative results will help refine the model for each of the validation activities. For example, if a TGH with high combined favorability encounters significant hydrothermal alteration but low heat flow, it will be critical to evaluate all of the models, not just the one with the negative result. With this perspective, each validation activity provides meaningful information that will improve the final model regardless of whether the model predictions are met with favorable results.

TEMPERATURE-GRADIENT HOLES

Justification

Geothermal exploration in Washington State has lagged behind other regions due to low electricity prices, copious precipitation that masks thermal anomalies (and requires much-deeper TG holes than in desert areas), challenging topography, and unfamiliar play types. Starting in the 1980s temperature-gradient holes were drilled in all three of the Play-Fairway study areas. The anomalously high temperature gradients determined from those early wells—along with regional geology and tectonics—were instrumental in identifying these areas as geothermal prospects worthy of additional study. If these results were found in known geothermal resource areas (KGRAs), additional shallow drilling would have already occurred to map the extent and temperature of the geothermal resource, perhaps as a campaign of closely spaced shallow TG holes and (or) a regular grid of shallow temperature probes to map the extent of a shallow outflow zone (for example, Olmsted and others, 1975; Olmsted, 1977; Hill, 1979).

The geophysical and geological data collected during Phase 2 of this project provide a geothermal context to the prior TGH results. Further, the new data has allowed development of geothermal favorability maps which provide testable hypotheses regarding the heat sources, permeability, and occurrence of fluid-filled fractures that together constitute a viable geothermal system. Unfortunately, the geophysical datasets do not provide direct or unique evidence of geothermal resources at depth—the geophysical signals could be related to unexpected lithology, alteration, or structure. Testing the predictions of the favorability model is only possible through additional

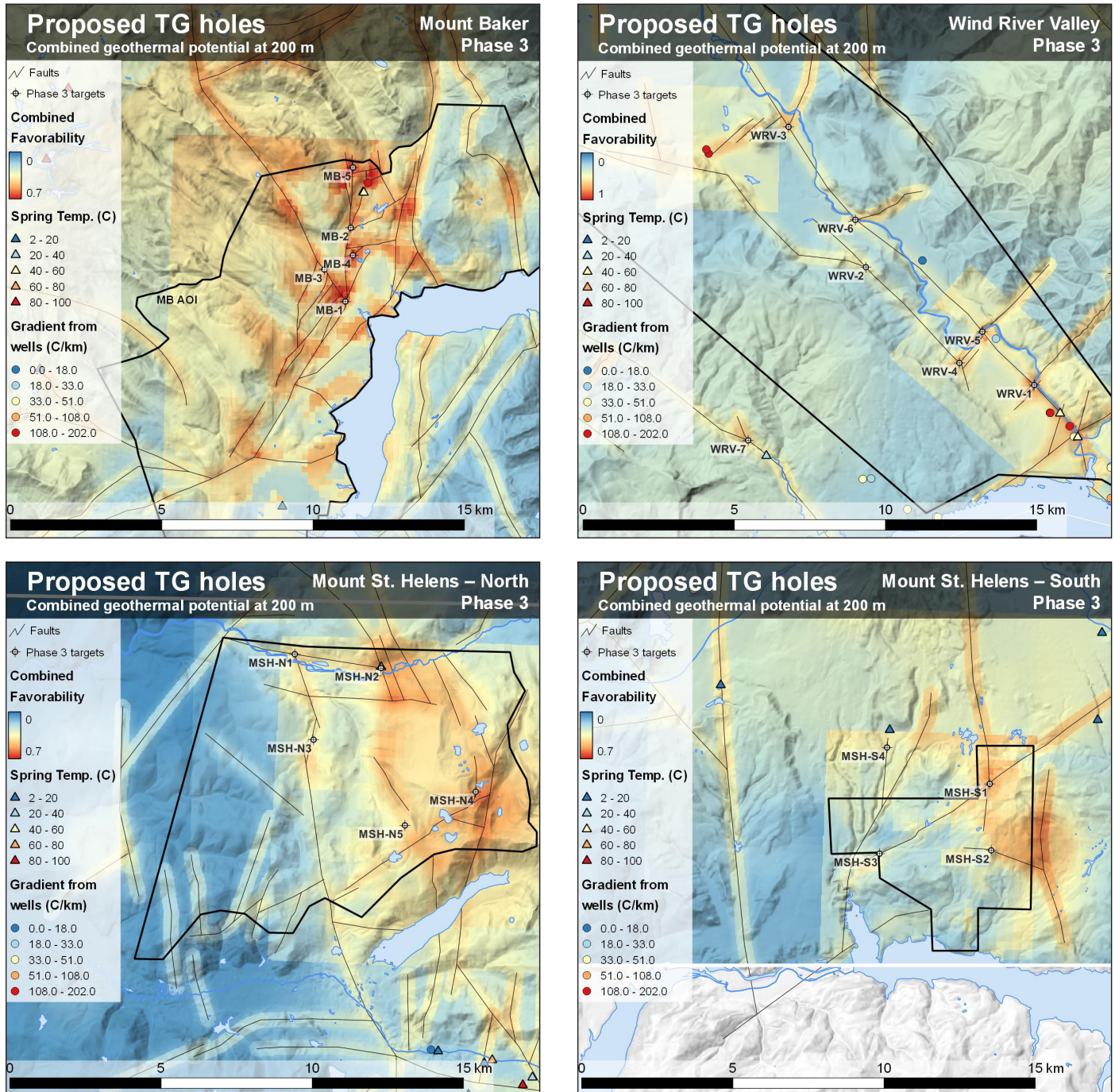


Figure 12. Proposed temperature-gradient holes (TGH) at the Mount Baker (upper left), Wind River Valley (upper right) and Mount St. Helens northern and southern AOIs (bottom). Maps show major faults at 200 m depth and favorability values from the combined geothermal model. Values are scaled to 0.7 which is the maximum value achieved in any of the three study areas.

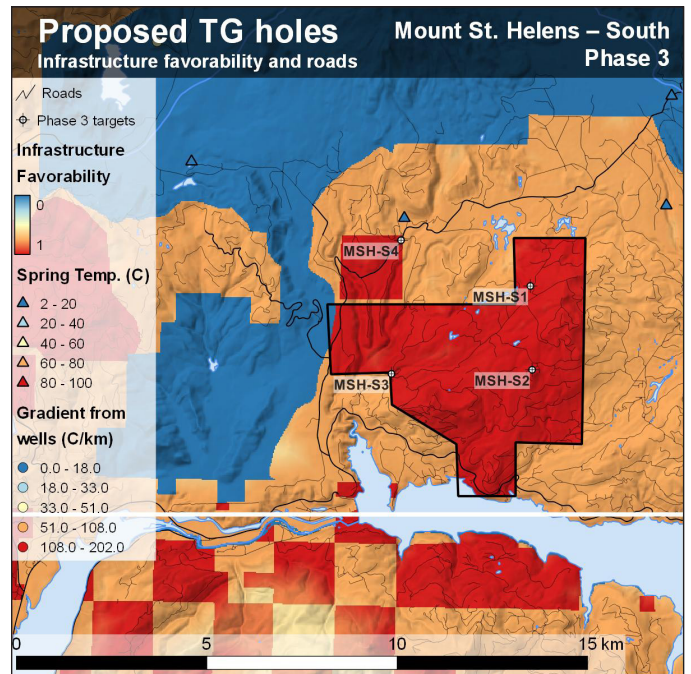
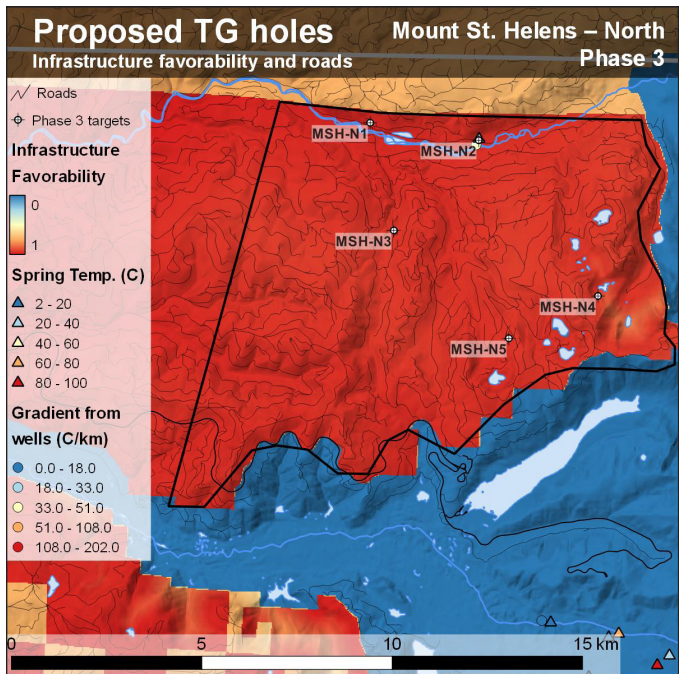
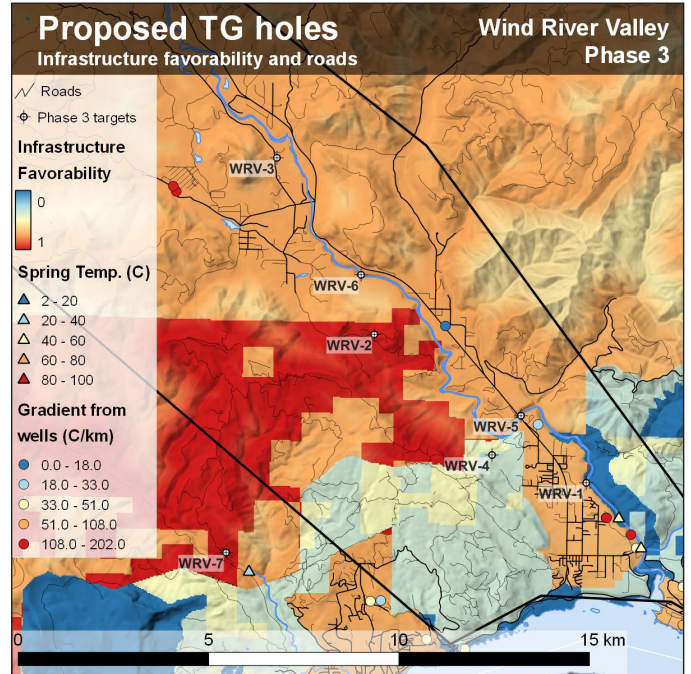
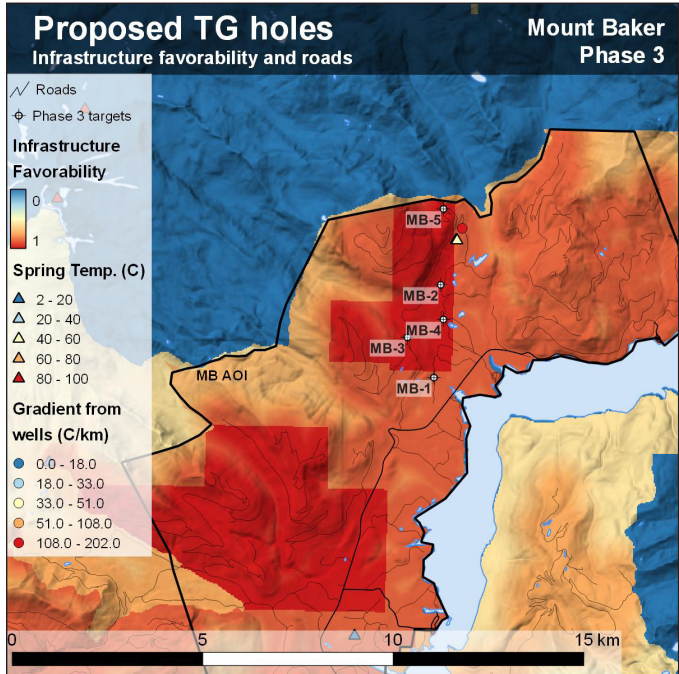


Figure 13. Proposed temperature-gradient holes (TGH) showing infrastructure model and major roads. Paved roads have a thicker line weight than gravel forest roads.

Table 20. Validation metrics for four aspects of temperature-gradient holes.

Metric	Strongly positive result	Moderately positive result	Negative result
Geothermal gradient in high-favorability location	>60°C/km	>30°C/km but <60°C/km	<30°C/km
Favorable convective cell	Convective cell >80°C	Above-regional conductive gradient	Cold meteoric convective cell only
Permeability (rough constraint)	Low flow-rate conductive zone above high flow-rate convective zone	Low flow-rate conductive zone	Low flow-rate meteoric convective zone only
Hydrothermal alteration	Mineral-filled fractures and altered matrix with structural/petrographic evidence of high temperatures and recency	Mineral-filled fractures and altered matrix	Little or no alteration

temperature-gradient drilling to determine where heat flow is anomalously high above convecting geothermal fluids.

Specific Proposed Actions

A total of 20 temperature-gradient-hole sites are proposed (Figs. 12 and 13; Table 19) with depths ranging from 700–1,600 ft; budgetary considerations will likely limit the possible number of TG holes to fewer than 7. The sites are specifically targeted to intersect areas of high conductive heat flow and (or) geothermal outflow based on the Phase 2 favorability, confidence, and risk models, and combined with additional expert analysis and synthesis of the subsurface and surficial datasets. Compared to a gridded TGH program with many holes, this targeted and cost-effective approach is necessarily focused on drilling in areas with a confluence of positive indicators that permeability and fluids are transporting heat to economic drilling depths.

More sites were selected and will be permitted than are possible to drill with the available budget. This approach is being used to reduce the likelihood that a site will not be drillable due to difficulties encountered during permitting, obtaining access to private land, or due to new information learned during nearby drilling. Each site is ranked by its combined model favorability (Table 19). It is fully expected that the actual drilling priorities will be revised during Phase 3 through discussions with project partners, stakeholders, and the DOE. State legislation passed in 2017 allows the consolidation of permits for TG holes, removes their depth limitation, and updates and streamlines the SEPA process.

Validation Metrics

Any data from a new TGH is of great value to Washington State and can be used to successfully update the model results. Specifically, the data can be used to evaluate four key aspects of a geothermal system at the drill site: (1) overall temperature gradient; (2) presence or absence of a hot convective (isothermal) cell; (3) an approximate constraint on permeability; and (4) evidence of hydrothermal alteration. A range of outcomes are considered in this context and listed in Table 20.

CORE ANALYSIS

Justification

The analysis of core from the deeper temperature-gradient wells is the only practical way to evaluate the predictions of the permeability model at depth during this stage of the

Table 19. Favorability ranking for proposed drill sites and comparison to nearby hot springs and temperature-gradient results.

Study area and drill site	Final combined favorability	Final combined confidence	Final 'risk' (conf x fav)
MB	MB-1	0.61	0.29
	MB-2	0.50	0.33
	MB-3	0.46	0.28
	MB-4	0.64	0.35
	MB-5	0.64	0.35
	Mount Baker Hot Springs (44 °C)	0.48	0.33
	DNR83-3 TGH (200 °C/km)	0.62	0.39
MSH North	MSHN-1	0.41	0.11
	MSHN-2	0.52	0.21
	MSHN-3	0.36	0.10
	MSHN-4	0.55	0.34
	MSHN-5	0.41	0.18
	DNR83-1 TGH (50 °C/km)	0.52	0.21
MSH South	MSHS-1	0.51	0.14
	MSHS-2	0.43	0.13
	MSHS-3	0.33	0.09
	MSHS-4	0.36	0.09
WRV	WRV-1	0.51	0.38
	WRV-2	0.33	0.09
	WRV-3	0.44	0.15
	WRV-4	0.49	0.23
	WRV-5	0.40	0.26
	WRV-6	0.39	0.09
	WRV-7	0.40	0.12
TGH at Shipherds Hot Spring (161 °C/km)	0.50	0.38	
TGH at St. Martin Hot Spring (166 °C/km)	0.55	0.37	

Table 21. Core-analysis activities and goals.

Activity	Data Goal	Purpose/Test
Core: structural mapping	Fracture type, aperture, density, and attitude. Petal-centerline fractures to constrain stress state.	Test compatibility with predictions of near-surface local stress model and maximum coulomb stress
Core: thin-section and XRD mineralogy, XRF elemental chemistry	Alteration and paragenetic history of the rock and fracture filling	Validate role of fractures in subsurface flow. Identify upflow/downflow zones and role of matrix porosity

development process. Core analysis also augments the detailed and spatially robust surface data. Collecting core while drilling is a cost-effective and useful means of evaluating the predictions of the Phase 2 permeability model in the subsurface by identifying fracture density and aperture, mineral fillings and alteration, and measurements of matrix permeability, thermal conductivity, and identification of open or filled fractures that could serve—or have served—as fluid-flow pathways.

Specific Proposed Actions

Two main aspects of core analysis are considered: (1) detailed micro-structural mapping of core, and (2) petrological thin sections with chemical analyses (Table 21). After completion of Phase 3 activities, a core-storage facility operated by the Washington Geological Survey will preserve the core and samples of cuttings for future study. The core and cuttings will be made available to researchers outside of the current Phase 3 group, provided that they propose analyses that are deemed useful by the current group and the materials are judiciously used.

Validation Metrics

By collecting and analyzing cores that were obtained where favorable conditions were identified from modeling in Phase 2 we hope to validate that there are abundant fractures in the subsurface and to test compatibility with predictions of the near-surface local stress model and maximum coulomb stress.

STRUCTURAL ASSESSMENT OF PERMEABILITY POTENTIAL MODEL

Justification

The permeability potential model uses the geometry of large active faults and the remote stress/strain conditions that drive slip to predict conditions that promote: (1) dilatancy in the fault zone conducive to sustaining a vertically extensive permeable conduit, and (2) extensive volumes of active smaller faults and

fractures that can kinematically maintain large volumes of reservoir porosity and permeability.

Validation and iterative improvement of this model can be achieved through detailed structural analysis in the field. Abundant natural outcrops—as well as quarries and road cuts—allow the detailed characterization of fault zone structures and fault-related damage. The type, attitude, and kinematics of these structures, along with evidence for their role in fluid flow from mineralization and alteration, can be used to test the predictions of the permeability potential model. Which faults are included in the geomechanical models depend on their size and likelihood of activity, either from their attitude in the stress/strain field, or from direct evidence such as seismicity. Improved understanding of recent slip on outcropping faults may also be revealed by its impact on the landscape evident in additional lidar analysis verified by fieldwork.

Within active fault zones, fractures exhibiting dilatancy indicate conduit/reservoir potential whereas the lack of dilatancy is consistent caprock behavior. This distinction is further bolstered by mineralization along the fracture where minerals such as quartz/chalcedony/opal are consistent with upwelling fluids and calcite with descending recharge fluids; extensive alteration of the fractured wall rock and formation of clays indicates caprock development. Alteration of these types has already been identified in at least one of the play areas (Czajkowski and others, 2014), where permeability structure evolution can be further determined from laboratory analysis of field samples (Fetterman and Davatzes, 2011)(Table 22).

Importantly, both the conceptual basis for the permeability potential models—and their predictions—will be refined in light of these new data. Specifically, formal sensitivity analyses can be carried out to characterize the variability in model predictions due to uncertainty in fault geometry, mechanical properties, and remote boundary conditions. Additional cross-validations can be performed between the maximum coulomb stress and Phase 2 MT and seismic tomography

Table 22. Structural assessment activities and goals.

Activity	Data Goal	Purpose/Test
Lidar, augmented analysis and gradient mapping	Attitude and distribution of small faults mechanically interacting with larger faults; Geomorphic indicators of fault kinematics and evidence for recent fault activity (tectonic geomorphology)	Test compatibility with predictions of near-surface local stress model and maximum coulomb stress; Determine which faults should be included/excluded during geomechanical modeling
Outcrop mapping	Fault zone kinematics; Verify lidar interpretations	Test compatibility with predictions of near-surface local stress model and maximum coulomb stress
Outcrop sampling: Thin-section and XRD mineralogy, XRF elemental chemistry	Alteration and paragenetic history of the rock and fracture filling	Test role of faults/fractures as conduits and comparison to modeled slip and dilation tendency and slip gradients

which are non-uniquely sensitive to the distribution of porous, saturated, hot volumes of rock in the subsurface.

Specific Proposed Actions

A structural geology and field-based permeability survey at or close to the drill site is a non-drilling validation method that can evaluate the predictions of the Phase 2 permeability model (for example, Davatzes and others, 2005). This survey consists of four main tasks: (1) detailed structural mapping of fault zone characteristics to guide numerical simulations of fault slip and stress perturbation; (2) detailed fault maps and fracture patterns to validate the permeability model; (3) analysis of existing borehole data to improve constraints on rock mechanical properties, stress state, and fracture populations, and; (4) detailed analysis of lidar lineaments identified in Phase 2 (Table 22).

Validation Metrics

Successful validation will be measured by completion of a detailed structural analysis in the areas surrounding drill sites and a comparison to the favorability model from Phase 2. The analysis will result in a detailed structural map, revised lidar interpretation, outcrop sample analysis and alteration mineralogy, and a write-up of the results. The findings will then be compared to the favorability models, core samples, and results of drilling at the site.

PFA METHOD COMPARISON

Specific Proposed Actions

An independent assessment of the Washington PFA method will be undertaken by Jacob DeAngelo from the USGS using the methods developed for the Snake River Plain (SRP) PFA. This method involves using an automated series of processing steps for handling the data layers in the study. After an initial discussion of data types it was determined that the SRP method should be able to incorporate most, if not all, of the data examined by the Washington group. It was also determined that the weighting coefficients developed by the Washington PFA could be incorporated, as could most or all of the data relating to confidence mapping.

Justification

An independent assessment of the Washington PFA data using a different method provides an excellent opportunity to help validate both modeling approaches. Any major differences observed using the two approaches may reveal insights as to relative strengths or weaknesses of the respective approaches. New insights from TG holes can provide a direct test of the relative predictive strength of the two schemes. Furthermore, this provides an opportunity to test the ability of the SRP method to consume datasets from a different play.

Validation Metrics

Because the SRP method is built on a framework that was developed in a region of numerous benchmarks (DeAngelo and others, 2016), areas of agreement between the two models will highlight aspects of the two methods that are more likely

to predict a successful geothermal resource. Areas of disagreement will highlight aspects that either or both methods can improve upon.

Method Re-evaluation and Improvement

The results of all Phase 3 activities will be used to update and refine the Play-Fairway Analysis method. The goal of improving the model is so that Phase 3 model favorability will be a better predictor of high geothermal gradients and permeability pathways than the Phase 2 model. A comparison between Phase 2 and Phase 3 model results will highlight the model improvements and provide refined targets for future exploration and development. Most importantly, validation and refinement of the method will provide confidence in the approach that will allow it to be quickly scaled up and used in other locations throughout Washington State to aid in initial exploration of geothermal resources.

Permitting Pathway and Known Constraints

The permitting pathway and restricted timeline for completing temperature-gradient holes is the largest logistical challenge for any Phase 3 proposal. We are confident that there is a clear and robust path towards the successful permitting and drilling of at least 7 of the 20 proposed sites. Table 23 compiles the permitting logistics, land ownership, and drilling details for each of the proposed sites; Tables 19 and 23 serve as the decision-making framework moving forward.

In Washington State, there are at least 9 components to a successful temperature-gradient hole. Each is listed below along with a brief summary of the issue.

Drilling permit—This permit is issued by the regulatory component of our parent agency (DNR). We are well aware of the necessary forms and procedures and are confident that the necessary permits will be issued so long as all required aspects of the permit are properly planned and executed.

NEPA—For all sites on DNR- or privately-owned land, the DOE and DNR are the administrative authorities; on all others, the U.S. Forest Service (USFS) and DNR. We have talked with our contacts at DNR and the State Archaeologist who works with DOE on NEPA to alert them of this proposal; they have the preliminary drill sites and will be able to review them as soon as the funding decision is made.

SEPA—Only sites on DNR- or privately-owned land must obtain SEPA approval. The SEPA contacts at DNR have informed us that they can adopt the NEPA findings or do a programmatic SEPA for all of the drilling targets.

Access—The ability to access the drill site is of considerable importance. The proposed sites are preferentially focused on private timber land (Weyerhaeuser Corp., The Agnew Company, and Pacific Corp.) with existing geothermal leases (AltaRock Energy), National Forest land with an existing geothermal lease (Cyrq Energy) and DNR-owned land; private land without geothermal leases is the least favored ownership type.

Private timber land—All but one site at MSH are in this category. We have worked closely with the two major land-owners in the past and have secured a letter of support from

Table 23. Proposed drill sites, land status, permitting information, and other logistics.

Study area and drill site	Target TD	Land owners	Geothermal lease holder	Letters of support	Timeline	NEPA	SEPA	Permit to drill	Driller	
MB	MB-1	1,600 ft	USFS	Cyrq Energy	Yes: Mount Baker–Snoqualmie National Forest District Ranger, and Snohomish County Public Utilities District	July or August 2018	USFS/ DNR	Adopt NEPA or 1 SEPA for all targets	Yes; DNR	USGS
	MB-2	1,600 ft	USFS			July or August 2018	USFS/ DNR	Adopt NEPA or 1 SEPA for all targets	Yes; DNR	USGS
	MB-3	1,600 ft	USFS			July or August 2018	USFS/ DNR	Adopt NEPA or 1 SEPA for all targets	Yes; DNR	USGS
	MB-4	1,600 ft	USFS			July or August 2018	USFS/ DNR	Adopt NEPA or 1 SEPA for all targets	Yes; DNR	USGS
	MB-5	1,600 ft	USFS			July or August 2018	USFS/ DNR	Adopt NEPA or 1 SEPA for all targets	Yes; DNR	USGS
MSH North	MSHN-1	700 ft	Weyerhaeuser and The Agnew Company	AltaRock Energy Inc.	Yes: Weyerhaeuser verbal from The Agnew Company	July 2018	DOE/ DNR	Adopt NEPA or 1 SEPA for all targets	Yes; DNR	USGS
	MSHN-2	1,600 ft	Weyerhaeuser and The Agnew Company			July 2018	DOE/ DNR	Adopt NEPA or 1 SEPA for all targets	Yes; DNR	USGS
	MSHN-3	700 ft	Weyerhaeuser and The Agnew Company			July 2018	DOE/ DNR	Adopt NEPA or 1 SEPA for all targets	Yes; DNR	USGS
	MSHN-4	1,600 ft	Weyerhaeuser and The Agnew Company			July 2018	DOE/ DNR	Adopt NEPA or 1 SEPA for all targets	Yes; DNR	USGS
MSH South	MSHS-1	1,600 ft	Pacific Corp	AltaRock Energy Inc.	Verbal	June or July 2018	DOE/ DNR	Adopt NEPA or 1 SEPA for all targets	Yes; DNR	USGS
	MSHS-2	1,600 ft	Pacific Corp			June or July 2018	DOE/ DNR	Adopt NEPA or 1 SEPA for all targets	Yes; DNR	USGS
	MSHS-3	1,600 ft	Pacific Corp			June or July 2018	DOE/ DNR	Adopt NEPA or 1 SEPA for all targets	Yes; DNR	USGS
	MSHS-4	1,600 ft	DNR			DNR	Yes	June or July 2018	DOE/ DNR	Adopt NEPA or 1 SEPA for all targets
WRV	WRV-1	1,600 ft	Wilkins—commercial Timber	---	Not yet	June or July 2018	DOE/ DNR	Adopt NEPA or 1 SEPA for all targets	Yes; DNR	USGS
	WRV-2	1,600 ft	DNR	DNR	Yes	June or July 2018	DOE/ DNR	Adopt NEPA or 1 SEPA for all targets	Yes; DNR	USGS
	WRV-3	1,600 ft	Hollis—private	---	Not yet	June or July 2018	DOE/ DNR	Adopt NEPA or 1 SEPA for all targets	Yes; DNR	USGS
	WRV-4	1,600 ft	Birkenfeld—private	---	Not yet	June or July 2018	DOE/ DNR	Adopt NEPA or 1 SEPA for all targets	Yes; DNR	USGS
	WRV-5	1,600 ft	Skamania County	---	Not yet	June or July 2018	DOE/ DNR	Adopt NEPA or 1 SEPA for all targets	Yes; DNR	USGS
	WRV-6	1,600 ft	USFS	---	Not yet	June or July 2018	DOE/ DNR	Adopt NEPA or 1 SEPA for all targets	Yes; DNR	USGS
	WRV-7	1,600 ft	DNR	DNR	Yes	June or July 2018	DOE/ DNR	Adopt NEPA or 1 SEPA for all targets	Yes; DNR	USGS

Weyerhaeuser (Appendix K) and verbal support from Pacific Corp. and The Agnew Company. Our industry partner in this project is AltaRock and they support the drilling targets on their geothermal leases.

National Forest land—All sites at MB are in this category. We have been in close contact with the USFS Geologist and Ranger who supervise permitted activities in the region and they are planning on including this project in the upcoming year's list of permitted activities (see letters of support in Appendix K). In addition, AltaRock has a master services agreement with Cyrq Energy, the current geothermal lease holder at MB, to manage all of Cyrq's geothermal resources, including operating power plants and geothermal prospects.

Cyrq acquired the leases from Gradient Resources and continues to pay the annual fees.

DNR-managed land—Two sites at WRV and one site at MSH-S are in this category. We have worked closely with the Leasing and Product Sales team at DNR to ensure that there are no obstacles to drilling a TGH on DNR-managed lands. See letter of support in Appendix K.

Private land—Five sites at WRV are in this category. We have worked closely with at least one of the private landowners in the past (most-favorable site, WRV-5) and believe that we will be able to successfully secure access again. We have recently contacted the remaining landowners and have not yet received responses back. Although many locals in the area are

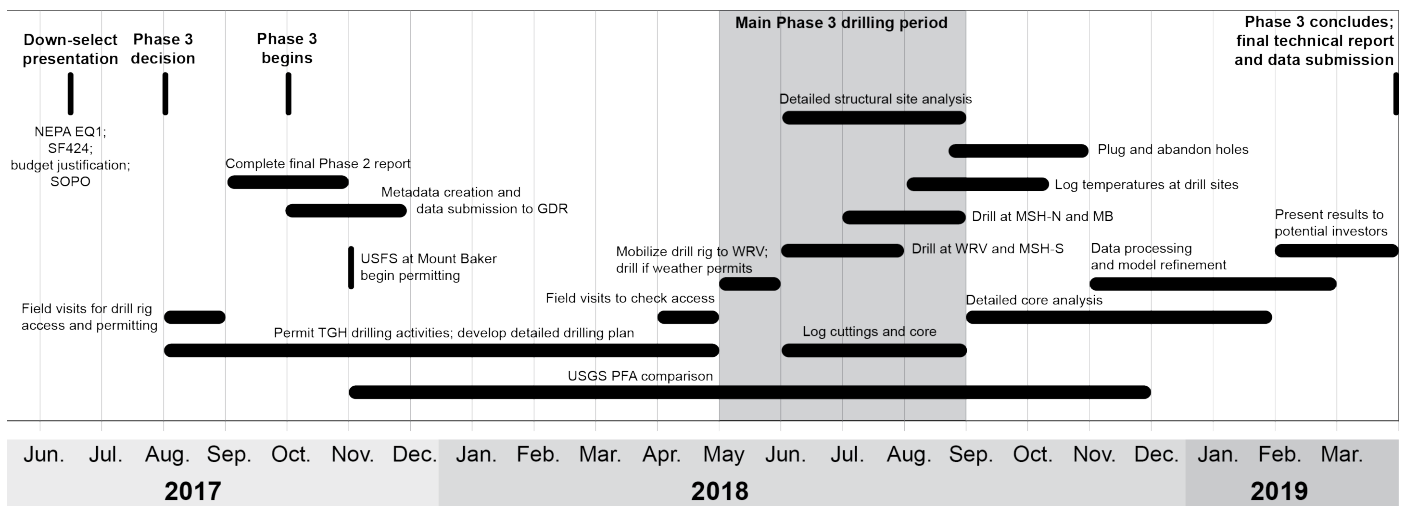


Figure 14. Timeline for conclusion of Phase 2 and proposed validation activities.

in favor of geothermal development, we consider these targets as the most at-risk for land-access issues.

Weather restrictions—Drilling is possible at low-elevation sites such as Wind River for much of the year; high-elevation sites at MSH (two of the sites) are the most restrictive and may only be available from late May/early June through early November. Sites at low elevation in MSH and at MB are likely available from April through late November.

Environmental restrictions—Several listed species occur in Washington State and there can be time-of-day, seasonal, and location restrictions that apply. These restriction are largely mitigatable and are determined in the SEPA/NEPA process. The drill targets are all located on the shoulders or dead ends of gravel logging roads or forest service roads where drilling will not disturb any sensitive areas. Multiple backup drill sites have been proposed as a contingency in case the top-rated sites have a cultural or wildlife issue.

Well-depth restrictions—The regulation that controls the geothermal permitting process for TG well drilling in Washington was recently amended and streamlined: a public comment requirement was eliminated; one application for multiple wells is now allowed; and a previous 750-ft depth restriction was removed.

Available and capable drillers—We have been working with the head of the USGS drilling program in Las Vegas (Steve Crawford) to develop a plan for using USGS drill rigs and operators. Additionally, Tacoma Pump and Drilling is a local operator that was the preferred driller for AltaRock at the Newberry geothermal site and drilled shot-holes for the iMUSH project around Mount. St. Helens in 2015; they are capable of serving as a backup operator if the USGS is unable to provide drilling support.

Successful plug and abandonment—Each of the sites has a plan to plug and abandon the well and this task is in the budget and timeline.

Phase 3 Timeline

The timeline shown in Figure 14 provides a clear path towards successful drilling and completion of all proposed Phase 3 activities within the 18-month performance period. Permitting

will begin as soon as a Phase 3 award decision is made; all of the permitting agencies are well aware of the proposed activities. Major drilling operations will occur from May to September of 2018; data logging and hole abandonment will occur into the early fall. Detailed core analysis will occur after structural characterization of the drill sites. The method comparison will begin shortly after submission of the Phase 2 data to the Geothermal Data Repository (GDR). The Play-Fairway Analysis method will be updated once new data is available and a report, updated model, and all new data will be submitted at the conclusion of the Phase 3 performance period.

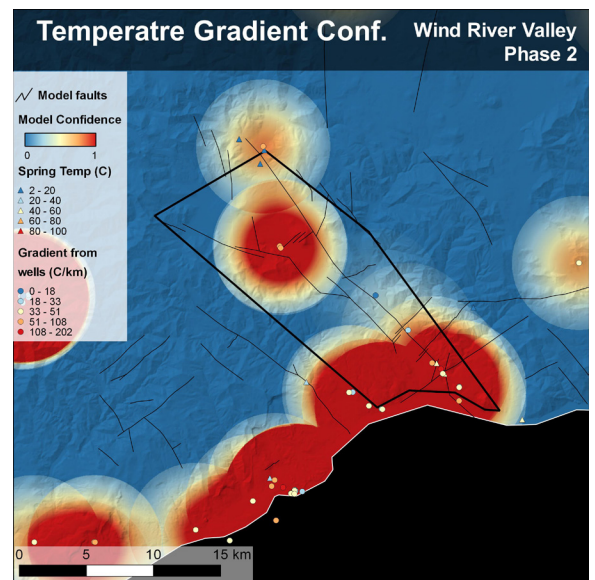
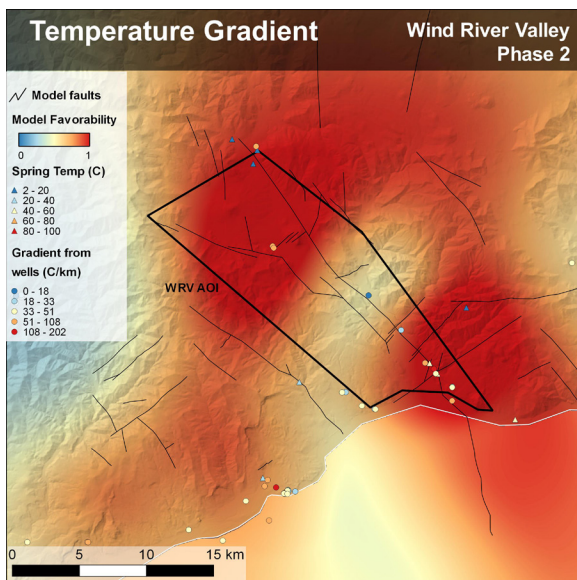
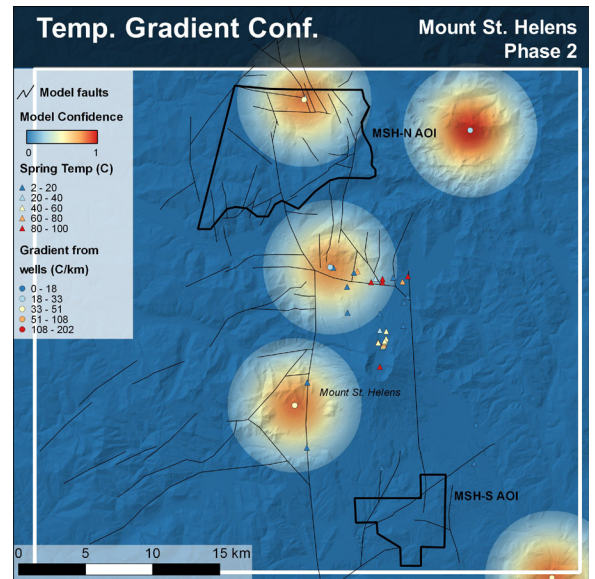
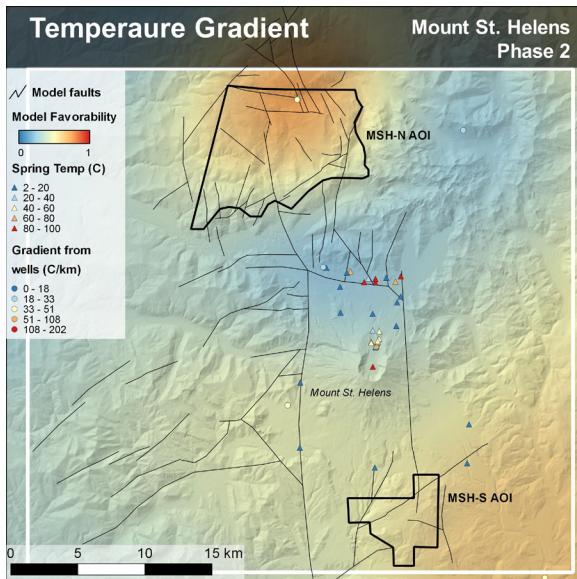
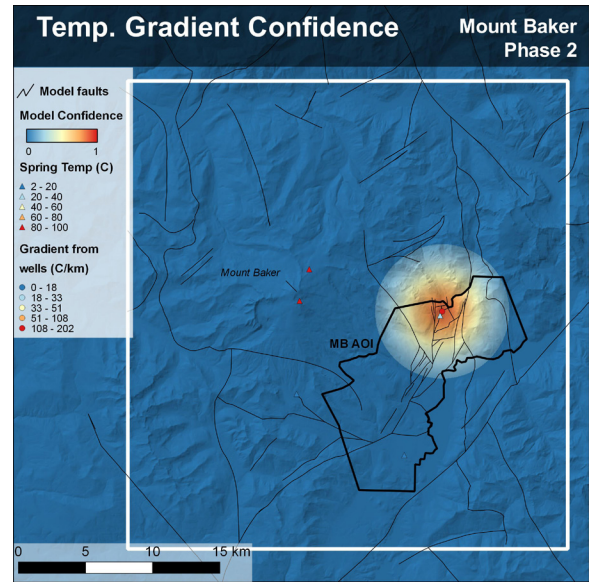
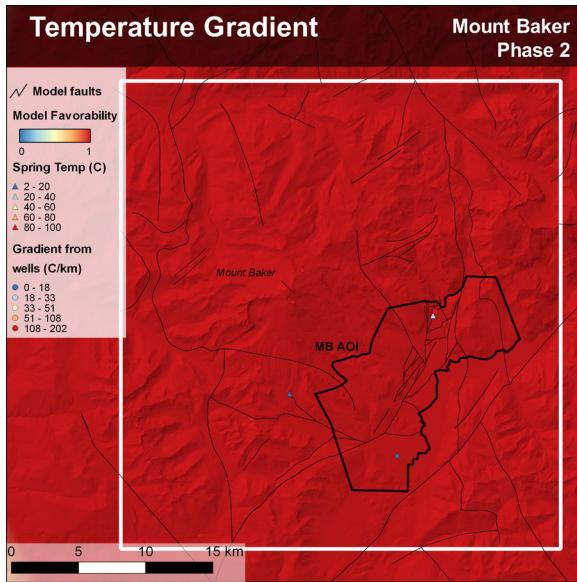
REFERENCES

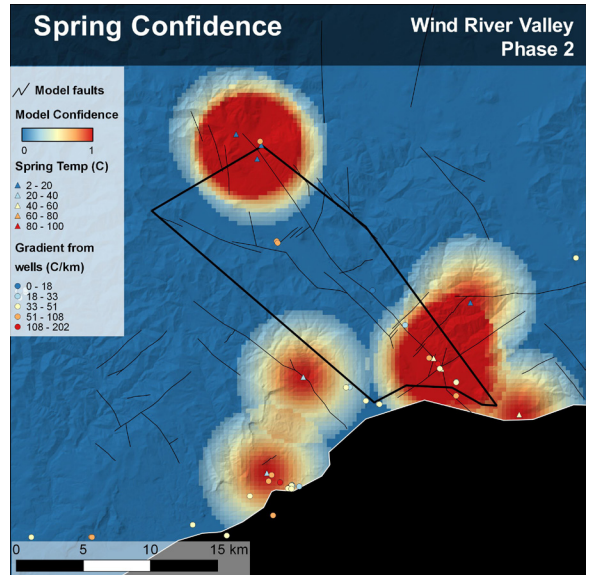
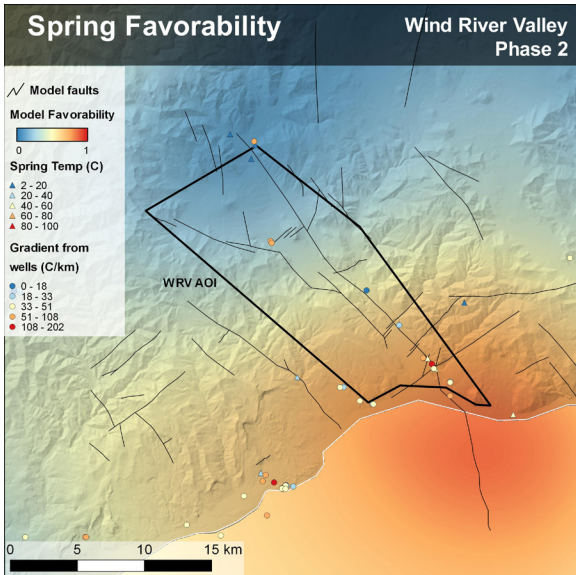
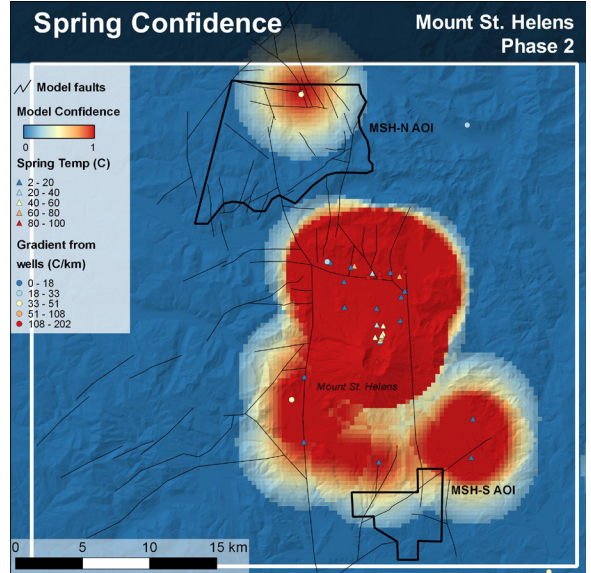
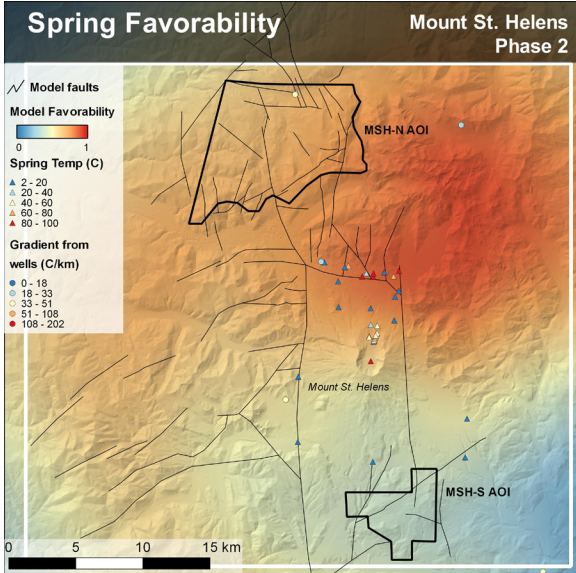
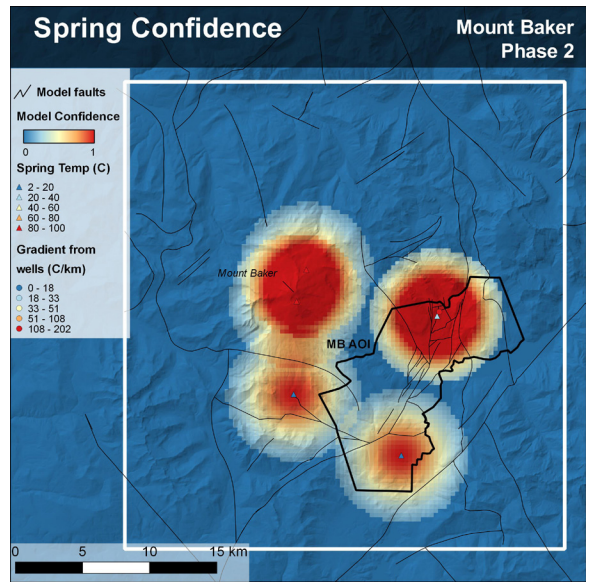
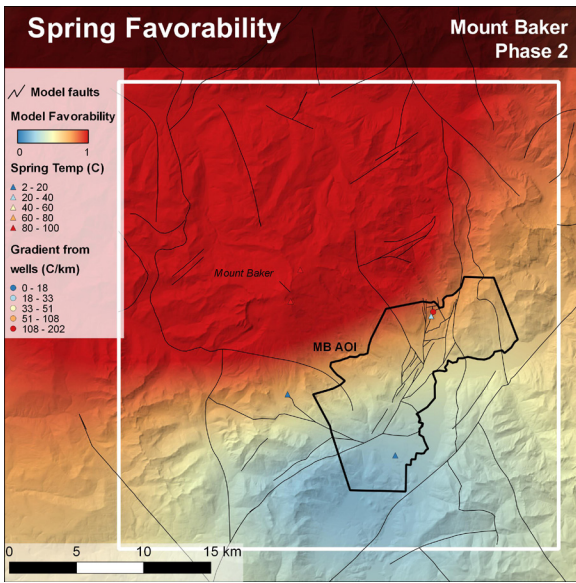
- Boschmann, D. E.; Czajkowski, J. L.; Bowman, J. D., 2014, Geothermal favorability model of Washington State: Washington Division of Geology and Earth Resources Open File Report 2014-02, 1 plate, scale 1:900,000, 20 p. [http://www.dnr.wa.gov/publications/ger_ofr2014-02_geothermal_favorability.pdf]
- Bucknam, R. C.; Hemphill-Haley, E.; Leopold, E. B., 1992, Abrupt uplift within the past 1700 years at southern Puget Sound, Washington: Science, v. 258, no. 5088, p. 1611-1614.
- Carranza, E. J. M.; Wibowo, H.; Barritt, S. D.; Sumintadireja, P., 2008, Spatial data analysis and integration for regional-scale geothermal potential mapping, West Java, Indonesia: Geothermics, v. 37, no. 3, p. 267-299.
- Crider, J. G.; Frank, D.; Malone, S. D.; Poland, M. P.; Werner, C.; Caplan-Auerbach, J., 2011, Magma at depth: a retrospective analysis of the 1975 unrest at Mount Baker, Washington, USA: Bulletin of Volcanology, v. 73, p. 175-189.
- Curewitz, D. and Karson, J. A., 1997, Structural settings of hydrothermal outflow—fracture permeability maintained by fault propagation and interaction: Journal of Volcanology and Geothermal Research, v. 79 p. 149-168.
- Czajkowski, J. L.; Bowman, J. D.; Fusso, L. A.; Boschmann, D. E., 2013, Geologic mapping and geothermal assessment of the Wind River Valley, Skamania County, Washington: Washington Division of Geology and Earth Resources Open File Report 2014-01, 30 p., 1 plate, scale 1:24,000.
- Davatzes, N. C.; Eichhubl, Peter; Aydin, Atilla, 2005, Structural evolution of fault zones in sandstone by multiple deformation mechanisms: Moab fault, southeast Utah: GSA Bulletin, v. 117, no. 1-2, p. 135-148.

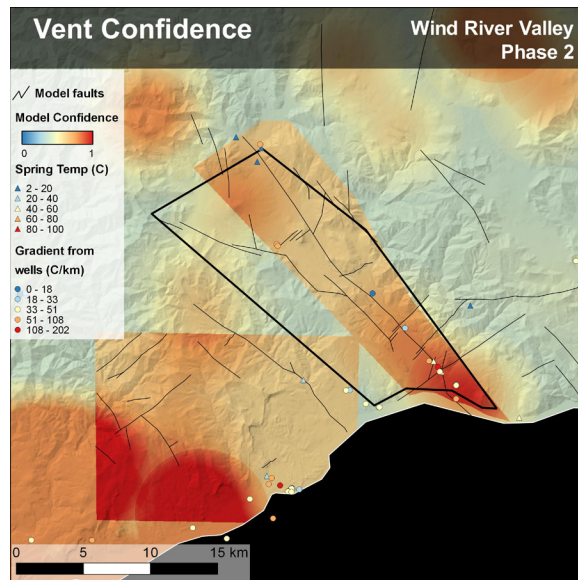
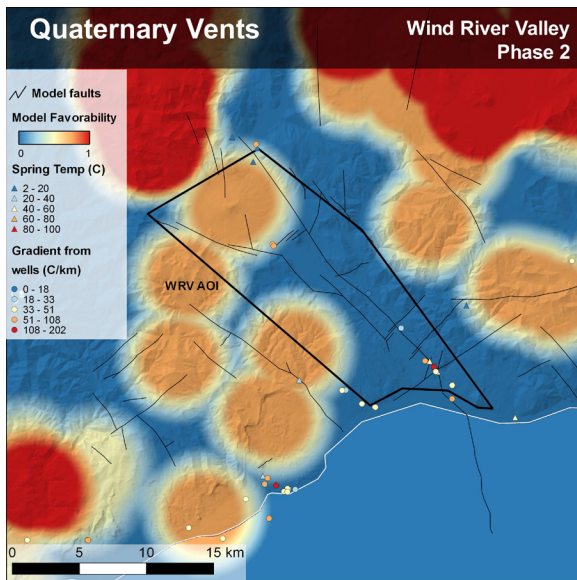
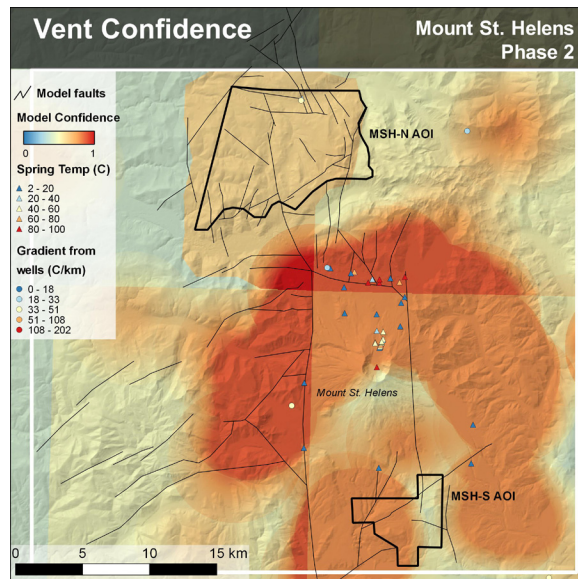
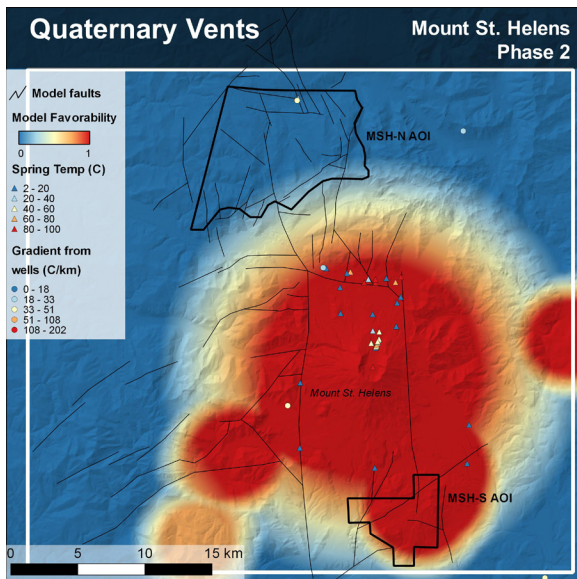
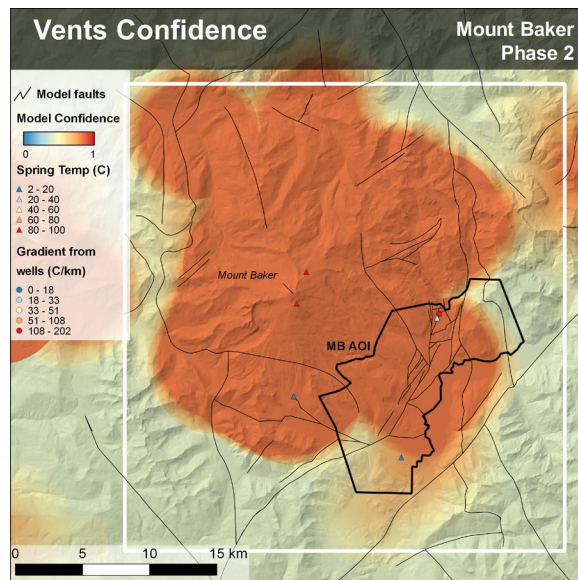
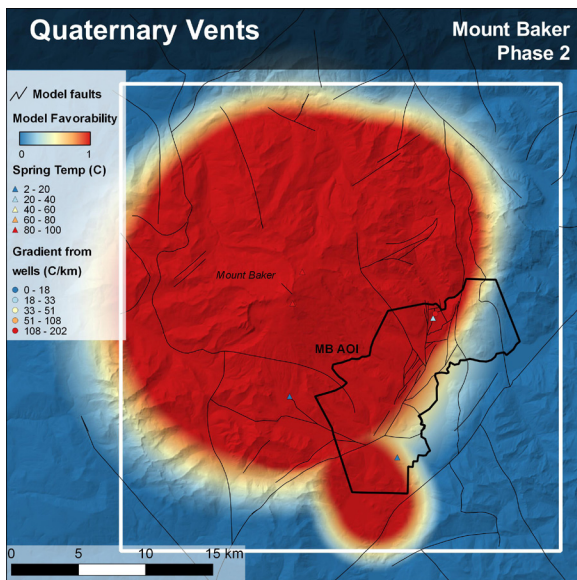
- DeAngelo, J.; Shervais, J. W.; Glen, J. M.; Nielson, D.; Garg, S.; Dobson, P.; Gasperikova, E.; Sonnenthal, E.; Visser, C.; Liberty, L. M.; Siler, D.; Evans, J. P.; Santellanes, S., 2016, GIS methodology for geothermal play fairway analysis—example from the Snake River Plain Volcanic Province: Stanford Geothermal Workshop, 10 p.
- Eberhart-Phillips, D.; Oppenheimer, D. H., 1984, Induced seismicity in the Geysers Geothermal Area, California: *Journal of Geophysical Research: Solid Earth*, v. 89, iss. B2, p. 2156-2202.
- Ekström, G.; Abers, G. A.; Webb, S. C., 2009, Determination of surface-wave phase velocities across USArray from noise and Aki's spectral formulation: *Geophysical Research Letters*, v. 36, iss. 18.
- Evarts, R. C.; Ashley, R. P.; Smith, J. G., 1987, Geology of the Mount St. Helens area—record of discontinuous volcanic and plutonic activity in the Cascade Arc of southern Washington: *Journal of Geophysical Research*, v. 92, no. B10, p. 10,155-10,169.
- Evarts, R. C.; Ashley, R. P., 1990, Preliminary geologic map of the Goat Mountain quadrangle, Cowlitz County, Washington: U.S. Geological Survey Open-File Report OF-90-632, scale 1:24,000.
- Fetterman, J. A.; Davatzes, N. C.; 2011, Evolution of porosity in fractures in the Newberry Volcano Geothermal System, Oregon, USA—Feedback between deformation and alteration: *GRC Transactions*, v. 35, p. 339-346.
- Fleck, R. J.; Hagstrum, J. T.; Alvert, A. T.; Evarts, R. C.; Conrey, R. W., 2014, $^{40}\text{Ar}/^{39}\text{Ar}$ geochronology, paleomagnetism, and evolution of the Boring volcanic field, Oregon and Washington, USA: *Geosphere*, v. 10, no. 6, p. 1283-1314.
- Goepel, K. D., 2013, Implementing the Analytic Hierarchy Process as a standard method for multi-criteria decision making in corporate enterprises—a new AHP Excel template with multiple inputs: *Proceedings of the International Symposium on the Analytic Hierarchy Process*.
- Haney, M. M.; Mikesell, T. D.; van Wijk, K.; Nakahara, H., 2012, Extension of the spatial autocorrelation (SPAC) method to mixed-component correlations of surface waves: *Geophysical Journal International*, v. 191, no. 1, p. 189-206.
- Hodge, B. E.; Crider, J.G., 2010, Investigating mechanisms of edifice deflation, 1981-2007, at Mount Baker volcano, Washington, United States: *Journal of Geophysical Research*, v. 115, B04401, doi:10.1029/2009JB006730.
- Hole, J. A.; Zelt, B. C., 1995, 3-D finite-difference reflection travel times: *Geophysical Journal International*, v. 121: p. 427-434. doi:10.1111/j.1365-246X.1995.tb05723.x
- Iovenitti, J.; Blackwell, D.; Sainsbury, J.; Tibuleac, I. ; Waibel, A.; Cladouhos, T.; Karlin, R.; Isaaks, E.; Clyne, M.; Ibser, F. H.; Callahan, O.; Kennedy, B. M.; Wannamaker, P., 2012, Towards developing a calibrated EGS exploration methodology using the Dixie Valley Geothermal System, Nevada: Thirty-Seventh Workshop on Geothermal Reservoir Engineering Proceedings, Stanford University, Stanford, California, January 30-February 1, SGP-TR-194.
- Johri, M., 2012, Fault damage zone—observations, dynamic modeling, and implications on fluid flow: Stanford University PhD Dissertation, SRB 131, 194 p.
- Lees, J. M.; Wu, H., 2000, Poisson's ratio and porosity at Coso geothermal area, California: *Journal of Volcanology and Geothermal Research* v. 95, p. 157-173.
- McCaffrey, R.; Qamar, A. I.; King, R. W.; Wells, R.; Khazaradze, G.; Williams, C. A.; Stevens, C. W.; Vollick, J. J.; Zwick, P. C., 2007, Fault locking, block rotation and crustal deformation in the Pacific Northwest: *Geophysical Journal International*, v. 169, no. 3, p. 1315-1340.
- Mignan, A.; Landtwing, D.; Kästli, P.; Mena, B.; Wiemer, S., 2015, Induced seismicity risk analysis of the 2006 Basel, Switzerland, Enhanced Geothermal System project: Influence of uncertainties on risk mitigation, *Geothermics*, v. 53, p. 133-146.
- O'Connell, R. J.; Budiansky, B., 1974, Seismic velocities in dry and saturated cracked solids: *Journal of Geophysical Research*, v. 79, no. 35, p. 5,412-5,426.
- Olmsted, F. H.; Glancey, P. A.; Harril, J. R.; Rush, R. E.; Van Denburgh, A. S., 1975, Preliminary hydrogeologic appraisal of selected hydrothermal systems in northern and central Nevada: U.S. Geological Survey Open-File Report 75-56, p. 267.
- Olmsted, F. H., 1977, Use of temperature surveys at a depth of 1 meter in geothermal exploration in Nevada, U.S. Geological Survey Professional Paper 1044-B.
- Personius, S. F.; Briggs, R. W.; Nelson, A. R.; Schermer, E. R.; Maharrey, J. Z.; Sherrod, B. L.; Spaulding, S. A.; Bradley, L., 2014, Holocene earthquakes and right lateral slip on the left-lateral Darrington-Devils Mountain fault zone, northern Puget Sound, Washington: *Geosphere*, v. 10, no. 6, p. 1482-1500.
- Saaty, T. L., 2008, Decision making with the analytical hierarchy process: *International Journal of Service Sciences*, v. 1, no. 1, p. 83-98.
- Schultz, R. A., 1993, Brittle strength of basaltic rock masses with applications to Venus: *Journal of Geophysical Research*, v. 98, no. E6, p. 10,883-10,895.
- Shapiro, N. M.; Campillo, M., 2004, Emergence of broadband Rayleigh waves from correlations of the ambient seismic noise: *Geophysical Research Letters*, v. 31, L07614.
- Stanley, W. D.; Johnson, S. Y.; Qamar, A. I.; Weaver, C. S.; Williams, J. M., 1996, Tectonics and seismicity of the southern Washington Cascade range: *Bulletin of the Seismological Society of America*, v. 86, p.1-18, 1996.
- Tabor, R. W.; Haugerud, R. A.; Hildreth, W.; Brown, E. H., 2003, Geologic map of the Mount Baker 30- by 60-minute quadrangle, Washington, Prepared in cooperation with the Washington State Department of Natural Resources, Division of Geology and Earth Resources. Pamphlet to accompany Geologic Investigations Series I-2660, U.S. Department of the Interior, U.S. Geologic Survey.
- Thomas, A. L., 1993, *Poly3D*—a three-dimensional, polygonal-element, displacement discontinuity boundary element computer program with applications to fractures, faults and cavities in the Earth's crust: M.S. thesis, Stanford University, California.
- Tibuleac, I. M.; Pullammanappallil, S.; Faulds, J.; McLachlan, H., 2012, Development of a low cost method to estimate the seismic signature of a geothermal field from ambient seismic noise analysis: *GRC Transactions*, v. 36.
- Vidale, J. E., 1990, Finite-difference calculation of traveltimes in three dimensions. *Geophysics*, v. 55, no. 5, p. 521-526.
- Waite, G. P.; Moran, S. C., 2009, V_p structure of Mount St. Helens, Washington, USA, imaged with local earthquake tomography: *Journal of Volcanology and Geothermal Research*, v. 182, no. 1-2, p. 113-122.
- Wannamaker, P. E.; Rose, P. E.; Doerner, W.; Berard, B.; McCulloch, J.; Nurse, K., 2004, Magnetotelluric surveying and monitoring at the Coso geothermal area, California, in support of the enhanced geothermal systems concept—survey parameters and initial results: 29th Workshop on Geothermal Reservoir Engineering Proceedings, Stanford University, Stanford California, January 26-28, SGP- TR-175.
- Washington Division of Geology and Earth Resources, 2016, Surface geology, 1:100,000--GIS data, November 2016: Washington Division of Geology and Earth Resources Digital Data Series DS-18, version 3.1, previously released June 2010.

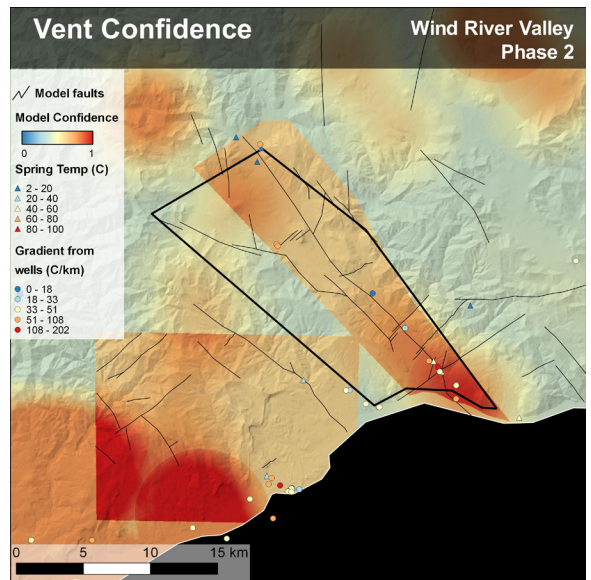
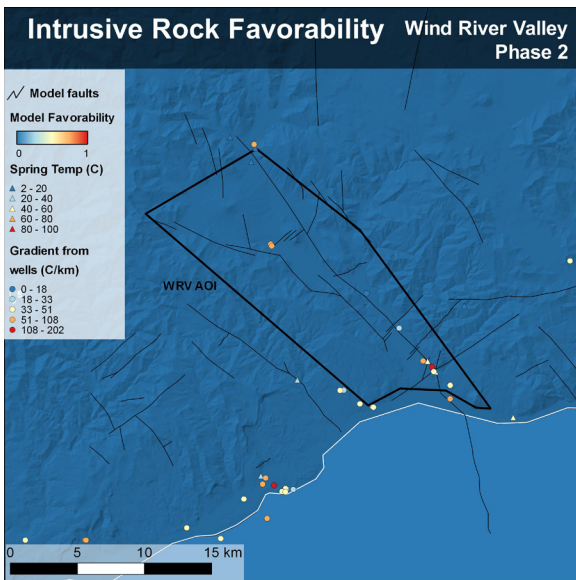
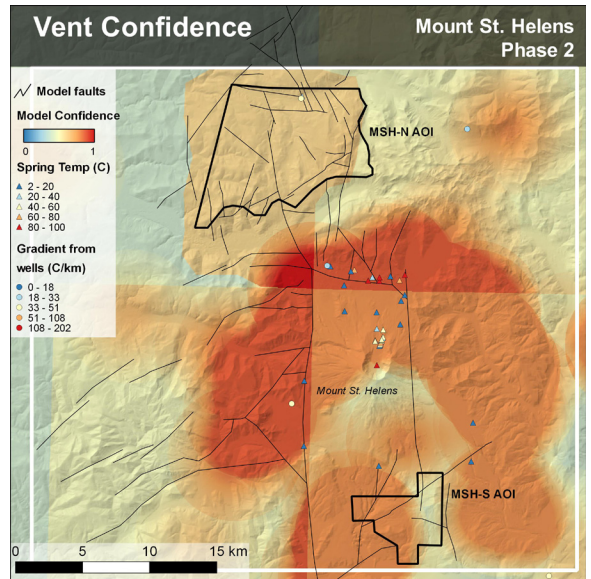
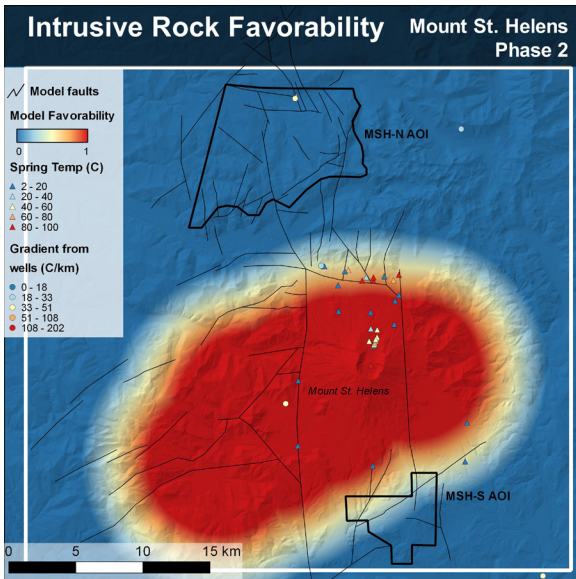
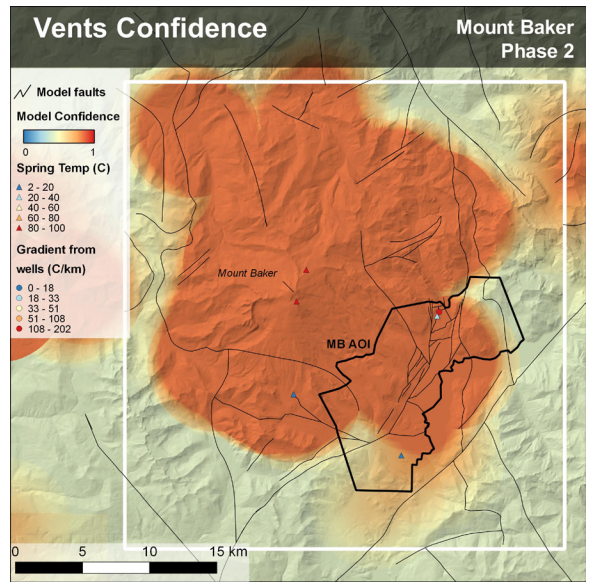
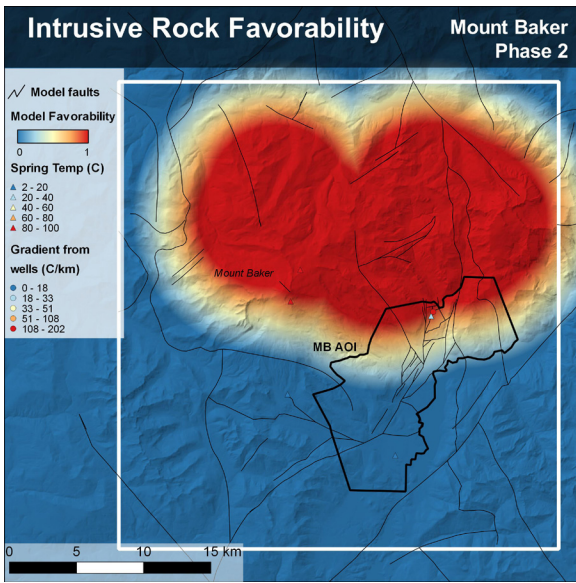
- Weaver, C. S.; Grant, W. C.; Shemeta, J. E., 1987, Local crustal extension of Mount St. Helens, Washington: *Journal of Geophysical Research*, v. 92, no. B10, p. 10,170-10,178.
- Zhu, T. Y., 2012, Some useful numbers on the engineering properties of materials (geologic and otherwise): GEOL 615, Department of Geophysics, Stanford University.

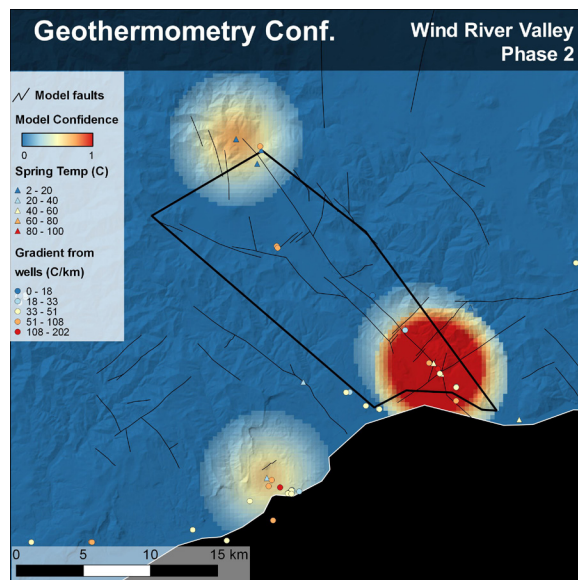
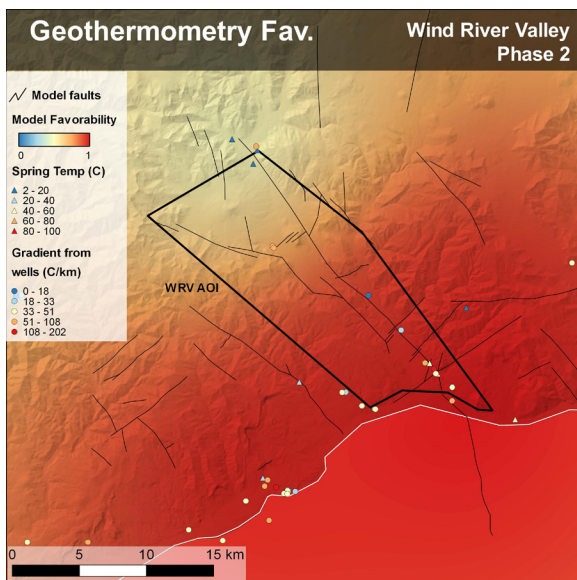
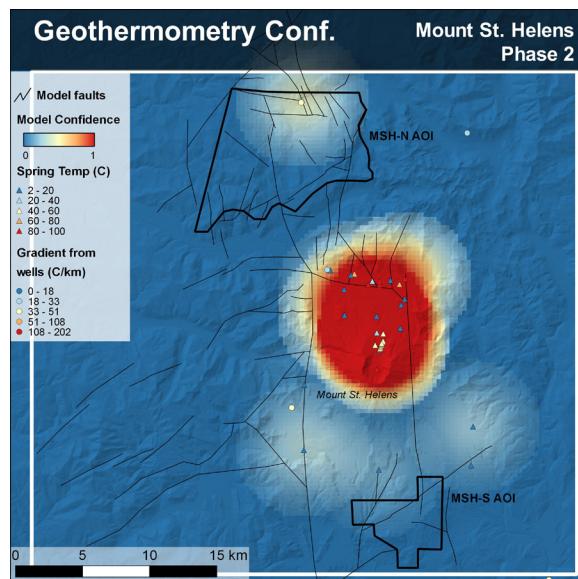
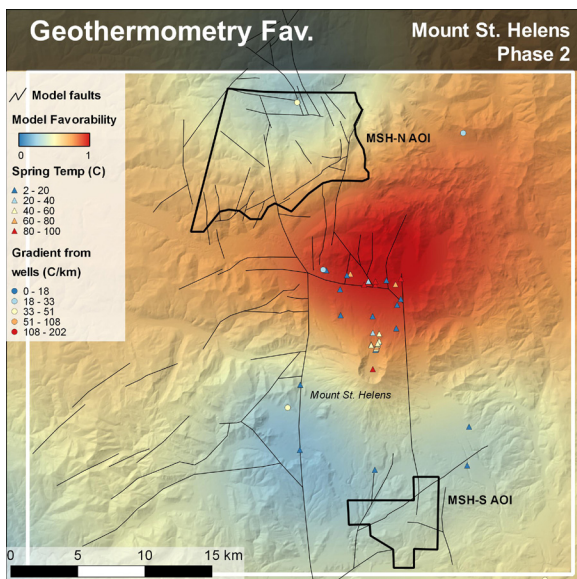
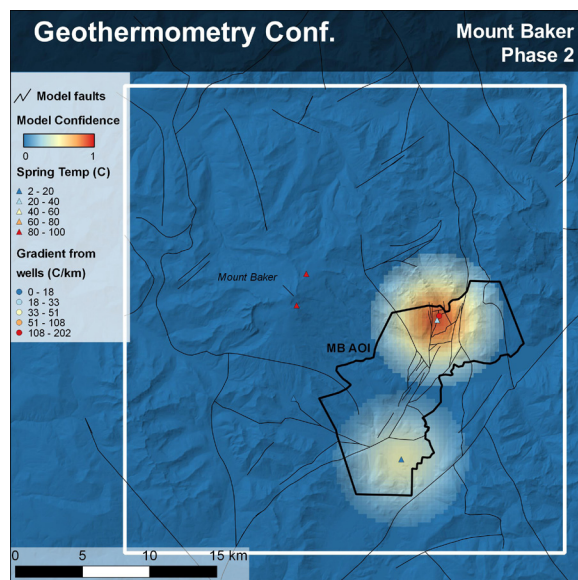
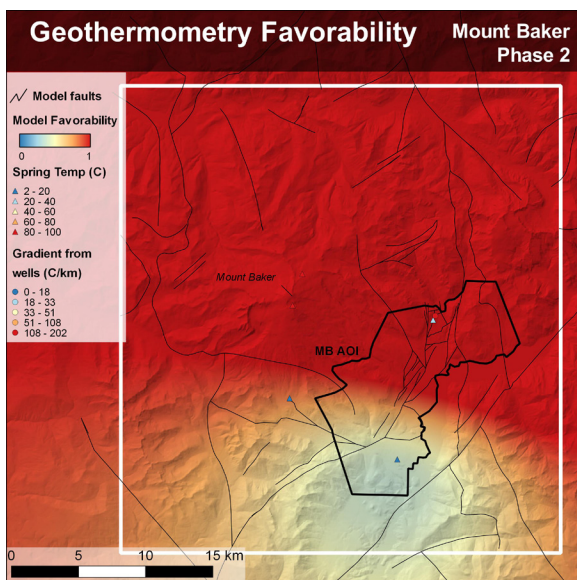
Appendix A. Intermediate Favorability and Confidence Results

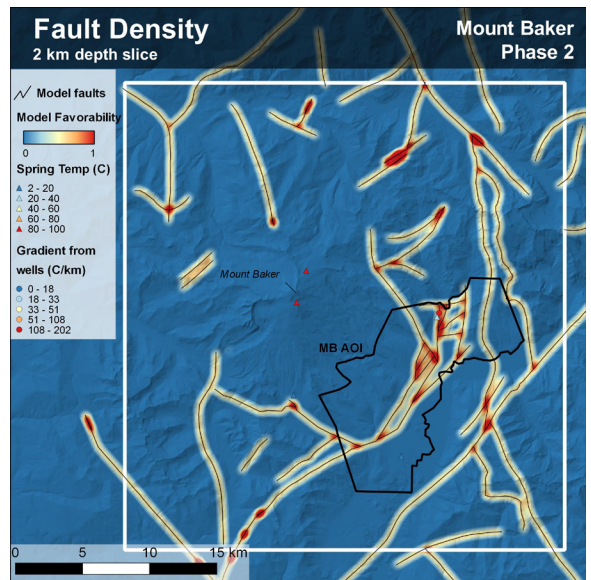
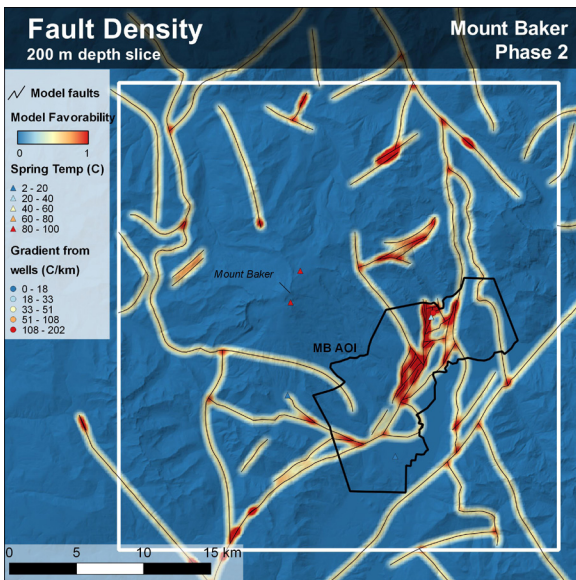
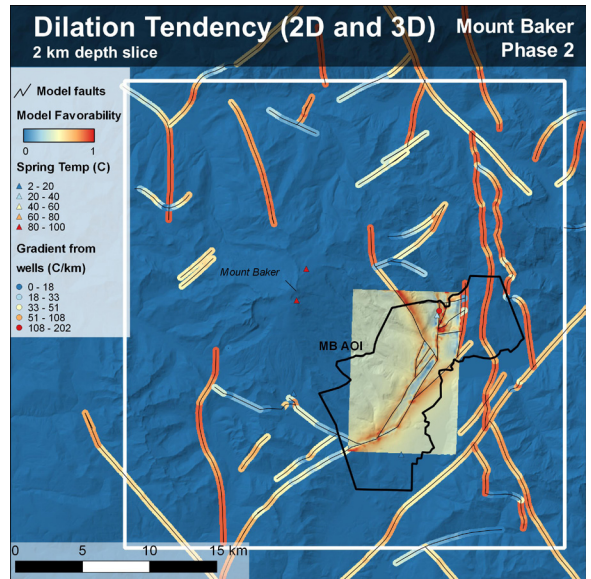
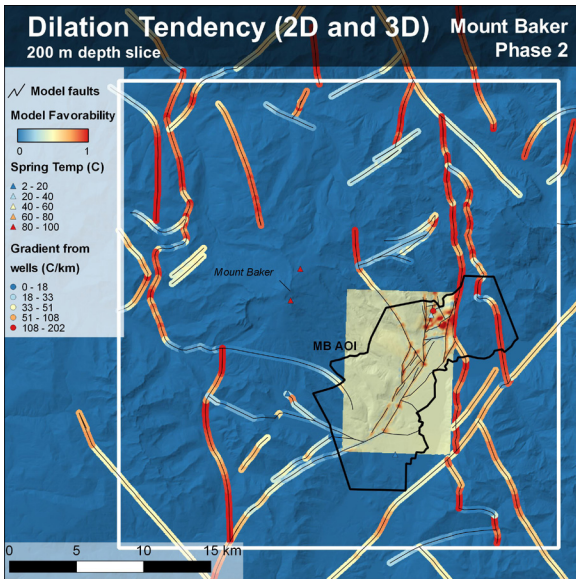
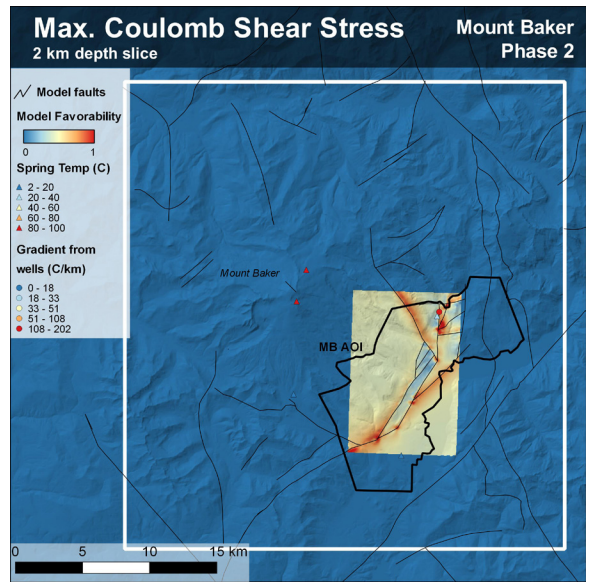
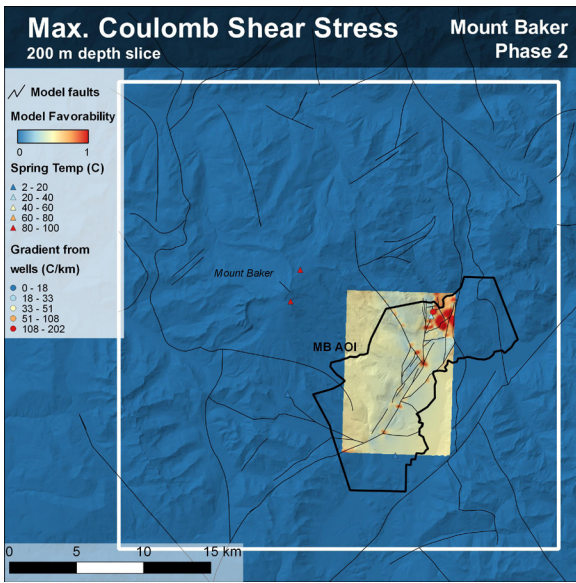


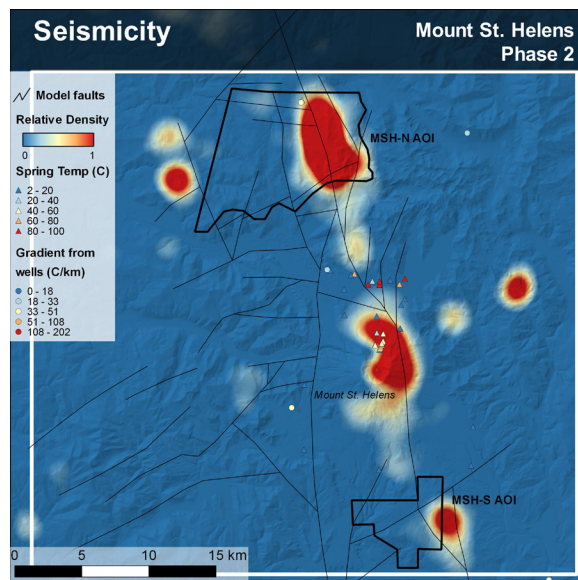
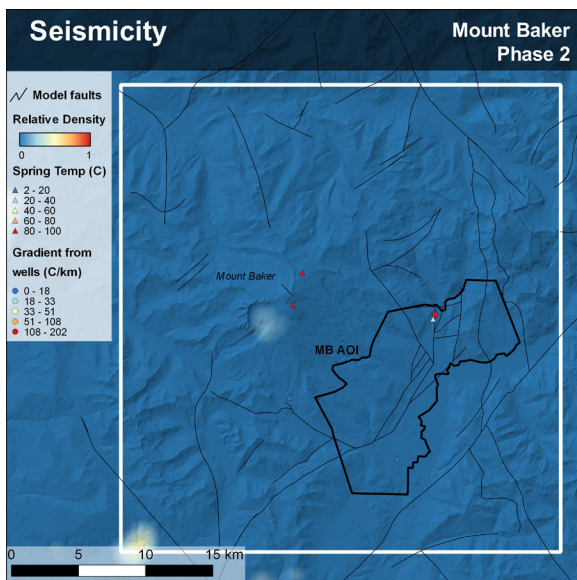
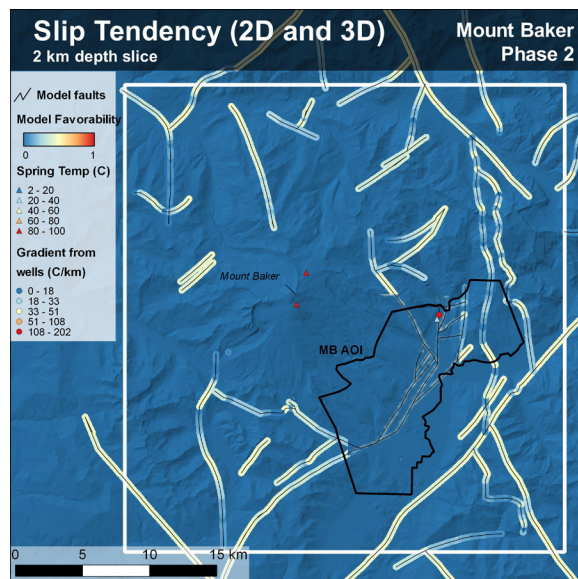
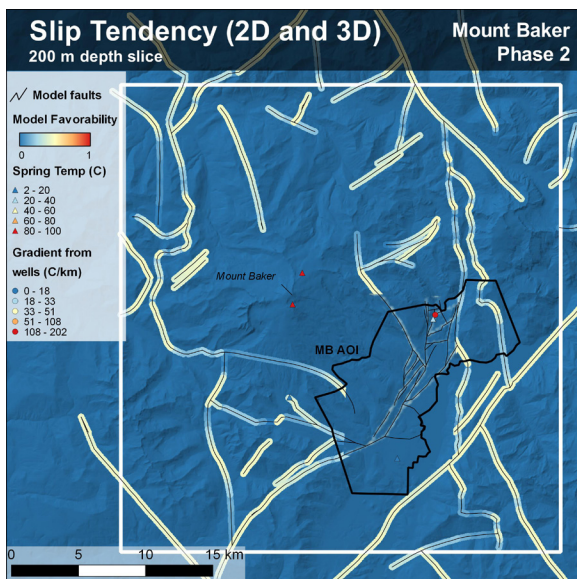
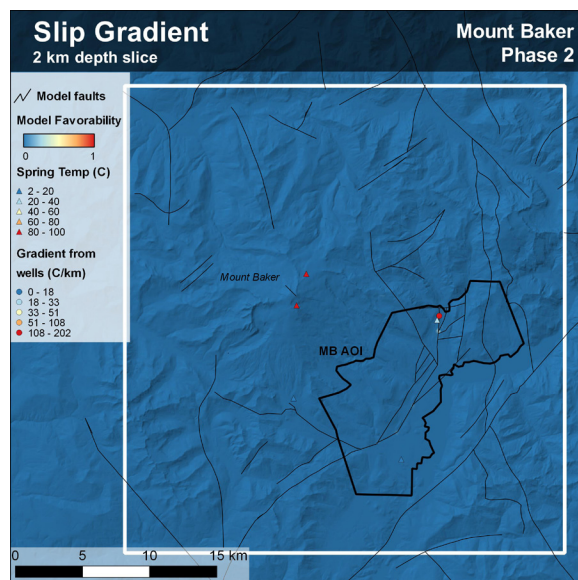
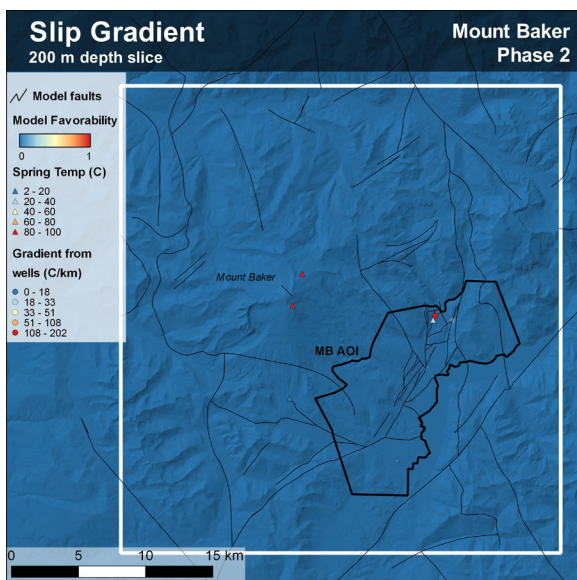


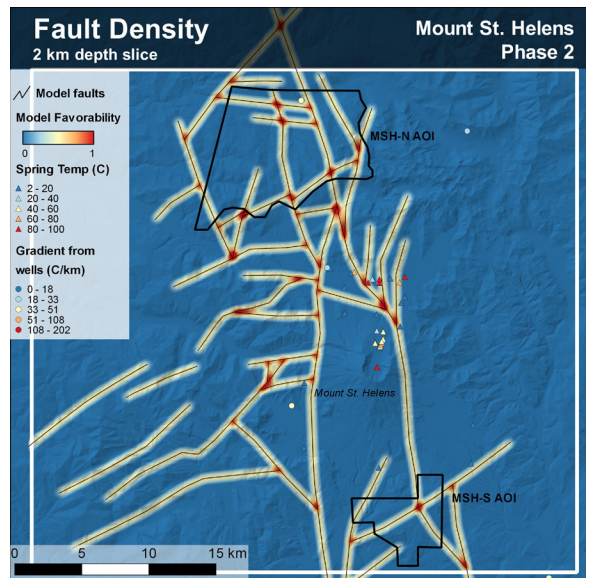
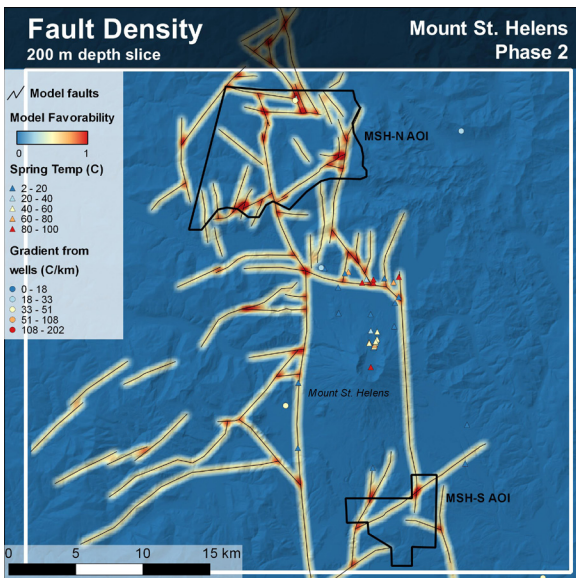
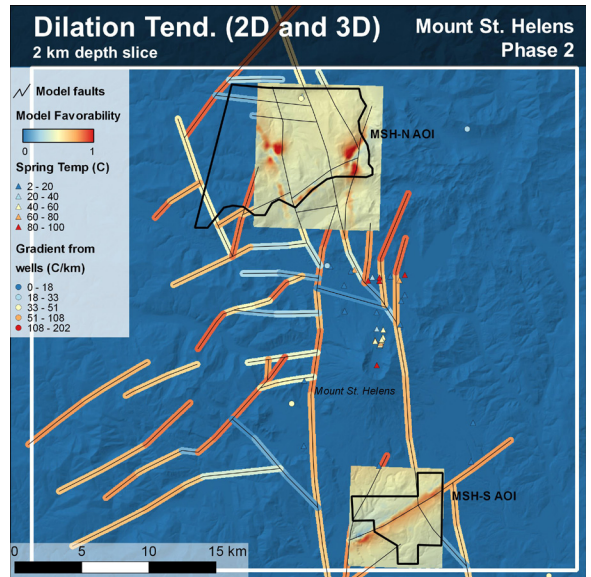
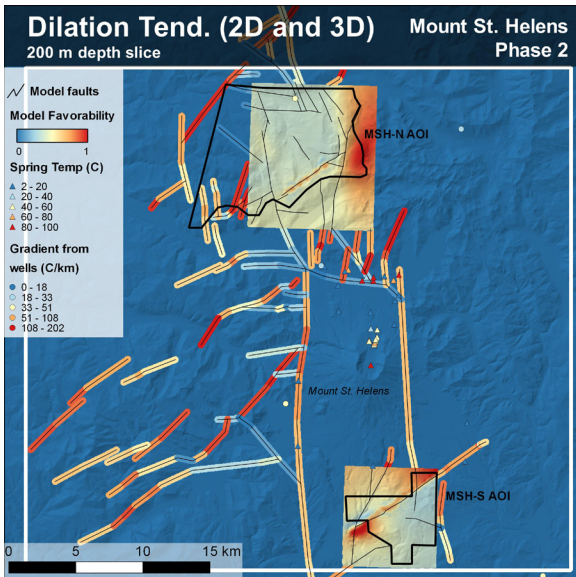
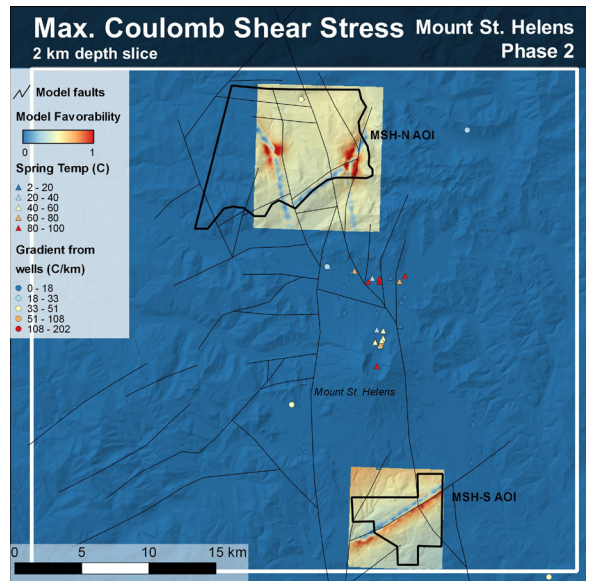
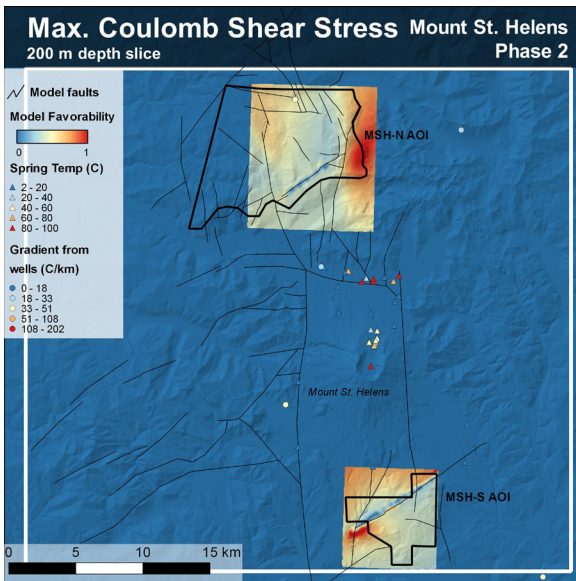


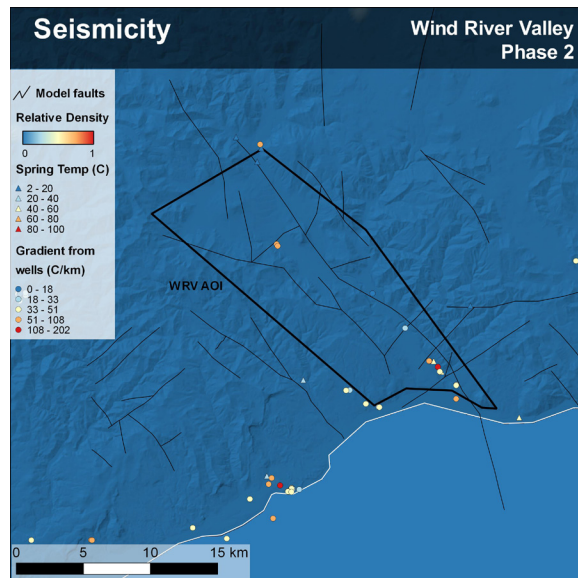
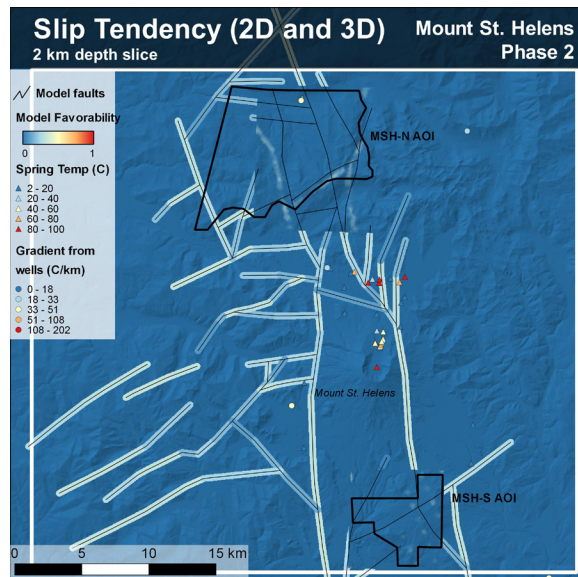
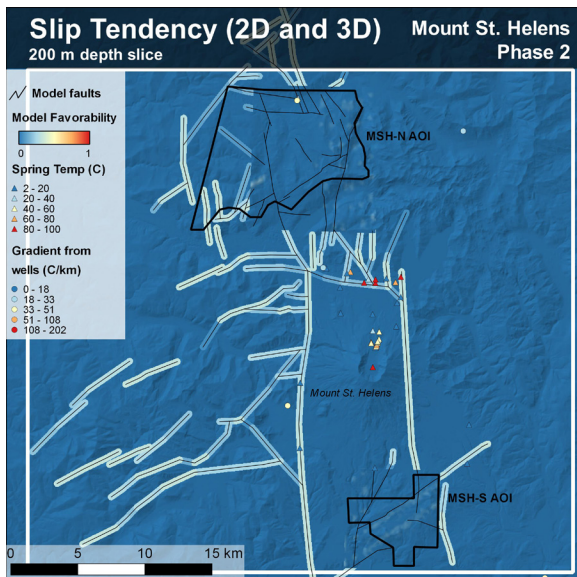
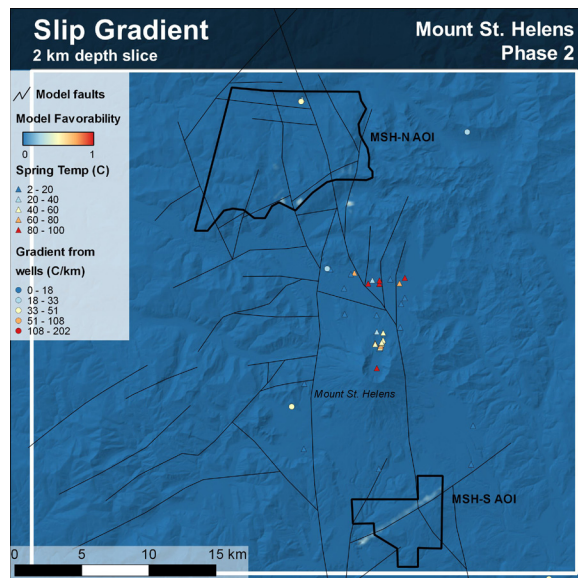
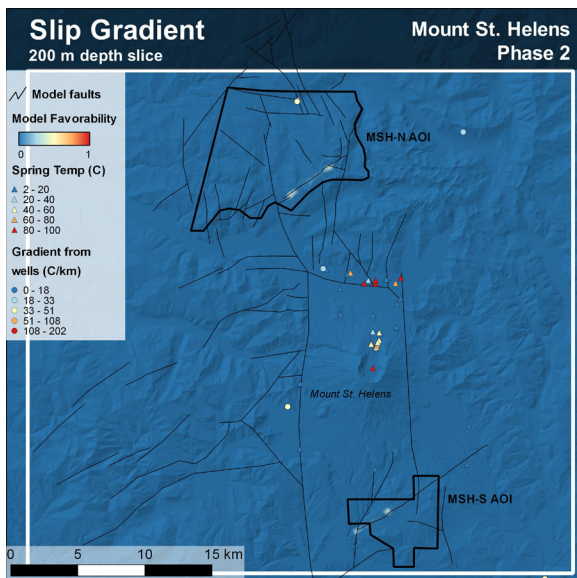


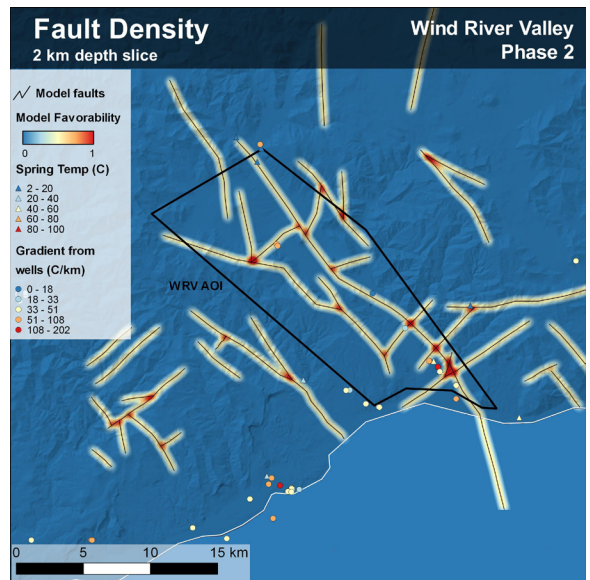
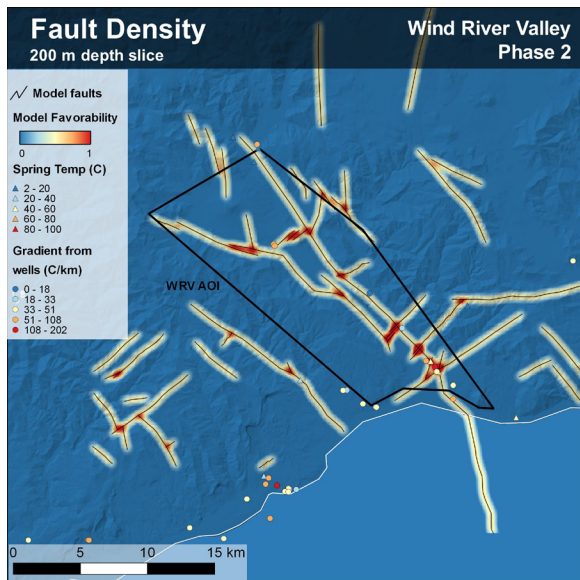
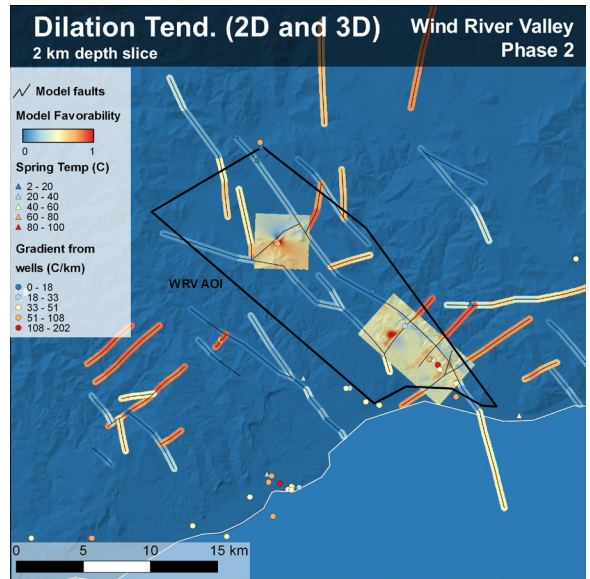
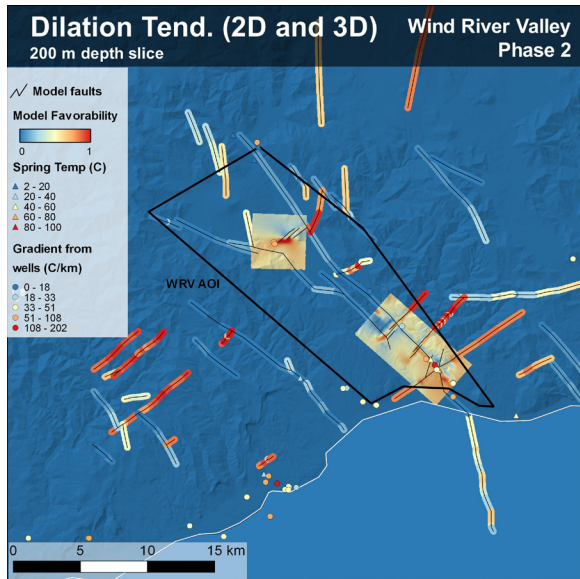
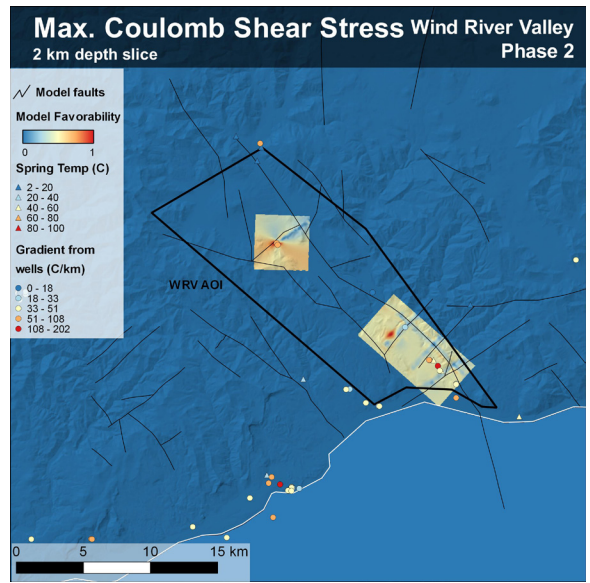
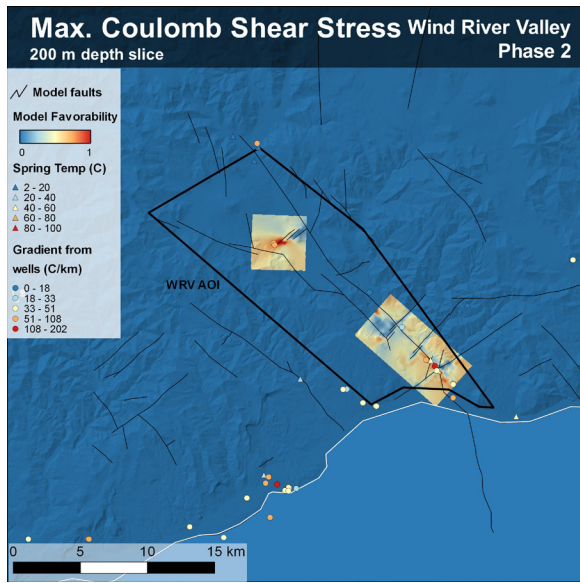


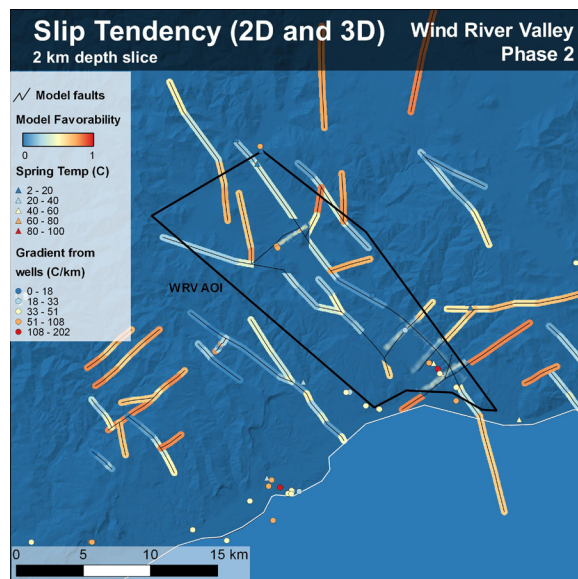
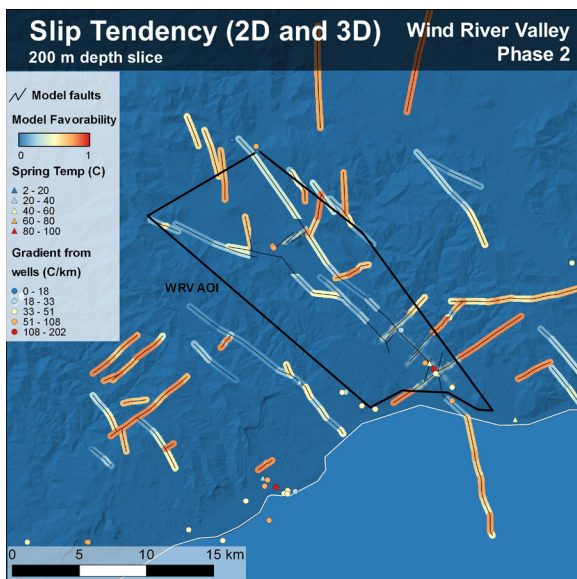
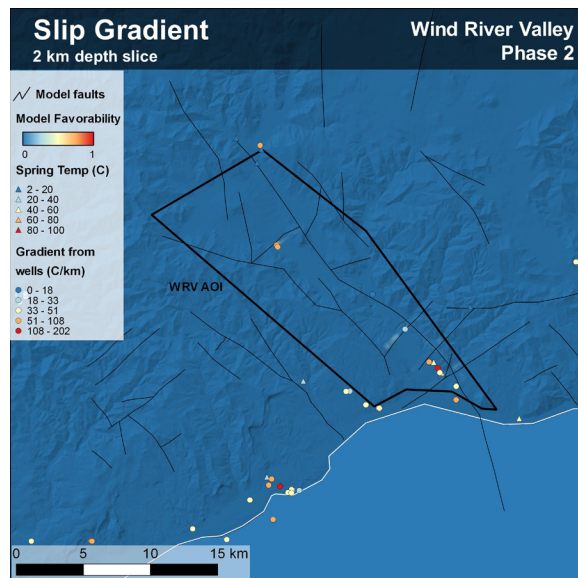
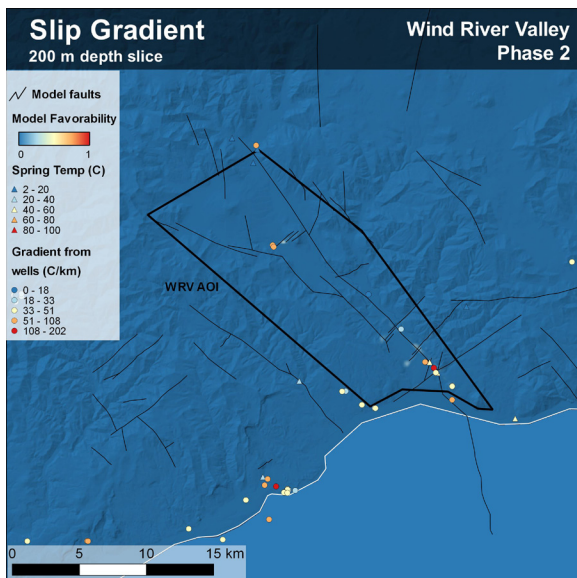


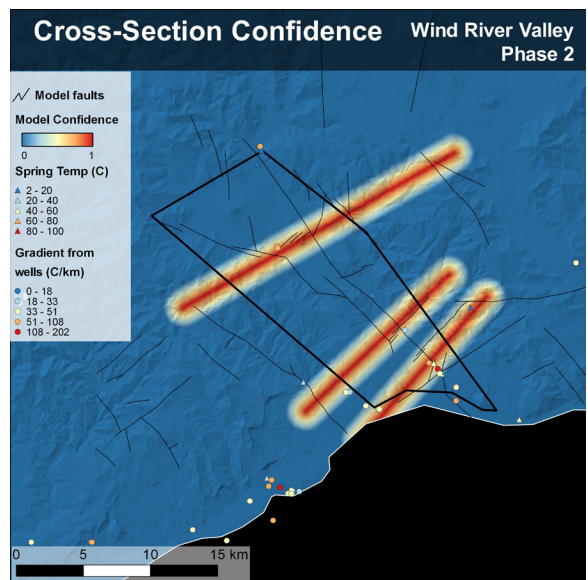
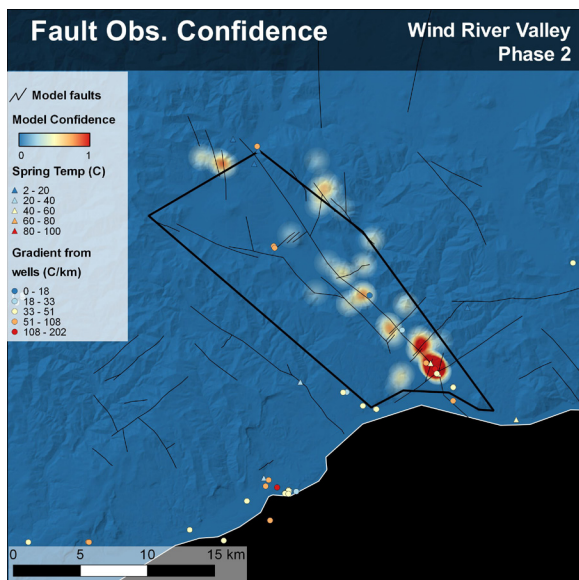
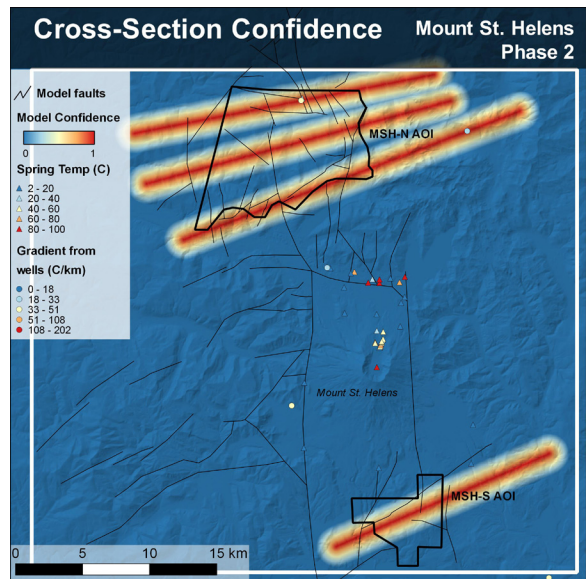
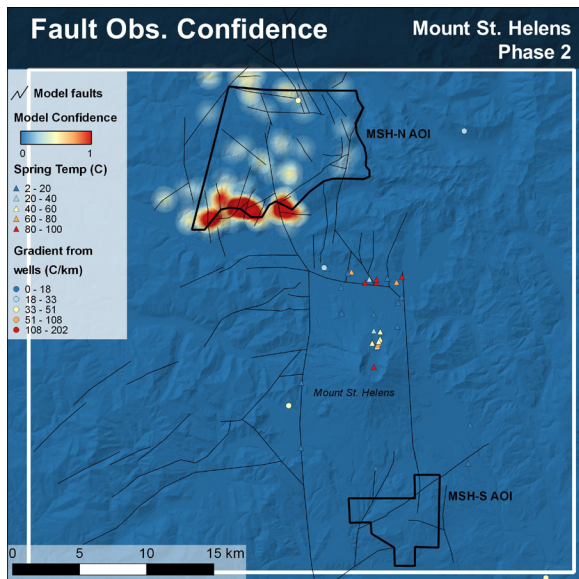
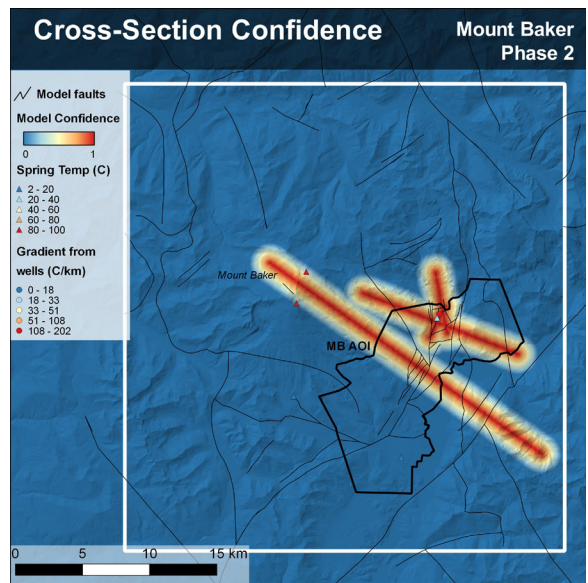
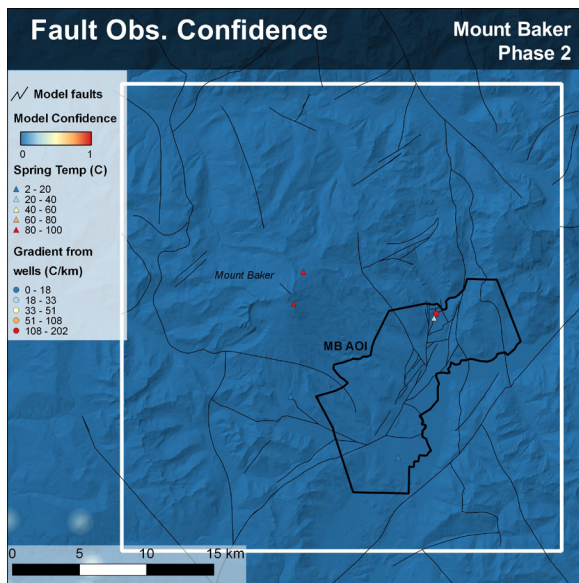


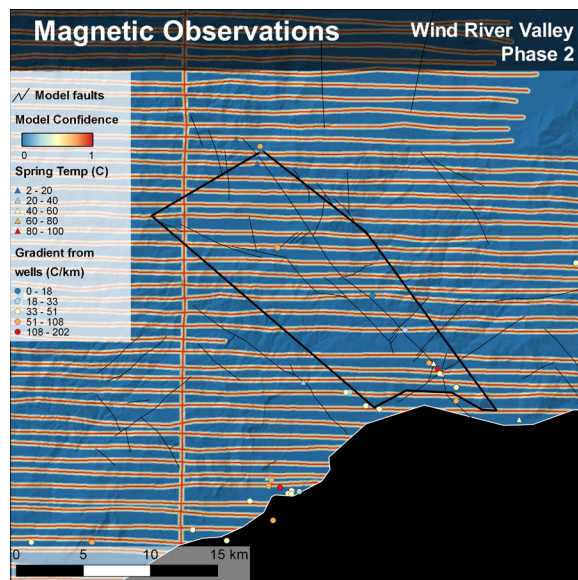
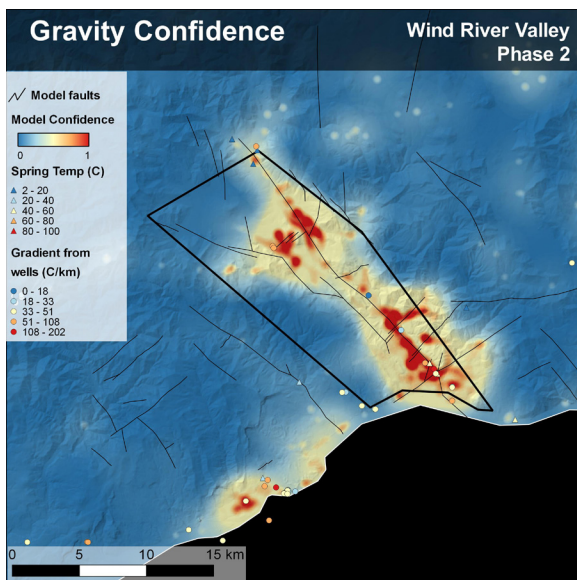
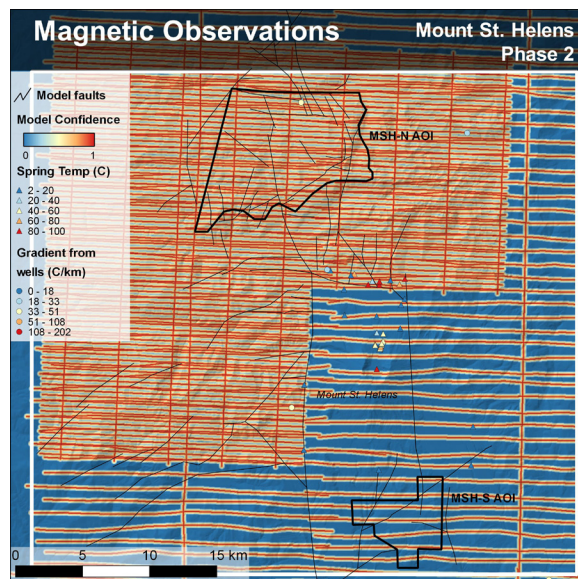
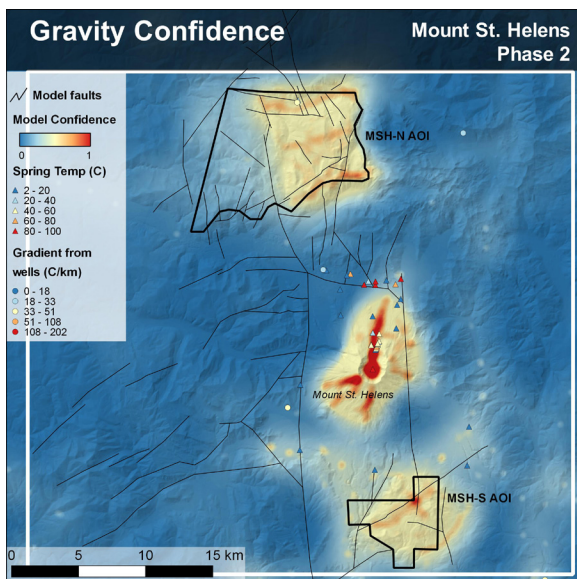
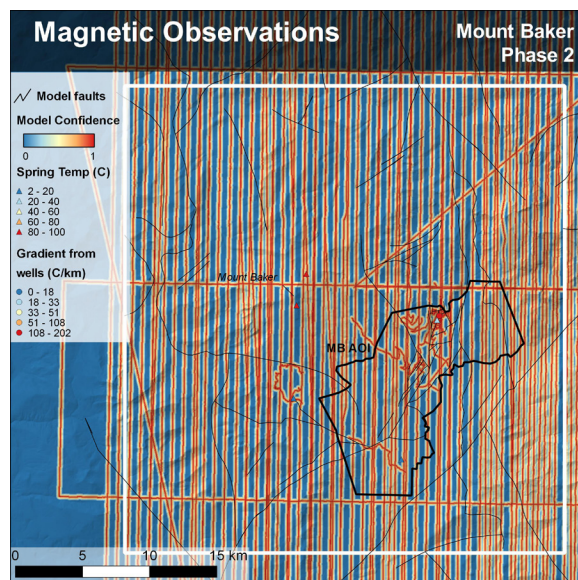
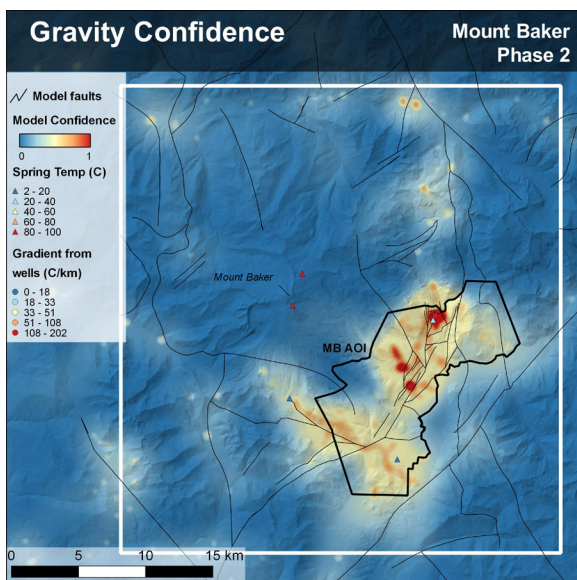


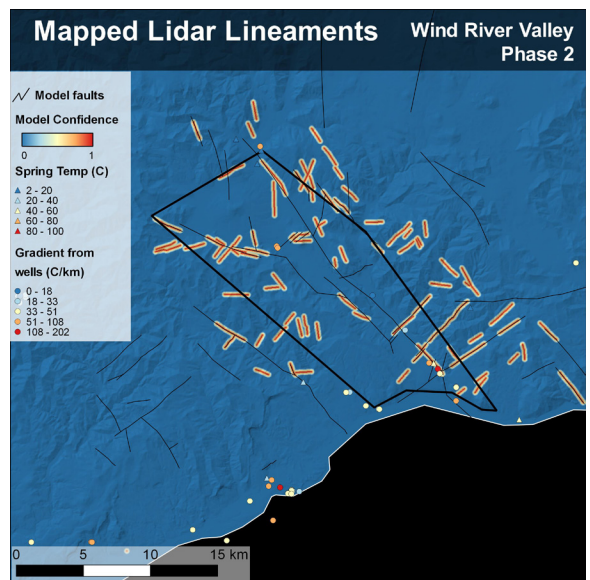
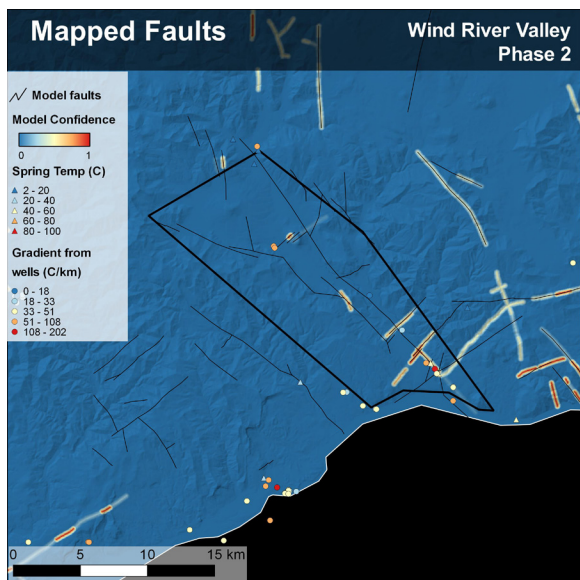
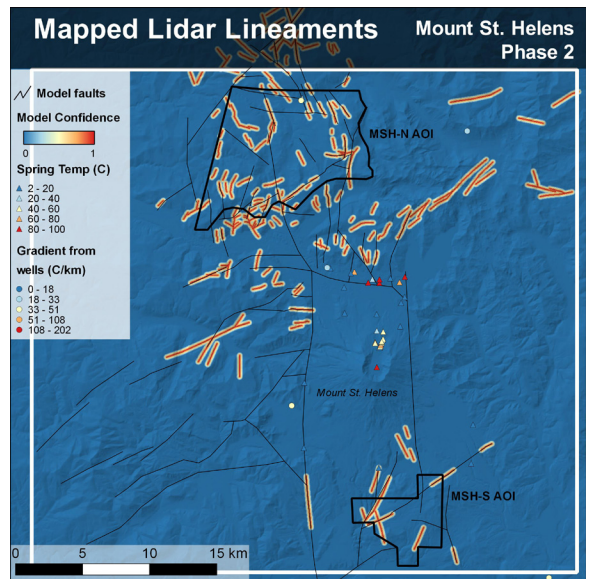
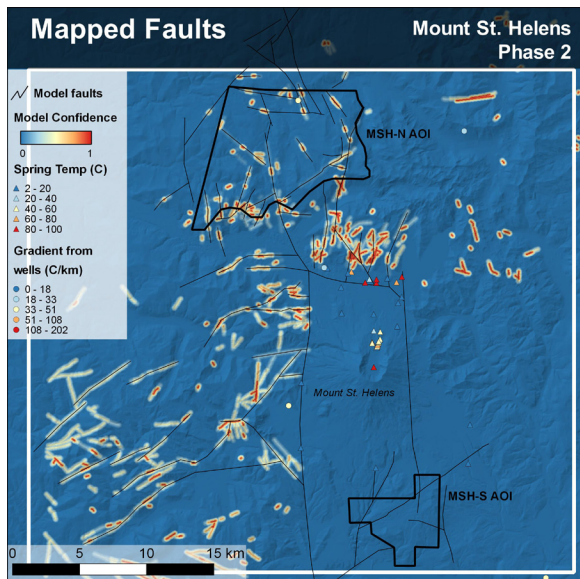
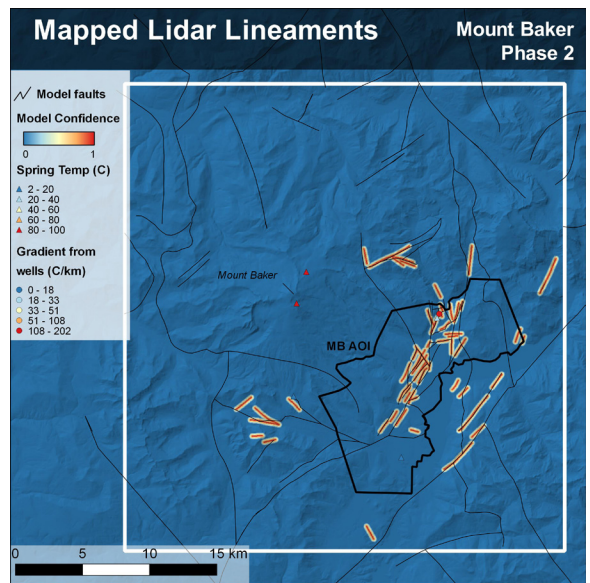
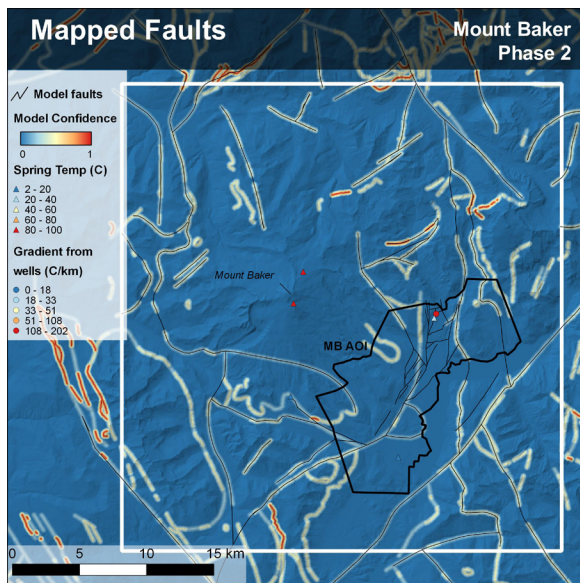


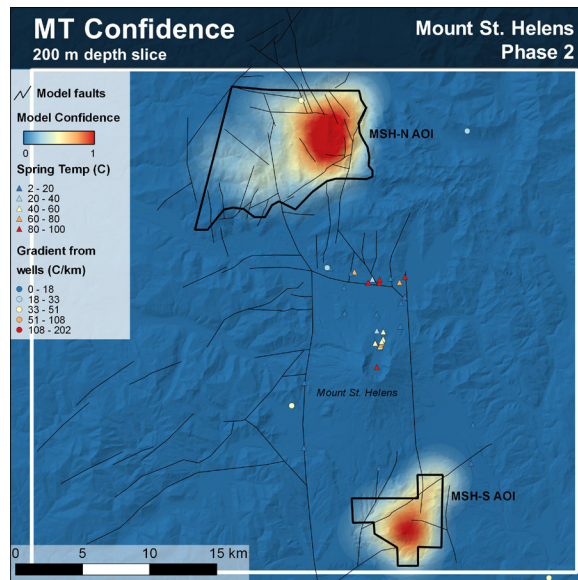
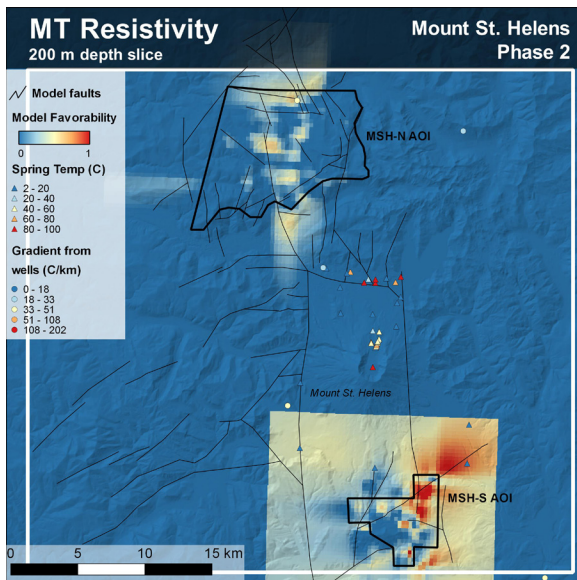
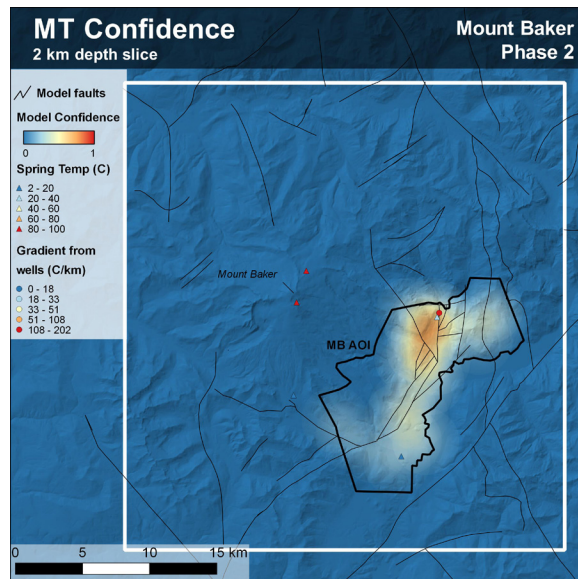
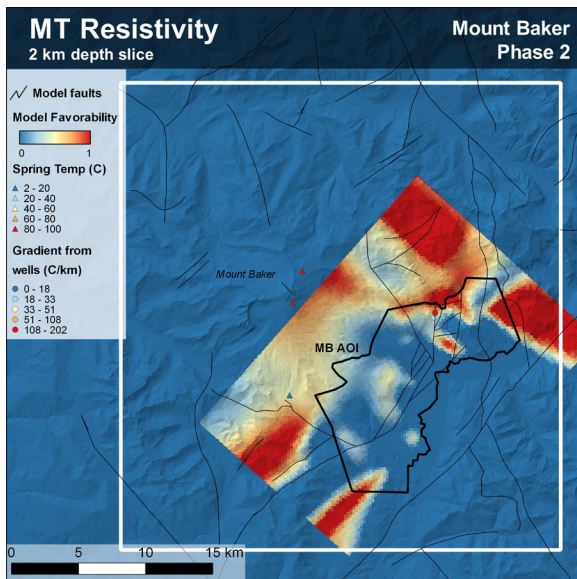
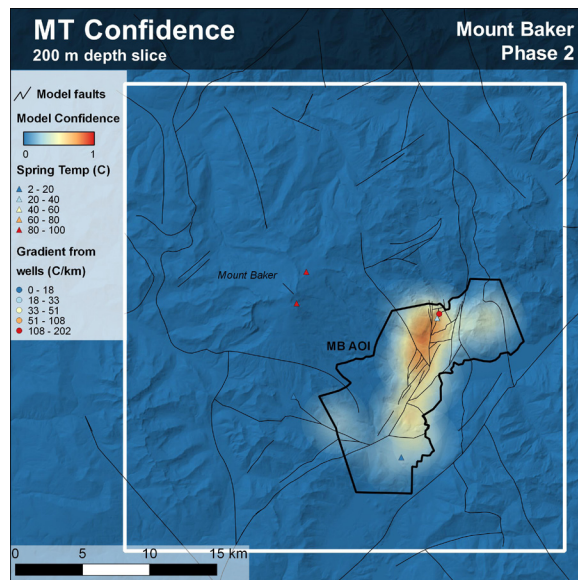
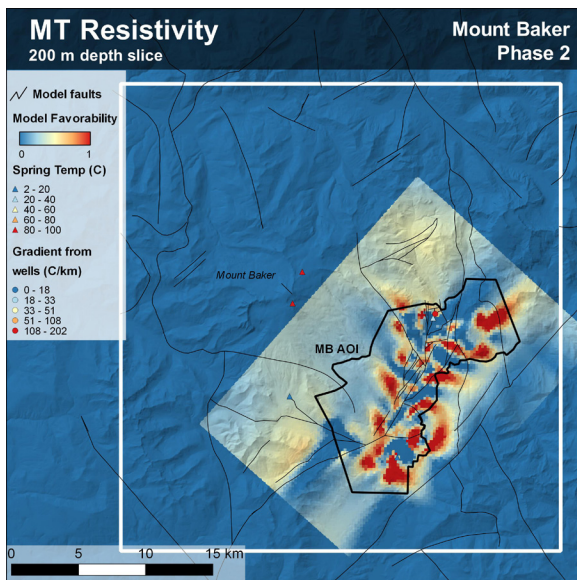


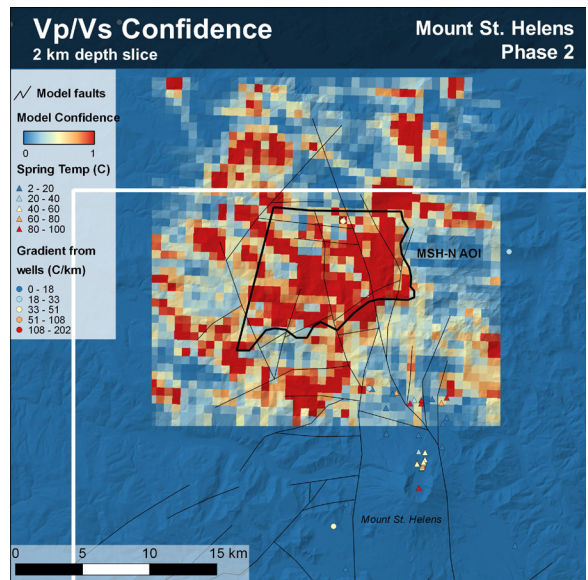
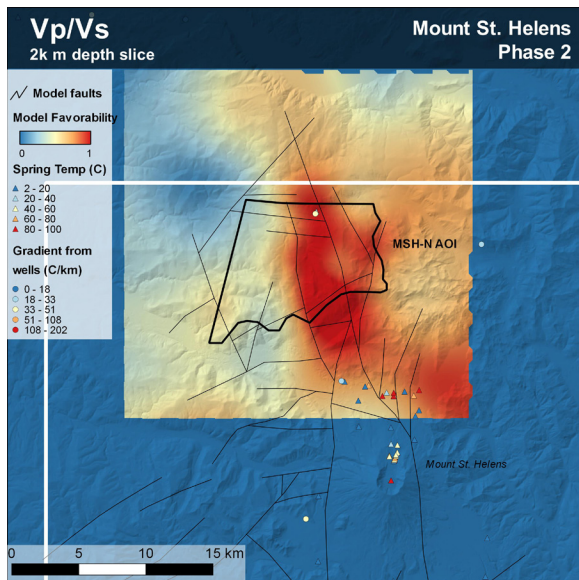
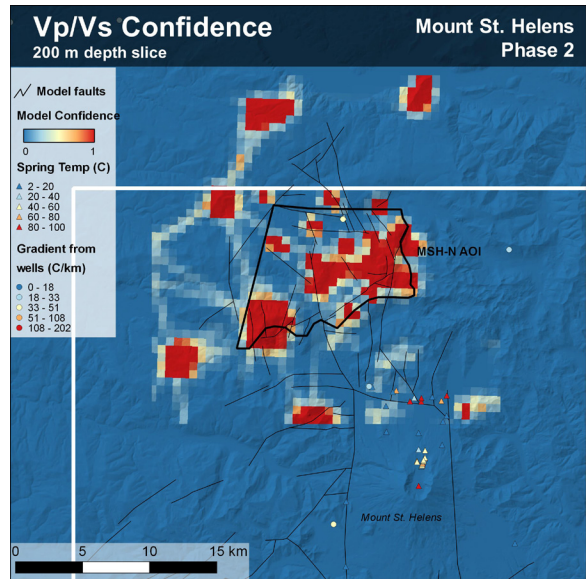
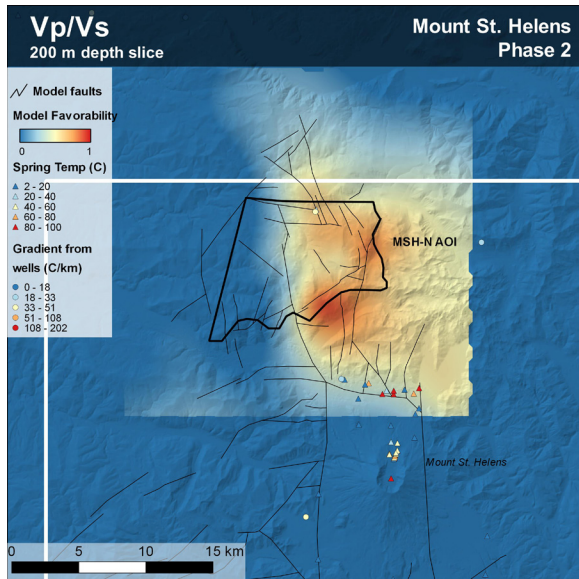
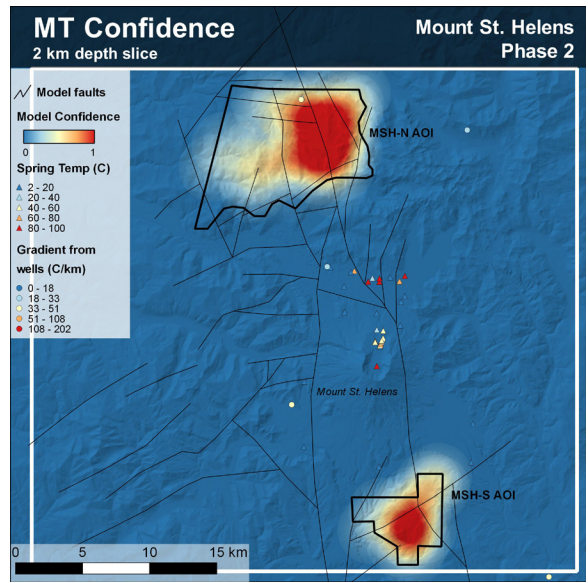
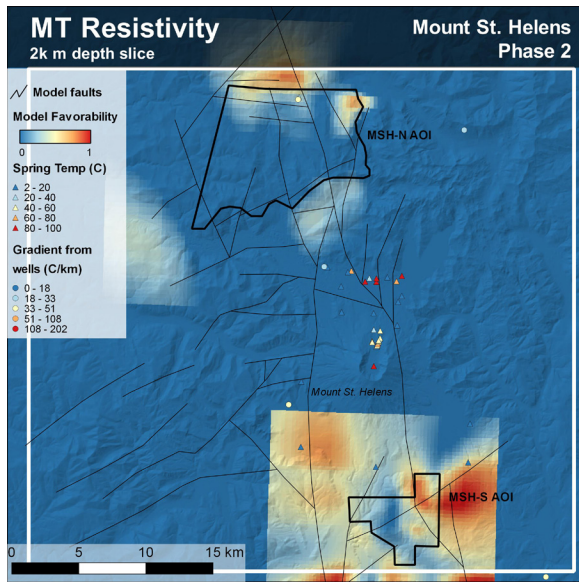


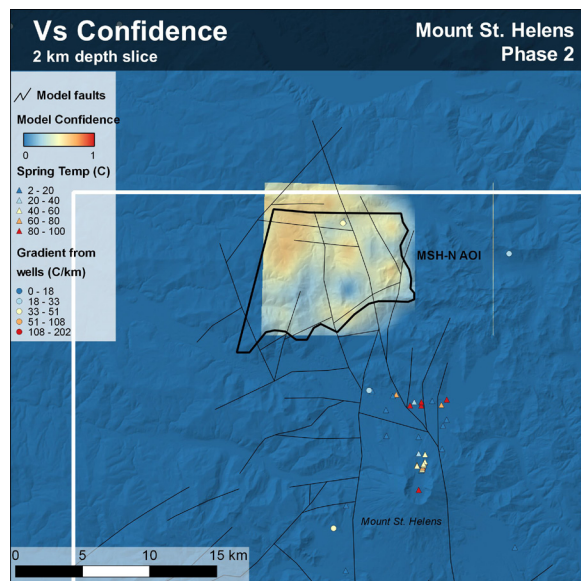
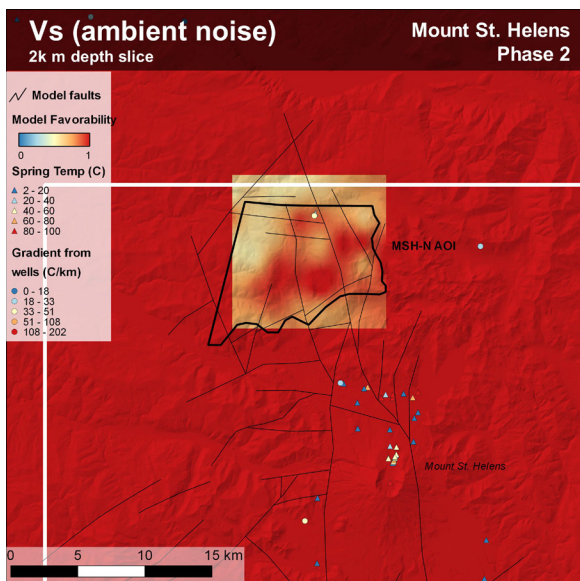
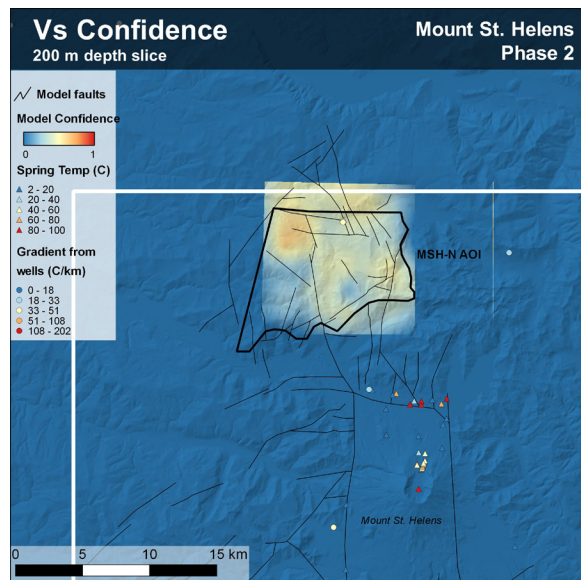
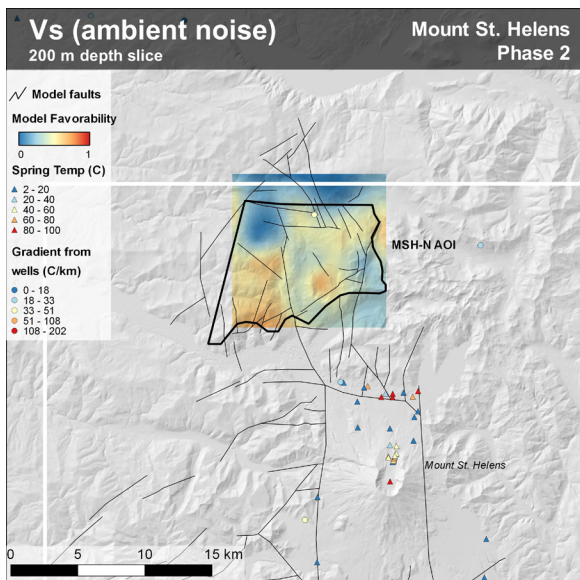


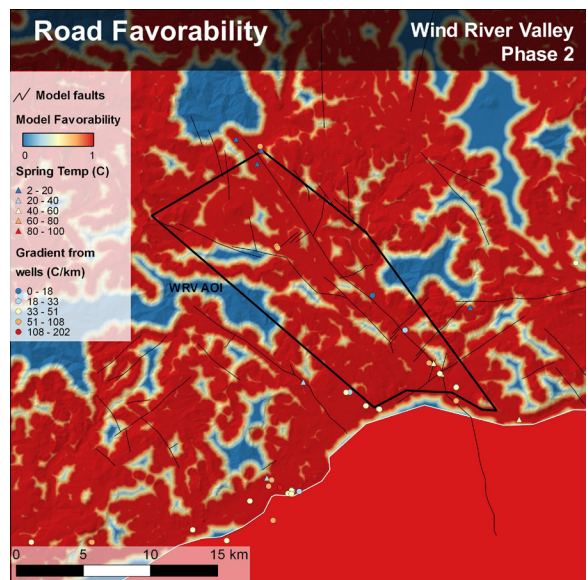
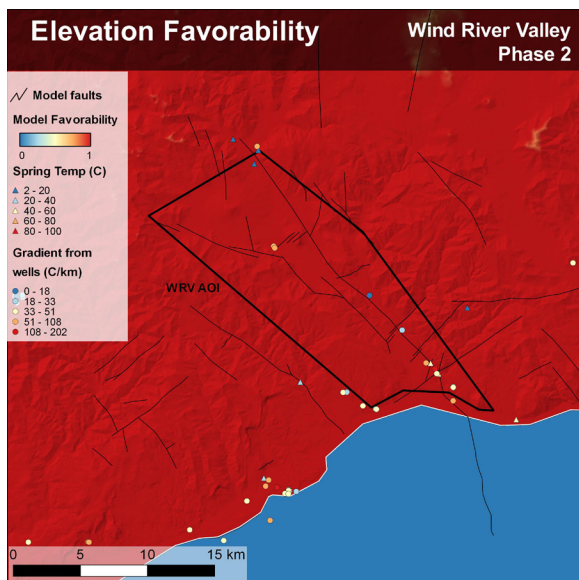
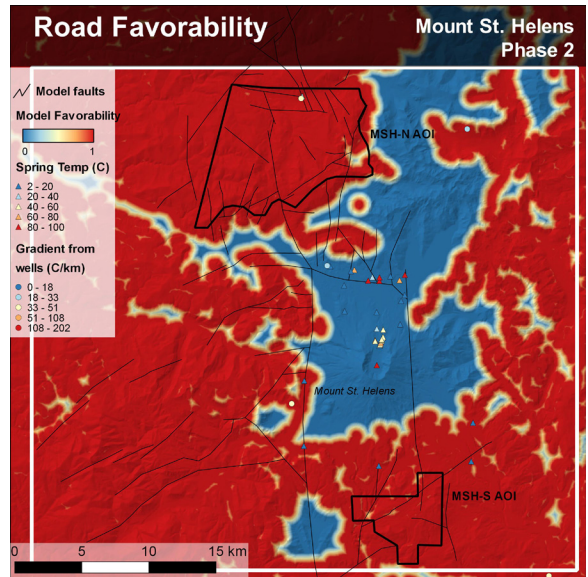
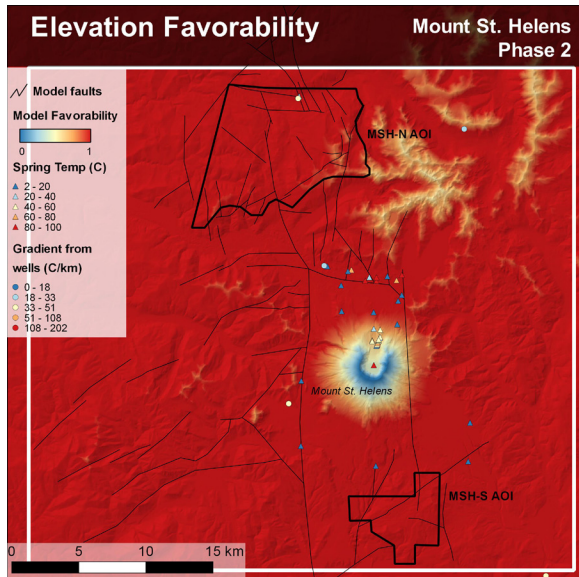
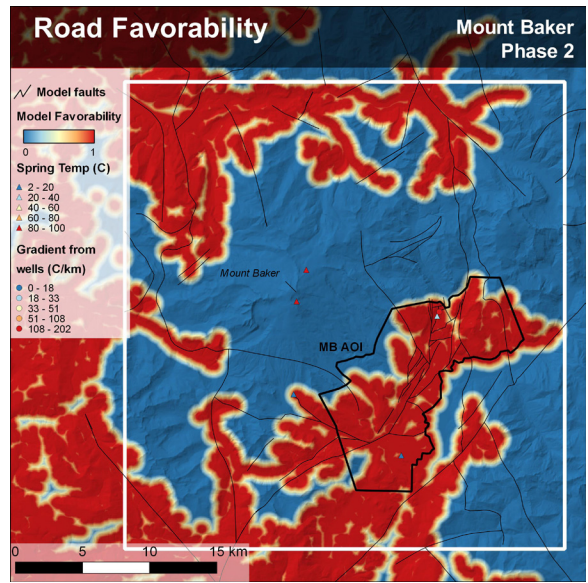
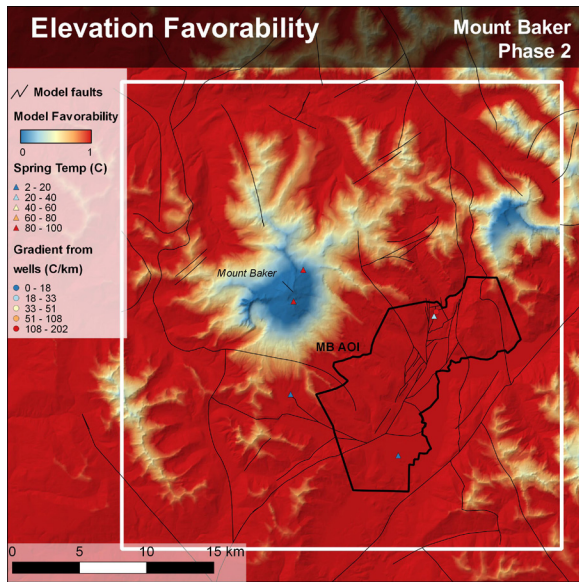


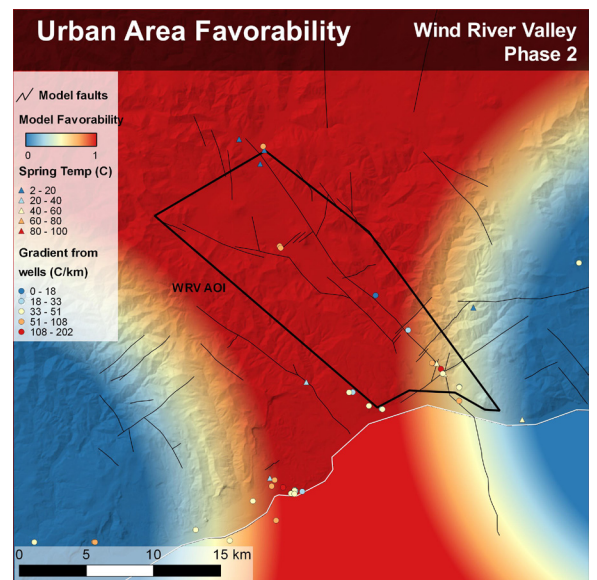
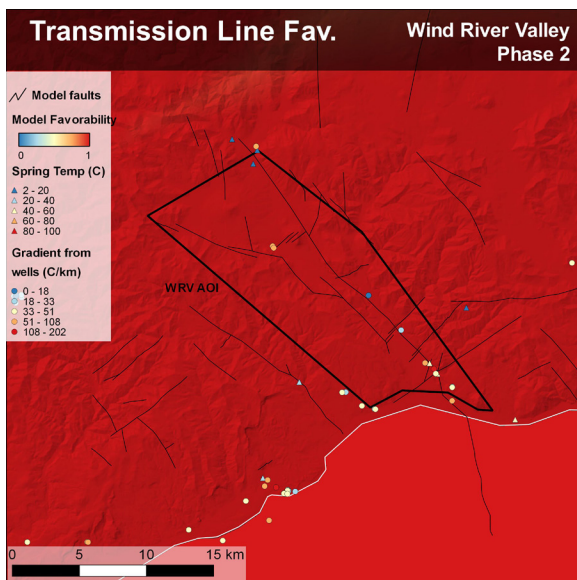
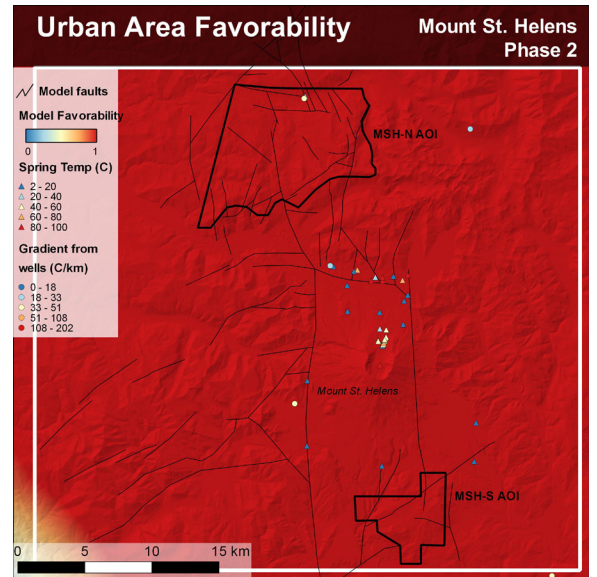
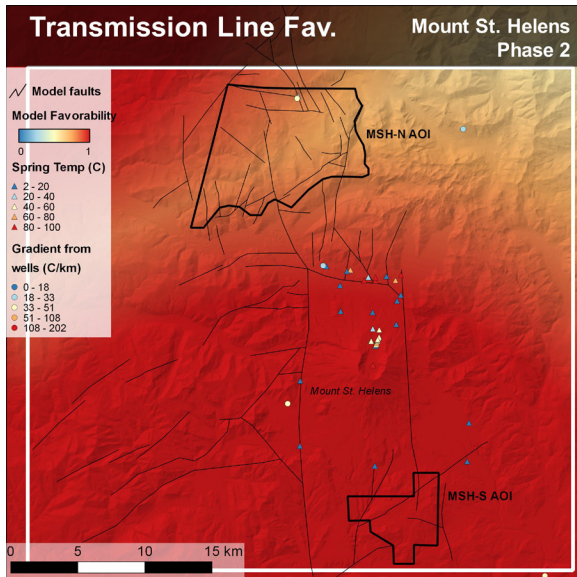
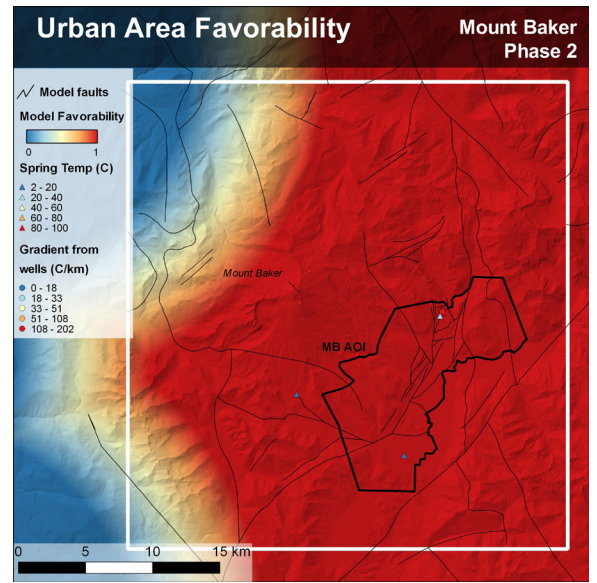
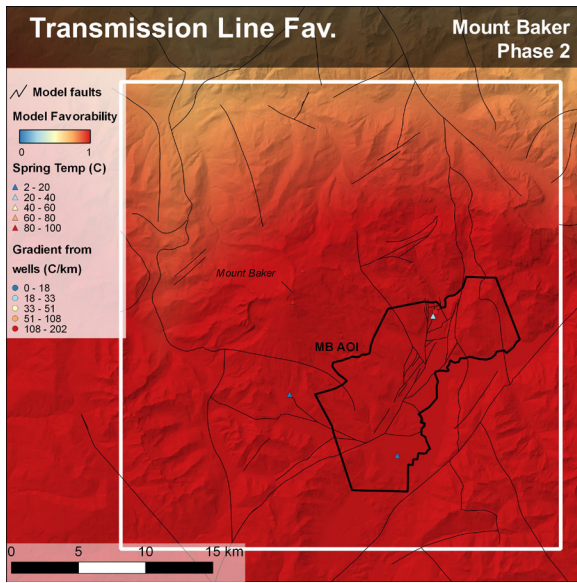


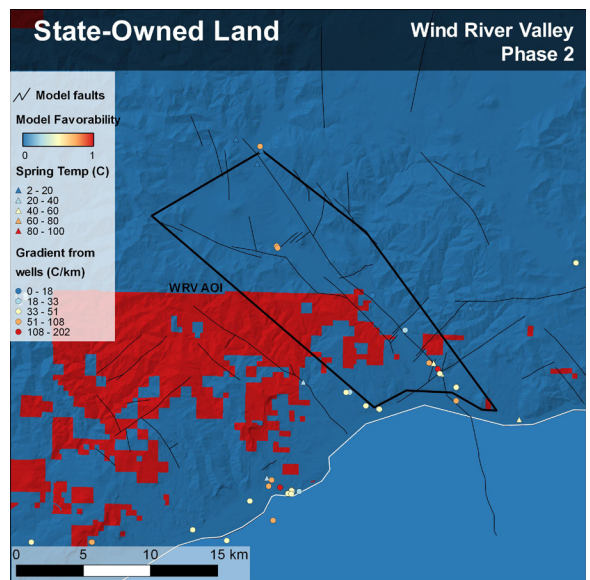
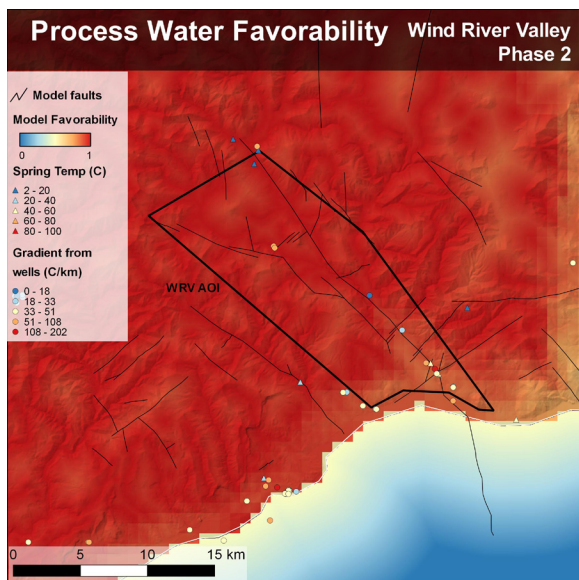
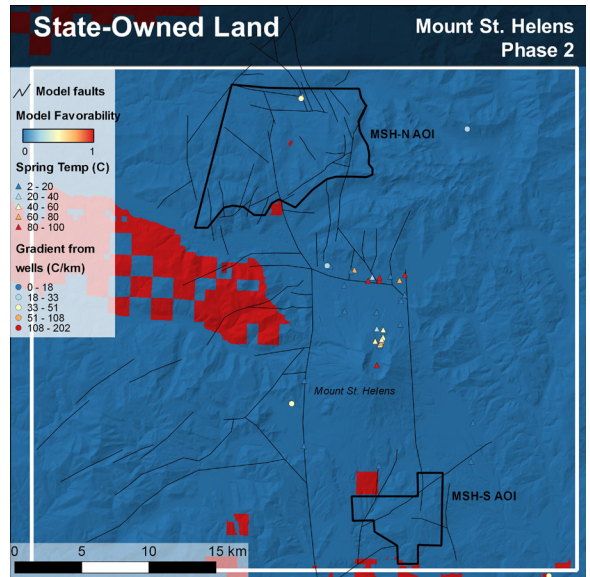
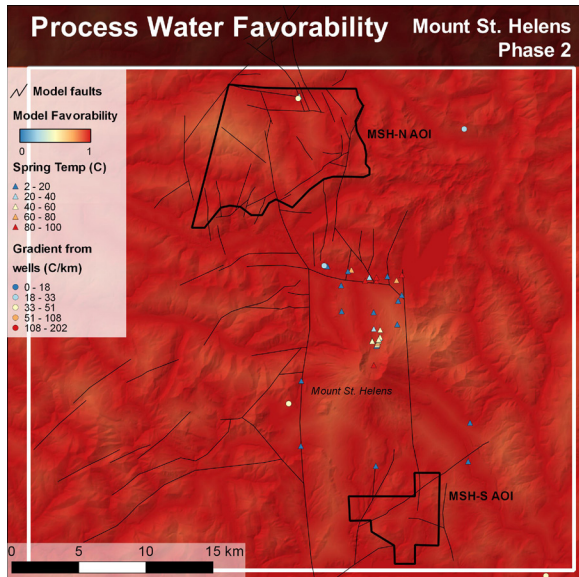
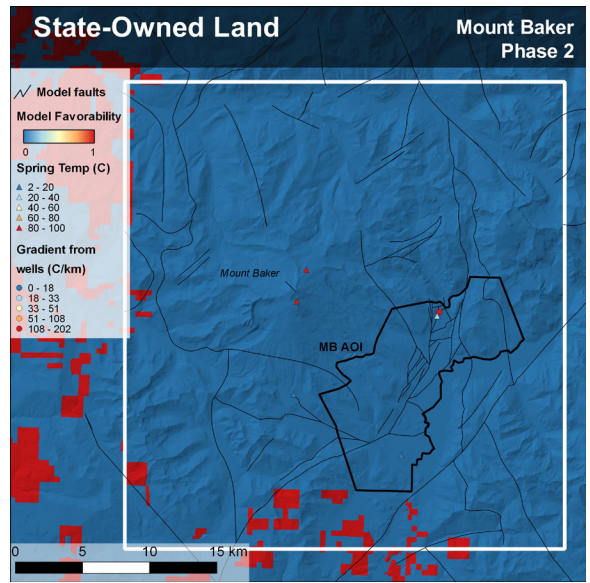
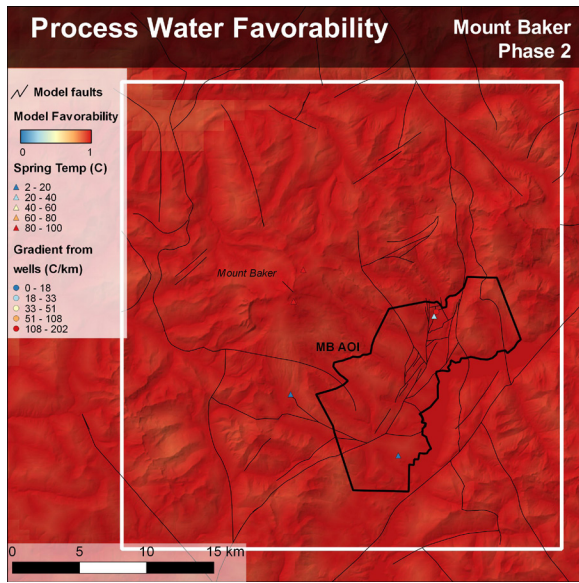


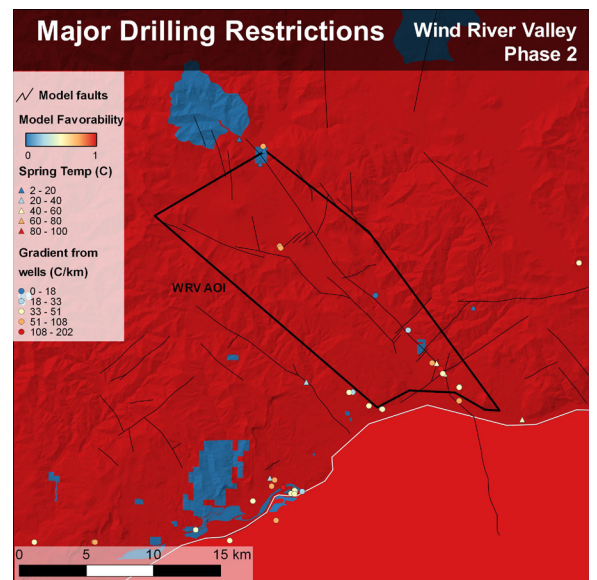
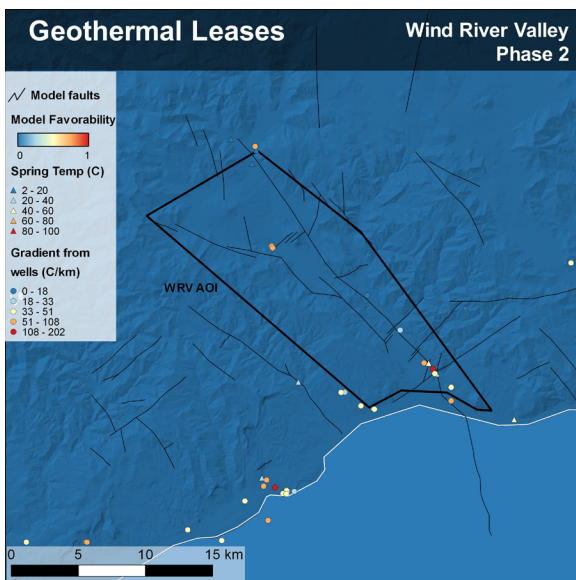
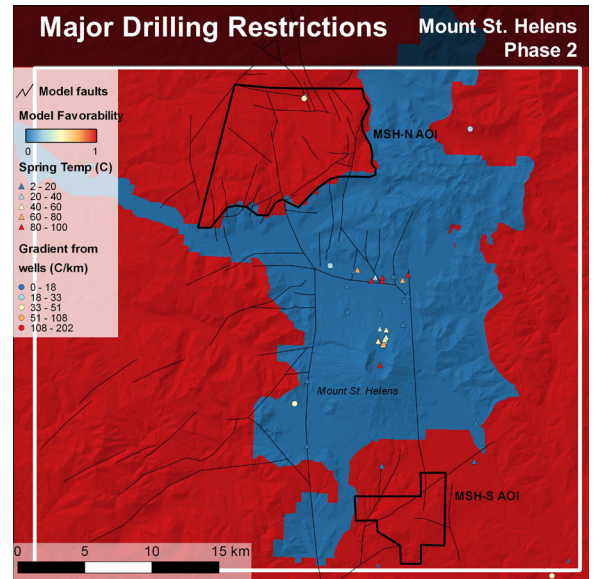
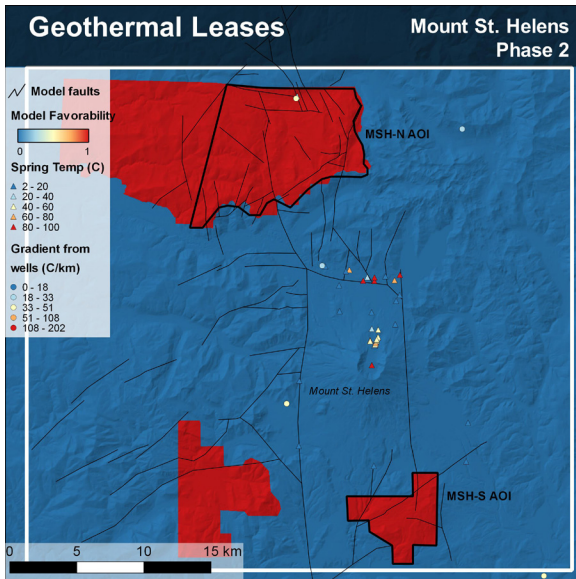
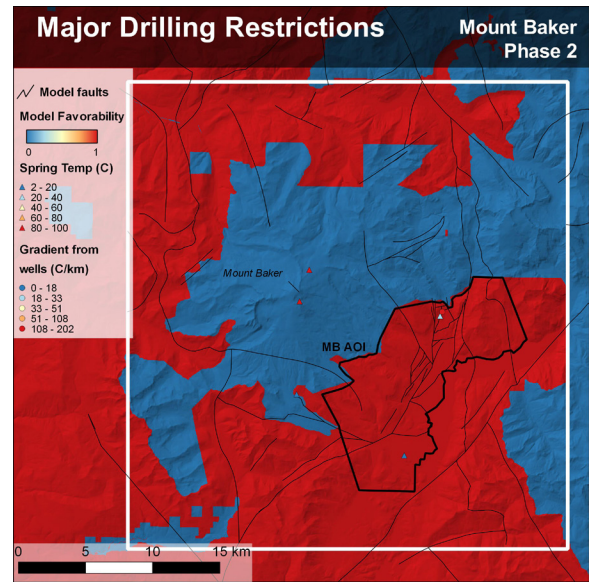
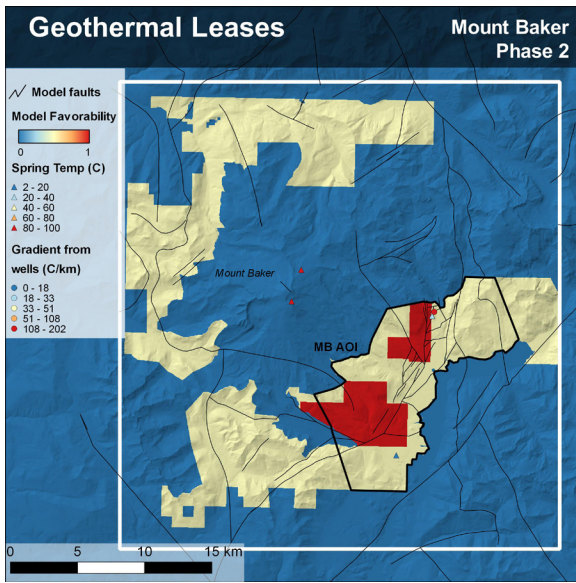




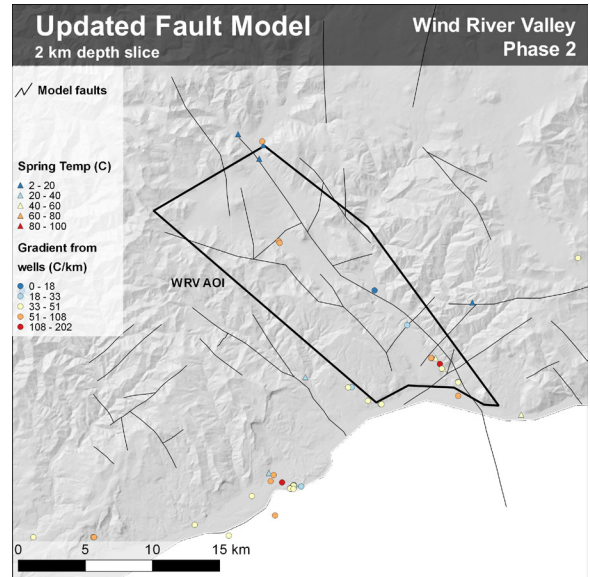
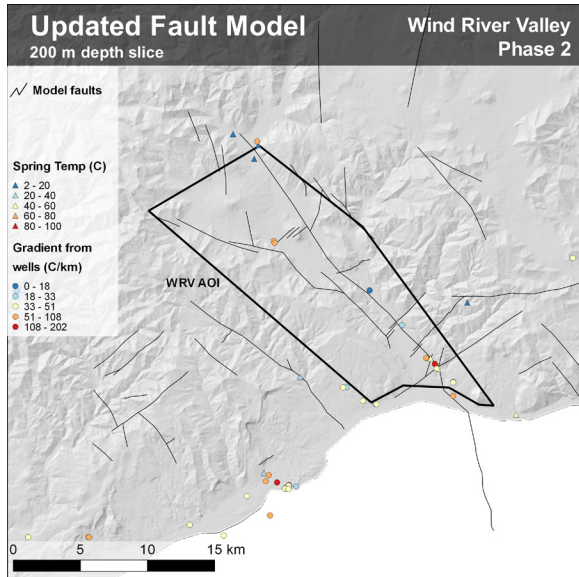
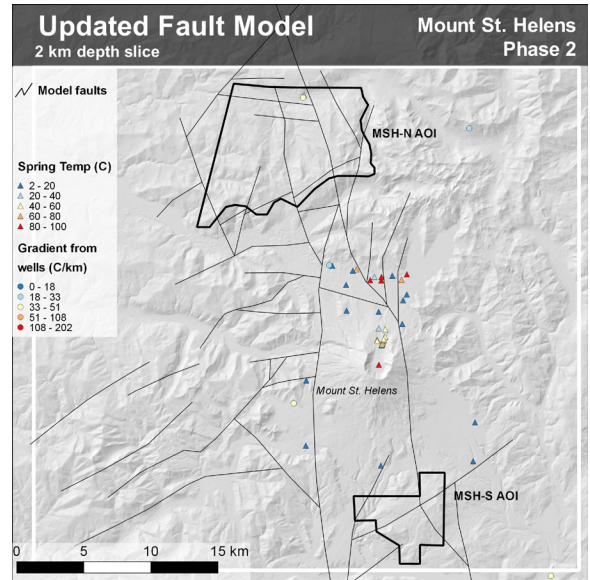
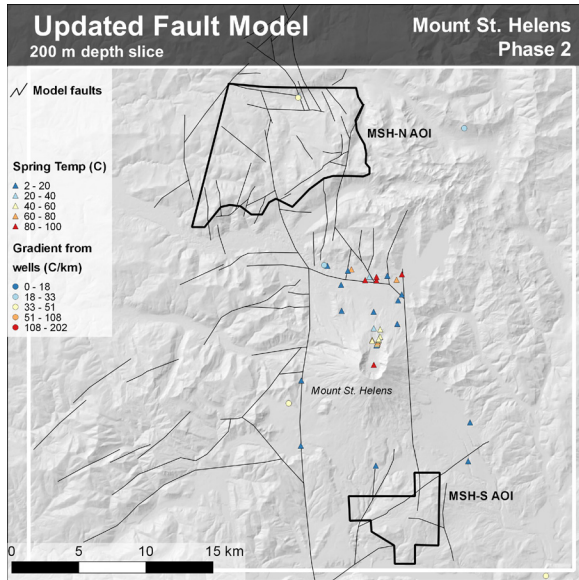
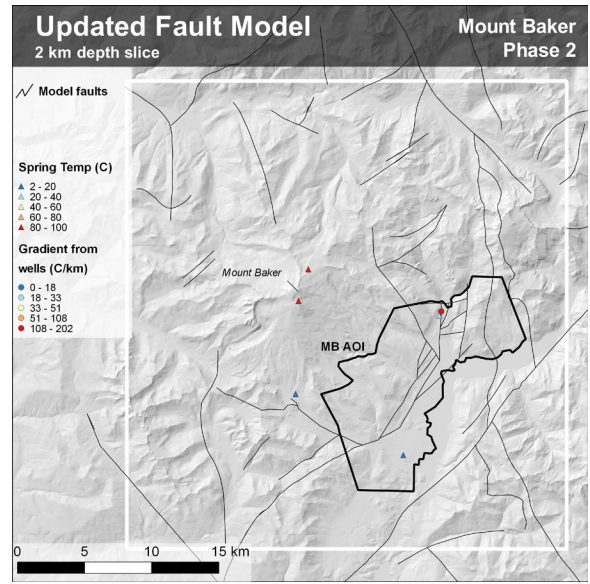
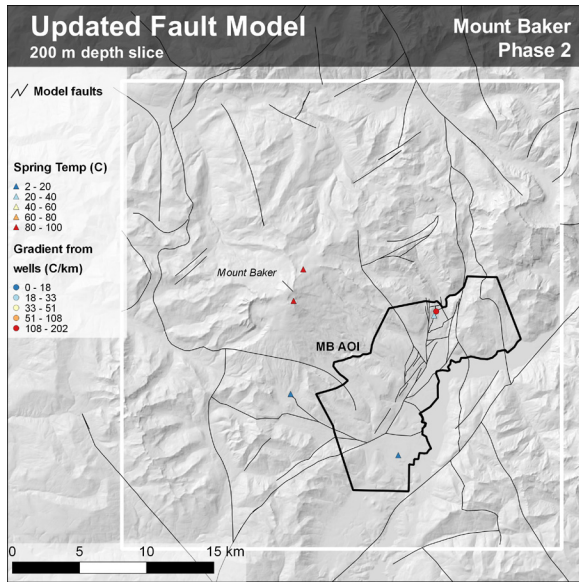








Appendix B. Updated Phase 2 Fault Models



Appendix C. Results of MT Surveys

Play Fairway Analysis: Mount Baker, WA, Magnetotelluric Measurements

Jared R. Peacock¹

¹U.S. Geological Survey

October 23, 2017

1 Introduction

This report describes the magnetotelluric portion of the Washington Play Fairway geothermal assessment, specifically the Mount Baker play (Figure 1).

2 Magnetotelluric Method

Magnetotellurics (MT) is a passive electromagnetic geophysical method that measures the Earth's electrical response to natural time-varying magnetic fields. MT is an inductive process where natural time-varying magnetic fields diffuse into the Earth which induce electrical currents in the subsurface. Depth of penetration of the diffusing magnetic field depends on subsurface resistivity and the frequency of the inducing magnetic field. The time-varying magnetic source is two-fold, one that operates at frequencies of less than 1 Hz and a second that operates at frequencies larger than 1 Hz. The magnetic source for frequencies less than 1 Hz is interaction of the Earth's natural magnetic field with solar wind, a collection of charged particles emitted from the sun, which can be visibly observed as auroras. The magnetic source for frequencies larger than 1 Hz is guided waves (the waveguide being the cavity between the Earth's surface and the ionosphere) from lightning strikes around the globe. Note, the vertically impinging time-varying magnetic field is elliptically polarized in the horizontal plane. Thus, the Earth's electrical response contains information about subsurface resistivity structure as a function of frequency and direction. In the frequency domain (ω) this is a simple linear transformation (1) of the inducing magnetic field (\mathbf{H}) into an electric field (\mathbf{E}) via a transfer function (\mathbf{Z}), where \mathbf{Z} is a complex rank 2 tensor that contains all the information about subsurface resistivity structure.

$$\mathbf{E}(\omega) = \mathbf{Z}(\omega)\mathbf{H}(\omega) \quad (1)$$

Similarly, the impinging magnetic field and induced horizontal electrical currents can generate a secondary magnetic field in the vertical direction. This is known as a geomagnetic depth sounding (GDS) and is again a linear transformation in the frequency domain (2), where the transfer function \mathbf{W} provides information on direction and relative strength of electrical currents. The geomagnetic depth sounding is useful for locating lateral boundaries.

$$H_z(\omega) = \mathbf{W}(\omega)\mathbf{H}(\omega) \quad (2)$$

3 Magnetotelluric Data

MT is measured in the field by using induction coils to measure the time-varying magnetic source for frequencies between 1000–0.001 Hz, and electric dipoles to measure the Earth's electrical response. Because the magnetic source field is polarized, orthogonal directions of the fields need to be measured to get a complete description of the fields. In all measurements collected for this project induction coils and electric

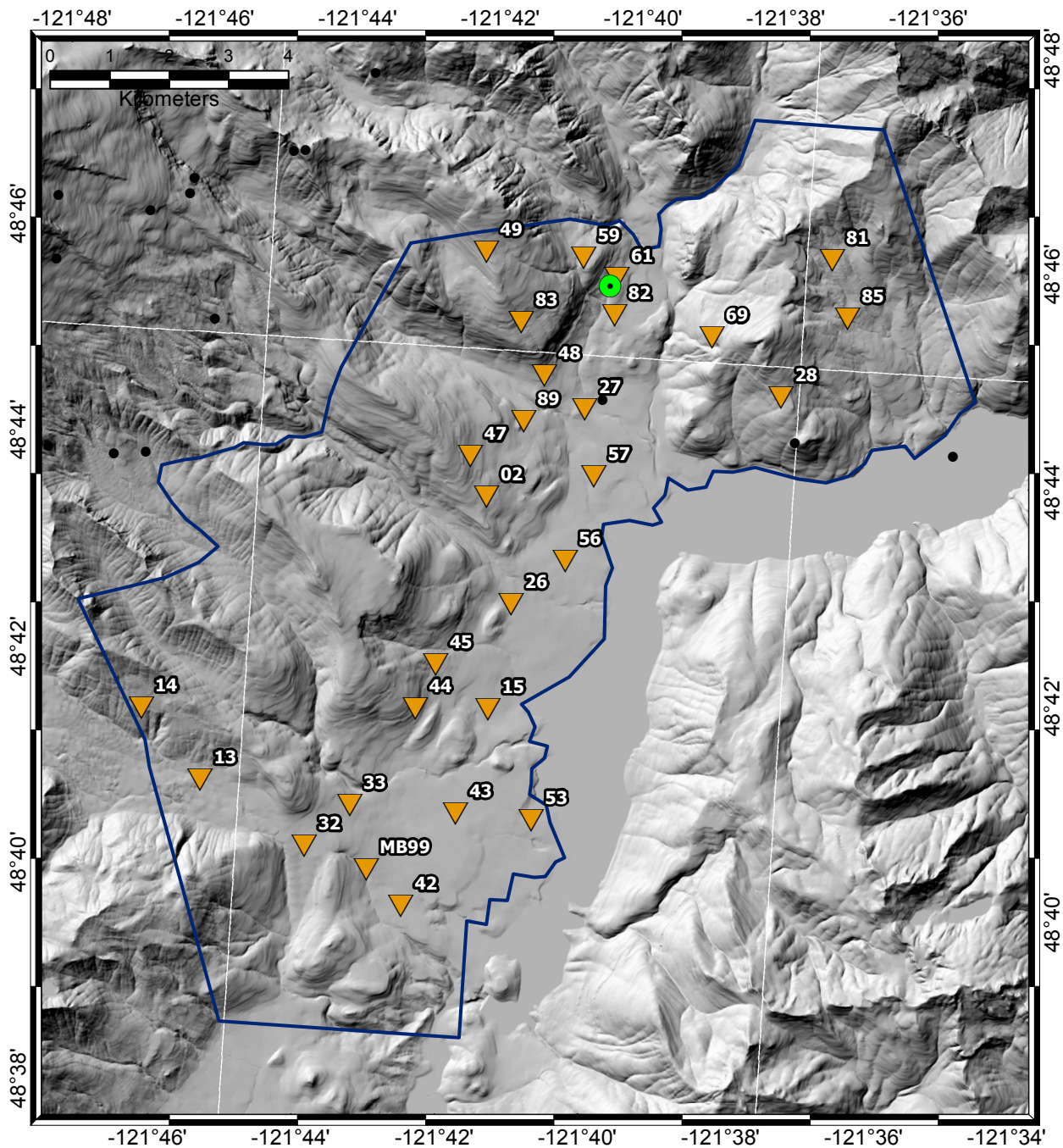


Figure 1: Area of interest at Mount Baker (yellow line), location of MT stations collected for this survey (orange triangles), and hot springs (green circle).

dipoles were aligned with geomagnetic north and east and a vertical induction coil was either buried or tied to a tree to get the vertical magnetic field. MT data was collected at 41 stations with a ZEN 32-bit data logger developed by Zonge International, magnetic fields were measured with ANT-4 induction coils, and electric fields were measured with Ag-AgCl reference electrodes from Borin on 50-100 m dipoles. The data was collected on a repeating schedule of 5 min at 4096 samples/s, 15 min at 1024 samples/s, and 7 hours and 40 minutes at 256 samples/s over a 2024 hour period. To get time series data into the frequency domain and get estimations of Z and W , the processing code provided by Zonge International was used in

conjunction with BIRRP written by [Chave & Thomson \(2004\)](#). Simultaneous measurements were used as remote references to reduce noise and bias in the data.

4 Inverse Modeling

MT and GDS response functions were modeled in three-dimensions (3-D) using the code ModEM developed by [Egbert & Kelbert \(2012\)](#); [Kelbert *et al.* \(2014\)](#). Input data was edited using the EDI editor in MTpy ([Krieger & Peacock, 2014](#)) to remove obvious outliers in the data and suppress bias in the modeling. All data was interpolated onto 23 frequencies in the range of 6250.001 Hz. The model mesh (north, east, depth) was 72 x 70 x 40 with dimensions of 103000 x 102600 x 169360 m, where spacing within the station area was 200 m increasing by 1.4 away from the station area. The first layer was set to 10 m and increases logarithmically downwards. Inversions were run on NASAs high-end computing capability (HECC) Pleiades super computer, where average run times were on the order of 18 hours.

To get to a preferred model the following scheme was used. Invert all components of the data with an error floor of $0.12\sqrt{Z_{xy} \cdot Z_{yx}}$ and an error floor of 0.10 for the GDS components and run ModEM with a covariance of 0.40 in all directions using different starting models of a 1000, 100, and 10 Ohm-m half space. Reduce error floors to $0.05\sqrt{Z_{xy} \cdot Z_{yx}}$ and an error floor of 0.03 and run ModEM with a covariance of 0.30 in all directions using the final iteration from the previous run as the starting model. Invert just the GDS components with an error floor of 0.03 with a covariance of 0.40 using starting models of a 1000, 100, and 10 Ohm-m half space. Compute the geometric average of all models to enhance common features and suppress uncommon features. Run ModEM with error floors of $0.10\sqrt{Z_{xy} \cdot Z_{yx}}$ and an error floor of 0.05 and a covariance of 0.40 using the average model as the starting model. Then reduce error floors to $0.05\sqrt{Z_{xy} \cdot Z_{yx}}$ and an error floor of 0.03 for GDS components and run ModEM with a covariance of 0.30 in all directions using the final iteration from the previous run as the starting model. Features in the preferred model were tested for sensitivity to location, geometry, and resistivity value.

5 Resistivity Model Features

Many interesting features are observed in the resistivity model. For the purpose of this report only those features in the top 10 km will be described (Figure 2). The first observation is that the near surface (top 1 km) is heterogeneous, which is caused by multiple glacial periods, land slides, flooding, and volcanic activity. Most of the conductive anomalies in the near surface are related to a collection of clay minerals, fluids, and conducting phases such as graphite or sulfides. At the bottom of the first figure in Appendix A there is a semicircular conductive feature which is related to sediment transport from Boulder Creek into the lake towards the dam. For the purposes of this study, only those conductive anomalies in the near surface with a deeper conductive anomaly will be interpreted.

The deep features include 2 narrow conductive zones oriented northwest towards Mount Baker.

The area around the hot springs is the most conductive and has the most structure.

6 Preliminary Interpretation

Where the hot spring are there is a thin conductor near the surface at around 30 Ohm-m which coincides with measured resistivity of the spring water. The thin conductor seems to originate from a deeper fault or other permeable structure to the north where there appears to be conductive body at the near surface extending down to 3 km where temperatures could reach the estimated 170 C of the springs source (Figure 3). There seems to no connection to a deeper conductor in the area, but could be influenced by a deep conductor under Mt. Baker, interpreted as a zone of partial melt at around 10 km. The conceptual model here is that meteoric water seeps into deep faults north of the spring down to a depth of 2-3 km, where the temperature is around 170 C. The warm water then upflows towards the south and out through a permeable near surface layer. The flow is not fast as the flow into the spring is low.

A few EW conductors are imaged under the survey area that extend from near the surface to 4 or 5 km, these could be faults associated with Mt. Baker, glacial gouges, or a combination. They are most

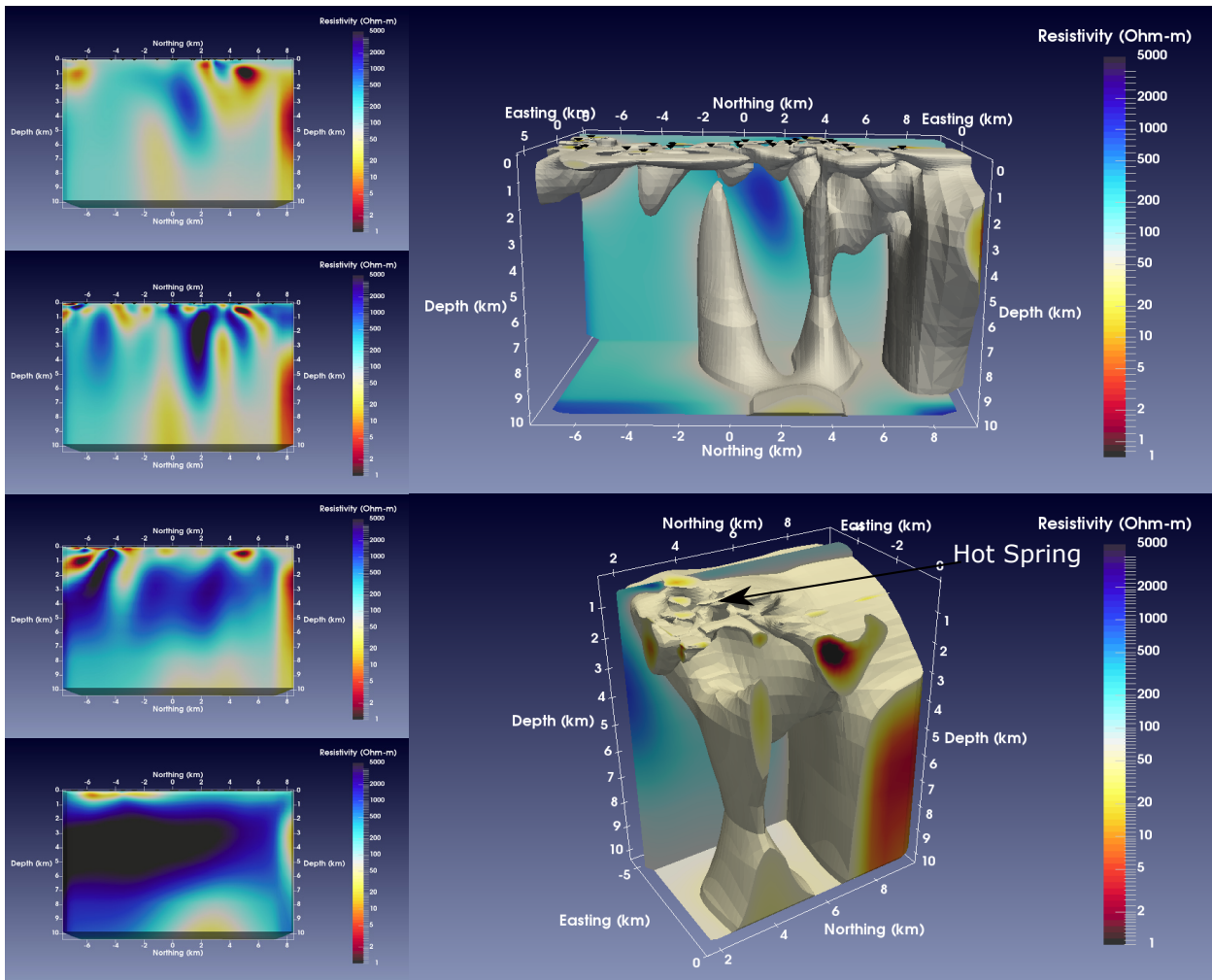


Figure 2: Different views of the resistivity model and main anomaly C1. Left: looking west through the resistivity model, where the top panel is the furthest west profile and each panel is a 3 km step west. Top Right: looking west. Bottom Right: looking northwest at the hot springs.

likely permeable and contain fluids. We cannot decipher whether the fluids circulate or not. An estimated temperature just based on regional heat flow would be around 170, similar to the estimated Baker Hot Spring reservoir temperature.

Other interesting features in the model that were surprising. We could image the lake, and the path of deposition from the rivers into Baker lake and down towards the dam.

7 Geothermal Potential

The location with the highest potential for geothermal would be just to the north of the Baker hot springs, where there is a conductive body suggestive of a hydrothermal reservoir at 3-4 km depth. The estimated temperature from geochemistry is 170 C.

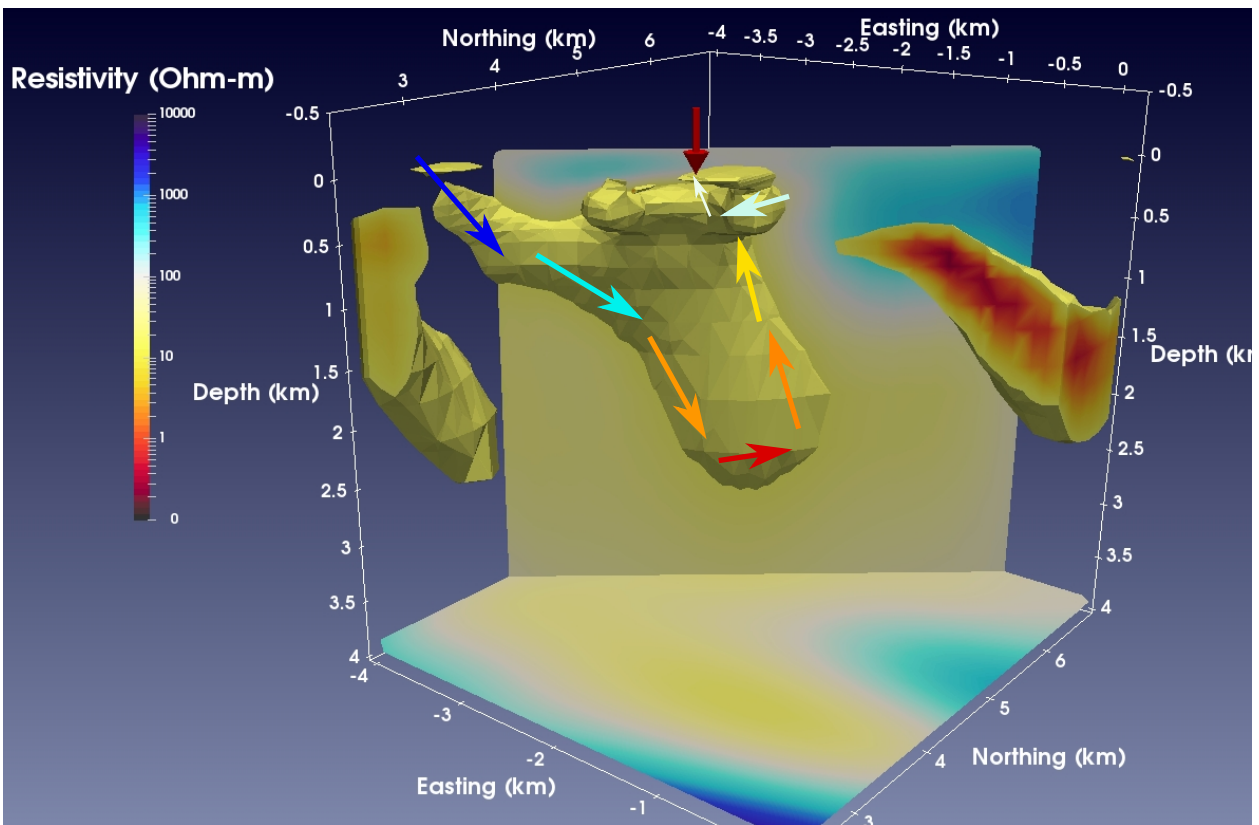


Figure 3: A closer look at the conductive anomaly associated with the Baker Hot Springs. The view is looking to the east northeast. The red arrow at the surface mark the location of the hot spring. The threshold on the resistivity is 10 Ohm-m. The thought is that cold meteoric water seeps down through deep faults to a depth of around 3 km (cool colored arrows), then heats up (red arrows) and up flows to the Baker Hot Spring while mixing with near surface meteoric water.

References

- Chave, A. D., & Thomson, D. J. 2004. Bounded influence magnetotelluric response function estimation. *Geophys. J. Int.*, **157**, 988–1006.
- Egbert, G. D., & Kelbert, A. 2012. Computational recipes for electromagnetic inverse problems. *Geophys. J. Int.*, **189**, 251–267.
- Kelbert, A., Meqbel, N. M., Egbert, G. D., & Tandon, K. 2014. ModEM: a modular system for inversion of electromagnetic geophysical data. *Computer Geoscience*, **66**, 40–53.
- Krieger, L., & Peacock, J. R. 2014. MTPy: a Python toolbox for magnetotellurics. *Computers & Geoscience*, **72**, 167–175.

A Depth Slices

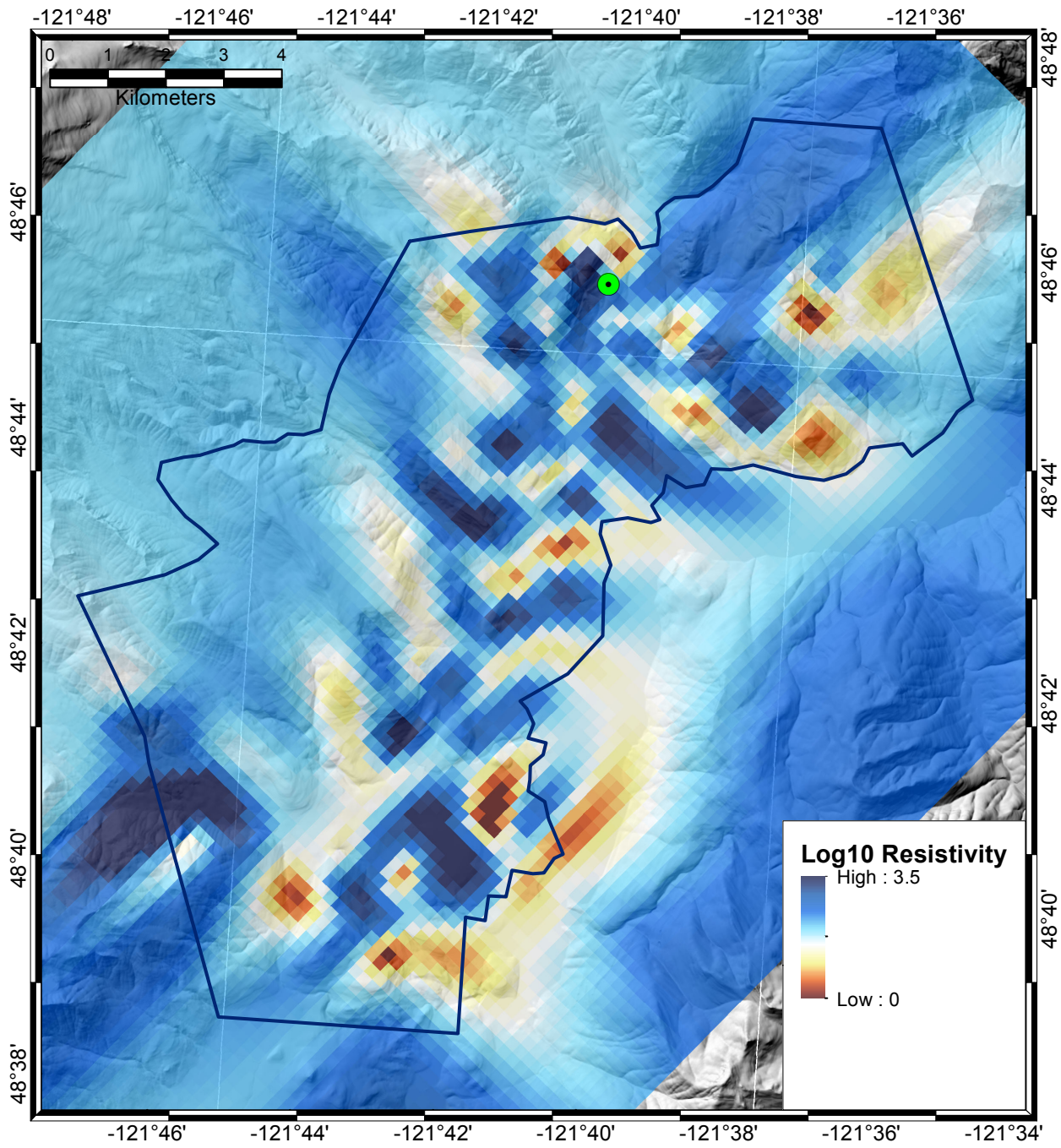


Figure 4: Depth slice at 290 m. Green dot is hot spring location.

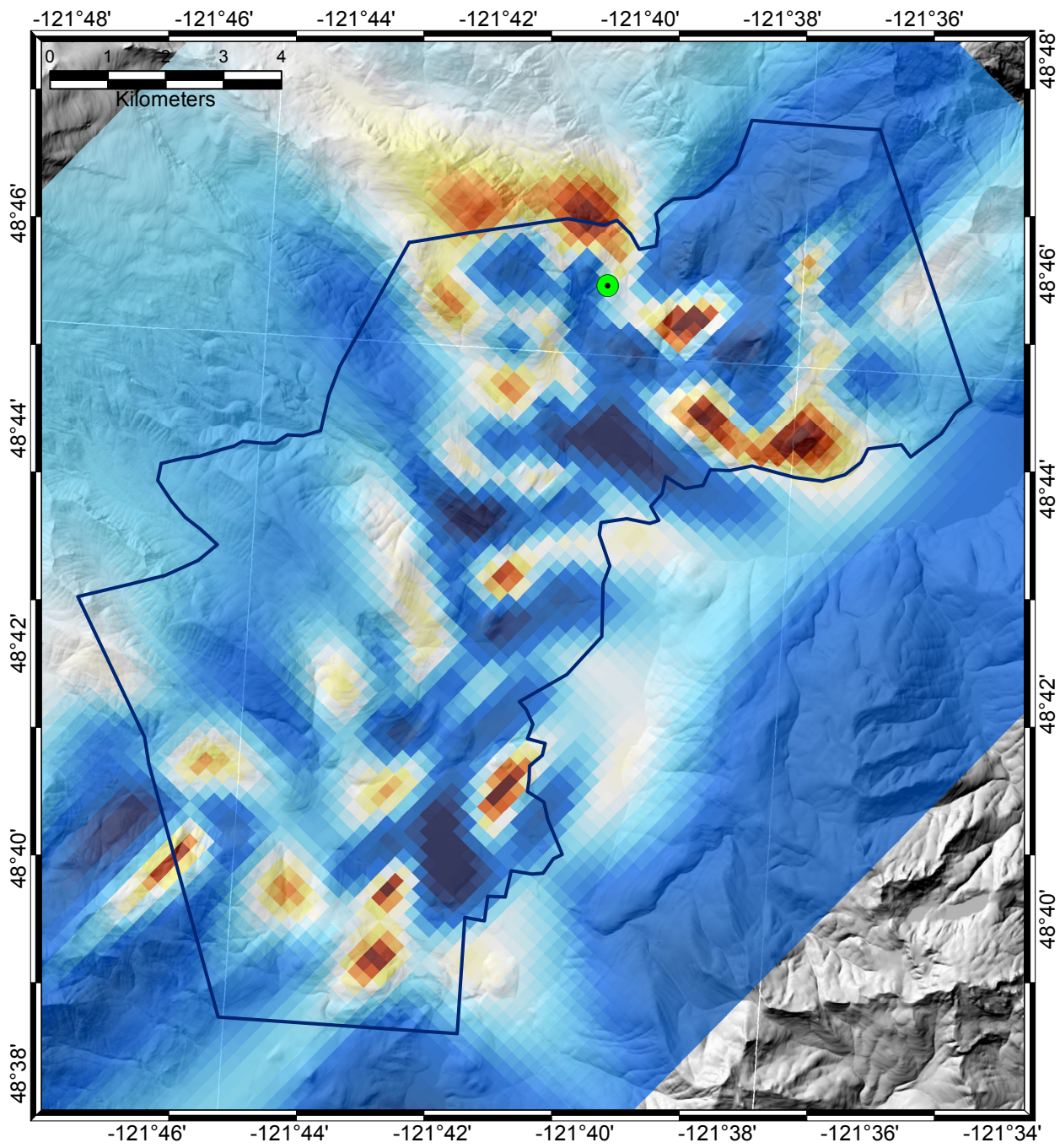


Figure 5: Depth slice at 560 m. Green dot is hot spring location.

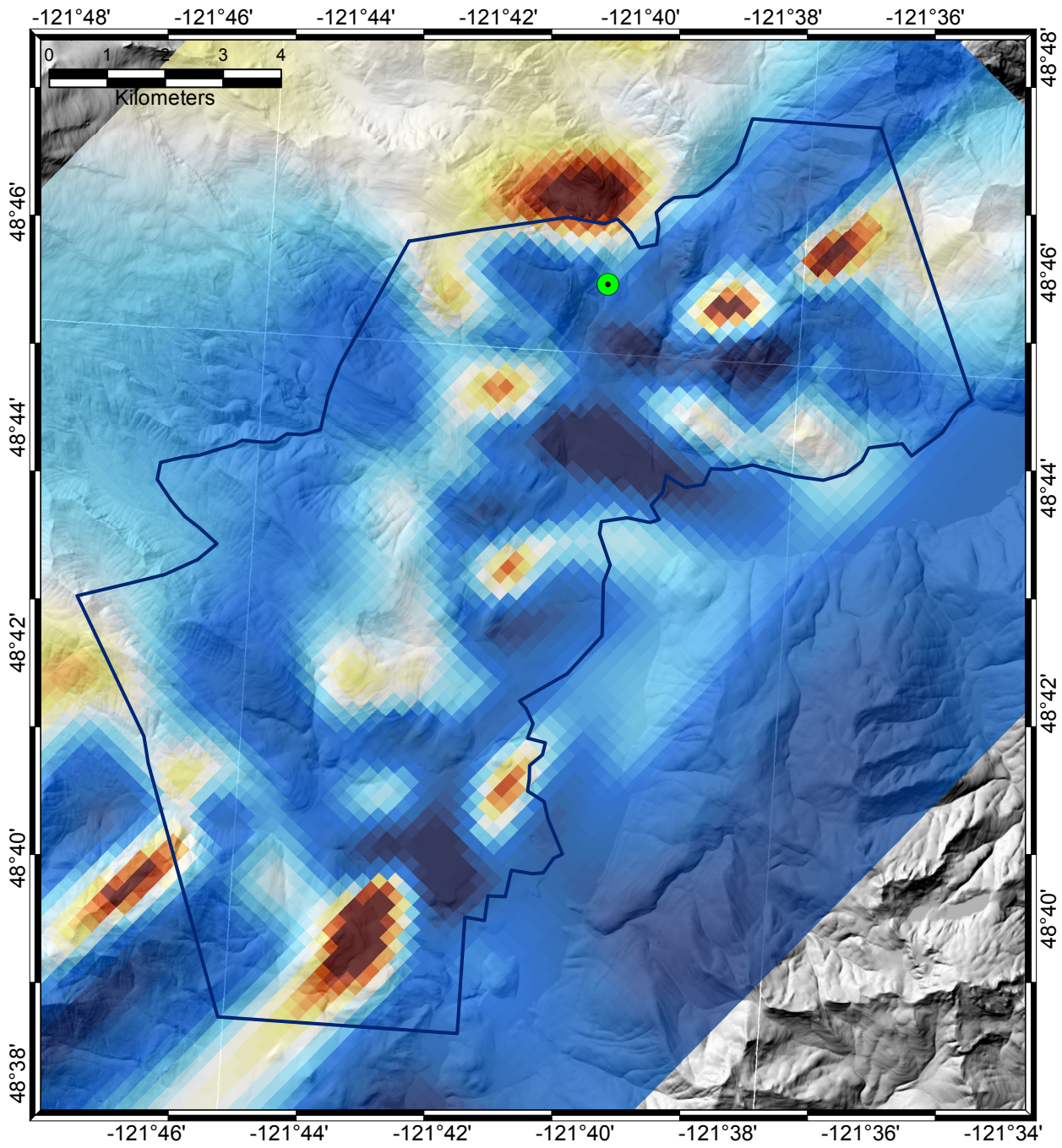


Figure 6: Depth slice at 960 m. Green dot is hot spring location.

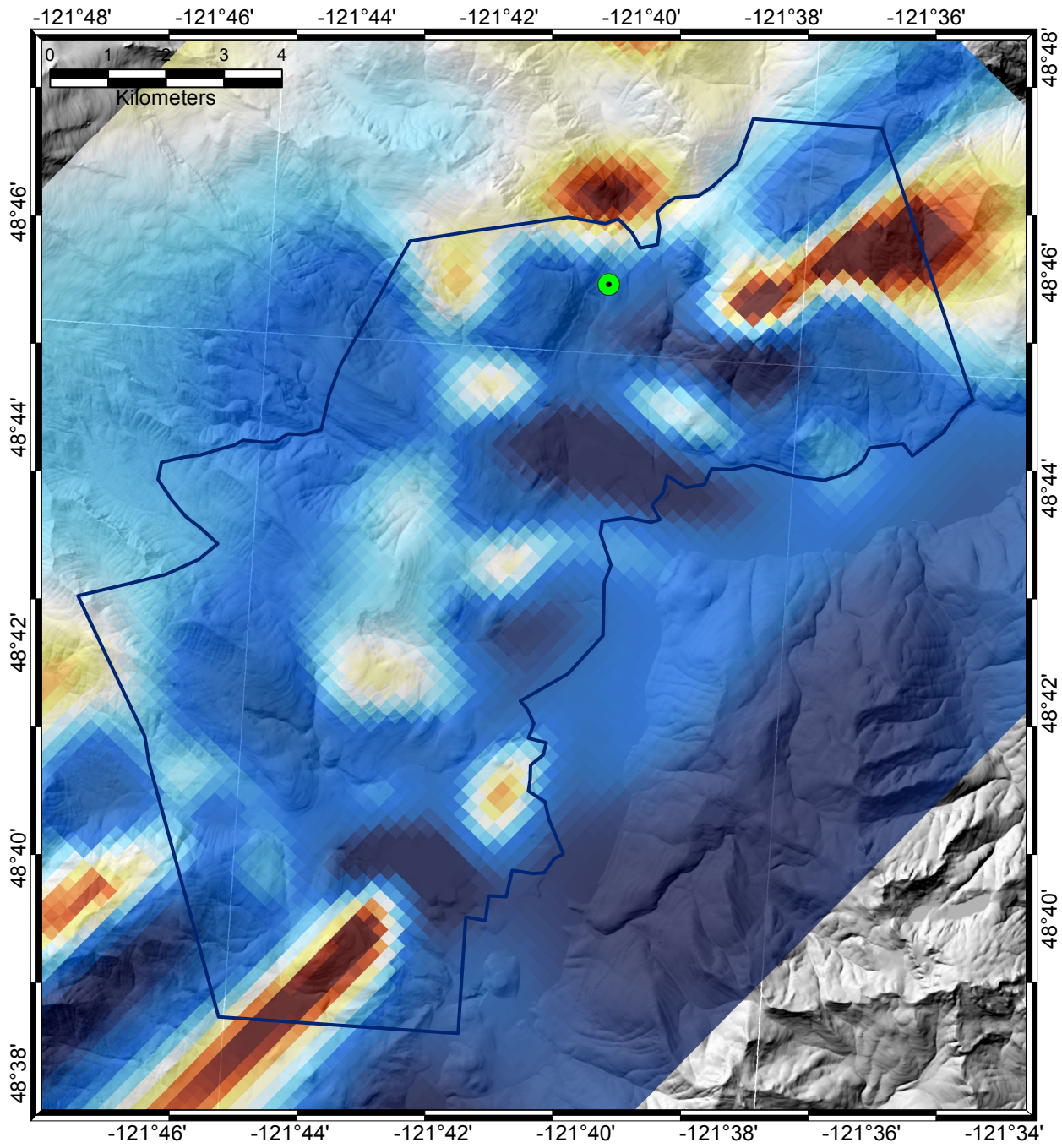


Figure 7: Depth slice at 1460 m. Green dot is hot spring location.

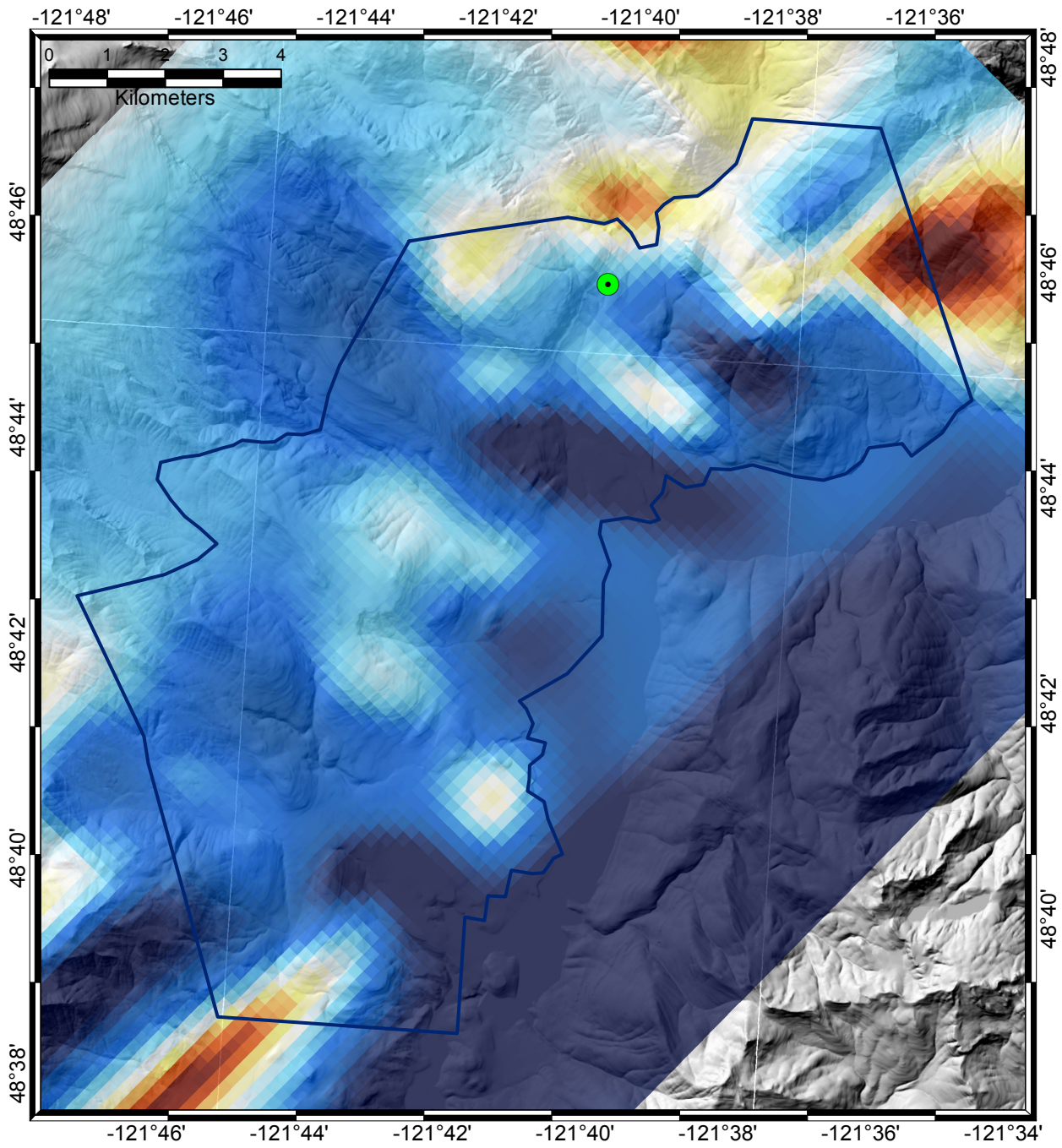


Figure 8: Depth slice at 2160 m. Green dot is hot spring location.

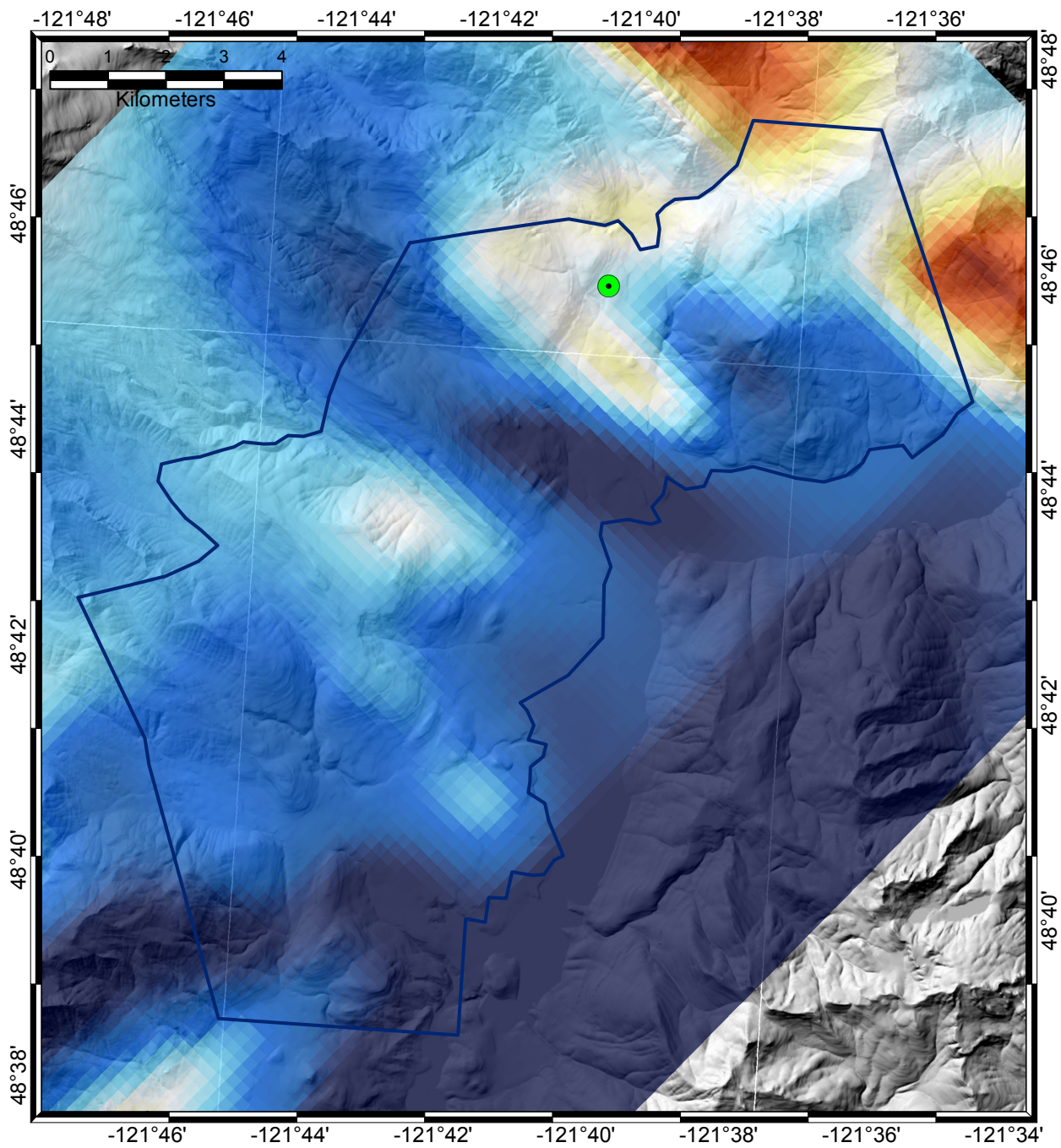


Figure 9: Depth slice at 3260 m. Green dot is hot spring location.

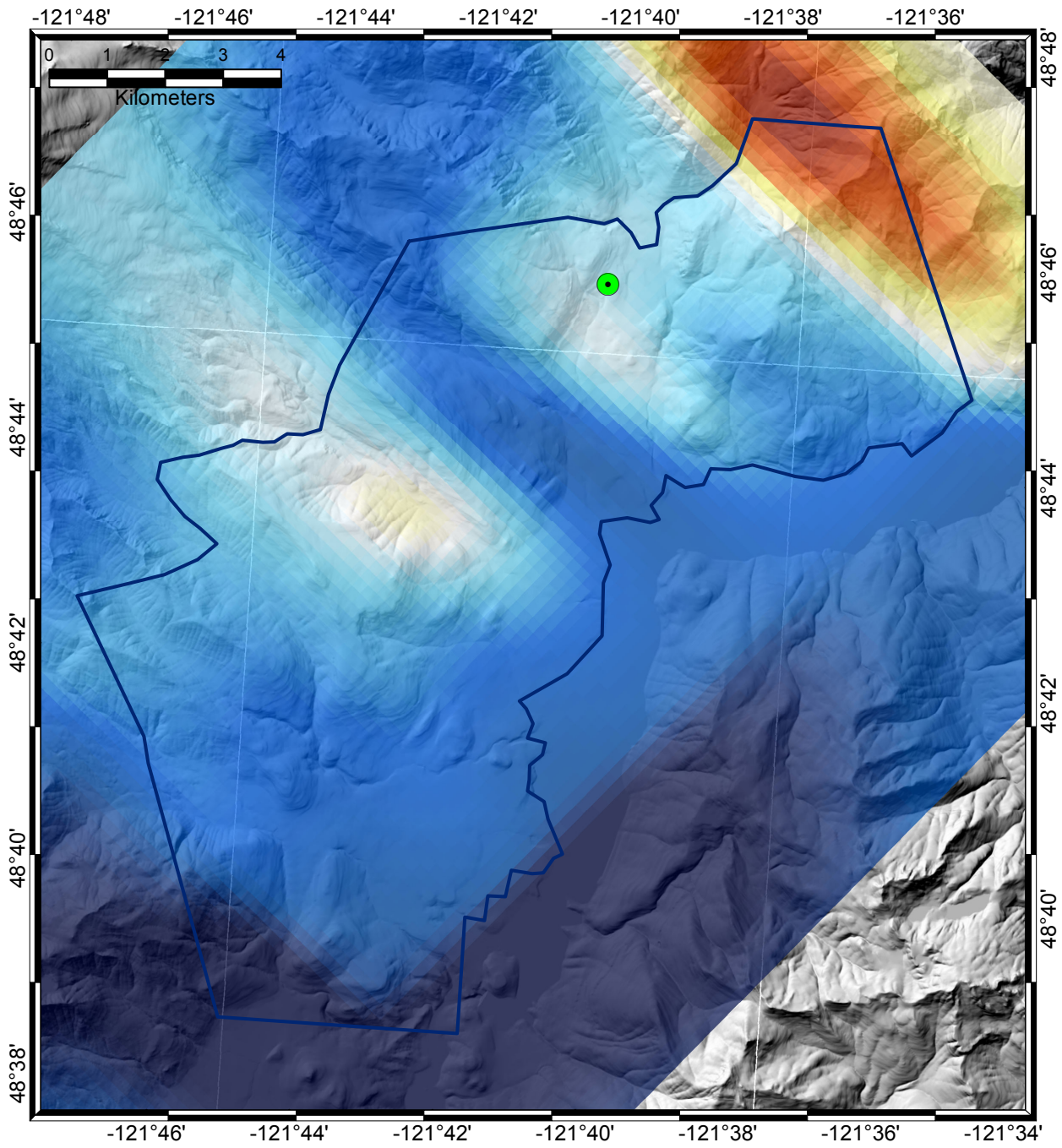


Figure 10: Depth slice at 5860 m. Green dot is hot spring location.

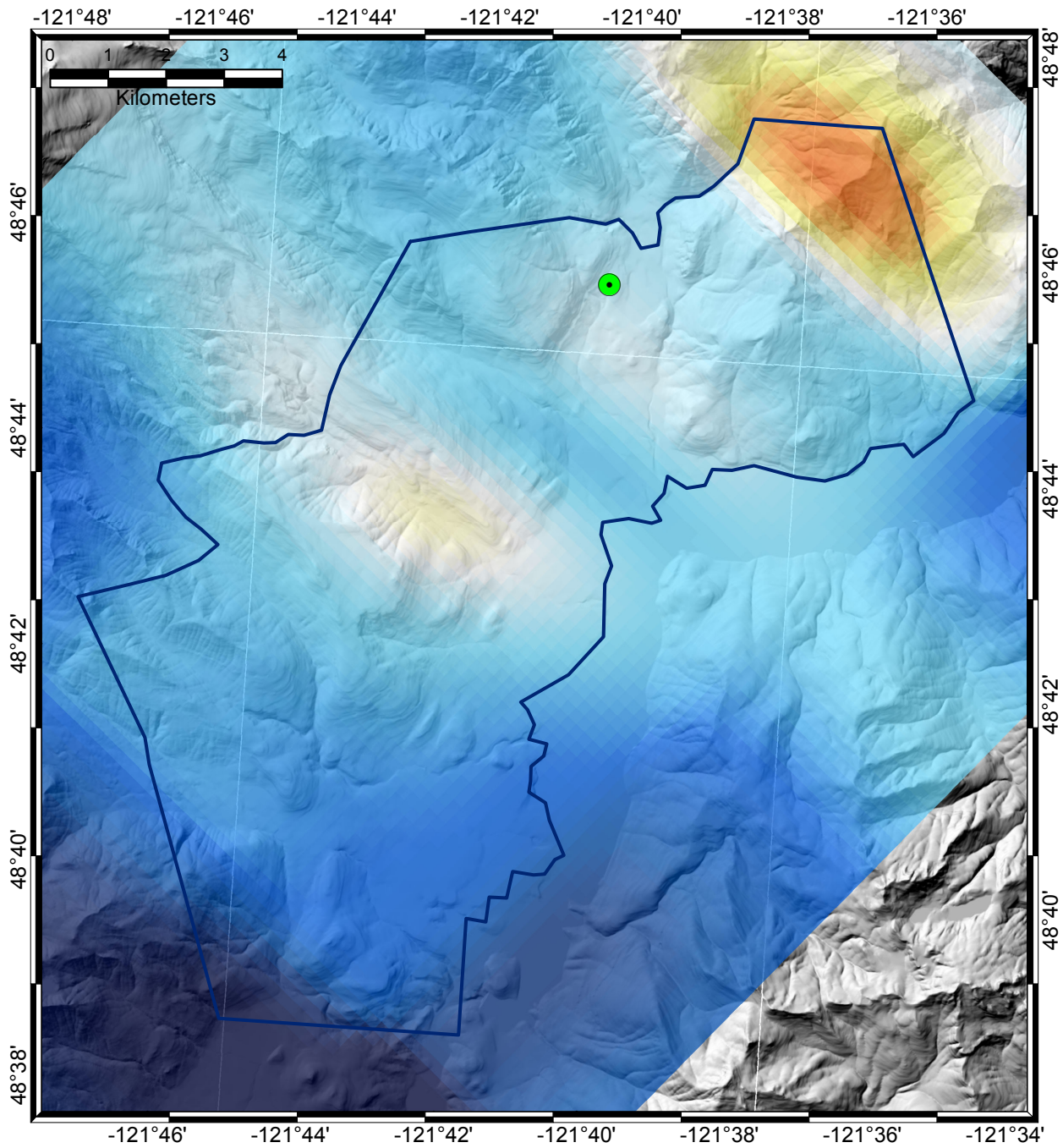


Figure 11: Depth slice at 7860 m. Green dot is hot spring location.

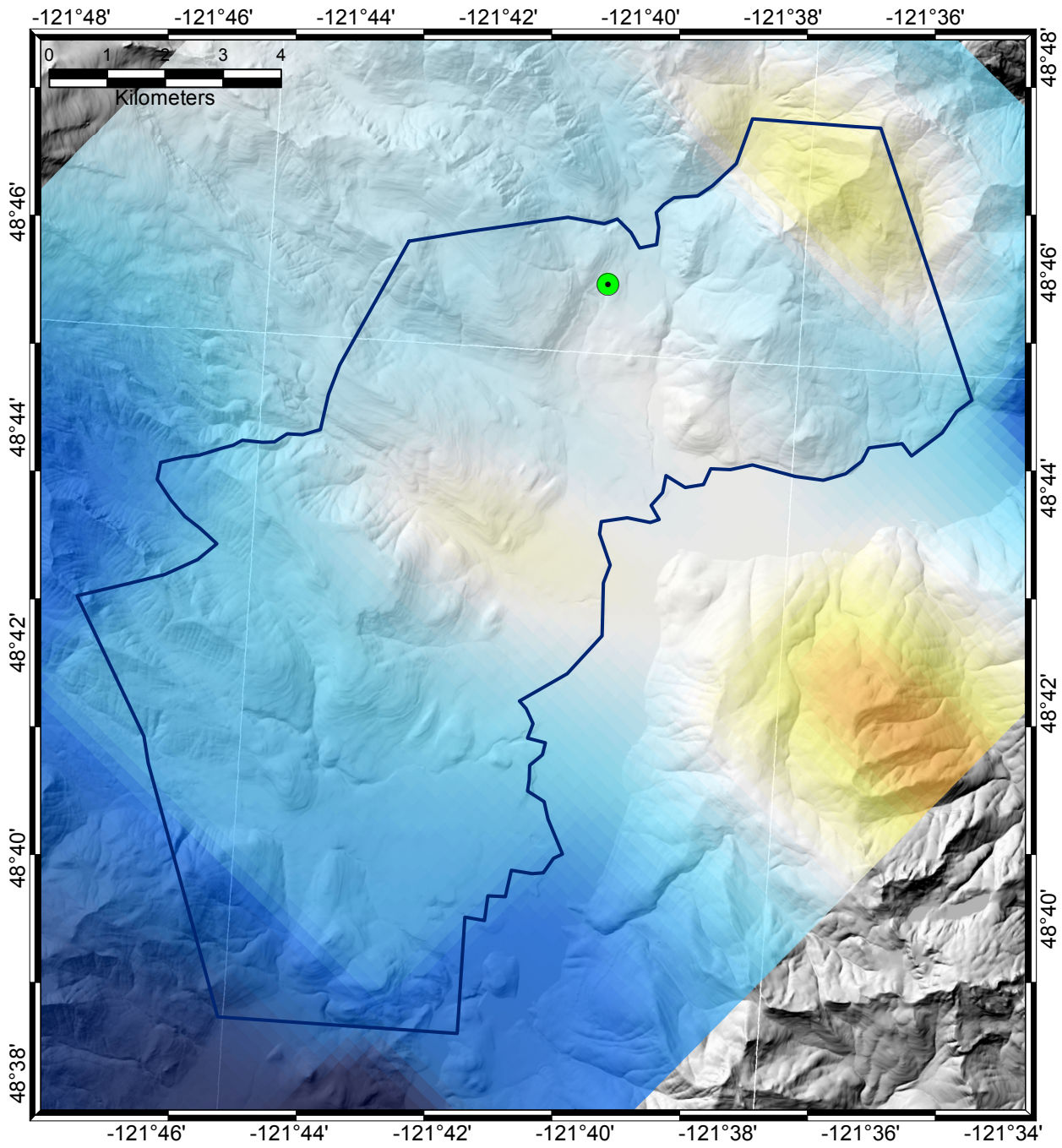
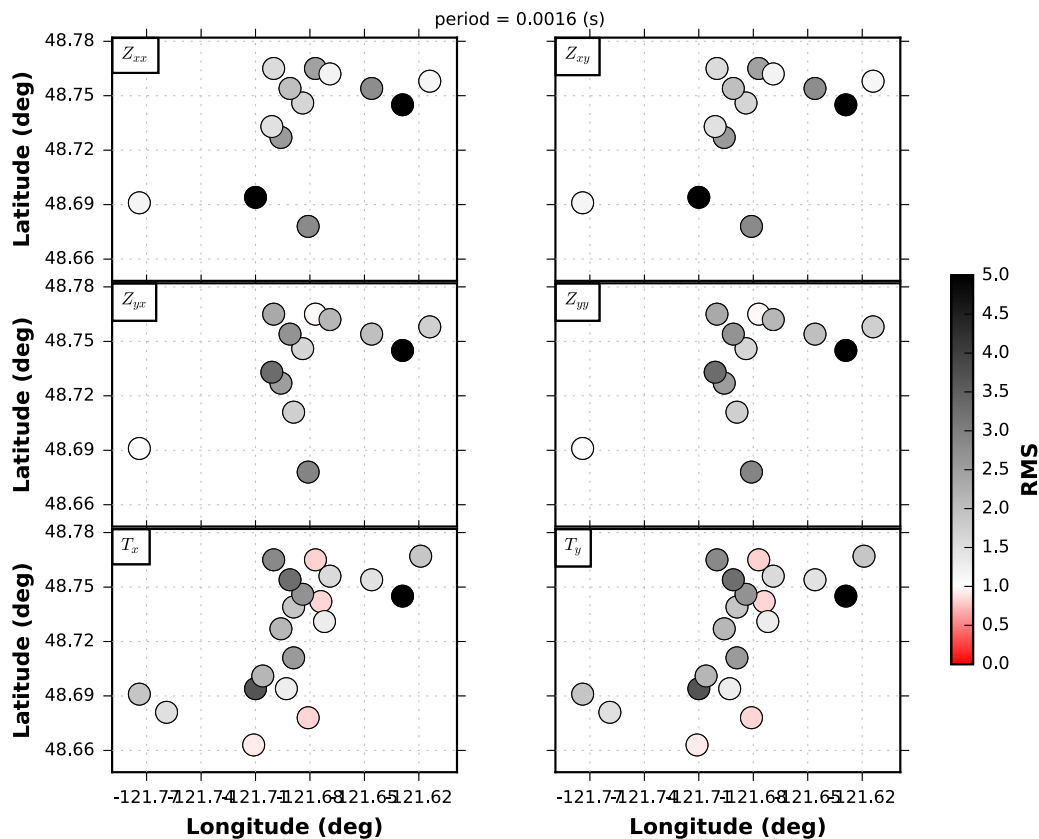
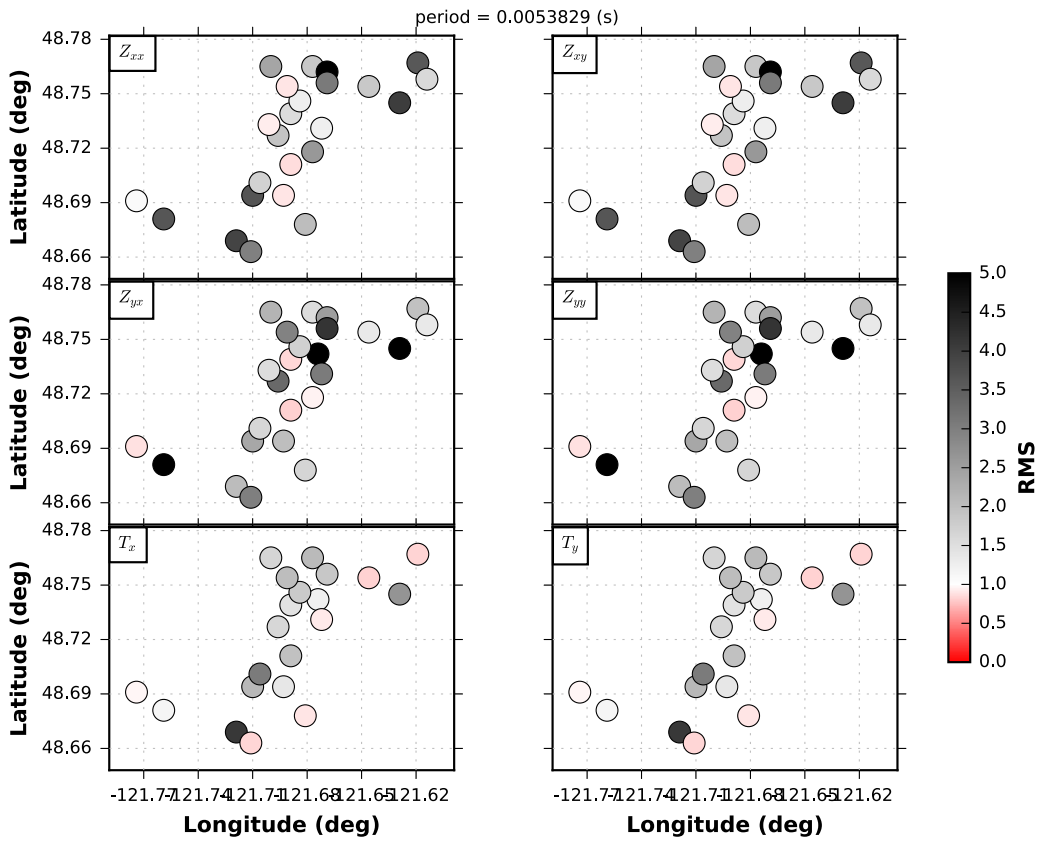
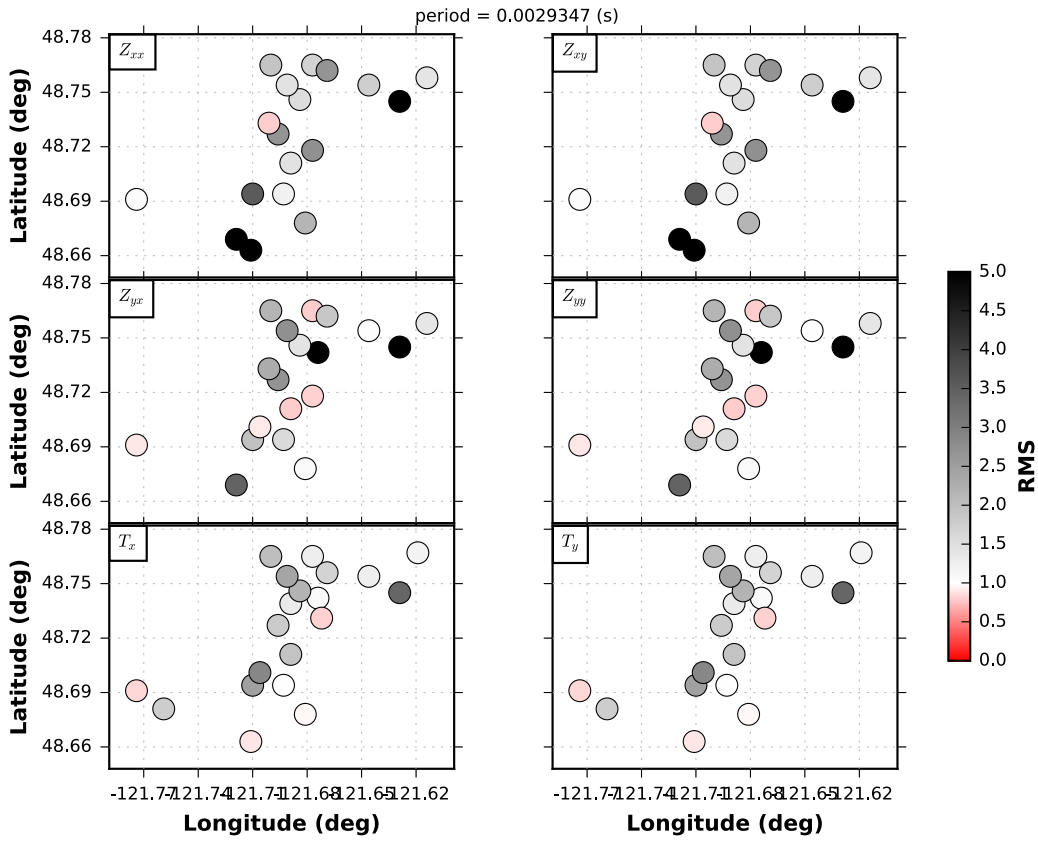


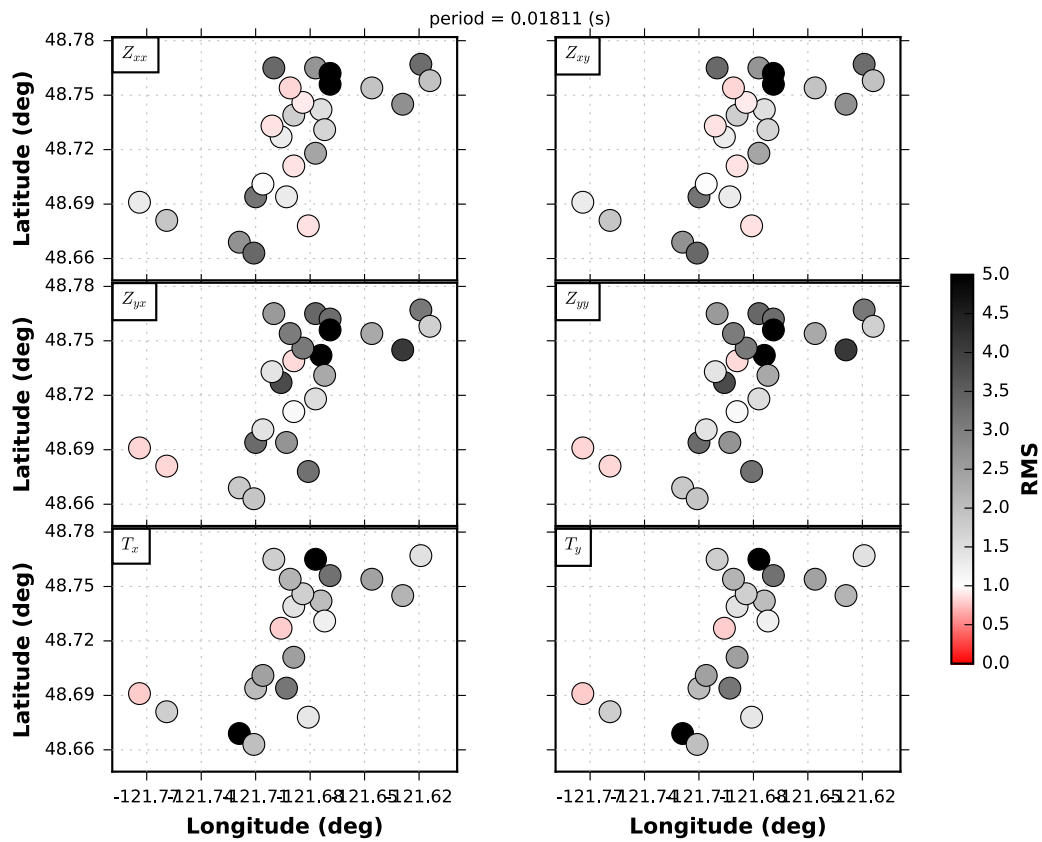
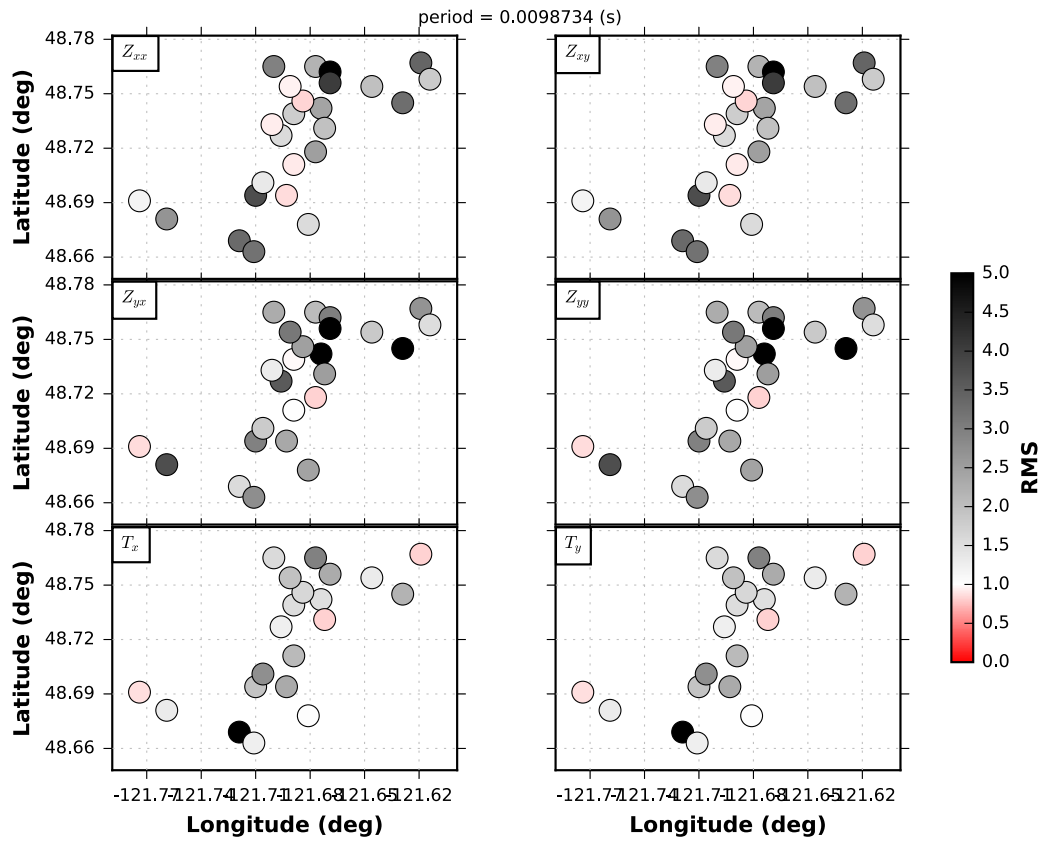
Figure 12: Depth slice at 11860 m. Green dot is hot spring location.

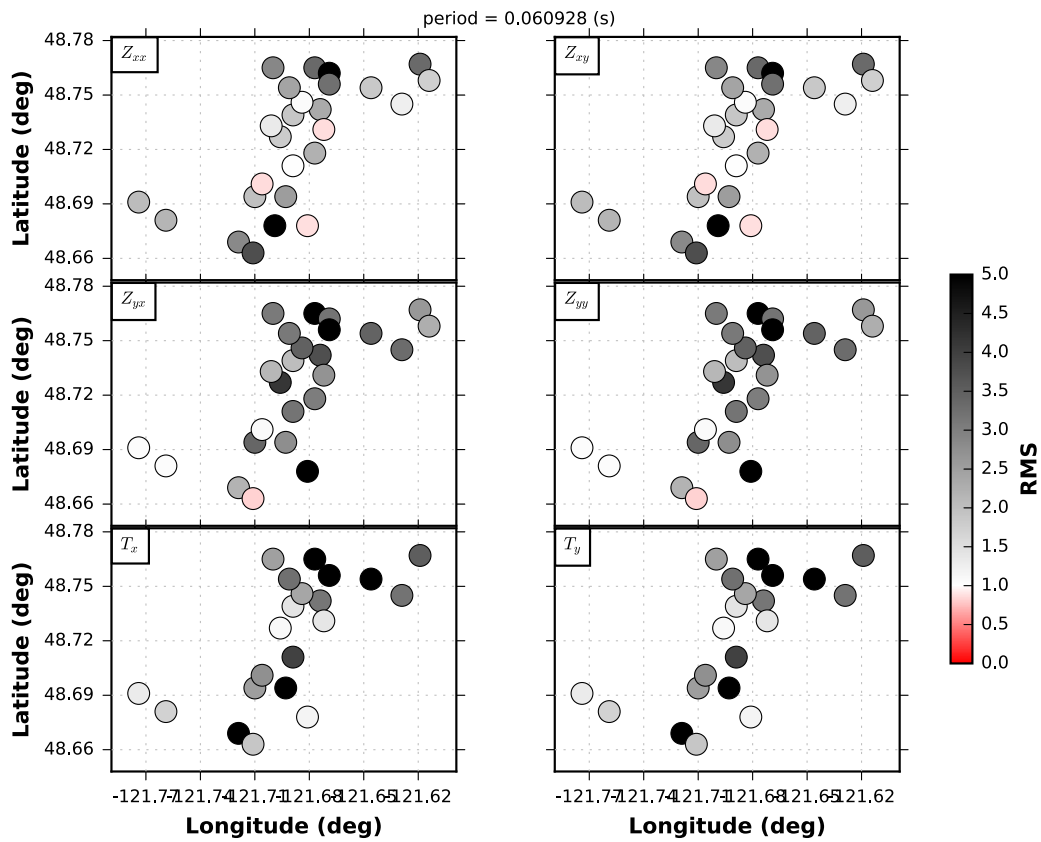
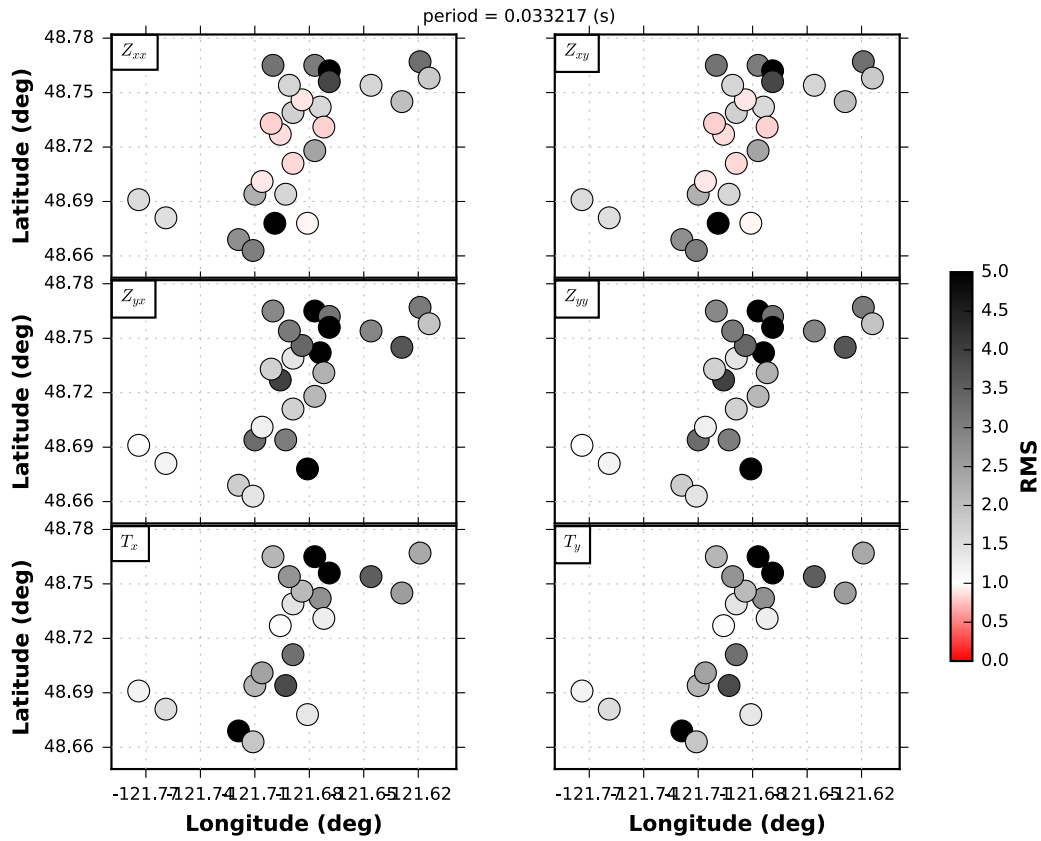
B Model RMS Maps

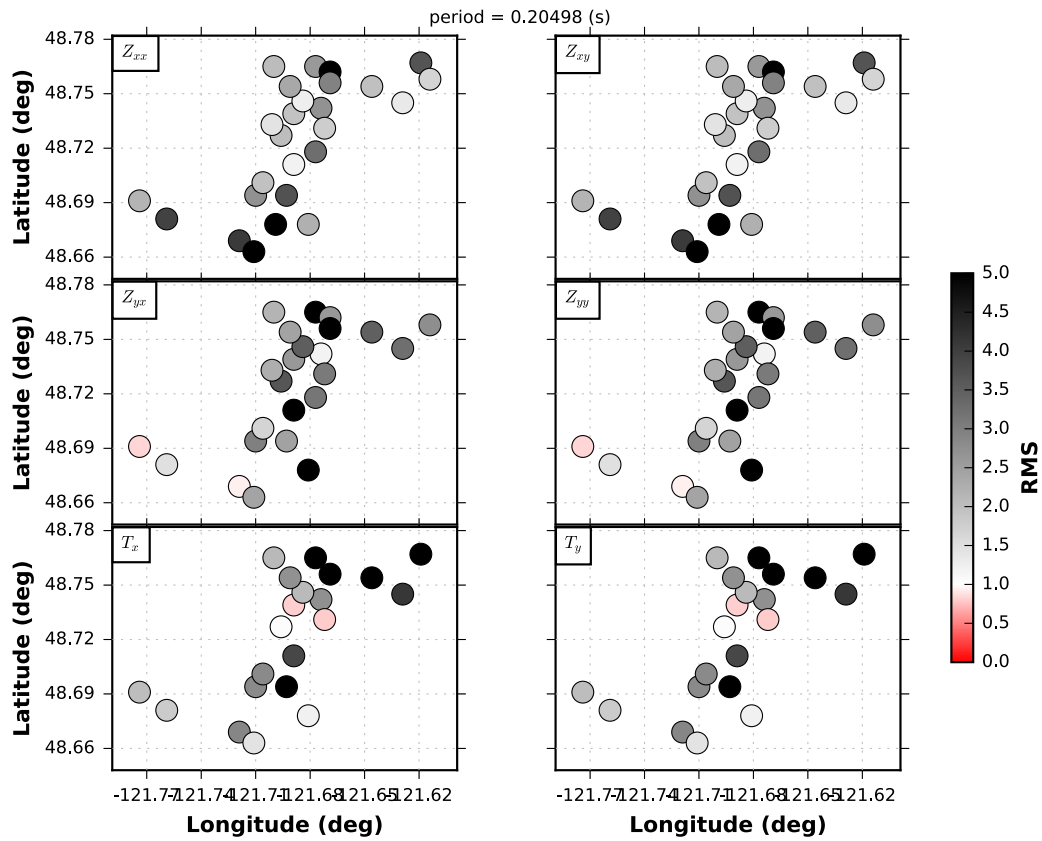
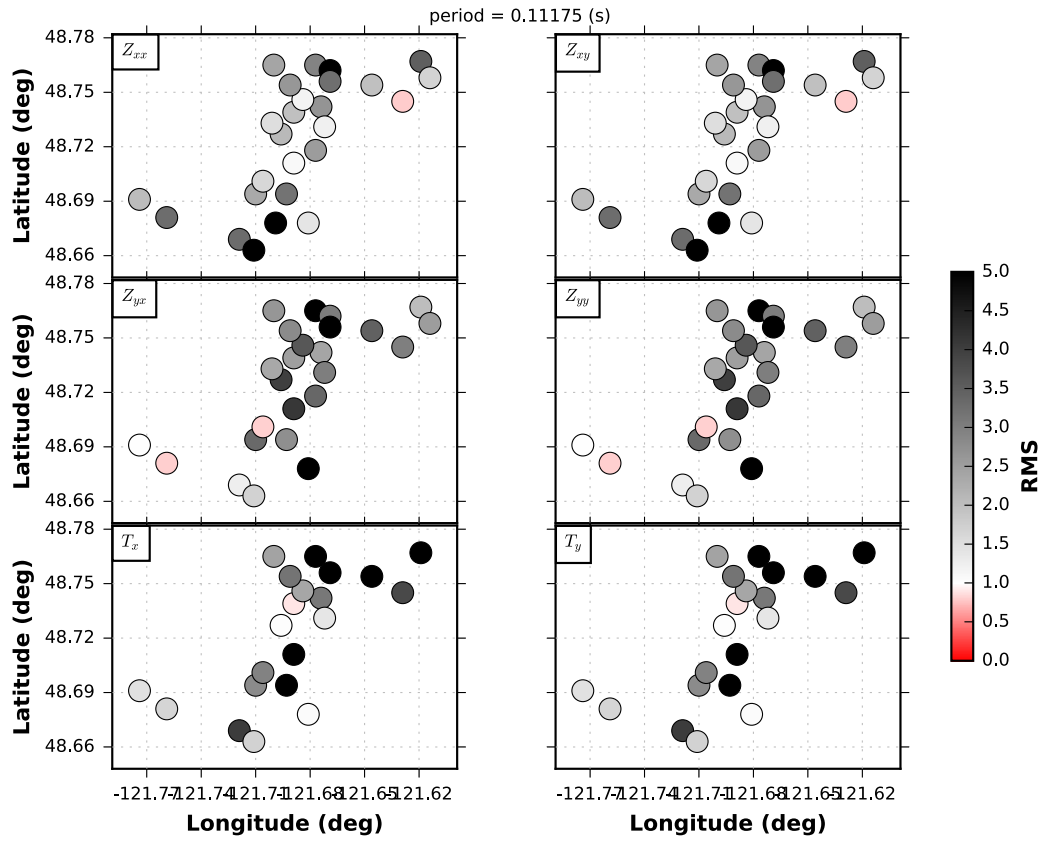
The maps in this section show the normalized root-means-squared (nRMS) error of the misfit between the MT response of the data and the resistivity model within the given error floors. Black color means the difference between the data and model response is large and the fit is poor, whereas red colors means the model is over fitting the data within the given error. White colors around and nRMS of 1 are optimal fits. The off-diagonal components of \mathbf{Z} typically have more weight than the diagonal components, which is related to the physics of induction. However, in this experiment, the diagonal components are nearly the same magnitude as the off-diagonal components and have influence in the model. The GDS magnitudes are relatively small (< 0.3) but still influence the shape and orientation of the main anomaly C1.

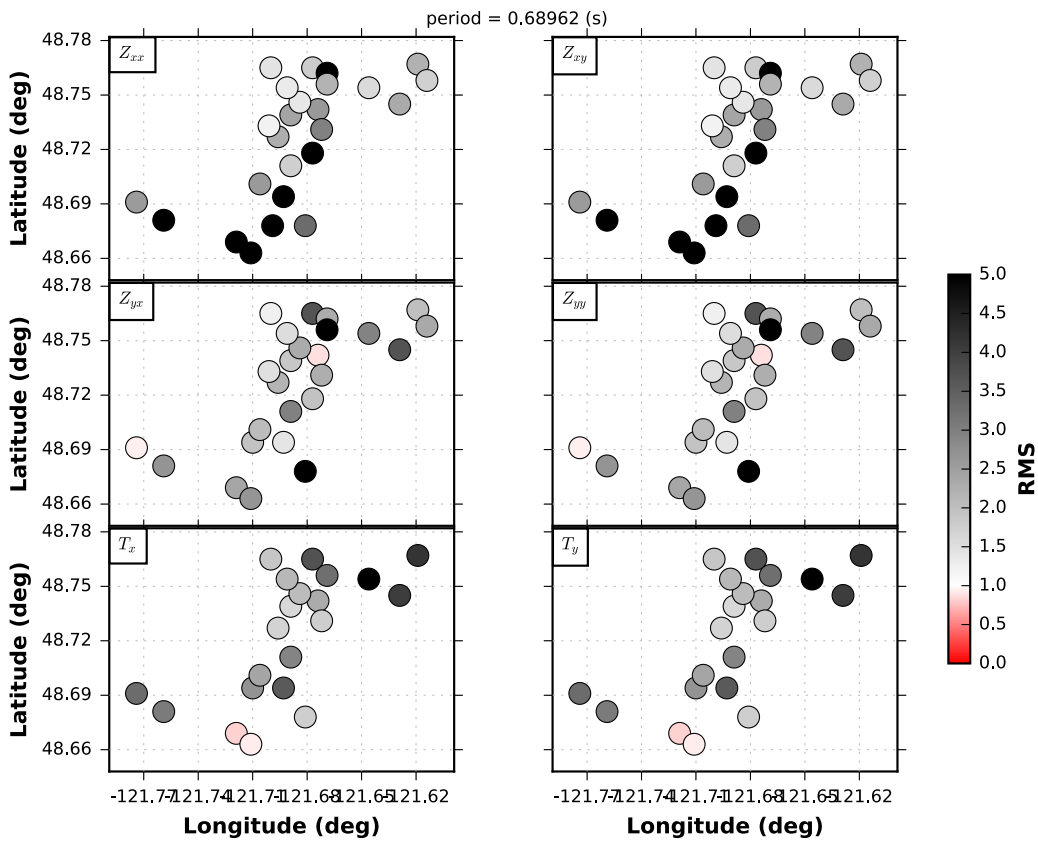
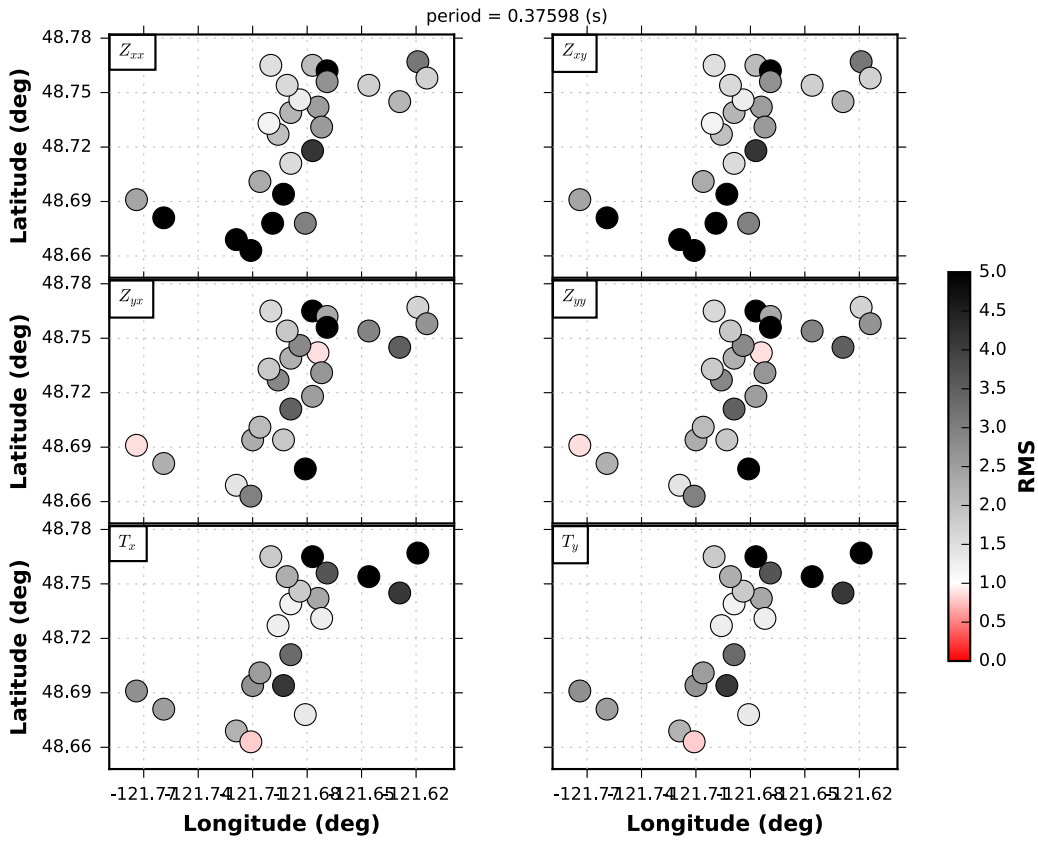


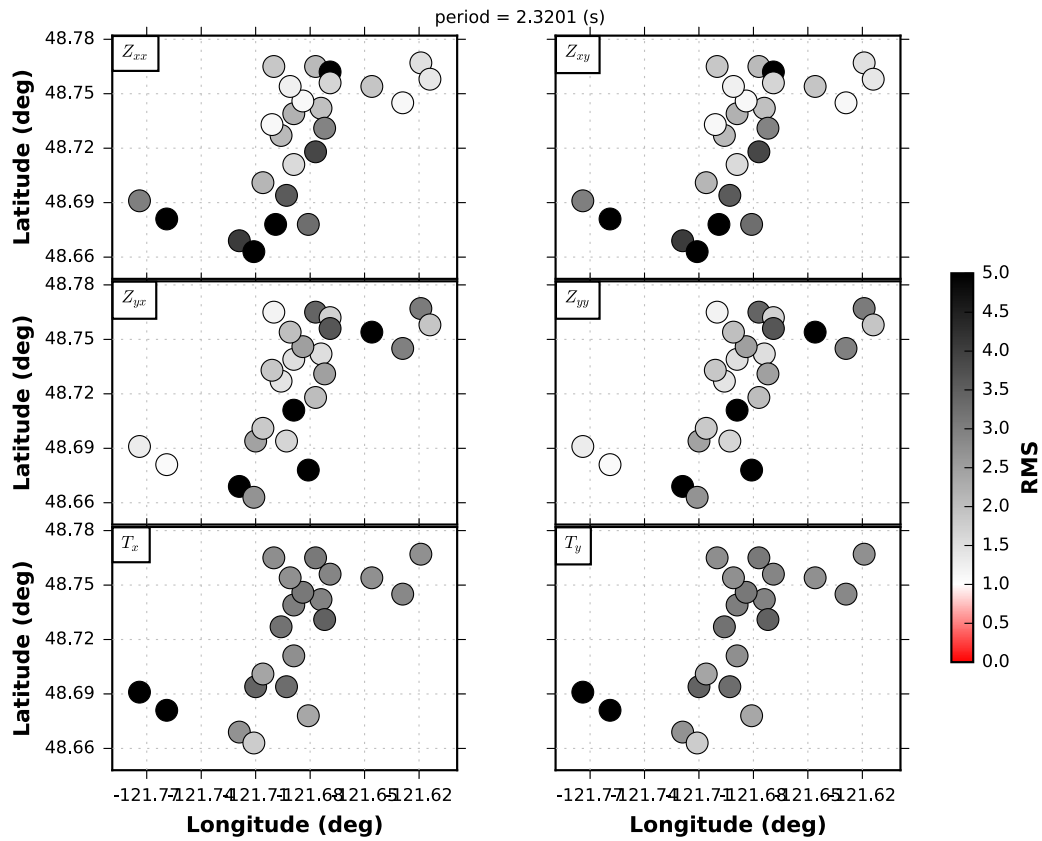
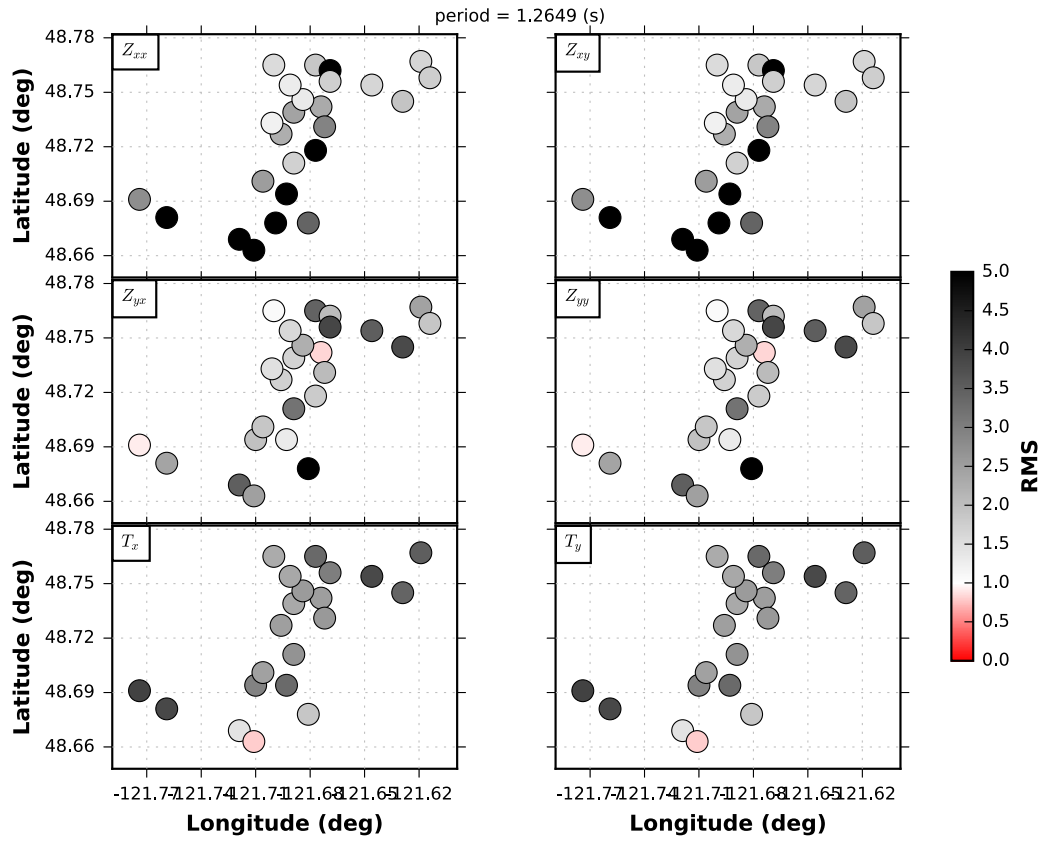


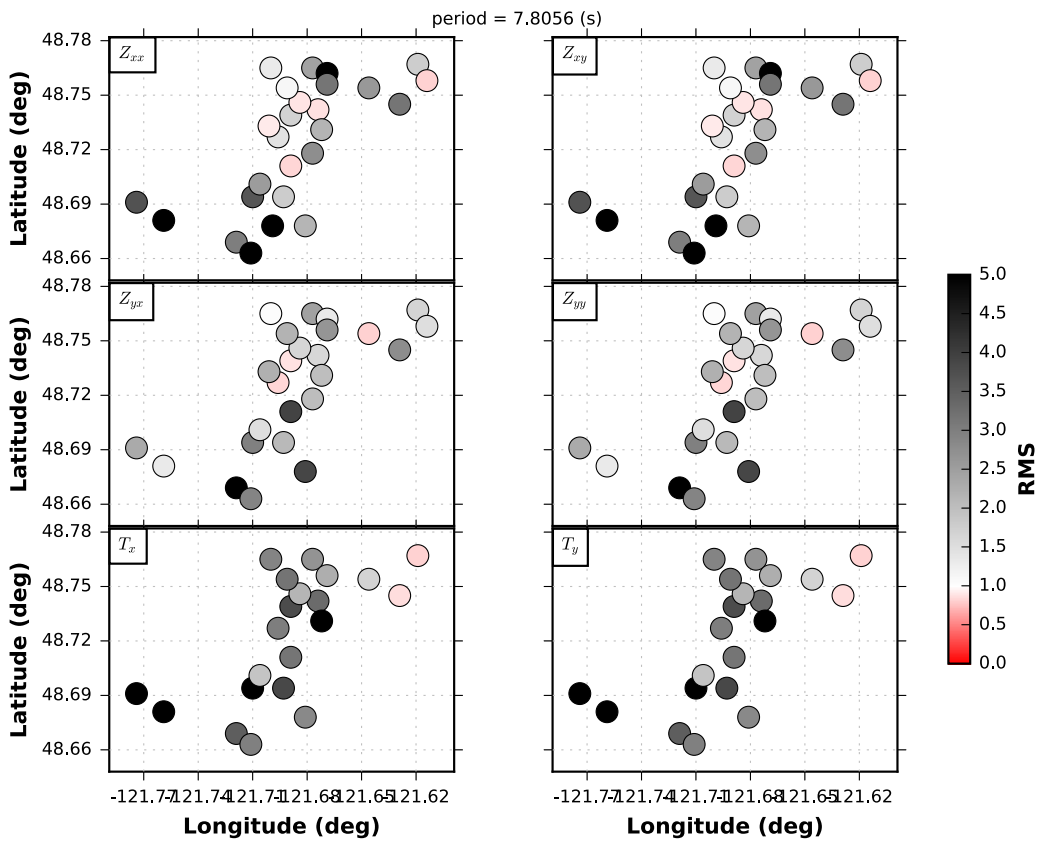
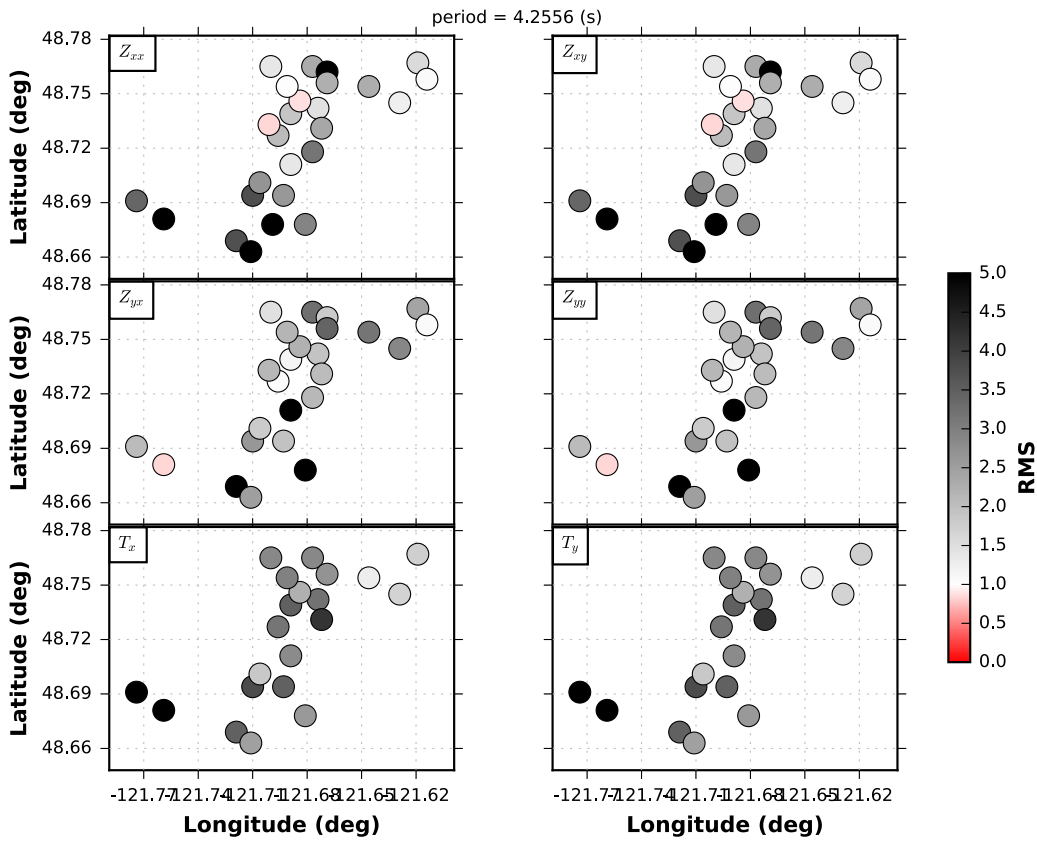


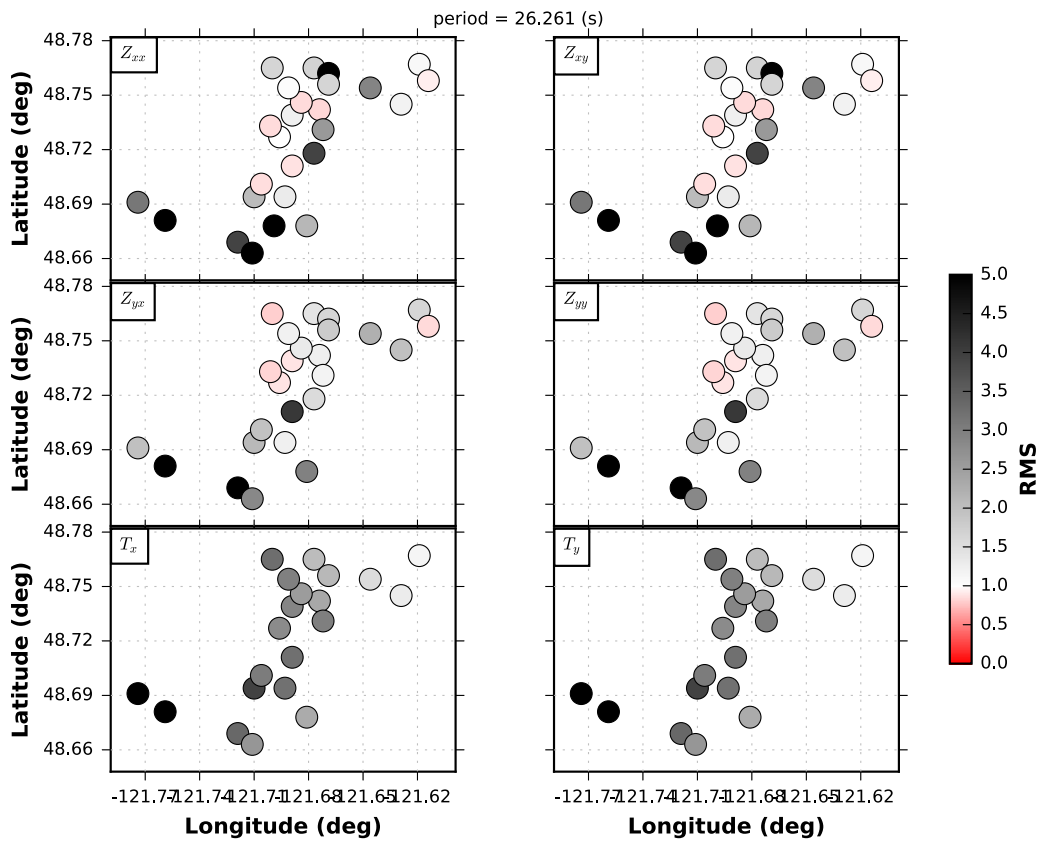
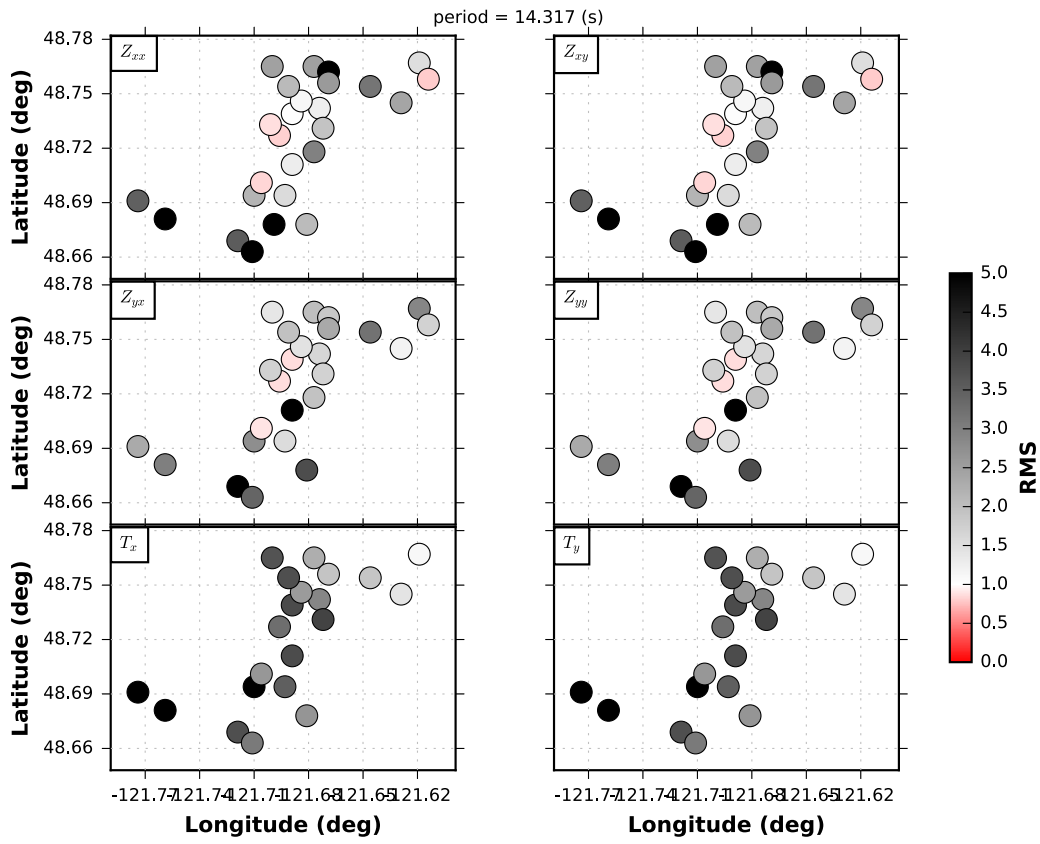


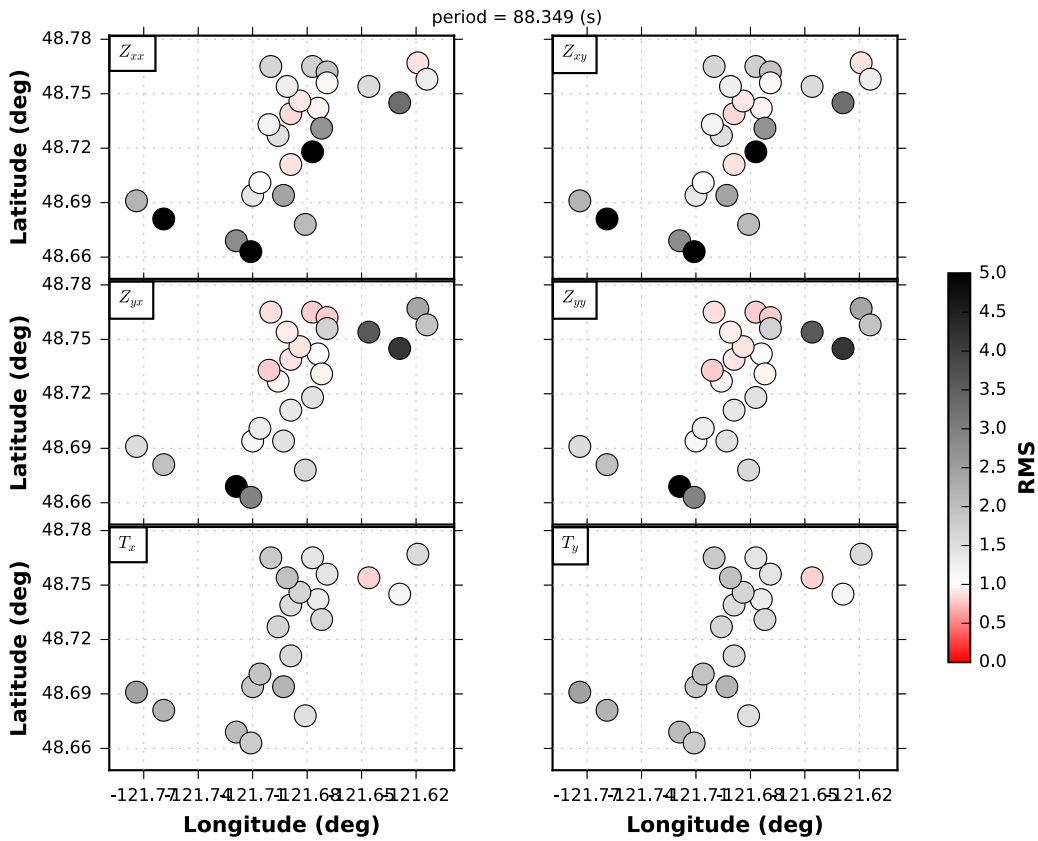
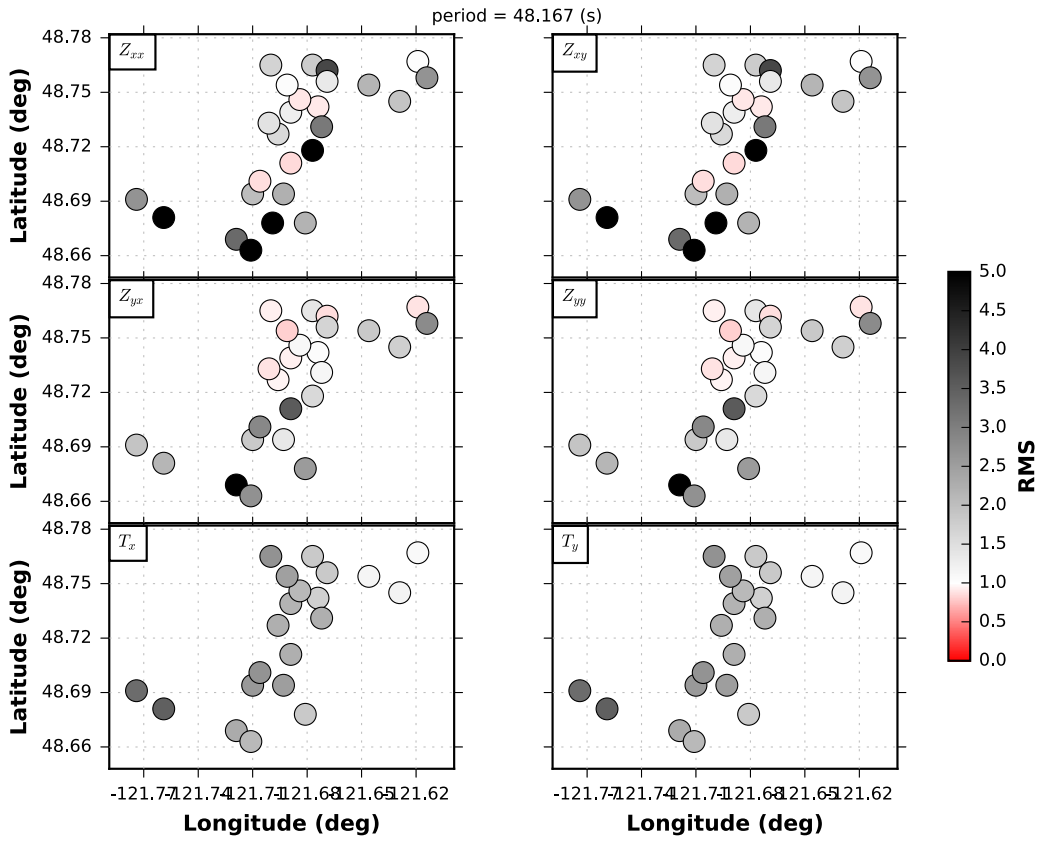


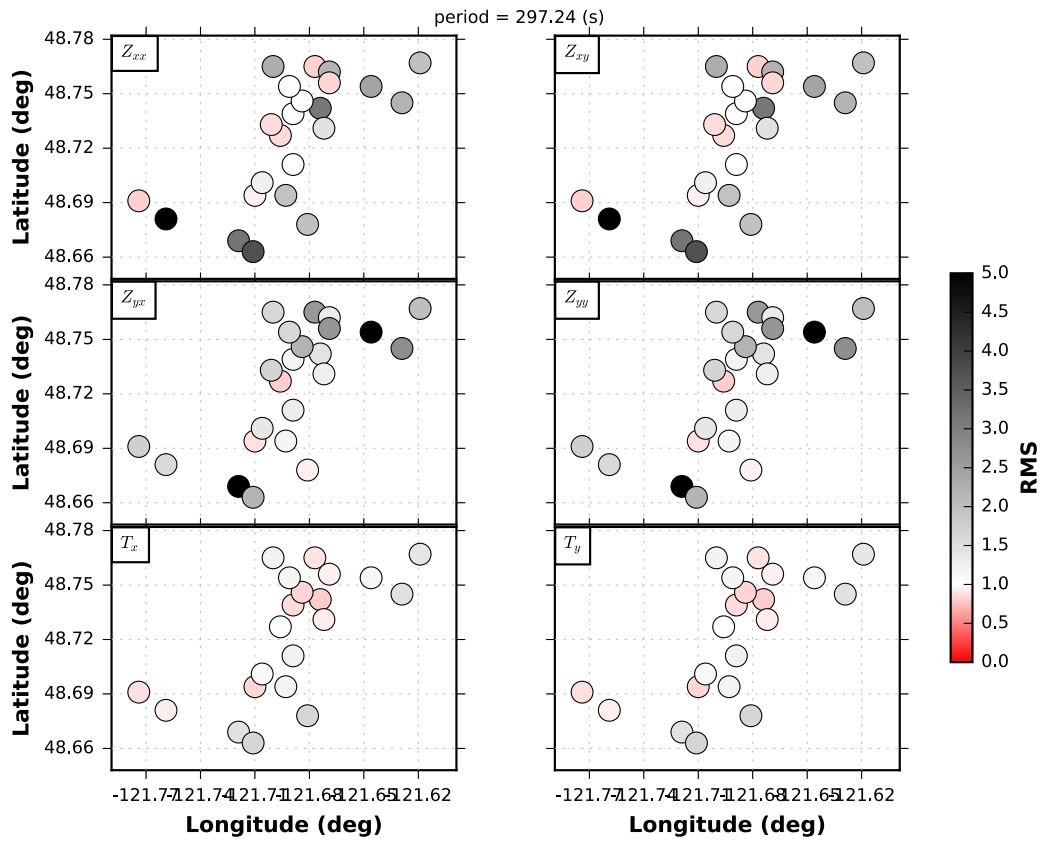
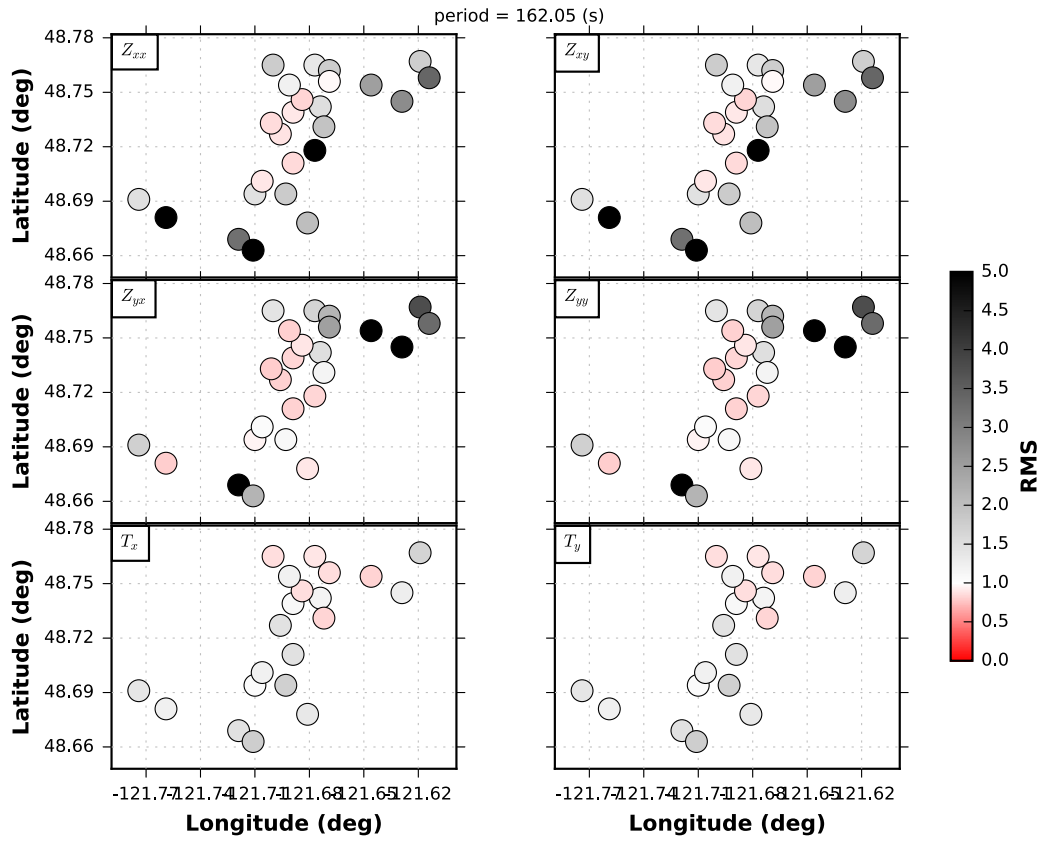


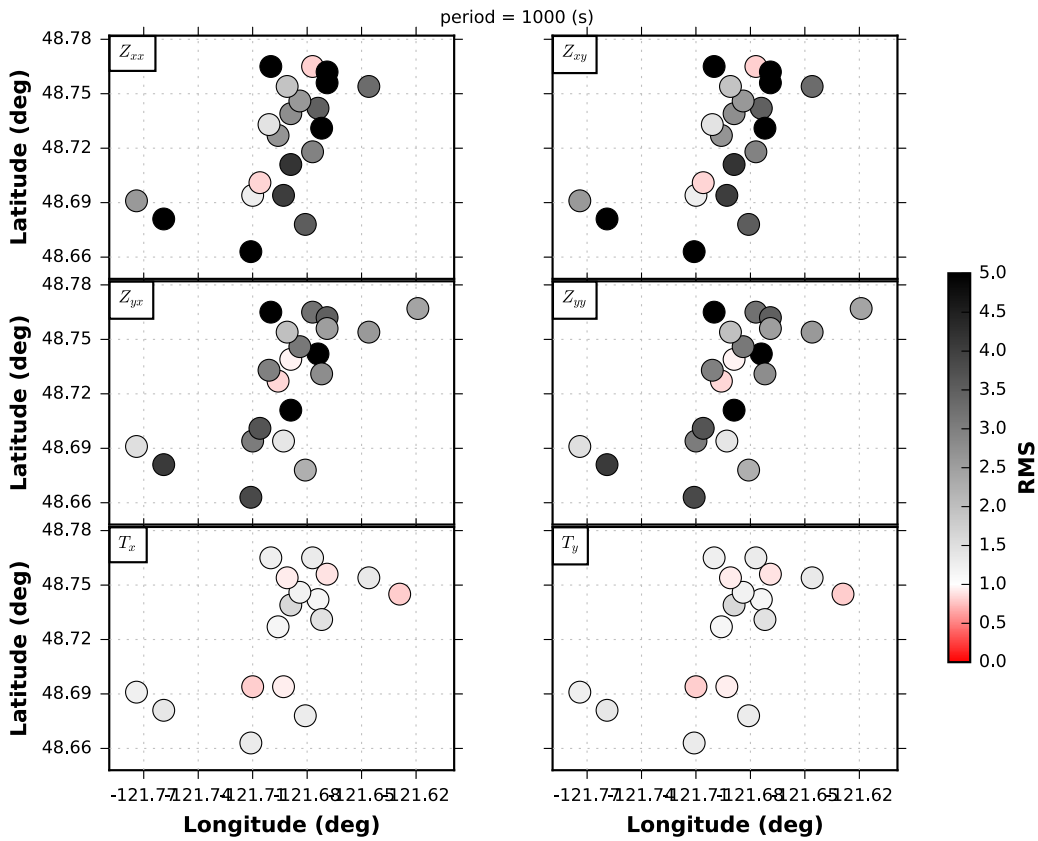
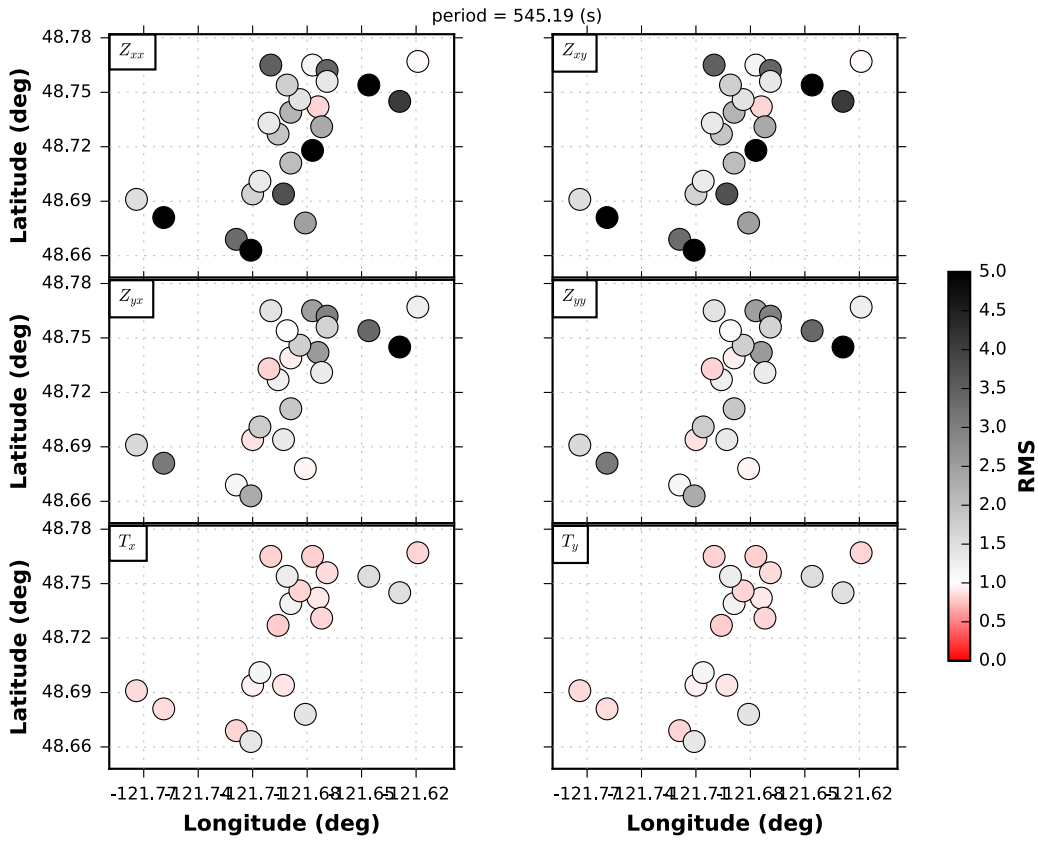






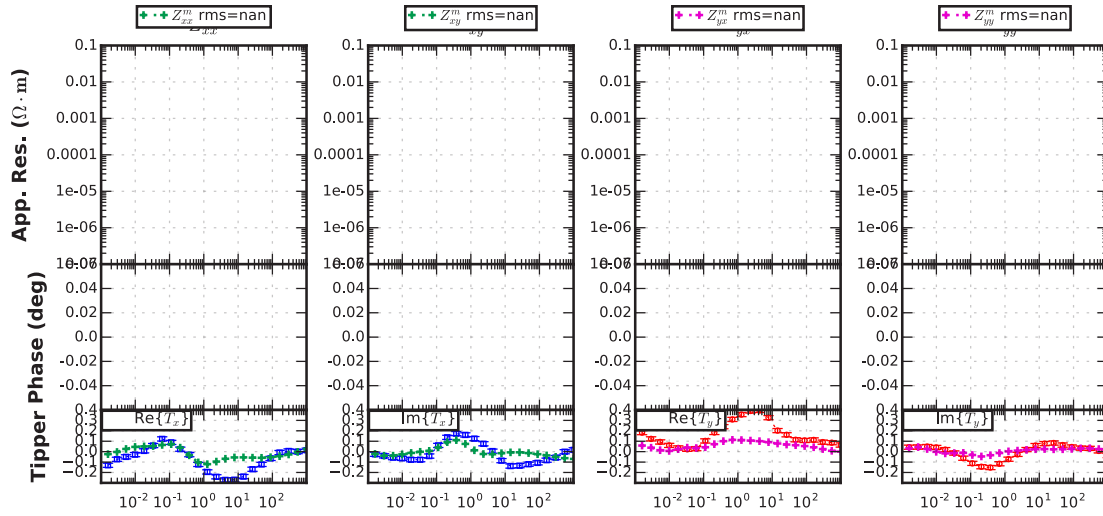




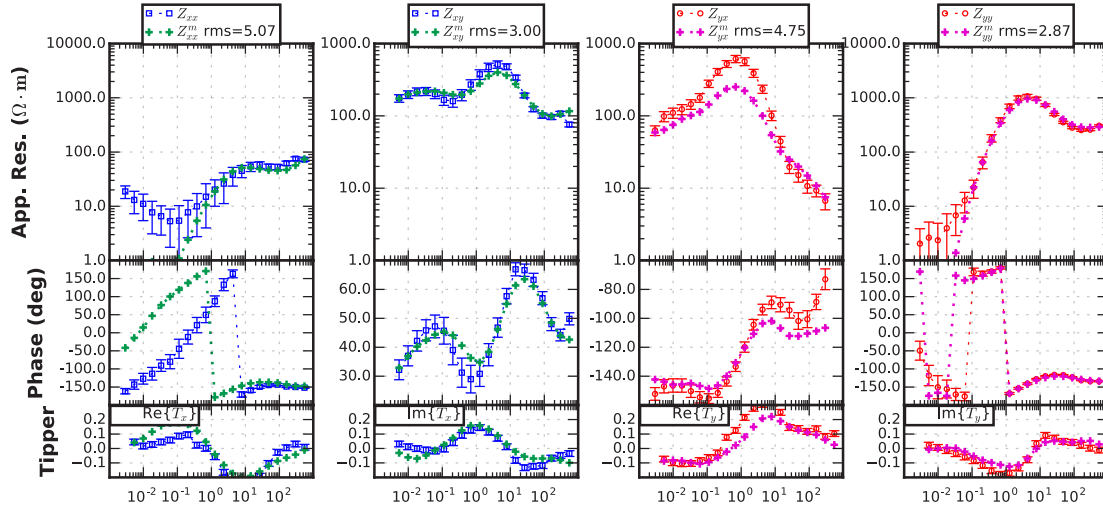


C Data & Model MT Responses (NEED TO REDO)

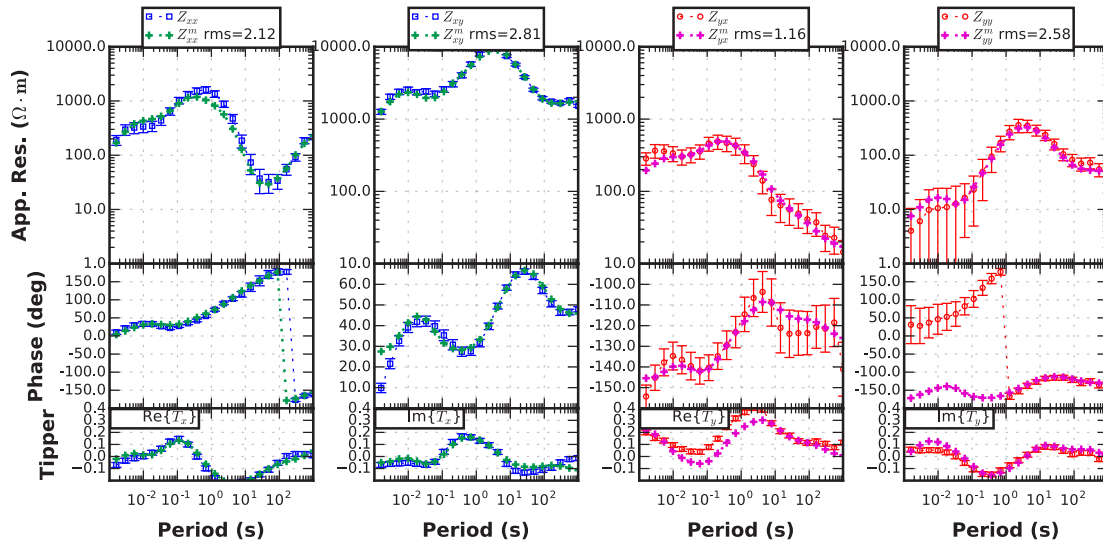
89



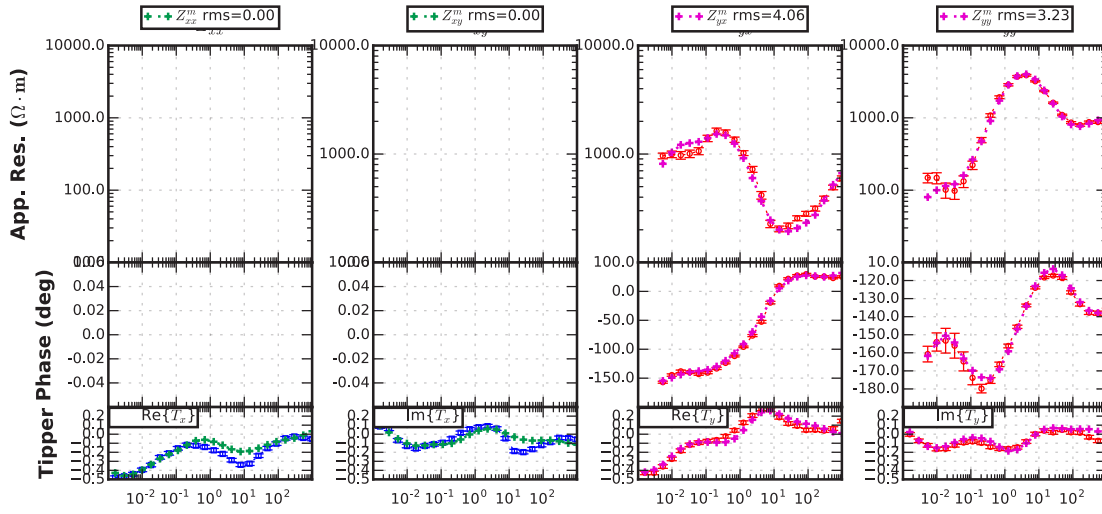
mb99



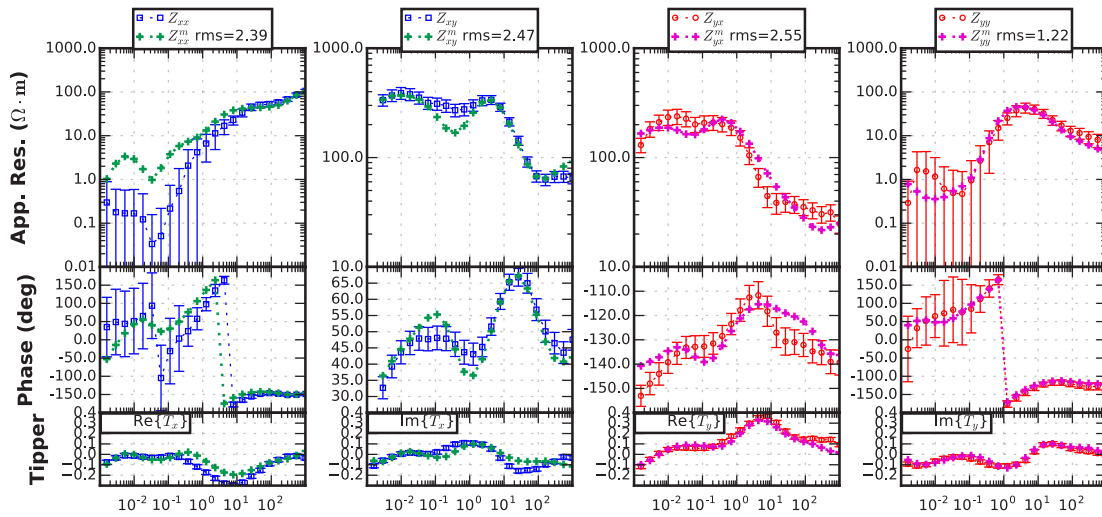
mb02



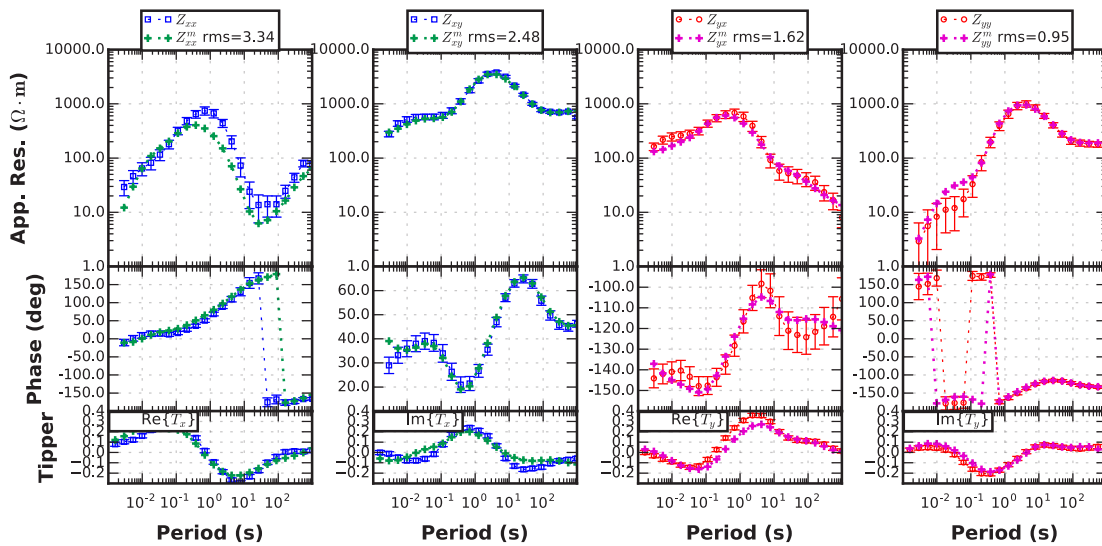
mb13

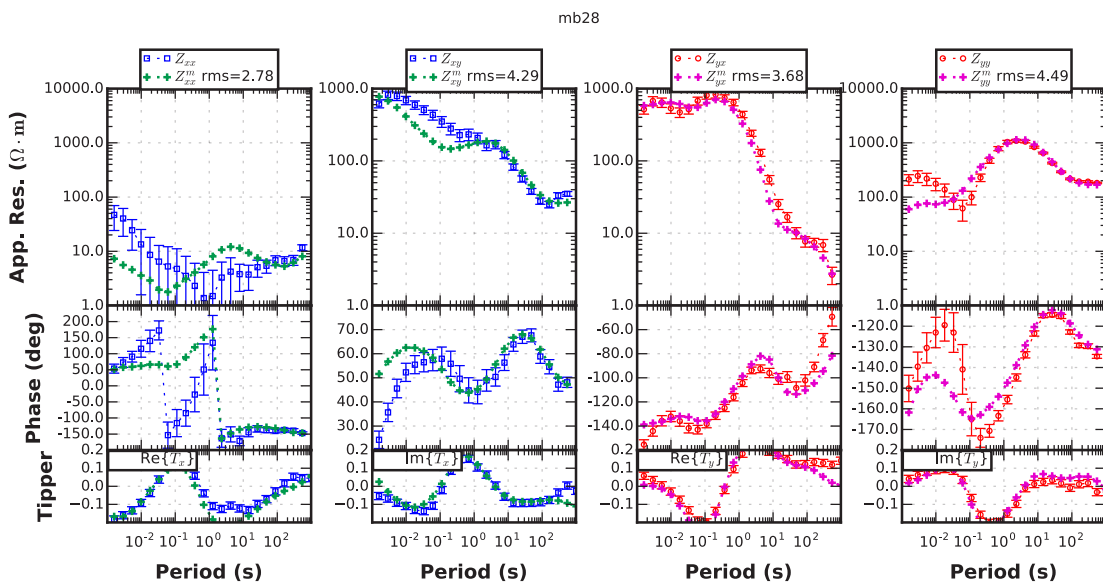
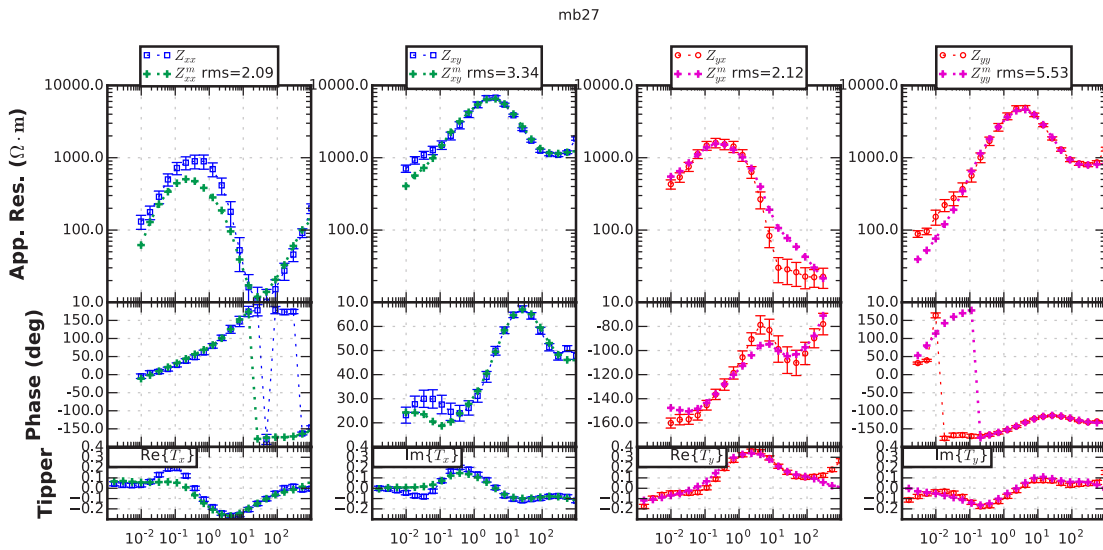
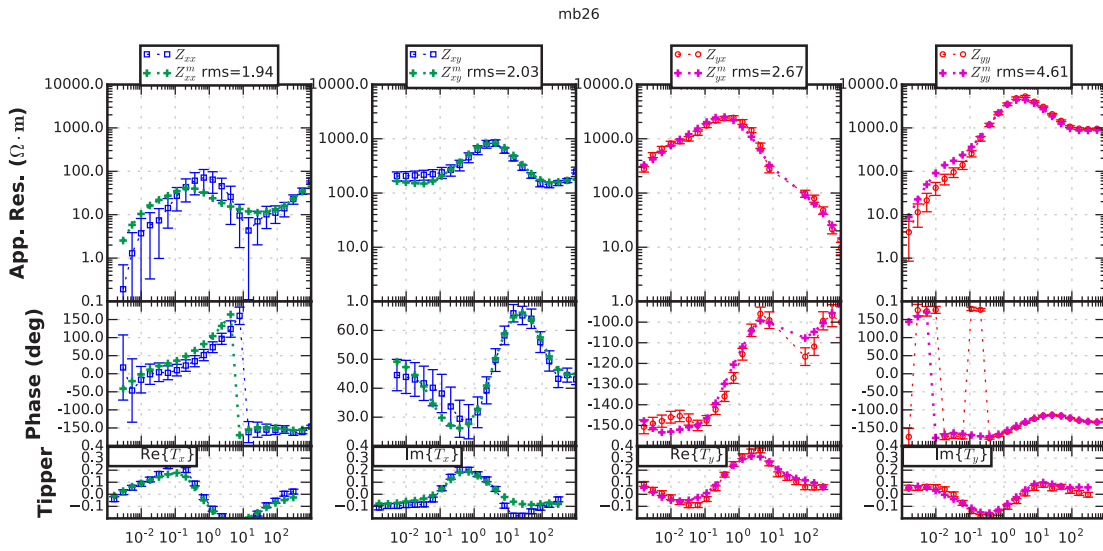


mb14

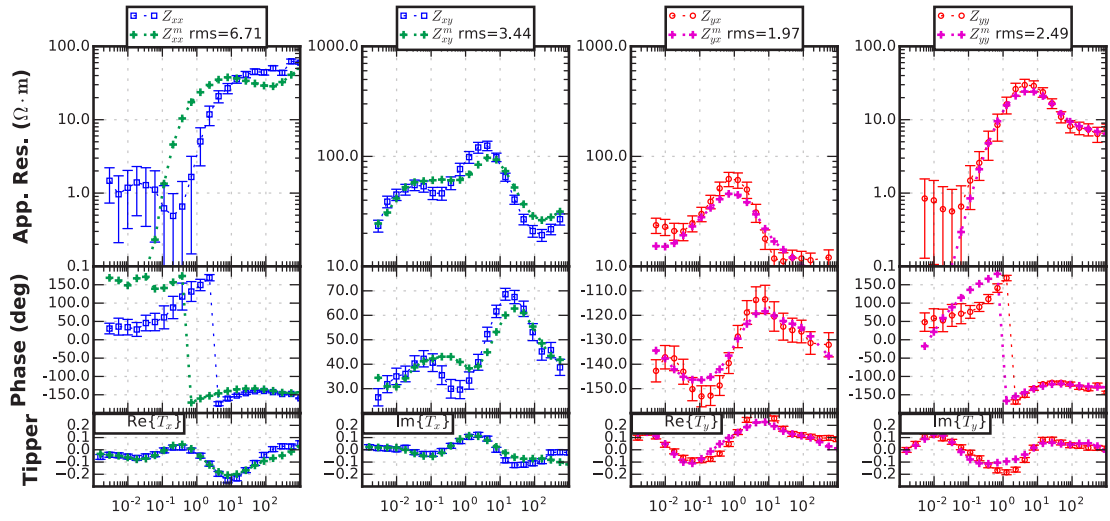


mb15

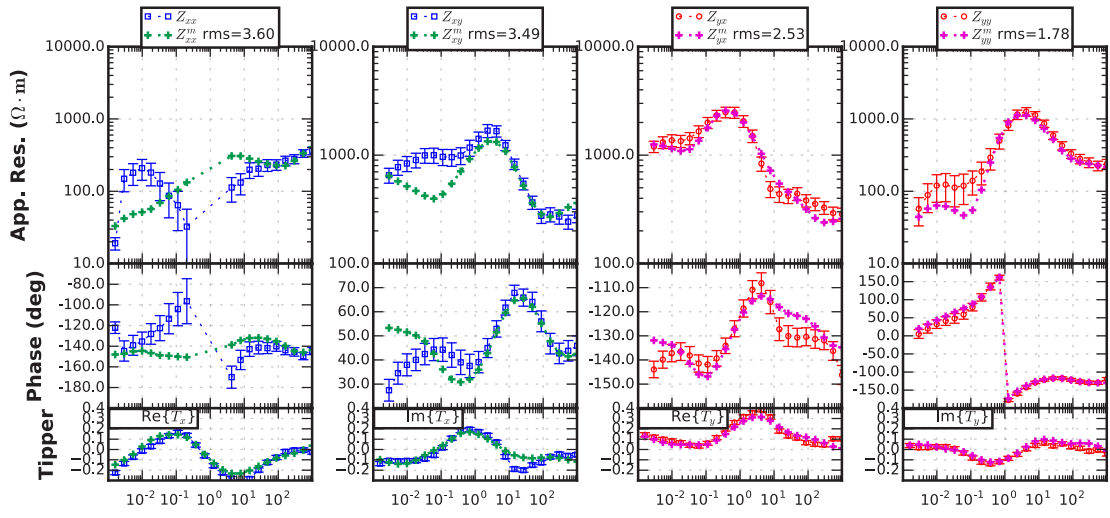




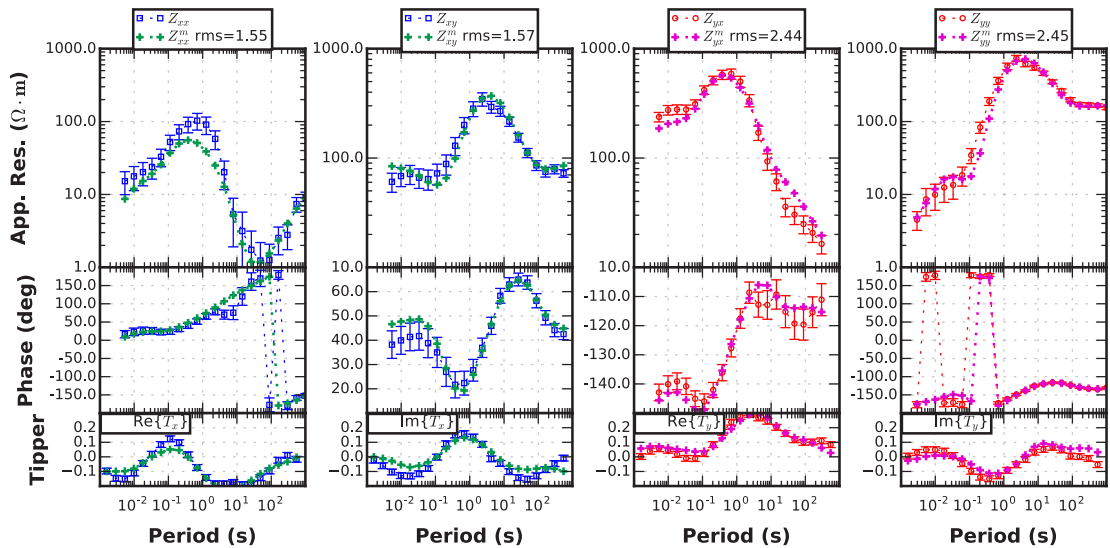
mb42

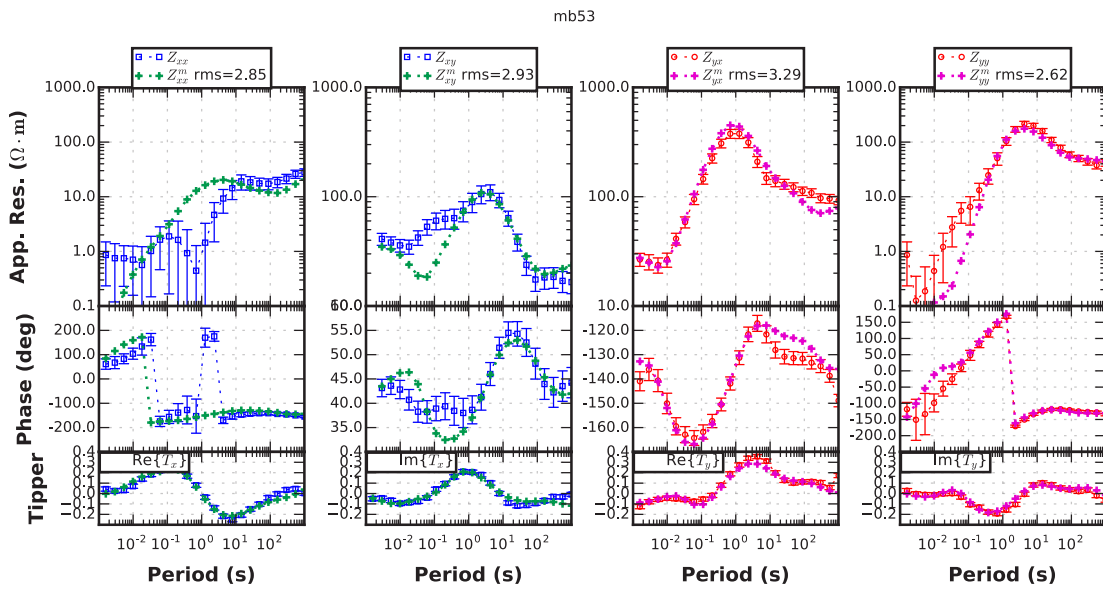
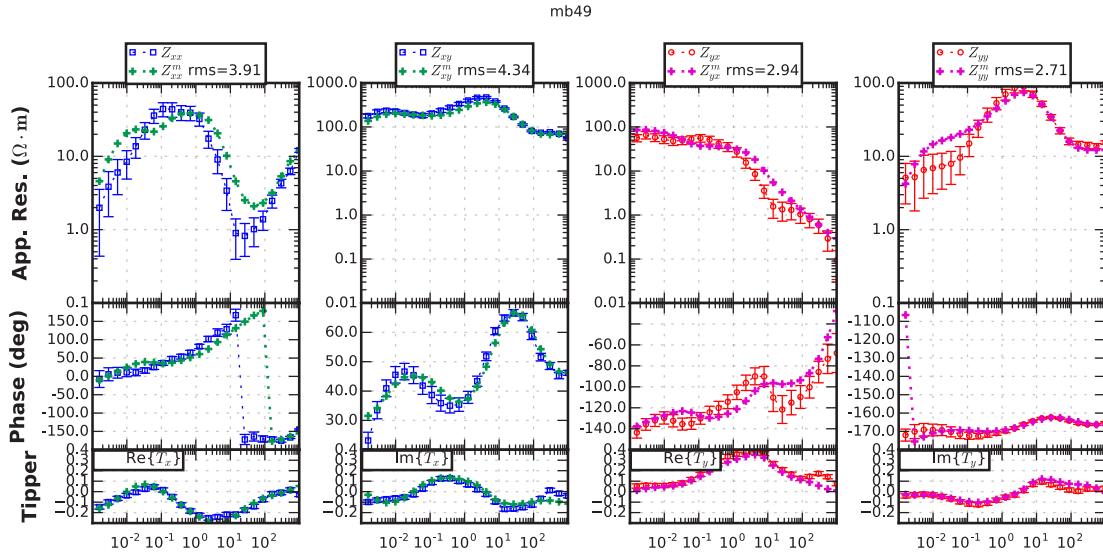
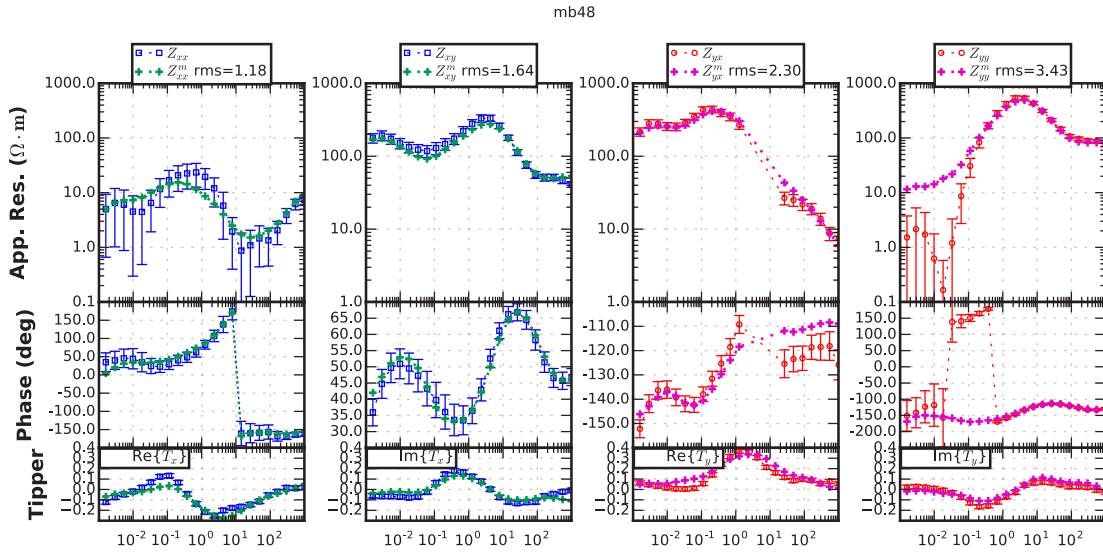


mb44

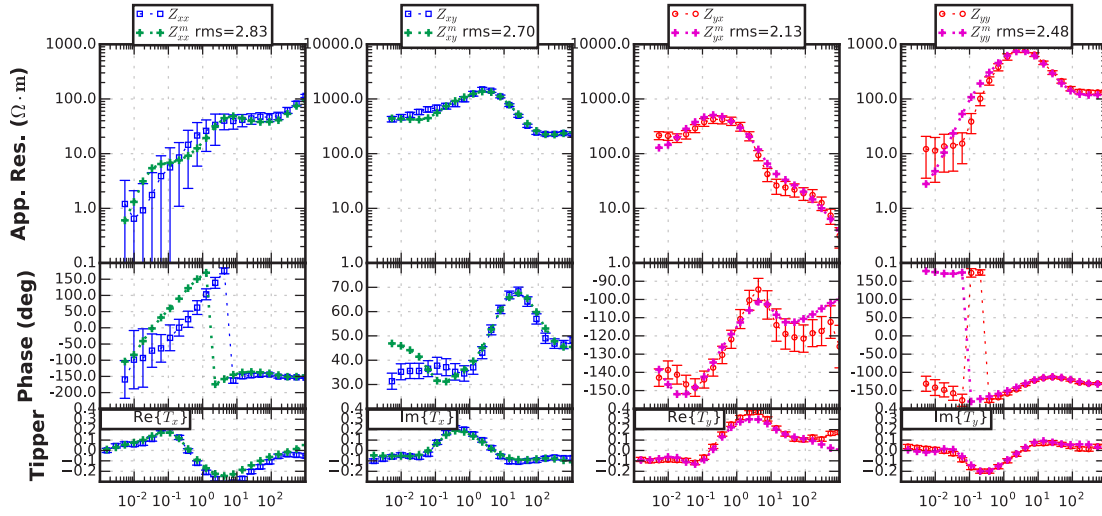


mb45

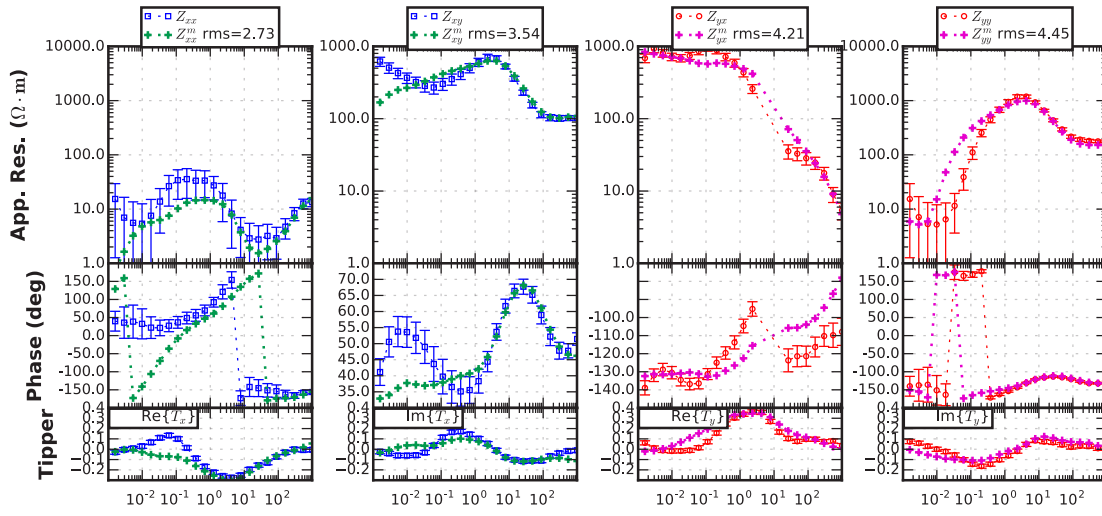




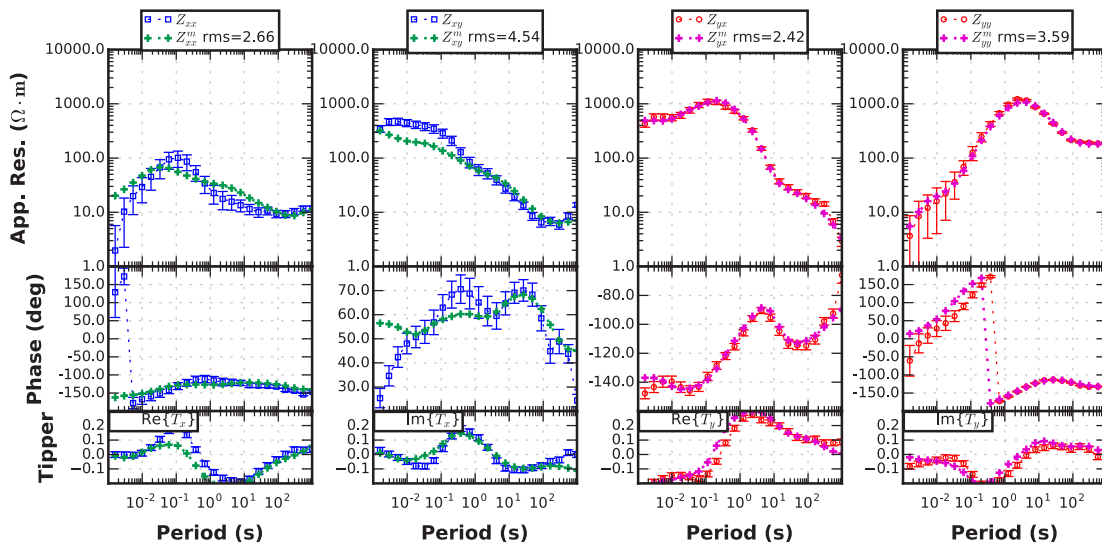
mb57



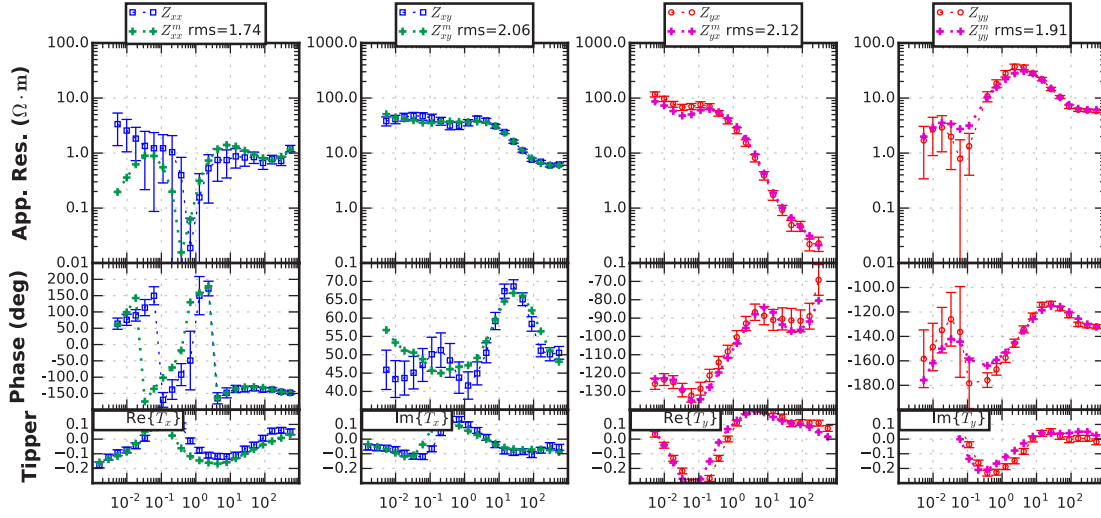
mb59



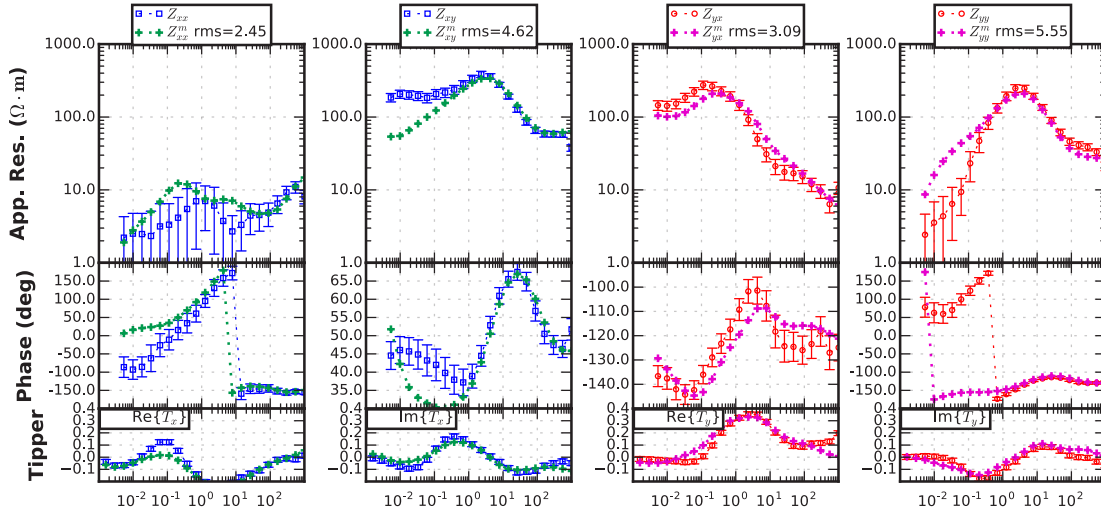
mb69



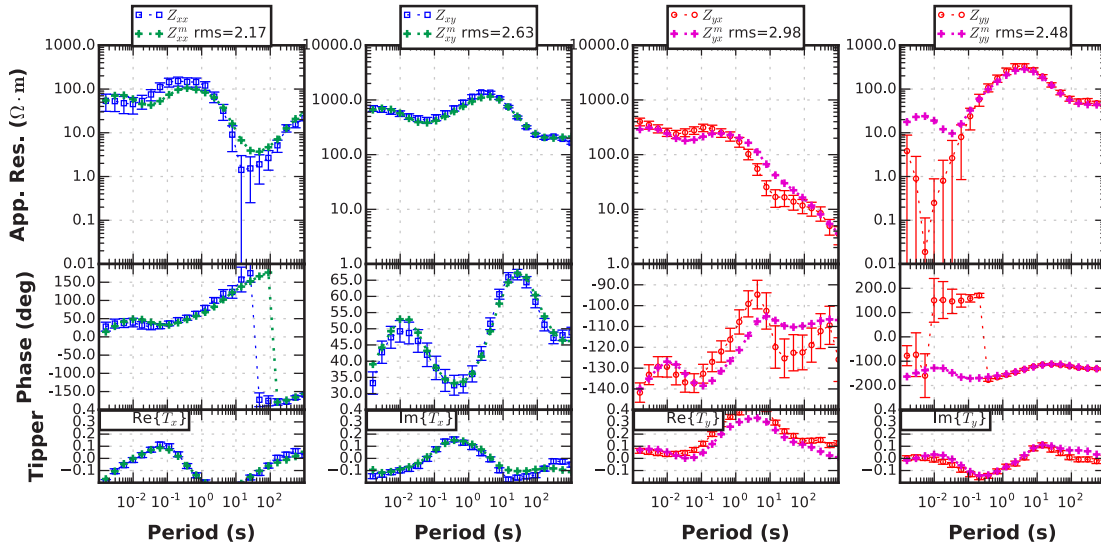
mb81



mb82



mb83



Play Fairway Analysis: North Mount St. Helens, WA, Magnetotelluric Measurements

Jared R. Peacock¹

¹U.S. Geological Survey

January 18, 2017

1 Introduction

This report describes the magnetotelluric portion of the Washington Play Fairway geothermal assessment, specifically the northern area of interest of Mount St. Helens (Figure 1).

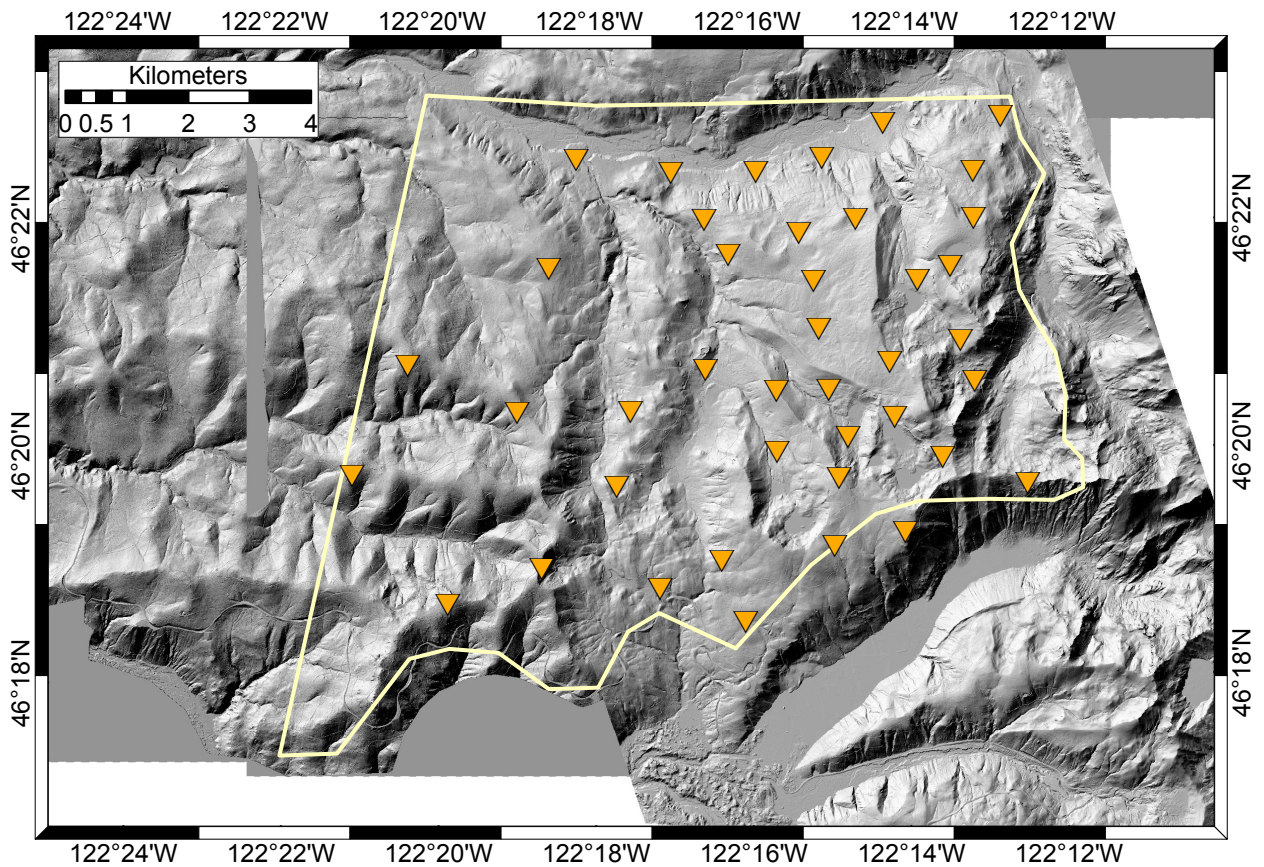


Figure 1: Area of interest north of Mount St. Helens (yellow line) and location of MT stations (orange triangles).

2 Magnetotelluric Method

Magnetotellurics (MT) is a passive electromagnetic geophysical method that measures the Earth's electrical response to natural time-varying magnetic fields. MT is an inductive process where natural time-varying magnetic fields diffuse into the Earth which induce electrical currents in the subsurface. Depth of penetration of the diffusing magnetic field depends on subsurface resistivity and the frequency of the inducing magnetic field. The time-varying magnetic source is two-fold, one that operates at frequencies of less than 1 Hz and a second that operates at frequencies larger than 1 Hz. The magnetic source for frequencies less than 1 Hz is interaction of the Earth's natural magnetic field with solar wind, a collection of charged particles emitted from the sun, which can be visibly observed as auroras. The magnetic source for frequencies larger than 1 Hz is guided waves (the waveguide being the cavity between the Earth's surface and the ionosphere) from lightning strikes around the globe. Note, the vertically impinging time-varying magnetic field is elliptically polarized in the horizontal plane. Thus, the Earth's electrical response contains information about subsurface resistivity structure as a function of frequency and direction. In the frequency domain (ω) this is a simple linear transformation (1) of the inducing magnetic field (\mathbf{H}) into an electric field (\mathbf{E}) via a transfer function (\mathbf{Z}), where \mathbf{Z} is a complex rank 2 tensor that contains all the information about subsurface resistivity structure.

$$\mathbf{E}(\omega) = \mathbf{Z}(\omega)\mathbf{H}(\omega) \quad (1)$$

Similarly, the impinging magnetic field and induced horizontal electrical currents can generate a secondary magnetic field in the vertical direction. This is known as a geomagnetic depth sounding (GDS) and is again a linear transformation in the frequency domain (2), where the transfer function \mathbf{W} provides information on direction and relative strength of electrical currents. The geomagnetic depth sounding is useful for locating lateral boundaries.

$$H_z(\omega) = \mathbf{W}(\omega)\mathbf{H}(\omega) \quad (2)$$

3 Magnetotelluric Data

MT is measured in the field by using induction coils to measure the time-varying magnetic source for frequencies between 1000–0.001 Hz, and electric dipoles to measure the Earth's electrical response. Because the magnetic source field is polarized, orthogonal directions of the fields need to be measured to get a complete description of the fields. In all measurements collected for this project induction coils and electric dipoles were aligned with geomagnetic north and east and a vertical induction coil was either buried or tied to a tree to get the vertical magnetic field. MT data was collected at 41 stations with a ZEN 32-bit data logger developed by Zonge International, magnetic fields were measured with ANT-4 induction coils, and electric fields were measured with Ag-AgCl reference electrodes from Borin on 50-100 m dipoles. The data was collected on a repeating schedule of 5 min at 4096 samples/s, 15 min at 1024 samples/s, and 7 hours and 40 minutes at 256 samples/s over a 2024 hour period. To get time series data into the frequency domain and get estimations of \mathbf{Z} and \mathbf{W} , the processing code provided by Zonge International was used in conjunction with BIRRP written by [Chave & Thomson \(2004\)](#). Simultaneous measurements were used as remote references to reduce noise and bias in the data.

4 Inverse Modeling

MT and GDS response functions were modeled in three-dimensions (3-D) using the code ModEM developed by [Egbert & Kelbert \(2012\)](#); [Kelbert *et al.* \(2014\)](#). Input data was edited using the EDI editor in MTpy ([Krieger & Peacock, 2014](#)) to remove obvious outliers in the data and suppress bias in the modeling. All data was interpolated onto 23 frequencies in the range of 6250.001 Hz. The model mesh (north, east, depth) was 73 x 85 x 40 with dimensions of 129050 x 132050 x 169360 m, where spacing within the station area was 250 m increasing by 1.4 away from the station area. The first layer was set to 10 m and increases logarithmically downwards. Inversions were run on NASA's high-end computing capability (HECC) Pleiades super computer, where average run times were on the order of 18 hours.

To get to a preferred model the following scheme was used. Invert all components of the data with an error floor of $0.12\sqrt{Z_{xy} \cdot Z_{yx}}$ and an error floor of 0.10 for the GDS components and run ModEM with a covariance of 0.40 in all directions using different starting models of a 1000, 100, and 10 Ohm-m half space. Reduce error floors to $0.05\sqrt{Z_{xy} \cdot Z_{yx}}$ and an error floor of 0.03 and run ModEM with a covariance of 0.30 in all directions using the final iteration from the previous run as the starting model. Invert just the GDS components with an error floor of 0.03 with a covariance of 0.40 using starting models of a 1000, 100, and 10 Ohm-m half space. Compute the geometric average of all models to enhance common features and suppress uncommon features. Run ModEM with error floors of $0.10\sqrt{Z_{xy} \cdot Z_{yx}}$ and an error floor of 0.05 and a covariance of 0.40 using the average model as the starting model. Then reduce error floors to $0.05\sqrt{Z_{xy} \cdot Z_{yx}}$ and an error floor of 0.03 for GDS components and run ModEM with a covariance of 0.30 in all directions using the final iteration from the previous run as the starting model. Features in the preferred model were tested for sensitivity to location, geometry, and resistivity value.

5 Resistivity Model Features

Many interesting features are observed in the preferred model; however, for the purpose of this report only those features in the top 10 km will be described (Figure 2). The most striking feature is C1, an elongated conductive body ($<30 \Omega\text{m}$) that strikes north-northwest across the middle of the survey area with a width of about 2 km. The top of C1 is on average around 4 km extending down to 10 km depth with a slight dip to the west. The most conductive part of C1 ($<5 \Omega\text{m}$) is near the middle of the body at 5 km depth dipping south to 8 km. C1 increases in width further to the north, shallows to 2 km depth, and becomes more conductive.

C2 is a spur shaped like a thumb that comes off C1 to the east at 4 km north of the center and reaches up to about 2 km depth. C2 is more resistive than C1 ($>25 \Omega\text{m}$).

R1 is a resistive ($>500 \Omega\text{m}$) structure to the west of C1 that extends from the surface down to a depth of 10 km. The eastern edge of R1 has a westerly dip.

R2 is a resistive ($>500 \Omega\text{m}$) structure to the east of C1 that extends from the surface down to a depth of 10 km.

6 Preliminary Interpretation

C1 lies directly west and above the seismically active Mount St. Helens shear zone (SHZ) (Weaver *et al.*, 1987), and is sandwiched between resistive blocks R1 and R2. The resistivity values of R1 and R2 suggest these anomalies are cold with little porosity or conducting mineral phases like dense plutonic rocks. Thus, R1 and R2 are plutons that correspond to the Spirit Lake Pluton to the east and the Spud Mountain Pluton to the west (Lees & Crosson, 1989).

Geologic composition of the SHZ is not yet fully understood. Waite & Moran (2009) suggest the SHZ is a structural weakness that lies between 2 strong plutonic bodies and Moran *et al.* (1999) interpret the SHZ as being composed of weak sedimentary rock of the Carbonado formation. De Siena *et al.* (2014) found the SHZ to attenuate seismic waves along strike, suggestive of a dense fracture network. They interpret the SHZ as being filled with Tertiary marine sediments.

The low resistivity value of the body juxtaposed to the SHZ is suggestive of a zone of fluids, clay rich lithology, or both. The fact that the eastern edge of C1 is where earthquakes occur could indicate an impermeable boundary. Fluids, either meteoric or sourced from deep, flowing along the fault could get trapped in the porous sedimentary rocks to the west of the fault plane enhancing electrical conductivity. C1 is not homogenous, but appears to have a conductive core and less conductive outer area which is also suggestive of fluids, where the center is highly fractured nucleus and away from the center fracture density diffuses. The most conductive part of C1 is at around 5 km, which would be around 200°C (depending on thermal gradient) hot enough to cause hydrothermal alteration, which would increase the conductivity.

To the north of C1, at the edge of the survey boundary is a hot spring, which appears conductive ($50\text{--}70 \Omega\text{m}$) in the resistivity model (Figure 2 top left, Figure 3). The source of the hot spring could be C1, where the path from the hot spring to C1 is a shallow west dipping fault to 1 km, then an east dipping fault that connects to C1 at 2-3 km. The geochemistry of the hot spring waters could confirm or eliminate connection

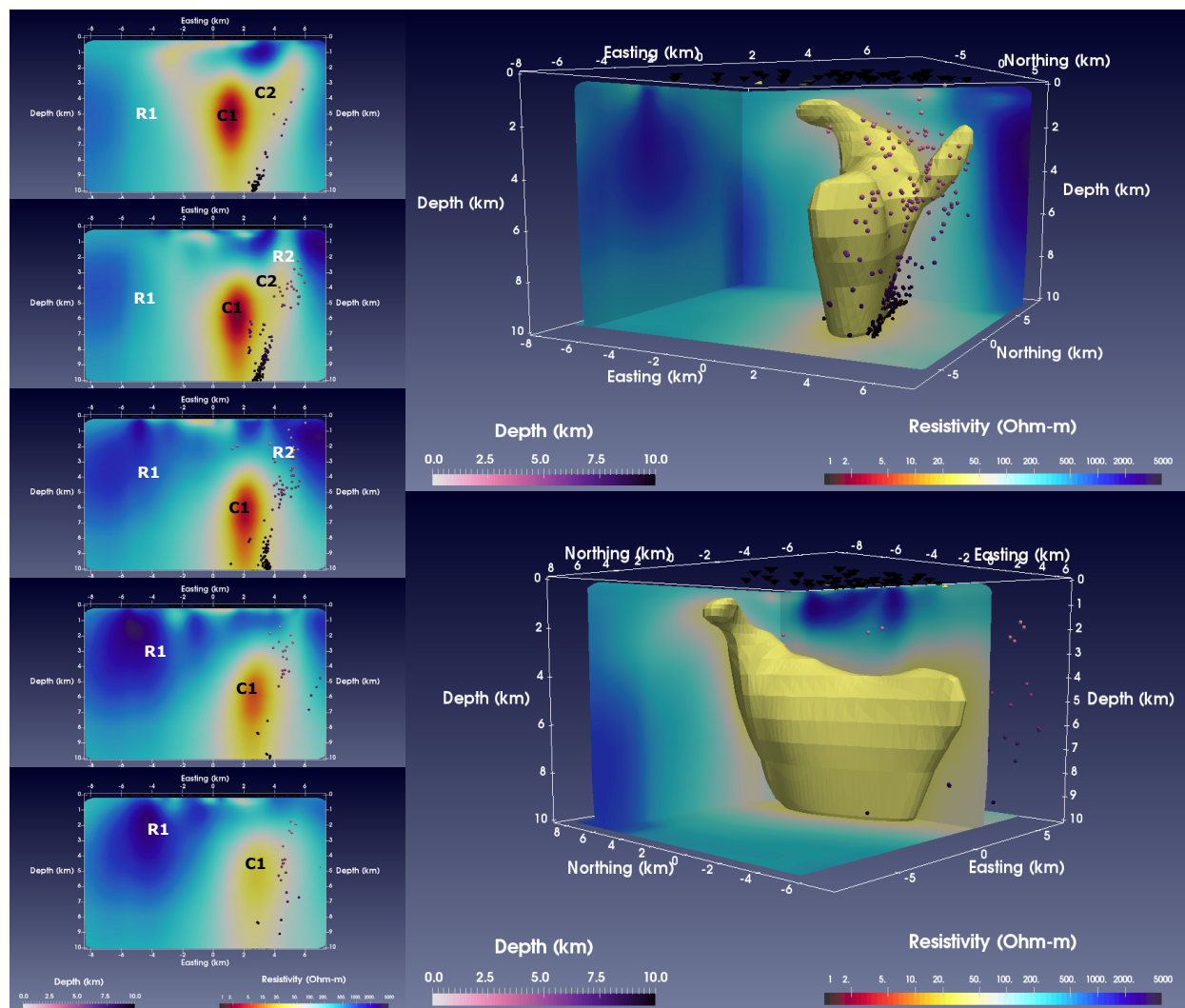


Figure 2: Different views of the resistivity model and main anomaly C1. Left: looking north through the resistivity model each panel is a 2 km step north. Resistivity anomalies are labeled as discussed in the text. Top Right: looking northeast at the C1. Bottom Right: looking north-northwest along C1.

to C1. Not many earthquakes occur in this region, suggesting either the fluids are in an equilibrium stress state with the surrounding host rock, the area is warm enough to reduce brittle failure, or something else.

C2, the thumb coming off of C1 could be a narrow pathway for fluids. However, there is no surface manifestation of upwelling fluids in the vicinity of C2, suggesting either fluids get trapped before effusing to the surface, downwelling of fluids, an old fluid pathway that is mineralized, or something else.

Interestingly, relocated earthquakes from Trenton (source?) form a distinct fault plane below about 5 km, above 5 km the earthquakes are more diffuse and clustered towards in the resistive area between C1 and C2. Not sure what causes these earthquakes, if it is movement of fluids, then the fluids must be freshwater because the earthquake zone is resistive. There is no surface manifestation of upwelling fluids in that area, which could mean those earthquakes are in response to regional or local stress field changes. The fact that they are more diffuse shallower could suggest splashing faults from the deeper fault plane, which could be a good target for an enhanced geothermal system.

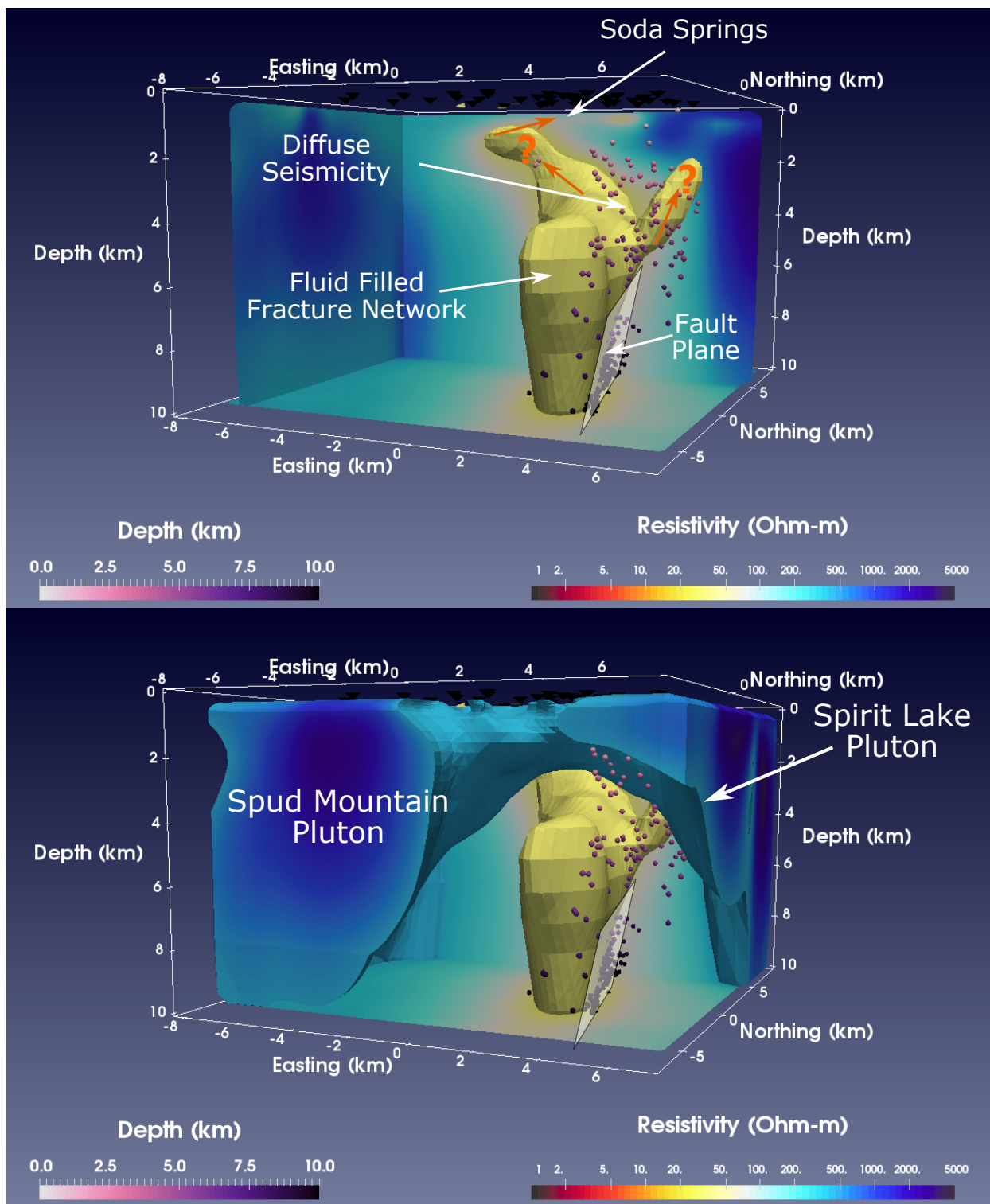


Figure 3: Views of 3-D resistivity model with preliminary interpretations. Orange arrows and question marks indicate possible fluid flow pathways and direction.

6.1 Outstanding Questions

Why do the earthquakes occur only on one side of the conductive zone? If C1 is a fluid filled fracture network, you might expect the earthquakes to occur inside the zone, but if the east boundary of C1 is an impermeable fault plane then perhaps fluids from C1 move around and change the stress field along the fault plane, which then slips when past critical stress?

6.2 Estimate of Physical Properties

TODO: estimate porosity, temperature, salinity from resistivity. Find any chemical analysis of Soda Springs

6.3 Preliminary Geologic Interpretation

Generally, the main feature is a highly fractured fluid filled sedimentary unit that is located between two plutons, the Spud Mountain Pluton to the west and the Spirit Lakes Pluton to the east (Figure 4). Within this sedimentary unit there is a sub-vertical fault plane dipping west that is well defined below 5 km, but more diffuse near the surface. A possible fluid connection from the sedimentary unit to the surface is located at the north end of the survey area at Soda Springs. The other interesting feature is a possible narrow zone of fluids in the northwest corner of the survey that comes off of the sedimentary zone.

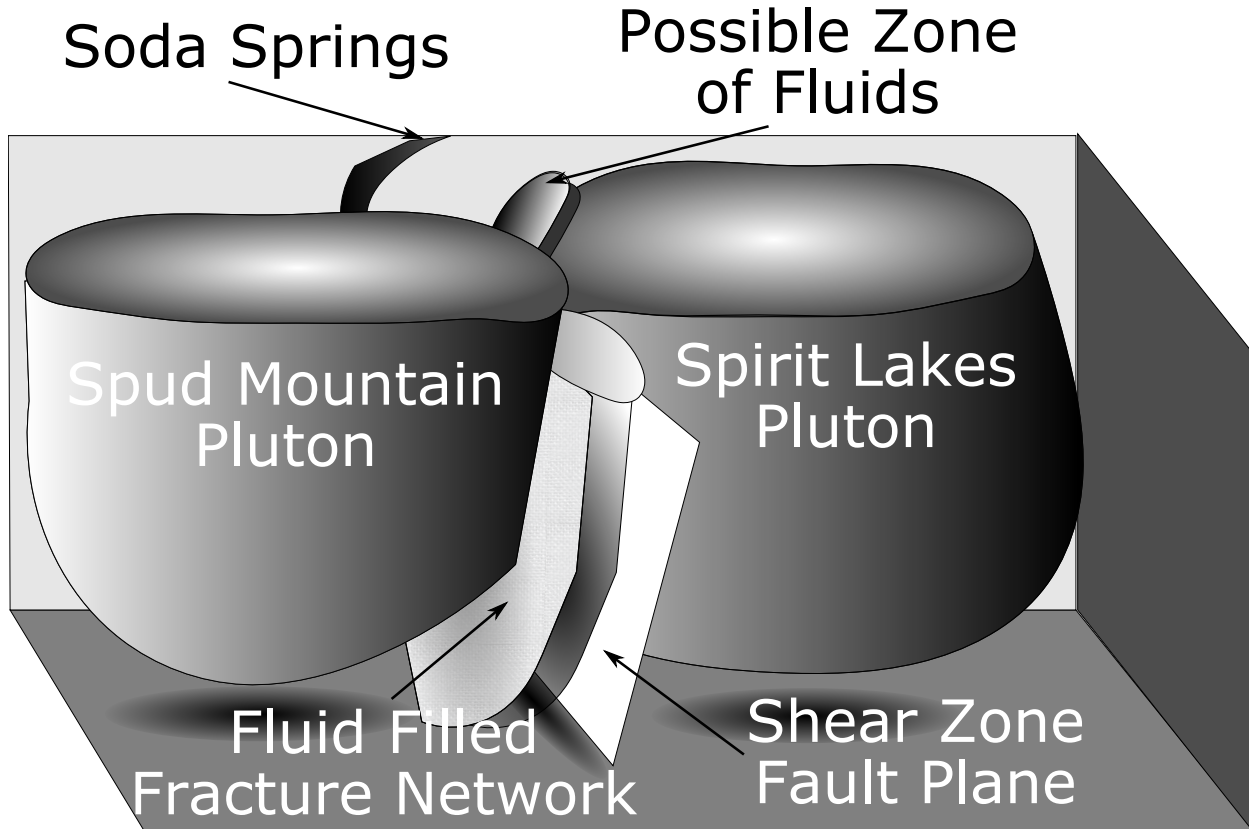


Figure 4: Schematic cartoon of geological features.

7 Geothermal Potential

From the resistivity model, the optimal location for geothermal potential from the resistivity model appears to be in the northern part of the survey area. This is where there is a known spring, and C1 is at its shallowest (around 3 km). Another zone might be the area of C2.

References

- Chave, A. D., & Thomson, D. J. 2004. Bounded influence magnetotelluric response function estimation. *Geophys. J. Int.*, **157**, 988–1006.
- De Siena, L., Thomas, C., Waite, G. P., Moran, S. C., & Klemme, S. 2014. Attenuation and scattering tomography of the deep plumbing system of Mount St. Helens. *Journal of Geophysical Research: Solid Earth*, **119**, 8223–8238.
- Egbert, G. D., & Kelbert, A. 2012. Computational recipes for electromagnetic inverse problems. *Geophys. J. Int.*, **189**, 251–267.
- Kelbert, A., Meqbel, N. M., Egbert, G. D., & Tandon, K. 2014. ModEM: a modular system for inversion of electromagnetic geophysical data. *Computer Geoscience*, **66**, 40–53.
- Krieger, L., & Peacock, J. R. 2014. MTpy: a Python toolbox for magnetotellurics. *Computers & Geoscience*, **72**, 167–175.
- Lees, J. M., & Crosson, R. S. 1989. Tomographic inversion for three-dimensional velocity structure at Mount St. Helens using earthquake data. *Journal of Geophysical Research*, **94**(B5), 5716–5728.
- Moran, S. C., Lees, J. M., & Malone, S. D. 1999. P wave crustal velocity structure in the greater Mount Rainier area from local earthquake tomography. *Journal of Geophysical Research*, **104**(B5), 10,755–10,786.
- Waite, G. P., & Moran, S. C. 2009. V_p structure of Mount St. Helens, Washington, USA, imaged with local earthquake tomography. *Journal of Volcanology and Geothermal Research*, **182**, 113–122.
- Weaver, C. S., Grant, W. C., & Shemeta, J. E. 1987. Local Crustal extension at Mount St. Helens, Washington. *Journal of Geophysical Research*, **92**(B10), 10,170–10,178.

A Depth Slices

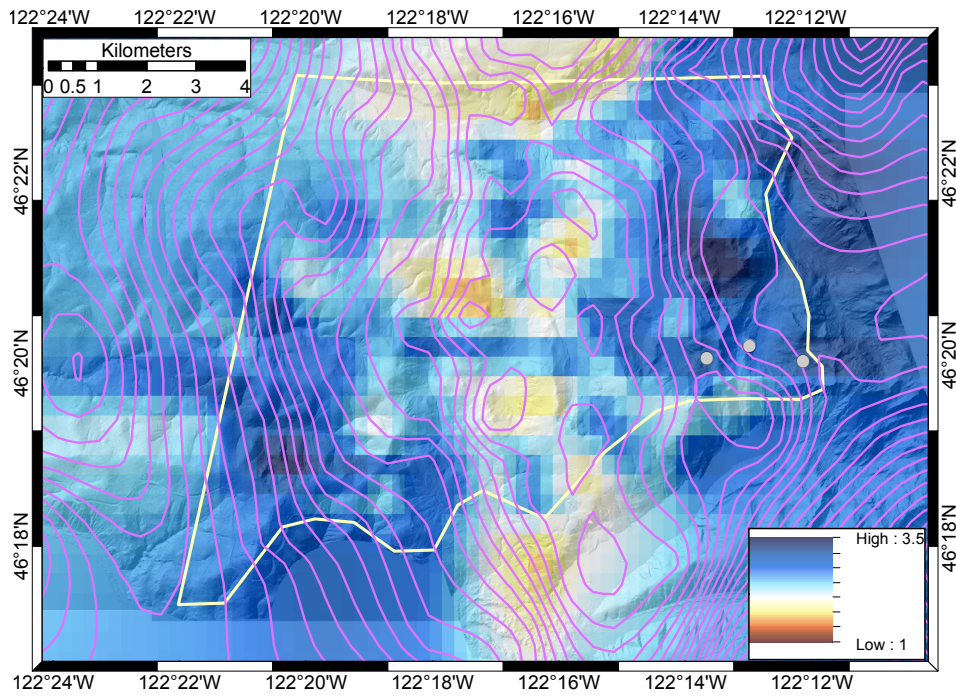


Figure 5: Resistivity depth slice at 290 m with isostatic gravity contours (magenta lines) and earthquake locations (gray circles) within 200 m of the depth slice.

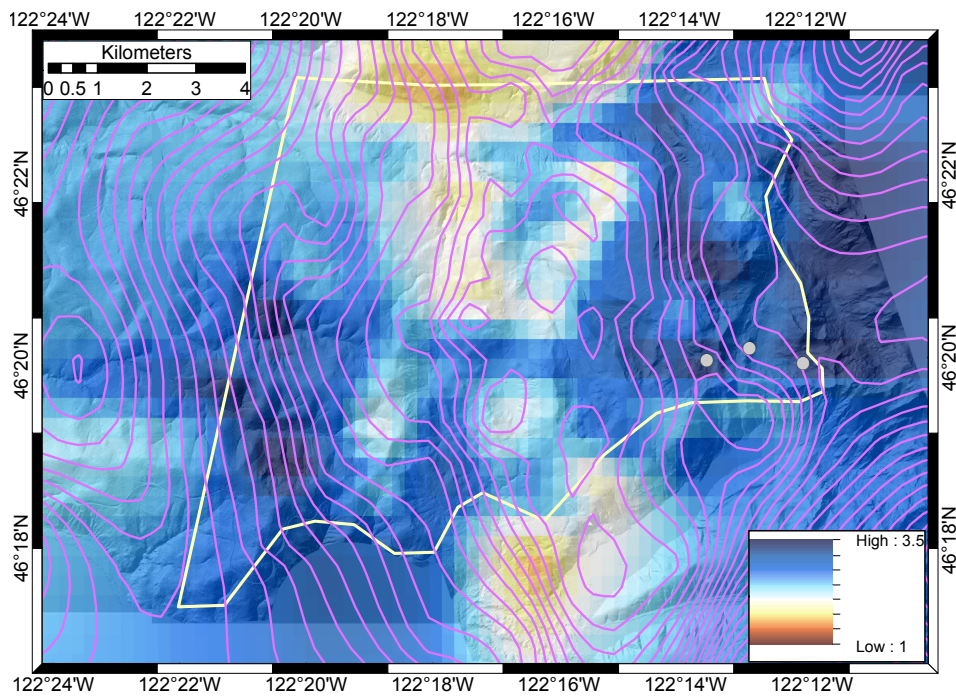


Figure 6: Resistivity depth slice at 560 m with isostatic gravity contours (magenta lines) and earthquake locations (gray circles) within 200 m of the depth slice.

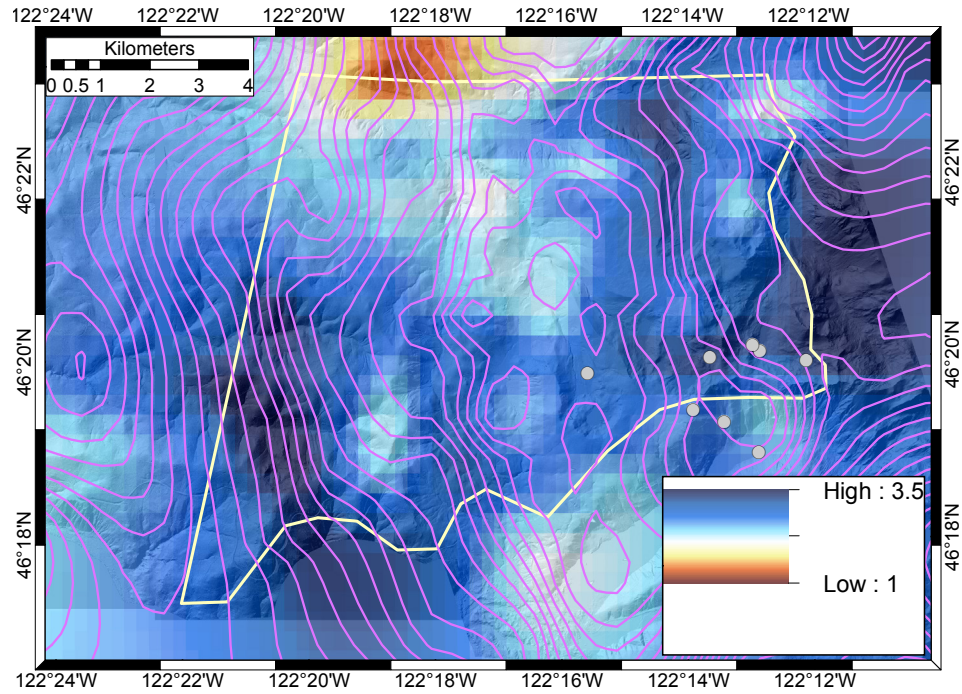


Figure 7: Resistivity depth slice at 960 m with isostatic gravity contours (magenta lines) and earthquake locations (gray circles) within 300 m of the depth slice.

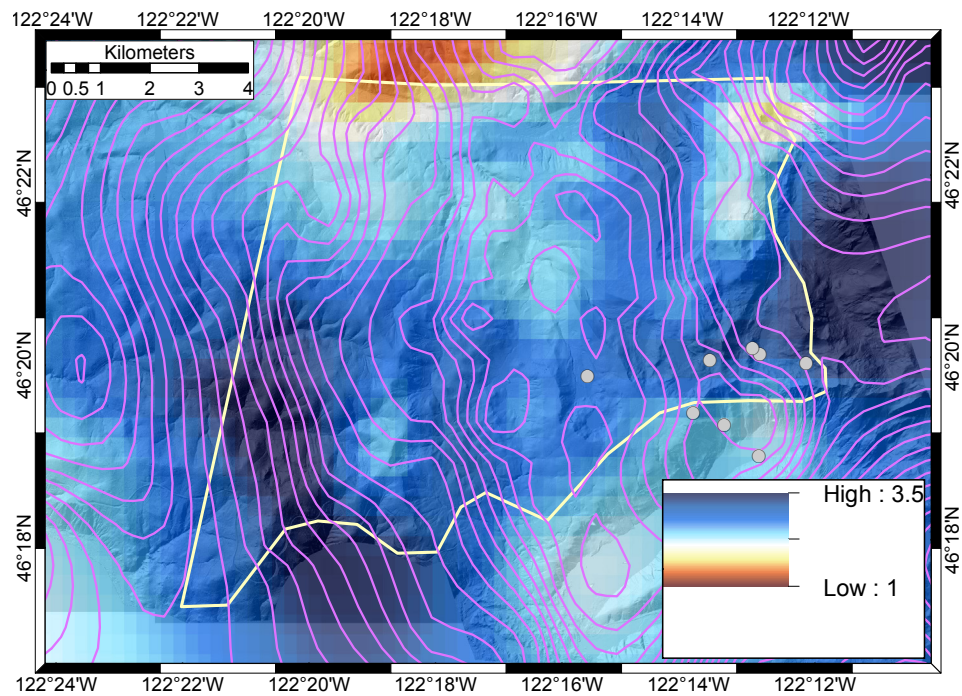


Figure 8: Resistivity depth slice at 1500 m with isostatic gravity contours (magenta lines) and earthquake locations (gray circles) within 500 m of the depth slice.

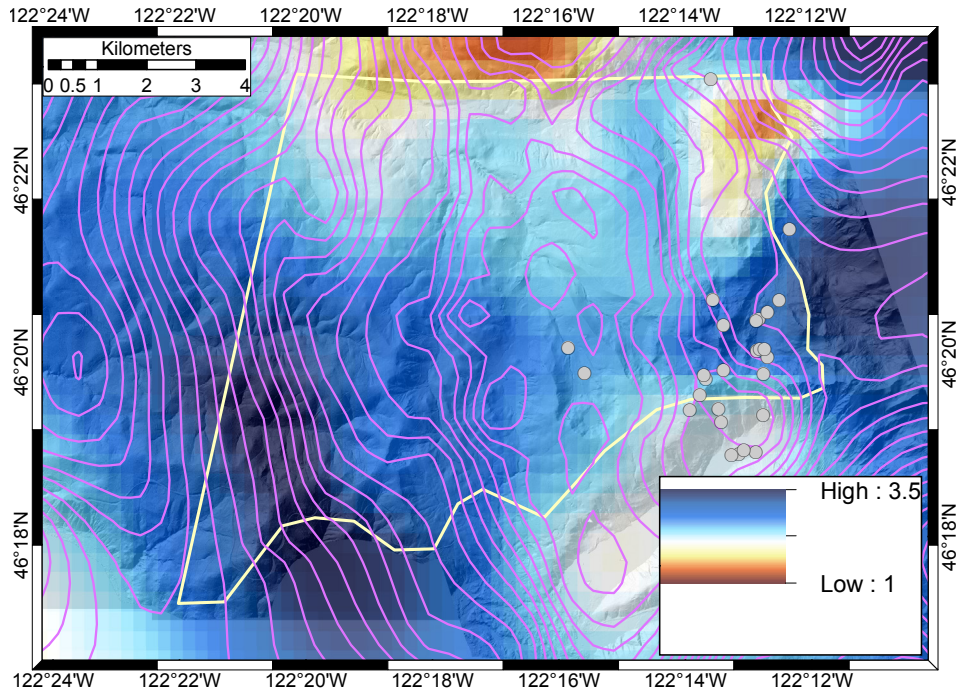


Figure 9: Resistivity depth slice at 2160 m with isostatic gravity contours (magenta lines) and earthquake locations (gray circles) within 1000 m of the depth slice.

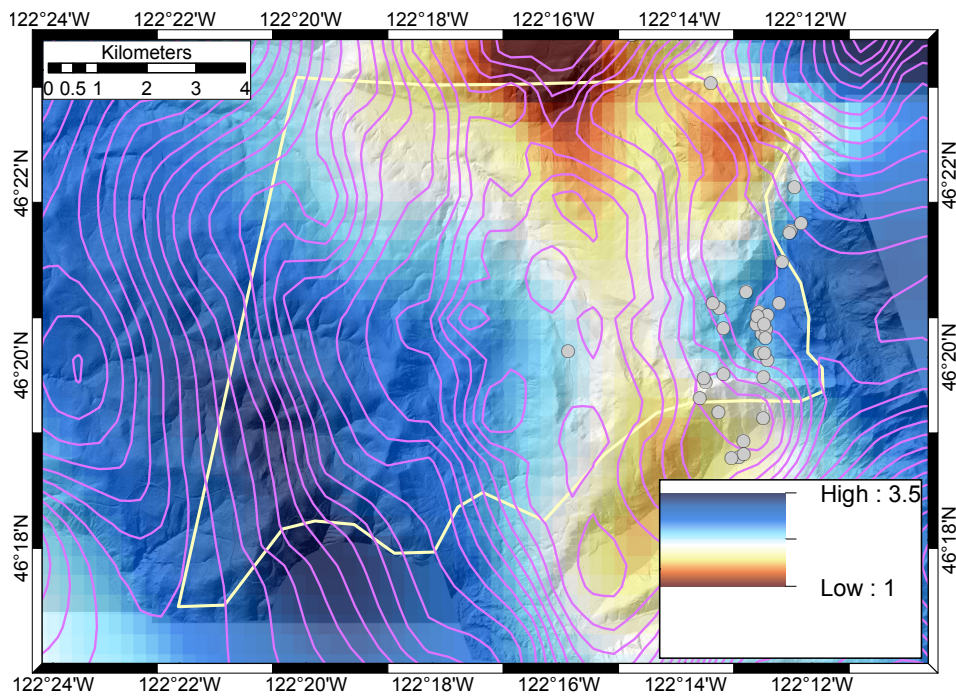


Figure 10: Resistivity depth slice at 3260 m with isostatic gravity contours (magenta lines) and earthquake locations (gray circles) within 1000 m of the depth slice.

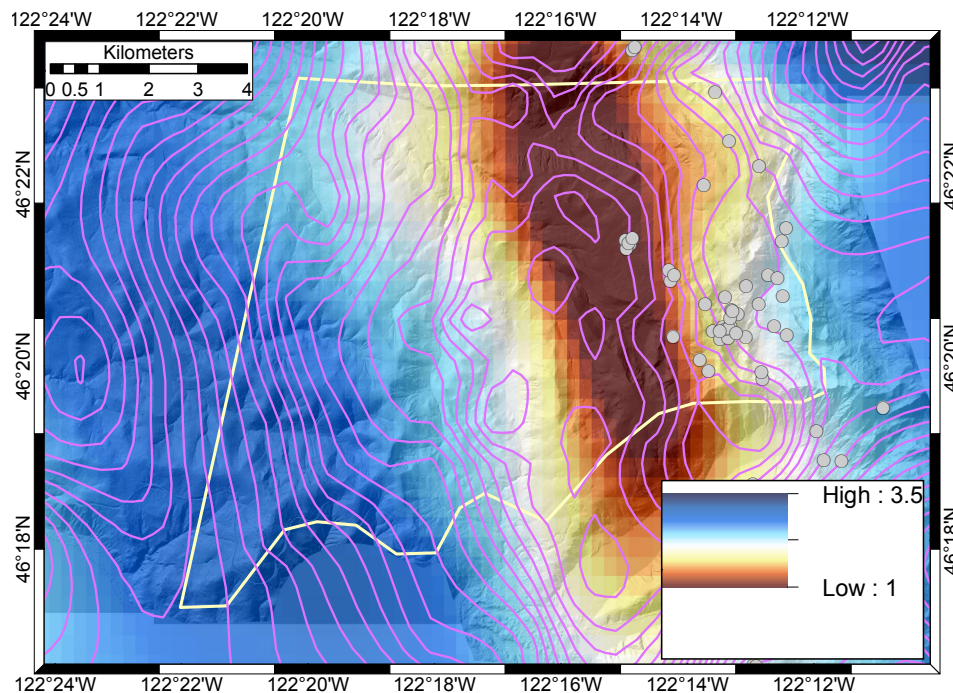


Figure 11: Resistivity depth slice at 5860 m with isostatic gravity contours (magenta lines) and earthquake locations (gray circles) within 1000 m of the depth slice.

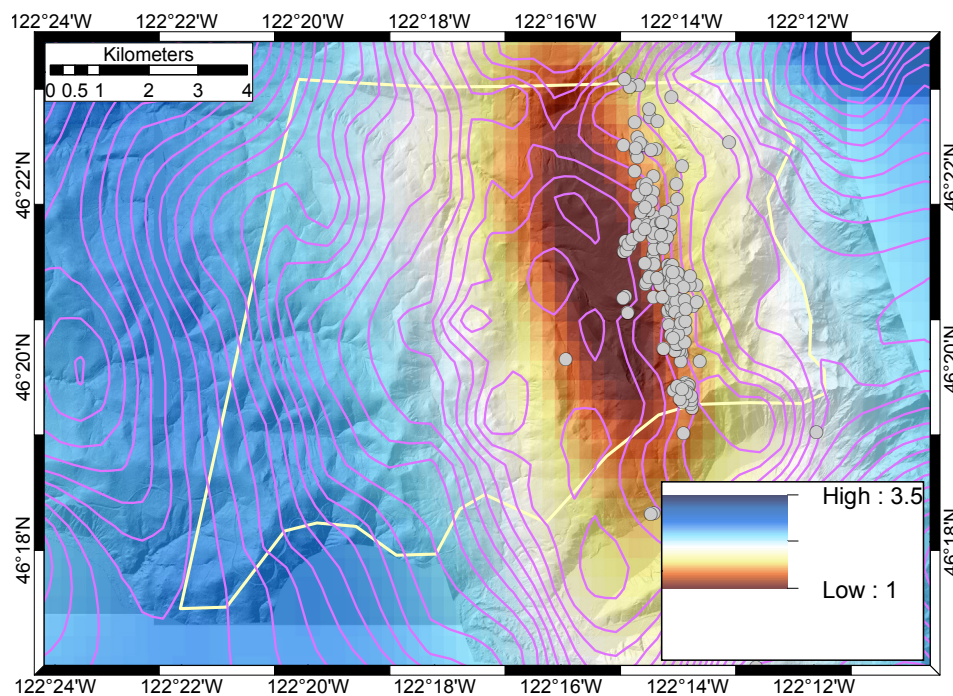


Figure 12: Resistivity depth slice at 7860 m with isostatic gravity contours (magenta lines) and earthquake locations (gray circles) within 1000 m of the depth slice.

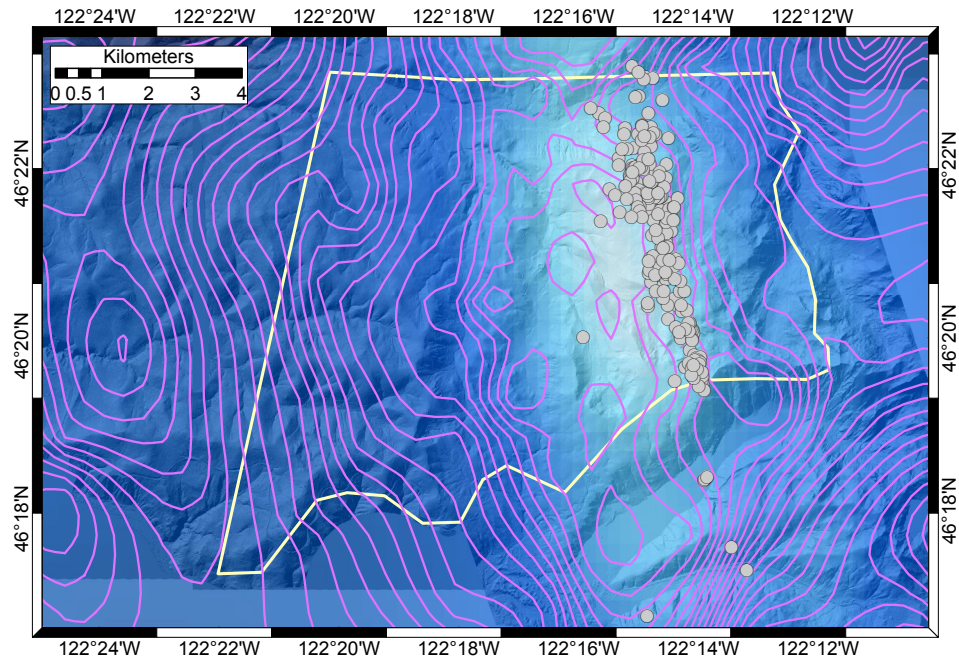
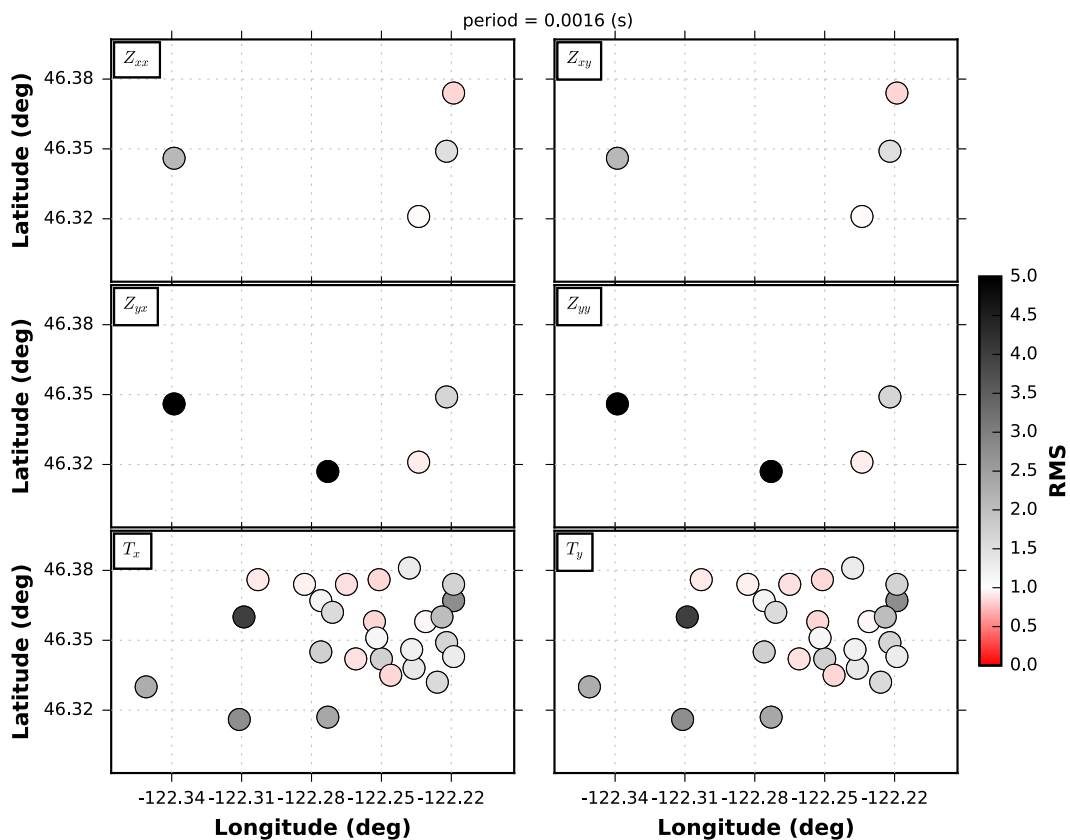
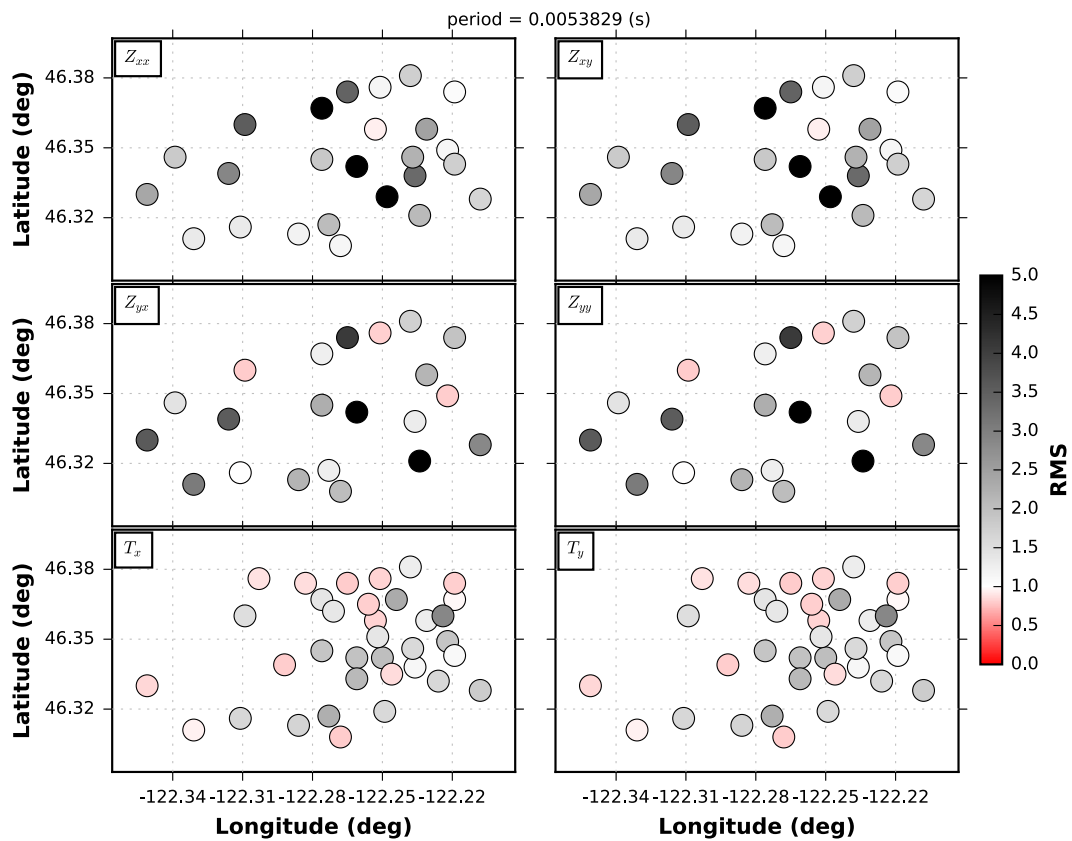
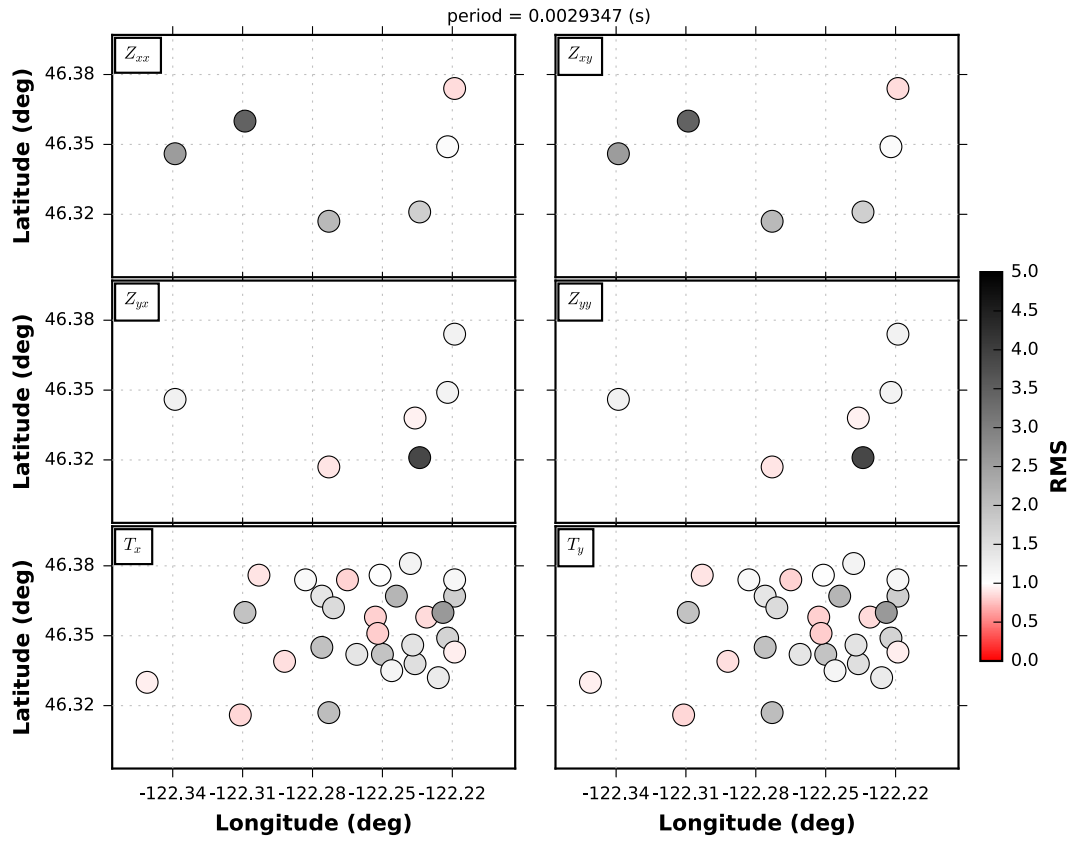


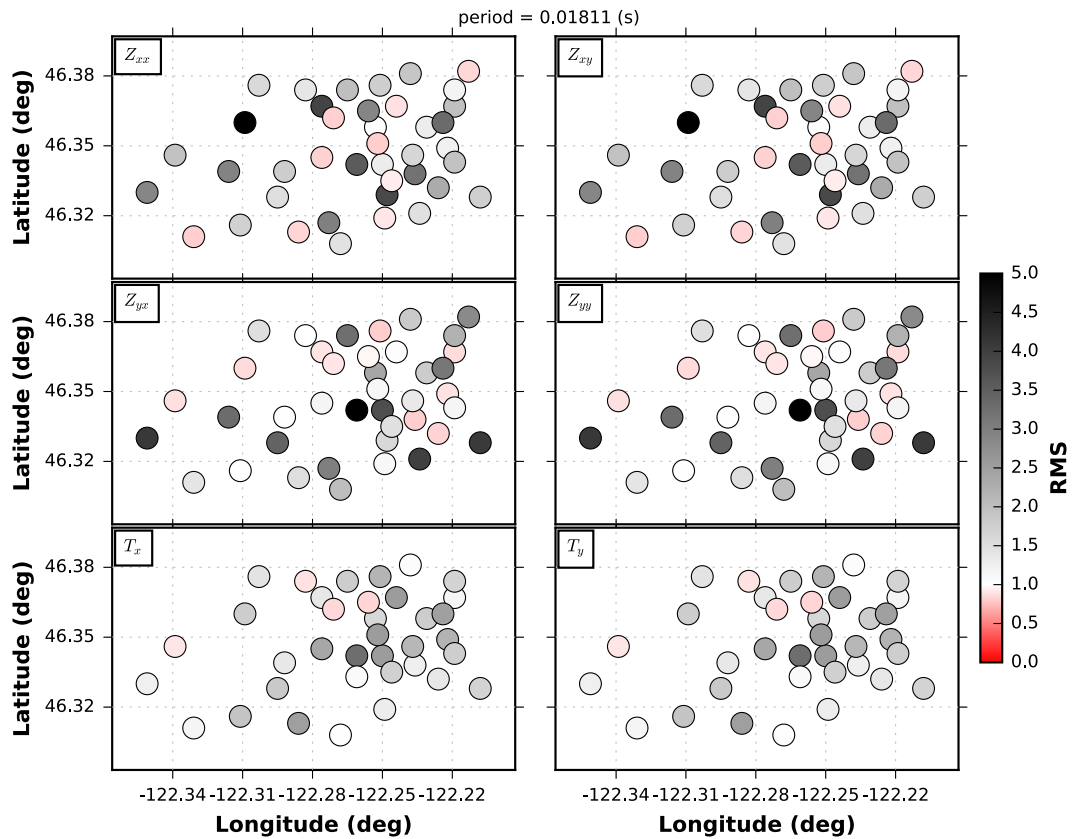
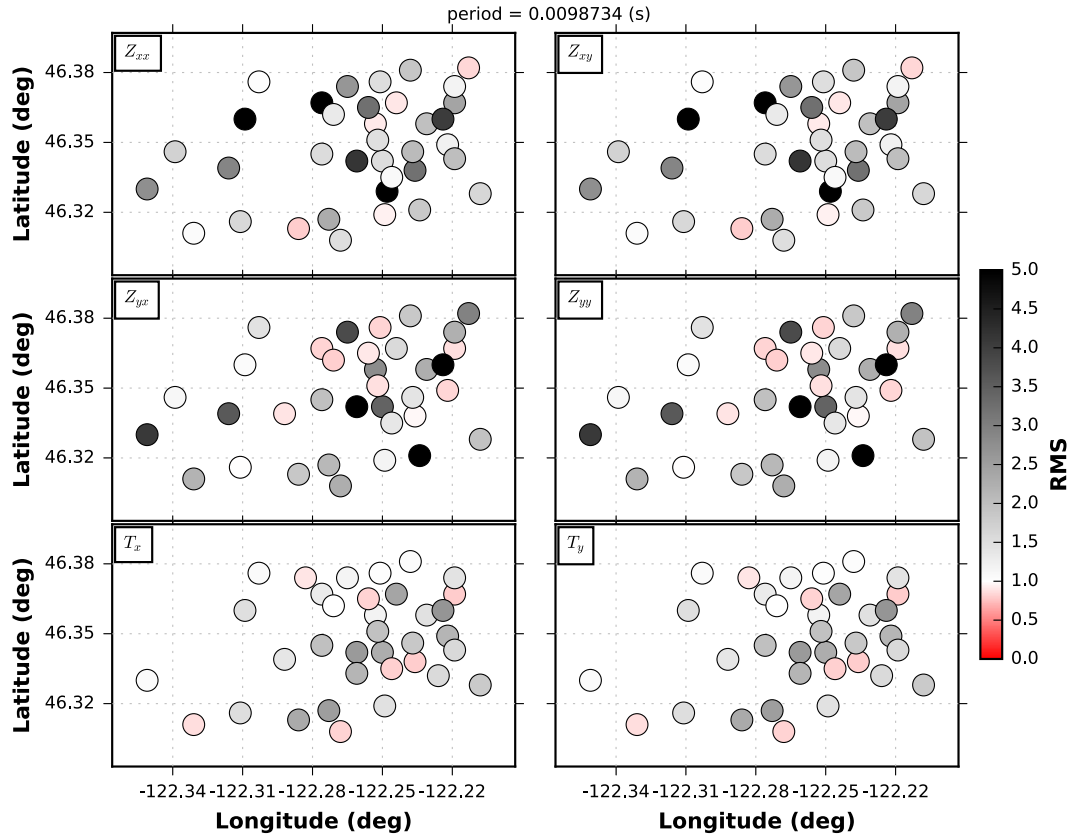
Figure 13: Resistivity depth slice at 11000 m with isostatic gravity contours (magenta lines) and earthquake locations (gray circles) within 2000 m of the depth slice.

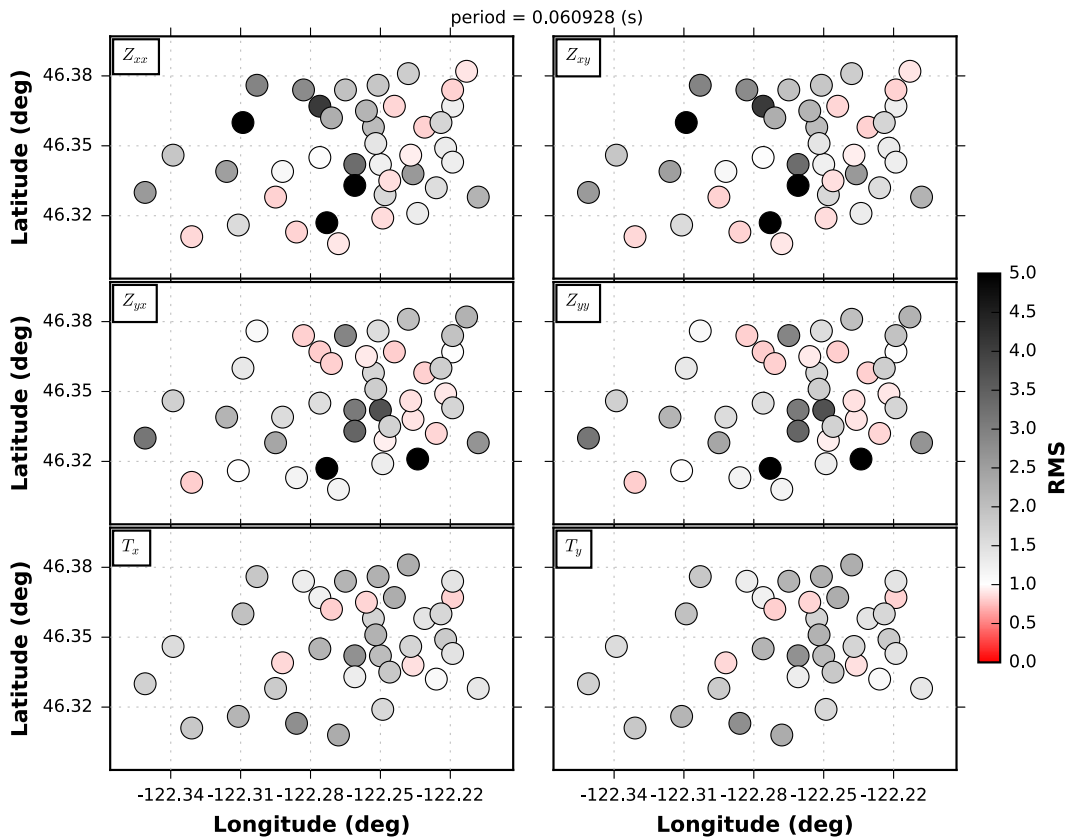
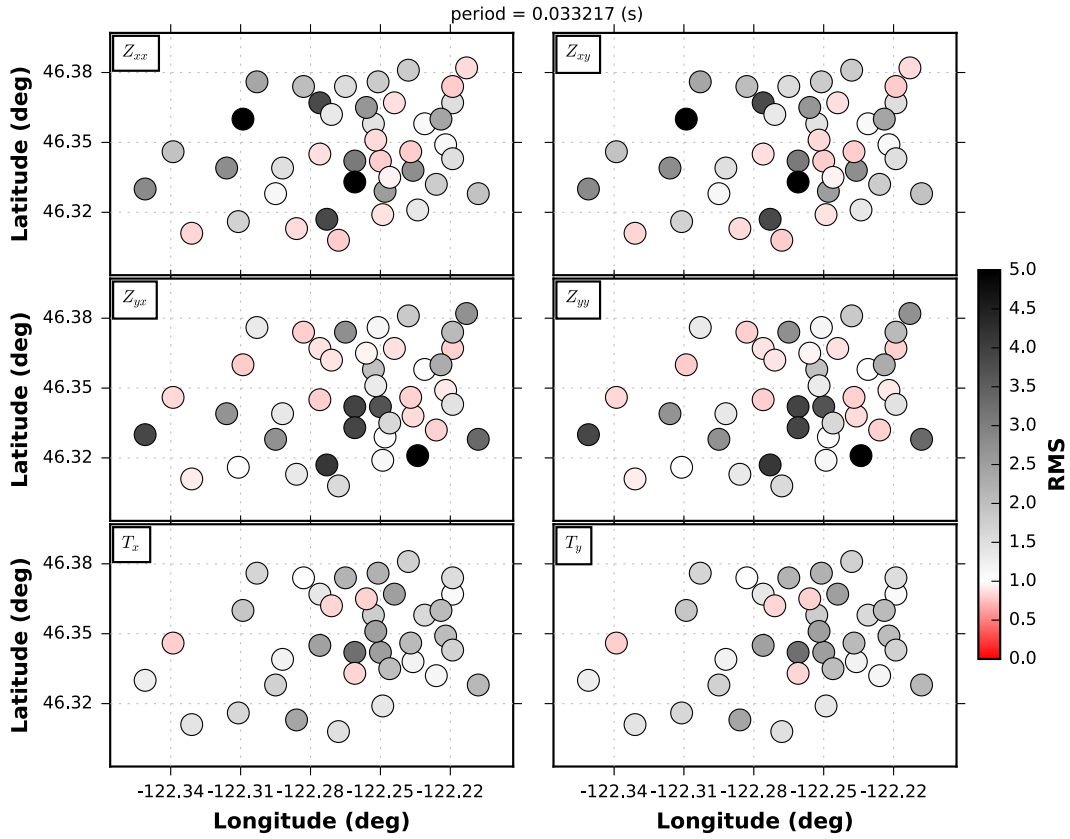
B Model RMS Maps

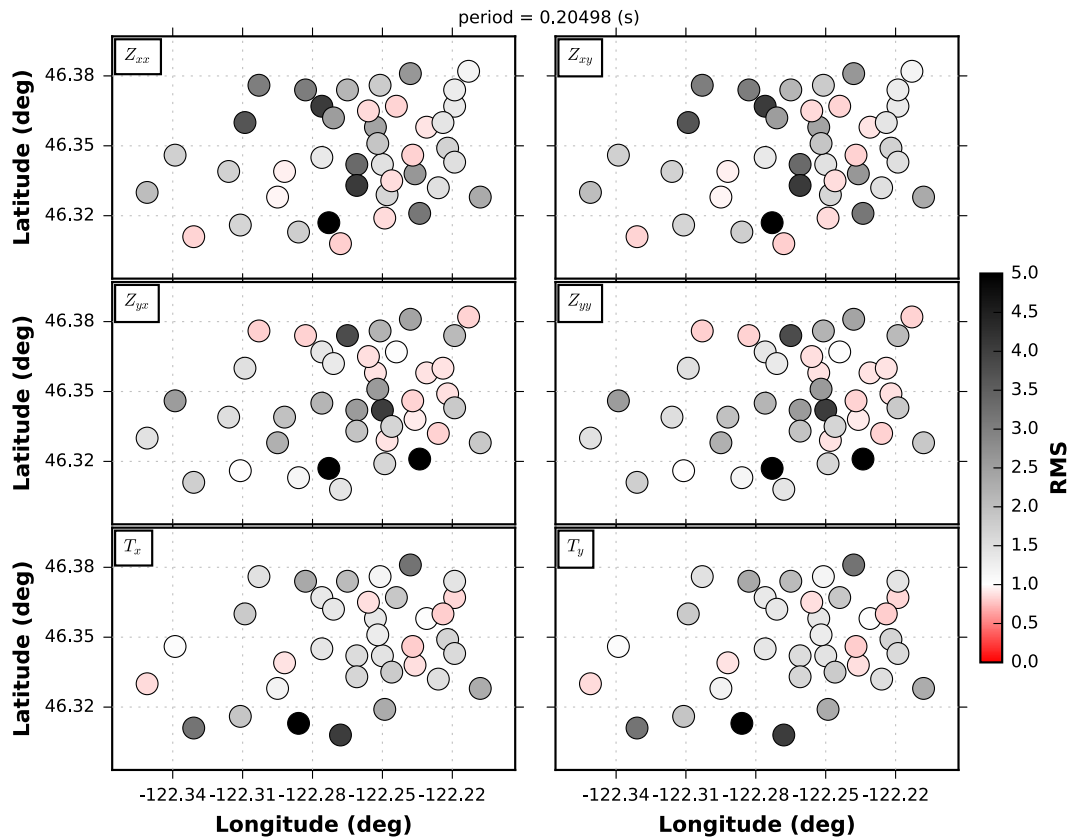
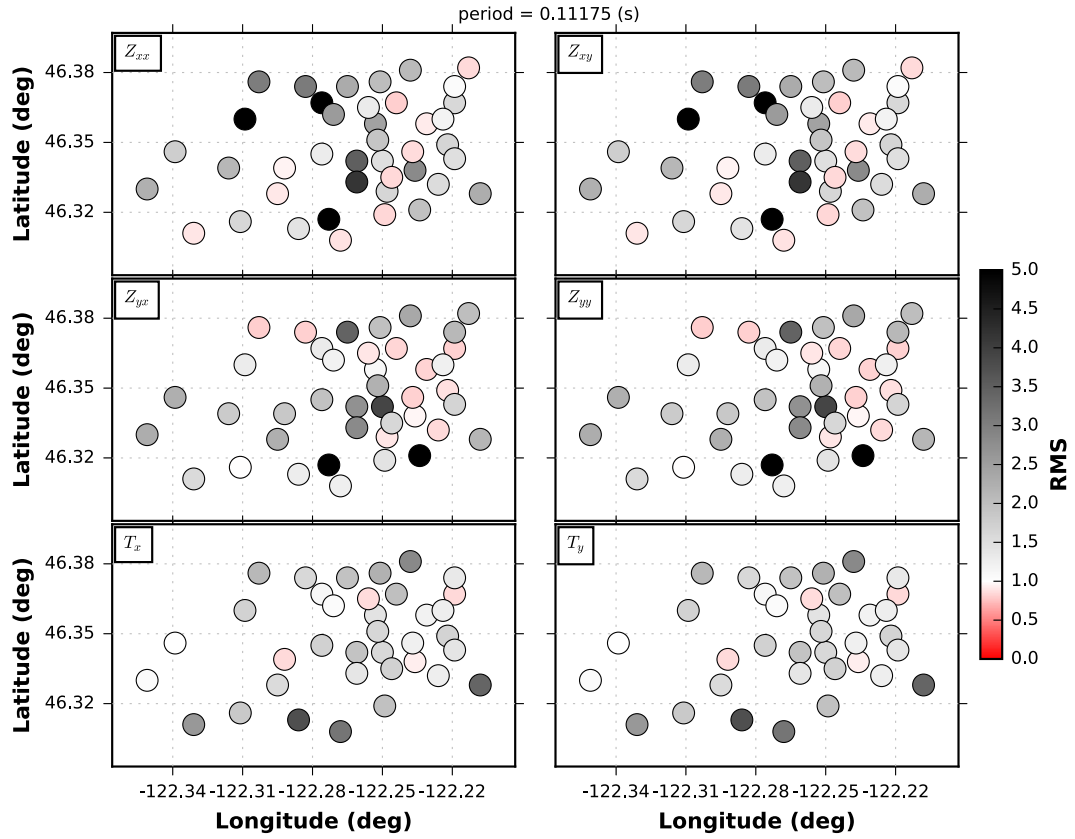
The maps in this section show the normalized root-means-squared (nRMS) error of the misfit between the MT response of the data and the resistivity model within the given error floors. Black color means the difference between the data and model response is large and the fit is poor, whereas red colors means the model is over fitting the data within the given error. White colors around and nRMS of 1 are optimal fits. The off-diagonal components of \mathbf{Z} typically have more weight than the diagonal components, which is related to the physics of induction. However, in this experiment, the diagonal components are nearly the same magnitude as the off-diagonal components and have influence in the model. The GDS magnitudes are relatively small (< 0.3) but still influence the shape and orientation of the main anomaly C1.

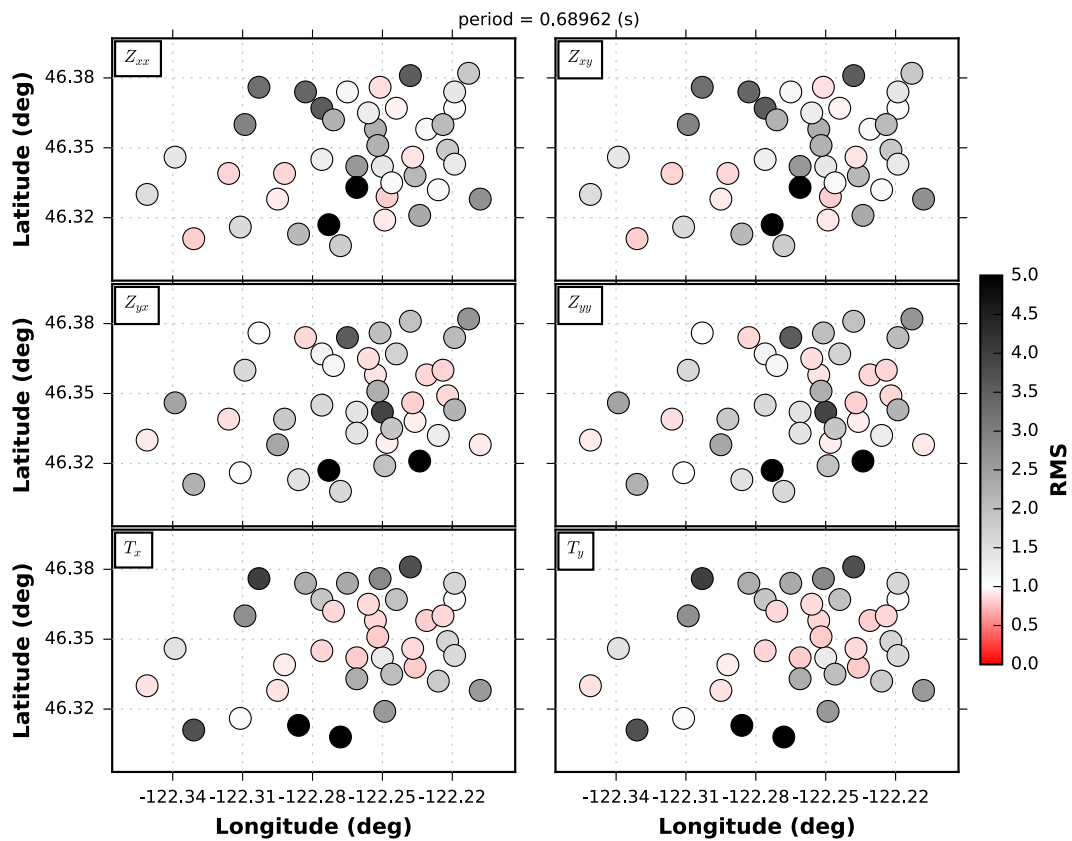
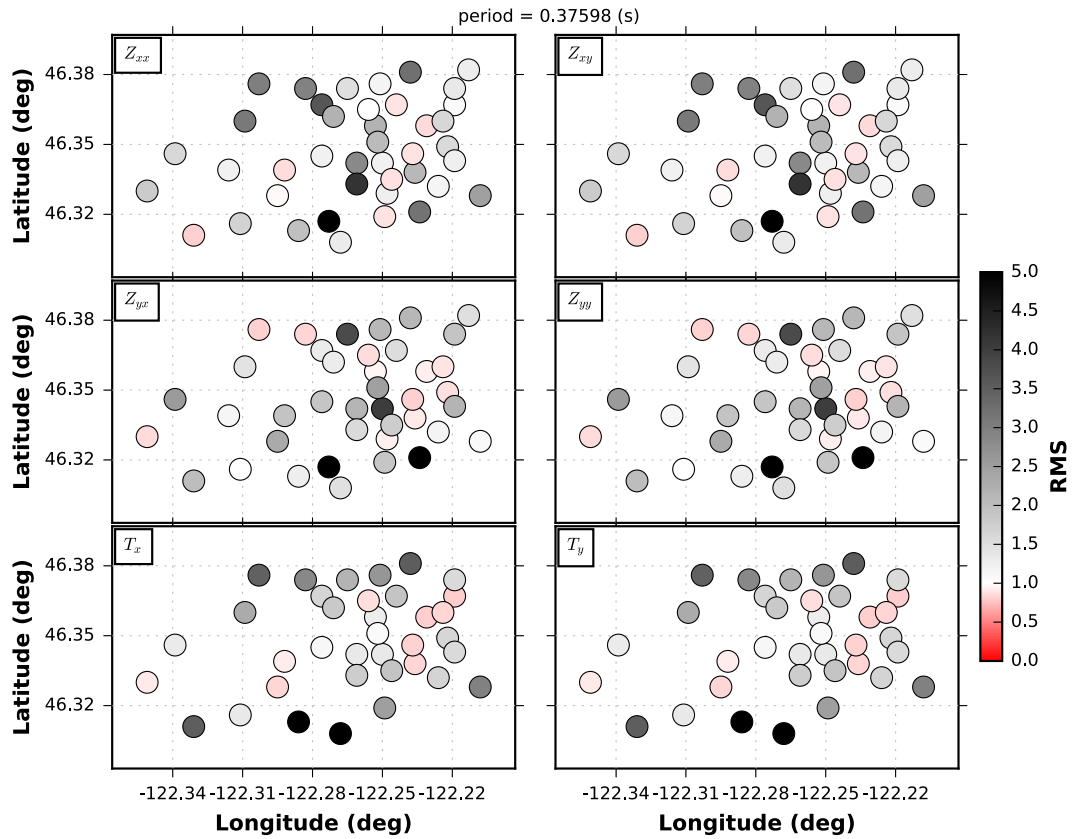


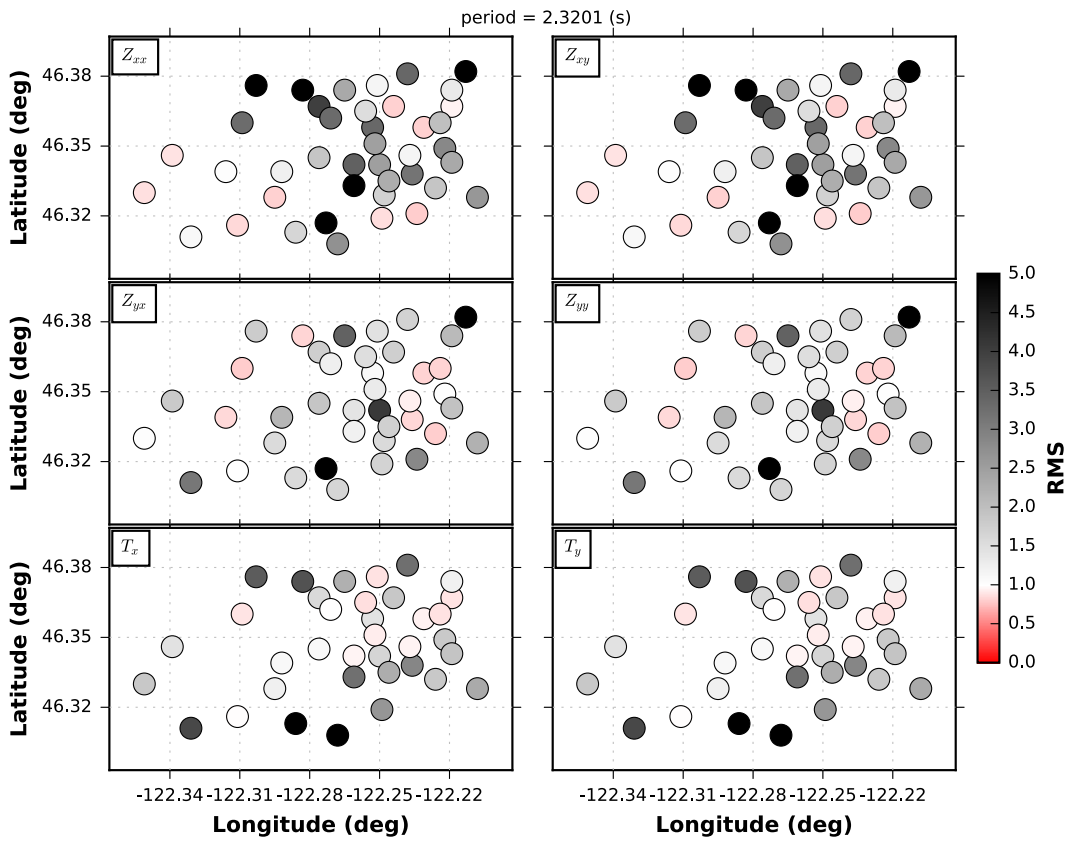
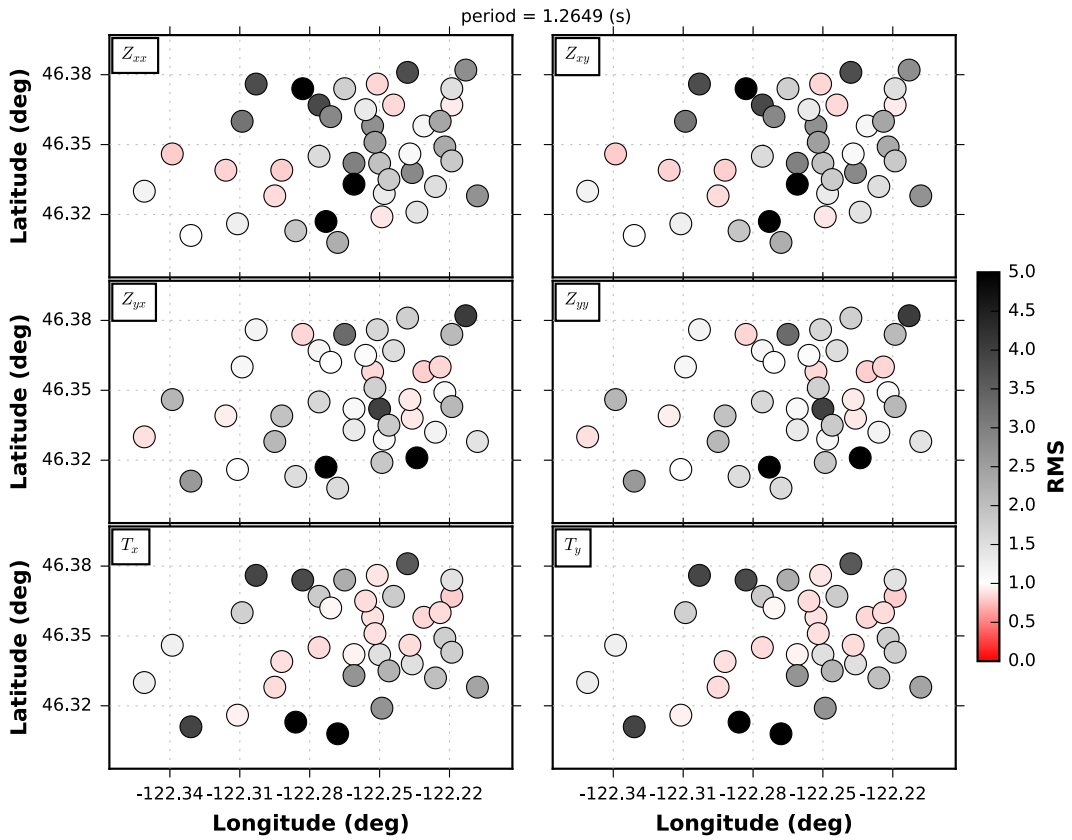


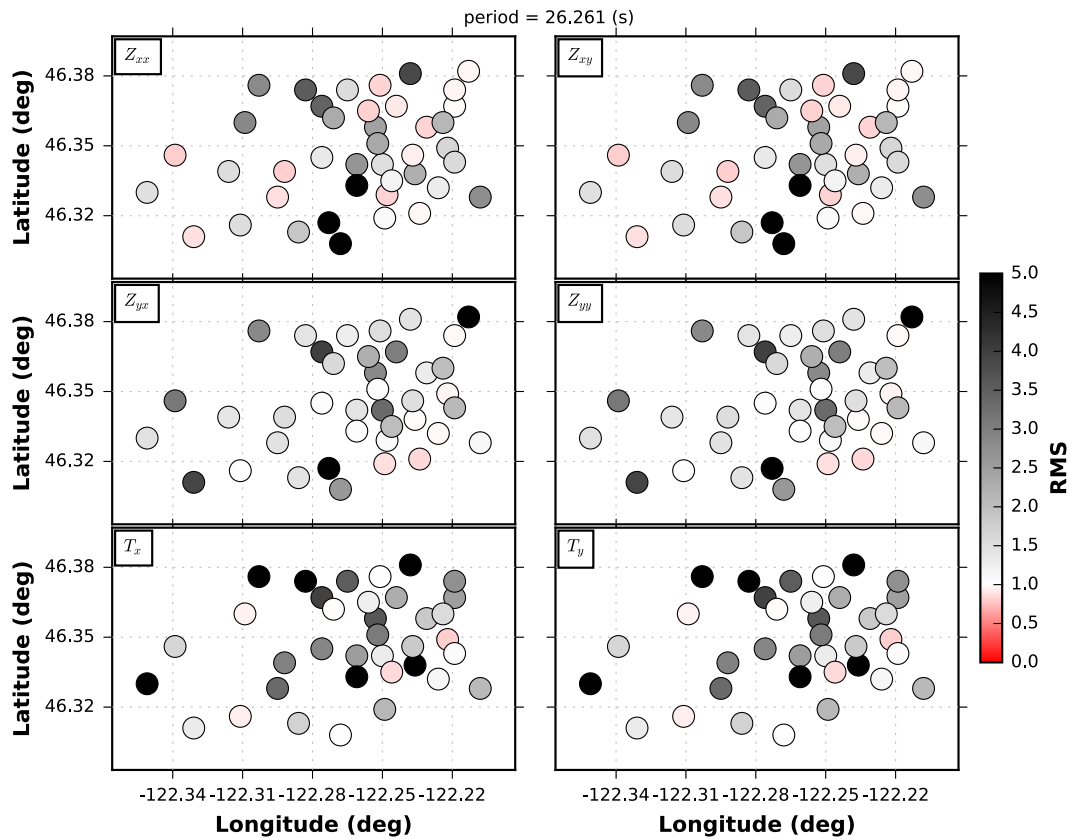
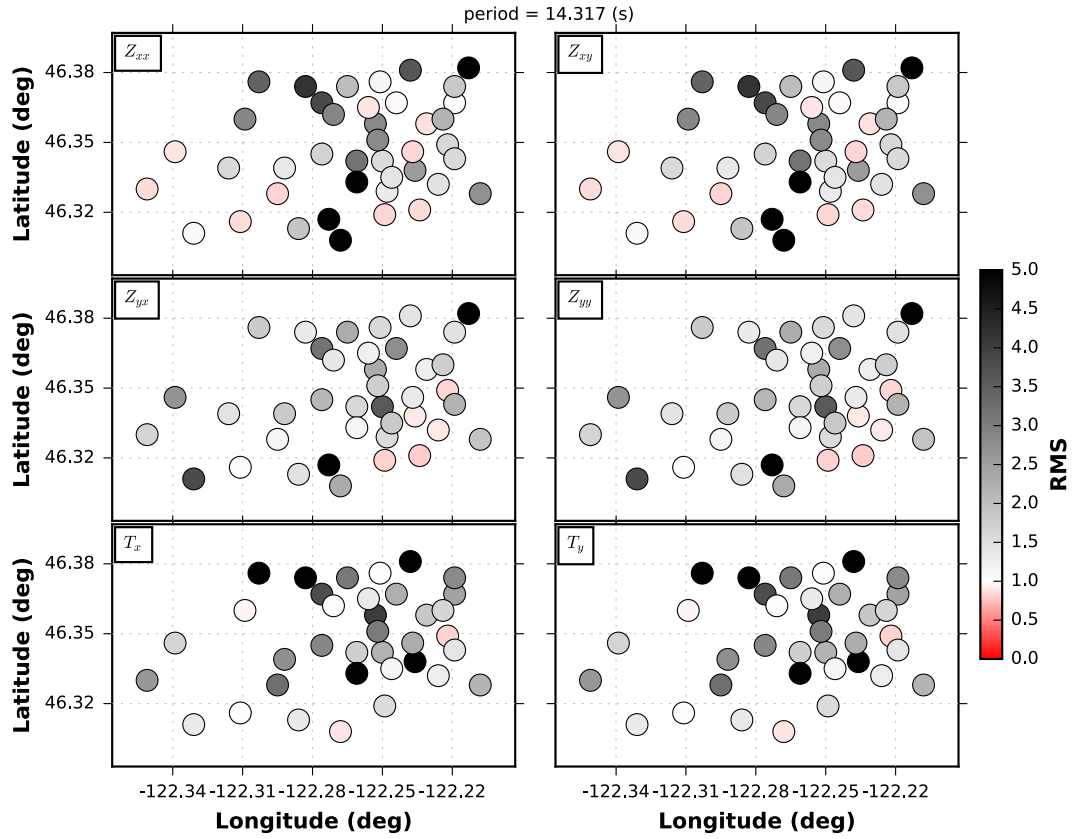


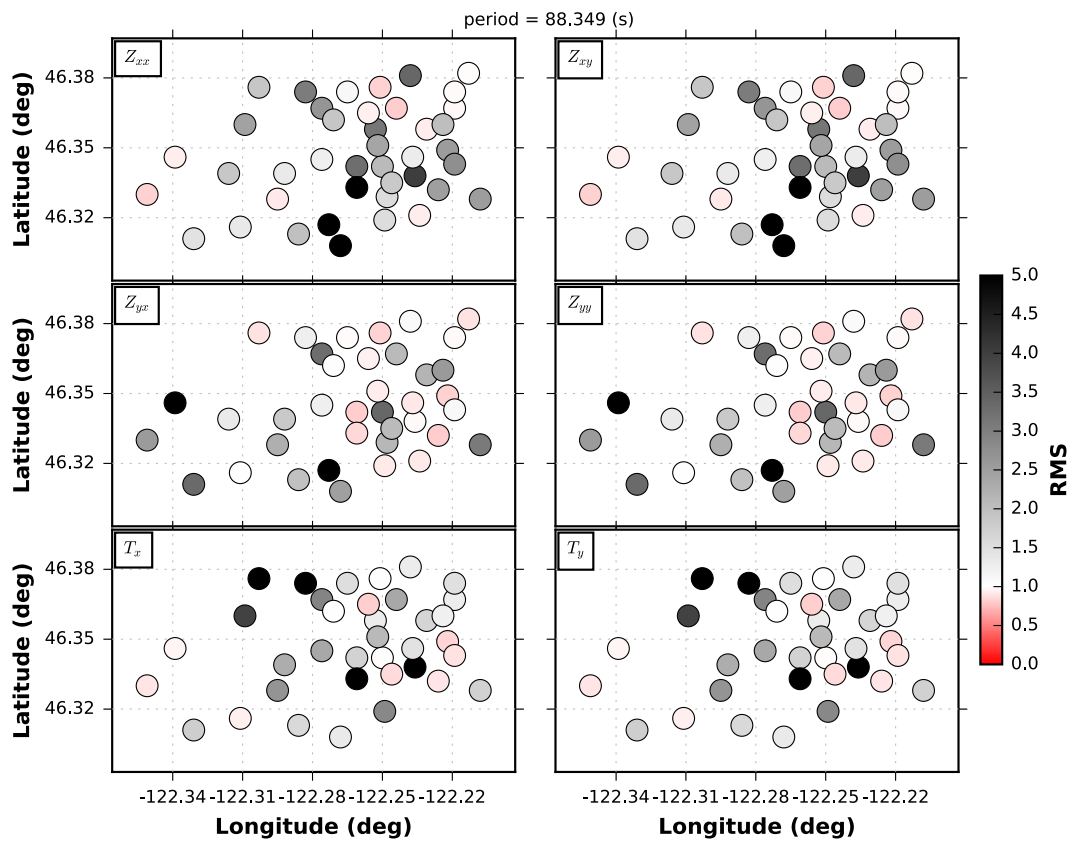
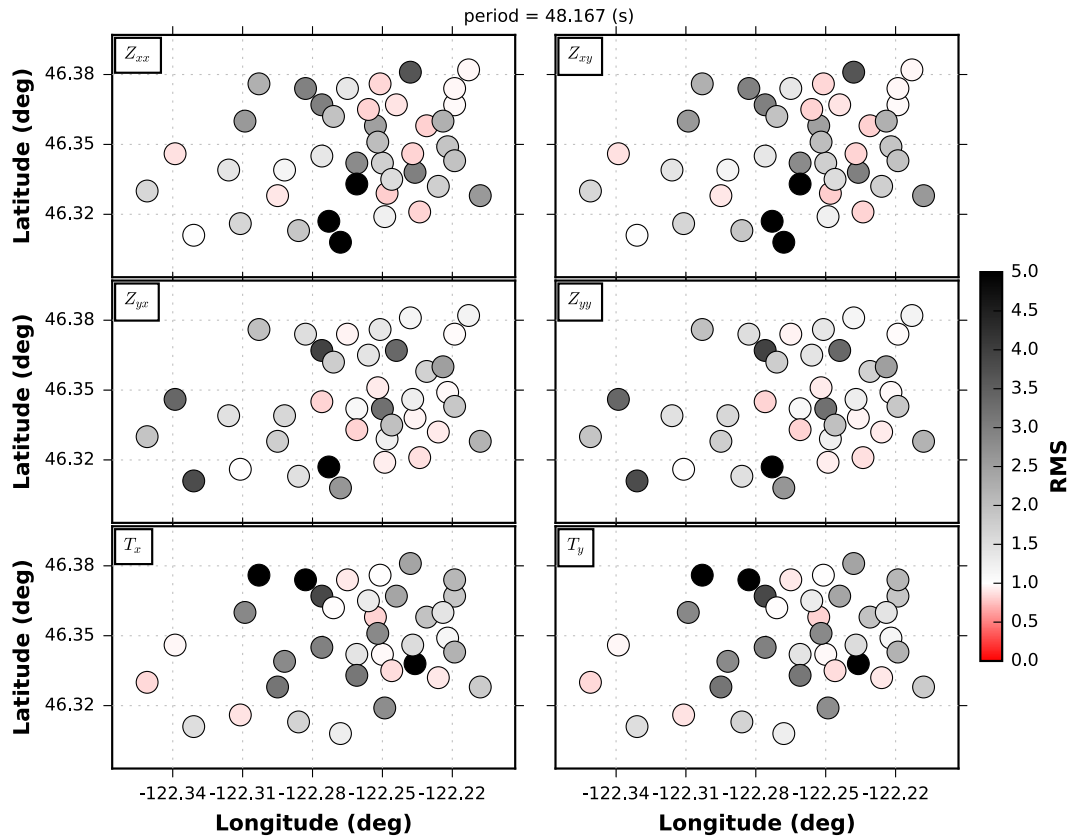


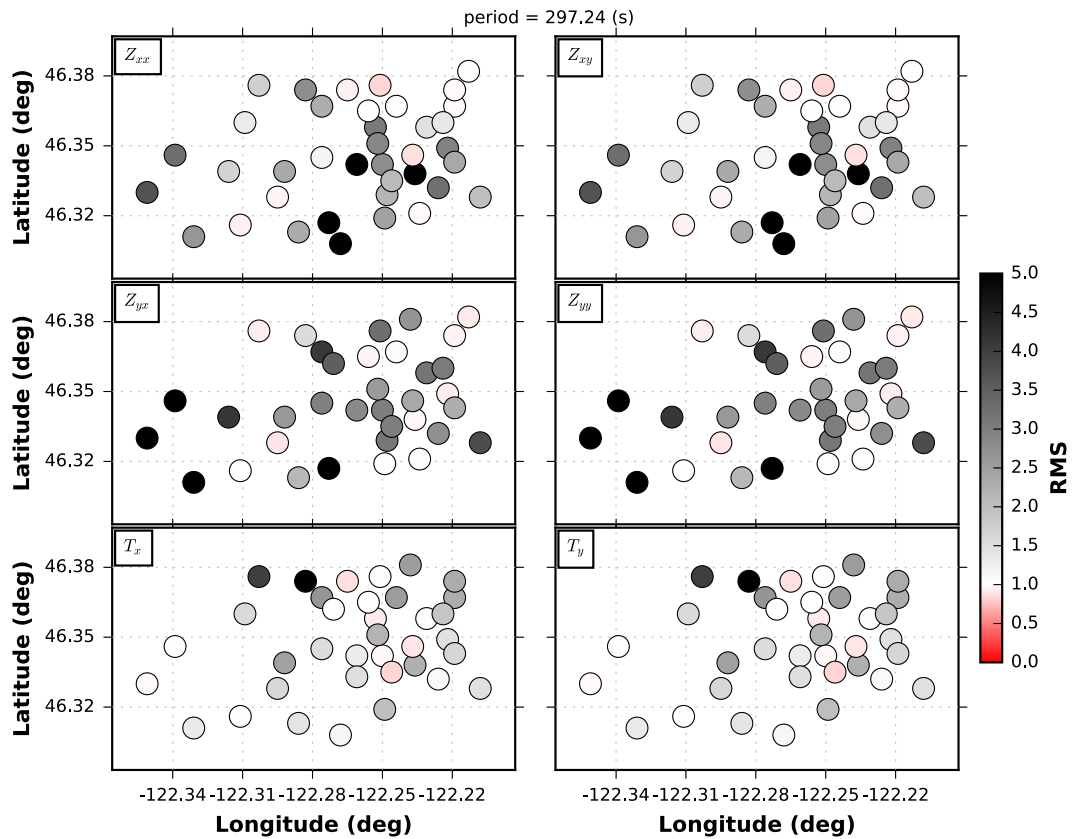
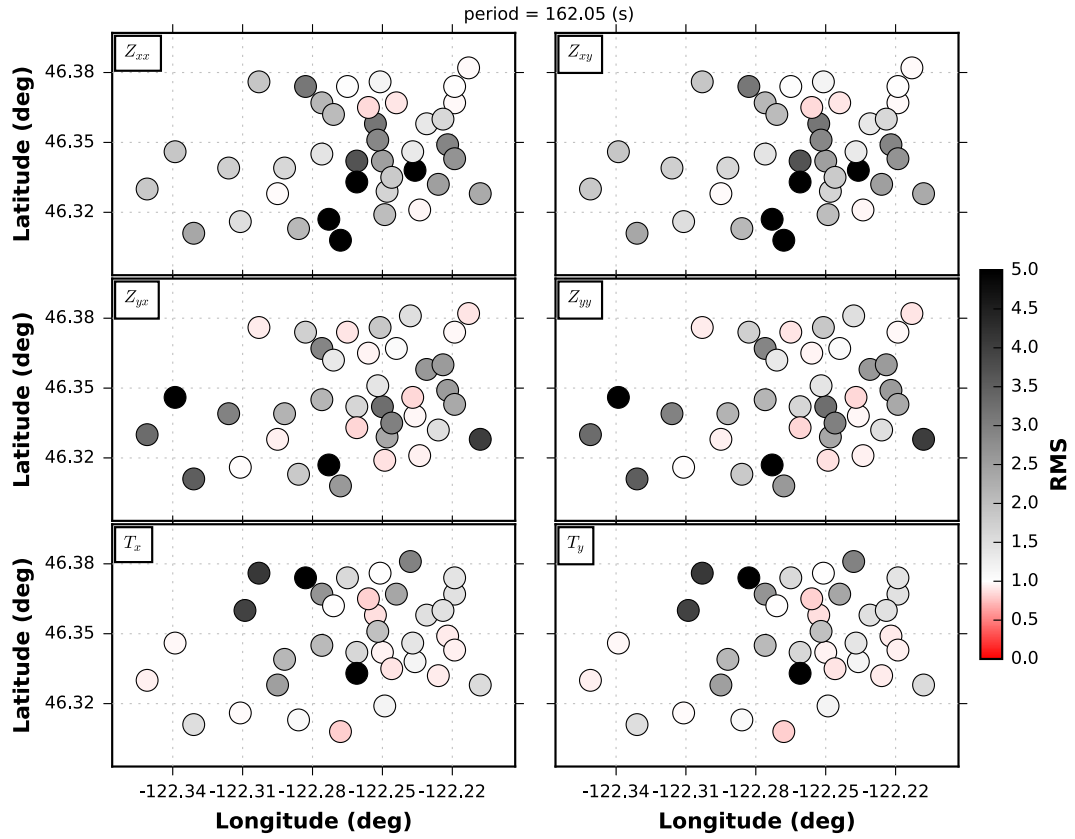


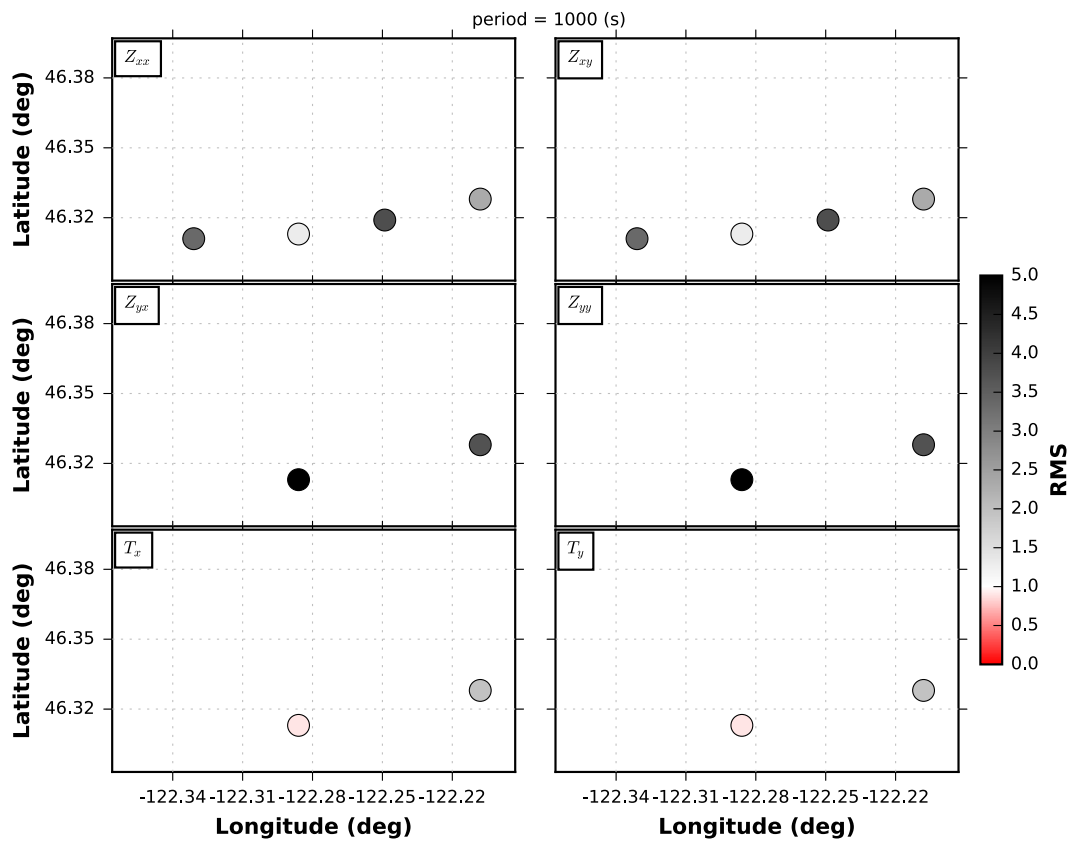
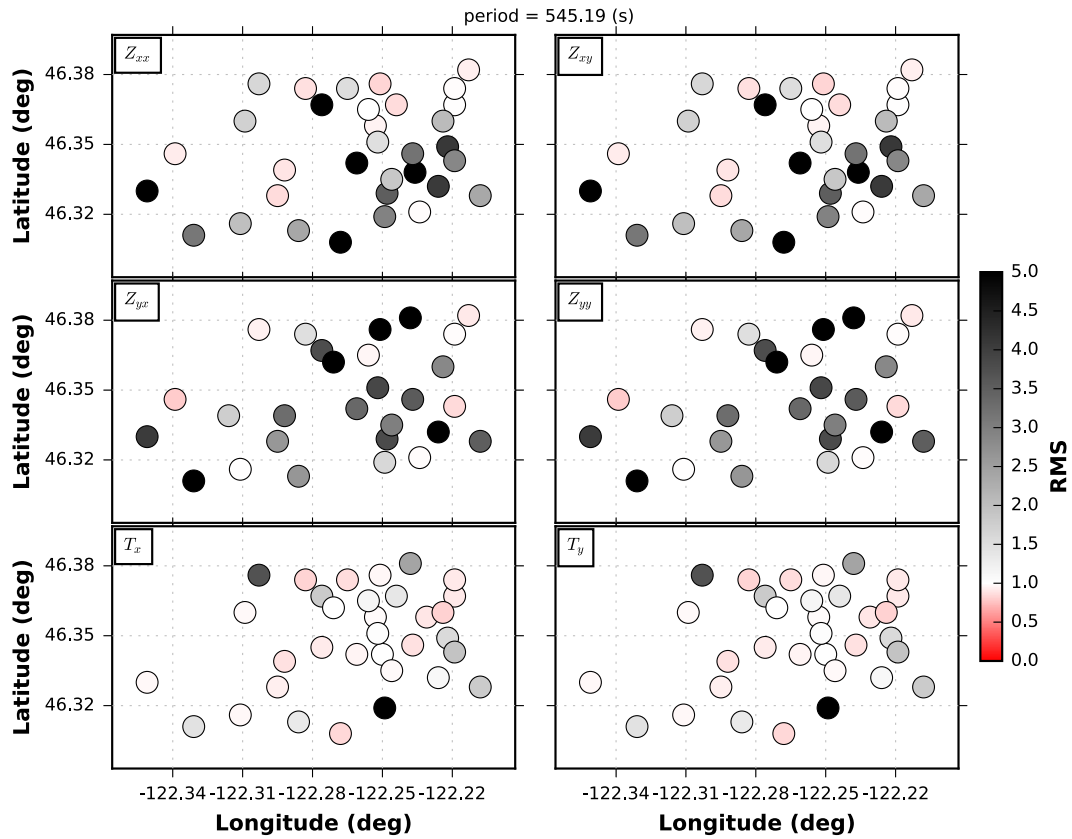




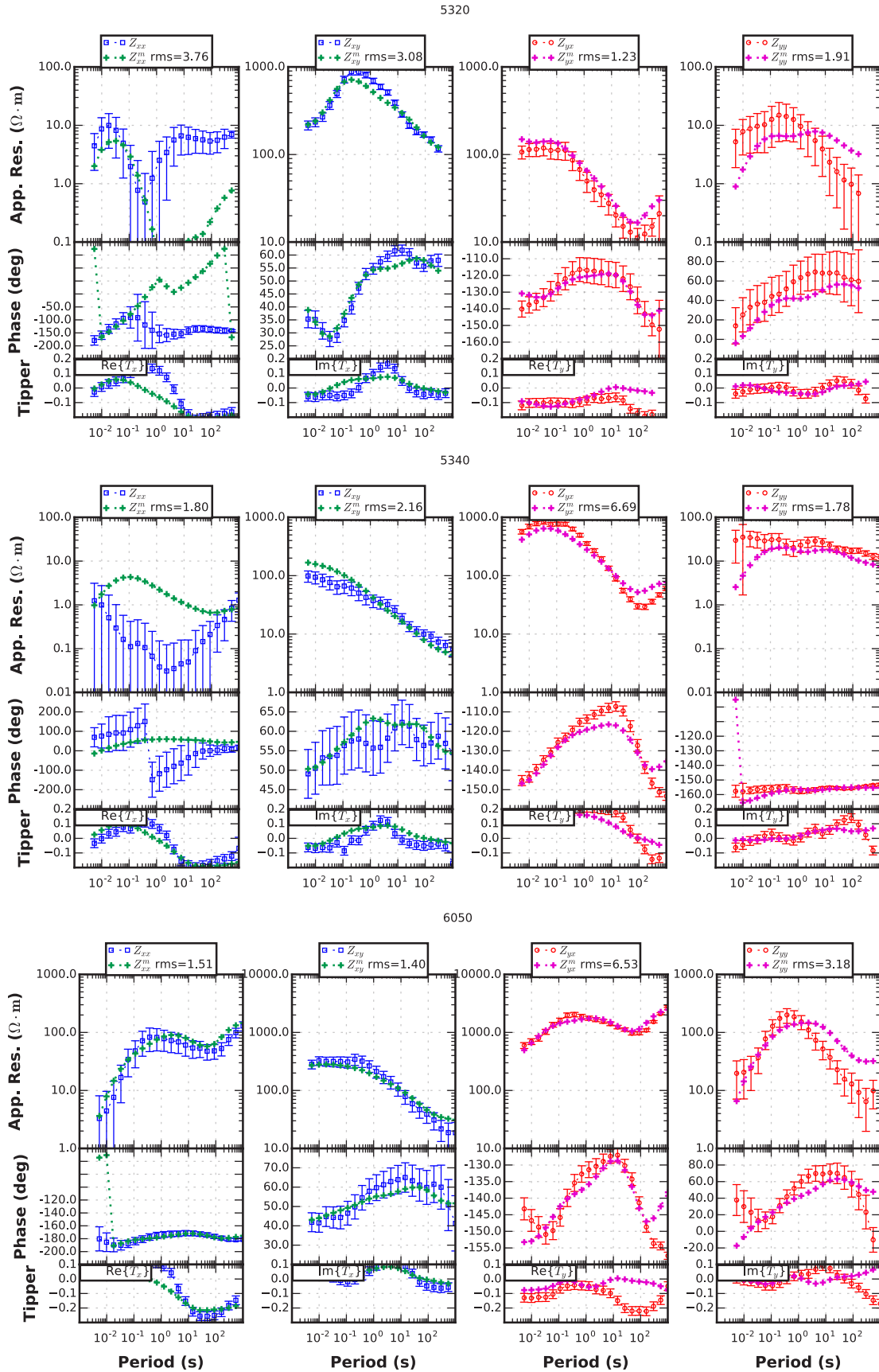




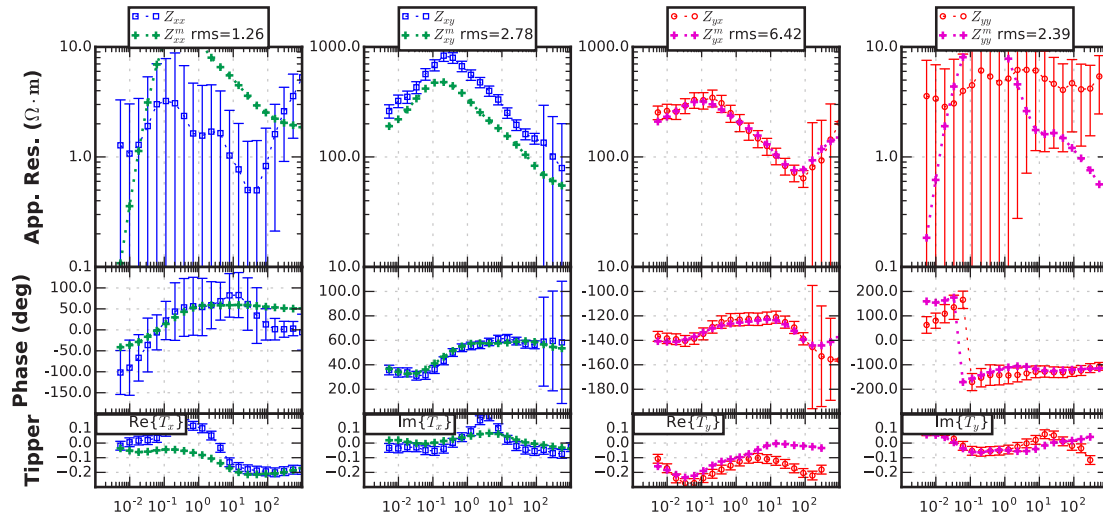




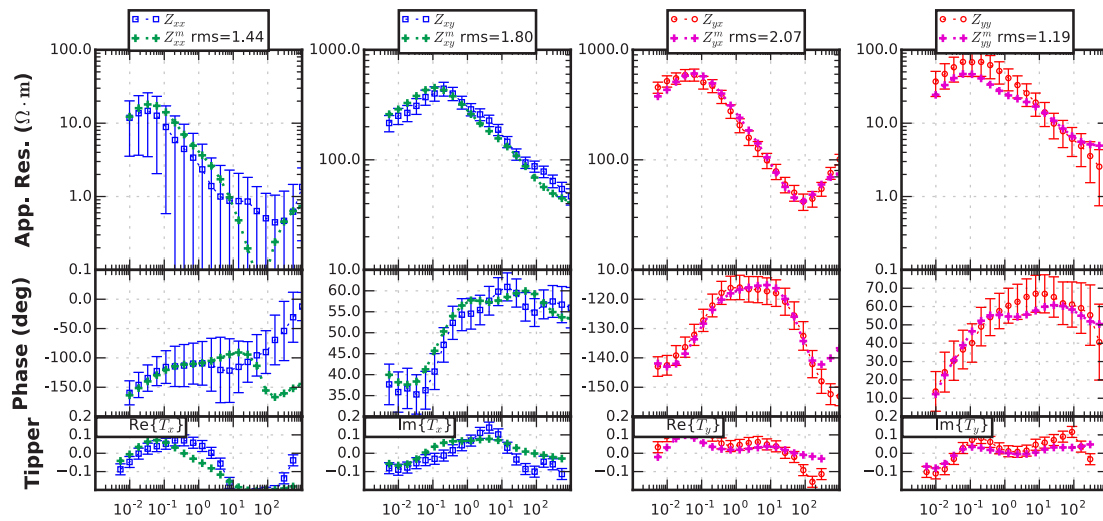
C Data & Model MT Responses



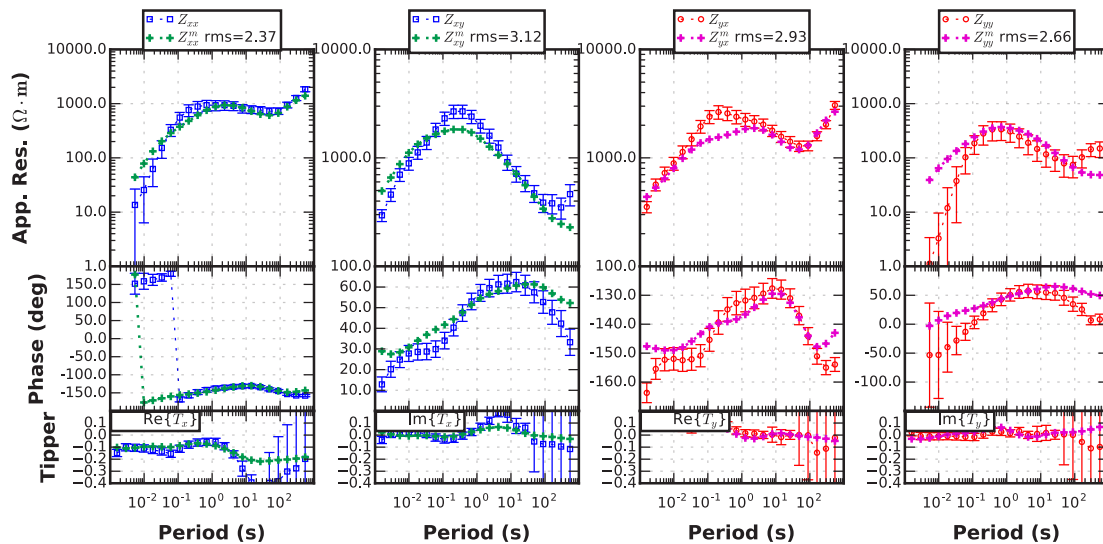
6320

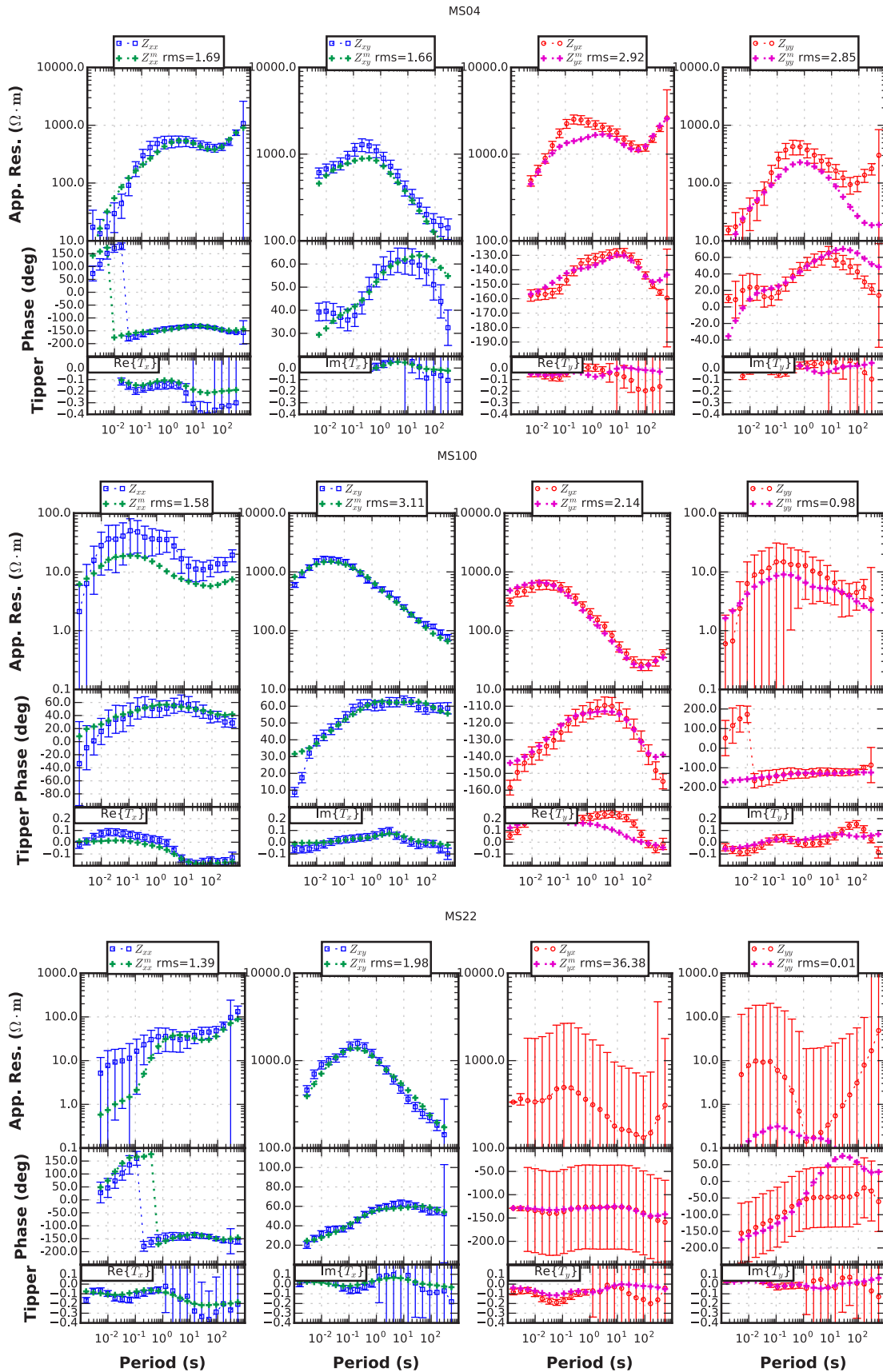


6460

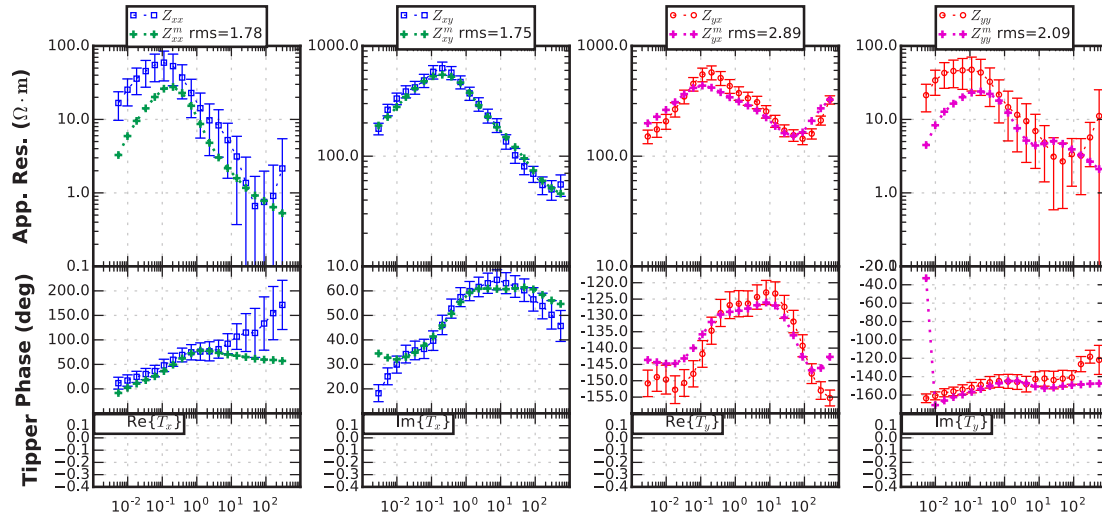


MS03

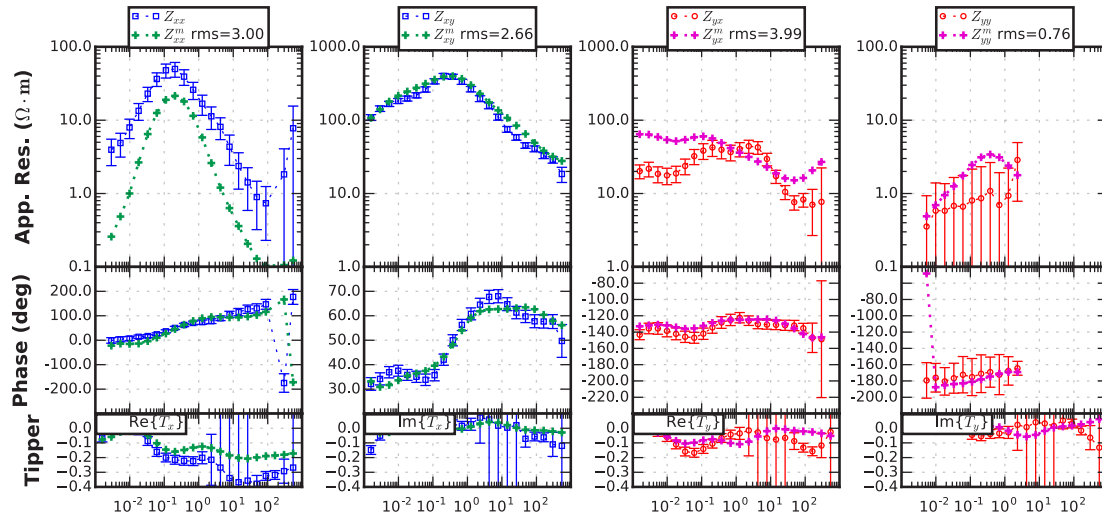




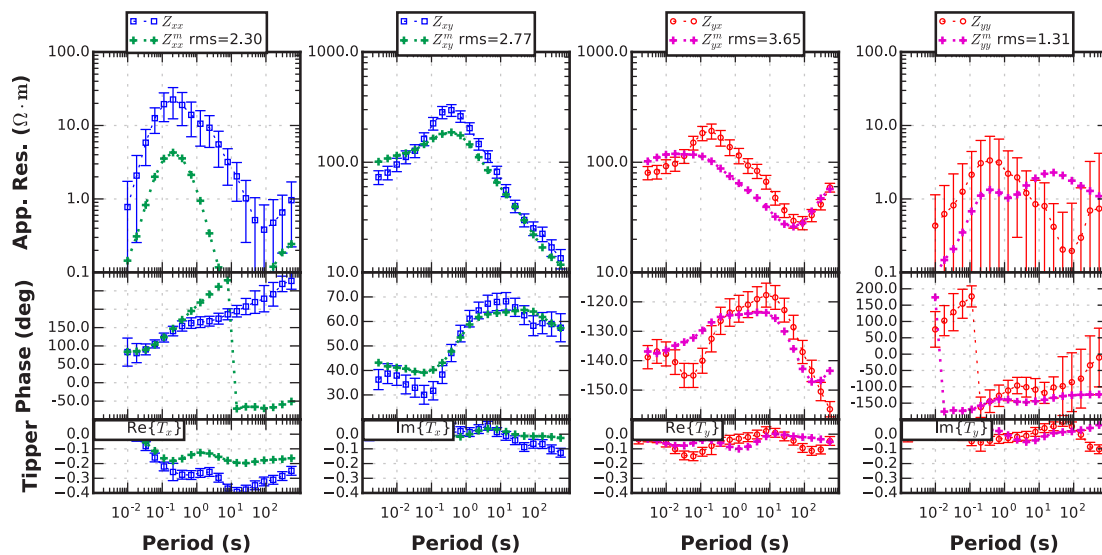
MS24

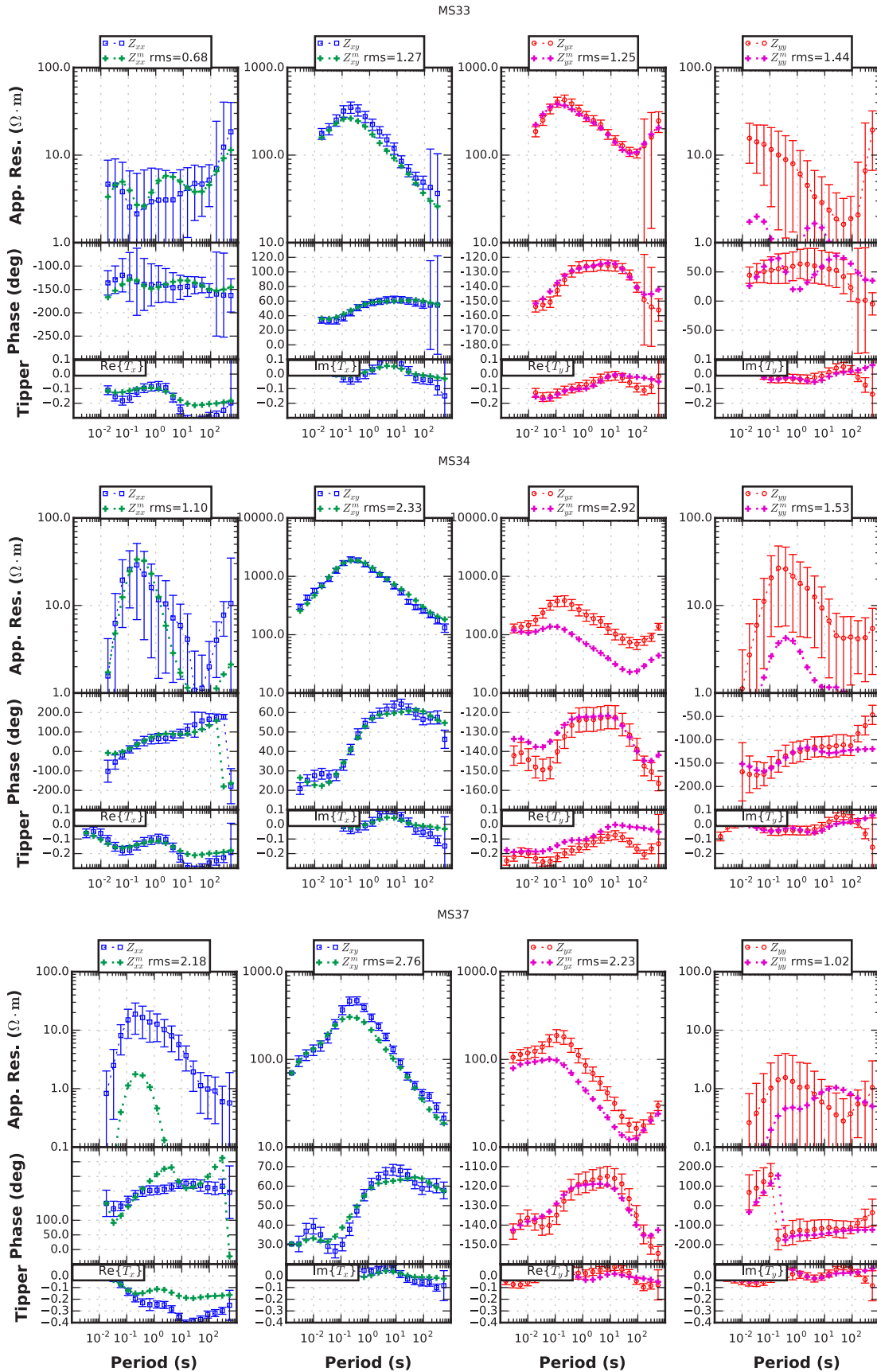


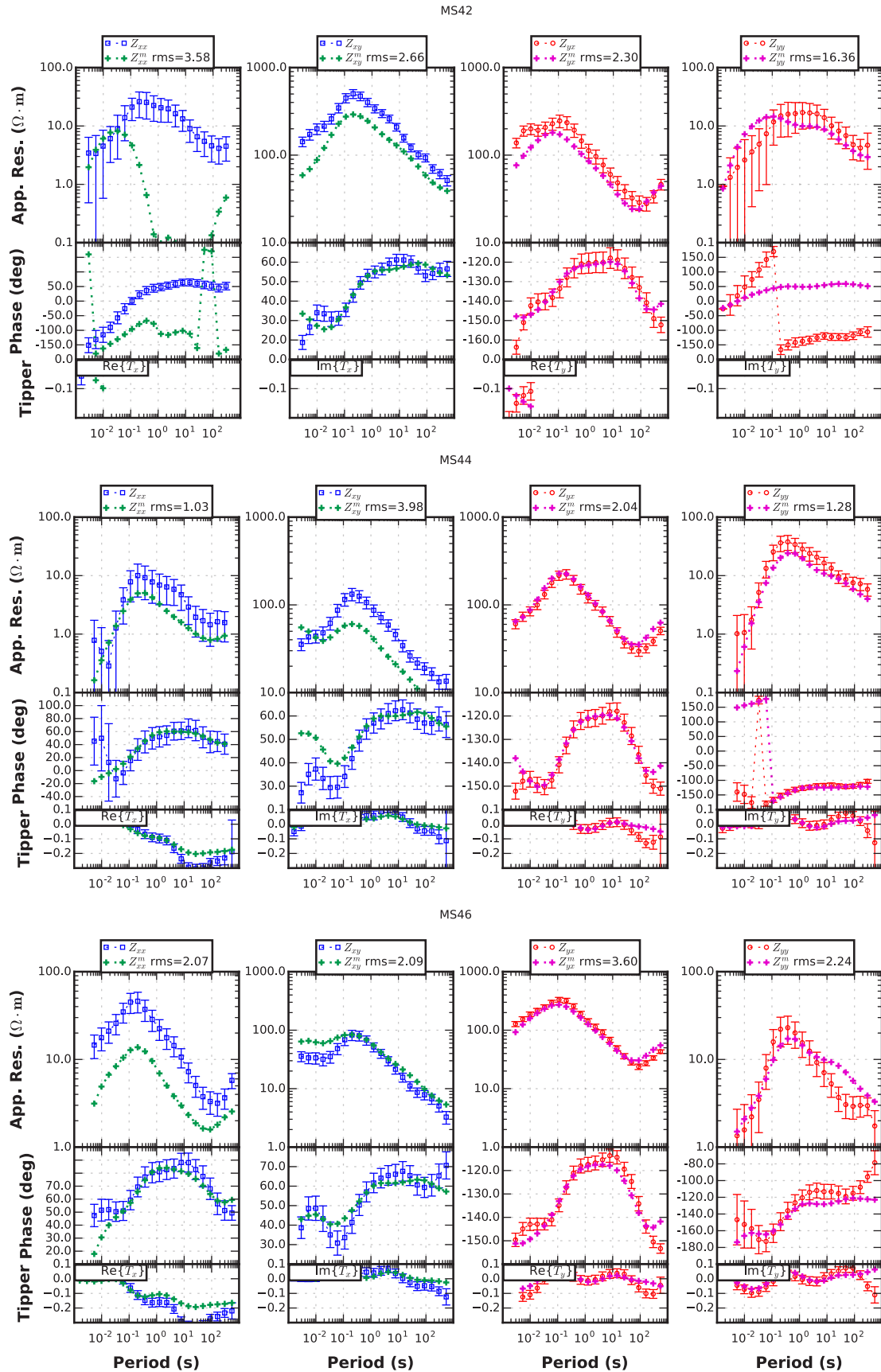
MS25

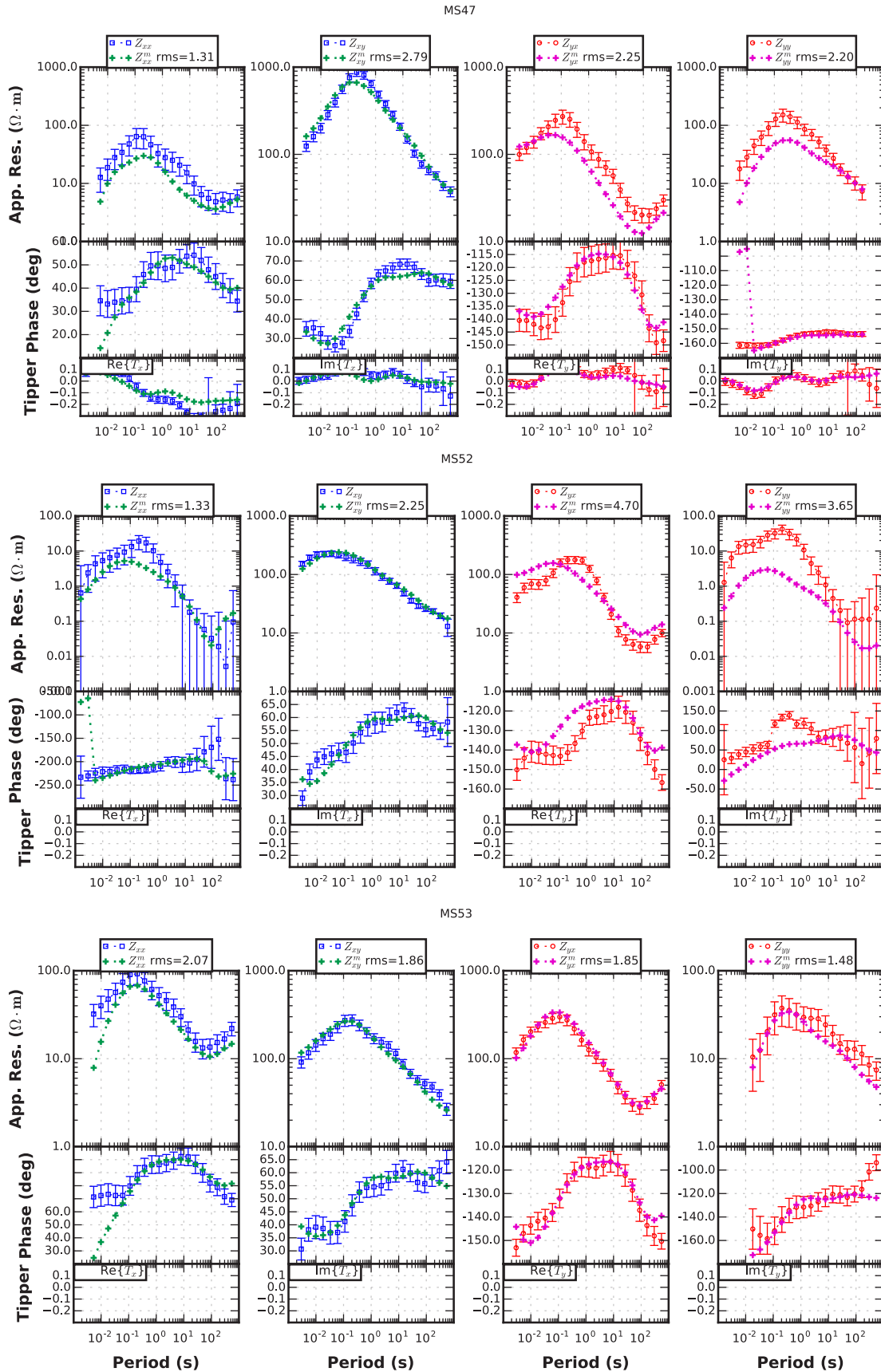


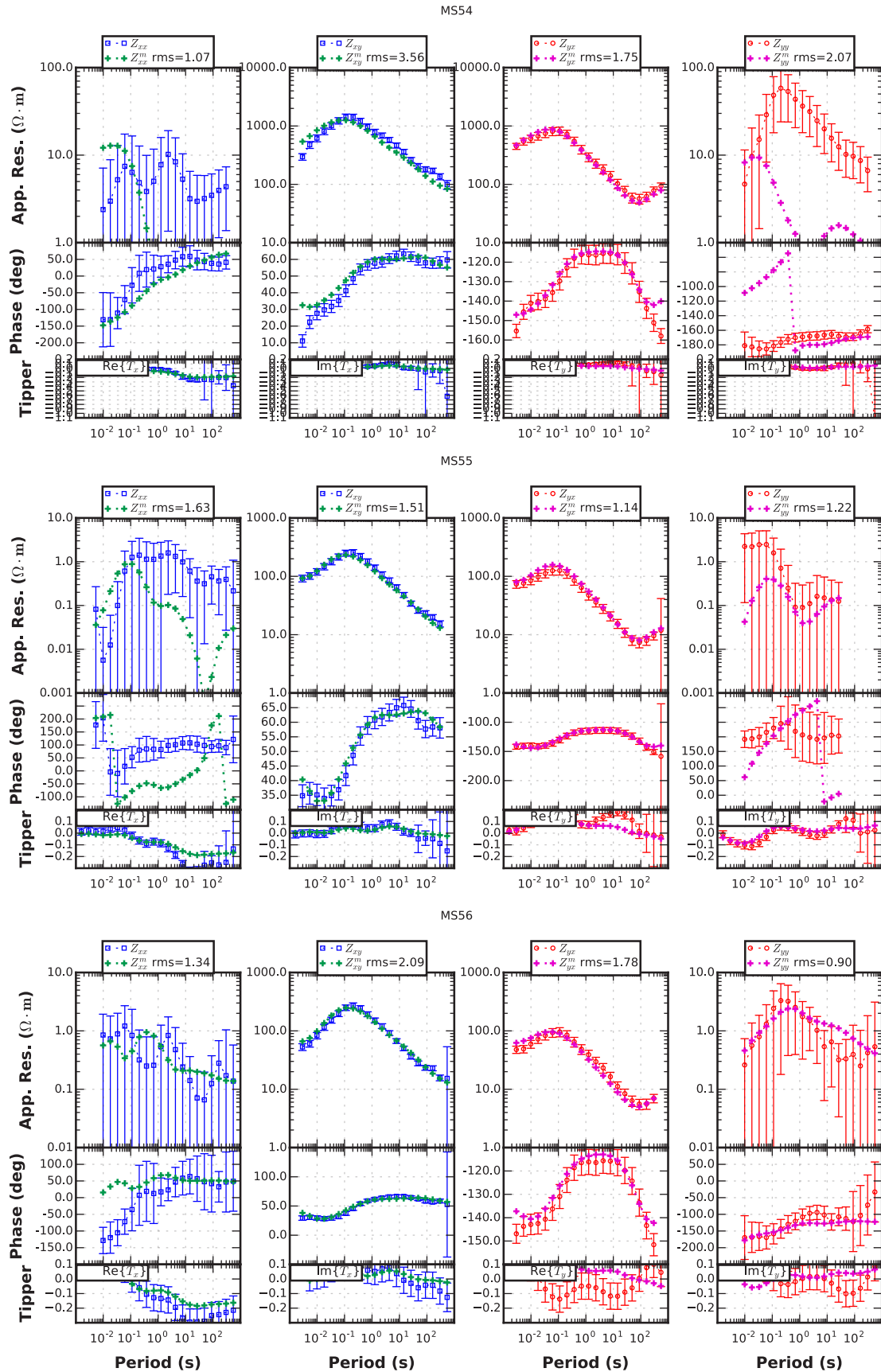
MS26

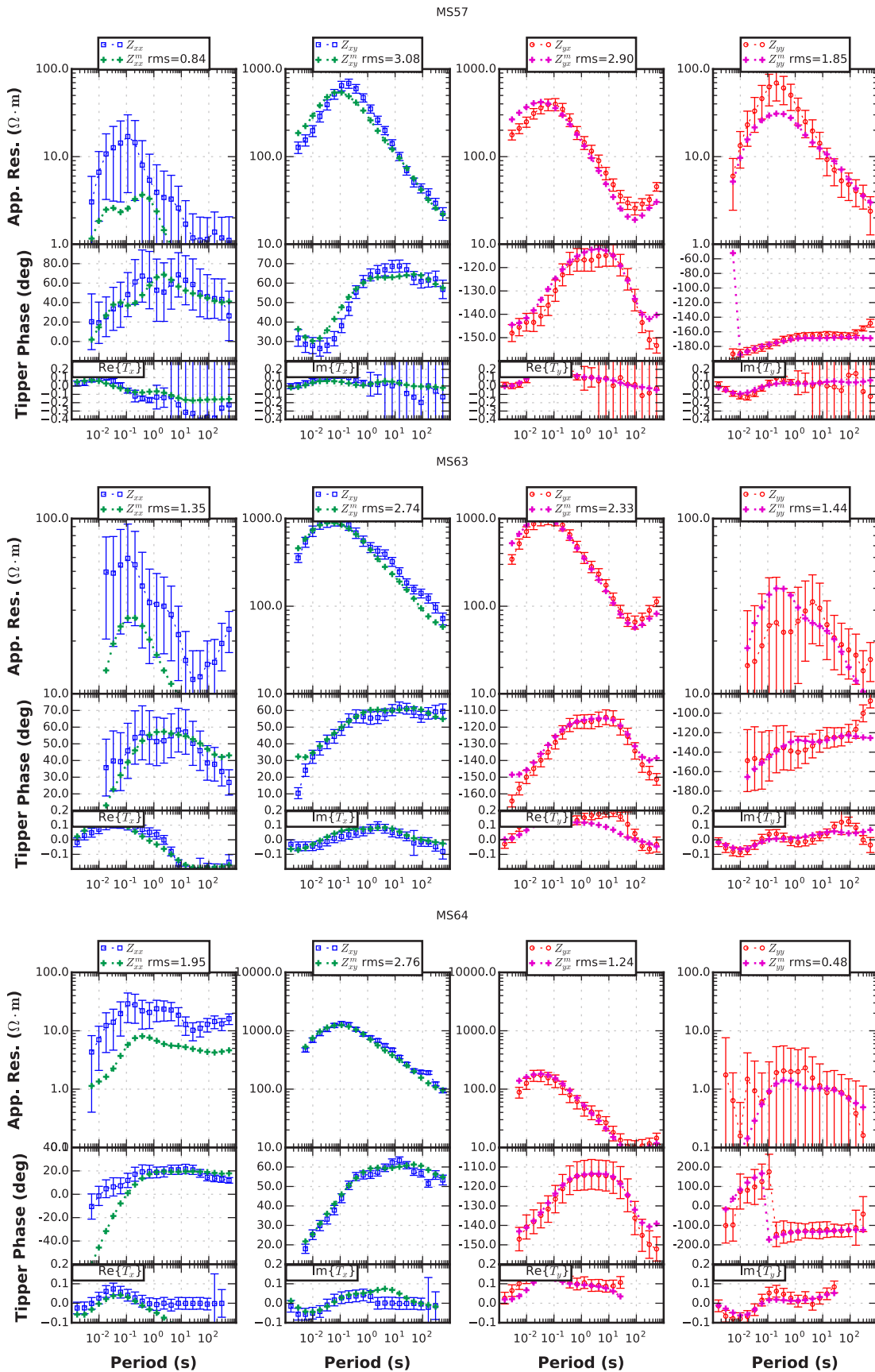




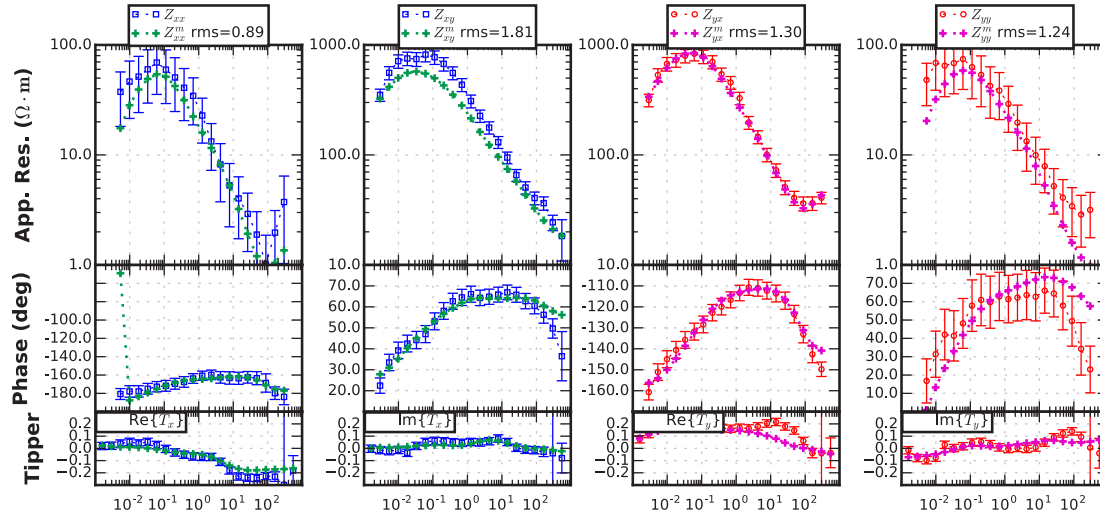




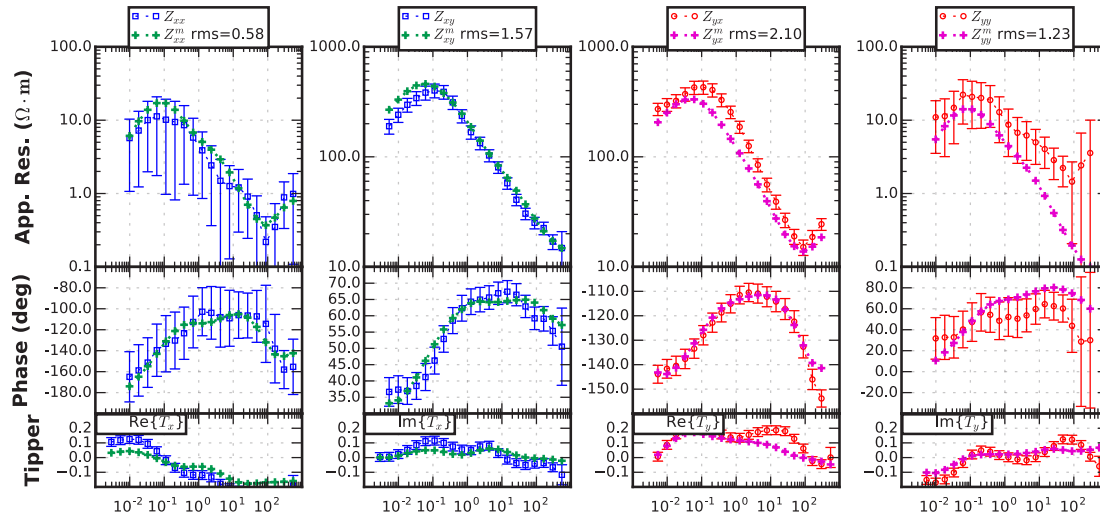




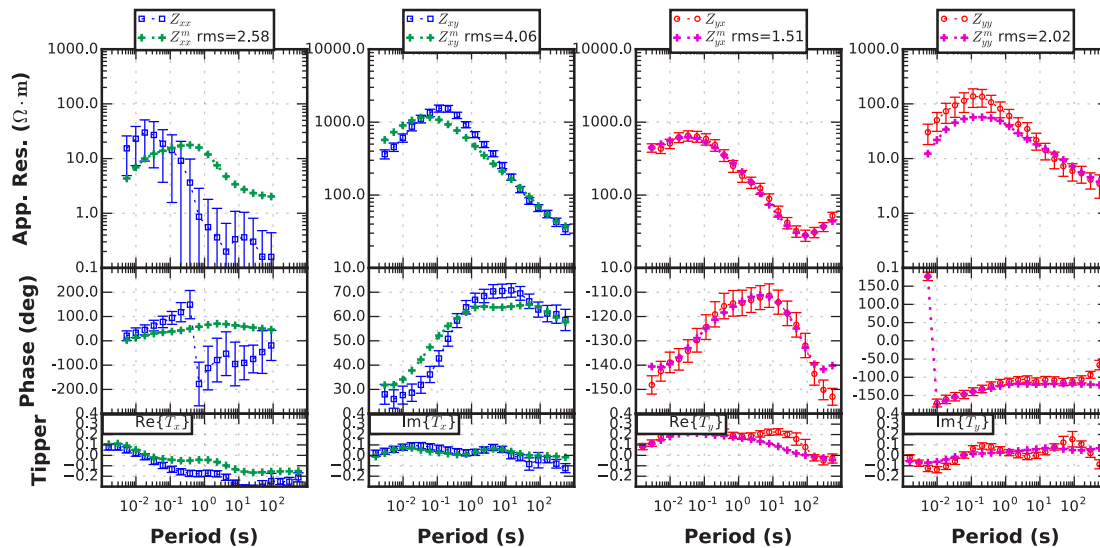
MS65

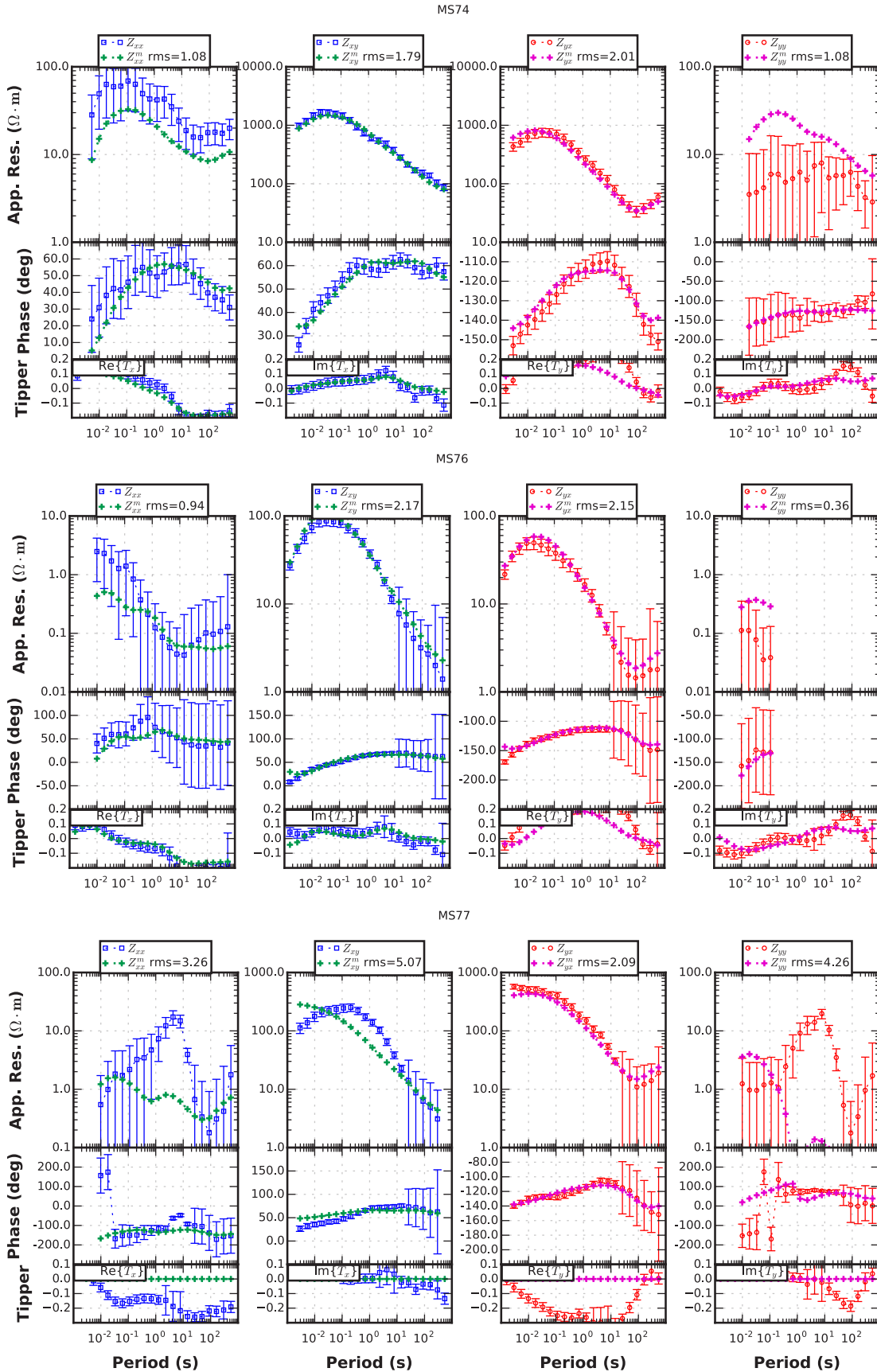


MS66

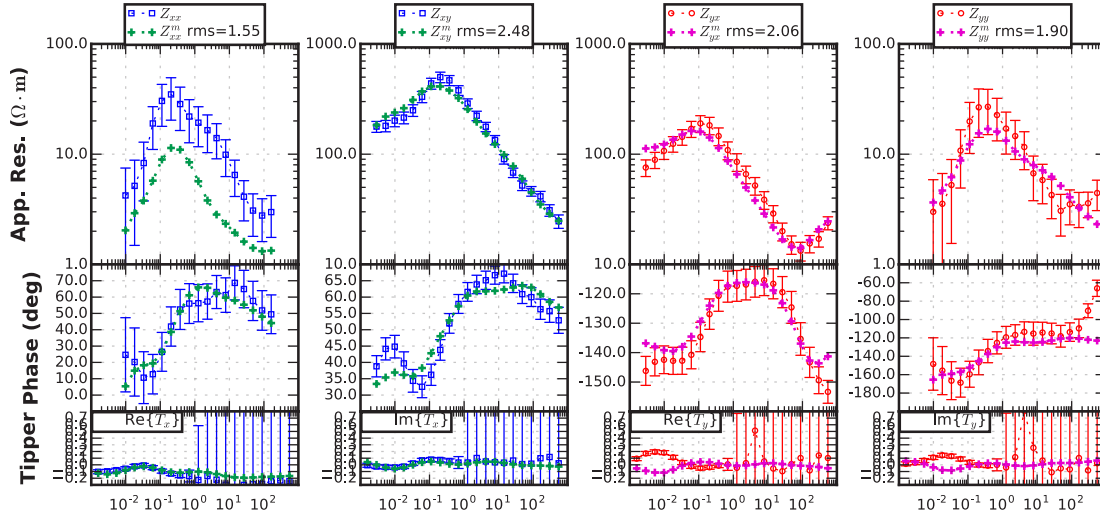


MS67

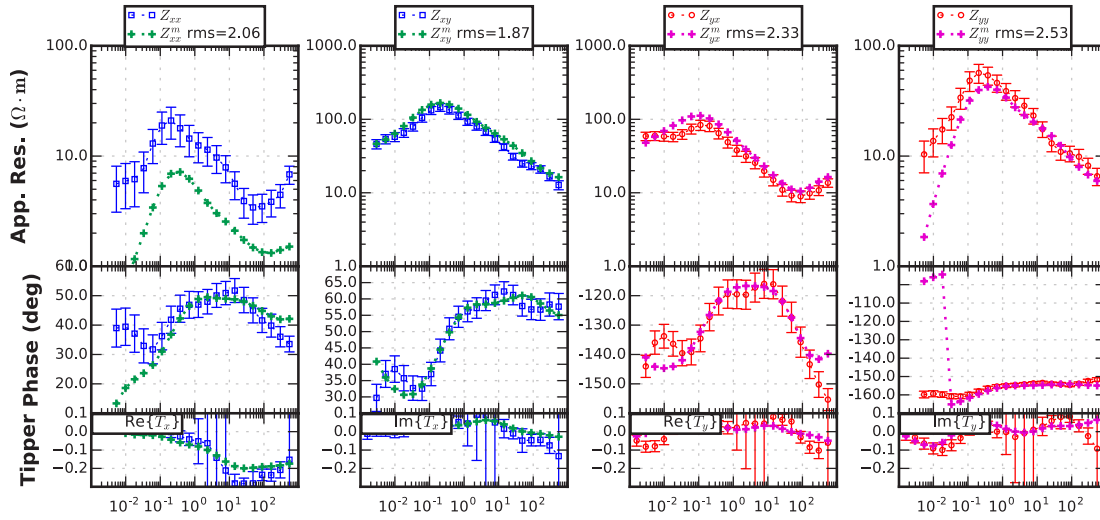




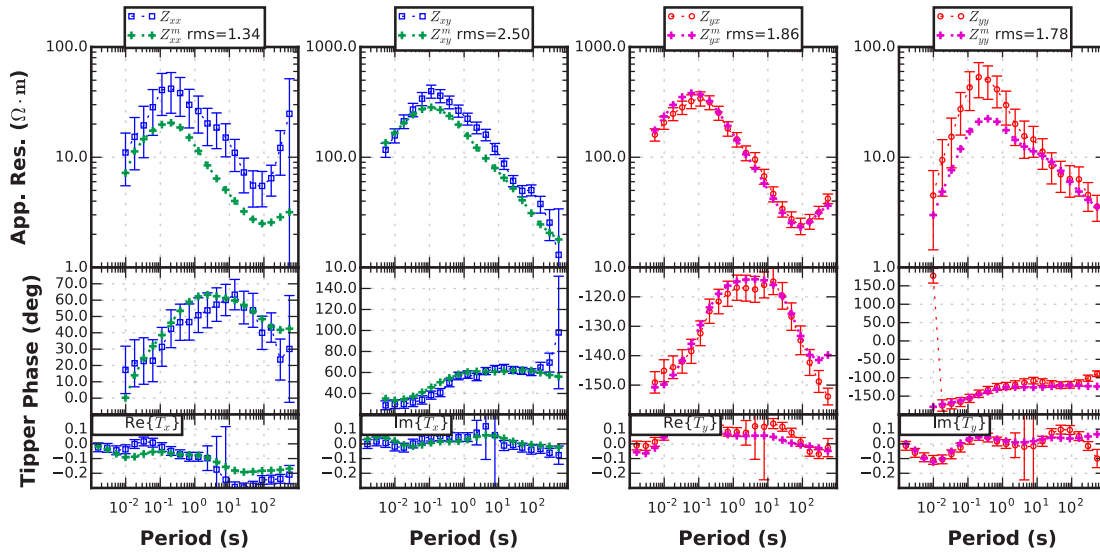
MS81

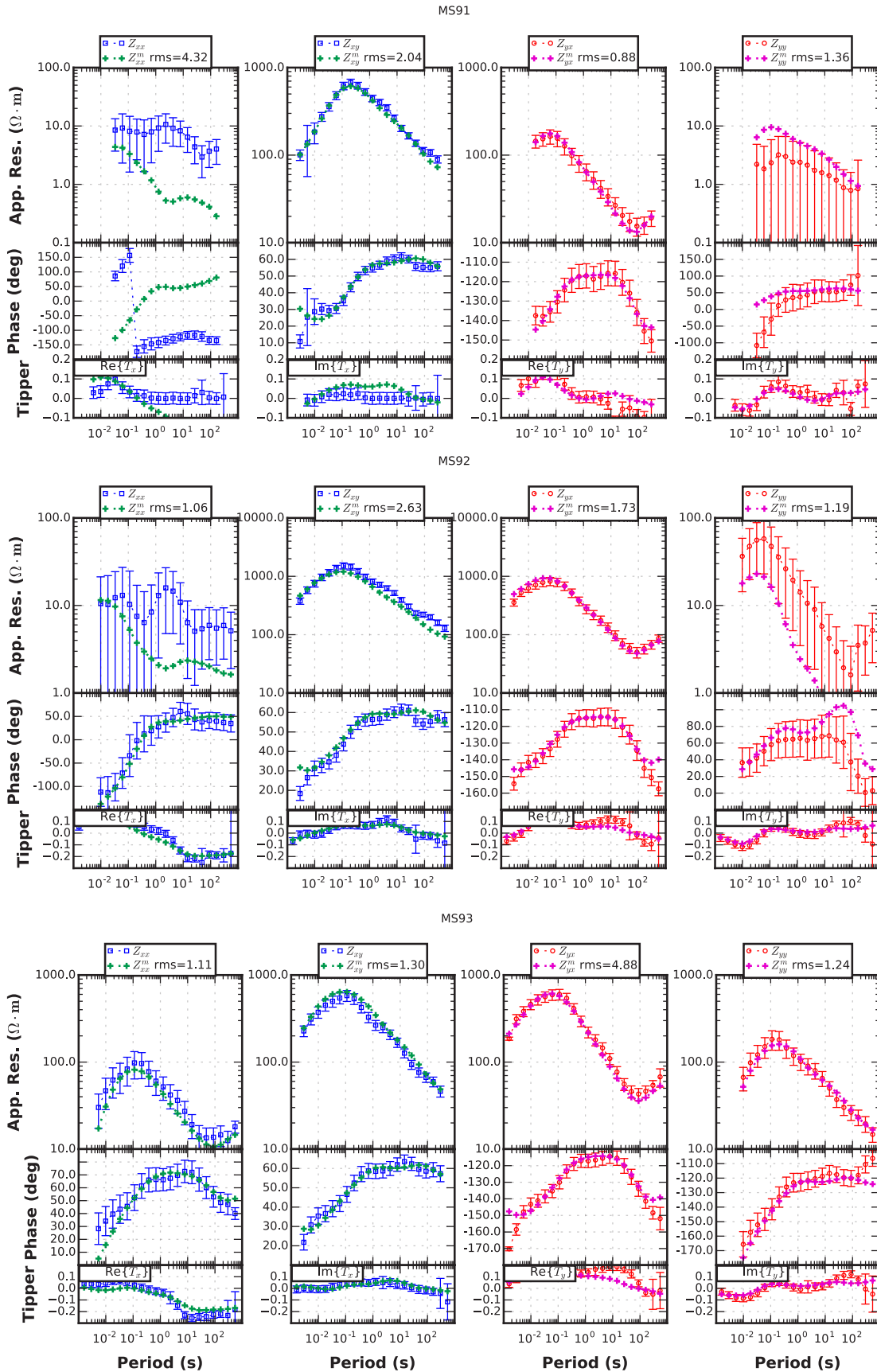


MS84

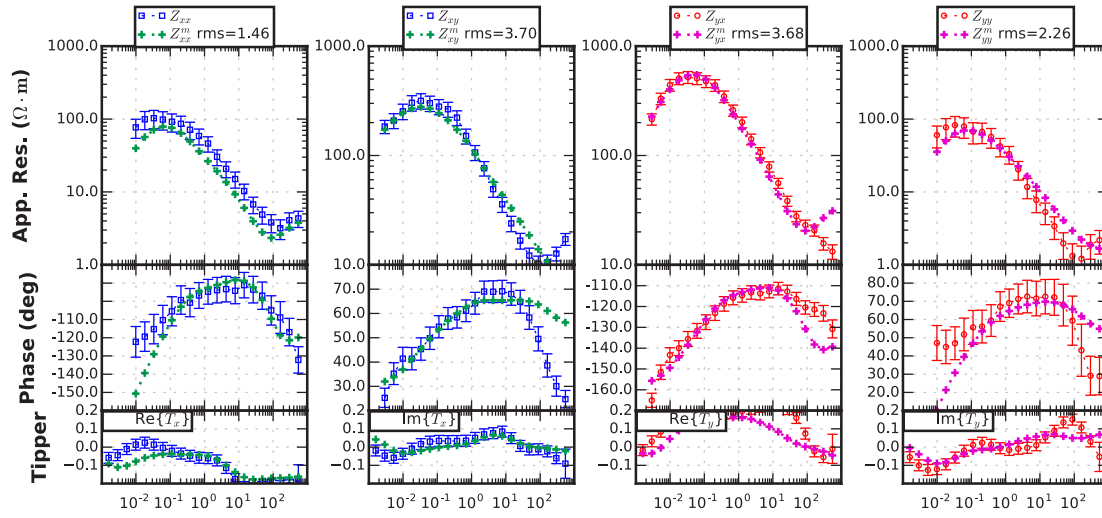


MS86

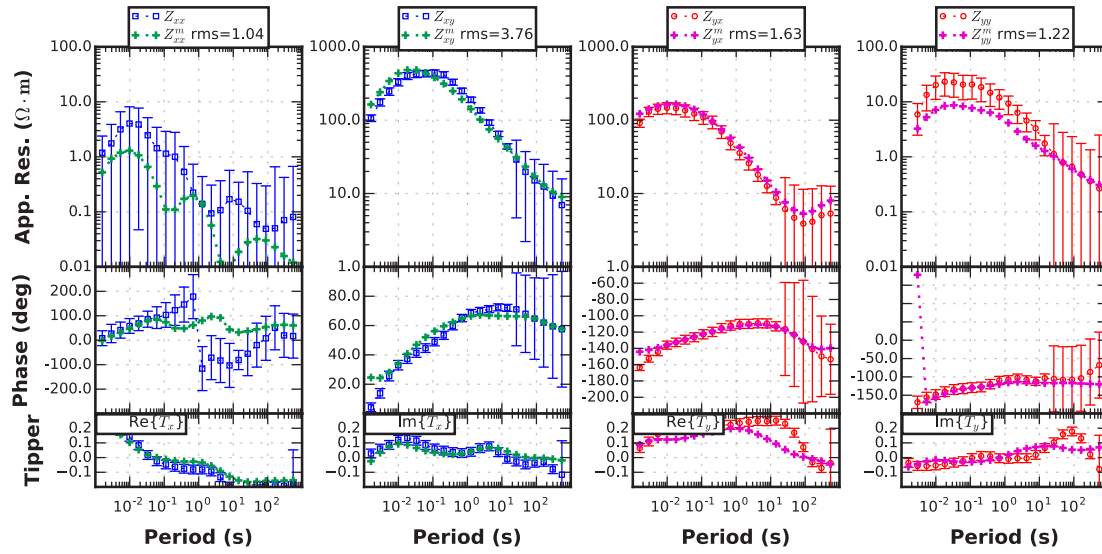




MS96



MS97



Play Fairway Analysis: South Mount St. Helens, WA, Magnetotelluric Measurements

Jared R. Peacock¹

¹U.S. Geological Survey

January 18, 2017

1 Introduction

This report describes the magnetotelluric portion of the Washington Play Fairway geothermal assessment, specifically the southern area of interest of Mount St. Helens (Figure 1).

2 Magnetotelluric Method

Magnetotellurics (MT) is a passive electromagnetic geophysical method that measures the Earth's electrical response to natural time-varying magnetic fields. MT is an inductive process where natural time-varying magnetic fields diffuse into the Earth which induce electrical currents in the subsurface. Depth of penetration of the diffusing magnetic field depends on subsurface resistivity and the frequency of the inducing magnetic field. The time-varying magnetic source is two-fold, one that operates at frequencies of less than 1 Hz and a second that operates at frequencies larger than 1 Hz. The magnetic source for frequencies less than 1 Hz is interaction of the Earth's natural magnetic field with solar wind, a collection of charged particles emitted from the sun, which can be visibly observed as auroras. The magnetic source for frequencies larger than 1 Hz is guided waves (the waveguide being the cavity between the Earth's surface and the ionosphere) from lightning strikes around the globe. Note, the vertically impinging time-varying magnetic field is elliptically polarized in the horizontal plane. Thus, the Earth's electrical response contains information about subsurface resistivity structure as a function of frequency and direction. In the frequency domain (ω) this is a simple linear transformation (1) of the inducing magnetic field (\mathbf{H}) into an electric field (\mathbf{E}) via a transfer function (\mathbf{Z}), where \mathbf{Z} is a complex rank 2 tensor that contains all the information about subsurface resistivity structure.

$$\mathbf{E}(\omega) = \mathbf{Z}(\omega)\mathbf{H}(\omega) \quad (1)$$

Similarly, the impinging magnetic field and induced horizontal electrical currents can generate a secondary magnetic field in the vertical direction. This is known as a geomagnetic depth sounding (GDS) and is again a linear transformation in the frequency domain (2), where the transfer function \mathbf{W} provides information on direction and relative strength of electrical currents. The geomagnetic depth sounding is useful for locating lateral boundaries.

$$H_z(\omega) = \mathbf{W}(\omega)\mathbf{H}(\omega) \quad (2)$$

3 Magnetotelluric Data

MT is measured in the field by using induction coils to measure the time-varying magnetic source for frequencies between 1000–0.001 Hz, and electric dipoles to measure the Earth's electrical response. Because the magnetic source field is polarized, orthogonal directions of the fields need to be measured to get a complete description of the fields. In all measurements collected for this project induction coils and electric

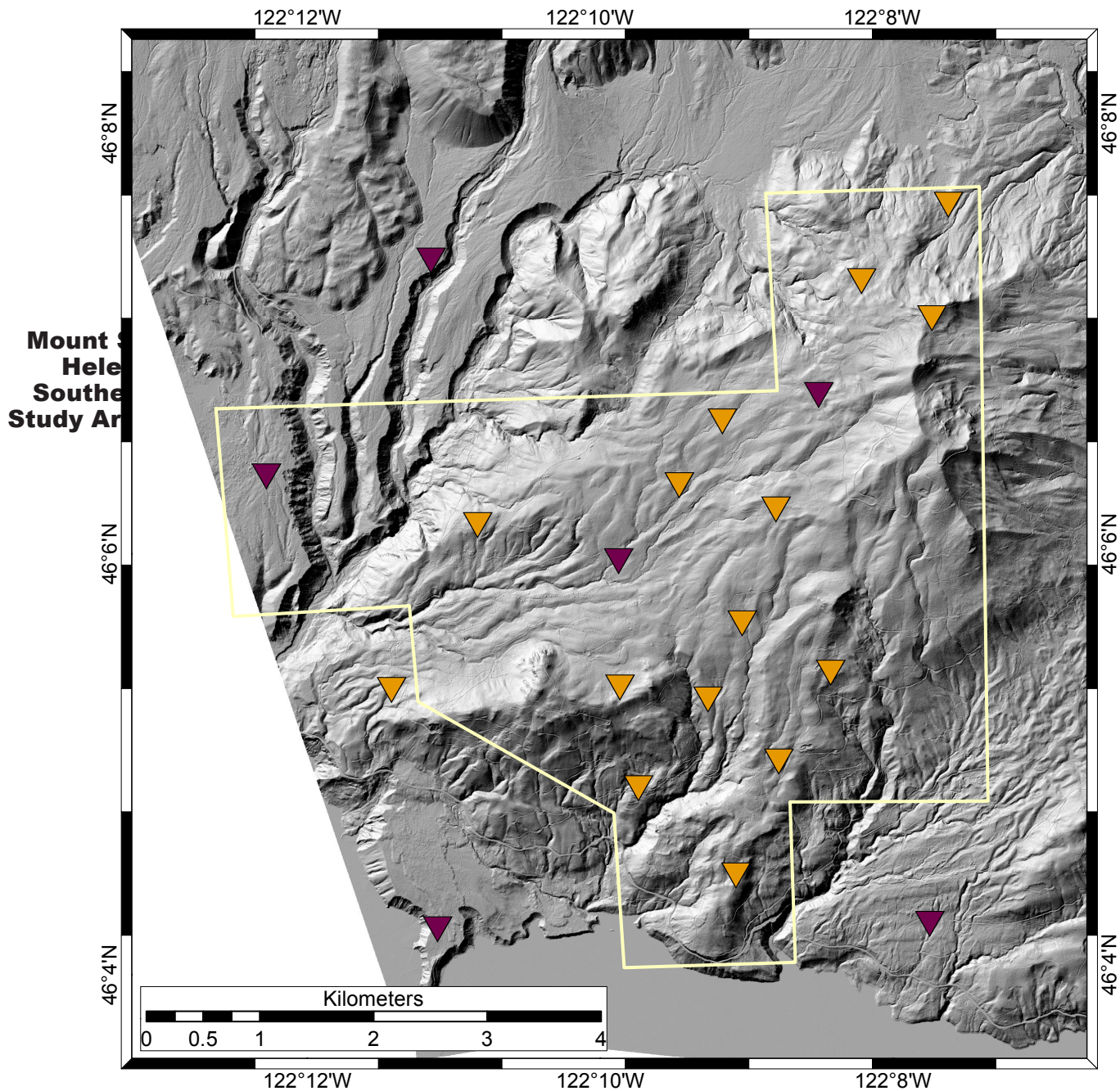


Figure 1: Area of interest south of Mount St. Helens (yellow line), location of MT stations collected for this survey (orange triangles), and existing MT stations.

dipoles were aligned with geomagnetic north and east and a vertical induction coil was either buried or tied to a tree to get the vertical magnetic field. MT data was collected at 41 stations with a ZEN 32-bit data logger developed by Zonge International, magnetic fields were measured with ANT-4 induction coils, and electric fields were measured with Ag-AgCl reference electrodes from Borin on 50-100 m dipoles. The data was collected on a repeating schedule of 5 min at 4096 samples/s, 15 min at 1024 samples/s, and 7 hours and 40 minutes at 256 samples/s over a 2024 hour period. To get time series data into the frequency domain and get estimations of Z and W , the processing code provided by Zonge International was used in conjunction with BIRRP written by [Chave & Thomson \(2004\)](#). Simultaneous measurements were used as

remote references to reduce noise and bias in the data.

4 Inverse Modeling

MT and GDS response functions were modeled in three-dimensions (3-D) using the code ModEM developed by Egbert & Kelbert (2012); Kelbert *et al.* (2014). Input data was edited using the EDI editor in MTpy (Krieger & Peacock, 2014) to remove obvious outliers in the data and suppress bias in the modeling. All data was interpolated onto 23 frequencies in the range of 6250.001 Hz. The model mesh (north, east, depth) was 72 x 70 x 40 with dimensions of 103000 x 102600 x 169360 m, where spacing within the station area was 200 m increasing by 1.4 away from the station area. The first layer was set to 10 m and increases logarithmically downwards. Inversions were run on NASAs high-end computing capability (HECC) Pleiades super computer, where average run times were on the order of 18 hours.

To get to a preferred model the following scheme was used. Invert all components of the data with an error floor of $0.12\sqrt{Z_{xy} \cdot Z_{yx}}$ and an error floor of 0.10 for the GDS components and run ModEM with a covariance of 0.40 in all directions using different starting models of a 1000, 100, and 10 Ohm-m half space. Reduce error floors to $0.05\sqrt{Z_{xy} \cdot Z_{yx}}$ and an error floor of 0.03 and run ModEM with a covariance of 0.30 in all directions using the final iteration from the previous run as the starting model. Invert just the GDS components with an error floor of 0.03 with a covariance of 0.40 using starting models of a 1000, 100, and 10 Ohm-m half space. Compute the geometric average of all models to enhance common features and suppress uncommon features. Run ModEM with error floors of $0.10\sqrt{Z_{xy} \cdot Z_{yx}}$ and an error floor of 0.05 and a covariance of 0.40 using the average model as the starting model. Then reduce error floors to $0.05\sqrt{Z_{xy} \cdot Z_{yx}}$ and an error floor of 0.03 for GDS components and run ModEM with a covariance of 0.30 in all directions using the final iteration from the previous run as the starting model. Features in the preferred model were tested for sensitivity to location, geometry, and resistivity value.

5 Resistivity Model Features

For the purpose of this report only those features in the top 10 km will be described (Figure 2). Two main features are observed in the 3-D resistivity model.

C1 is a conductive zone ($< 30 \Omega\text{m}$) elongated in the north-south direction and is located in the northeast corner of the survey area. C1 begins near the surface and extends down to 3 km, where there is a possible connection to deeper conductive body to the east.

R1 is a resistive ($>200 \Omega\text{m}$) structure in the middle of the survey area that strikes north-northwest and is the western boundary of the seismic zone. R1 extends from near the surface down past 10 km.

6 Preliminary Interpretation

R1 is a resistive anomaly ($> 150 \Omega\text{m}$) that appears to have deep root with some connections to the surface. Being in a volcanic region, it is reasonable to assume R1 is a pluton. The eastern boundary of R1 strikes north-northwest in line with the Mount St. Helens shear zone (SHZ), and has a slight dip to the west. Seismicity data from the North Pacific Seismic Network in this area is diffuse, which could be an effect of a limited velocity model or from the geology. Unlike the survey area north of Mount St. Helens the fault plane is not well characterized by seismicity, nor by the resistivity model. Moreover, no distinct conductive feature is associated with the SHZ except in the northern part of the survey.

C1 is located on the north east side of the SHZ and is 2 km above most of the seismicity. A connection to a deeper conductor is present to the east. This connection could be a current pathway for fluids to flow from deep. If the deep extension is a fluid pathway then C1 in the shallow surface could be a collection of those fluids. Similarly, if the fluids come from deep, they will have enhanced heat and could cause hydrothermal alteration where the most conductive part is the top as seen in Appendix A. However, there is no manifestation of hot springs in the area. Need to check on evidence for hydrothermal alteration. Another possibility is a collection of meteoric fluids in a fractured media. Not sure on the nature of the media,

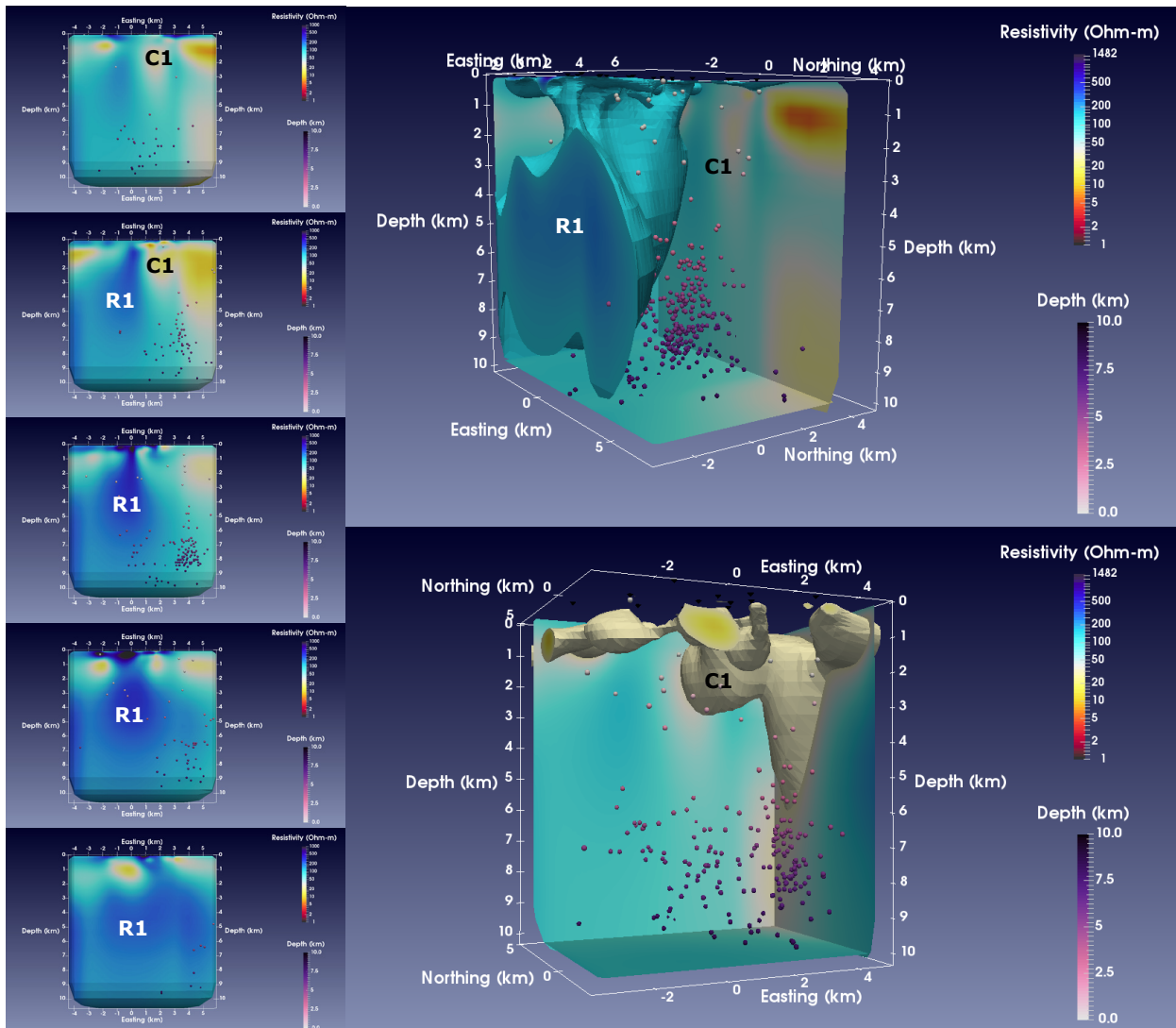


Figure 2: Different views of the resistivity model and main anomaly C1. Left: looking north through the resistivity model, where the top panel is the furthest north profile and each panel is a 1.5 km step south. . Resistivity anomalies are labeled as discussed in the text. Top Right: looking northwest at R1. Bottom Right: looking north-northeast at C1.

probably sediments similar to up north. Also, C1 appears to be aseismic, which could suggest elevated temperatures.

The zone between R1 and C1 is where most of the seismicity occurs, suggesting a weaker rock to the east of R1. This could be the same lithology as in the north, a densely fractured marine sedimentary unit. This unit is wider at this survey location than up north, which is supported by the diffuse seismicity and the resistivity model. The fact that the conductivity to the east of the SHZ is lower suggests a smaller density of fractures within the sedimentary unit, unless the fractures are filled with freshwater which would be unlikely in a marine sedimentary unit.

6.1 Outstanding Questions

Any proof of hydrothermal activity in the northeastern part of the survey area?

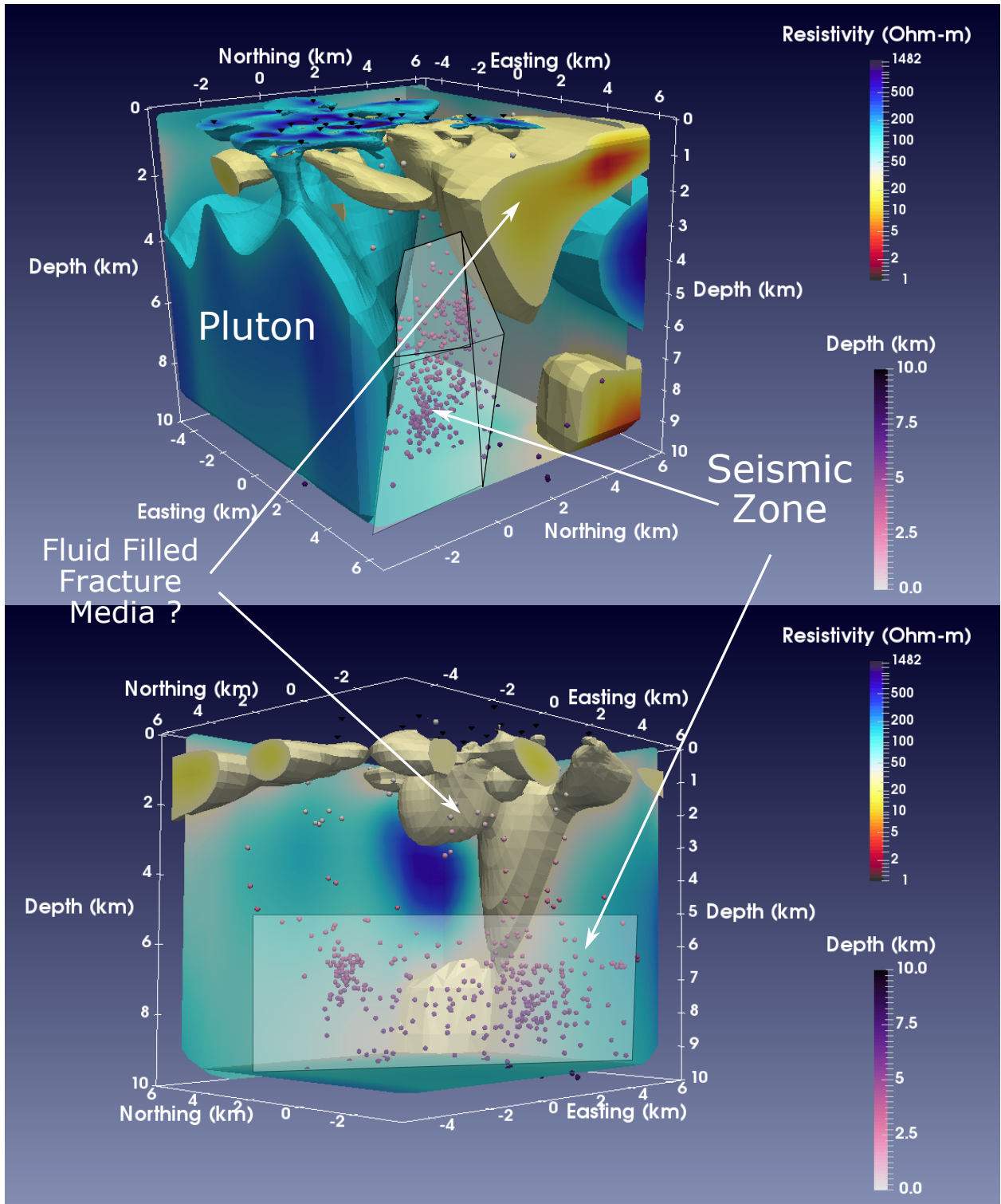


Figure 3: Views of 3-D resistivity model with preliminary interpretations.

6.2 Estimate of Physical Properties

TODO: estimate porosity, temperature, salinity from resistivity. Find any chemical analysis of Soda Springs

6.3 Preliminary Geologic Interpretation

On the southwestern side of the survey area is a pluton that extends from ~2 km down past 10 km with a few connections to the surface near the center of the survey area. The western boundary of the pluton strikes north-northwest with a slight dip to the west. West of the pluton is a seismic zone where most of the activity is below 5 km. The lithology of the seismic zone is likely to be the same sedimentary unit as in the north survey, but is wider and likely less fractured. In the northeast of the survey area could be a collection of fluids, either meteoric or crustal in origin.

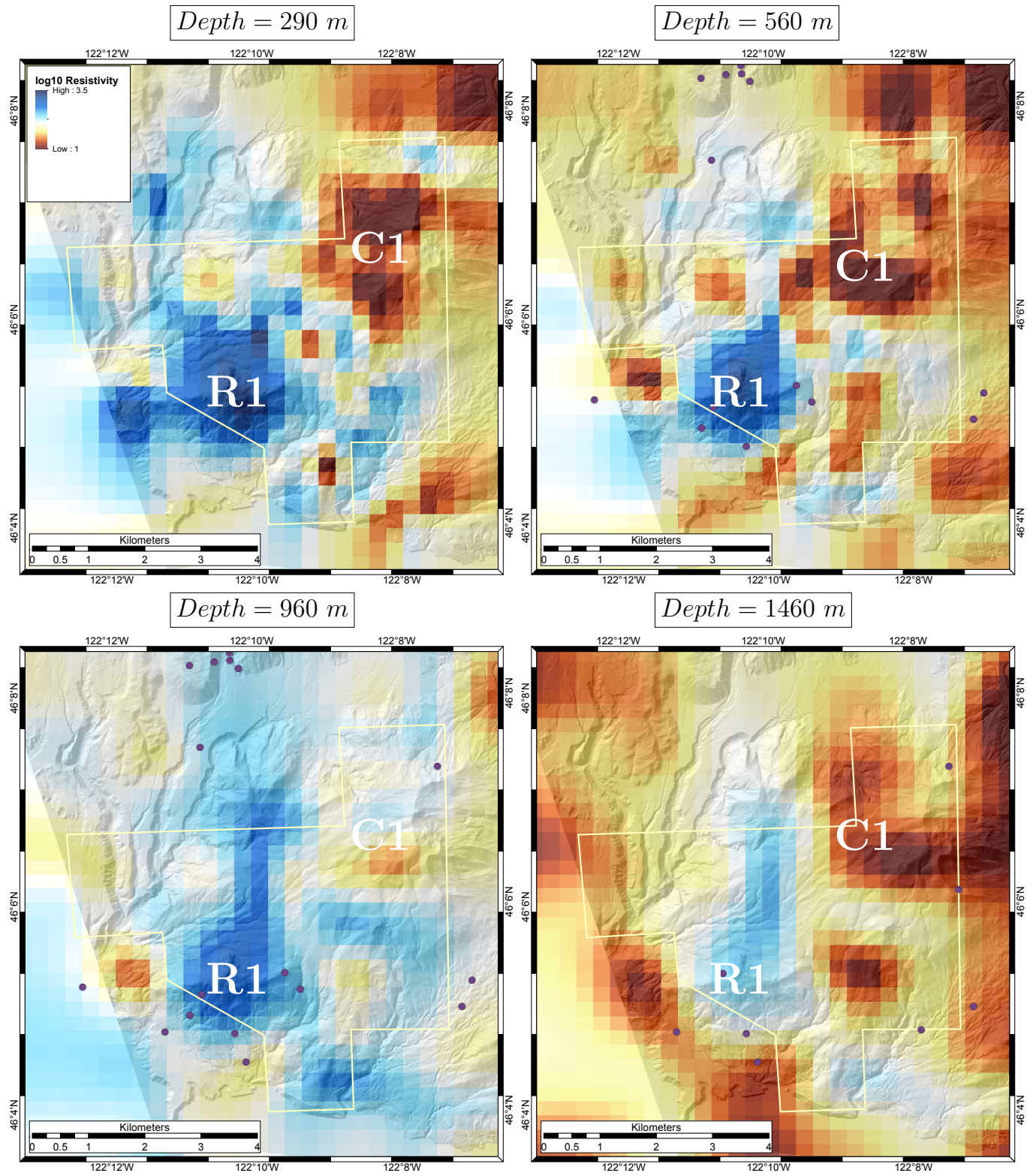
7 Geothermal Potential

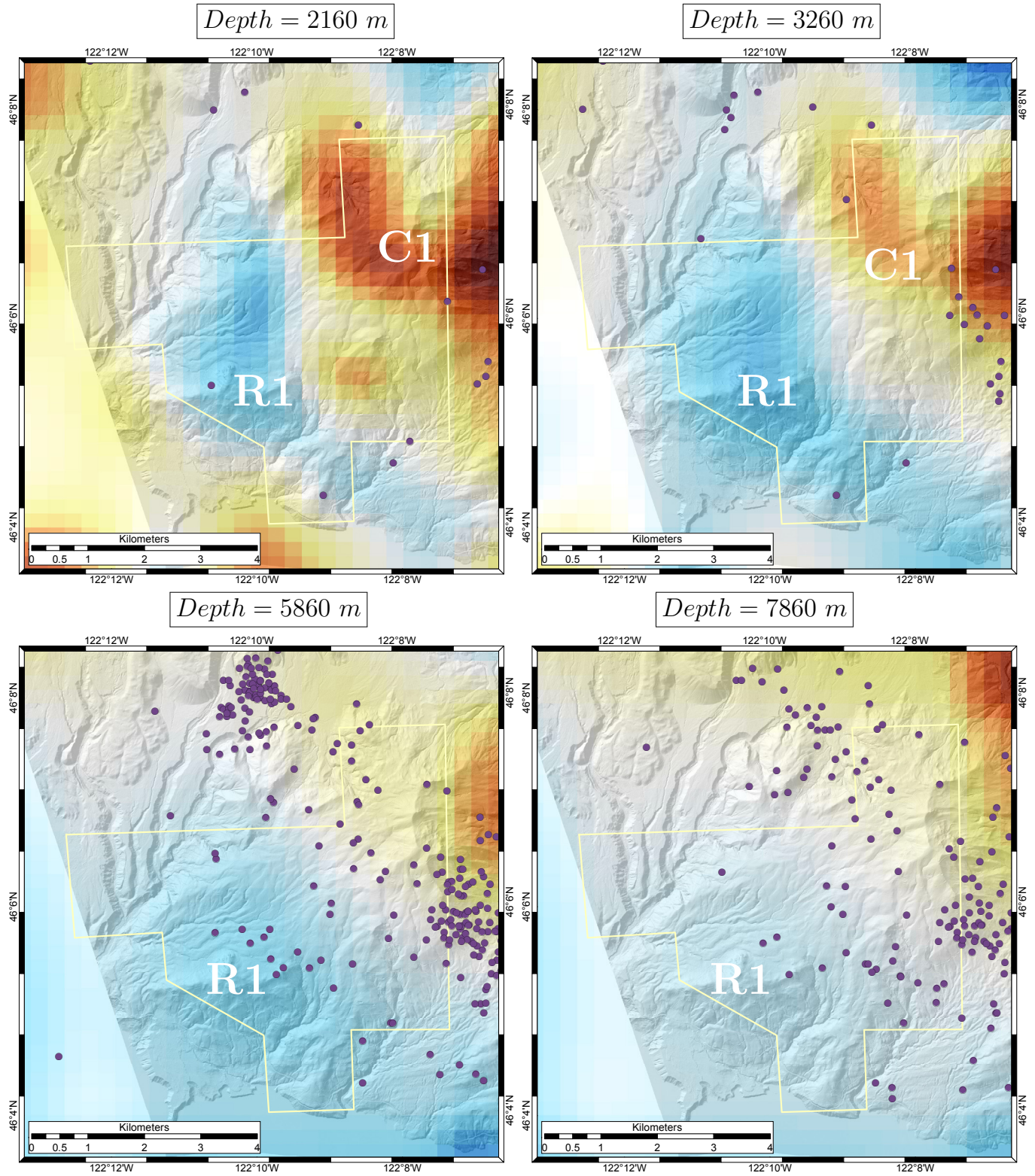
From the resistivity model, the optimal location for geothermal potential from the resistivity model appears to be in the northeastern part of the survey area where a potential collection of fluids could exist from near the surface to 3 km depth.

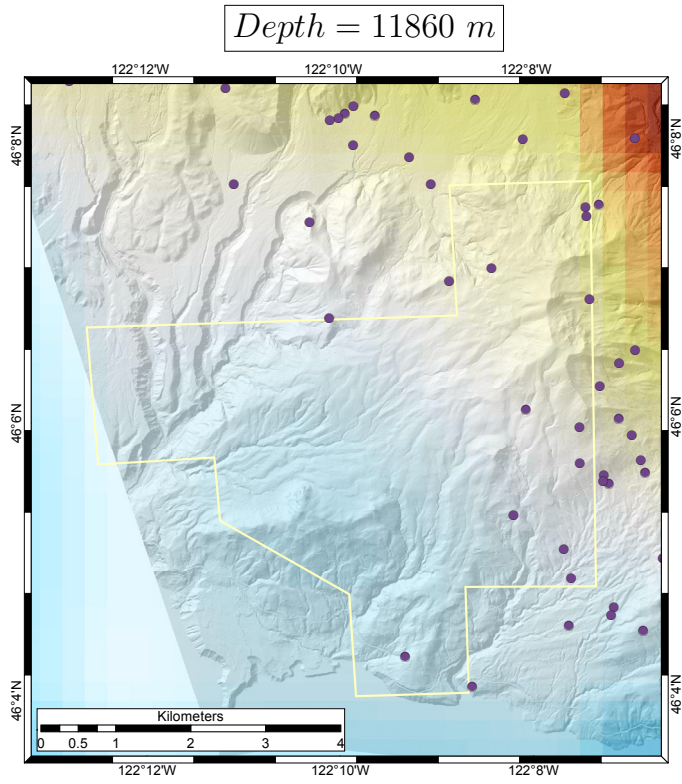
References

- Chave, A. D., & Thomson, D. J. 2004. Bounded influence magnetotelluric response function estimation. *Geophys. J. Int.*, **157**, 988–1006.
- De Siena, L., Thomas, C., Waite, G. P., Moran, S. C., & Klemme, S. 2014. Attenuation and scattering tomography of the deep plumbing system of Mount St. Helens. *Journal of Geophysical Research: Solid Earth*, **119**, 8223–8238.
- Egbert, G. D., & Kelbert, A. 2012. Computational recipes for electromagnetic inverse problems. *Geophys. J. Int.*, **189**, 251–267.
- Kelbert, A., Meqbel, N. M., Egbert, G. D., & Tandon, K. 2014. ModEM: a modular system for inversion of electromagnetic geophysical data. *Computer Geoscience*, **66**, 40–53.
- Krieger, L., & Peacock, J. R. 2014. MTpy: a Python toolbox for magnetotellurics. *Computers & Geoscience*, **72**, 167–175.
- Lees, J. M., & Crosson, R. S. 1989. Tomographic inversion for three-dimensional velocity structure at Mount St. Helens using earthquake data. *Journal of Geophysical Research*, **94**(B5), 5716–5728.
- Moran, S. C., Lees, J. M., & Malone, S. D. 1999. P wave crustal velocity structure in the greater Mount Rainier area from local earthquake tomography. *Journal of Geophysical Research*, **104**(B5), 10,755–10,786.
- Waite, G. P., & Moran, S. C. 2009. V_p structure of Mount St. Helens, Washington, USA, imaged with local earthquake tomography. *Journal of Volcanology and Geothermal Research*, **182**, 113–122.
- Weaver, C. S., Grant, W. C., & Shemeta, J. E. 1987. Local Crustal extension at Mount St. Helens, Washington. *Journal of Geophysical Research*, **92**(B10), 10,170–10,178.

A Depth Slices

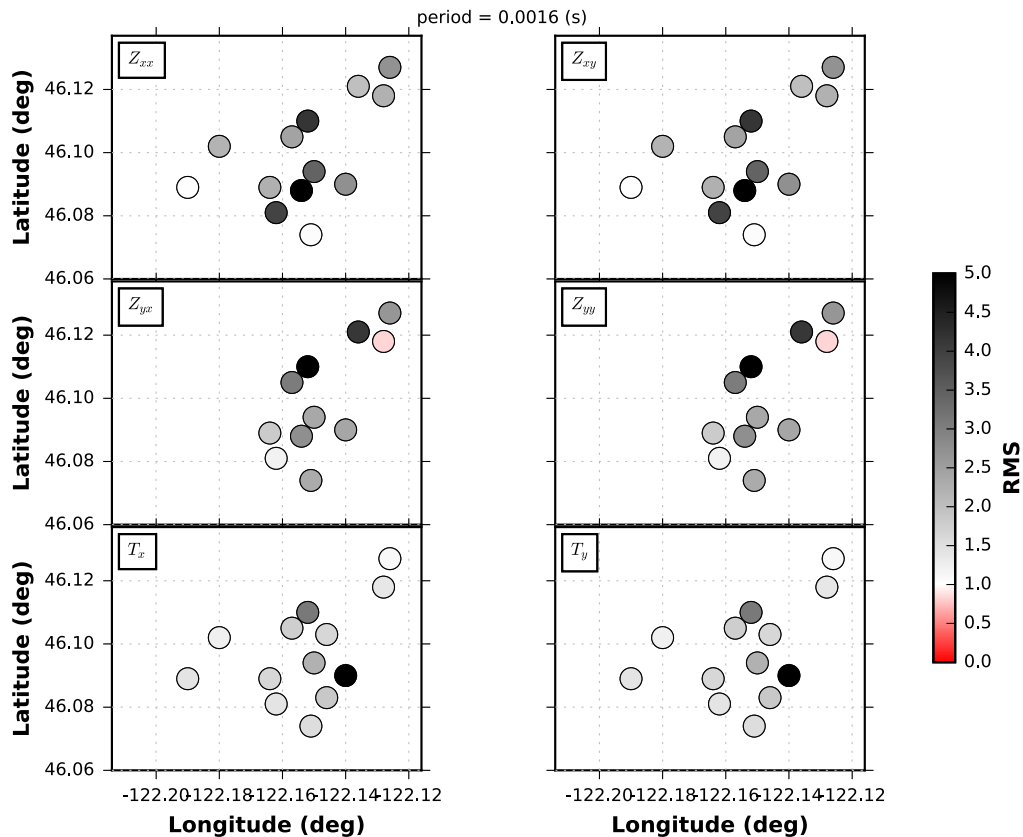


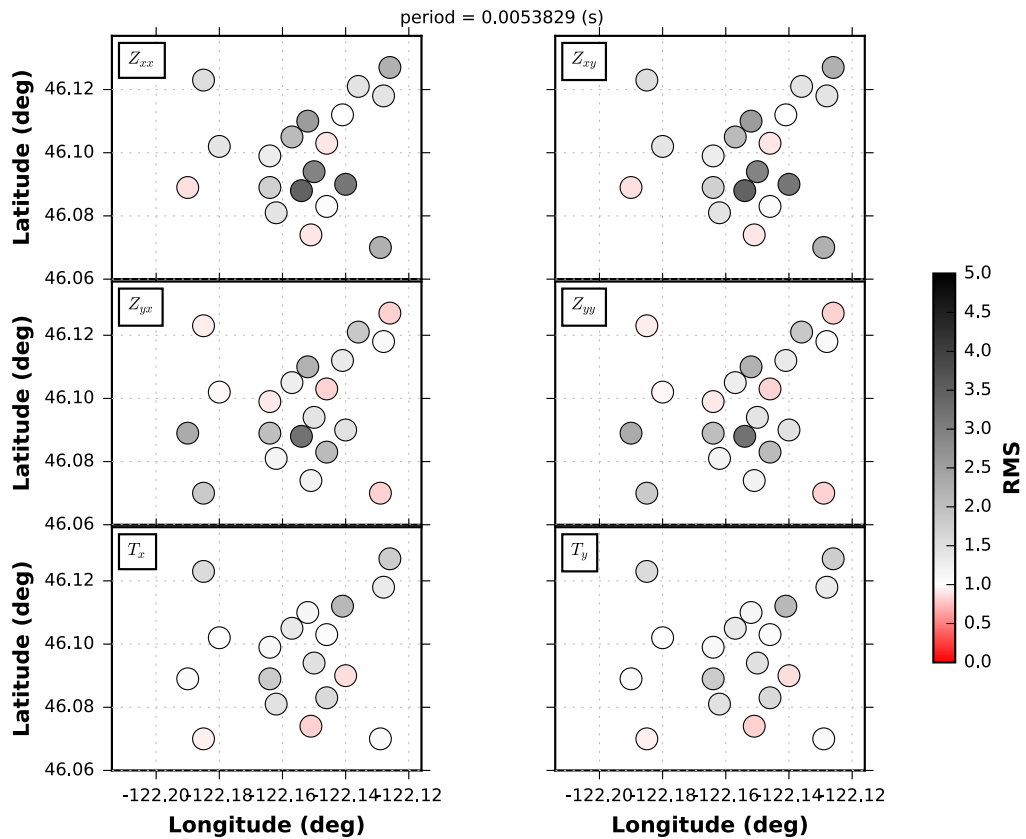
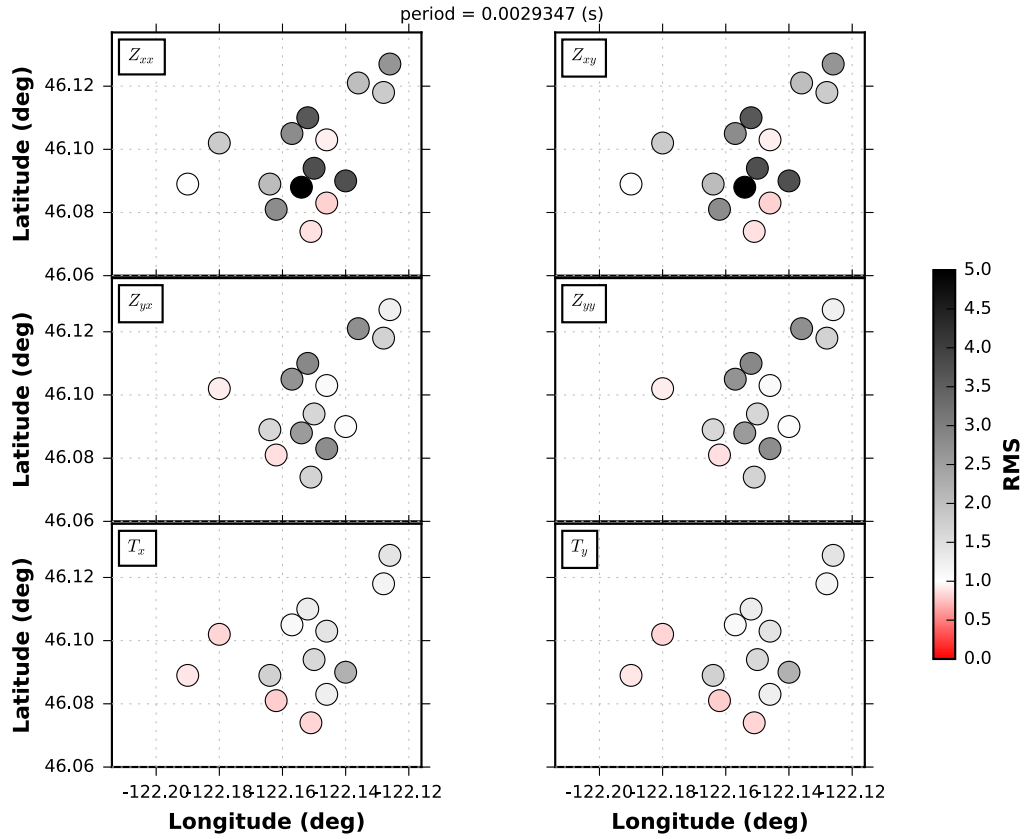


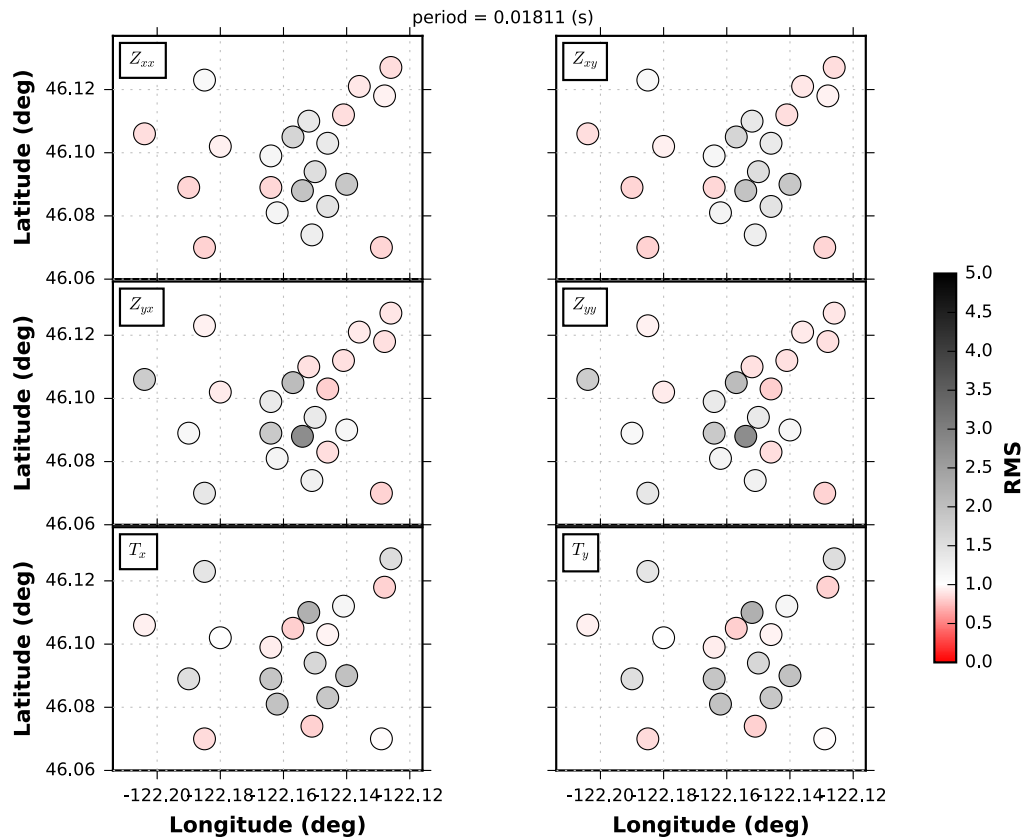
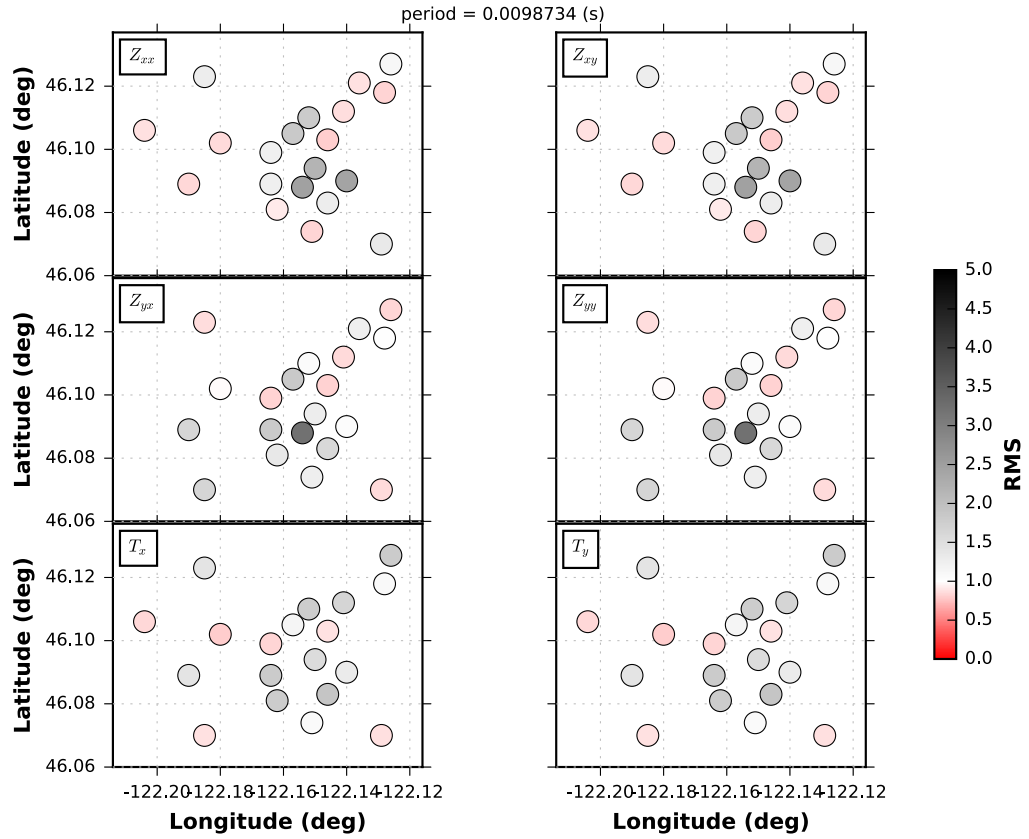


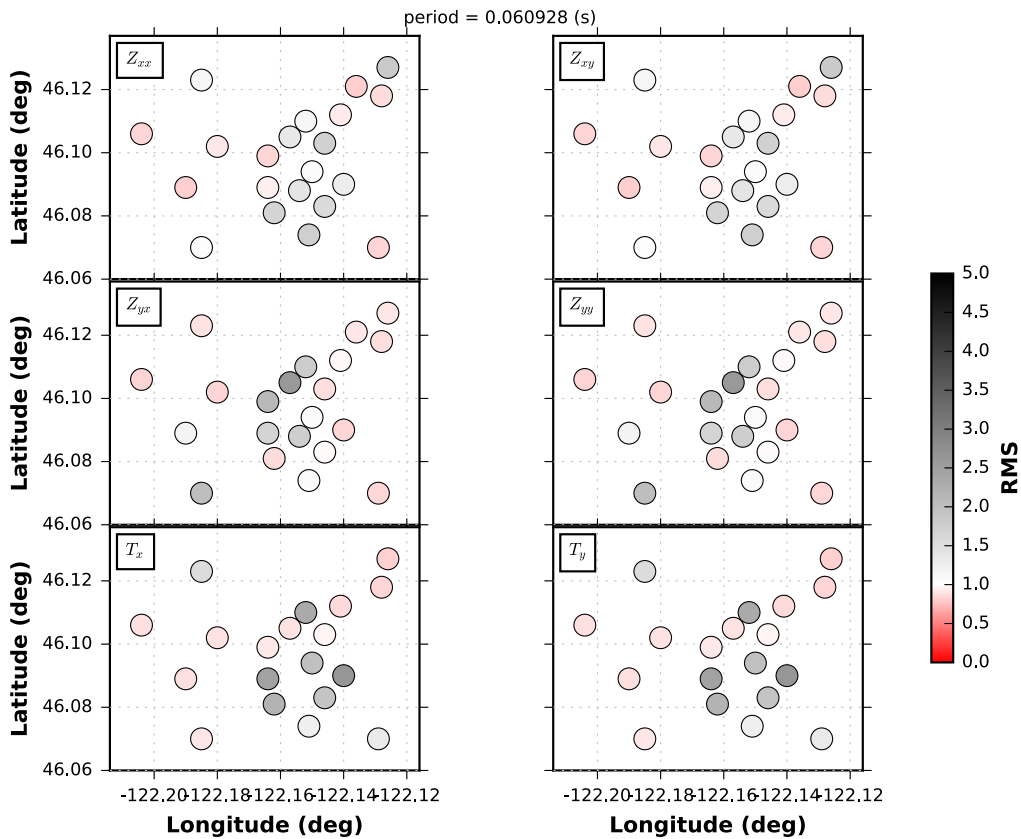
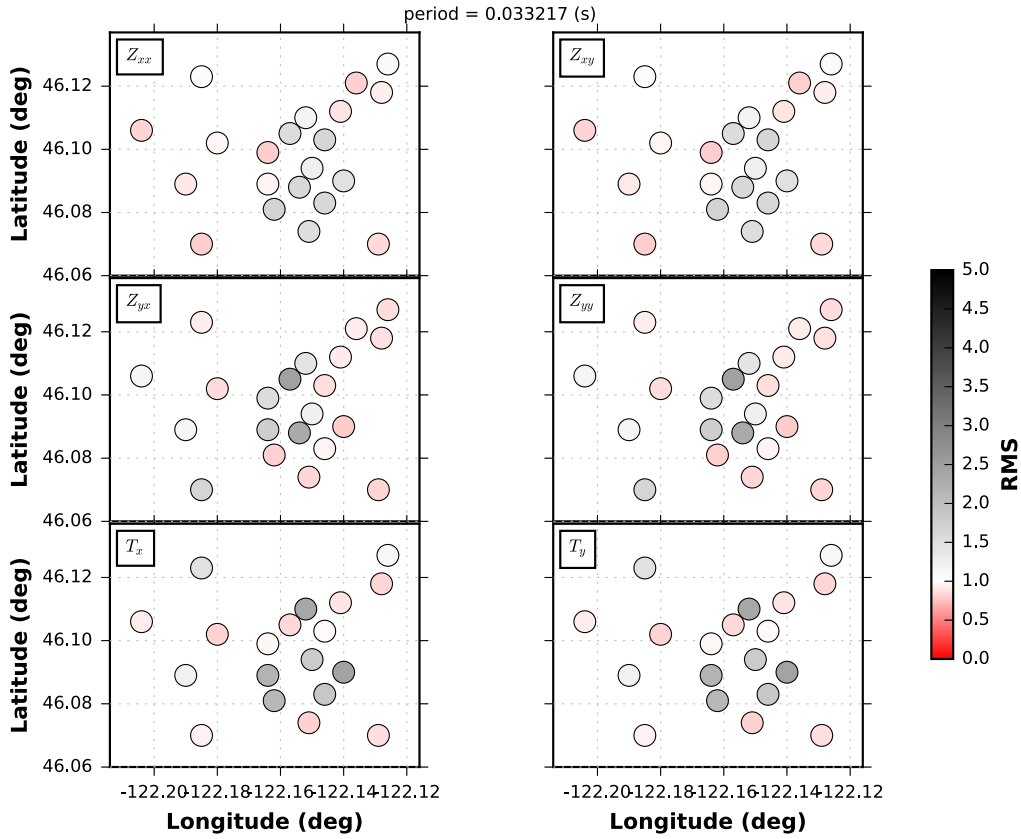
B Model RMS Maps

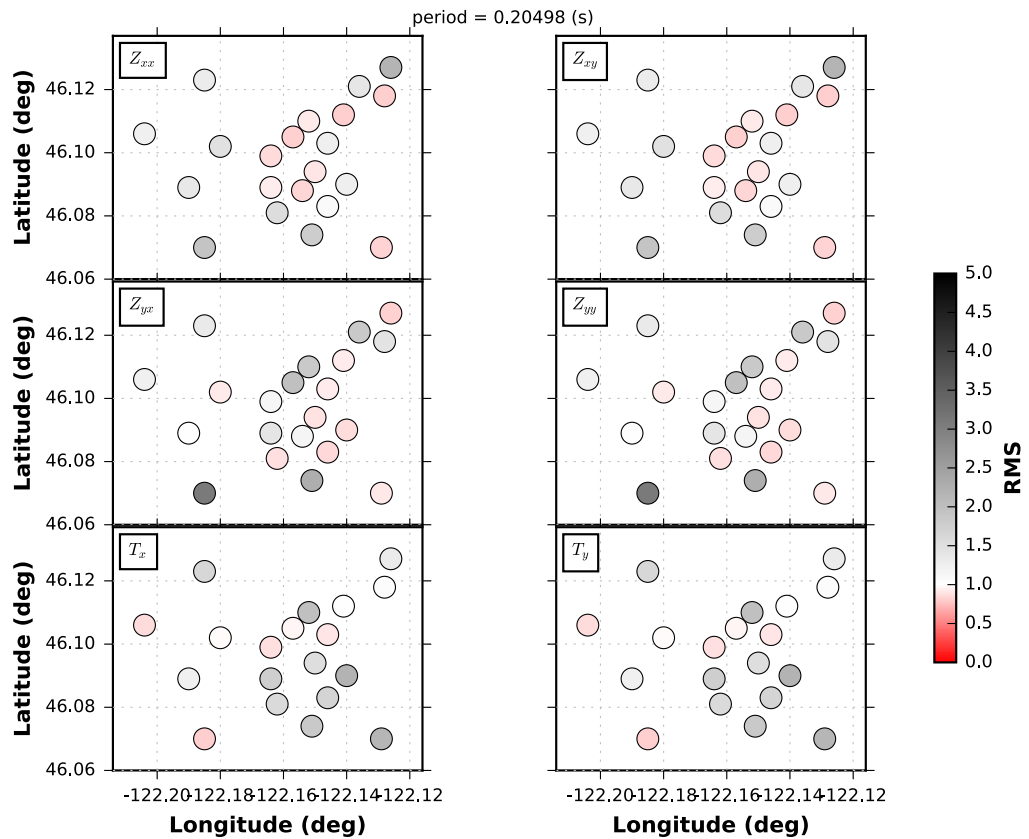
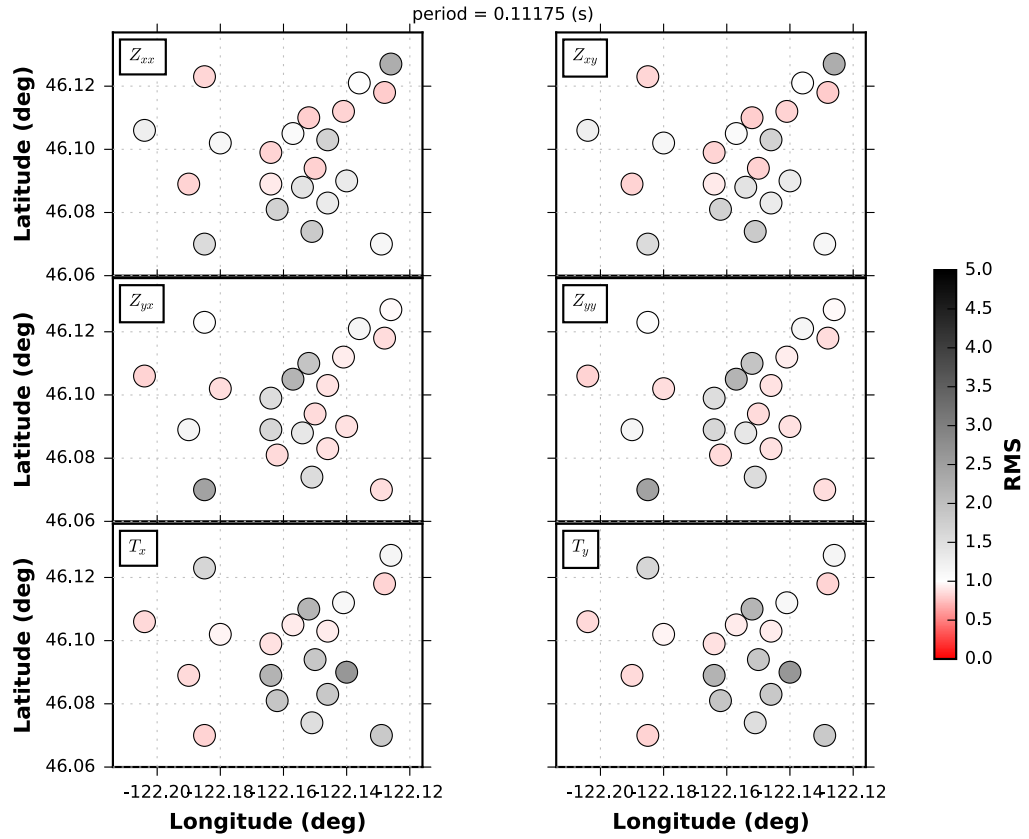
The maps in this section show the normalized root-means-squared (nRMS) error of the misfit between the MT response of the data and the resistivity model within the given error floors. Black color means the difference between the data and model response is large and the fit is poor, whereas red colors means the model is over fitting the data within the given error. White colors around and nRMS of 1 are optimal fits. The off-diagonal components of \mathbf{Z} typically have more weight than the diagonal components, which is related to the physics of induction. However, in this experiment, the diagonal components are nearly the same magnitude as the off-diagonal components and have influence in the model. The GDS magnitudes are relatively small (< 0.3) but still influence the shape and orientation of the main anomaly C1.

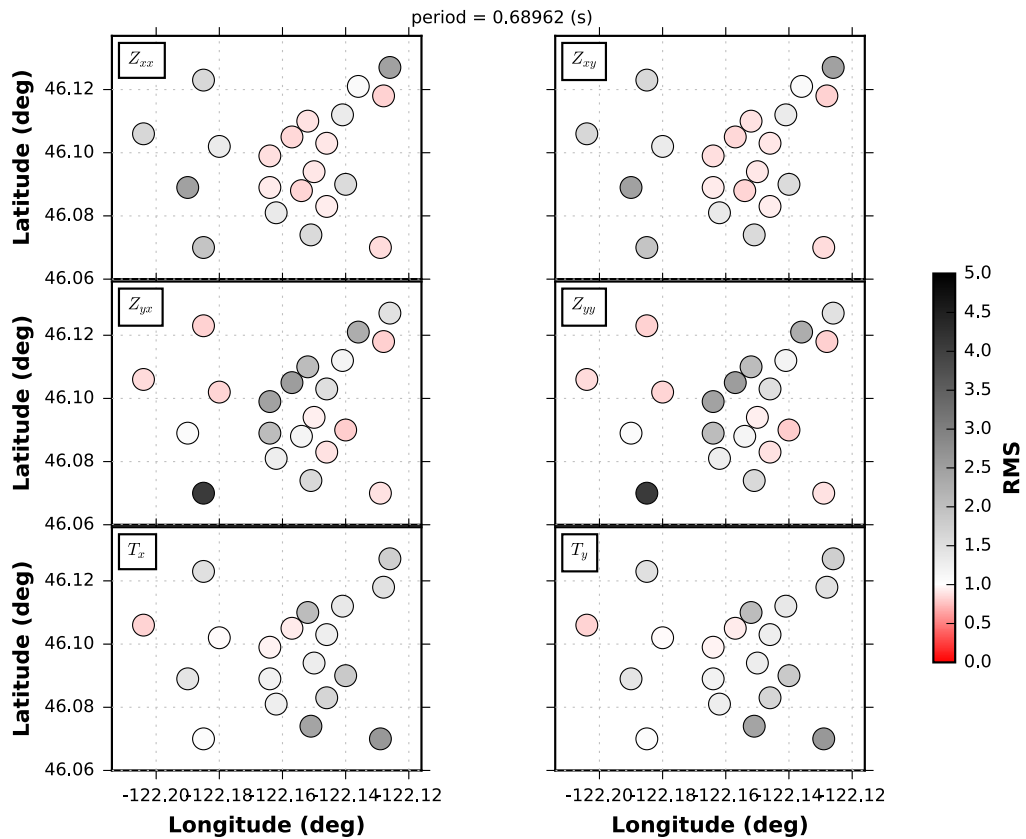
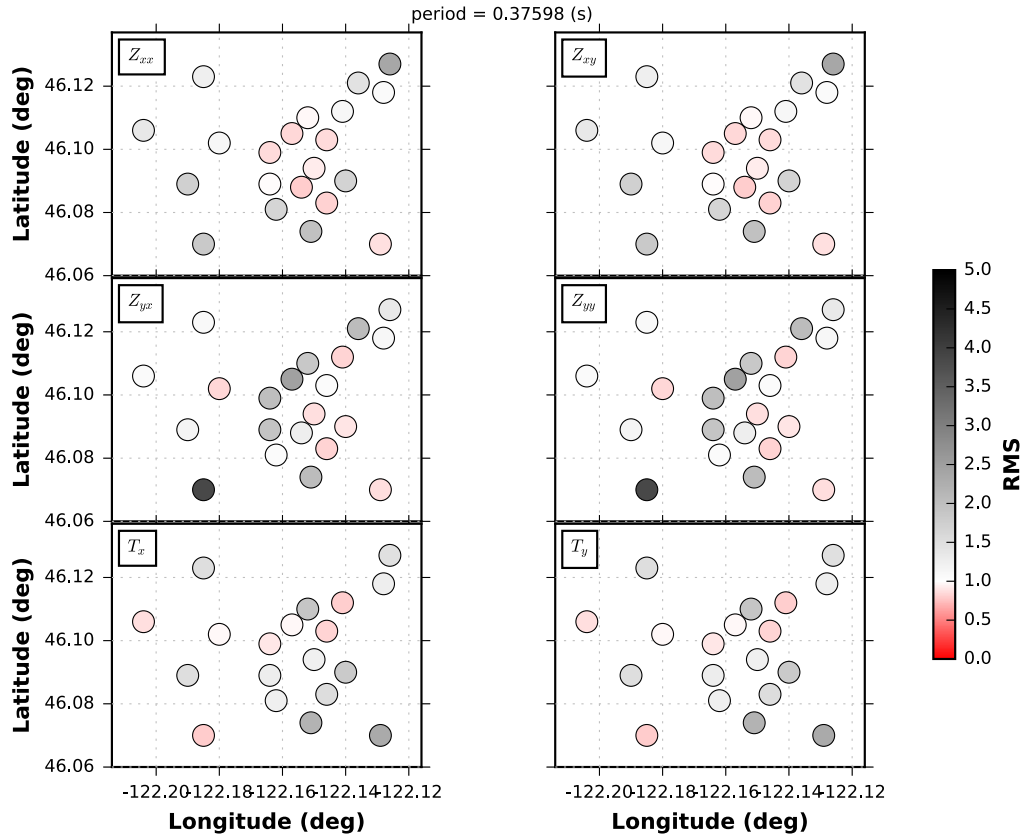


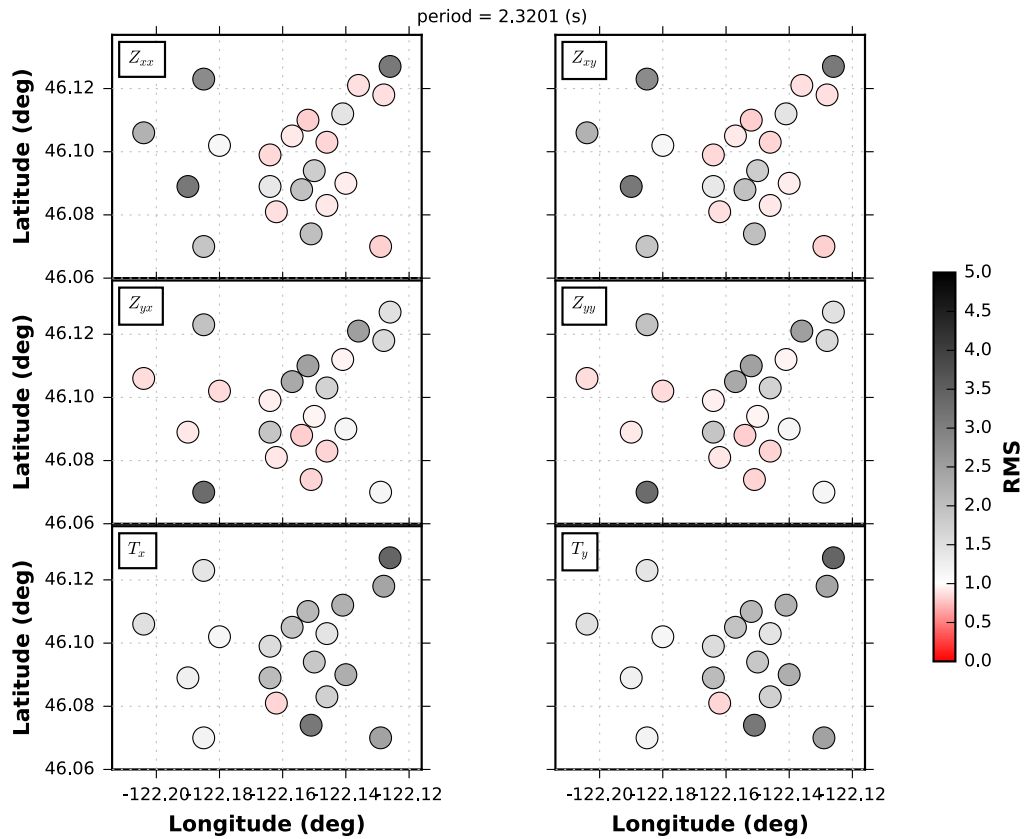
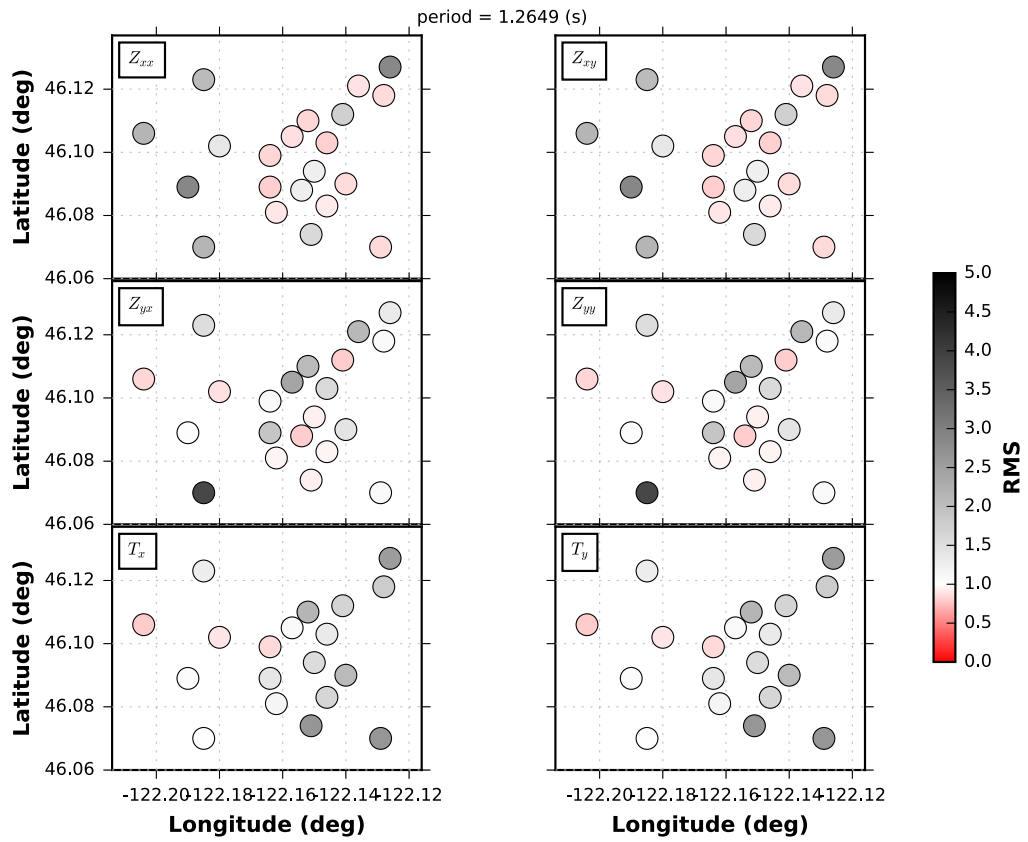


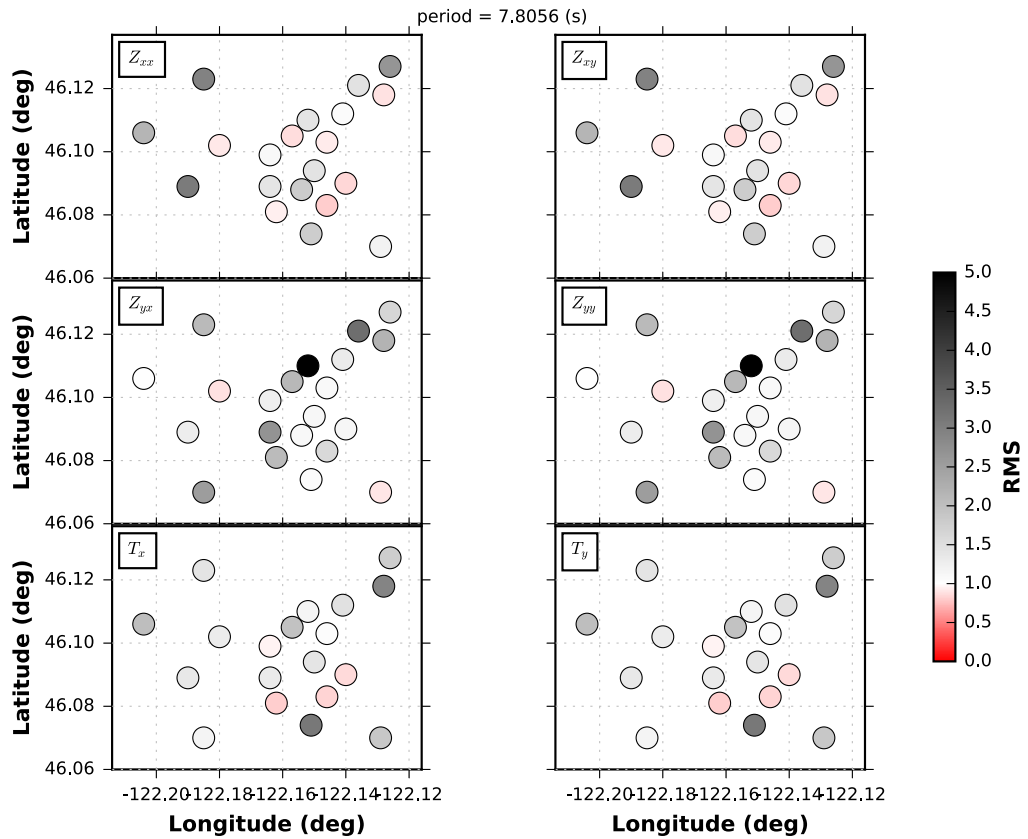
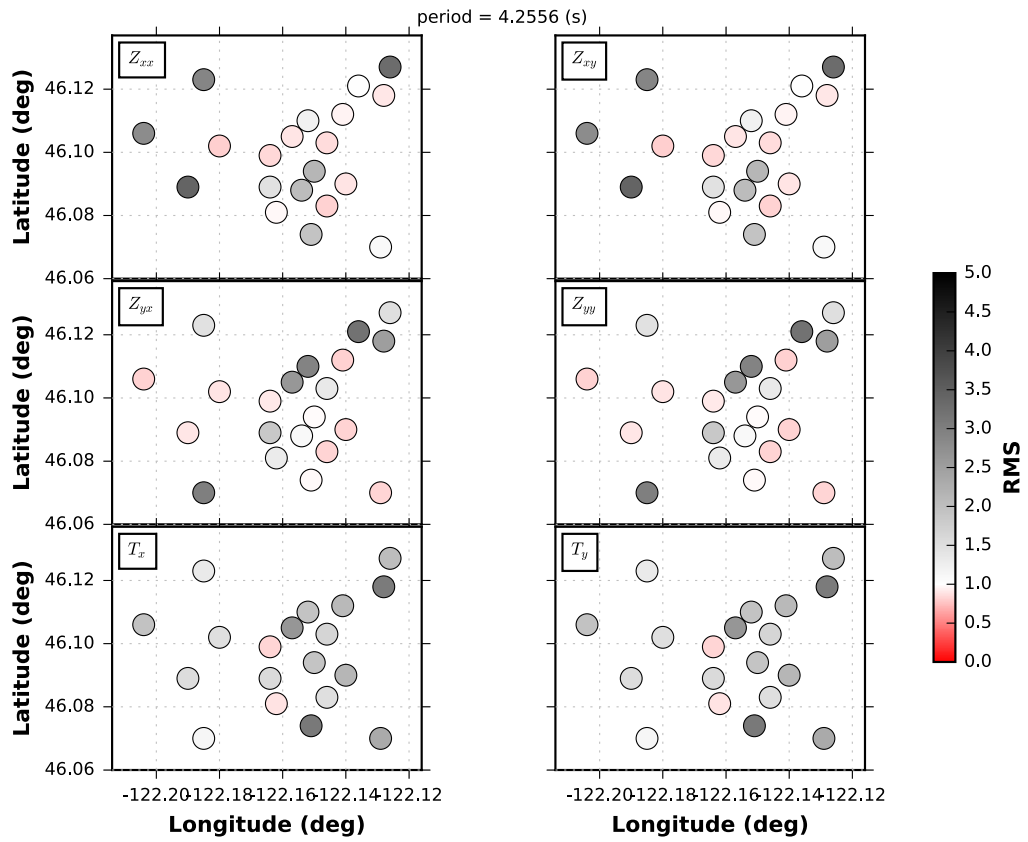


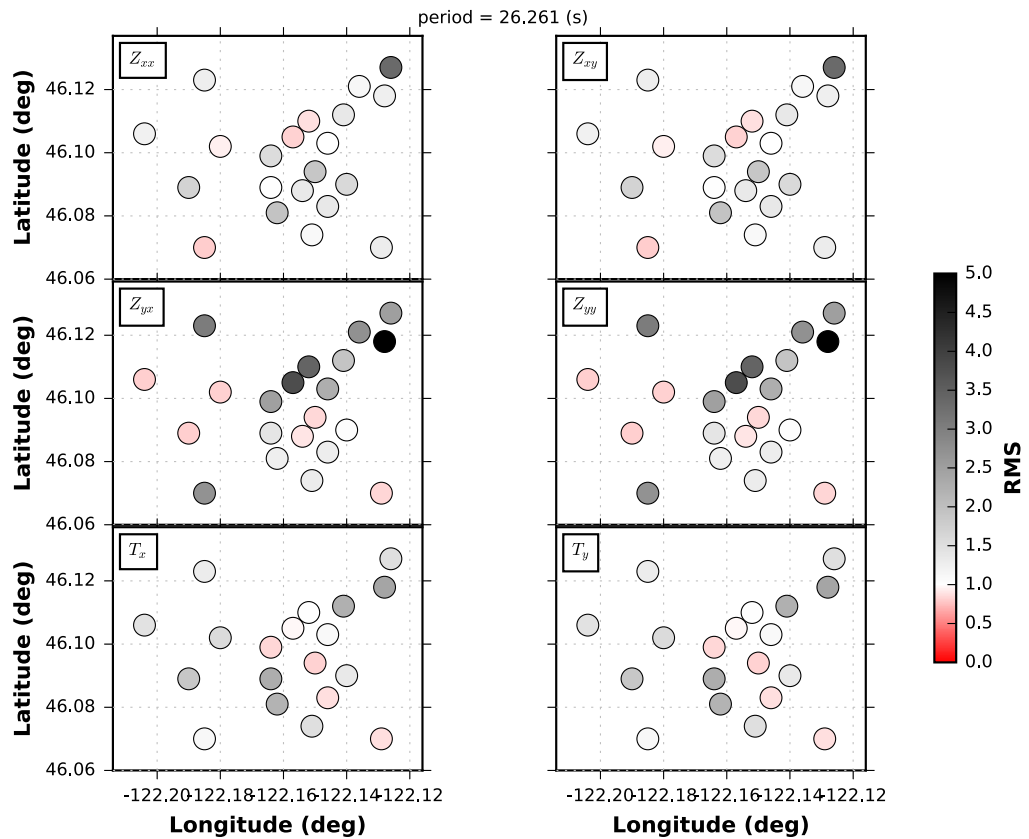
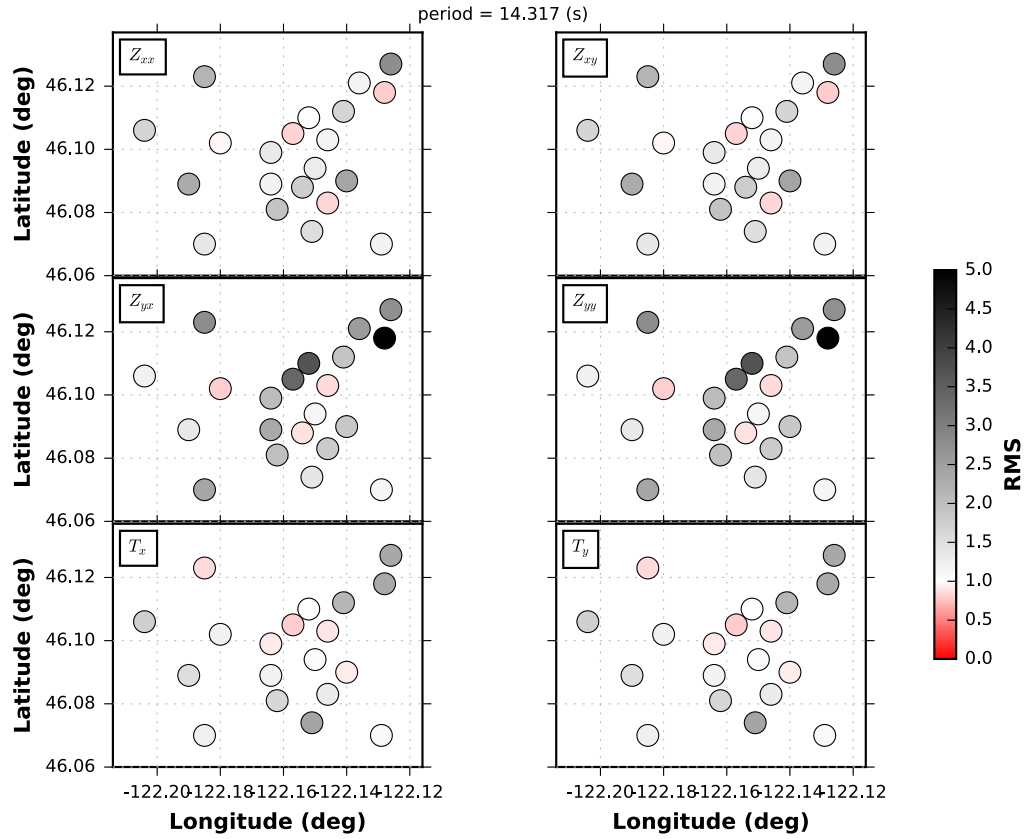


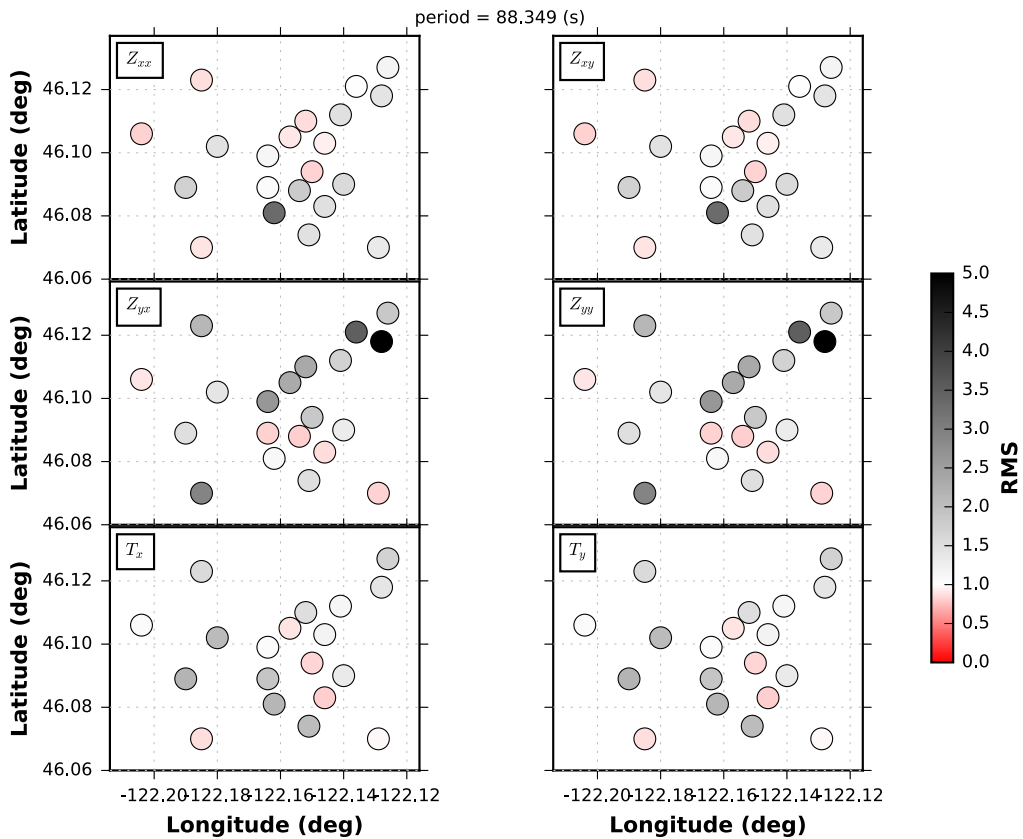
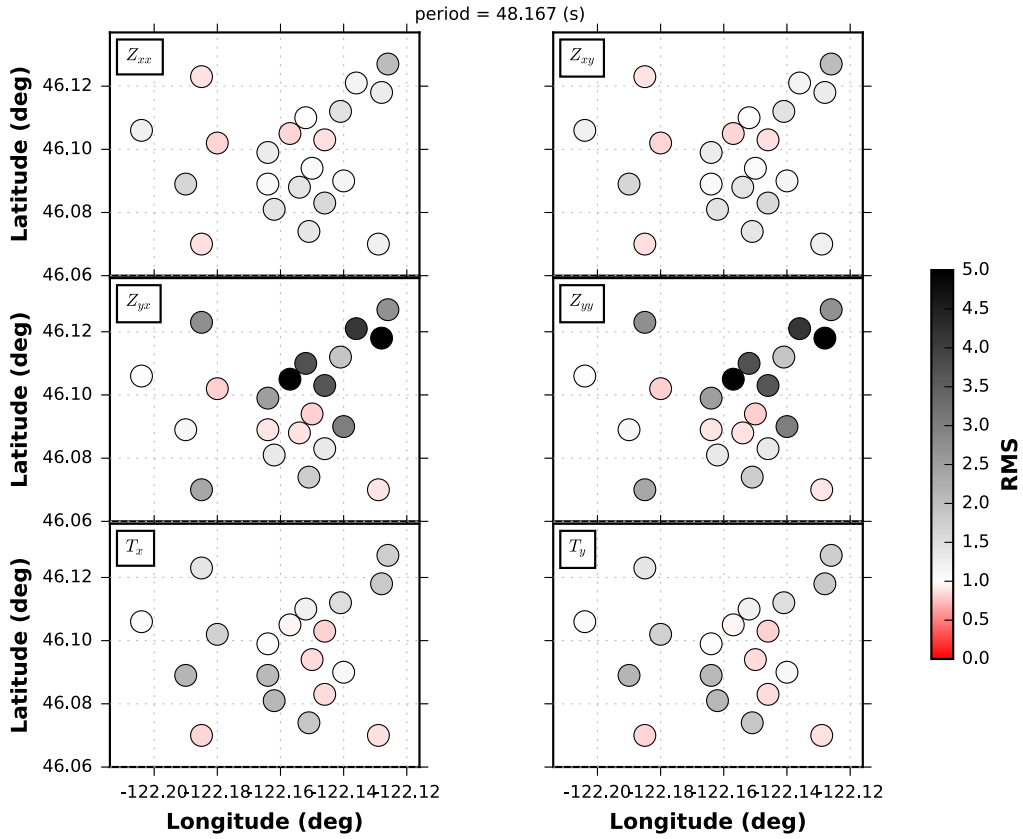


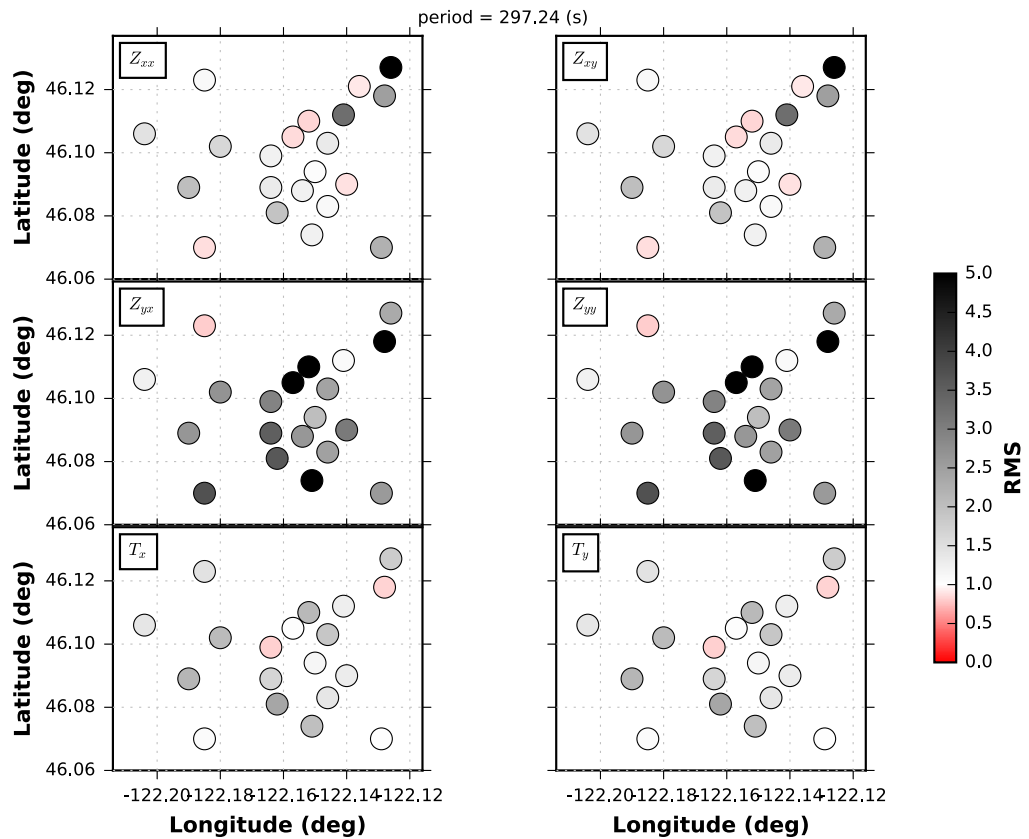
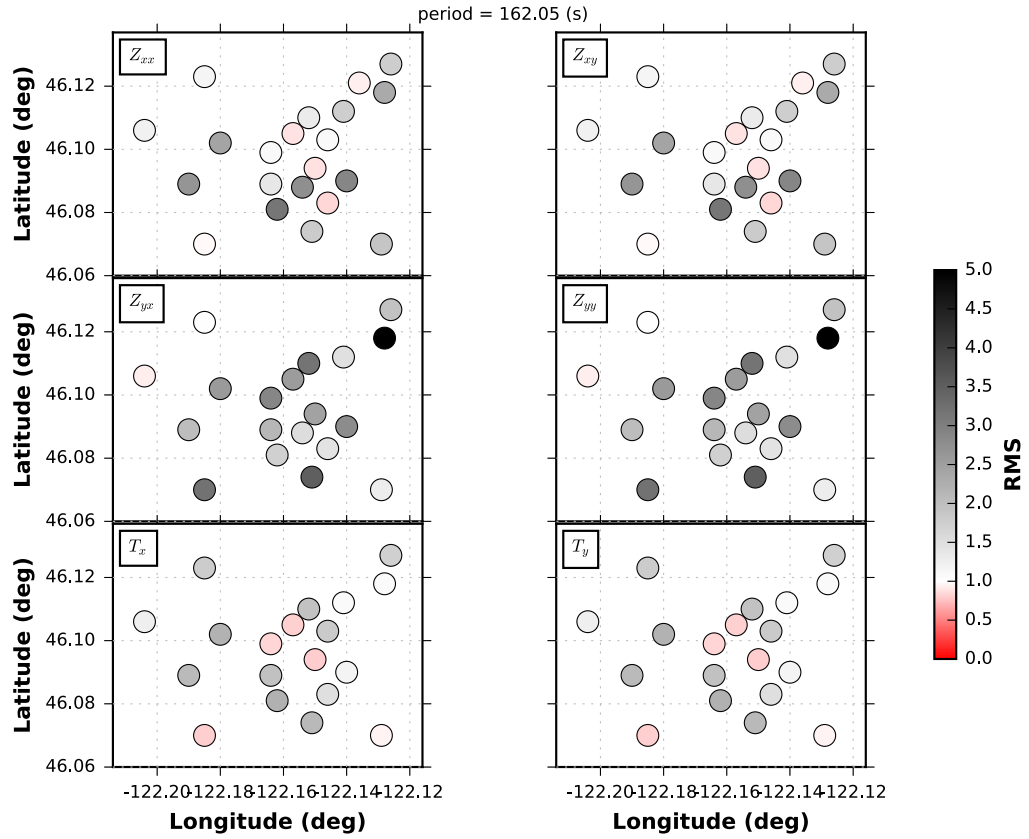


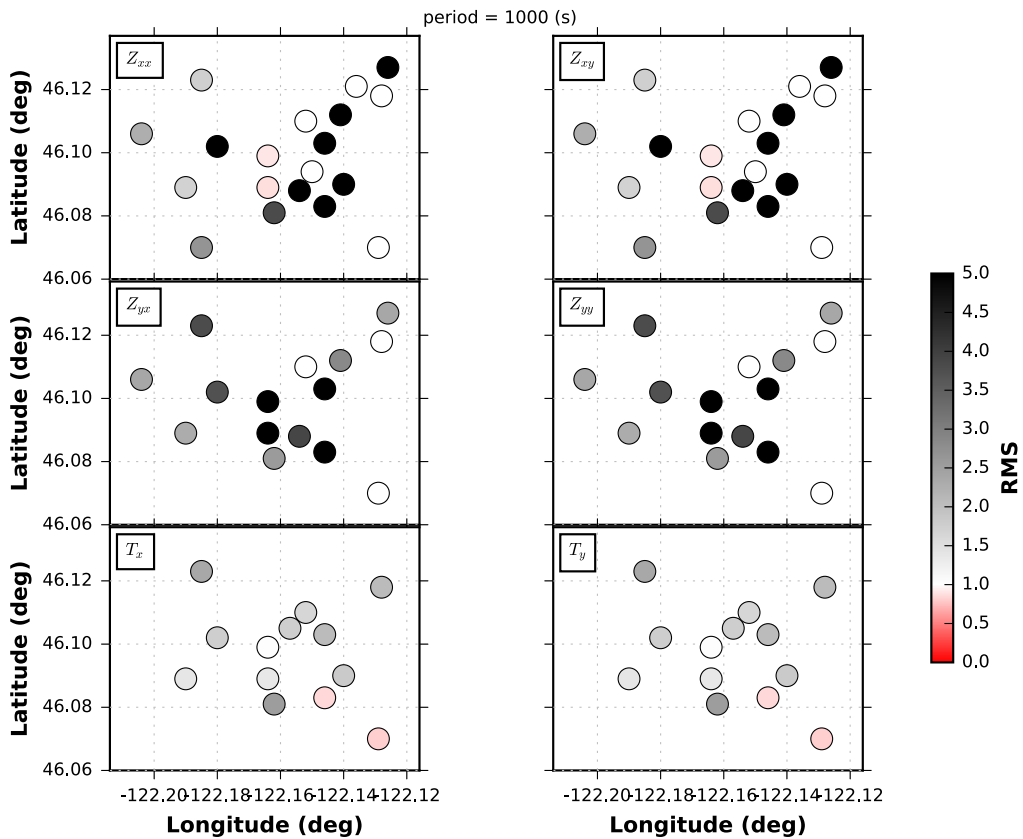
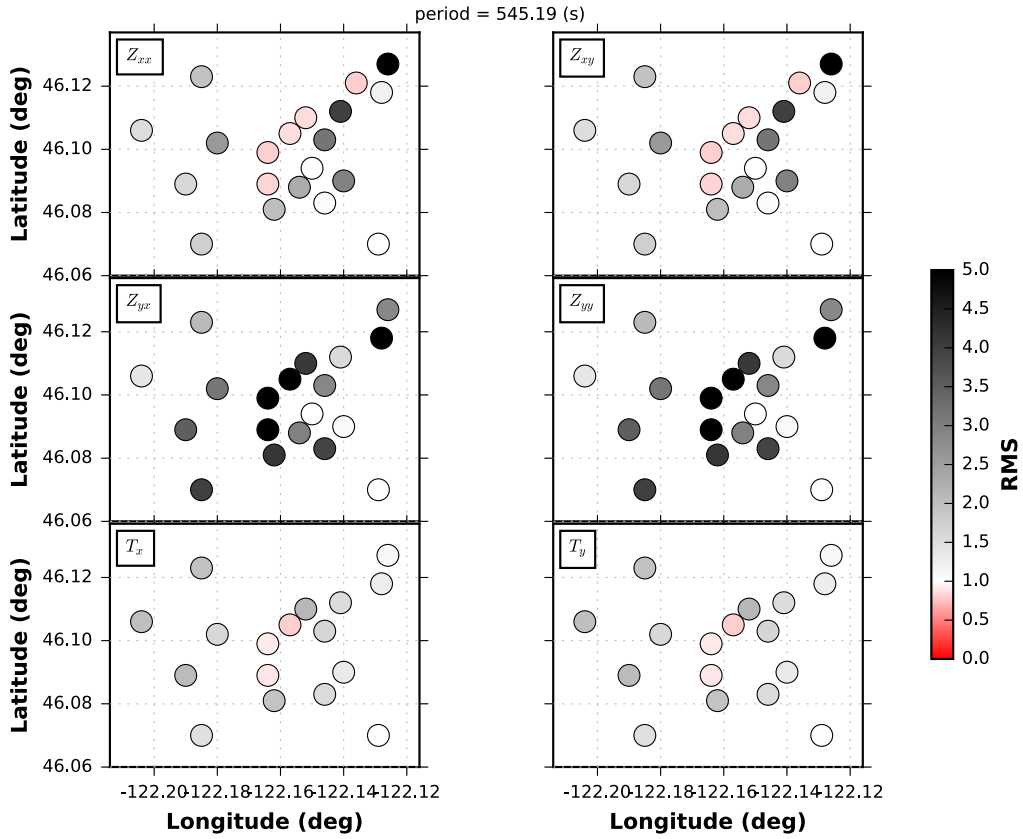




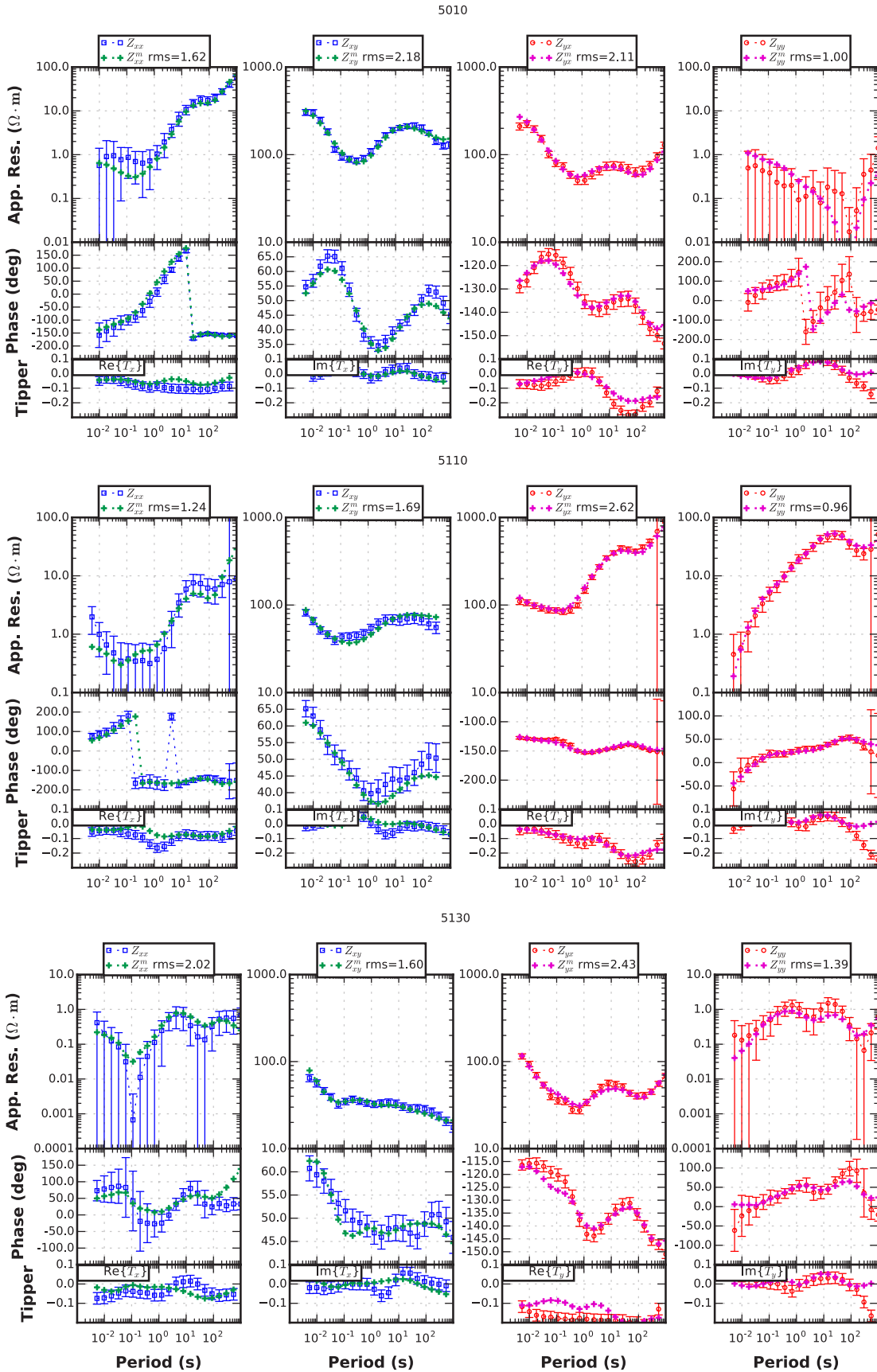




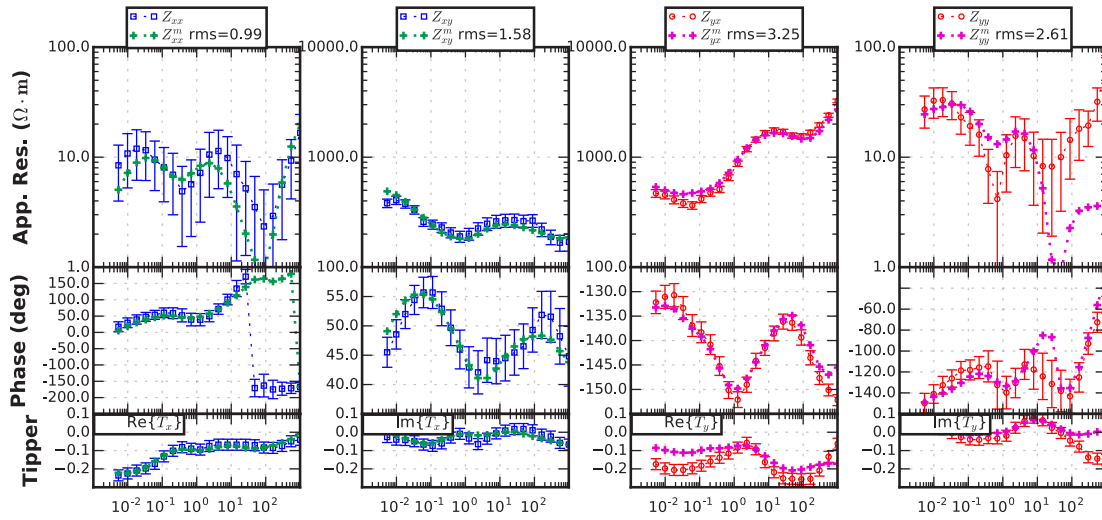




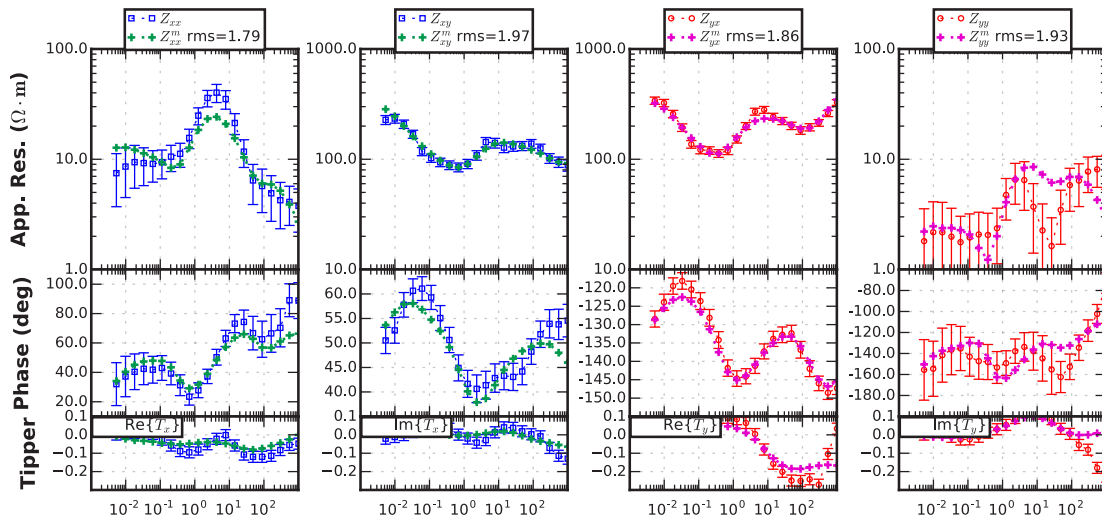
C Data & Model MT Responses



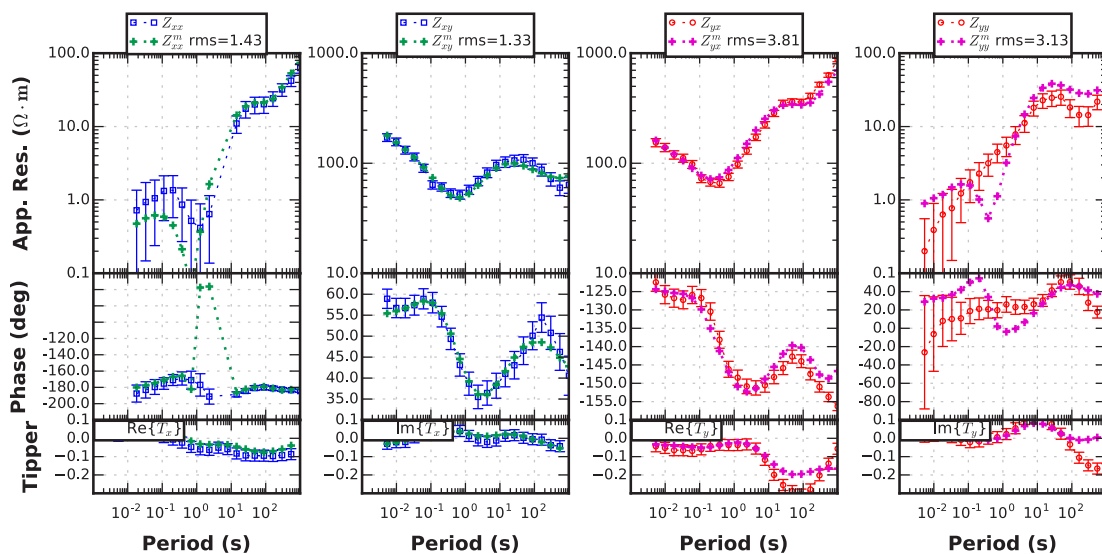
5150

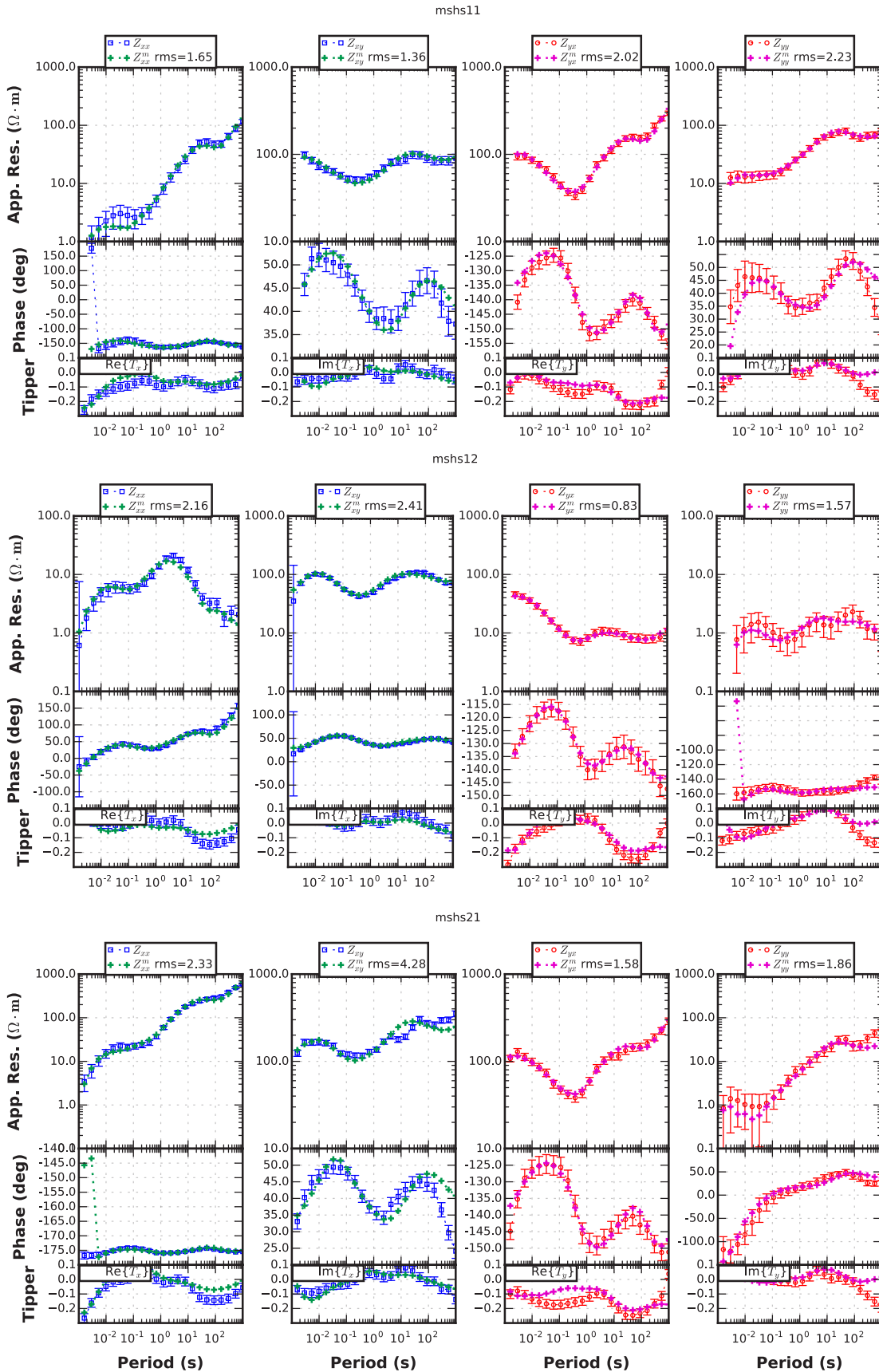


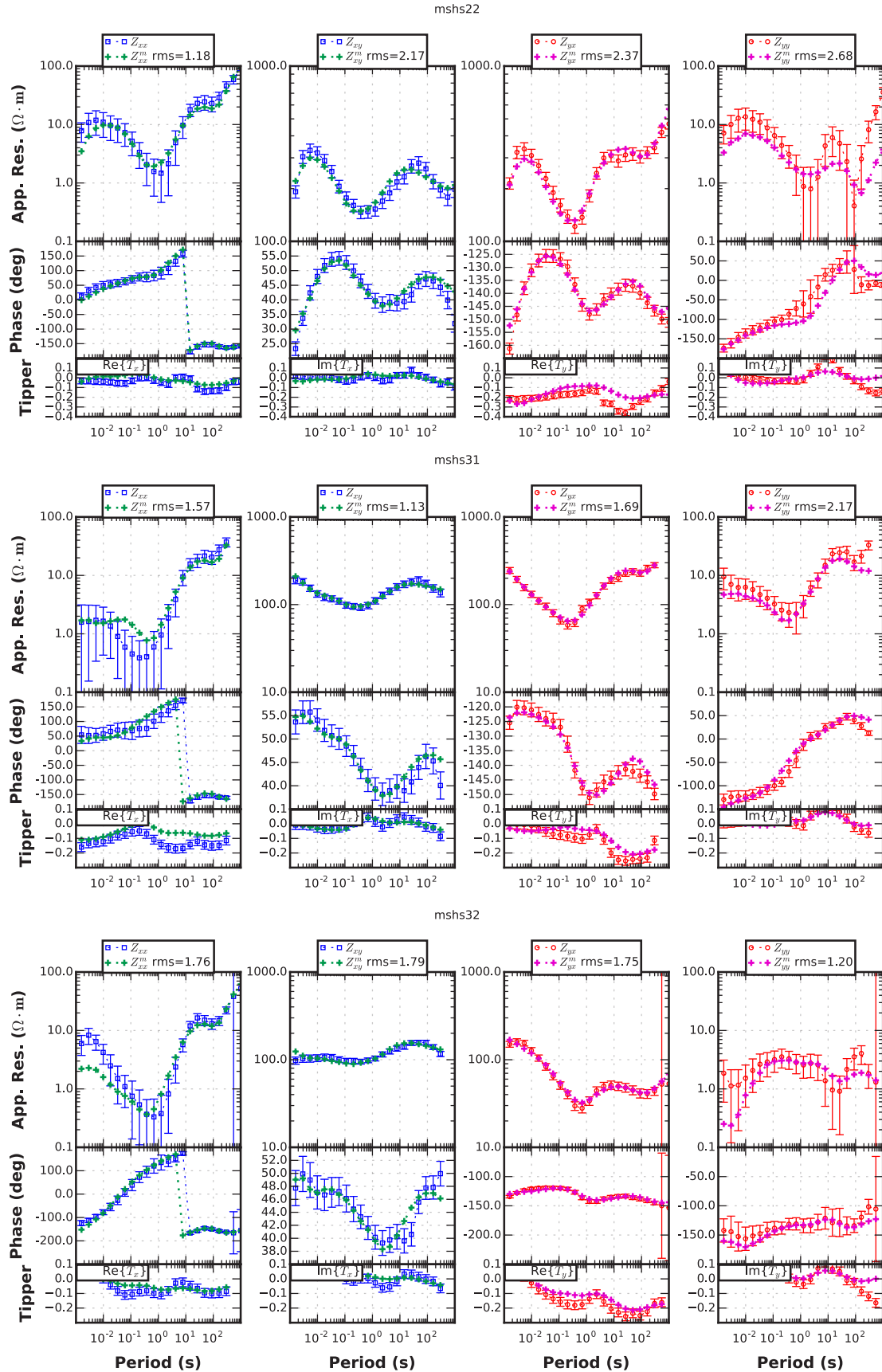
5310

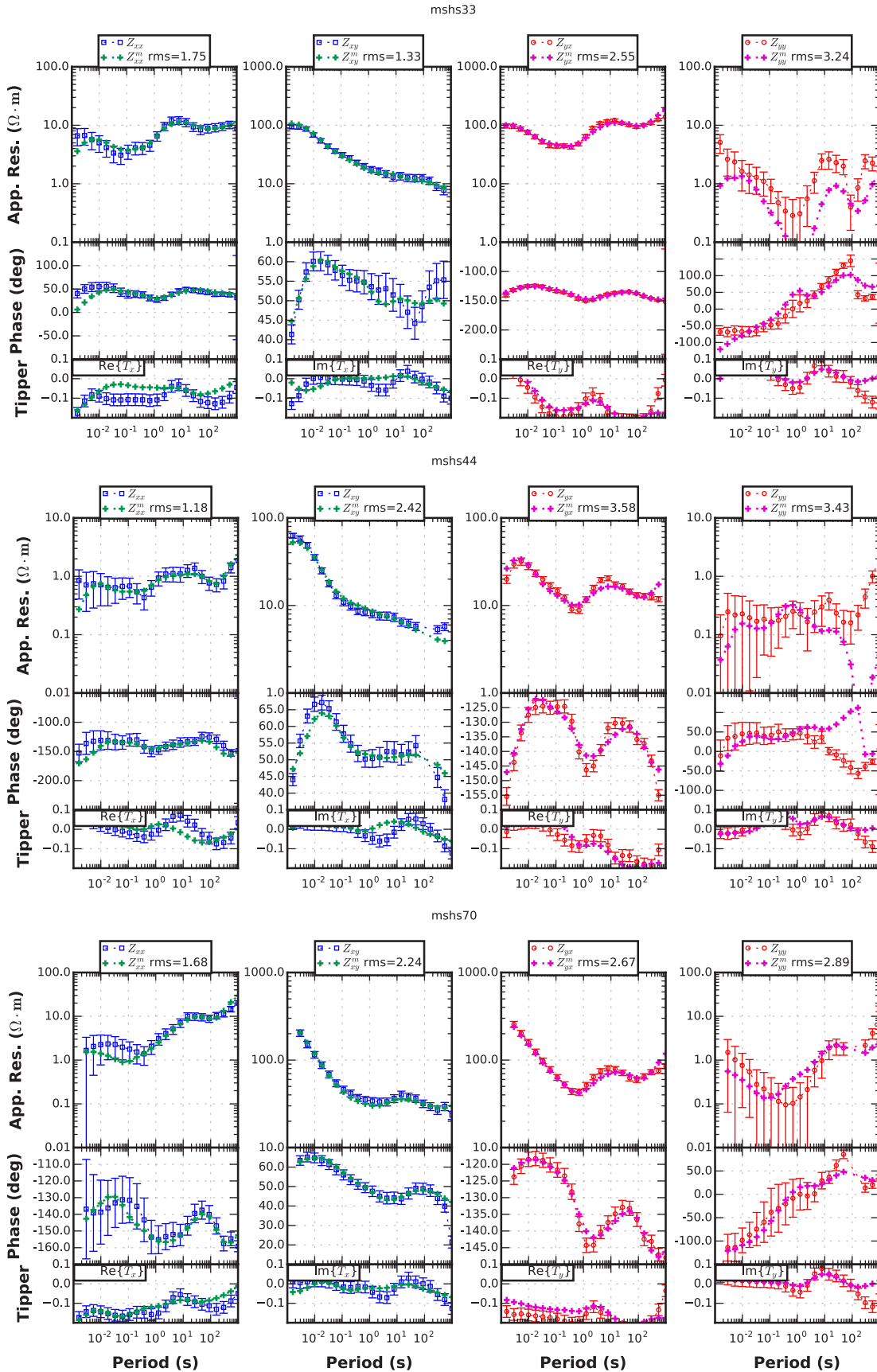


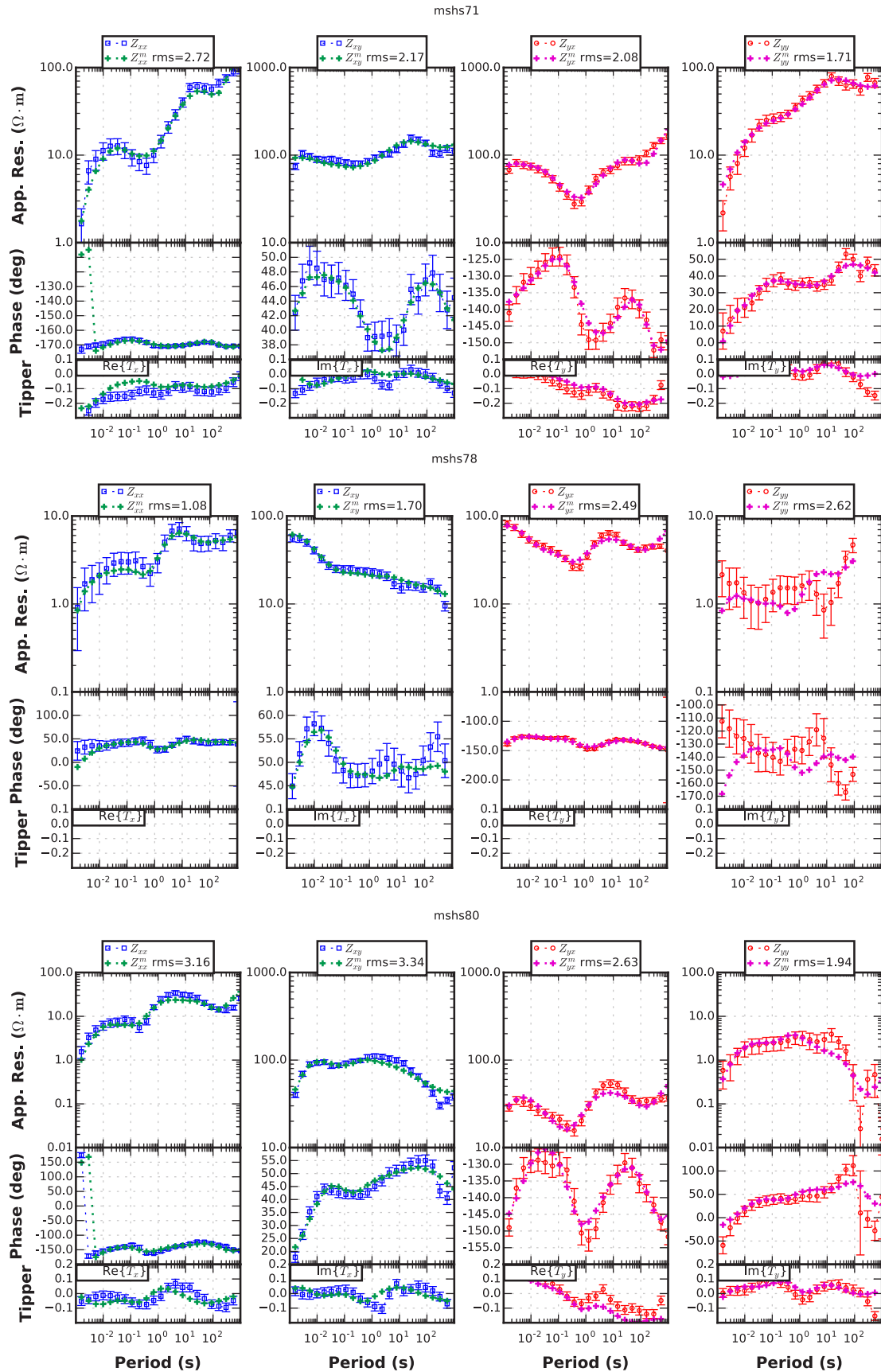
6120

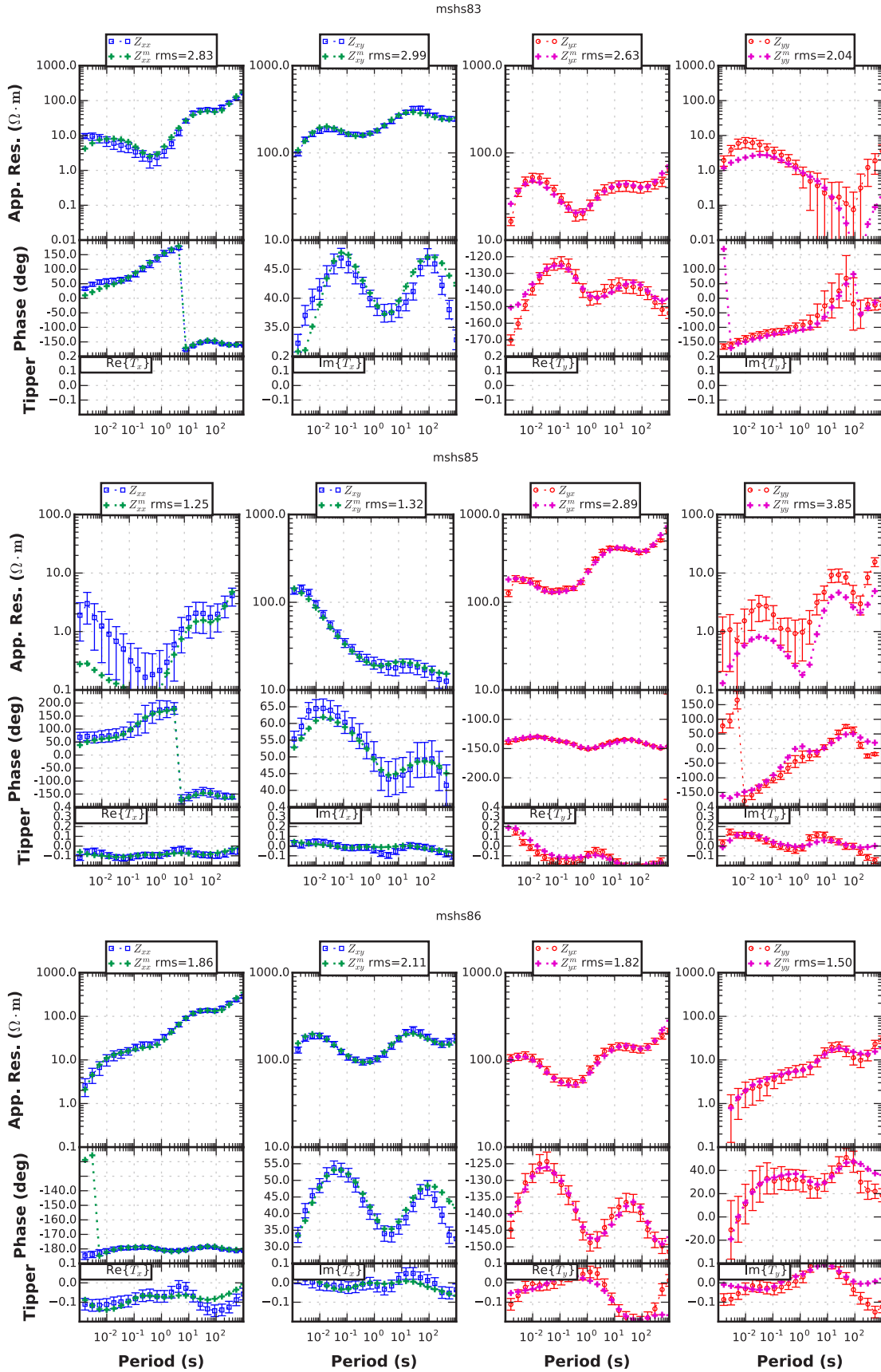












Appendix D. Results of Passive-Seismic Surveys

Ambient Noise Tomography

Kayla Crosbie

Background

Ambient noise tomography (Shapiro and Campillo (2004)) has been used for the past decade to image the crust using microseisms. Unlike earthquakes, a sometimes sparse source which limits the resolution, microseisms create a nearly diffuse, continuous wavefield. Brenguier et al. (2007) brought ambient noise tomography to a smaller scale (a 10 km wide caldera) for the first time with a dense array when imaging Piton de la Fournaise volcano. For geothermal applications, the resolution needed to be localized even further to image 1-5 km bodies. To accomplish this, denser arrays and lower period noise (usually 5-100 s) is used. Yang et al. (2011) imaged a known geothermal area in the Coso region of southeastern California using 3-10s period Rayleigh waves and stations spaced between 0.5km and 12 km. However, it was thought that discarding velocities from station pairs where the wavelength was 3 times the spacing or less was necessary, which limited the resolution. Luo et al. (2015) showed that velocities could be used for station pairs with a distance equal to the wavelength, increasing the resolution of local scale tomography tremendously. Caló et al. (2013) studied the Soultz geothermal plant in northern Alsace, France, decreasing the period of surface waves to 1-5 s. Using group velocities and picking travel times they found low velocities at the edge of the geothermal boreholes. Recently, a hydrothermal reservoir at Lazufre volcanic area was imaged by Spica et al. (2015), using FTAN to obtain group velocities between 1-8 s. Tibuleac et al. (2011, 2015) imaged the Soda Lake, Nevada region for geothermal exploration using much lower periods (0.1-3 s) to create a favorability model using shear and compressional velocity calculated from F-k analysis.

To further the resolution of this seismic array using ambient noise tomography, we used mixed-component correlations of ambient noise at 0.3-2.5 s, to minimize the “ghost lag”, a signal that arrives before the Rayleigh wave (Haney et al., 2012). This ghost lag was more apparent for the smaller array compared to larger networks, making the measurement of phase velocities difficult. Using this new method, 3 km wide low velocity features were imaged.

Data

The seismic stations have a 3 km grid spacing, with a clustered three on the shear zone having a 1 km spacing, and an aperture of 9 km (see Appendix XX for geometry). The broadband seismometers are Geotech KS200M, which measure continuously at 100 sps. Nine of the digitizers are Geotech Smart24 dataloggers, while the other 11 are Reftek 130 dataloggers (see Appendix XX for equipment descriptions). Despite shady conditions for the solar panel power system, the data is continuous, cutting out in the last week of the deployment due to snow. Station MF85 was severely rotated from north from a bad install, and the radial component

of these cross correlations were not used due to time constraints prohibiting rotating the raw seismograms and redoing analysis.

Method

Preprocessing and Cross Correlating

Cross correlation of radial-vertical (RZ) components of 20 stations yields 190 ray paths between stations. All three components of waveforms are prepared for cross correlation similar to Bensen et al. (2007). Seismograms are detrended and windowed to 100s then pre-whitened, bandpass filtered between 0.05-20 Hz, envelope normalized, and tapered. The windows are much smaller than an hour because high frequency noise is being used. Similar to Haney et al. (2012) the relative amplitudes between the three components are preserved when envelope normalizing, by dividing each trace by the rms of all three envelopes plus a water level. Pre-whitening preserves relative amplitudes as well by dividing the complex spectrum by the sum of the squares of the absolute values of each spectrum plus a water level. Combining the three components, nine cross correlations are computed per station pair for 50 second-long preprocessed waveforms. This tensor is then rotated to output the RZ correlation. Using the RZ correlation as opposed to the ZZ correlation gives good Rayleigh wave signals between stations without the ghost lag as seen when comparing the panels in figure 1. The ZZ correlation has a strong signal at nearly 0 seconds, which made calculating physically reasonable phase velocities complicated.

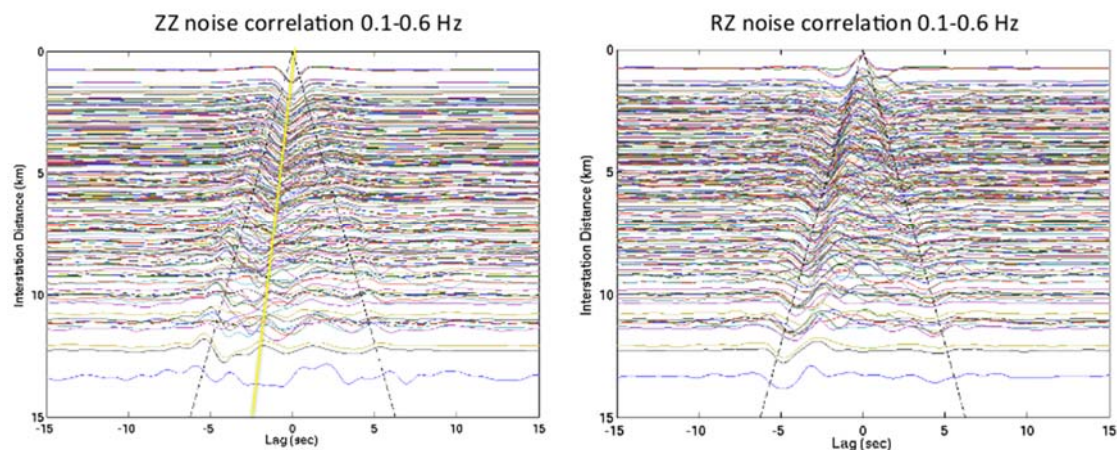


Figure 1. A comparison of the ZZ correlation and the RZ correlation filtered to 0.1-0.6 Hz. The ZZ correlation shows a signal (indicated by the yellow line) near zero lag which is gone in the RZ correlation.

Dispersion Curves

Phase velocities are calculated using the theory of the frequency domain method developed for spatial autocorrelation by Aki (1957), updated for ambient noise by Ekström et al. (2012), and applied to RZ correlations by Haney et al. (2012). The real part of the spectrum of vertical cross correlations for a perfectly

diffuse, far-field wavefield of ambient noise is a zeroeth order Bessel function of the first kind (J_0) (Ekstrom et al., 2012). For an RZ correlation, the real spectrum (ρ) is a first order Bessel function of the first kind (J_1) with frequency (ω), distance between stations (r), and phase velocity (c) as arguments (Haney et al., 2012).

$$Re(\rho) = J_1\left(\frac{\omega r}{c}\right)$$

Variations from an azimuthally symmetric wavefield give amplitude modulations to these Bessel functions. Following the method of Jin et al. (2015) the real part of the spectrum is fit to an amplitude modulated bessel function by minimizing the misfit, a function enforcing smoothness of the dispersion curve, and another function forcing the slope of the dispersion curve with respect to frequency to be negative. Each of these functions are weighted, and the total function minimized is as follows:

$$\epsilon^2 = \sum \|\alpha J_1(\omega r/c) - Re(\rho)\|^2 + a \sum \|\nabla^2(r/c)\|^2 + b \sum \left\| \frac{d(r/c)}{d\omega} X\left(\frac{d(r/c)}{d\omega}\right) \right\|^2$$

Weights are constants a and b , the amplitude modulation of the Bessel function is α , and X is a Heaviside function. An example of a spectrum is shown in figure 2 with the fit in pink. In the panel below it is the calculated dispersion curve.

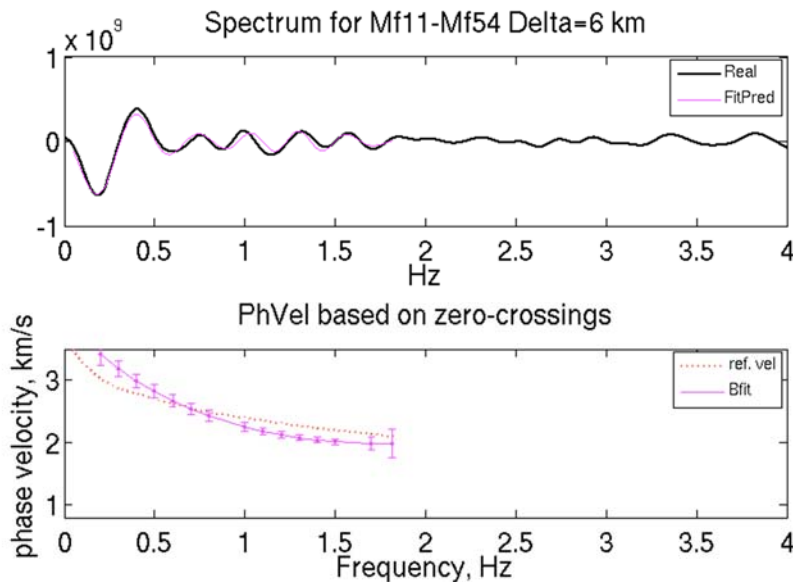


Figure 2. Top: The real part of the spectrum is plotted in black with the fit in pink. Bottom: The calculated dispersion curve in pink calculated from the fit. The reference velocity in dotted red is used in the calculation as a starting point.

Finite Frequency Inversion

Calculated phase velocities that have above 3 times the standard deviation and wavelengths less than 1 times the station spacing are thrown out for quality control. Phase velocities of all station pairs are inverted for tomographic maps using a damped least squares inversion that uses finite frequency methods (Zhou et al., 2005, Lin et al., 2009) where sensitivity kernels that are outside the ray are taken into account when inverting for structure along the ray path between stations. The more ray crossings the better constrained that grid pixel is for the map. When the resolution matrix has a resolution of zero, this defines what inversion results are

used for the second inversion for depth (A contour of well defined area is plotted on figures 9 and 10). In figure 3 an example phase velocity map is shown with the resolution matrix plotted in the bottom left. The calculated error and ray paths are also shown.

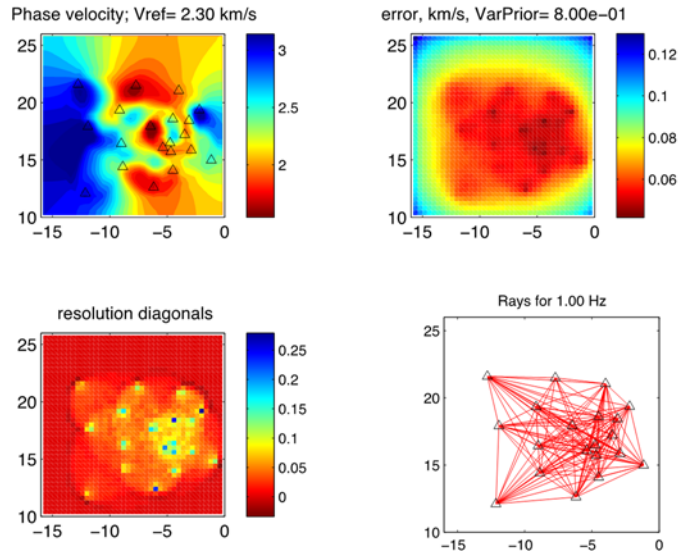


Figure 3. Top left: Inversion using finite frequency methods for phase velocity map at one 1 Hz . Top right: calculated error. Bottom left: Resolution matrix. Bottom right: Ray paths for each station pair used.

Slant Stacking

Before inverting phase velocities for 1D shear velocity structures, a shear velocity starting model is necessary. An average dispersion curve was computed using slant stacking, which finds where the Rayleigh wave signal is most coherent filtered at narrow bandwidths. Slant stacking sums the envelope of the cross correlations by shifting them by different slownesses (inverse of velocity) and outputting the sum at different time offsets, tau. A plot of this stack looks like figure 4, where the peak gives the group velocity of the Rayleigh wave at this frequency band. The error bar was defined where the peak dropped to 5% of its maximum value.

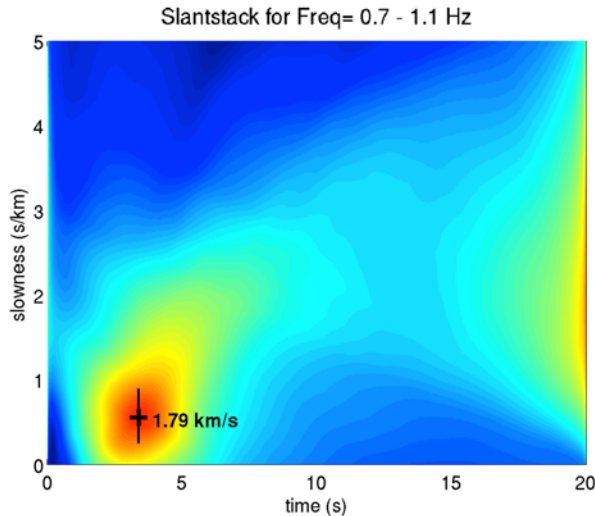


Figure 4. Group velocity slant stacking. The center of the peak shows the slowness of the Rayleigh wave at 0.7-1.1 Hz. Error bars are where the peak drops from the maximum by 5%.

After repeating this for several bandwidths, the group velocity (U) dispersion curve is fit to a polynomial. This polynomial is used to calculate a phase velocity dispersion curve by expressing $1/U$ as a polynomial and calculating coefficients for the inverse phase velocity polynomial $1/c$:

$$\sum_{k=0}^N (k+1)a_k w^k = \sum_{k=0}^N b_k w^k$$

a_k are coefficients for the $1/c$ polynomial and b_k are coefficients for the $1/U$ polynomial. This polynomial has a constant added, so the phase velocity curve is shifted up to match some phase velocities calculated from slant stacking done on the full correlograms, rather than the envelopes. The final dispersion curve, including average phase velocities from ambient noise tomography on a larger array iMUSH and Janiszewski et al. (2016 AGU poster) surface wave earthquake tomography is plotted in figure 5.

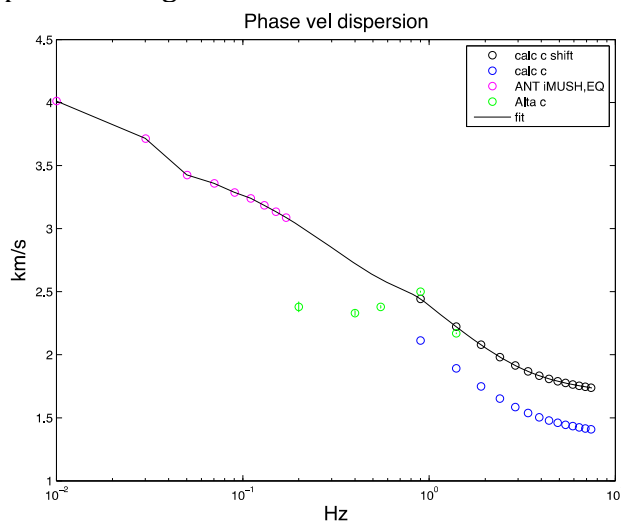


Figure 5. Dispersion curve (black line) used for 1D average shear velocity start model. Pink points are phase velocities from ambient noise tomography on iMUSH array and EQ tomography on western

US by Janiszewski et al. (2016 AGU poster). Green is phase velocity from slant stacking on Play Fairway array. Blue is calculated phase velocity from slant stacking on envelopes for group velocity on Play Fairway array. Black points are the shifted dispersion curve of the blue points.

Phase velocities are inverted iteratively with damping for shear velocity at depth in 1D profiles under each pixel by fitting the dispersion curve and updating a starting model (Herrmann, 2013). The starting model for this inversion is the end model from ambient noise on the iMUSH array, with more layers in the top 5 km. Velocities are decreased in some of these top layers to account for common sediment velocities that were not captured by the iMUSH study. Figure 6 shows the starting model and the final model using the slant stacking dispersion curve, where the final model is the starting model for the MSH Play Fairway ambient noise tomography inversion.

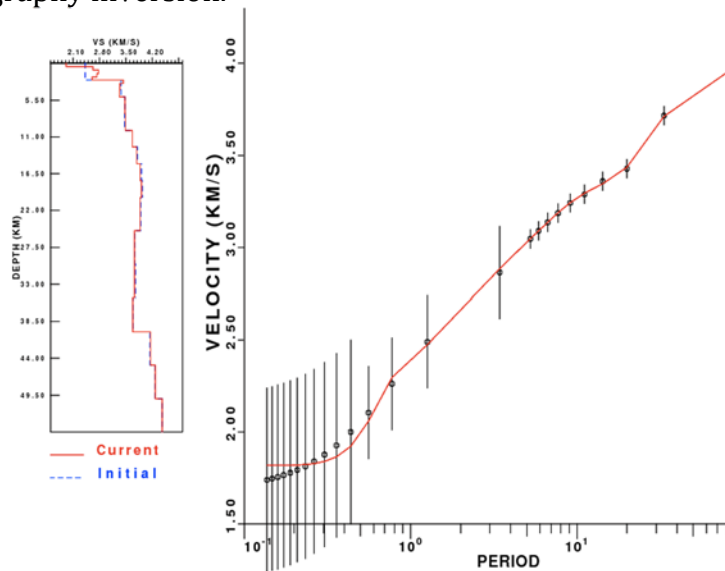


Figure 6. Left: 1D shear velocity inversion result (red) and starting model (blue). Right: the fit to the dispersion curve from slant stacking and higher period results from iMUSH and earthquake surface wave tomography (Janiszewski et al. 2016 AGU poster) used to calculate shear velocity.

Ambient Noise Tomography Shear Velocity Inversion

Using the sensitivity kernel of phase velocity with respect to depth (figure 7), the phase velocities are inverted for depth the same way as the starting model was inverted for described above. The frequencies used are only sensitive to about 4 km depth, so results to only those depths are presented.

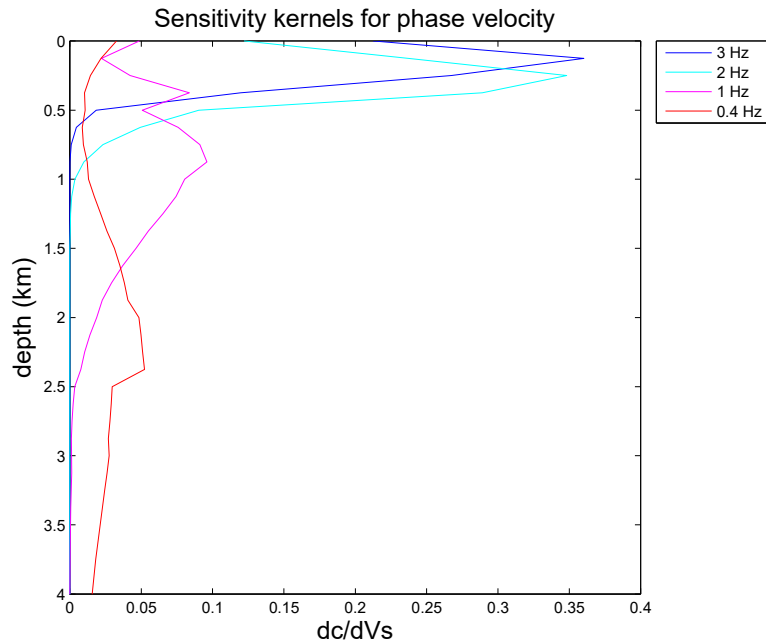


Figure 7. Sensitivity kernel for each of the frequencies used. Shows how deep the structure of the phase velocity is sensitive to.

Results

Phase velocities at four example frequencies are shown in figure 8. Shear velocities at different depth slices are shown in figures 9 and 10. The faults in grey and seismicity in white are plotted. One transect that intersects a slow velocity zone in a well-constrained area of the map is plotted in figure 11.

In the phase velocity maps (figure 8) in general the center of the array has a north-south slow velocity zone between the fast velocity zones of Spud Mountain and Spirit Lake plutons. The shear velocity maps show a similar pattern to the phase velocity maps at shallower slices (figure 9), showing the possible locations of the plutons and slow velocity zone between them. The deeper slices (figure 10) show the St Helens seismic zone as a boundary between the faster and slower velocity zone. The transect (figure 11) shows the depth of the slowest velocity zone in the middle of the array which is maximum around 2.5 km depth.

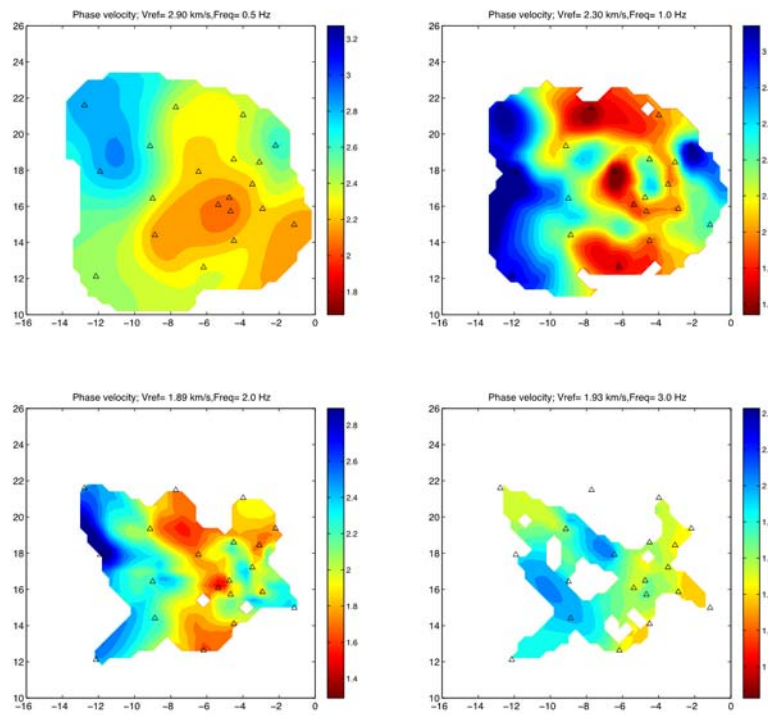


Figure 8. Phase velocity maps at four different frequencies plotted where resolution is greater than 0.

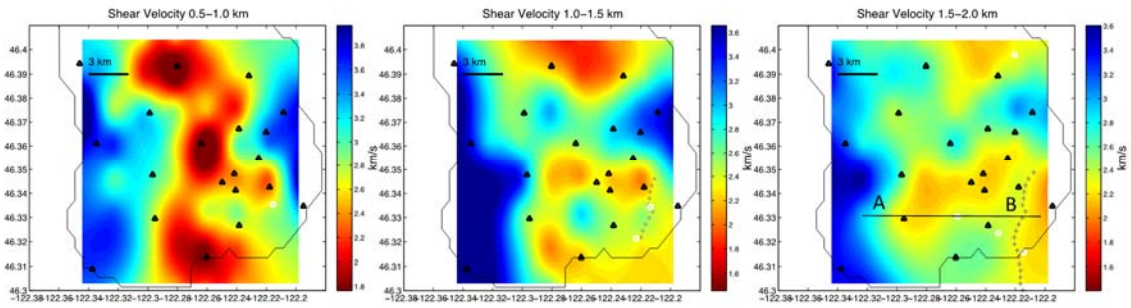


Figure 9. Shear velocity maps for shallow depth slices (see titles). Seismicity white circles, mapped faults grey crosses. Line where A-B transect is projected (Figure 11) is on right plot. The black contour outlines where the resolution matrix was nonzero in the most resolved phase velocity map.

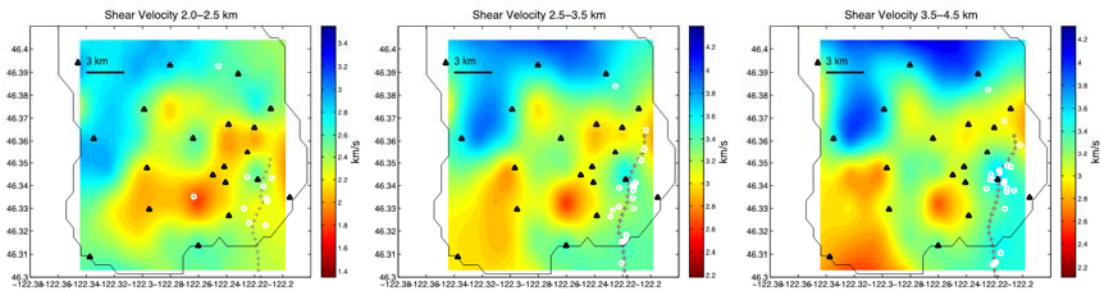


Figure 10. Shear velocity maps for deepest depths labelled in titles. Seismicity in white and mapped fault in grey.

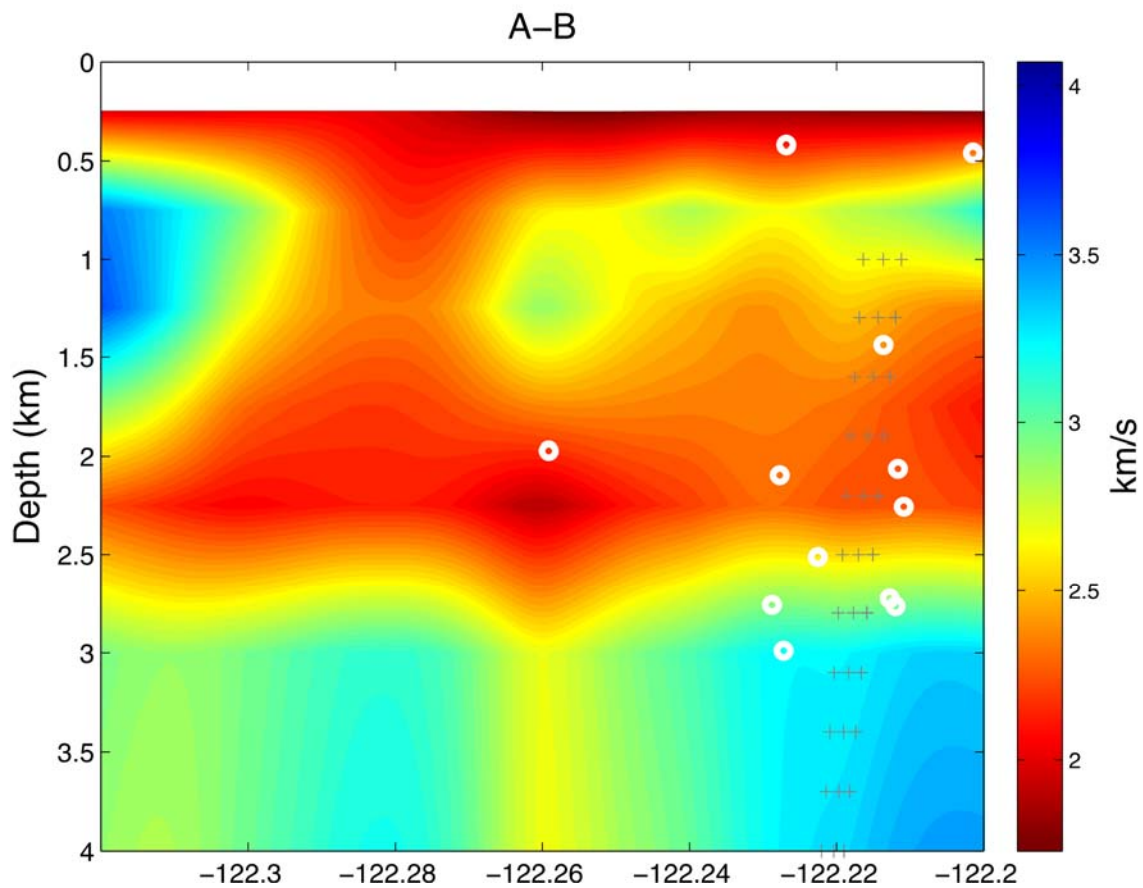


Figure 11. Transect A-B. The fault and seismicity is mapped with depth along the transect to show the E-W sloping trend.

Carl Ulberg

Play Fairway project, MSH-north

Local earthquake tomography and earthquake relocation results

4/7/17

Tomography

We performed local earthquake seismic tomography, using data from the 20 stations of the Play Fairway analysis, along with 70 iMUSH stations (imush.org), and permanent PNSN network stations¹. The Play Fairway instruments were located above the Mount St. Helens seismic zone (SHZ) 15 km NNW of Mount St. Helens with an array diameter of ~12 km and average station spacing of ~2 km, while the iMUSH instruments were centered on Mount St. Helens with an array diameter of ~100 km and average station spacing of ~10 km. The data consisted of P- and S-wave arrival times from ~300 local earthquakes (~60 within the Play Fairway footprint, 40 of which occurred during the deployment). In total there were ~5300 P-wave and ~2500 S-wave arrivals which represented raypaths through the model volume, with 559 P-wave and 414 S-wave arrivals observed at Play Fairway stations. We picked earthquake P- and S- arrival times using the seismic software package Antelope, and inverted them to obtain 3-D seismic velocity models with the program struct3dp, written by Bob Crosson. This program uses a conjugate gradient least squares method, with joint hypocenter and velocity inversion, using 3-D eikonal-based travel time computation (Vidale, 1990; Hole and Zelt, 1995).

Major features of the 3-D seismic velocity models include low P- and S-wave velocities along the SHZ, possibly related to fluids or fractures. High velocities at shallow depths to the east and west of the SHZ likely correspond to the Spirit Lake and Spud Mountain plutons, respectively. There are high V_p/V_s ratios just to the west of the SHZ, which could indicate the presence of fluids, since S-waves are more sensitive to fluids. Currently the P and S velocity models are inverted separately, but a simultaneous inversion or an inversion to obtain the V_p/V_s ratio directly would provide a more robust result for the V_p/V_s ratio.

Earthquake relocation and focal mechanisms

There were approximately 20 events in the PNSN catalog within the Play Fairway array footprint during its deployment. These were relocated as a part of the seismic tomographic inversion, and 20 more were detected using the Antelope seismic software. Focal mechanisms were calculated for several of these. Earthquake focal mechanisms along the SHZ are similar to previous results, exhibiting right lateral shear, with T axes oriented in a NW-SE direction (Weaver et al, 1987). Earthquakes ~15km WSW of the SHZ have T axes oriented closer to E-W.

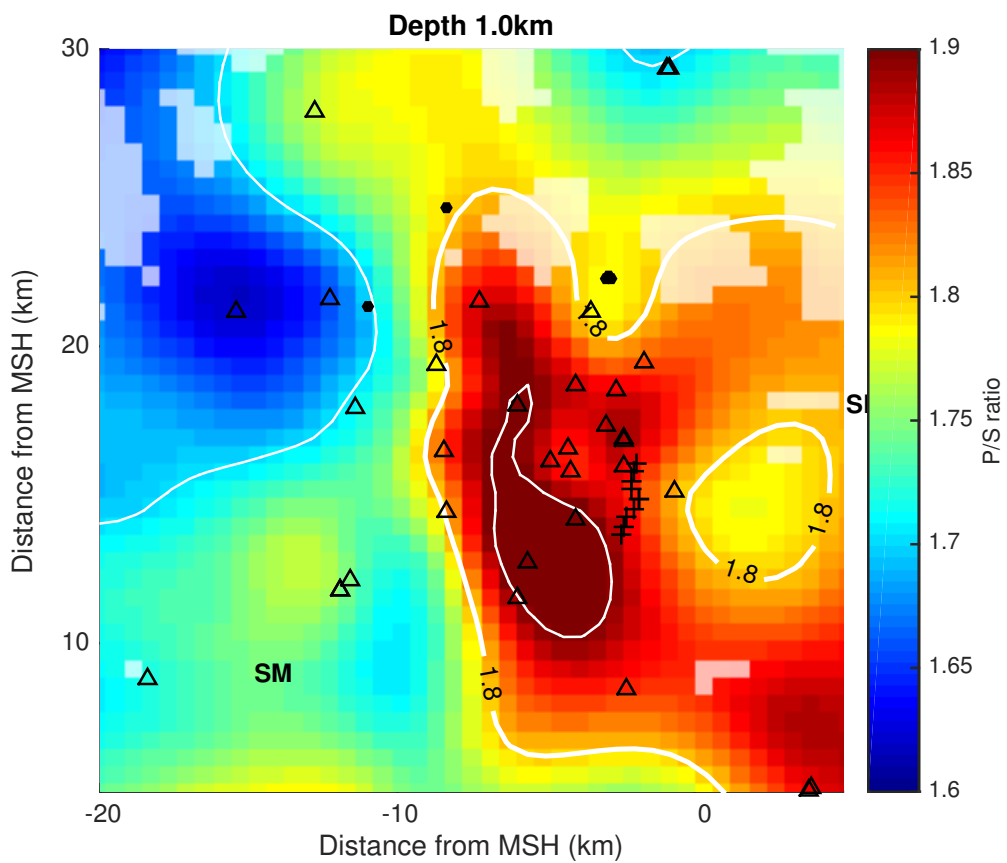
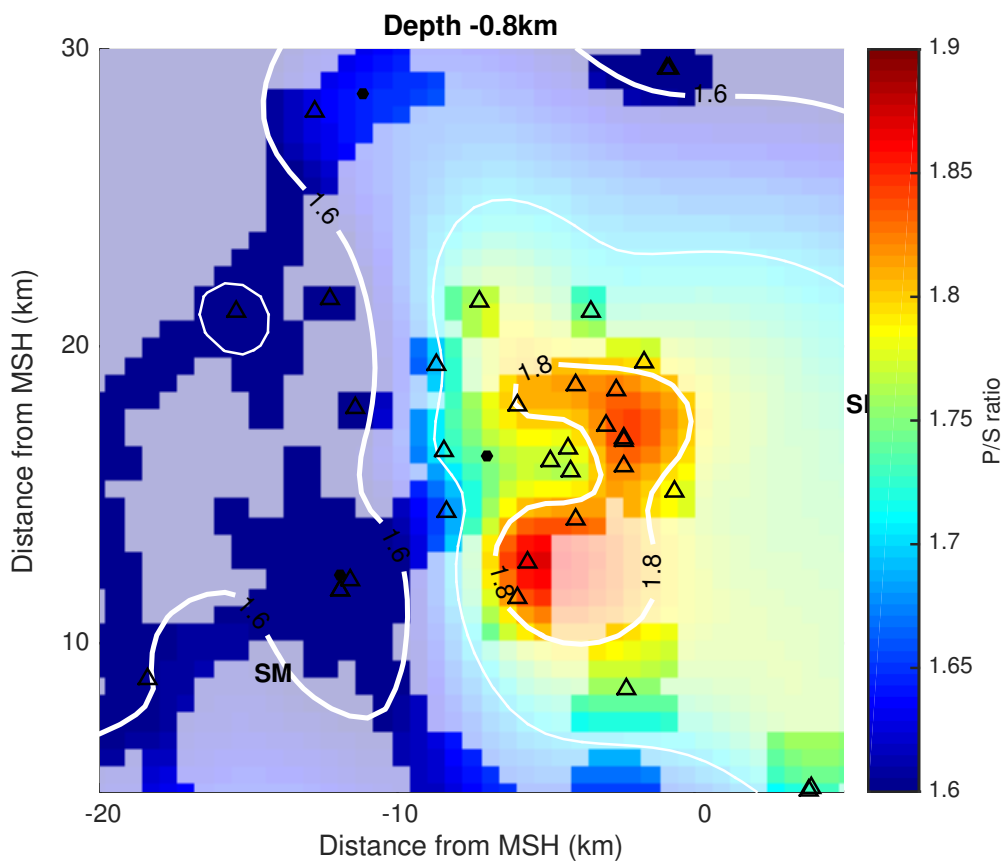
¹ Play Fairway seismic stations used Geotech KS2000M broadband seismometers with Reftek 130 and Smart24 dataloggers, iMUSH stations used Guralp CMG-3T broadband seismometers and Reftek 130 dataloggers, and PNSN stations are a mixture of short-period and broadband seismometers.

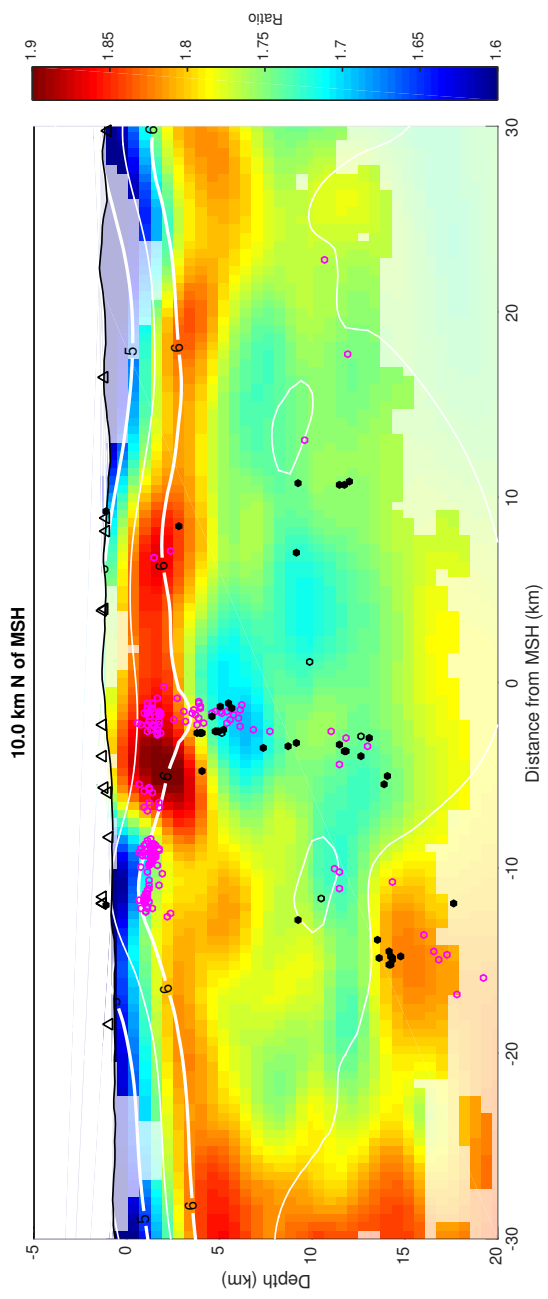
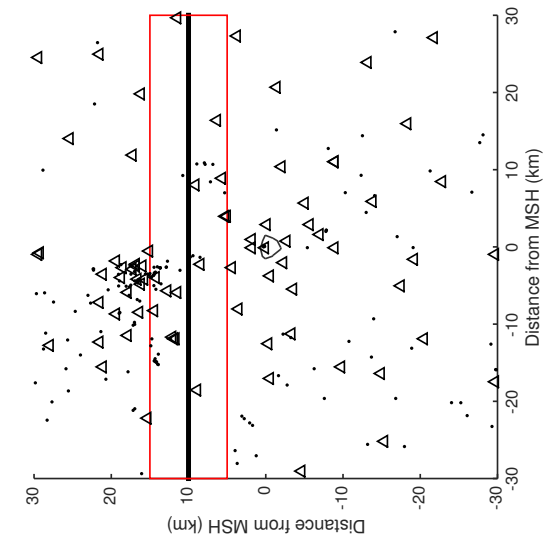
References

Hole, J.A., and B.C. Zelt, 3-D finite-difference reflection travel times, *Geophysical Journal International*, 121, 427-434, 1995.

Vidale, J.E., Finite-difference calculation of travel-times, *Geophysics*, vol. 55, no. 5, pp. 521-526, 1990.

Weaver, C.S., W.C. Grant, and J.E. Shemeta, Local crustal extension at Mount St. Helens, Washington, *Journal of Geophysical Research*, vol. 92, no. B10, pp. 10,170-10,178, 1987.





Appendix E. Results of Potential-Field Surveys

Potential Field Studies of Geothermal Systems along the Washington Cascade Range: Mount St. Helens, Mount Baker, and Wind River Valley

By ¹Brent Ritzinger, ¹William Schermerhorn, ²Megan Anderson, ¹Tait Earney and ¹Jonathan M.G. Glen

¹U.S. Geological Survey, 345 Middlefield Rd., Menlo Park, CA 94025

²Geology Department, Colorado College, 14 E. Cache La Poudre St, Colorado Springs, CO 80903,

INTRODUCTION

A recent study which adapts play fairway analysis (PFA) methodology to assess geothermal potential was conducted at three locations (Mount Baker, Mount St. Helens seismic zone, and Wind River valley) along the Washington Cascade Range (Forson et al. 2017). Potential field (gravity and magnetic) methods, which can detect subsurface contrasts in physical properties, provides a means for mapping and modeling subsurface geology and structure. As part of the WA-Cascade PFA project, we performed potential field studies by collecting high-resolution gravity and ground-magnetic data, and rock property measurements to (1) identify and constrain fault geometries, (2) constrain subsurface lithologic distribution, (3) study fault interactions, (4) identify areas favorable to hydrothermal flow, and ultimately (5) guide future geothermal exploration at each location.

DATA COLLECTION: ALL STUDY AREAS

PHYSICAL PROPERTY DATA

Rocks samples were collected for physical property measurements (density and magnetic susceptibility) in each of the three study areas. Rock property data are in Tables 1 through 3.

Grain, saturated-bulk, and dry-bulk densities of collected samples were determined by weighing each sample dry in air (W_a), saturated and submerged in water (W_w), and saturated in air (W_s). The three densities were computed using the following formulas.

$$\text{Grain density} = 1,000 \text{ kg/m}^3 \times W_a / (W_a - W_w),$$

$$\text{Saturated-bulk density} = 1,000 \text{ kg/m}^3 \times W_s / (W_s - W_w), \text{ and}$$

$$\text{Dry-bulk density} = 1,000 \text{ kg/m}^3 \times W_a / (W_s - W_w).$$

Magnetic susceptibility values were measured from outcrop locations, where density samples were extracted in the field, using a ZH instruments SM30 meter (resolution 1×10^{-7} SI units). Typically, a minimum of twelve measurements were made across a several meter-wide areas of outcrop.

GRAVITY DATA

New high precision gravity data were collected using Scintrex CG-5 and La Coste & Romberg gravity meters. Station locations and elevations were obtained using Trimble® GEOXH differential GPS devices. Additionally, newly collected gravity data were combined with pre-existing gravity data acquired from the PACES website (Pan American Center for Earth and Environmental Studies, 2016) to construct a regional gravity map.

Gravity data were reduced using standard methods (Blakely, 1995) and include the following corrections: (a) Earth-tide correction, which accounts for the gravitational effects of the sun and moon; (b) instrument drift, which compensates for drift in the instrument's spring; (c) latitude correction, which accounts for the variation of the Earth's gravity with latitude; (d) free-air correction, which accounts for variation of gravity due to elevation relative to sea level; (e) Bouguer correction, which corrects for the attraction of material between the station and sea level; (f) curvature correction, which corrects the Bouguer correction for the effect of the Earth's curvature; (g) terrain correction, which removes the effect of topography to a radial distance of 167 km around the station; (h) isostatic correction, which removes long wavelength variations in the gravity field related to the compensation at depth of topographic loads at the Earth's surface.

Terrain corrections, which account for the gravitational effect of topographic variation near a gravity station, were computed using a combination of manual and digital methods. Determining terrain corrections consisted of a three-part process. The innermost terrain corrections extend from the station to a distance of 68 meters and were estimated in the field using methods equivalent to Hayford and Bowie's (1912) zone B (Plouff, 2000). Inner-zone terrain corrections extend a radial distance of 68 m out to 2 km from the station and were estimated using digital elevation models (DEMs) as described in D. Plouff, USGS, unpub. software, (2006). Outer-zone terrain corrections, which extend from a radial distance of 2 to 167 km, were computed using a DEM derived from USGS 1: 250,000-scale topographic maps and an automated procedure (Plouff, 1966; Plouff, 1977; Godson and Plouff, 1988). Gravity data are provided in Tables 4 through 6.

Mount Baker

495 new gravity stations were collected in the Mount Baker (MB) Area of interest (AOI) from mid-July to mid-September 2016. All MB gravity data used base station COPO located at the U.S Post Office in Concrete, Washington, at an elevation of 230.1 ft., latitude 48° 32' 18.78" (N), and longitude 121° 45' 07.57" (W) with an observed gravity of 980,835.87 mGals. This base station had been tied to the absolute base station "Bellingham CA" at Western Washington University in Bellingham, WA at an elevation of 317.7 ft., latitude 48° 43' 59.962" (N), and longitude 122° 29' 05.475" (W) with an observed gravity value of 980,854.874 mGals.

Wind River Valley

604 new gravity stations were collected in the Wind River Valley (WRV) AOI from May to early July 2016. All WRV gravity stations used base station CARS located at the Skamania County Public Utility District building in Carson, WA at an elevation of 576.8 ft., latitude 45° 44' 00.1" (N), and longitude 121° 49' 10.6" (W) with an observed gravity of 980,575.34 mGals. This was tied to an absolute base station The Dalles AA located in The Dalles, OR at an elevation of 183.7 ft., latitude 45° 37' 31.11" (N), and longitude 121° 13' 31.17" (W) with an observed gravity of 980,599.779 mGals.

Mount St. Helens

297 new gravity stations were collected in the northern Mount St. Helens (MSH) AOI and 184 were collected in the southern in early July 2016. Gravity stations collected in MSH north used base station Mount St. Helens WYGT at the eastern post of the Weyerhaeuser access gate along the Spirit Lake Highway (504) in Cowlitz County at an elevation of 3062.1 ft. latitude 46° 18' 45.6" (N), and longitude 122° 16' 57.0" (W) with an observed gravity of 980,481.80 mGals. The primary base station was tied to absolute station JRO at Mt. St. Helens National Volcanic Monument, Johnston Ridge Volcanic Observatory in Skamania County, WA at an elevation of 4227.1 ft. at latitude 46° 16' 30.900" (N), and longitude 122° 12' 59.835", (W) with an observed gravity value of 980,397.796 mGals.

Gravity stations collected in MSH south used base station "CGPO" located at the U.S Post Office in Cougar, WA at an elevation of 576.8 ft., latitude 46° 02' 58.8" (N), and longitude 122° 18' 13.2" (W) with an observed gravity value of 980,628.49 mGals. The primary base station was tied to absolute base station Q 14 in Portland, OR at an elevation of 34.9 ft., latitude 45° 31' 42.9" (N), and longitude 122° 40' 35.1" (W) with an observed gravity of 980,631.947 mGals.

MAGNETIC DATA

Ground-magnetic data were collected using Geometrics® G858 and G859 cesium vapor magnetometers with integrated Global Positioning Systems (GPS). Magnetic intensity in nanoteslas (nT) and position were recorded simultaneously at 1-second intervals. The height of the magnetometer sensor above the ground surface was about 2 meters. A Geometrics® G856 proton-precession base-station magnetometer was used to record and correct for diurnal variations of the Earth's magnetic field during the time of the surveys. Cultural features (culverts, signs, metal gates, bridges, and vehicles) encountered during the survey were noted and their erroneous signals removed during data processing. Raw magnetic data were filtered using MagMap2000 software to remove cultural noise, correct for diurnal variations recorded by the base station magnetometer and merge the recorded GPS and magnetic data. Magnetic data are provided in Tables 7-9.

Mount Baker, Wind River Valley, Mount St. Helens

A total of ~93 line-km of magnetic data were collected at Mount Baker; 47 km of which were collected in mid July 2016 by the USGS Geophysical Unit of Menlo Park (GUMP) and 46 km were collected from Mid-August to late September 2016 by WWU students. Five new magnetic transects were collected in the MSH AOI and 4 transects were collected in the Wind River Valley AOI from May-early July, 2016.

References

- Bankey, V.A., Cuevas, D., Daniels, A.A., Finn, I., 2002. Hernandez and Project Members, Digital Data Grids for the Magnetic Anomaly Map of North America, USGS (2002), Open-File Report 02-414
- Blakely, R.J., 1995, Potential theory in gravity and magnetic applications: New York, Cambridge University Press, 441 p.
- Blakely, R. J., Wells, R. E., Sherrod, B. L., and Brocher, T. M., 2016, Segmentation of the Cascadia forearc in southwestern Washington-evidence from new potential-field data: AGU Fall Meeting, 12-16 December, abstract # GP34A-04.
- Forson, C., Steely, A.N., Cladouhos, T., Swyer, M., Davatzes, N., Anderson, M., Ritzinger, B., Glen, J., Peacock, J., Schermerhorn, W.W., Burns, E., and Stelling, P., 2017, Geothermal Play-Fairway Analysis of Washington State Prospects: Phase 2 Report and Phase 3 Proposal. Washington State Department of Natural Resources.
- Godson, R.H., and Plouff, Donald, 1988, BOUGUER version 1.0, a microcomputer gravity-terrain-correction program: U.S. Geological Survey Open-File Report 88-644-A, Documentation, 22 p.; 88-644-B, Tables, 61 p., 88-644-C, 5 1/4 - in diskette.
- Hayford, J.F., and Bowie, W., 1912, The effect of topography and isostatic compensation upon the intensity of gravity: U.S. Coast and Geodetic Survey Special Publication no. 10, 132 p.
- Pan-American Center for Earth and Environmental Studies (PACES), 2016, Online gravity data set for the United States: El Paso, University of Texas at El Paso (UTEP). [http://research.utep.edu/paces, accessed May 2016].
- Plouff, D., 1966, Digital terrain corrections based on geographic coordinates [abs.]: Geophysics, v. 31, no. 6, p. 1208.
- Plouff, D., 1977, Preliminary documentation for a FORTRAN program to compute gravity terrain corrections based on topography digitized on a geographic grid: U.S. Geological Survey Open-File Report 77-535, 45 p.
- Plouff, D., 2000, Field estimates of gravity terrain corrections and Y2K-compatible method to convert from gravity readings with multiple base stations to tide- and long-term drift-corrected observations: U.S. Geological Survey Open-File Report 00-140, 35 p.
- U.S Geological Survey, 1982, Aeromagnetic map of parts of the Cascade Range, southwestern Washington and northern Oregon Open-File Report 82-663
- <http://pubs.er.usgs.gov/publication/ofr82663>

PROFILES AND MODELING

Processed gravity and magnetic data were gridded and filtered using Oasis Montaj and forward modeled using the GM-SYS 2D software. Constructed models utilize data extracted from the gravity and magnetic grids (Figures 1-16). The top panel of each model window displays a graph of the observed data as points and the model calculated response as a solid line; the model error is represented by the difference between the calculated and observed (Figures 17-25). The bottom panel displays the model bodies, the lateral extent of the modeled profile, and the depth of each model. The model bodies were assigned densities and susceptibilities based on values determined from rock-property measurements made in the field on outcrops, or from laboratory measurements performed on rock samples. The geometries of the model bodies were made to be consistent with the known surface geology and structure of the region by analysis of geologic maps and cross sections.

TABLES

Phase II Location	File Description	File name	File Location
Mount Baker	Rock Property database provided in csv. or xlxs. format	MB_RockProperties.xlsx	MB>MB_RockProperties

Table 1. Physical property measurements made on samples and outcrops from the Mount Baker study area. Table includes: sample name, rock type, Saturated-bulk densities (g/cc), magnetic susceptibility (SI volume units), Q-factors, and rock type. [see supplemental MB_RockProperties.xls]

Phase II Location	File Description	File name	File Location
Wind River Valley	Rock Property database provided in csv. or xlxs. format	WRV_RockProperties.xlsx	WRV>WRV_RockProperties

Table 2. Physical property measurements made on samples and outcrops from the Wind River Valley study area. Table includes: sample name, rock type, Saturated-bulk densities (g/cc), magnetic susceptibility (SI volume units), Q-factors, and rock type. [see supplemental file MWRV_RockProperties.xls]

Phase II Location	File Description	File name	File Location
Mount St. Helens	Rock Property database provided in csv. or xlxs. format	MSH_RockProperties.xlsx	MSH>MSH_RockProperties

Table 3. Physical property measurements made on samples and outcrops from the Mount St. Helens study area. Table includes: sample name, rock type, Saturated-bulk densities (g/cc), magnetic susceptibility (SI volume units), Q-factors, and rock type [see supplemental file MSH_RockProperties.xls]

Phase II Location	File Description	File name	File Location
Mount Baker	Gravity database provided in csv. or xlxs. format	MB_Gravity.csv	MB>Databases

Table 4. Gravity data collected within the Mount Baker study area. Table includes station name, location (Latitude, Longitude, Elevation), CBA, complete Bouguer anomaly; FAA, free-air anomaly; ISO, isostatic anomaly; OG, observed gravity; SBA, simple Bouguer anomaly; TTC, total terrain correction. Data are on the North American Datum 1927 (NAD27). Elevations are on the North American Vertical Datum 1929 (NAVD29). [see supplemental file MB_Gravity.xls]

Phase II Location	File Description	File name	File Location
Wind River Valley	Gravity database provided in csv. or xlsx. format	WRV_Gravity.csv	WRV>Databases

Table 5. Gravity data collected within the Wind River Valley study area. Table includes station name, location (Latitude, Longitude, Elevation), CBA, complete Bouguer anomaly; FAA, free-air anomaly; ISO, isostatic anomaly; OG, observed gravity; SBA, simple Bouguer anomaly; TTC, total terrain correction. Data are on the North American Datum 1927 (NAD27). Elevations are on the North American Vertical Datum 1929 (NAVD29). [see supplemental file WRV_Gravity.xls]

Phase II Location	File Description	File name	File Location
Mount St. Helens	Gravity database provided in csv. or xlsx. format	Helens_North_Gravity.xlsx	MSH>Databases
Mount St. Helens	Gravity database provided in csv. or xlsx. format	Helens_South_Gravity.xlsx	MSH>Databases

Table 6. Gravity data collected within the Mount St. Helens study area. Table includes station name, location (Latitude, Longitude, Elevation), CBA, complete Bouguer anomaly; FAA, free-air anomaly; ISO, isostatic anomaly; OG, observed gravity; SBA, simple Bouguer anomaly; TTC, total terrain correction. Data are on the North American Datum 1927 (NAD27). Elevations are on the North American Vertical Datum 1929 (NAVD29). [see supplemental file Helens_North_Gravity.xls & Helens_South_Gravity.xls]

Phase II Location	File Description	File name	File Location
Mount Baker	Magnetic database provided in csv. or xlsx. format	MB_Magnetic_Surveys.csv	MB>Databases

Table 7. Ground magnetic data collected within the Mount Baker study area. Table includes: Latitude, Longitude, Elevation, Line number, Total Field anomaly (in nanotesla). Data are on the North American Datum 1983 (NAD83). Elevations are on the North American Vertical Datum 1929 (NAVD29) [see supplemental file MB_Magnetic_Surveys.csv]

Phase II Location	File Description	File name	File Location
Wind River Valley	Magnetic database provided in csv. or xlsx. format	WRV_Magnetic_Surveys.csv	WRV>Databases

Table 8. Ground magnetic data collected within the Wind River Valley study area. Table includes: Latitude, Longitude, Elevation, Line number, Total Field anomaly (in nanotesla). Data are on the North American Datum 1983 (NAD83). Elevations are on the North American Vertical Datum 1929 (NAVD29) [see supplemental file WRV_Magnetic_Surveys.csv]

Phase II Location	File Description	File name	File Location
Mount St. Helens	Rock Property database provided in csv. or xlsx. format	MSH_RockProperties.xlsx	MSH>MSH_RockProperties

Table 9. Ground magnetic data collected within the Mount St. Helens study area. Table includes: Latitude, Longitude, Elevation, Line number, Total Field anomaly (in nanotesla). Data are on the North American Datum 1983 (NAD83). Elevations are on the North American Vertical Datum 1929 (NAVD29) [see supplemental file MSH_Magnetic_Surveys.csv]

FIGURES

Wind River Valley

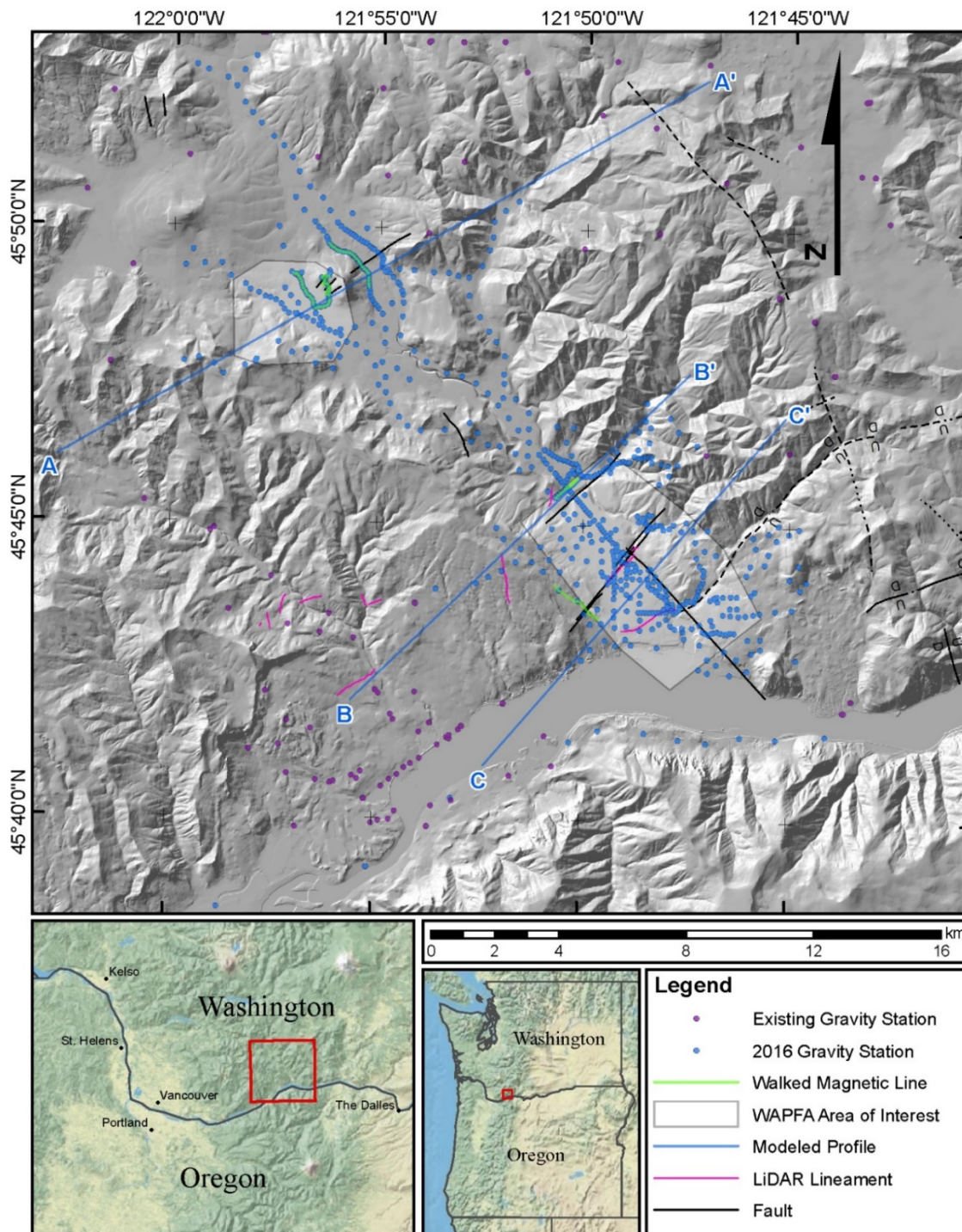


Figure 1. Location of gravity stations, walked magnetic lines, Lineaments and modeled profiles within the Wind River Valley AOI.

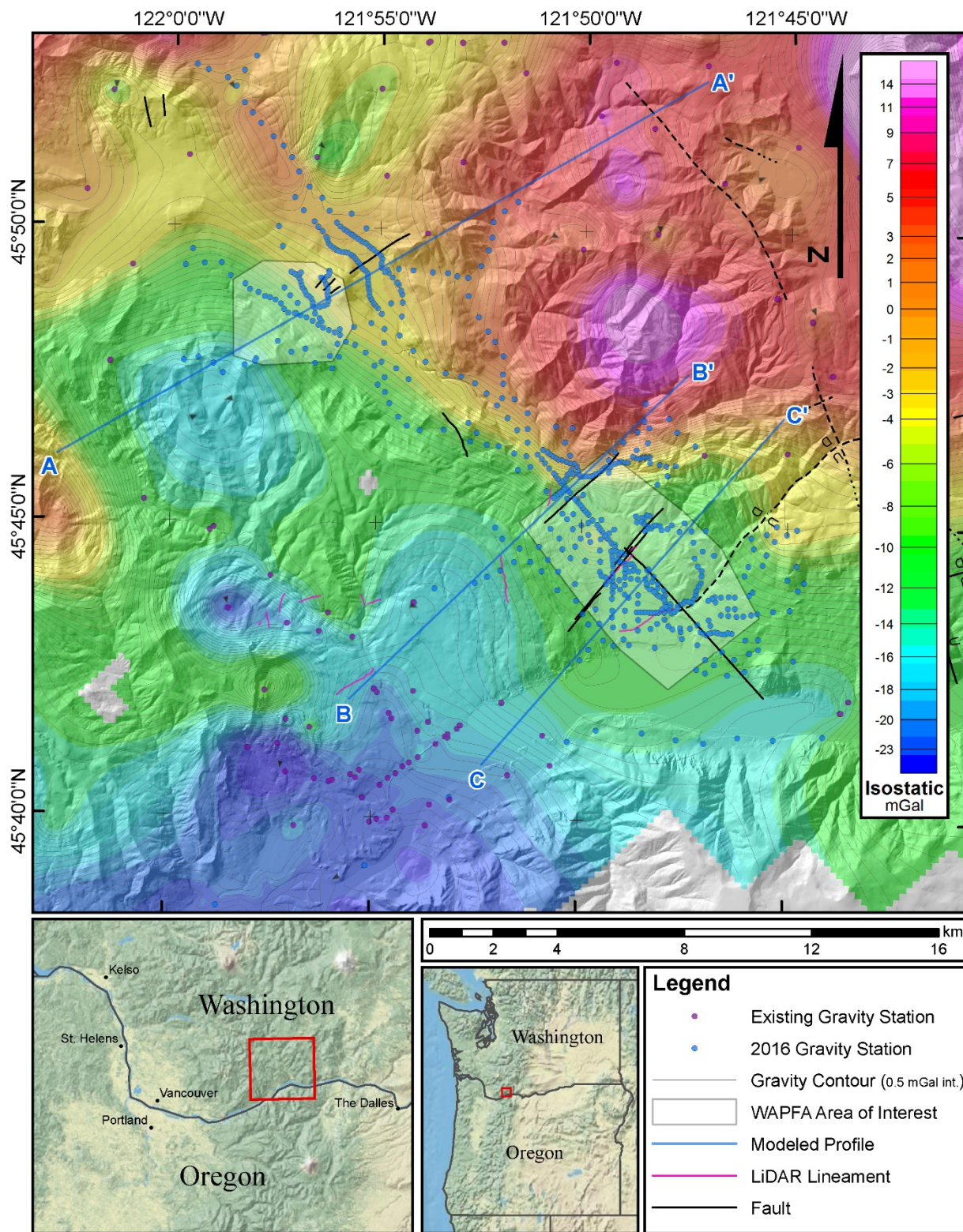


Figure 2. Isostatic gravity grid with contours, units in milligals produced from stations collected during this study and pre-existing stations.

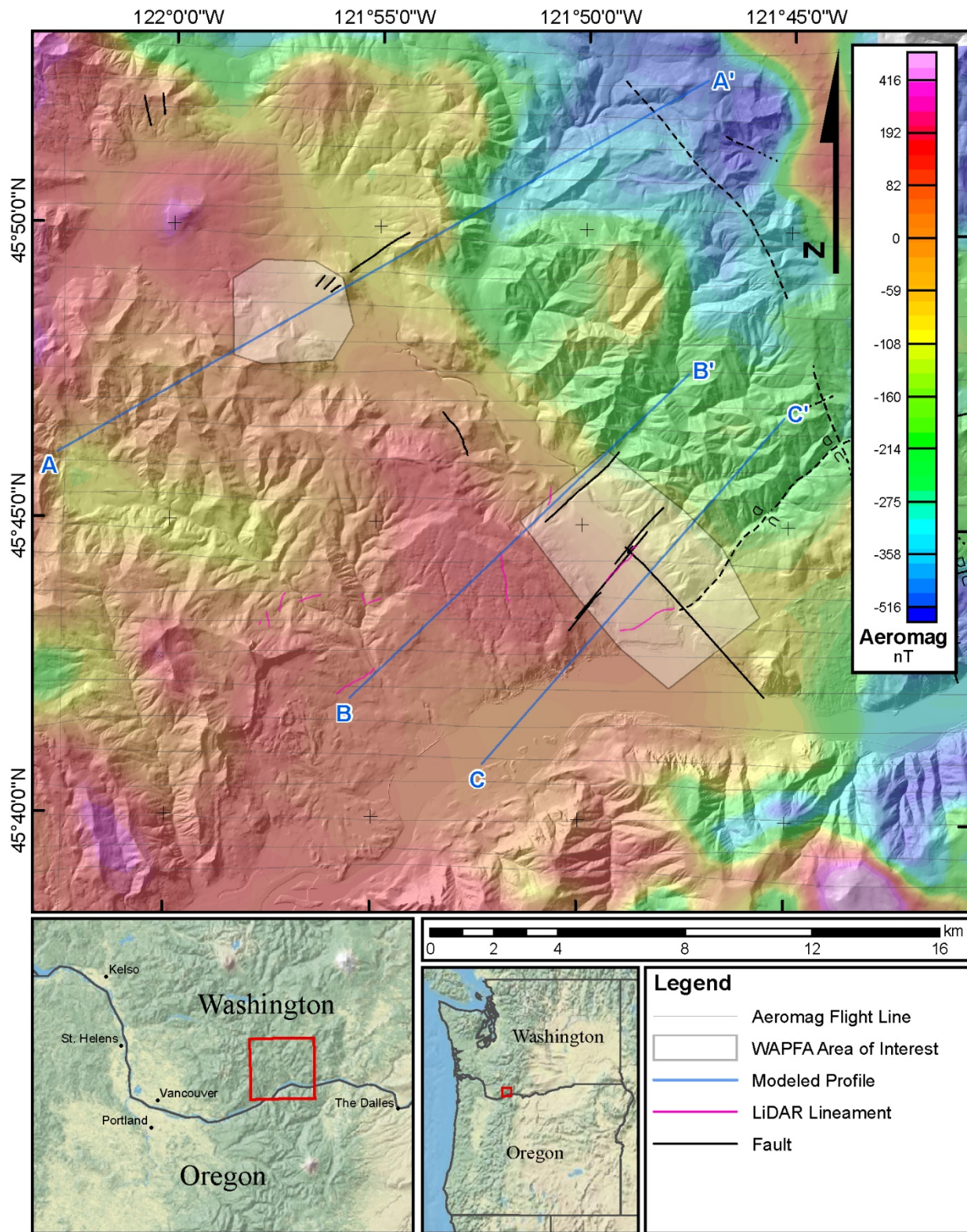


Figure 3. Reduced to Pole, Residual Aeromagnetic data flown in 1982. Flight lines included. (U.S Geological Survey, 1982)

Mount Baker

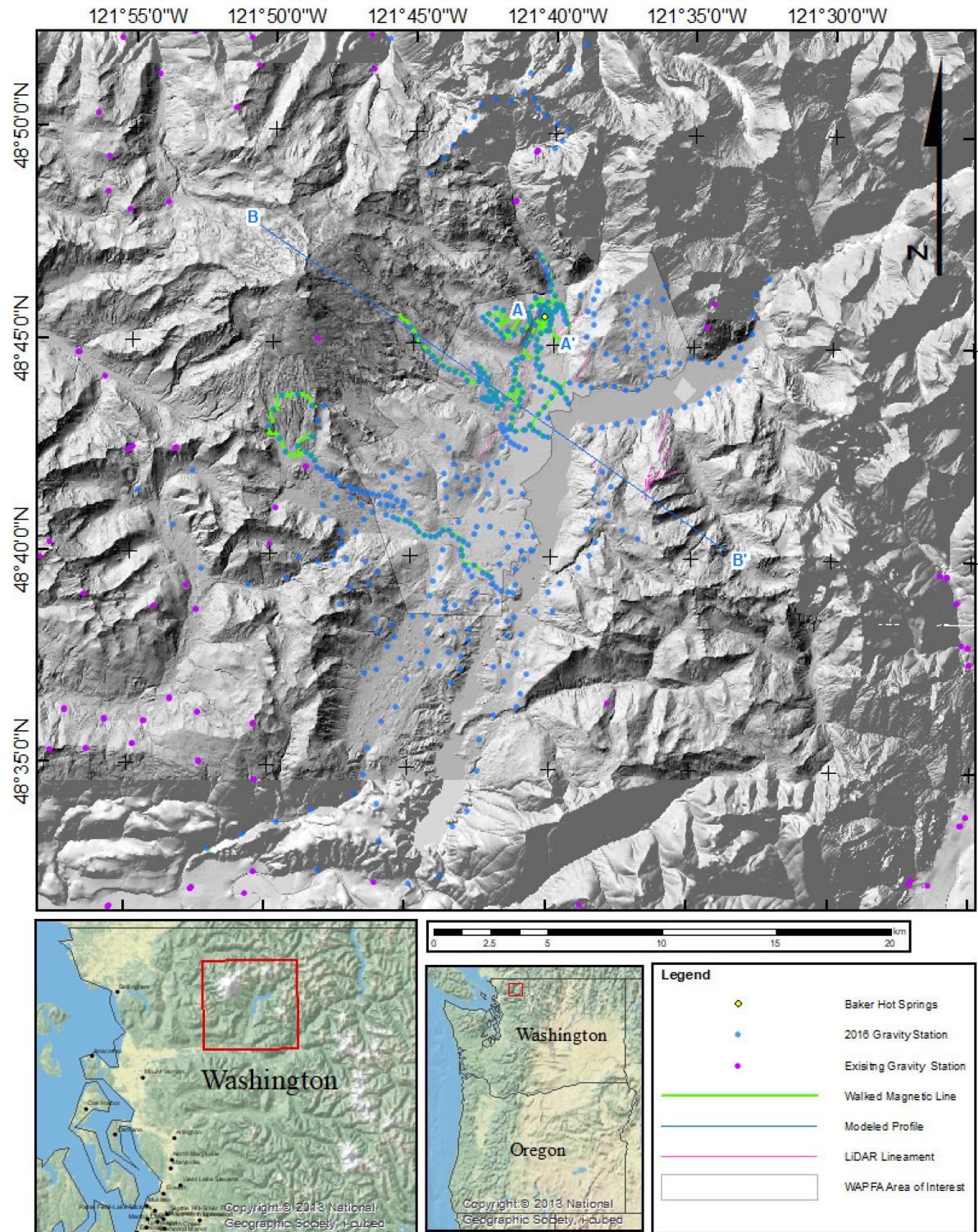


Figure 4. Location of gravity stations, walked magnetic lines, LIDAR lineaments, and modeled profiles across the Mount Baker study area.

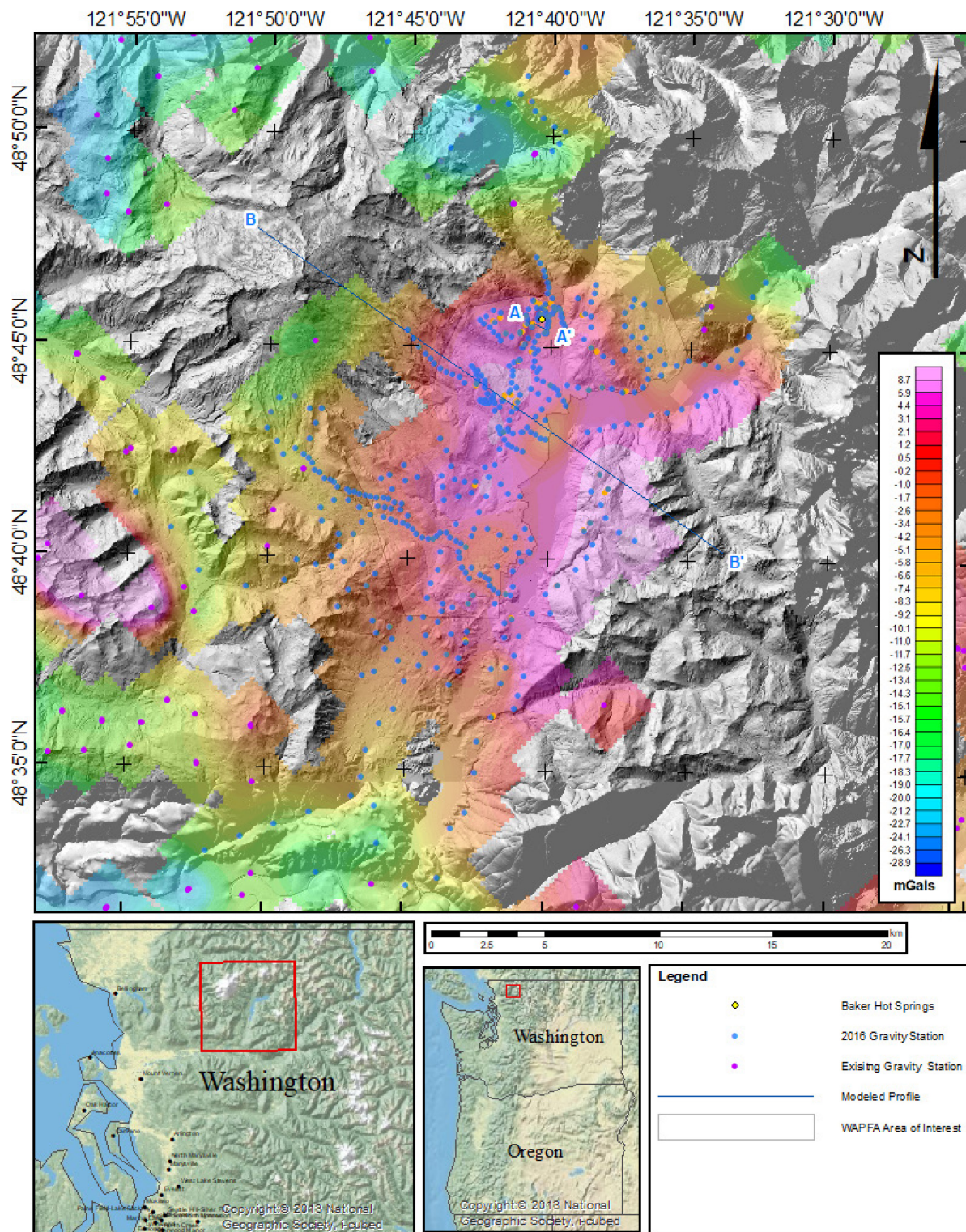


Figure 5. Isostatic gravity grid with contours produced from stations collected during this study and pre-existing stations across the Mount Baker study area.

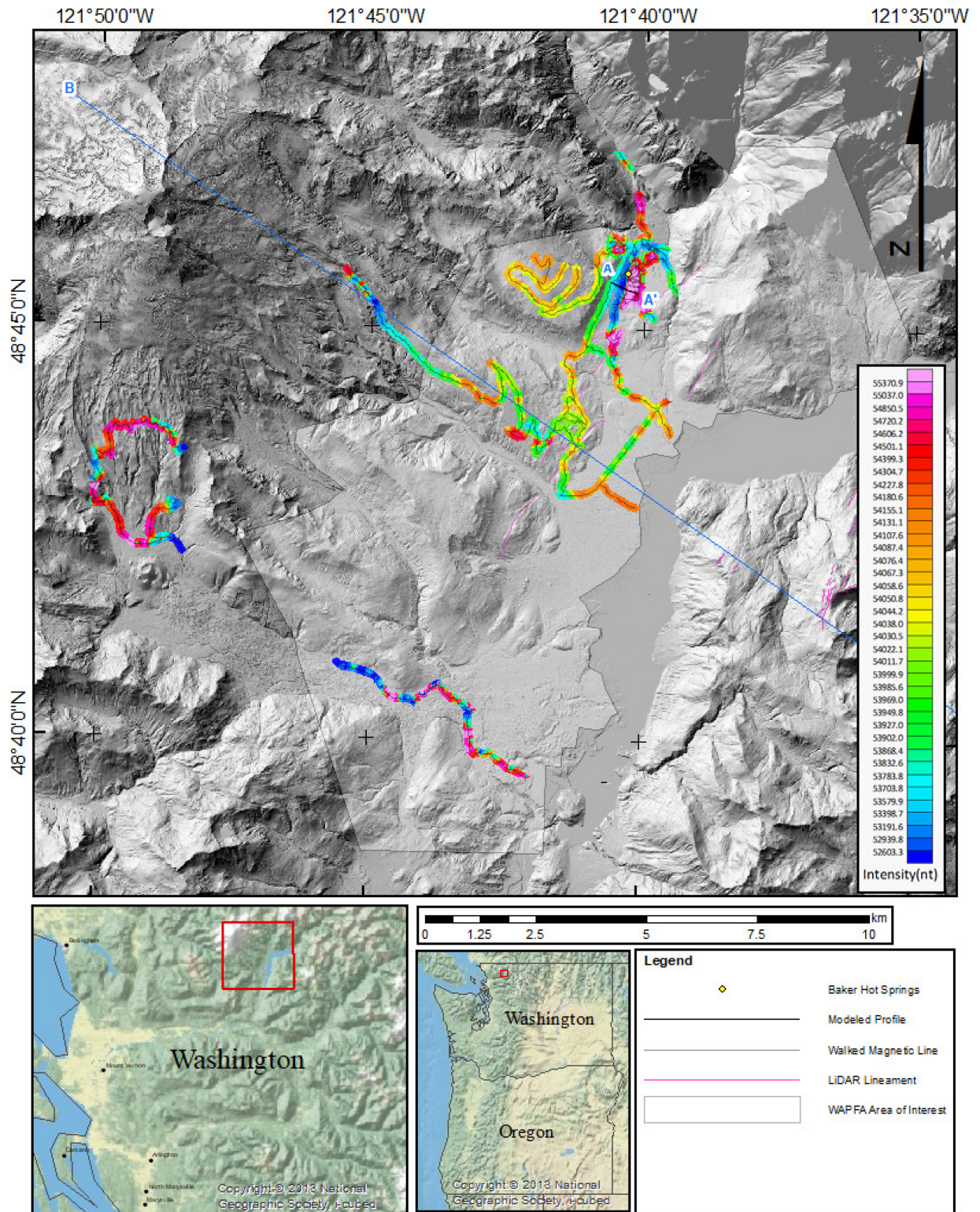


Figure 6 Total field magnetics produced from walked magnetic surveys (grid values in nanoteslas) collected within the Mount Baker study area.

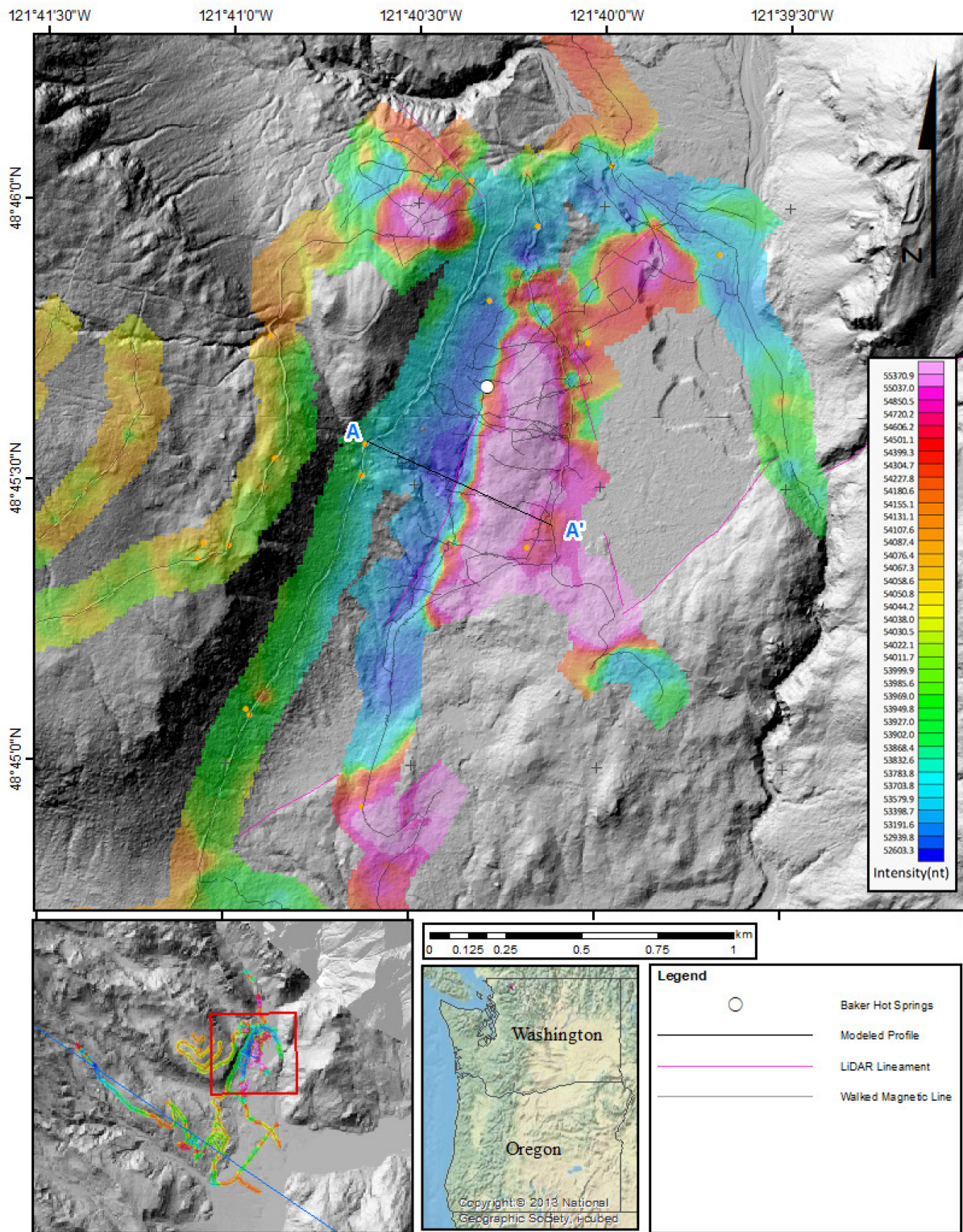


Figure 7. Grid of ground-magnetic data collected in the vicinity of the Baker Hot Springs Area of Interest. Profile A-A' corresponds the location of modeled cross-section shown in Figure 20.

Mount St. Helens North & South

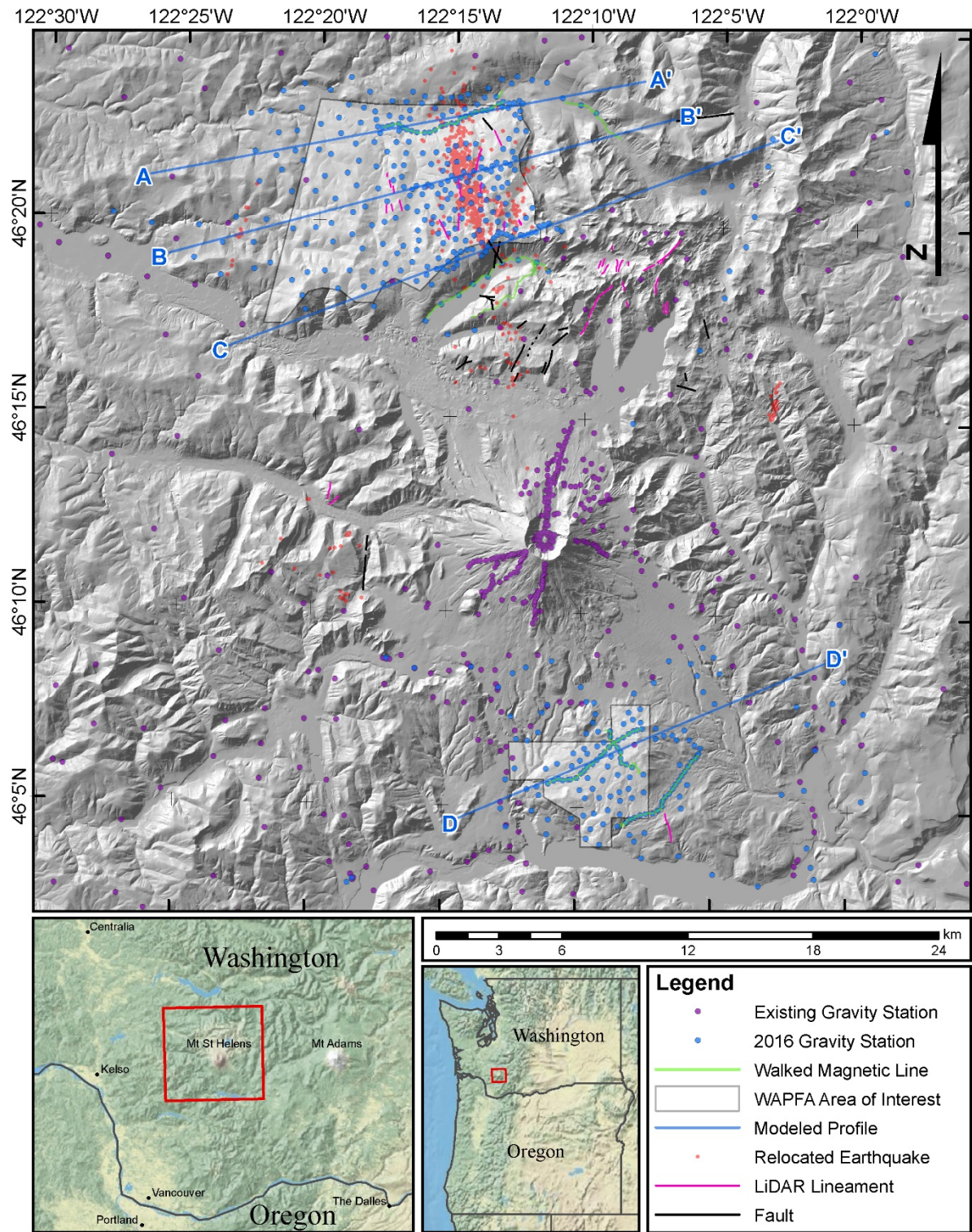


Figure 8. Location of gravity stations, walked magnetic lines, and modeled profiles across Northern and Southern Areas of Interest.

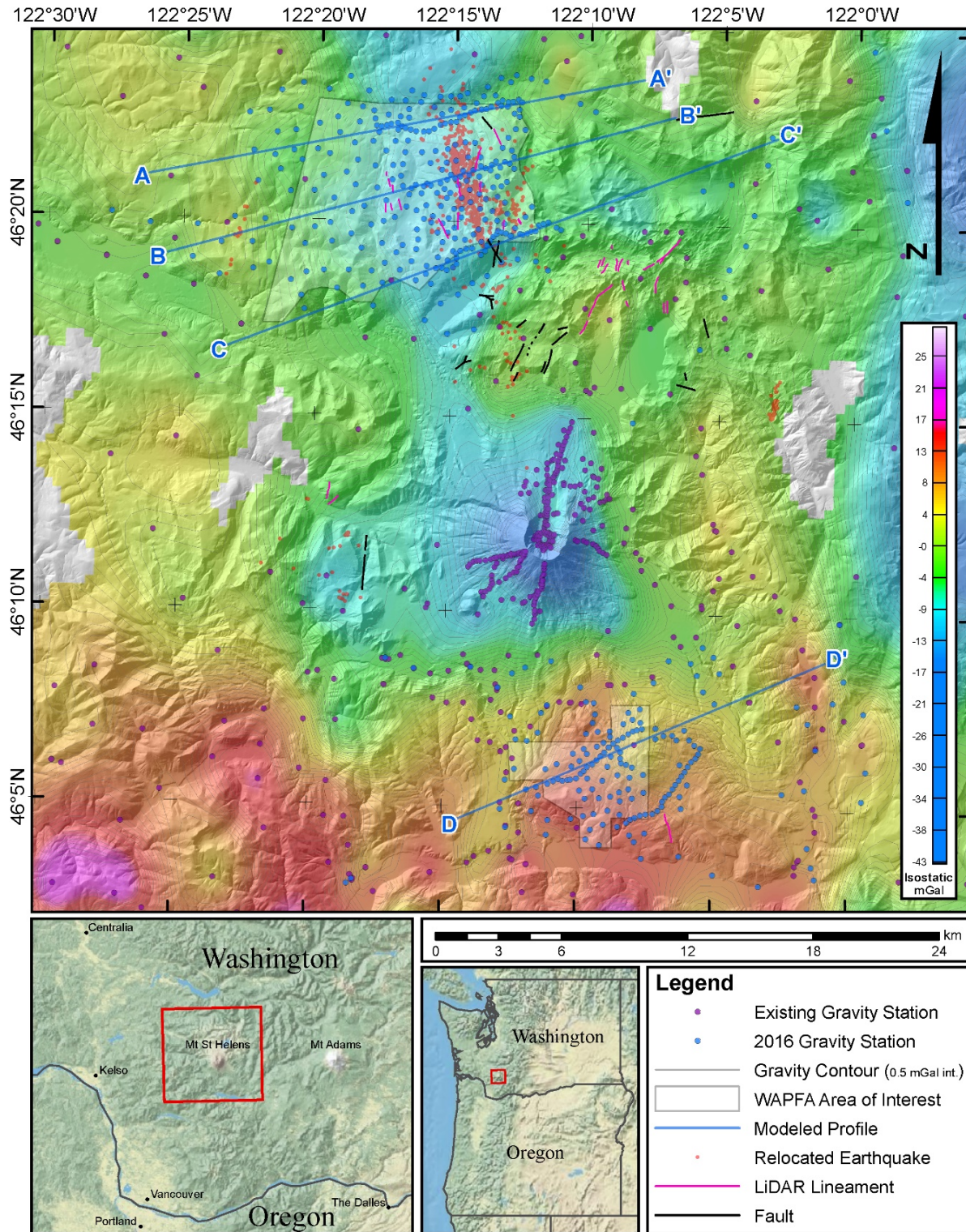


Figure 9. Isostatic gravity grid with contours, produced from stations collected during this study and pre-existing stations across Northern and Southern Areas of Interest.

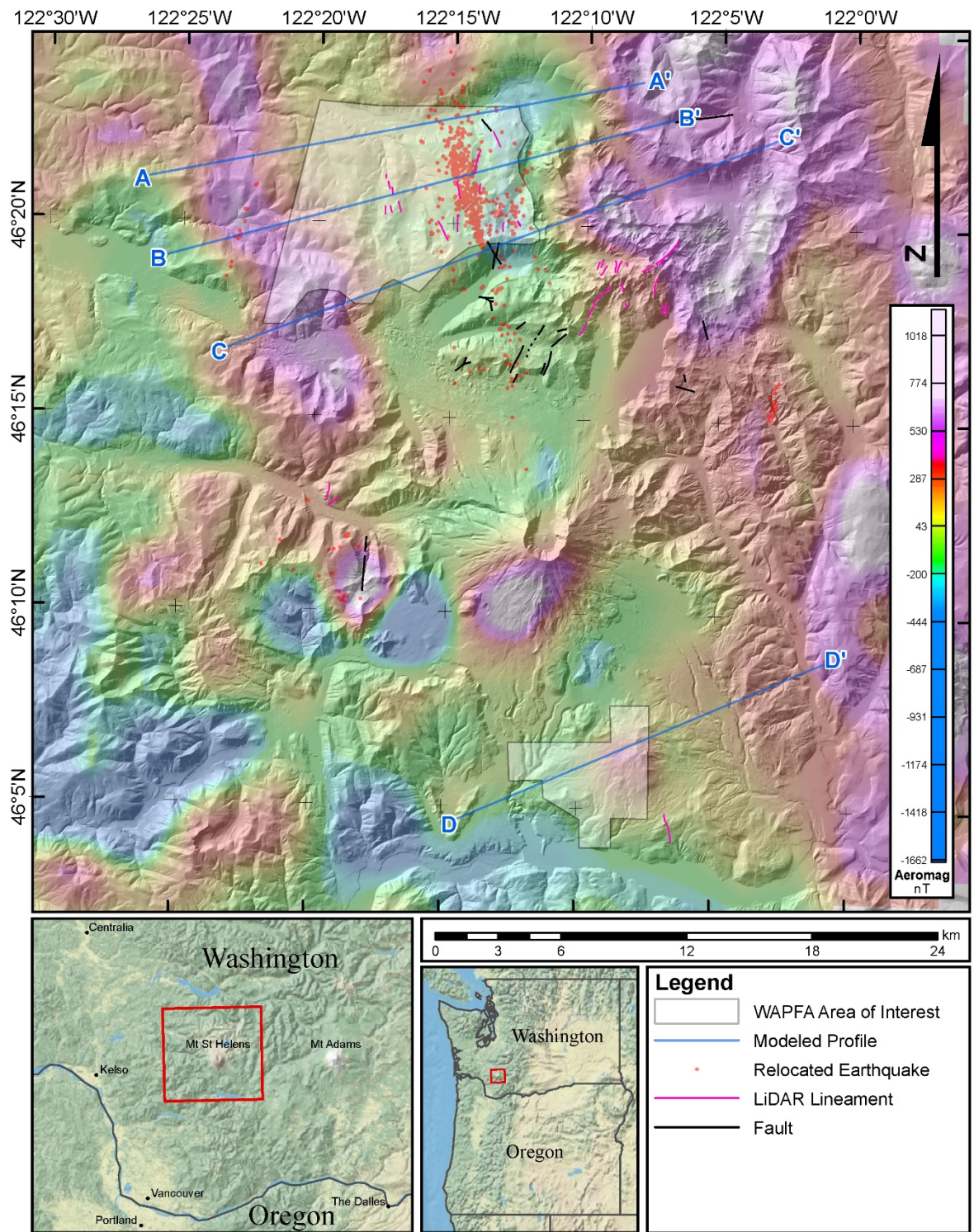


Figure 10. Reduced to Pole, Residual Aeromagnetic data for regional airborne survey flown in 1981 across Northern and Southern Areas of Interest (Blakely et al. 2016; Bankey et al. 2002).

Mount St. Helens Northern AOI

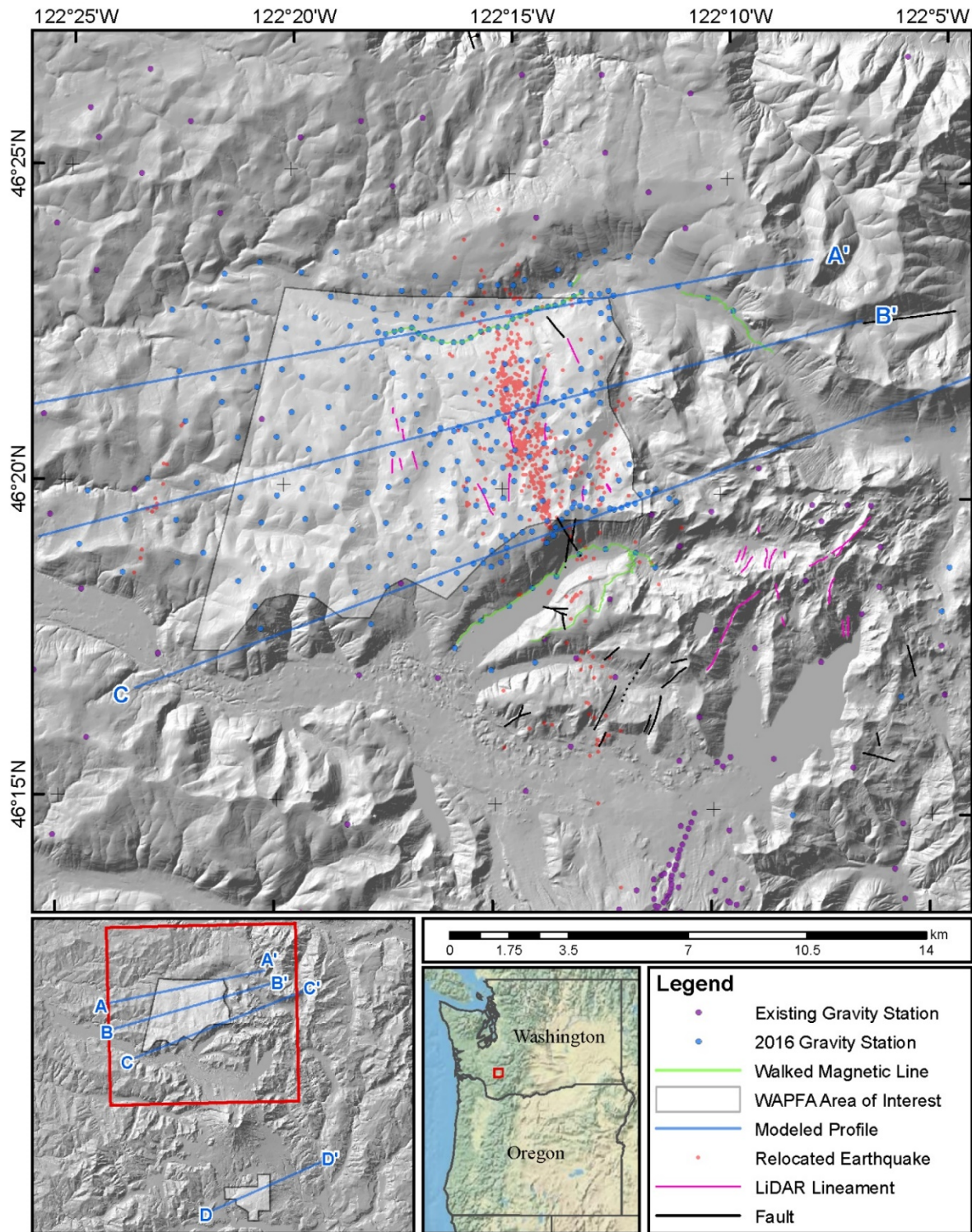


Figure 11. Location of gravity stations, walked magnetic lines, and modeled profiles within the Northern Area of Interest.

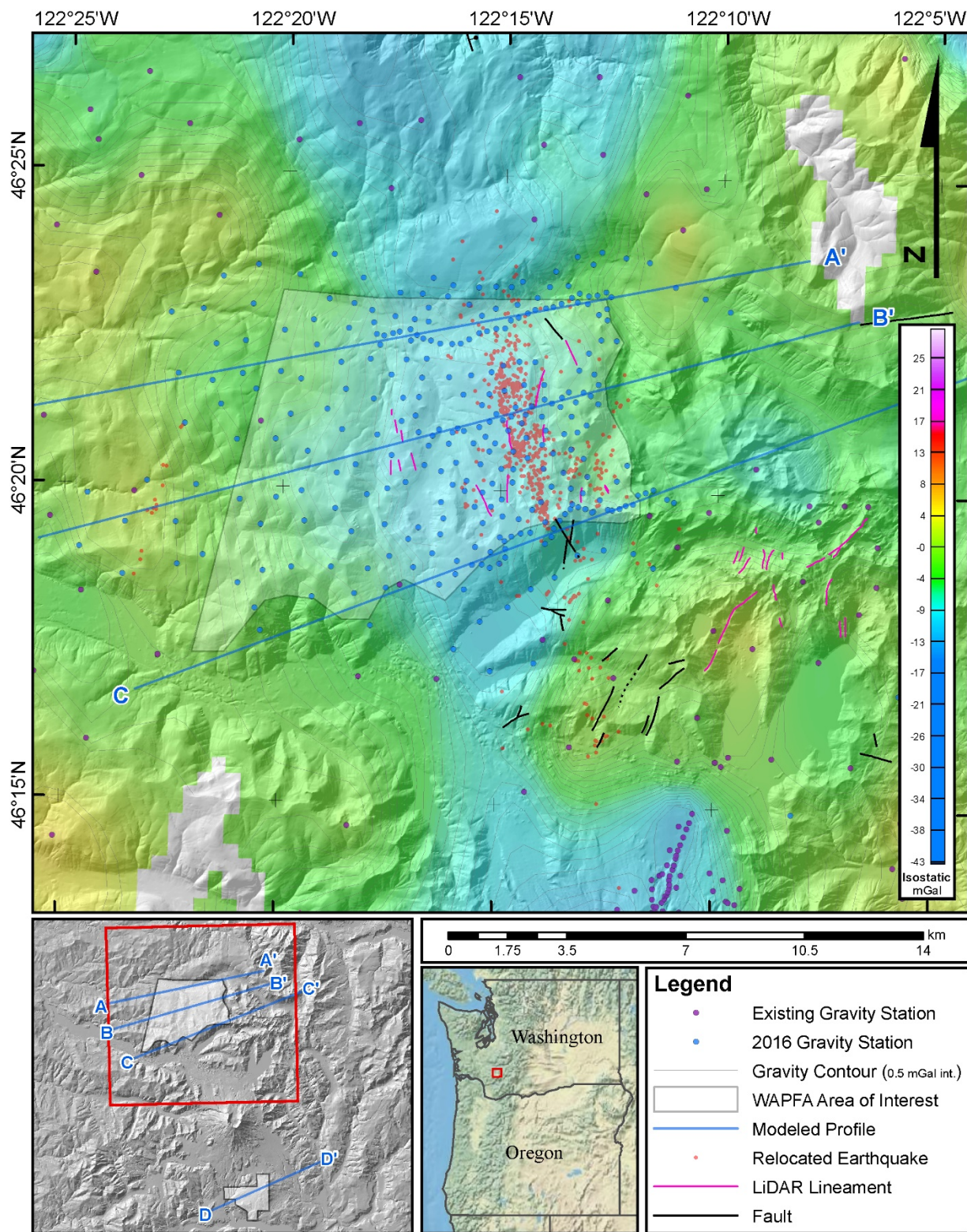


Figure 12. Isostatic gravity grid with contours, units in milligals produced from stations collected during this study and from pre-existing stations within the Northern Area of Interest.

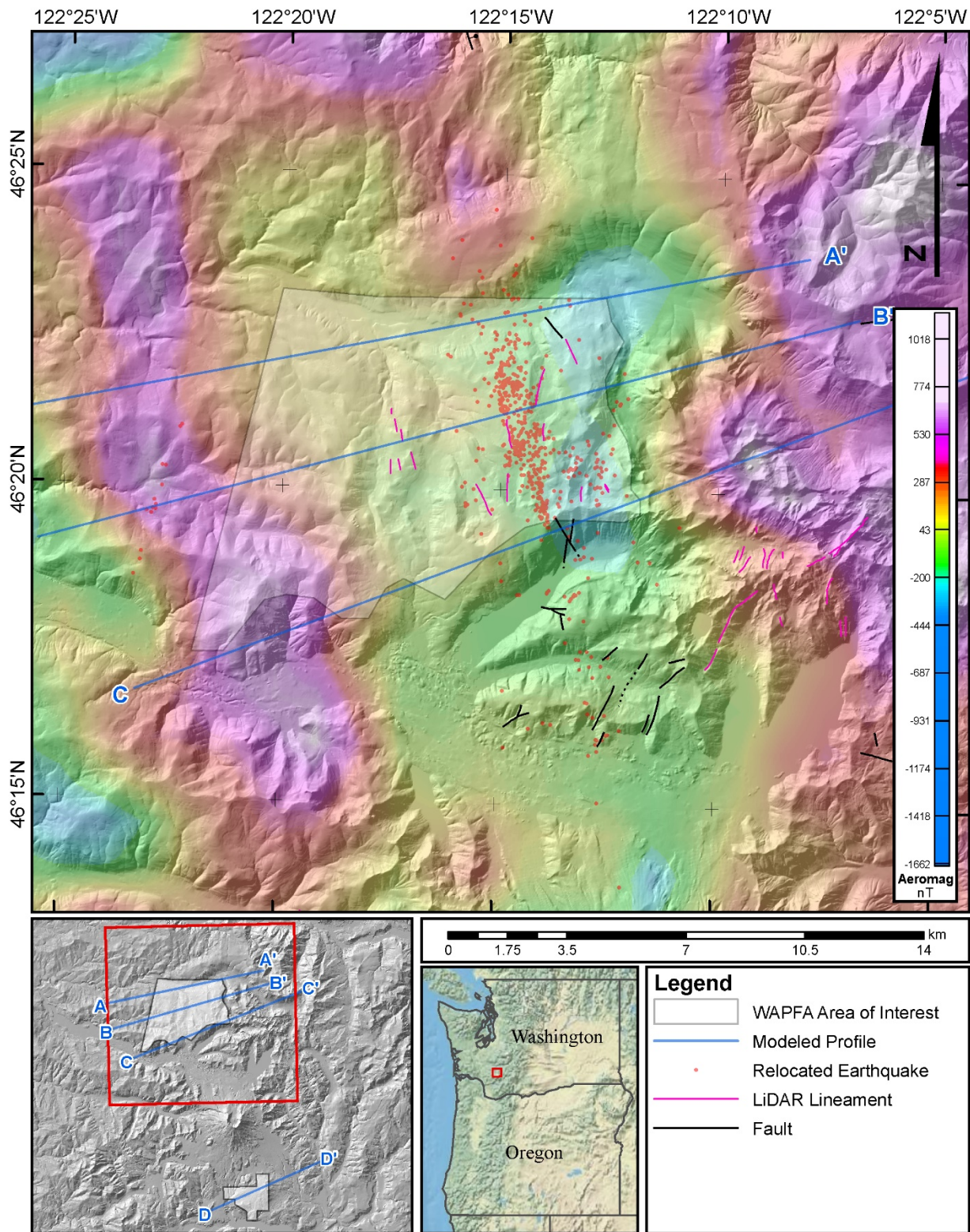


Figure 13. Reduced to Pole, Residual Aeromagnetic data within the Northern Area of Interest (Blakely et al. 2016).

Mount St. Helens Southern AOI

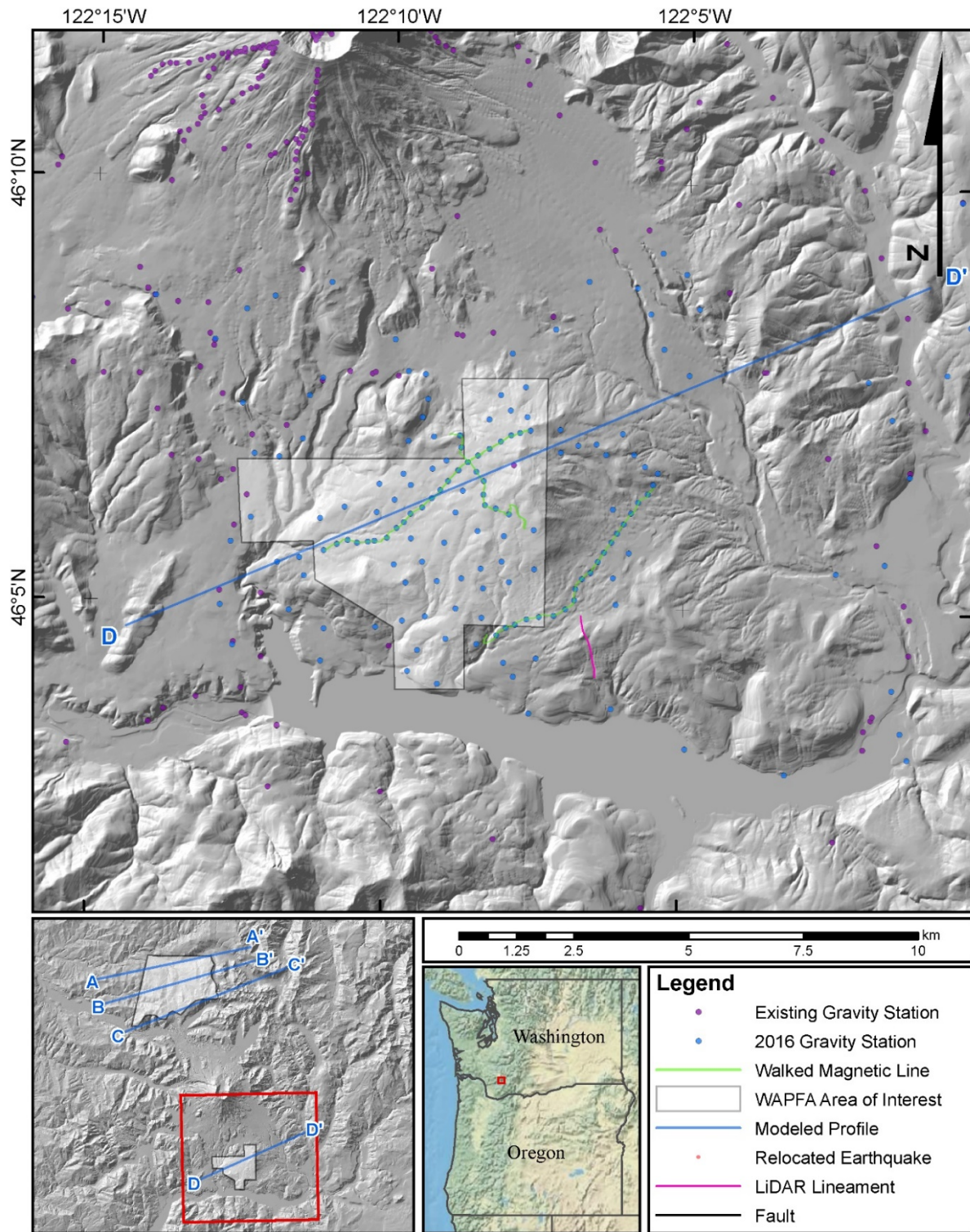


Figure 14. Location of gravity stations, walked magnetic lines, and modeled profiles within Southern Area of Interest.

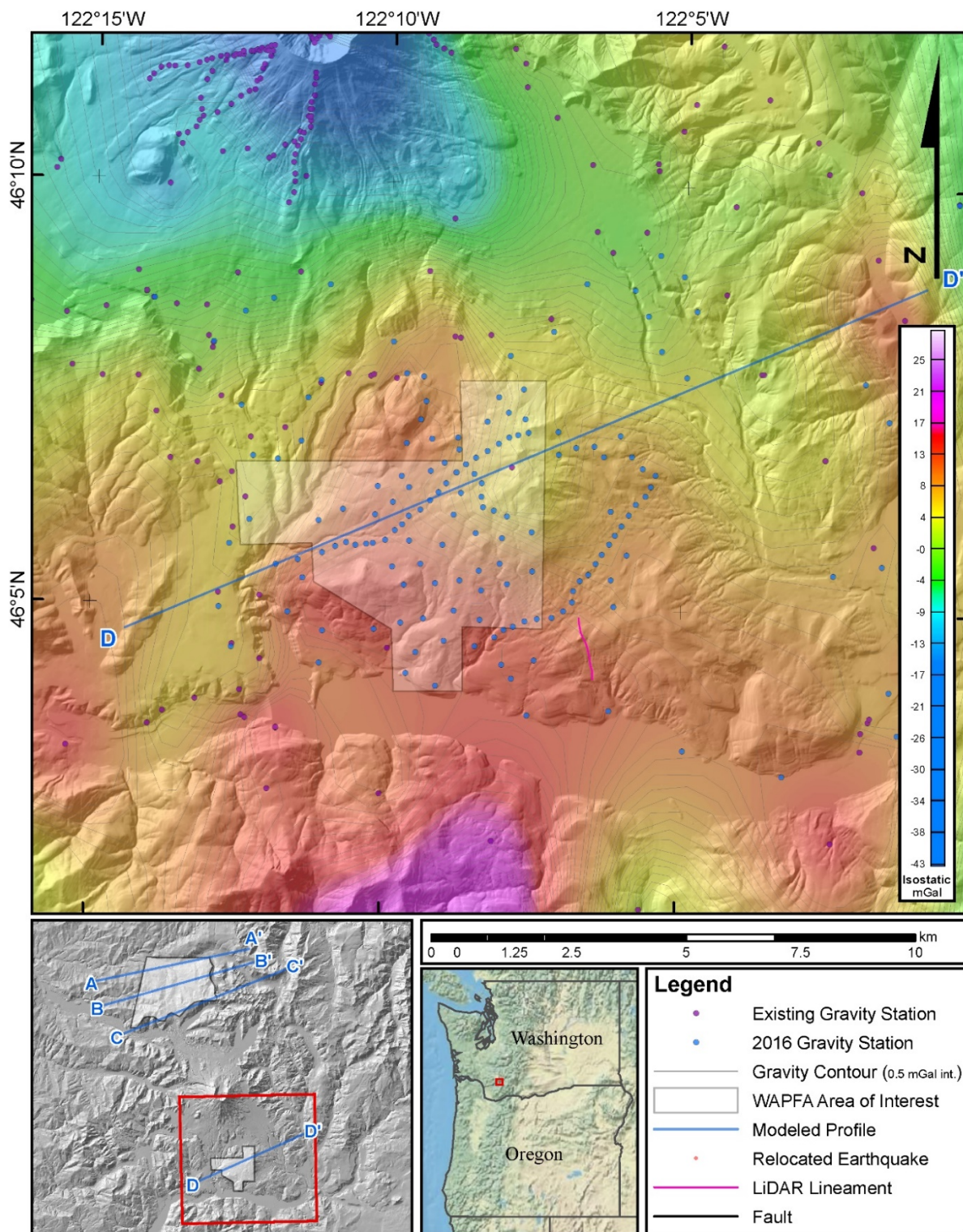


Figure 15. Isostatic gravity grid with contours, units in milligals produced from stations collected during this study and from pre-existing stations within Southern Area of Interest.

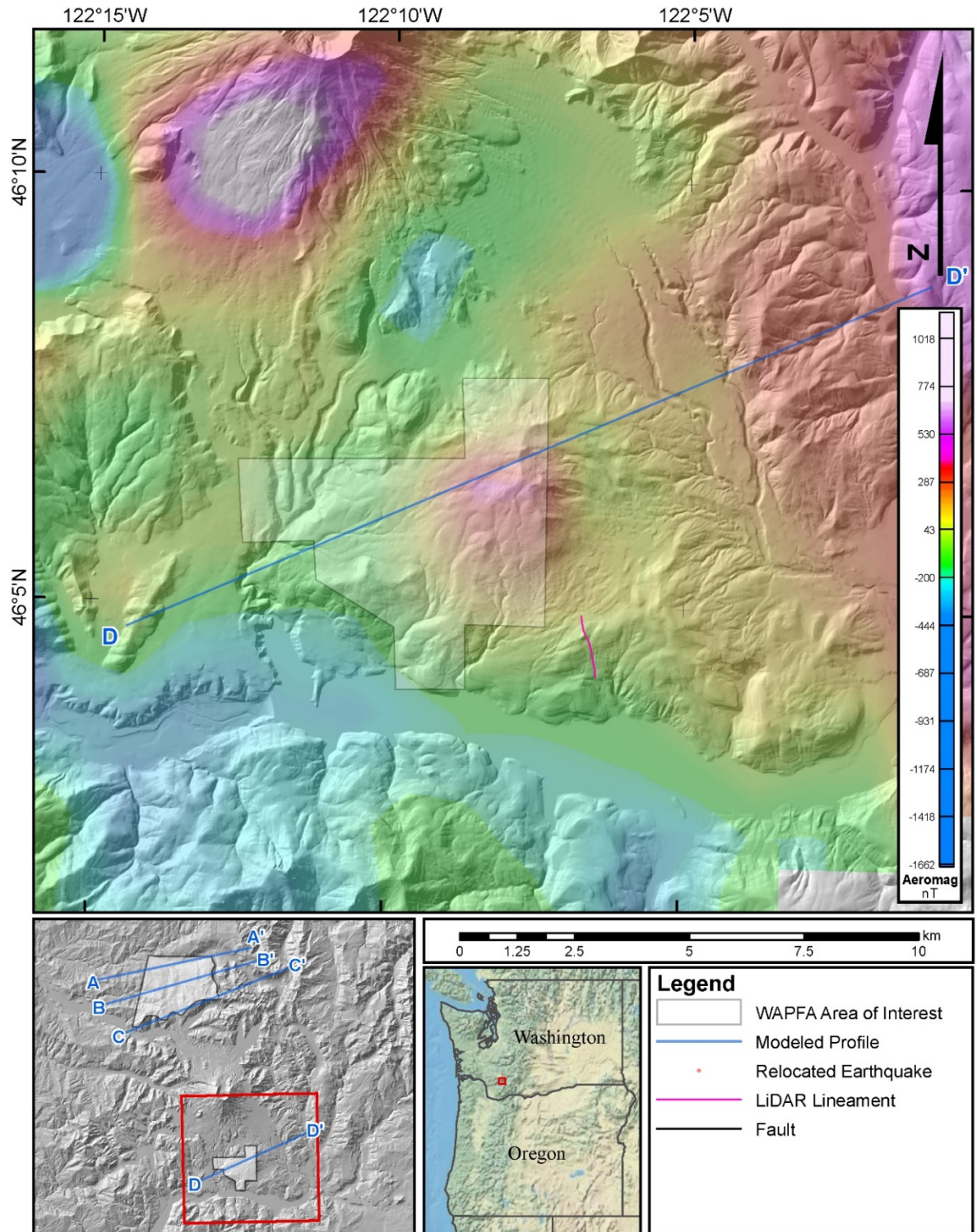


Figure 16. Reduced to Pole, Residual Aeromagnetic data within the Southern Area of Interest (Bankey et al. 2002).

Modeled Profiles: Wind River Valley

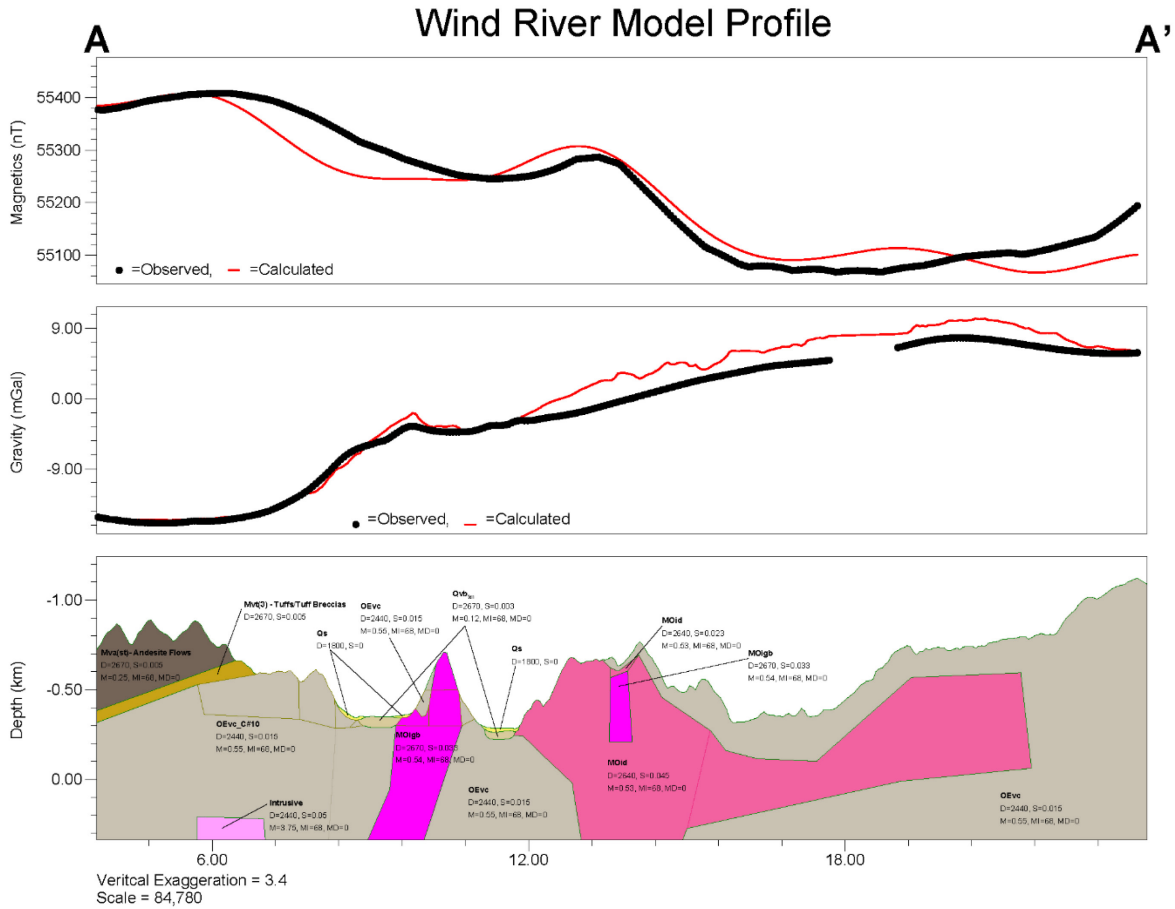


Figure 17. 2D Potential field model along profile AA' in the Wind River study area. Panels show observed (black circles) and model (red line) anomalies for magnetic (top) and gravity (middle) fields, and potential field model with individual model bodies colored by rock unit (bottom). Profile location shown on Figure 1.

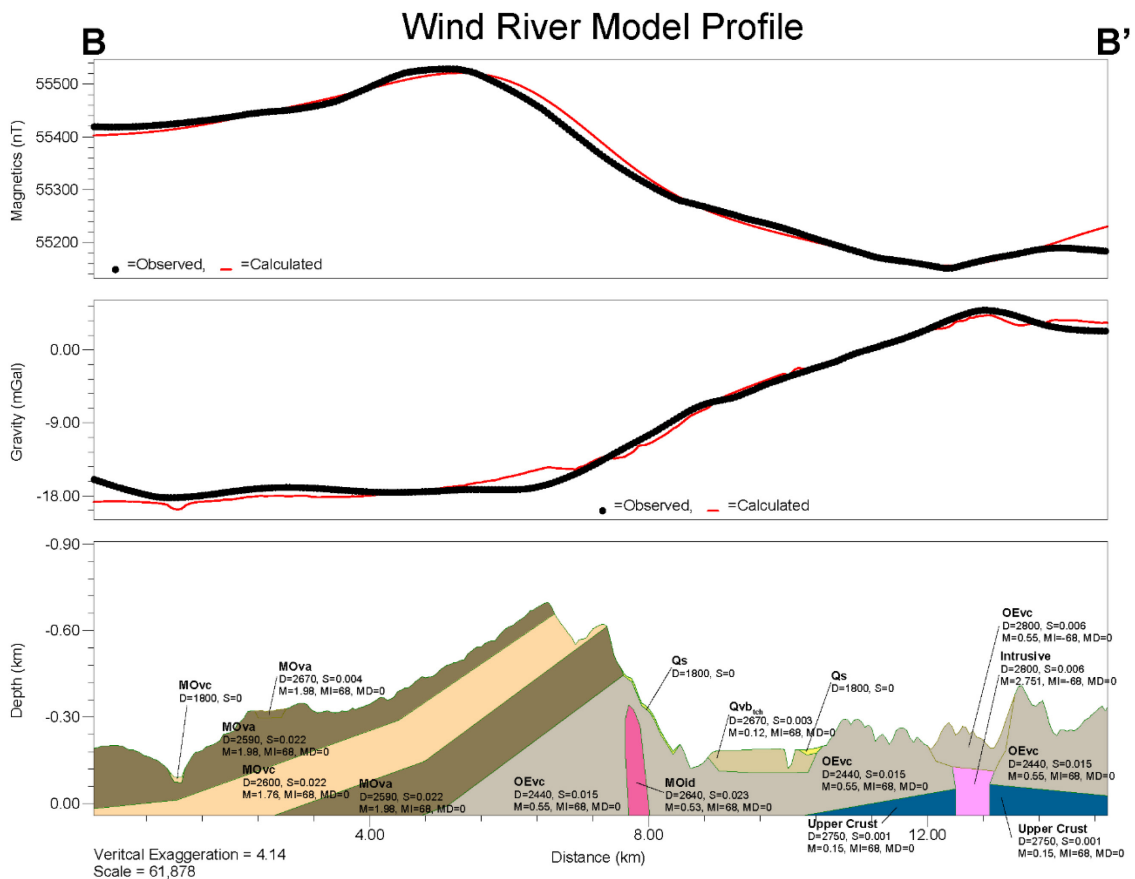


Figure 18. 2D Potential field model along profile BB' in the Wind River study area. Panels show observed (black circles) and model (red line) anomalies for magnetic (top) and gravity (middle) fields, and potential field model with individual model bodies colored by rock unit (bottom). Profile location shown on Figure 1.

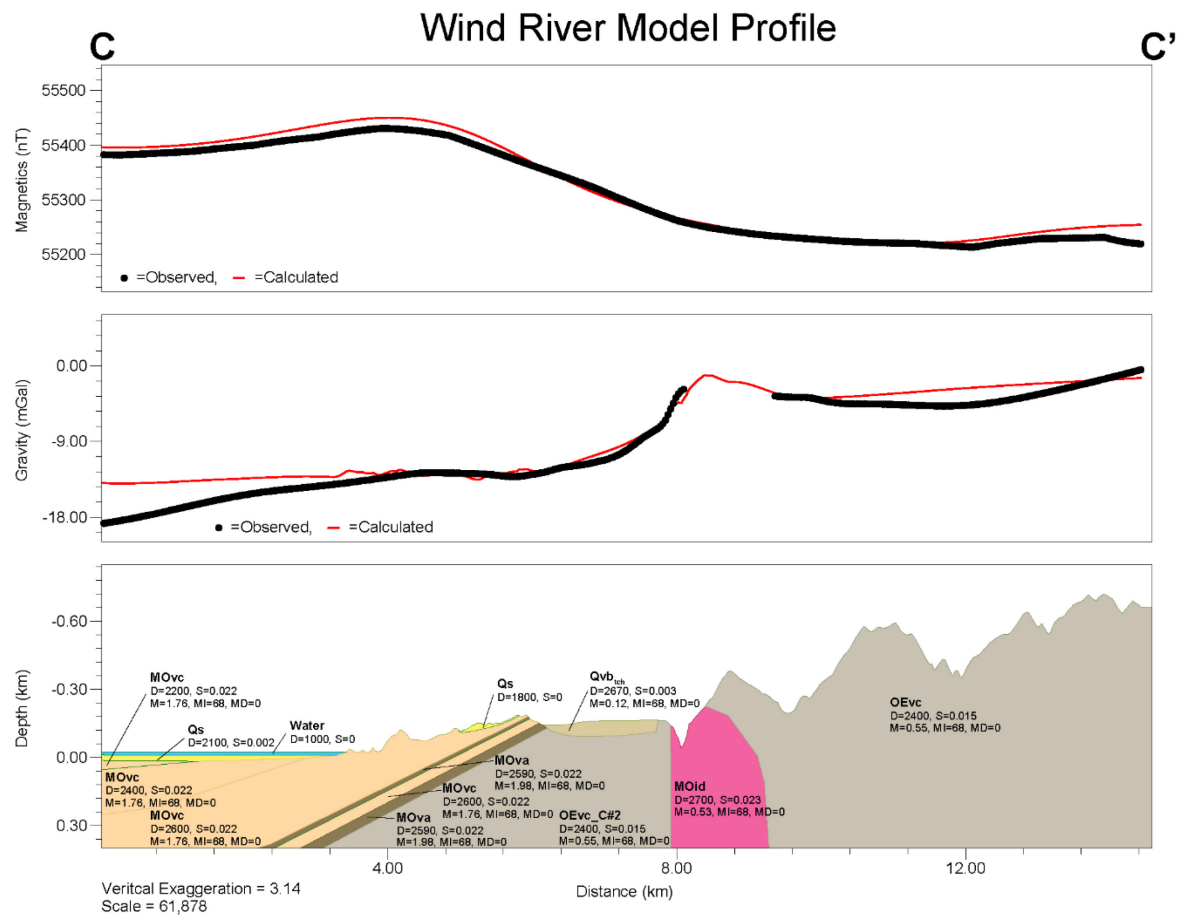


Figure 19. 2D Potential field model along profile CC' in the Wind River study area. Panels show observed (black circles) and model (red line) anomalies for magnetic (top) and gravity (middle) fields, and potential field model with individual model bodies colored by rock unit (bottom). Profile location shown on Figure 1.

Modeled Profiles: Mount Baker

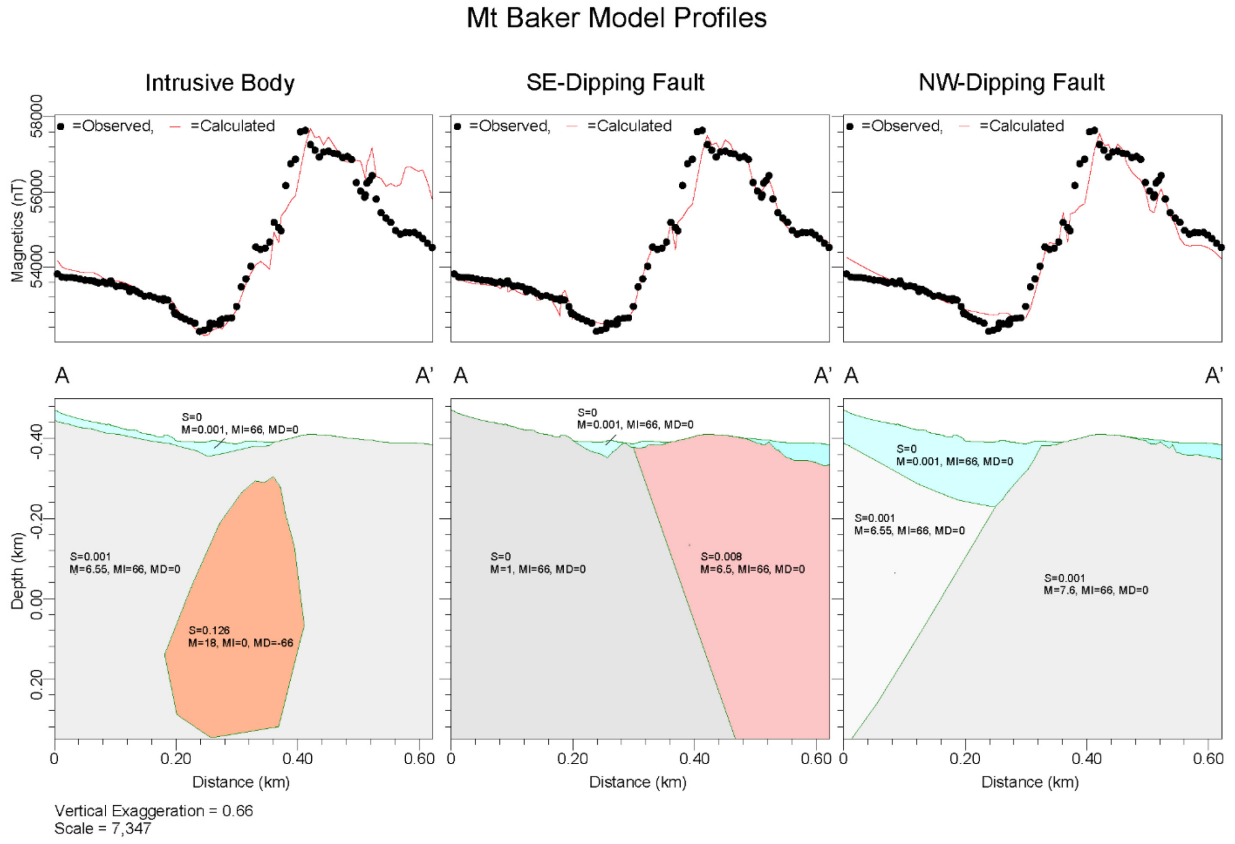


Figure 20. Three different 2D Potential field models along profile AA' in the Mount Baker study area. Top panels show observed (black circles) and model (red line) magnetic anomalies. Lower panels display potential field models with individual model bodies colored by rock unit. Profile location shown on Figures 4 and 7.

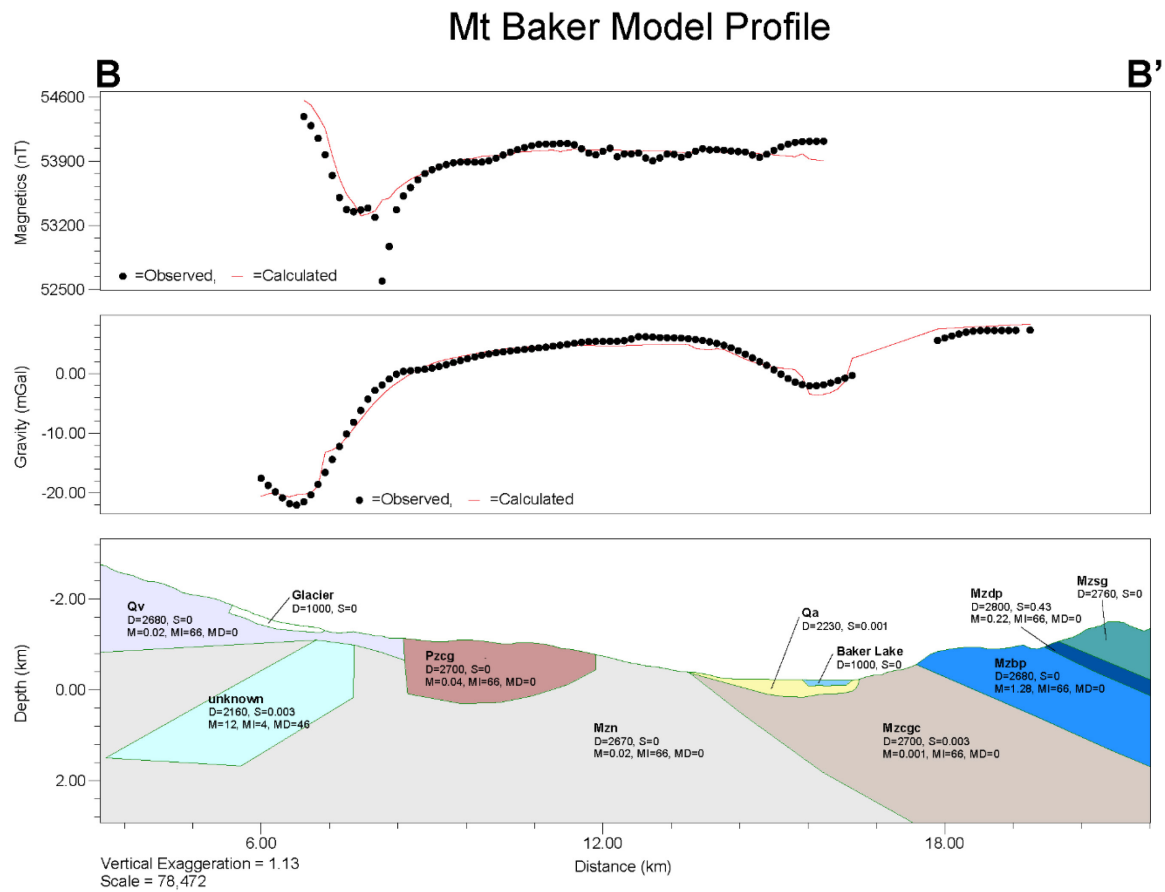


Figure 20. 2D Potential field model along profile BB' in the Mount Baker study area. Panels show observed (black circles) and model (red line) anomalies for magnetic (top) and gravity (middle) fields, and potential field model with individual model bodies colored by rock unit (bottom). Profile location shown on Figure 4.

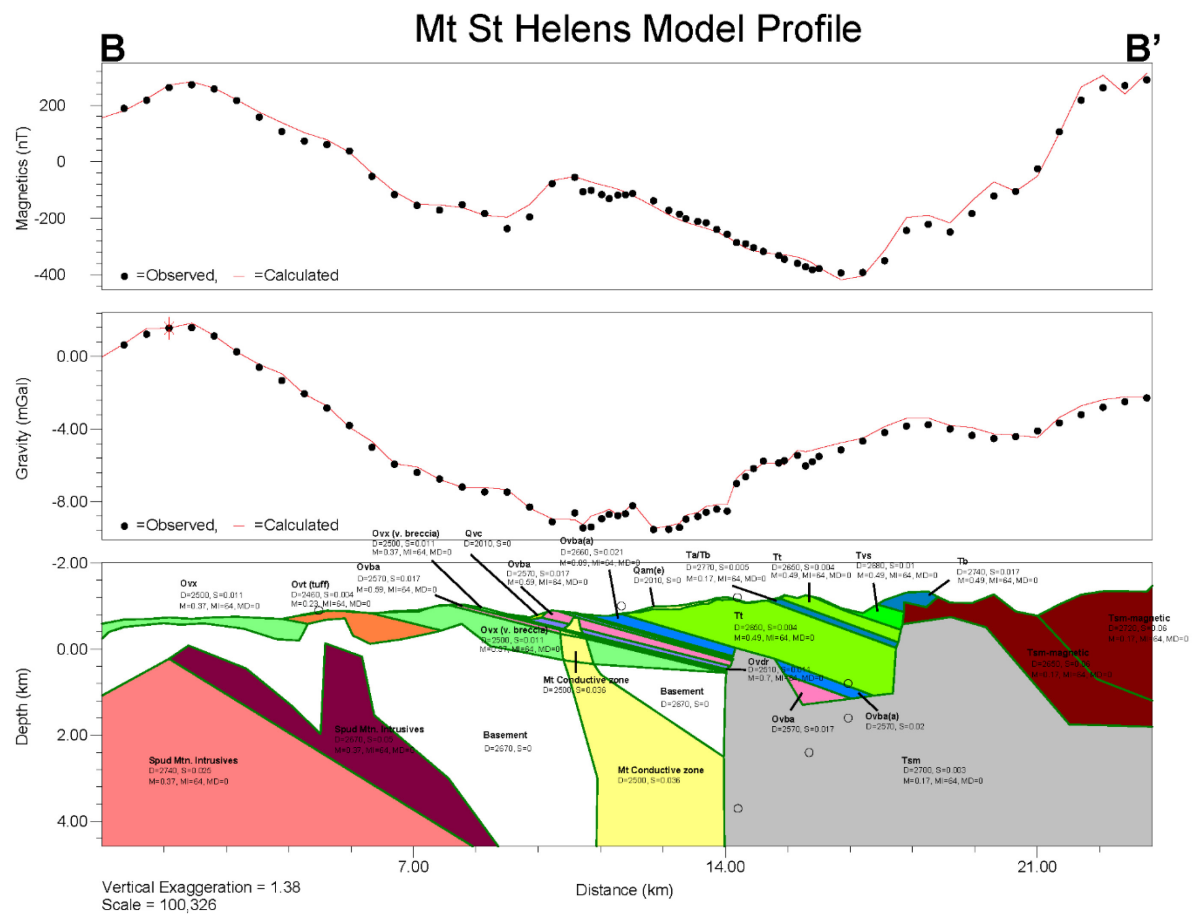
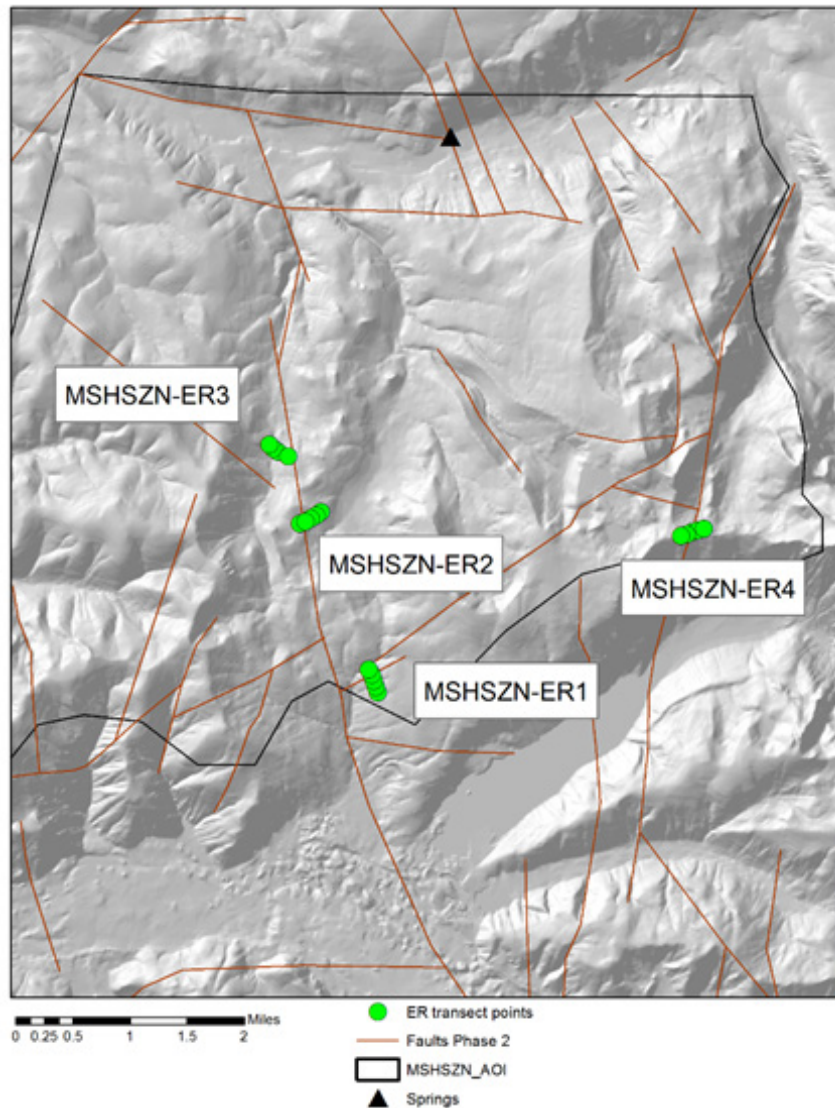
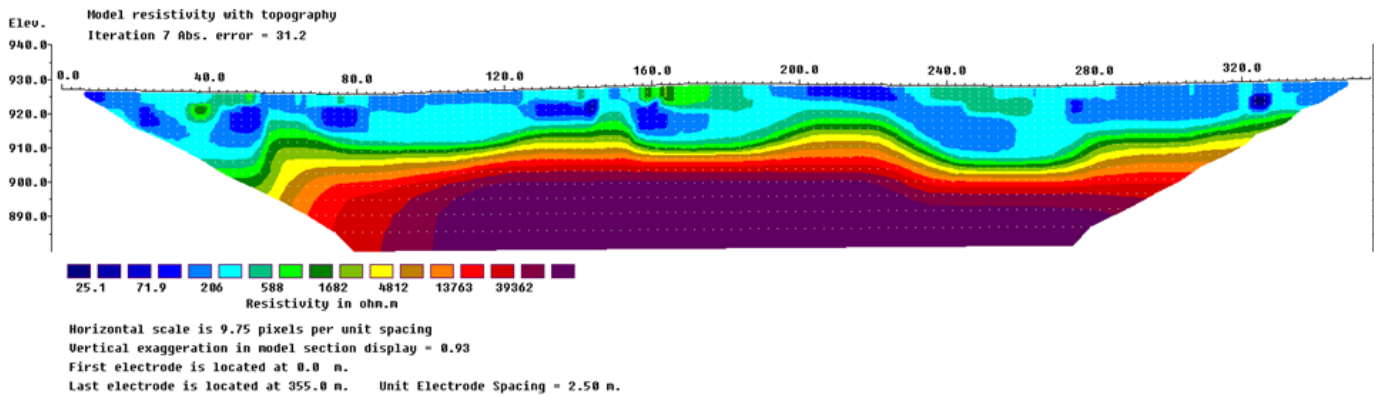


Figure 22. 2D Potential field model along profile BB' in the Mount St. Helens study area. Panels show observed (black circles) and model (red line) anomalies for magnetic (top) and gravity (middle) fields, and potential field model with individual model bodies colored by rock unit (bottom). Open circles are earthquake hypocenters from the PNSN catalog. Profile location shown in Figure 8.

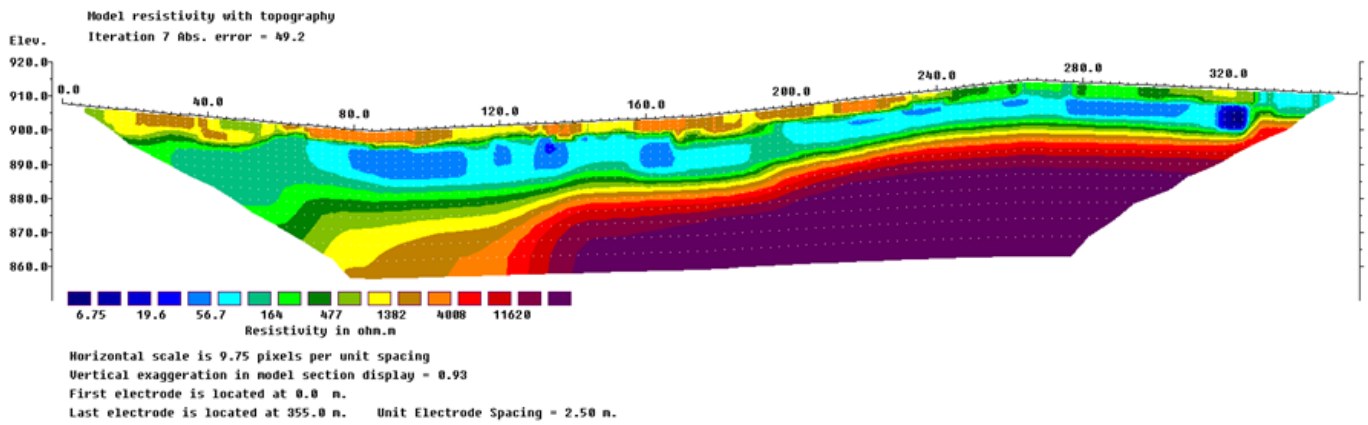
Appendix F. Results of Electrical Resistivity Surveys



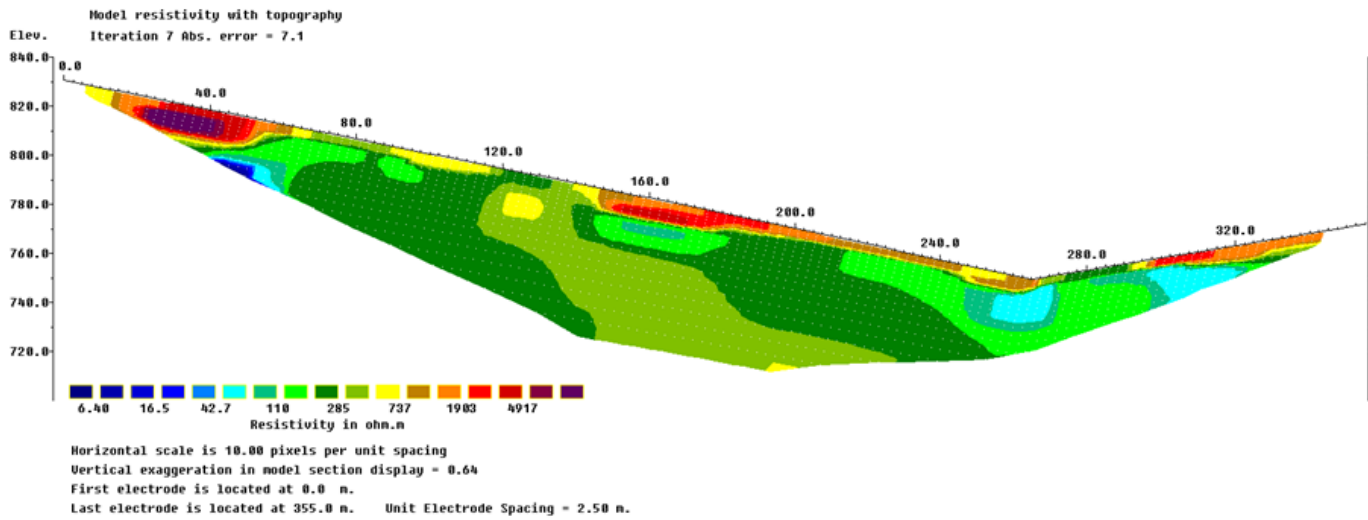
MSH_ER1_auto_remove.bin



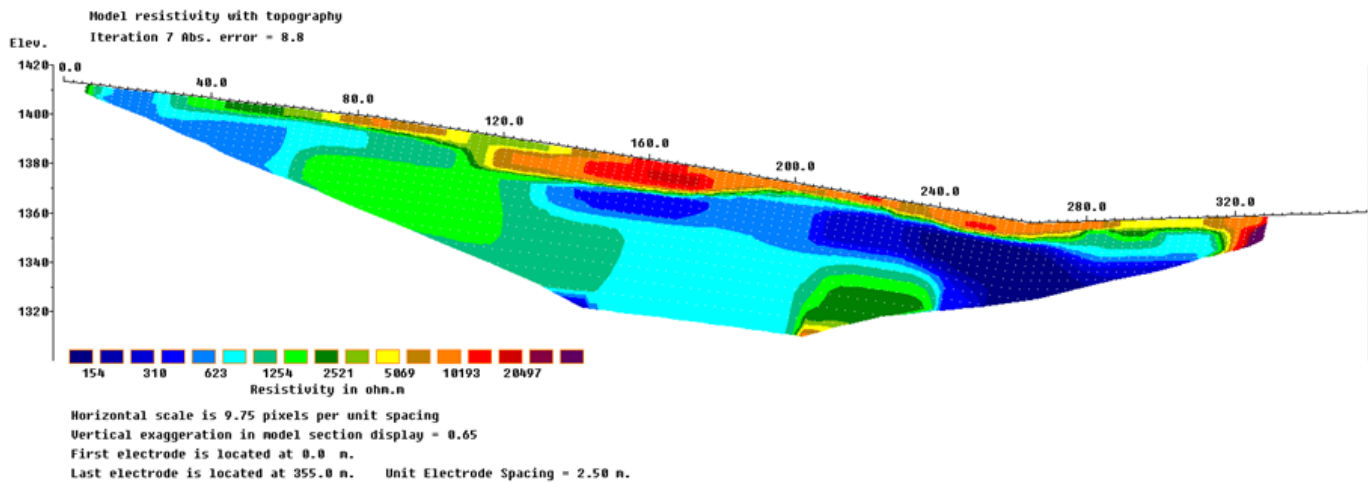
MSH_ER2_auto_remove.bin

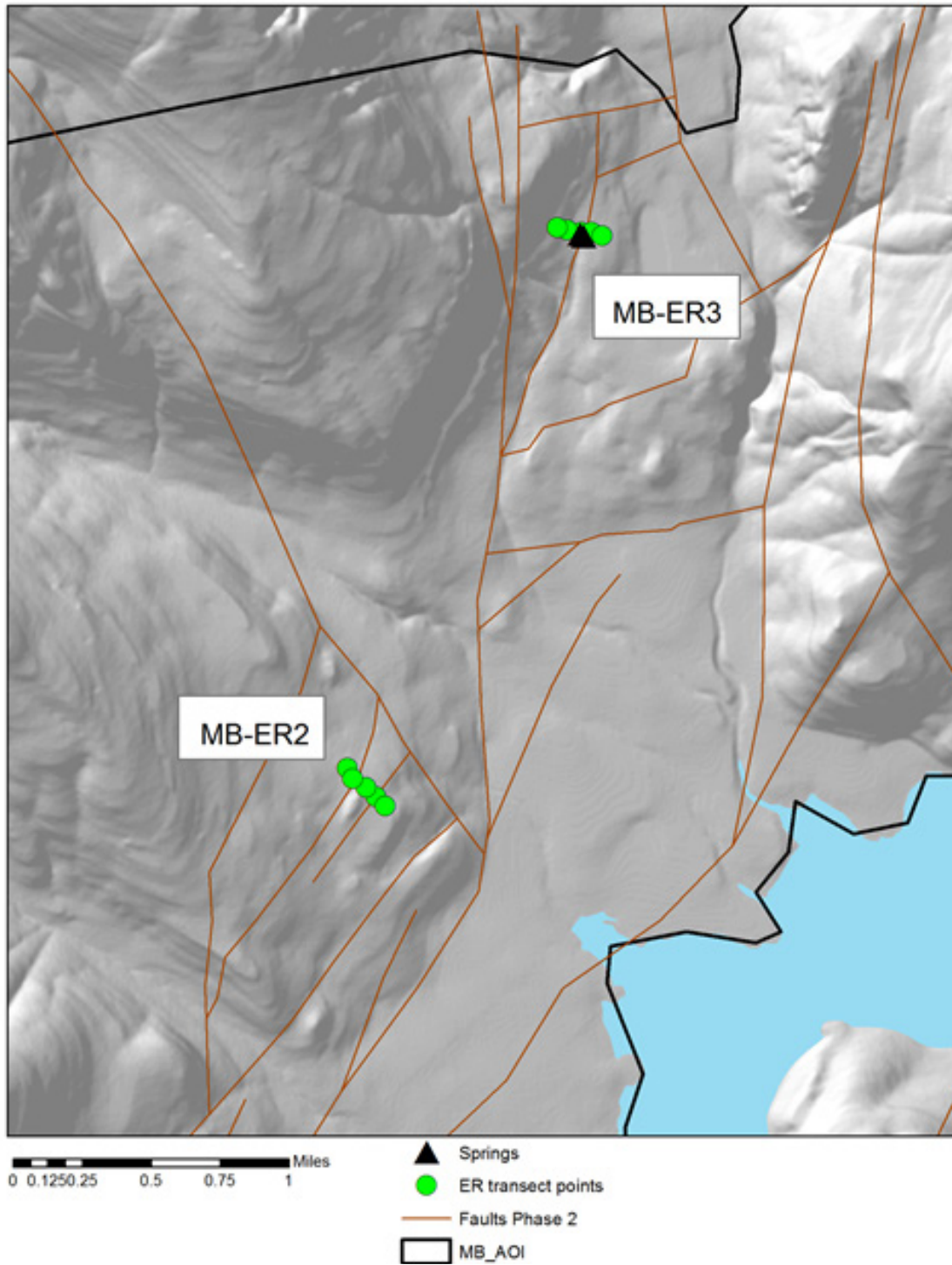


MSH_ER3_auto_remove.bin

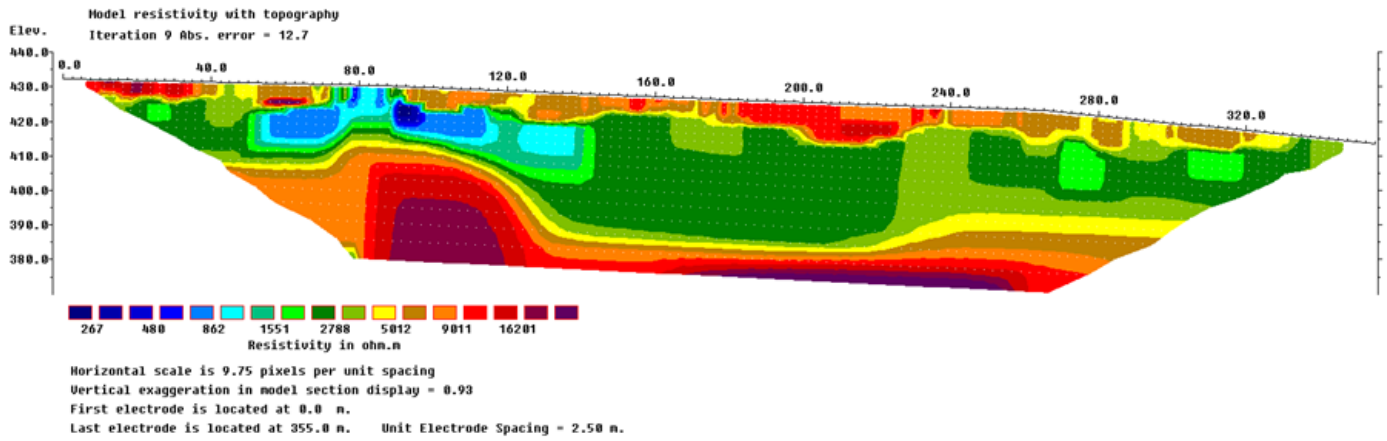


MSH_ER4_auto_remove.bin

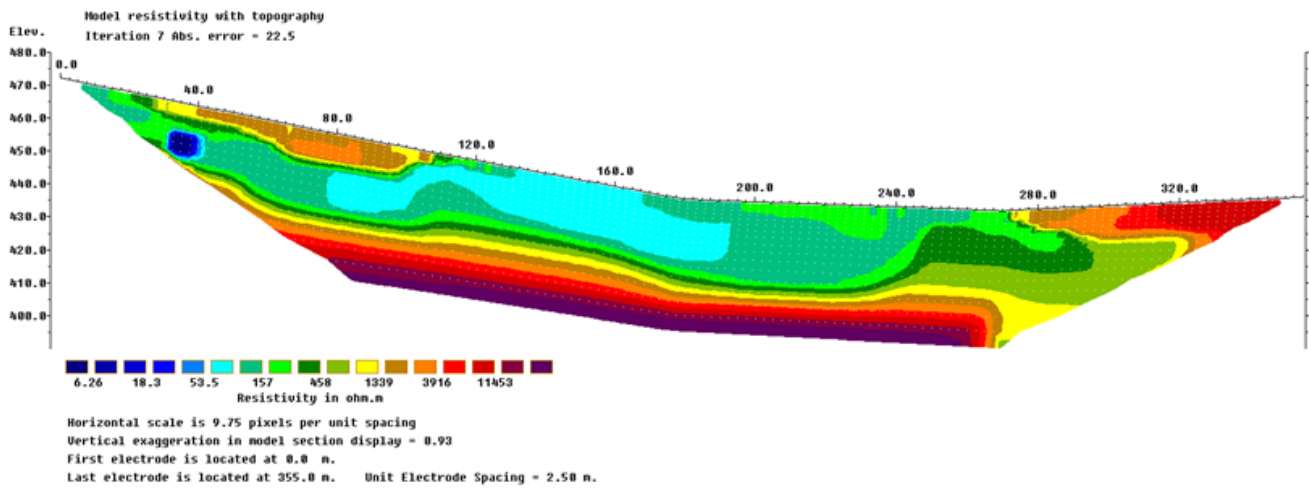




MB_ER2_auto_remove.bin



MB_ER3_auto_remove.bin



Appendix G. Results From New Geologic Mapping

OVERVIEW

Geologic mapping was undertaken in and around the Elk Lake 7.5-minute quadrangle northwest of Mount St. Helens during the summer of 2016. This quadrangle lies mostly within the MSH AOI and is adjacent to quadrangles on the east and north-east mapped at 1:24,000 scale by geologists from the USGS in the late 1990s. The purpose of the mapping was to document the lithologies exposed above the St. Helens shear zone, specifically look for evidence of recent faulting associated with the shear zone, and to document the tectonic history of the area with special emphasis on faults, fractures, and alteration.

Two geologists from the Washington Geological Survey completed the mapping over ~40 days of field mapping. Data were collected on paper maps and digitally on an iPad and iPhone using Avenza PDFMaps. Over 1,200 note points were taken. Topographic basemaps were provided by the USGS 7.5-minute quadrangle map and lidar with 2-m pixel size provided courtesy of Weyerhaeuser, Inc. Data and linework were compiled in *ArcGIS* and *QGIS* at a scale of 1:24,000. Limited mapping occurred south of the Spirit Lake Highway; the geology of this area was compiled from unpublished mapping by Russ Evarts and Roger Ashley of the U.S. Geological Survey (R. Evarts, USGS, written commun., 2016). A mapping campaign planned for the summer of 2018 will verify the mapping south of the Spirit Lake Highway. A full-scale map with complete legend, unit descriptions, and a pamphlet of major results will be published by the Washington Geological Survey in late 2018 or 2019 after the completion of final mapping.

The following maps show draft versions of the geologic map, a brief legend, and abbreviated unit descriptions. For clarity, fault observations and the regions with hornfels alteration are shown on a separate map from the labeled lithologies and bedding orientations. Draft GIS data will be uploaded to the Geothermal Data Repository, are available from the authors upon request, and will be available in their final form on the Washington Geologic Information Portal when the map is officially published.

UNIT DESCRIPTIONS

Holocene

- ml **Modified land**—Unsorted material placed to elevate or shape the land surface; found along the Spirit Lake Highway.
- Qda **Debris avalanche and lahar deposits from Mount St. Helens**—Unsorted diamicton associated with the 1980 eruption of Mount St. Helens. Commonly has hummocky topography; may be loose or compact; locally contains abundant organic material; local topography creates small closed depressions that may be filled with water.

Holocene–Pleistocene

- Qal **Alluvium**—Unsorted to well sorted boulder to pebble gravel, sand, and minor silt or clay; ranges from a few m to several-10s of m thick; commonly found along modern streams and rivers.
- Qls **Landslide deposits**—Unsorted diamicton to relatively cohesive and rotated blocks of bedrock or unconsolidated deposits.
- Qvc **Volcaniclastic colluvium and soil**—Moderately sorted sand, silt, clay, organic material, and ash-fall tephra; angular pebbles to cobbles or boulders rare; soil development varies but commonly well developed. Covers much of the map area; commonly 1–3 m thick and up to 6 m locally; often ash rich and lacking protolith clasts from underlying bedrock.
- Qoa **Older alluvium**—Unsorted to well sorted boulder to pebble gravel, sand, and minor silt or clay; ranges from a few meters up to ~50 m thick; commonly found along modern streams and rivers; no longer an active surface of deposition.

EVANS CREEK DRIFT:

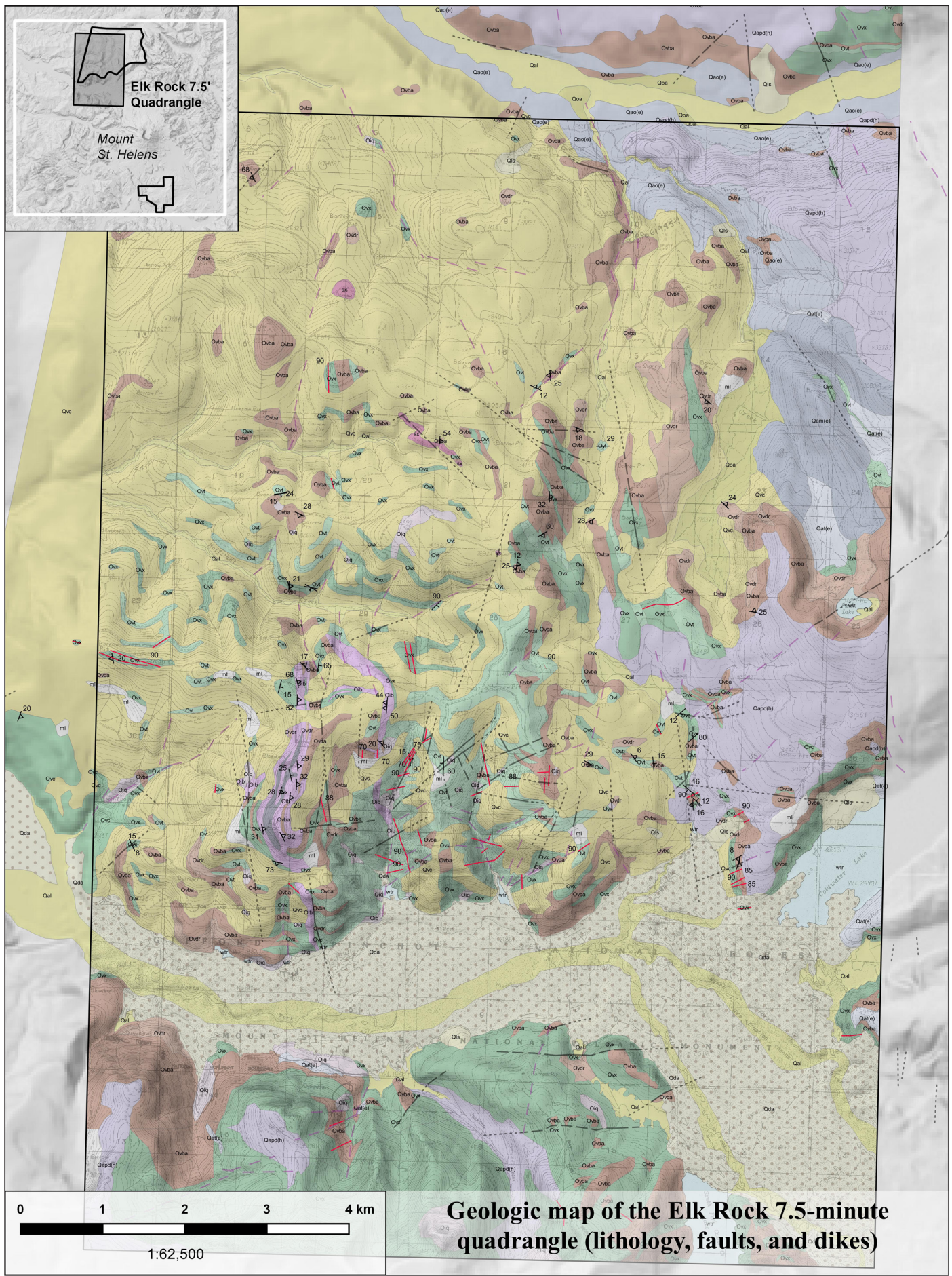
- Qat(e) **Till**—Unsorted cobble to boulder diamicton with a clayey to sandy matrix; moderately cohesive and compact. Weathering rinds on clasts are mostly <0.5 mm thick and few clasts are easily broken. Up to several 10s of m thick. Clasts generally derived from local up-slope regions.
- Qam(e) **Moraine deposits**—Unsorted cobble to boulder diamicton with a clayey to sandy matrix; moderately cohesive and compact. Weathering rinds on clasts are mostly <0.5 mm thick and few clasts are easily broken. Forms linear ridges along ‘U’-shaped valleys; locally up to 50–70 m thick. Clasts generally derived from nearby up-slope regions.
- Qao(e) **Outwash**—Moderately sorted pebble to cobble gravel, sandy gravel, and gravelly sand. Commonly forms stranded fluvial terraces along margins of larger stream or river valleys; terrace surfaces locally grade into till or moraine deposits.

HAYDEN CREEK DRIFT:

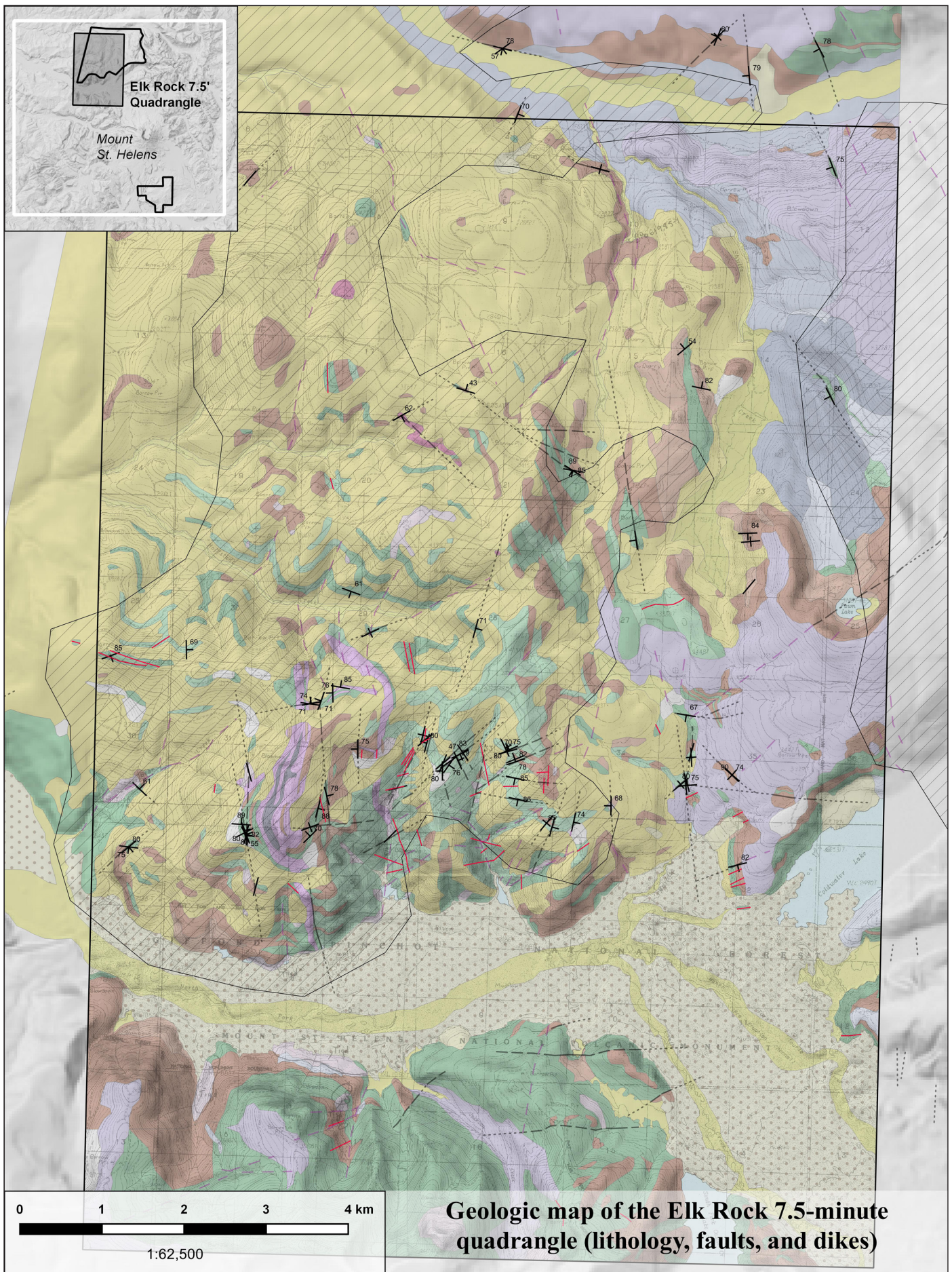
- Qapd(h) **Drift, undivided**—Unsorted cobble to boulder diamicton with a clayey to sandy matrix; commonly cohesive and compact. Weathering rinds on clasts are mostly >0.5 mm thick and many clasts are easily broken. Commonly forms a thick cover on high-elevation slopes up to 50 m thick. Clasts are a mixture of nearby up-slope lithologies and plutonic rocks derived from outside of the modern drainage area.

Oligocene

- Oib Basaltic dikes of Elk Mountain, xenolith rich**—Dark brown to black, aphyric to sparsely plagioclase-phyric basalt(?) with locally abundant angular xenoliths (<1–15 cm across) of gray to grayish green fine- to medium-grained quartz diorite. Intrudes units Ovc and Ovx in thick (up to 5 m) sills and dikes, most notably along the ridge of Elk Mountain. Margins of the dike are sharp to gradational with local injections of basalt into the country rock and broken and rotated pebble- to cobble-sized angular blocks of country rock incorporated into the dike margins. Where xenoliths are abundant the surrounding matrix commonly has flow banding and clasts show evidence for rotation. A new $^{39}\text{Ar}/^{40}\text{Ar}$ age from this unit is 35.9 Ma, although there is some evidence for contamination of the material (Appendix H; sample MSH16-108).
- Oiq Quartz diorite of Spud Mountain**—Gray to light green, microporphyritic to sub-equant porphyritic diorite, quartz diorite, and granodiorite. Mapped as small irregular intrusions into units Ovba, Ovc, Ovx, and Ovt; likely a larger contiguous intrusion at depth. Margins with country rock locally sheared or faulted and commonly altered to amphibole hornfels; pyrite mineralization with locally abundant magnetite is common along faulted margins of the intrusion. The mapped pattern of hornfels closely matches the mapped extent of outcrops of this unit and suggests that it may be related to pluton emplacement. A new $^{39}\text{Ar}/^{40}\text{Ar}$ age of this unit is 34.1 Ma (Appendix H; sample MSH16-109).
- Ovba Basalt to andesite**—Aphyric to plagioclase-rich highly porphyritic flows, dikes, and(or) sills; sparsely to moderately porphyritic basaltic andesite flows with 1–3 mm plagioclase most common. Black, dark blue, gray, or dark green. Vesicles and flow banding uncommon. Moderately indurated; very indurated where recrystallized into epidote-rich hornfels. Contains some autobrecciated flow tops, but primary textures are relatively uncommon. One dike near Coldwater Lake yielded an $^{39}\text{Ar}/^{40}\text{Ar}$ age of 34.6 Ma (Appendix H; sample MSH16-105).
- Ovdr Dacite to rhyolite**—Sparsely to moderately porphyritic flows, dikes, and(or) sills. Medium gray, lavender, or grayish pink. Parallel to chaotic flow banding with 0.5–1 mm thick laminations common and diagnostic. May contain small quartz phenocrysts.
- Ovc Volcaniclastic deposits**—Siltstone and sandstone with minor amounts of pebble conglomerate. Grains and clasts are rounded to sub-angular, moderately sorted, and indistinctly bedded. Commonly contains minor amounts of reworked tuffaceous material. Locally includes rocks that lack textures diagnostic of volcanic breccia (unit Ovx) or tuffaceous rocks (unit Ovt) yet have some indicators of sedimentary deposition. Typically green to blue and altered to epidote hornfels; buff to light green and less indurated where less altered.
- Ovx Volcanic breccia**—Unsorted mixture of angular to sub-angular pebble to large boulder-size clasts of various volcanogenic rocks including volcaniclastic deposits, ash-fall tuff, and flows. Matrix commonly present and consists of fine-grained, likely tuffaceous, material, and(or) sand and silt-size grains similar in lithology to the larger clasts. Usually light green or grayish green and moderately indurated. Locally dark green, purple, or blue and clayey where argillized; locally green or blue and very well indurated where altered to epidote hornfels. Bedding is generally not observable and contacts with other lithologies appear gradational (though rarely observed).
- Ovt Tuffaceous rocks**—Tuffaceous siltstone with sub-equal lapilli tuff. Generally buff to pale tan and moderately indurated with some primary textures visible; light to dark green and very well indurated with few or no primary textures visible where altered to epidote hornfels.
- sx Silicified rocks**—Tan, orange, brown, or white rocks with pervasive liesegang banding; primary textures not observable in outcrop; mostly recrystallized to quartz-rich lithologies; often contains pyrite and, less commonly, magnetite; protolith uncertain; very indurated.



Geologic map of the Elk Rock 7.5-minute quadrangle (lithology, faults, and dikes)



Geologic map of the Elk Rock 7.5-minute quadrangle (lithology, faults, and dikes)

Legend for the Geologic Map of the Elk Rock 7.5-minute Quadrangle

-  Hornfels alteration zone
-  Igneous dike (basalt/andesite)

Geologic Units

-  ml
-  Qal
-  Qda
-  Qls
-  Qvc
-  Qoa
-  Qat(e)
-  Qao(e)
-  Qam(e)
-  Qapd(h)
-  Oib
-  Oiq
-  Ovba
-  Ovdr
-  Ovc
-  Ovx
-  Ovt
-  sx
-  Water

Faults

-  Certain
-  Approximate
-  Inferred
-  Concealed
-  Lidar lineament

Symbols

-  Inclined bedding, showing strike and dip
-  Small inclined fault, showing strike and dip
-  Small vertical fault, showing strike
-  Inclined igneous dike, showing strike and dip
-  Inclined volcanic flow foliation, showing strike and dip
-  Shear zone or fault zone, showing trend

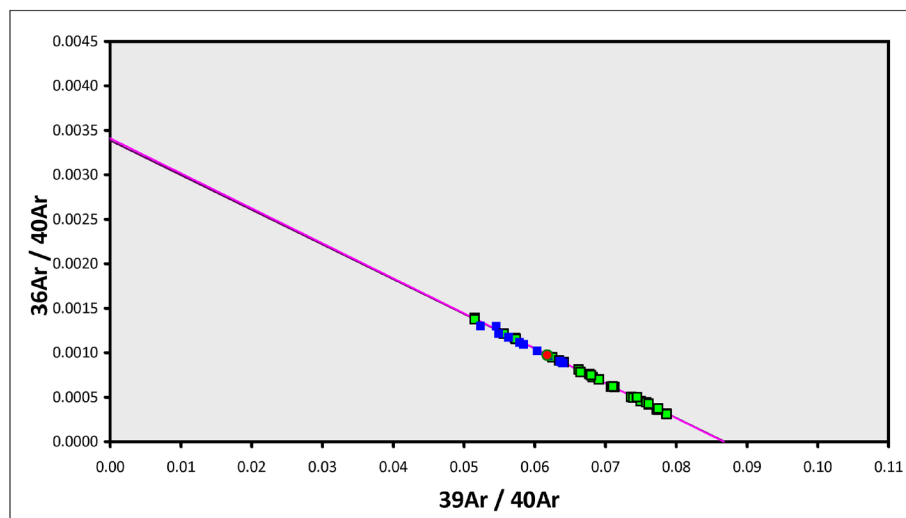
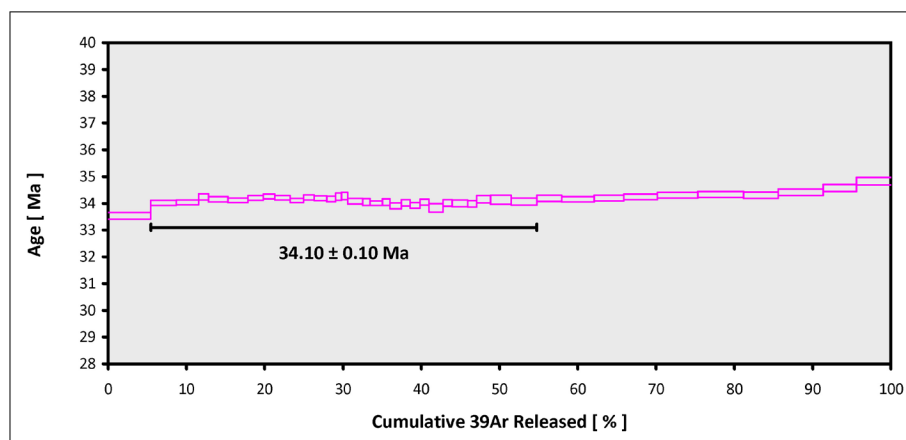
Appendix H. Results From New Geochronology

EXP#17D06530 > MSH16-109 > Groundmass > FORSON (16-46) CENTRAL CASCADES > NORTH MOUNT ST. HELENS 17-OSU-01 (1D15-17) > Incremental Heating > Dan Miggins

Information on Analysis and Constants Used in Calculations

Project = FORSON (16-46)
Sample = MSH16-109
Material = Groundmass
Location = North Mount St. Helens
Region = Central Cascades
Analyst = Dan Miggins
Irradiation = 17-OSU-01 (1D15-17)
Position = X: 0 | Y: 0 | Z/H: 19.79596 mm
FCT-NM Age = 28.201 ± 0.023 Ma
FCT-NM Reference = Kuiper et al (2008)
FCT-NM 40Ar/39Ar Ratio = 9.50852 ± 0.01227
FCT-NM J-value = 0.00165298 ± 0.00000213
Air Shot 40Ar/36Ar = 302.5450 ± 0.2693
Air Shot MDF = 0.99417103 ± 0.00061896 (LIN)
Experiment Type = Incremental Heating
Extraction Method = Undefined
Heating = 77 sec
Isolation = 0.00 min
Instrument = ARGUS-VI-D
Preferred Age = Undefined
Age Classification = Undefined
IGSN = Undefined
Rock Class = Undefined
Lithology = Undefined
Lat-Lon = Undefined - Undefined
Age Equations = Min et al. (2000)
Negative Intensities = Allowed
Collector Calibrations = 36Ar
Decay 40K = 5.530 ± 0.048 E-10 1/a
Decay 39Ar = 2.940 ± 0.016 E-07 1/h
Decay 37Ar = 8.230 ± 0.012 E-04 1/h
Decay 36Cl = 2.257 ± 0.015 E-06 1/a
Decay 40K(εC, β⁺) = 0.580 ± 0.009 E-10 1/a
Decay 40K(β⁻) = 4.950 ± 0.043 E-10 1/a
Atmospheric 40/36(a) = 295.50
Atmospheric 38/36(a) = 0.1869
Production 39/37(ca) = 0.0006756 ± 0.0000089
Production 38/37(ca) = 0.0000718 ± 0.0000092
Production 36/37(ca) = 0.0002663 ± 0.0000004
Production 40/39(k) = 0.003823 ± 0.000102
Production 38/39(k) = 0.012031 ± 0.000019
Production 36/38(d) = 262.80 ± 1.71
Scaling Ratio K/Ca = 0.430
Abundance Ratio 40K/K = 1.1700 ± 0.0100 E-04
Atomic Weight K = 39.0983 ± 0.0001 g

Results	40(a)/36(a) ± 2σ	40(r)/39(k) ± 2σ	Age ± 2σ (Ma)	MSWD	39Ar(k) (%,n)	K/Ca ± 2σ
Age Plateau						
Error Mean		11.51595 ± 0.01340 ± 0.12%	34.10 ± 0.10 ± 0.28%	3.98	49.34 0%	0.343 ± 0.045
			Full External Error ± 0.77 Analytical Error ± 0.04	1.53	2σ Confidence Limit	Error Magnification
Total Fusion Age		11.54279 ± 0.00733 ± 0.06%	34.18 ± 0.09 ± 0.26%		40	0.515 ± 0.000
			Full External Error ± 0.77 Analytical Error ± 0.02			
Normal Isochron						
Error Chron	293.12 ± 2.44 ± 0.83%	11.53902 ± 0.02703 ± 0.23%	34.17 ± 0.12 ± 0.35%	3.68	49.34 0%	0.343 ± 0.045
			Full External Error ± 0.78 Analytical Error ± 0.08	1.54	2σ Confidence Limit	Error Magnification
Inverse Isochron						
Error Chron	293.25 ± 2.43 ± 0.83%	11.53807 ± 0.02696 ± 0.23%	34.16 ± 0.12 ± 0.34%	3.67	49.34 0%	0.343 ± 0.045
			Full External Error ± 0.78 Analytical Error ± 0.08	1.54	2σ Confidence Limit	Error Magnification
				1.9145	31%	Spreading Factor



OSU Argon Geochronology Lab
 CEOAS Oregon State University, Corvallis, USA

EXP#17D06588 > MSH16-108 > Groundmass > FORSON (16-46)
CENTRAL CASCADES > NORTH MOUNT ST. HELENS
17-OSU-01 (1D18-17) > Incremental Heating > Dan Miggins

Information on Analysis and Constants Used in Calculations

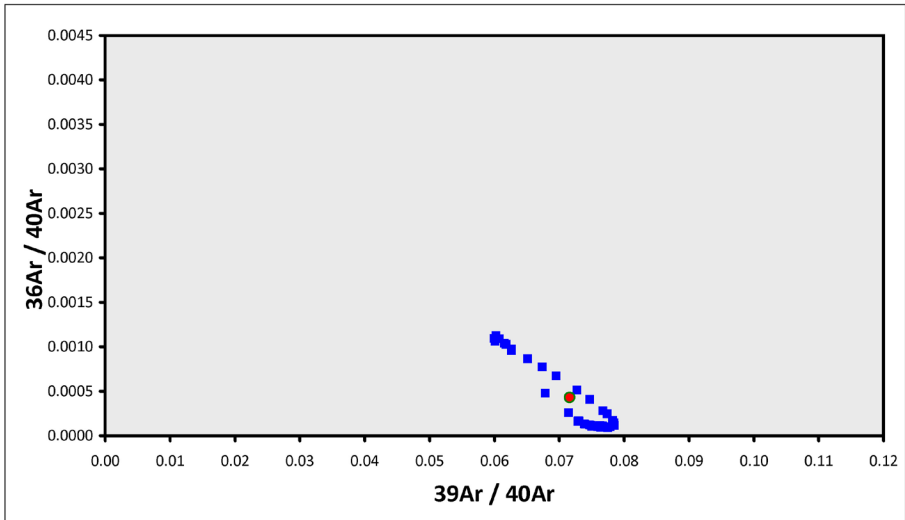
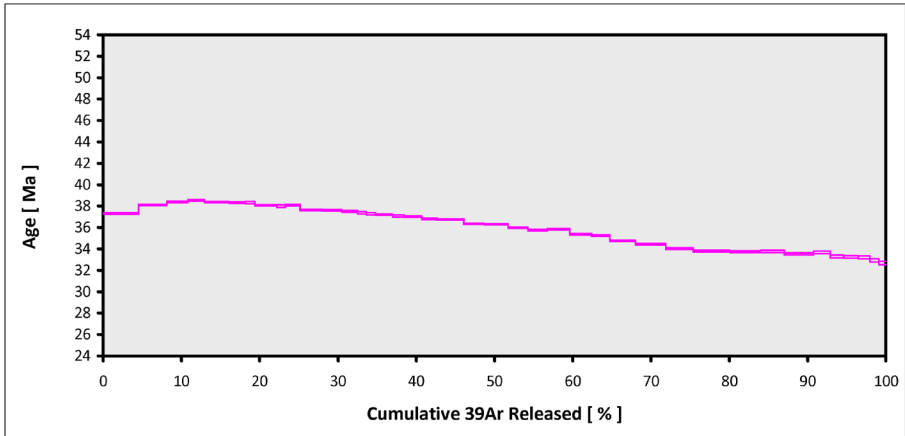
Project = FORSON (16-46)
 Sample = MSH16-108
 Material = Groundmass
 Location = North Mount St. Helens
 Region = Central Cascades
 Analyst = Dan Miggins
 Irradiation = 17-OSU-01 (1D18-17)
 Position = X: 0 | Y: 0 | Z/H: 23.85799 mm
 FCT-NM Age = 28.201 ± 0.023 Ma
 FCT-NM Reference = Kuiper et al (2008)
 FCT-NM 40Ar/39Ar Ratio = 9.54818 ± 0.01232
 FCT-NM J-value = 0.00164611 ± 0.00000212
 Air Shot 40Ar/36Ar = 302.5570 ± 0.2753
 Air Shot MDF = 0.99416133 ± 0.00062067 (LIN)
 Experiment Type = Incremental Heating
 Extraction Method = Undefined
 Heating = 77 sec
 Isolation = 0.00 min
 Instrument = ARGUS-VI-D
 Preferred Age = Undefined
 Age Classification = Undefined
 IGSN = Undefined
 Rock Class = Undefined
 Lithology = Undefined
 Lat-Lon = Undefined - Undefined
 Age Equations = Min et al. (2000)
 Negative Intensities = Allowed
 Collector Calibrations = 36Ar
 Decay 40K = 5.530 ± 0.048 E-10 1/a
 Decay 39Ar = 2.940 ± 0.016 E-07 1/h
 Decay 37Ar = 8.230 ± 0.012 E-04 1/h
 Decay 36Cl = 2.257 ± 0.015 E-06 1/a
 Decay 40K(EC,β⁺) = 0.580 ± 0.009 E-10 1/a
 Decay 40K(β⁻) = 4.950 ± 0.043 E-10 1/a
 Atmospheric 40/36(a) = 295.50
 Atmospheric 38/36(a) = 0.1869
 Production 39/37(ca) = 0.0006756 ± 0.0000089
 Production 38/37(ca) = 0.0000718 ± 0.0000092
 Production 36/37(ca) = 0.0002663 ± 0.0000004
 Production 40/39(k) = 0.003823 ± 0.000102
 Production 38/39(k) = 0.012031 ± 0.000019
 Production 36/38(d) = 262.80 ± 1.71
 Scaling Ratio K/Ca = 0.430
 Abundance Ratio 40K/K = 1.1700 ± 0.0100 E-04
 Atomic Weight K = 39.0983 ± 0.0001 g

Results	40(a)/36(a) ± 2σ	40(r)/39(k) ± 2σ	Age ± 2σ (Ma)	MSWD	39Ar(k) (%),n	K/Ca ± 2σ
---------	------------------	------------------	---------------	------	---------------	-----------

Age Plateau	Cannot Calculate					
Total Fusion Age		12.20507 ± 0.00445 ± 0.04%	35.97 ± 0.09 ± 0.26%		40	0.528 ± 0.000
			Full External Error ± 0.81			Analytical Error ± 0.01

Normal Isochron	Cannot Calculate					
-----------------	------------------	--	--	--	--	--

Inverse Isochron	Cannot Calculate					
------------------	------------------	--	--	--	--	--



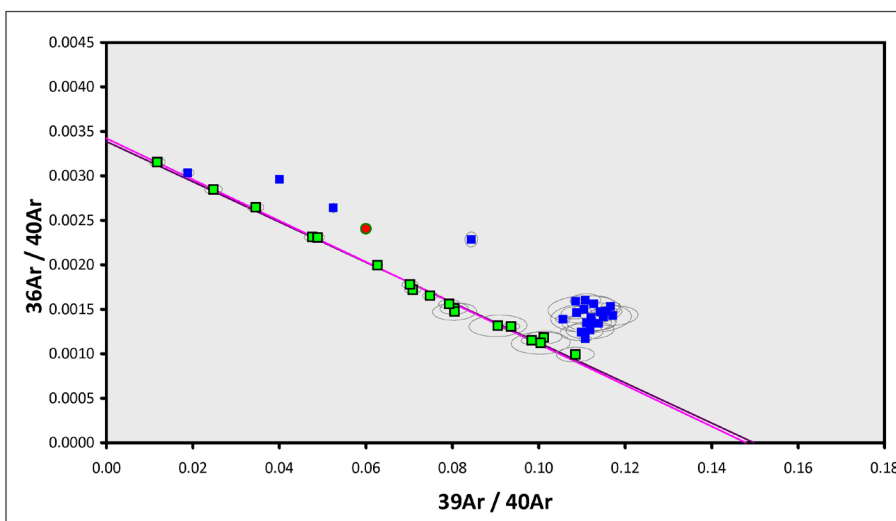
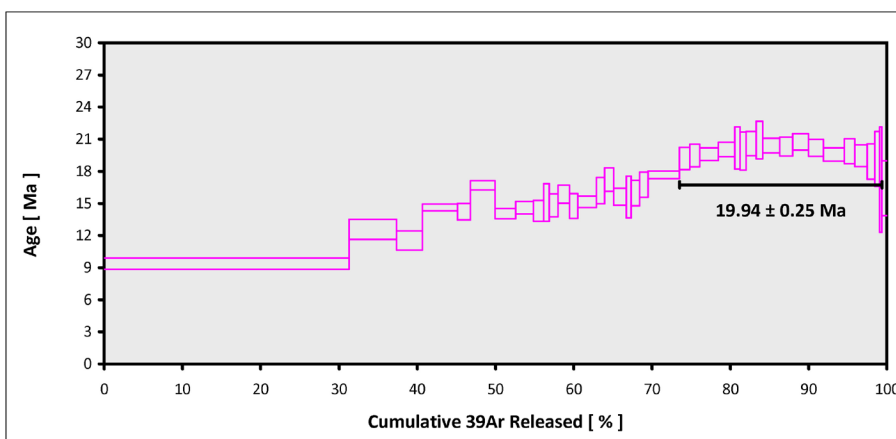
OSU Argon Geochronology Lab
 CEOAS Oregon State University, Corvallis, USA

EXP#17D06673 > WRV16-01 > K-Feldspar > FORSON (16-46)
SOUTHERN WASHINGTON > WIND RIVER VALLEY
17-OSU-01 (1D11-17) > Incremental Heating > Dan Miggins

**Information on Analysis
 and Constants Used in Calculations**

Project = **FORSON (16-46)**
 Sample = **WRV16-01**
 Material = **K-Feldspar**
 Location = **Wind River valley**
 Region = **Southern Washington**
 Analyst = **Dan Miggins**
 Irradiation = **17-OSU-01 (1D11-17)**
 Position = **X: 0 | Y: 0 | Z/H: 14.83 mm**
 FCT-NM Age = **28.201 ± 0.023 Ma**
 FCT-NM Reference = **Kuiper et al (2008)**
 FCT-NM 40Ar/39Ar Ratio = **9.47056 ± 0.01231**
 FCT-NM J-value = **0.00165961 ± 0.00000216**
 Air Shot 40Ar/36Ar = **302.5460 ± 0.2753**
 Air Shot MDF = **0.99417022 ± 0.00062070 (LIN)**
 Experiment Type = **Incremental Heating**
 Extraction Method = **Undefined**
 Heating = **77 sec**
 Isolation = **0.00 min**
 Instrument = **ARGUS-VI-D**
 Preferred Age = **Undefined**
 Age Classification = **Undefined**
 IGSN = **Undefined**
 Rock Class = **Undefined**
 Lithology = **Undefined**
 Lat-Lon = **Undefined - Undefined**
 Age Equations = **Min et al. (2000)**
 Negative Intensities = **Allowed**
 Collector Calibrations = **36Ar**
 Decay 40K = **5.530 ± 0.048 E-10 1/a**
 Decay 39Ar = **2.940 ± 0.016 E-07 1/h**
 Decay 37Ar = **8.230 ± 0.012 E-04 1/h**
 Decay 36Cl = **2.257 ± 0.015 E-06 1/a**
 Decay 40K(EC,β⁺) = **0.580 ± 0.009 E-10 1/a**
 Decay 40K(β⁻) = **4.950 ± 0.043 E-10 1/a**
 Atmospheric 40/36(a) = **295.50**
 Atmospheric 38/36(a) = **0.1869**
 Production 39/37(ca) = **0.0006756 ± 0.0000089**
 Production 38/37(ca) = **0.0000718 ± 0.0000092**
 Production 36/37(ca) = **0.0002663 ± 0.0000004**
 Production 40/39(k) = **0.003823 ± 0.000102**
 Production 38/39(k) = **0.012031 ± 0.000019**
 Production 36/38(d) = **262.80 ± 1.71**
 Scaling Ratio K/Ca = **0.430**
 Abundance Ratio 40K/K = **1.1700 ± 0.0100 E-04**
 Atomic Weight K = **39.0983 ± 0.0001 g**

Results	40(a)/36(a) ± 2σ	40(r)/39(k) ± 2σ	Age ± 2σ (Ma)	MSWD	39Ar(k) (%),n	K/Ca ± 2σ
Age Plateau		6.68119 ± 0.08088 ± 1.21%	19.94 ± 0.25 ± 1.23% Full External Error ± 0.51 Analytical Error ± 0.24	1.17 28% 1.69 1.0795	25.87 18 2σ Confidence Limit Error Magnification	0.219 ± 0.045
Total Fusion Age		4.82899 ± 0.06587 ± 1.36%	14.43 ± 0.20 ± 1.38% Full External Error ± 0.38 Analytical Error ± 0.20		40	0.064 ± 0.000
Normal Isochron	292.46 ± 4.30 ± 1.47%	6.75455 ± 0.12988 ± 1.92%	20.16 ± 0.39 ± 1.93% Full External Error ± 0.60 Analytical Error ± 0.39	1.09 35% 1.71 1.0462	25.87 18 2σ Confidence Limit Error Magnification	
Inverse Isochron	292.34 ± 4.31 ± 1.47%	6.76366 ± 0.13030 ± 1.93%	20.19 ± 0.39 ± 1.93% Full External Error ± 0.60 Analytical Error ± 0.39	1.09 36% 1.71 1.0443	25.87 18 2σ Confidence Limit Error Magnification	65% Spreading Factor



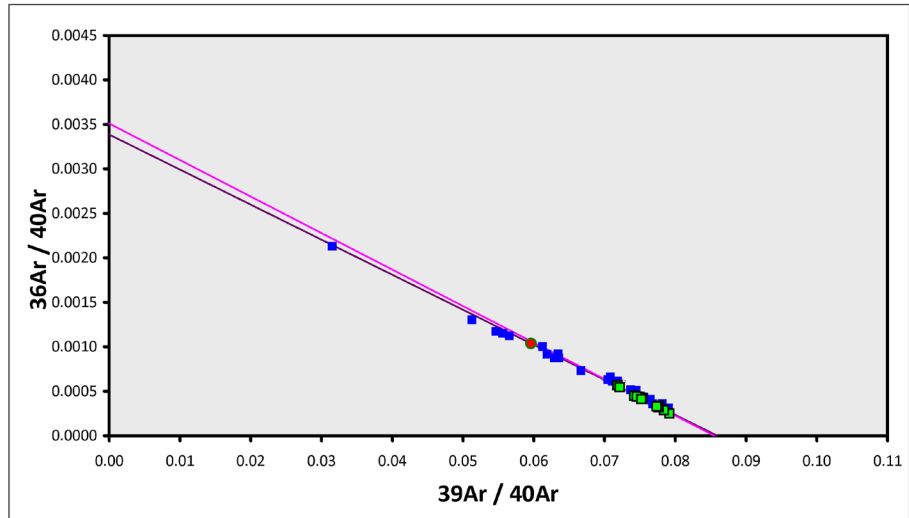
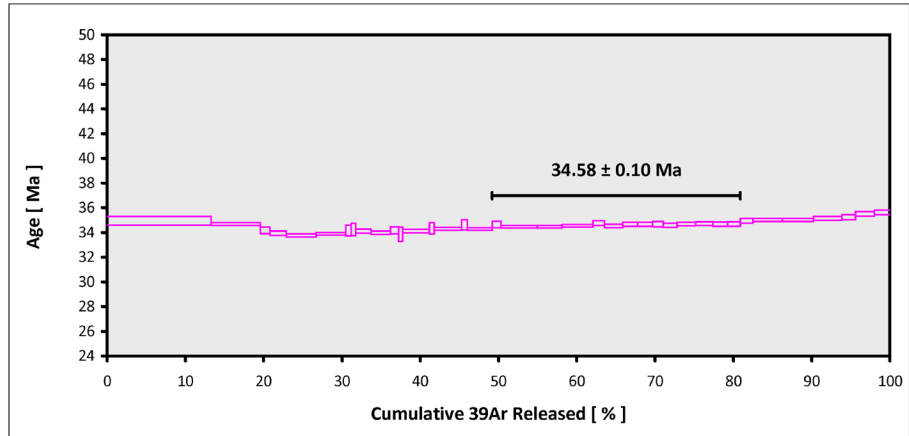
OSU Argon Geochronology Lab
 CEOAS Oregon State University, Corvallis, USA

EXP#17D06731 > 16-105 > K-Feldspar > FORSON (16-46)
CENTRAL CASCADES > NORTH MOUNT ST. HELENS
17-OSU-01 (1D12-17) > Incremental Heating > Dan Miggins

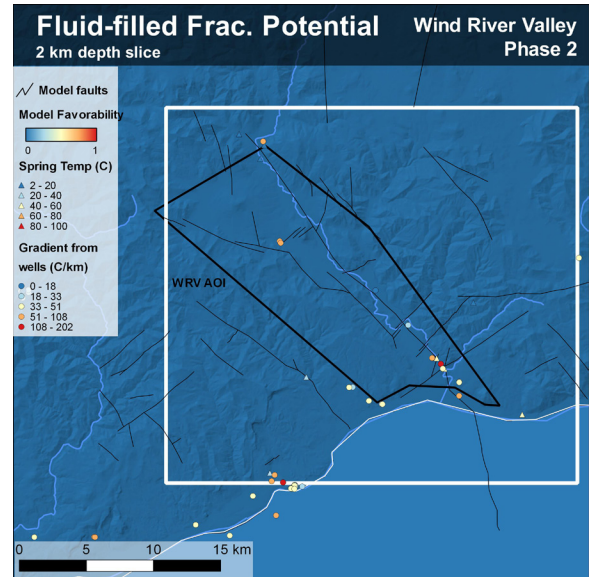
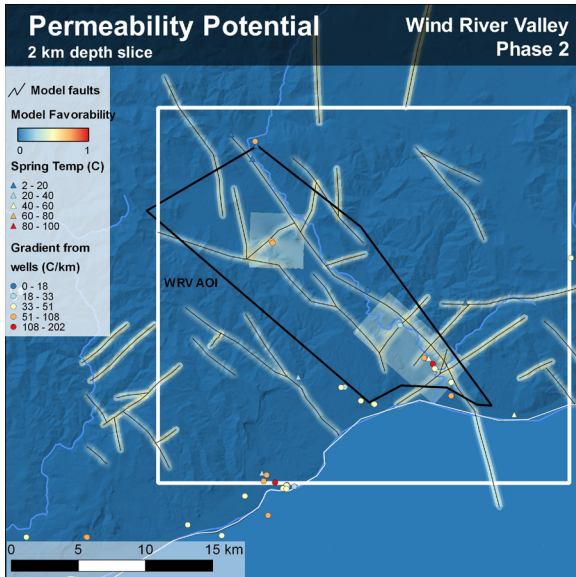
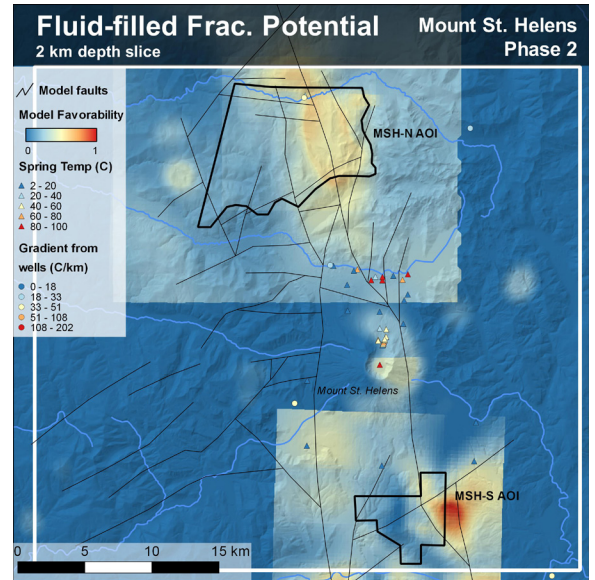
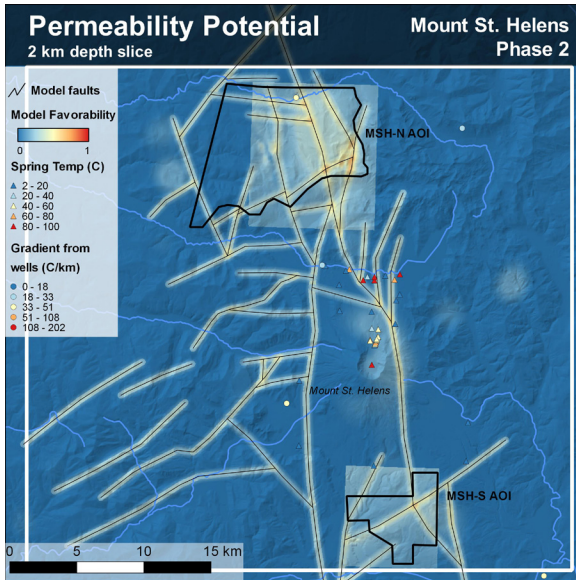
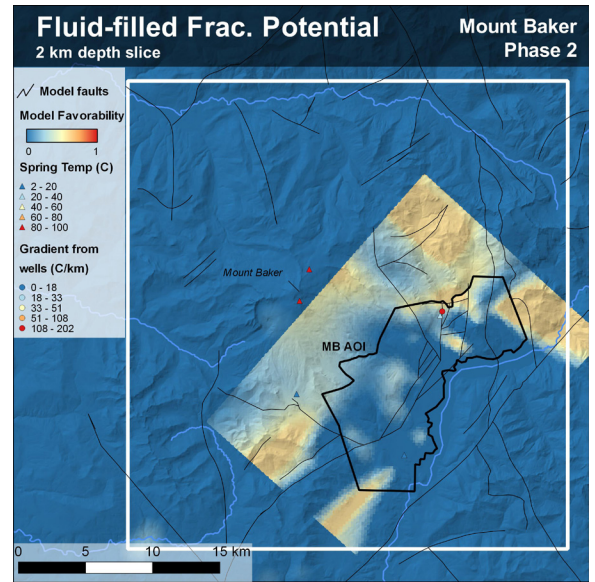
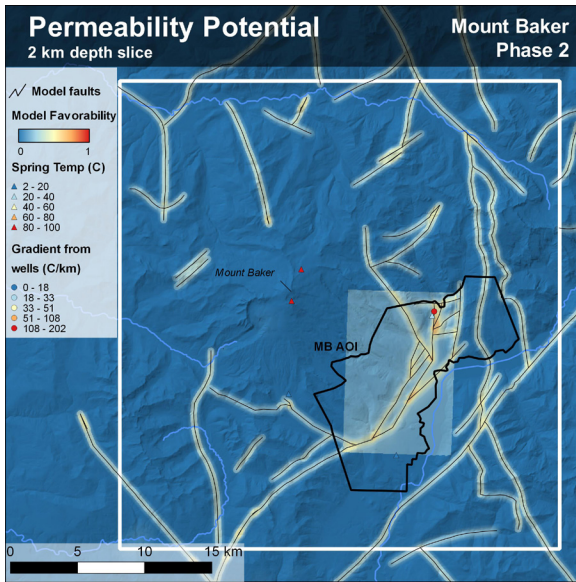
Information on Analysis and Constants Used in Calculations

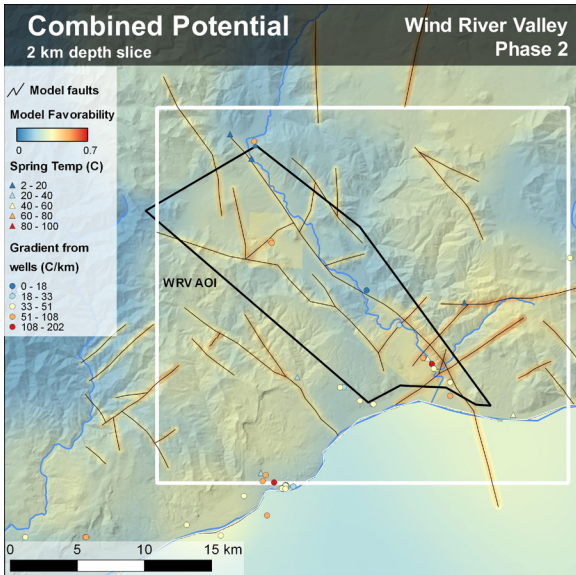
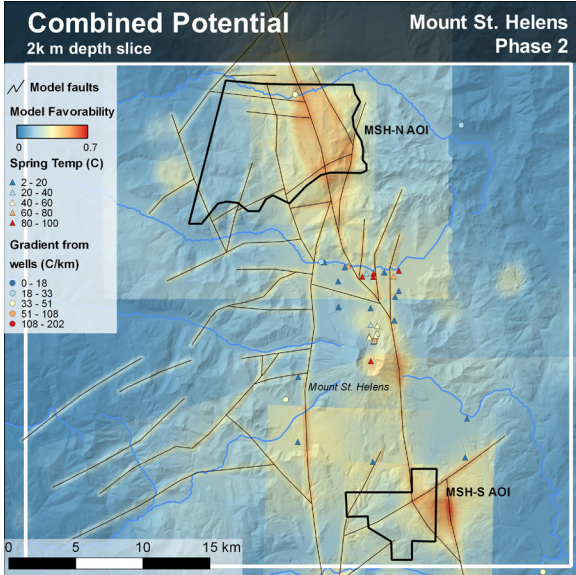
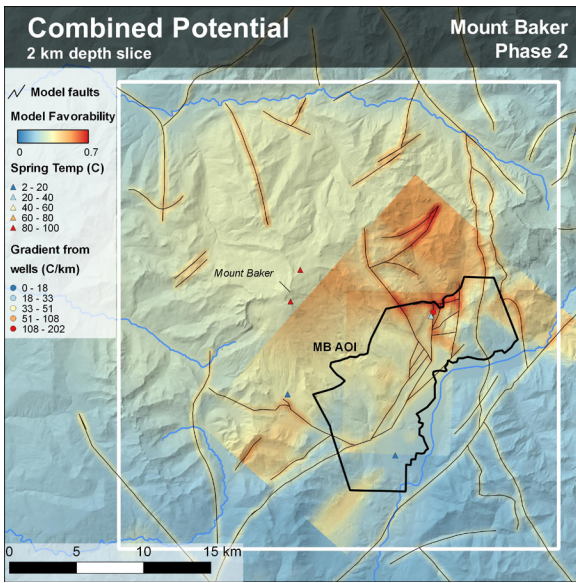
Project = FORSON (16-46)
 Sample = 16-105
 Material = K-Feldspar
 Location = North Mount St. Helens
 Region = Central Cascades
 Analyst = Dan Miggins
 Irradiation = 17-OSU-01 (1D12-17)
 Position = X: 0 | Y: 0 | Z/H: 16.1506 mm
 FCT-NM Age = 28.201 ± 0.023 Ma
 FCT-NM Reference = Kuiper et al (2008)
 FCT-NM 40Ar/39Ar Ratio = 9.47951 ± 0.01223
 FCT-NM J-value = 0.00165804 ± 0.00000214
 Air Shot 40Ar/36Ar = 302.5640 ± 0.2784
 Air Shot MDF = 0.99415567 ± 0.00062154 (LIN)
 Experiment Type = Incremental Heating
 Extraction Method = Undefined
 Heating = 77 sec
 Isolation = 0.00 min
 Instrument = ARGUS-VI-D
 Preferred Age = Undefined
 Age Classification = Undefined
 IGSN = Undefined
 Rock Class = Undefined
 Lithology = Undefined
 Lat-Lon = Undefined - Undefined
 Age Equations = Min et al. (2000)
 Negative Intensities = Allowed
 Collector Calibrations = 36Ar
 Decay 40K = 5.530 ± 0.048 E-10 1/a
 Decay 39Ar = 2.940 ± 0.016 E-07 1/h
 Decay 37Ar = 8.230 ± 0.012 E-04 1/h
 Decay 36Cl = 2.257 ± 0.015 E-06 1/a
 Decay 40K(εC,β⁺) = 0.580 ± 0.009 E-10 1/a
 Decay 40K(β⁻) = 4.950 ± 0.043 E-10 1/a
 Atmospheric 40/36(a) = 295.50
 Atmospheric 38/36(a) = 0.1869
 Production 39/37(ca) = 0.0006756 ± 0.0000089
 Production 38/37(ca) = 0.0000718 ± 0.0000092
 Production 36/37(ca) = 0.0002663 ± 0.0000004
 Production 40/39(k) = 0.003823 ± 0.000102
 Production 38/39(k) = 0.012031 ± 0.000019
 Production 36/38(d) = 262.80 ± 1.71
 Scaling Ratio K/Ca = 0.430
 Abundance Ratio 40K/K = 1.1700 ± 0.0100 E-04
 Atomic Weight K = 39.0983 ± 0.0001 g

Results	40(a)/36(a) ± 2σ	40(r)/39(k) ± 2σ	Age ± 2σ (Ma)	MSWD	39Ar(k) (%),n	K/Ca ± 2σ
Age Plateau						
Error Mean		11.64361 ± 0.01829 ± 0.16%	34.58 ± 0.10 ± 0.30%	2.01	31.70	0.152 ± 0.002
			Full External Error ± 0.78	1.78	2σ Confidence Limit	
			Analytical Error ± 0.05	1.4165	Error Magnification	
Total Fusion Age		11.65144 ± 0.01776 ± 0.15%	34.60 ± 0.10 ± 0.30%		38	0.177 ± 0.000
			Full External Error ± 0.78			
			Analytical Error ± 0.05			
Normal Isochron	284.60 ± 12.38 ± 4.35%	11.70424 ± 0.07127 ± 0.61%	34.76 ± 0.23 ± 0.66%	1.76	31.70	
			Full External Error ± 0.81	5%	14	
			Analytical Error ± 0.21	1.82	2σ Confidence Limit	
				1.3259	Error Magnification	
Inverse Isochron	284.88 ± 12.35 ± 4.33%	11.70306 ± 0.07126 ± 0.61%	34.75 ± 0.23 ± 0.65%	1.75	31.70	
			Full External Error ± 0.81	5%	14	
			Analytical Error ± 0.21	1.82	2σ Confidence Limit	
				1.3245	Error Magnification	
				9%	Spreading Factor	

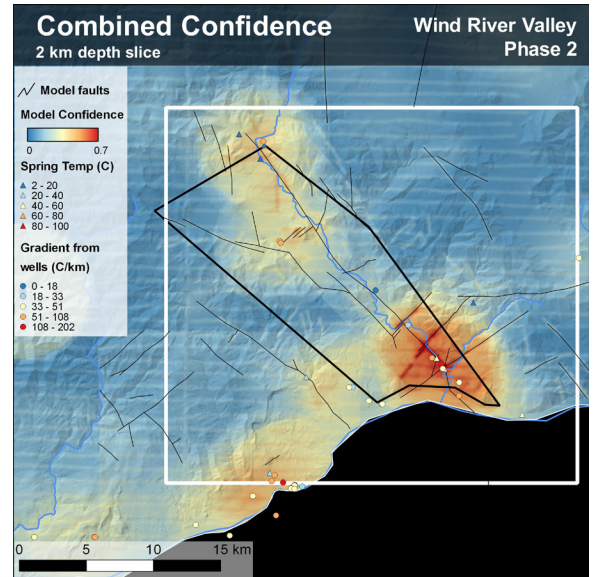
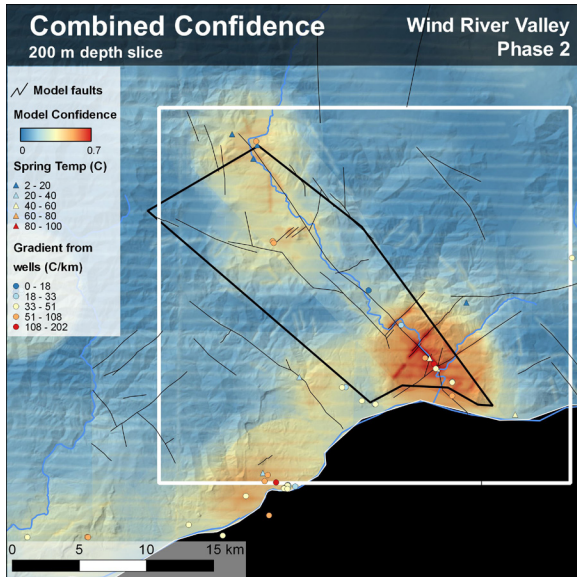
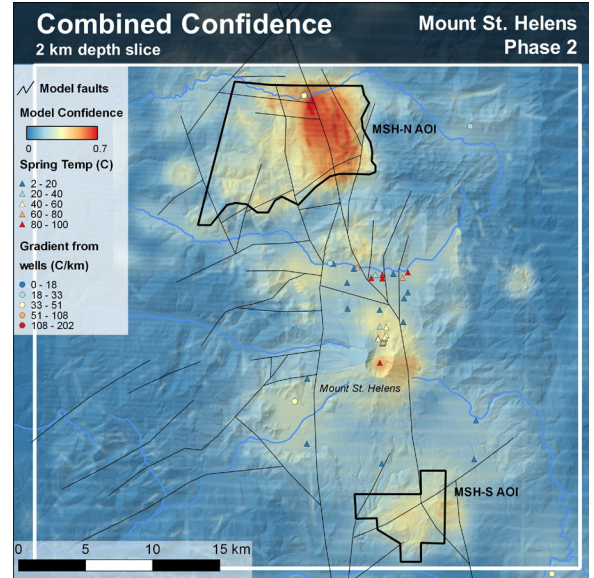
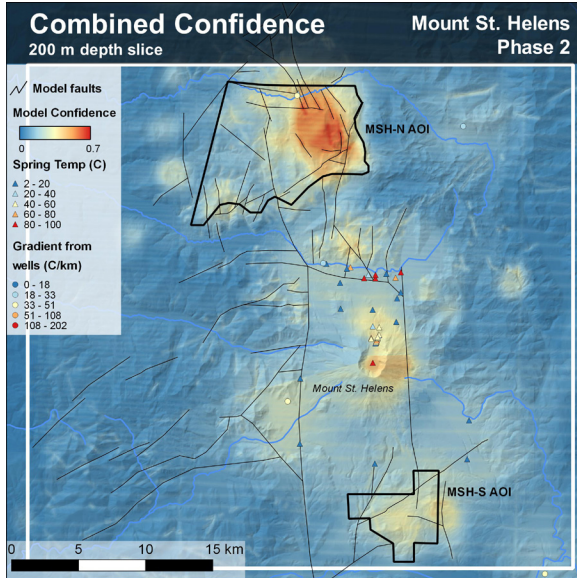
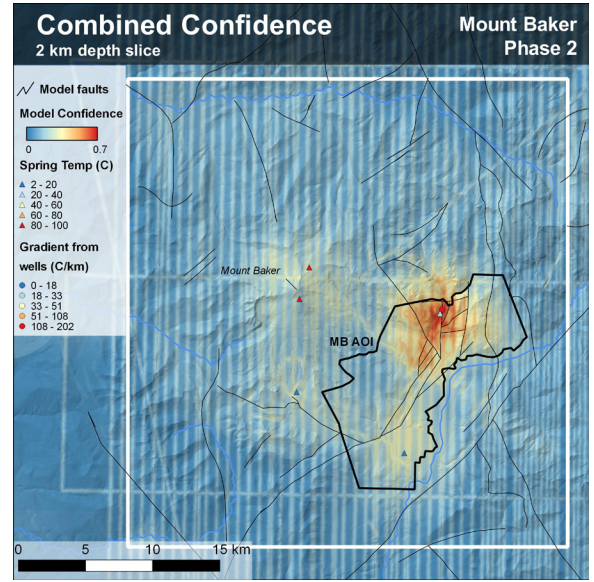
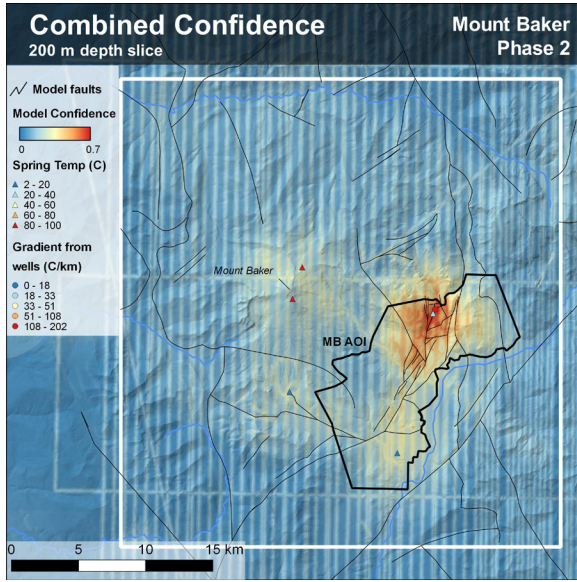


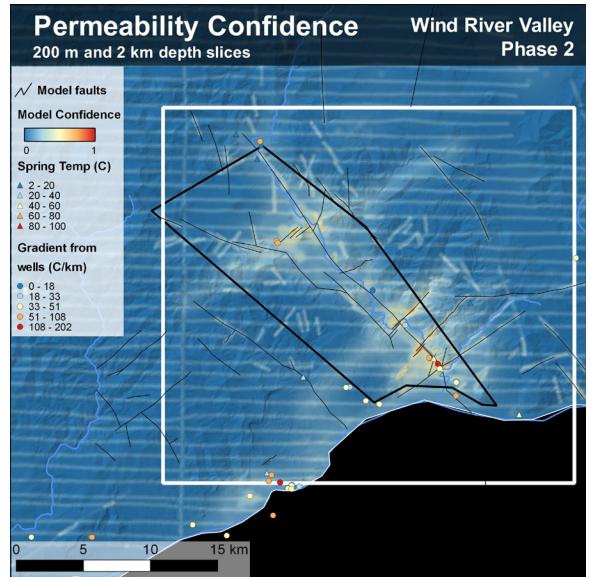
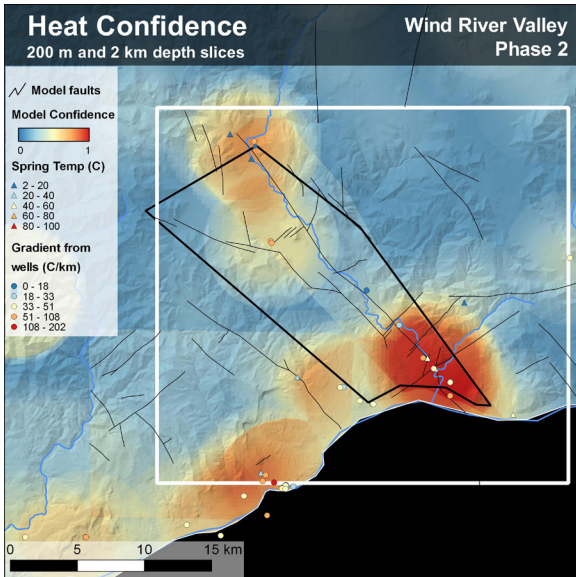
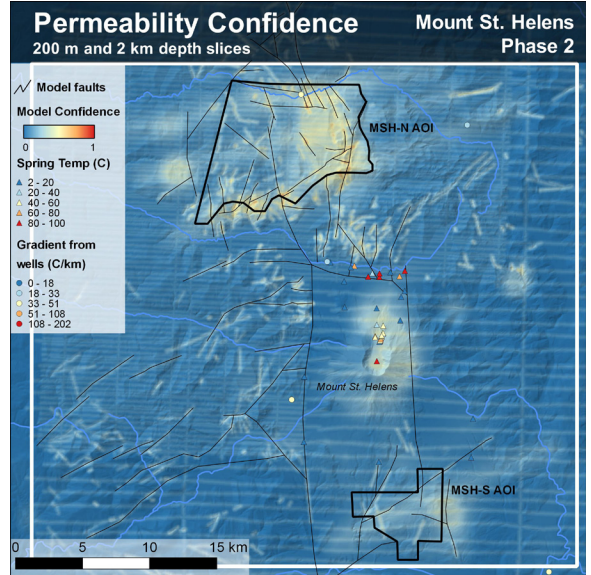
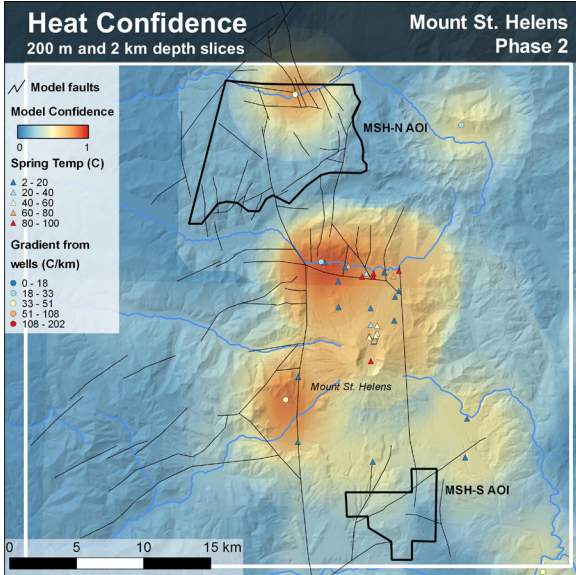
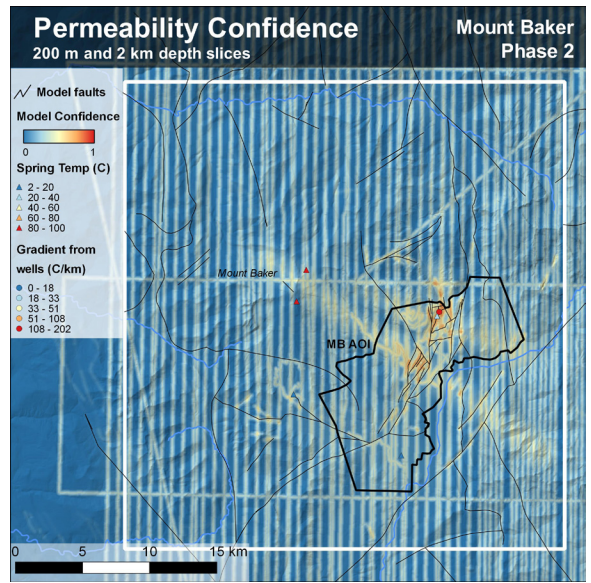
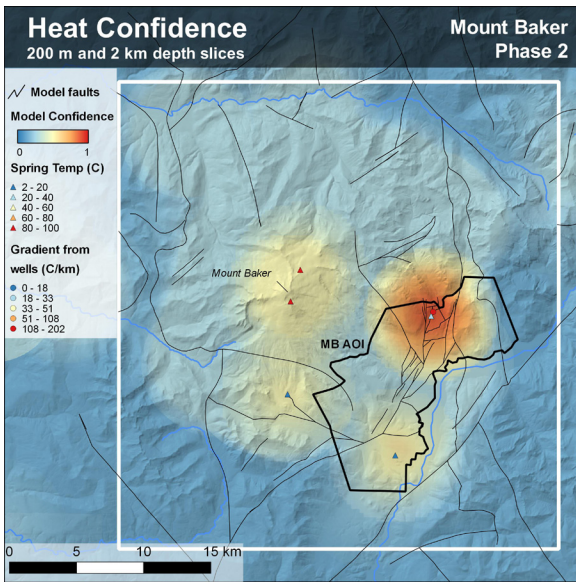
Appendix I. Favorability Model Results at 2-km Depth

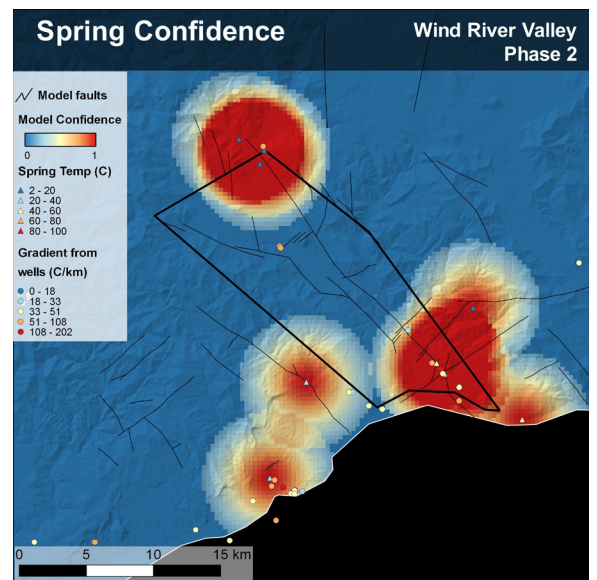
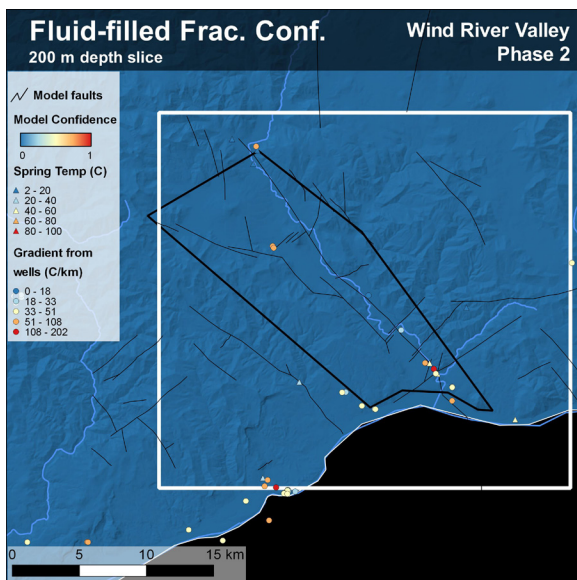
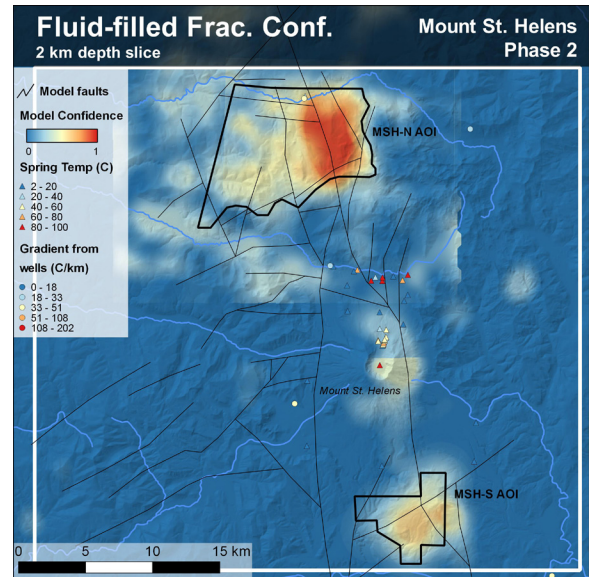
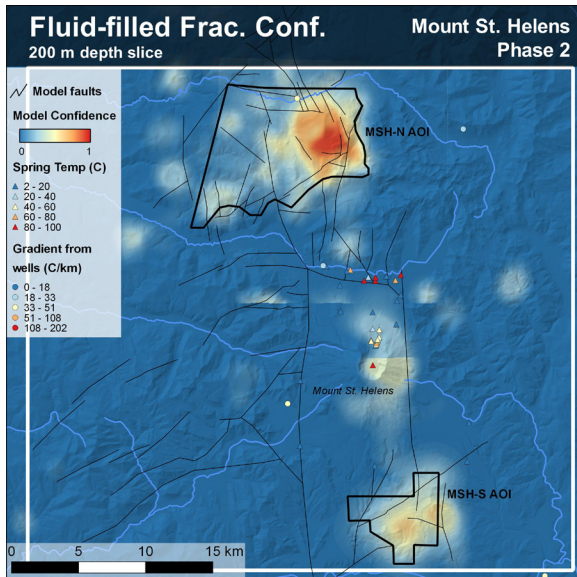
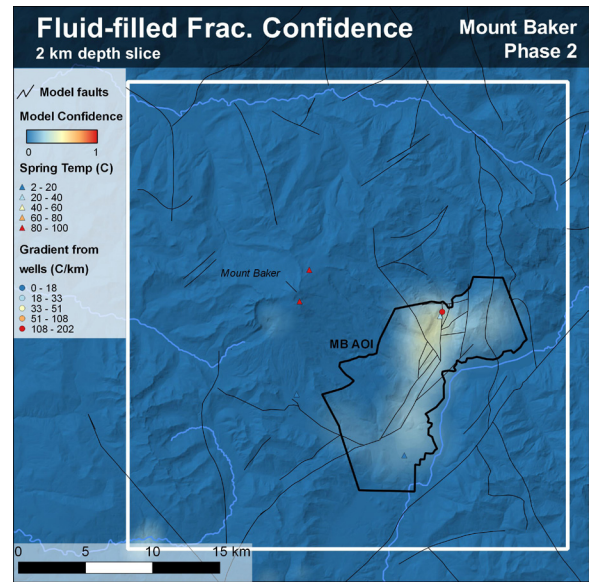
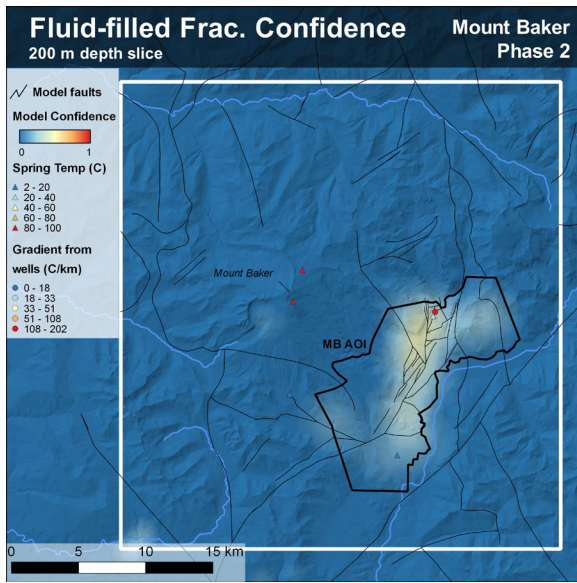




Appendix J. Confidence Model Results







Appendix K. Letters of Support

Energy & Natural Resources



Corporate Headquarters
220 Occidental Ave S
Seattle, WA 98104

May 25, 2017

David K. Norman
State Geologist
Washington Division of Geology and Earth Resources
MS 47007
Olympia, WA 98504

Re: Support for DOE Project

Dear Mr. Norman:

This letter confirms that Weyerhaeuser Company supports the Phase 3 proposal by the Washington Division of Geology and Earth Resources and AltaRock Energy to drill temperature gradient holes on Weyerhaeuser properties north of Mt St Helens in order to validate their findings in Phases 1 and 2 of their "Geothermal Play-Fairway Analysis of Washington State Prospects" as part of the Dept. of Energy funded project DOE-EE0006728.

AltaRock has optioned geothermal rights from Weyerhaeuser Company on lands in the Mount Saint Helen's area which will be explored as part of this project. Weyerhaeuser is amenable to promoting the development of renewable projects in Washington State including base-load energy sources like geothermal.

Weyerhaeuser has been a leader in the forest products industry since 1900. The company and its subsidiaries own and/or operate over 13 million acres in North America's most productive tree growing regions. Weyerhaeuser maintains an Energy and Natural Resources team to manage oil and gas, mineral, and renewable energy related activities on company lands.

Weyerhaeuser would like to see this project succeed and encourages the DOE to continue to financially support this project.

Sincerely,

A handwritten signature in black ink, appearing to read "D. S. Boyer".

David S. Boyer
Senior Geologist
Metals and Geothermal Business Development



United States
Department of
Agriculture

Forest
Service

Mt. Baker-Snoqualmie
National Forest
Mt. Baker Ranger District

810 Highway 20
Sedro-Woolley, WA 98284
(360) 856-5700

File Code: 2820

Date: 25 May 2017

David K. Norman
State Geologist, Division Manager
Washington Geological Survey
1111 Washington St. SE
MS 47007
Olympia, WA 98504

Dear Mr. Norman,

I have been made aware of your project proposal to conduct additional geothermal exploration within the Mt. Baker-Snoqualmie National Forest, Mt. Baker Ranger District. Although I do not have a complete description of the potential project, the Forest Geologist has informed me that you, in partnership with USGS, would like to drill 2-4 temperature gradient wells on National Forest System Lands to further delineate and better understand the resource. All sites would be located within the road prism of existing Forest Service roads.

After discussing this project with my staff, it was determined that completing the necessary environmental documents required for permitting this activity would not be possible this summer. I have already scheduled numerous projects this summer and do not have the capacity to take on any more. However, I have directed my environmental coordinator to list this project on our fiscal year 2018 program of work. This means that I will have staff time available at the start of the new fiscal year (October 1, 2017) to do the required environmental analysis and permitting. This would be contingent on the project being fully funded by Washington DNR through cost recovery, or some other method to fully fund the environmental team.

In summary, I do support your research and have directed my staff to schedule the appropriate environmental analysis and permitting for fiscal year 2018. If fully funded, and barring any extraordinary circumstances, I would expect to have a decision for you by either spring or early summer of 2018. I look forward to reviewing a complete and detailed project proposal.

Sincerely,

/s/ Erin Uloth

ERIN ULOTH
District Ranger





HILARY S. FRANZ
COMMISSIONER OF PUBLIC LANDS

**DEPARTMENT OF
NATURAL RESOURCES**

1111 WASHINGTON ST SE
MAIL STOP 47014
OLYMPIA, WA 98504-7014

360-902-1600
FAX 360-902-1789
TRS 711
FRCD@DNR.WA.GOV
WWW.DNR.WA.GOV

May 22, 2017

David K Norman
State Geologist
Washington Geological Survey
PO Box 47007
Olympia WA 98501

Re: Washington Geological Survey Supplemental Geothermal Proposal Submittal

Dear Mr. Norman,

The Department of Natural Resources (DNR) is the state's land manager responsible for 5.6 million acres of forest, range, agricultural, aquatic, and commercial lands and we support the Washington Geological Survey's proposal to collect new data on geothermal gradients, by drilling up to 10 new gradient holes as part of the U.S. Department of Energy's Award #DE-EERE-0006728, Hydrothermal Technologies Office, *Geothermal Play-Fairway Analysis, Phase 3*.

The Washington Geological Survey is the main source of geological products and information in the state to support decision making by Washington's government agencies, its business, and the public. As the state's land management agency, DNR is in a unique position to help develop geothermal energy by providing access. Furthering our understanding of geothermal energy in Washington is important, and this proposal will provide information for geothermal energy development.

As the Manager for Product Sales and Leasing on DNR state managed lands I support development of renewable energy in Washington. I believe this project is essential to developing Washington's geothermal energy potential and I urge your support.

Thank you for your time and consideration.

Sincerely,

Darin Cramer
Manager
Product Sales and Leasing Division
Department of Natural Resources

May 22, 2017

David K Norman
State Geologist
Washington Geological Survey
PO Box 47007
Olympia WA 98501

Re: Washington Geological Survey Supplemental Geothermal Proposal Submittal

Dear Mr. Norman,

We are writing to express our strong support for the Department of Natural Resources-Washington Geological Survey's proposal to collect new data geothermal gradients, by drilling up to 10 new -gradient holes as part of the U.S. Department of Energy's Award #DE-EERE-0006728, Hydrothermal Technologies Office, *Geothermal Play-Fairway Analysis, Phase 3*.

The Washington Geological Survey is regarded as the primary source of geological information in the state to support decision making by Washington's government agencies, its businesses, and the public. Snohomish County PUD has established a collaborative relationship with the Washington Geological Survey to evaluate the development of geothermal resources. Furthering our understanding of geothermal resources in Washington is important and this project will provide information that can be directly applied to commercial geothermal development projects.

We believe there is a strong possibility for successful geothermal development in Washington and Snohomish County PUD is extremely supportive of the Survey's proposal. Snohomish County PUD has taken a very proactive approach in the exploration of new renewable energy resource development in our region and believes that geothermal energy in particular has enormous potential to help ensure future energy needs are met in a sustainable way. Our ongoing geothermal exploration and development activities would be greatly facilitated by the activities described in your proposal.

As a major energy supplier of energy in Washington, Snohomish County PUD is committed to the development of geothermal energy, but without new and detailed information exploration will be risky. We are able to offer our expertise and support throughout the project and we will be able to attend progress meetings over the life of the project as needed.

We look forward to hearing that you have been successful in obtaining support from the Department of Energy for your proposal.

Sincerely,



Craig W. Collar
Senior Manager, Energy Resource Development
Snohomish County PUD



An equal opportunity university

Dr. Pete Stelling

Department of Geology

Tel: (360) 650-4095 ° Fax: (360) 650-7302 °
pete.stelling@wwu.edu

516 High St., MS 9080
Bellingham, Washington 98225-9080

May 22, 2017

Corina Forson
Washington Division of Geology and Earth Resources
Olympia, WA 98504-7007
(360) 902-1455

Re: Letter of Support for EERE Proposal (control number 0841-1525)

I am very excited to support the WA State Division of Geology and Earth Resources (WADGER) and other investigators in support of the Phase III proposal to the Office of Energy Efficiency and Renewable Energy (EERE) entitled "Geothermal Play-Fairway Analysis of Washington State Prospects." Washington State is a critical area for development of geothermal resources as it highlights the challenges faced by geothermal exploration in the Pacific Northwest. The advances made in Phase II of our understanding of the Mt. Baker, Mt. St. Helens and Wind River areas are very encouraging. Several of my students and I supported Phase II activities as field hands during geophysical surveys. One of these students took a lead role in the magnetic and gravity survey of Mt. Baker, and he has presented this work at the Stanford Geothermal Workshop and is in the process of writing this up to submit to the Journal of Geophysics. My students were thrilled to participate in Phase II of this project, and I anticipate a new group of students eager to support Phase III activities, likely as mud loggers on drill sites. I teach a Geothermal Energy class at Western Washington University in the spring each year, during which students learn how to identify diagnostic geothermal minerals among other things. These students would be ideally suited for geothermal mud logging work, and would be excited to be part of the project, even if they don't receive a salary. I would also be happy to support Phase II activities in any way that I can.

Sincerely,

A handwritten signature in black ink that reads "Pete Stelling".

Dr. Pete Stelling
Assistant Professor of Geology
Western Washington University